
Multiscale neuroimaging using synchrotron X-ray phase-contrast tomography

Giacomo E. Barbone

Ludwig-Maximilians-Universität München



München 2020

Multiscale neuroimaging using synchrotron X-ray phase-contrast tomography

Giacomo E. Barbone

Dissertation
an der Fakultät für Physik
der Ludwig-Maximilians-
Universität München

vorgelegt von
Giacomo Edoardo Barbone
aus Cambridge, MA (USA)

München, den 22. Oktober 2020

Erstgutachter/in: Prof. Dr. Paola Coan

Zweitgutachter/in: Prof. Dr. Guido Cavaletti

Tag der mündlichen Prüfung: 14. Dezember 2020

You climb one mountain, and see a higher one.

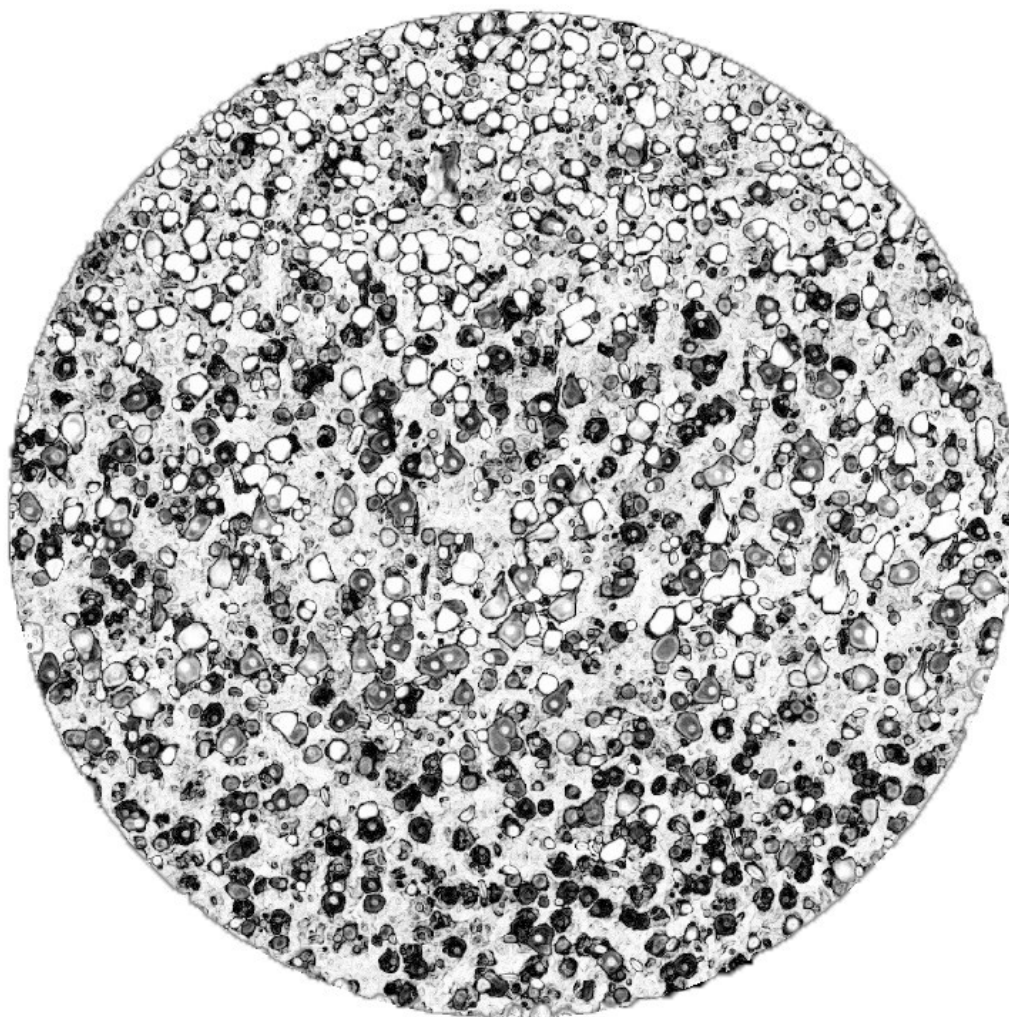
Dennis Bergkamp

It isn't the mountains ahead to climb that wear you out; it's the pebble in your shoe.

Mohammed Ali

It's not the mountain we conquer, but ourselves.

Sir Edmund Hillary



Abstract

X-ray phase-contrast tomography (X-PCI-CT) is an emerging imaging technology in the field of biomedicine. This methodology represents an advancement compared to traditional absorption-based X-ray CT in that it can measure phase-shift-inducing X-ray refraction effects in addition to photon attenuation effects. In this way, X-PCI-CT achieves considerably higher image contrast within weakly- or similarly- absorbing materials, e.g. biological soft tissues. Recently, high-resolution X-PCI-CT has been applied as a volumetric microscopy tool to a wide range of biomedical applications, e.g. cartilage, breast, lung and brain imaging. *Its post-mortem* implementation is increasingly being exploited as a virtual histological tool for label- and dissection-free 3D morphological visualizations and analyses of thick bio-samples.

This Thesis work explores the potential of state-of-the-art X-PCI-CT technology for *post-mortem* neuroimaging applications. Synchrotron X-ray sources in combination with so-called propagation-based and nano-holo-tomography X-PCI-CT setups were used to measure excised central nervous system (CNS) organs from various rodent animal models. Furthermore, proof-of-concept studies on donated human CNS organs were carried out using the same imaging methods. In order to validate and correlate the X-PCI-CT results, extensive multimodal neuroimaging data was obtained using established techniques, such as histology, immunohistochemistry, X-ray fluorescence microscopy, high-field 9.4 T magnetic resonance imaging (MRI), positron emission tomography (PET) and transmission electron microscopy (TEM).

By means of a multiscale approach using imaging systems providing voxel sizes starting from 46^3 and down to $0.1^3 \mu\text{m}^3$, full-organ to intra-cellular 3D visualizations of rodent brain and spinal cord neuroanatomy were achieved without the need for contrast agent injection. This approach enabled the study of brain glioblastoma, and of the effects of a spatially-fractionated X-ray radiation therapy, so-called microbeam radiation therapy (MRT), on nervous tissue and micro-vasculature. Interestingly, X-PCI-CT proved sensitive also to age-related intracellular toxic amyloid and tau protein buildup in the brains of a rodent animal model of Alzheimer's Disease (AD), and the obtained X-PCI-CT data could be exploited for a brain-wide 3D screening and quantification of cellular neurodegeneration. The technique was also successfully employed for the virtual 3D visualization of human spinal cords both before and after medullary soft-tissue dissection, and for the evaluation of cellular and vascular microstructure after different rodent spinal cord sample-preparation protocols, including different aldehyde fixations and osmium staining. Finally, X-PCI-CT was applied for a characterization of vascular abnormalities in a mouse animal model of hypertension, and for the quantitative interpretation of ^{18}F -Florbetaben amyloid-PET signal in an AD mouse model.

Overall, these case studies highlight the potential impact of X-PCI-CT imaging methodologies in the field of neuroimaging. Optimized experimental setups and data processing tools, used and implemented within this Thesis work, provided label-, dissection-free and quantifiable high spatial- and contrast-resolution 3D anatomically dense visualizations of the CNS multiscale nervous tissue structure, vasculature and pathology. By bridging a crucial gap in spatial resolution, multiscale X-PCI-CT results were found to contain complementary 3D information with respect to other currently-available state-of-the-art neuroimaging methodologies, and to present unique advantages, which can impact basic neuroscience research and anatomy medical education.

Zusammenfassung

Die Röntgenphasenkontrasttomographie (X-PCI-CT) ist eine entstehende Bildgebungstechnologie auf dem Gebiet der Biomedizin. Diese Methode stellt einen Fortschritt gegenüber der herkömmlichen Röntgen-CT auf Absorptionsbasis dar, da sie zusätzlich zu den Photonenschwächungseffekten phasenverschiebungsinduzierende Röntgenbrechungseffekte messen kann. Auf diese Weise erzielt X-PCI-CT einen erheblich höheren Bildkontrast in schwach oder ähnlich absorbierenden Materialien, z.B. biologische Weichteile. In letzter Zeit wurde hochauflösende X-PCI-CT als volumetrisches Mikroskopiewerkzeug für eine breite Palette biomedizinischer Anwendungen eingesetzt, z.B. Bildgebung von Knorpel, Brust, Lunge und Gehirn. Die *post-mortem* Implementierung wird zunehmend als virtuelles histologisches Werkzeug für markierungs- und sektionsfreie morphologische 3D-Visualisierungen und Analysen von dicken Bioproben genutzt.

In dieser Doktorarbeit wird das Potenzial der neuesten X-PCI-CT-Technologie für *post-mortem* Neuroimaging-Anwendungen untersucht. Synchrotron-Röntgenquellen in Kombination mit sogenannten propagationsbasierten und Nano-Holo-Tomographie X-PCI-CT Setups wurden verwendet, um Organe des ausgeschnittenen Zentralnervensystems (ZNS) aus verschiedenen Nagetier-Tiermodellen zu messen. Darüber hinaus wurden proof-of-concept Studien an gespendeten menschlichen ZNS-Organen mit denselben bildgebenden Verfahren durchgeführt. Um die X-PCI-CT-Ergebnisse zu validieren und zu korrelieren, wurden umfangreiche multimodale Neuroimaging-Daten unter Verwendung etablierter Techniken wie Histologie, Immunhistochemie, Röntgenfluoreszenzmikroskopie, Hochfeld-9,4-T-Magnetresonanztomographie (MRI) und Positronenemission Tomographie (PET) und Transmissionselektronenmikroskopie (TEM) erhalten.

Mittels eines Multiskalen-Ansatzes unter Verwendung von Bildgebungssystemen, die Voxelgrößen von 46^3 bis $0,1^3 \mu\text{m}^3$ bereitstellen, wurden Vollorgan- bis intrazelluläre 3D-Visualisierungen der Neuroanatomie des Gehirns und des Rückenmarks von Nagetieren ohne Kontrastmittelinjektion erzielt. Dieser Ansatz ermöglichte die Untersuchung von Gehirn-Glioblastomen und der Auswirkungen einer räumlich fraktionierten Röntgenstrahlentherapie, der sogenannten Mikrostrahl-Strahlentherapie (MRT), auf Nervengewebe und Mikrogefäße. Interessanterweise erwies sich X-PCI-CT auch als empfindlich gegenüber altersbedingten intrazellulären toxischen Amyloid- und Tau-Protein-Ansammlungen im Gehirn eines Nagetier-Tiermodells der Alzheimer-Krankheit (AD), und die erhaltenen X-PCI-CT-Daten konnten für eine Gehirnweites 3D-Screening und Quantifizierung der zellulären Neurodegeneration genutzt werden. Die Technik wurde auch erfolgreich zur virtuellen 3D-Visualisierung des menschlichen Rückenmarks sowohl vor als auch nach der medullären Weichteilsektion und zur Bewertung der zellulären und vaskulären Mikrostruktur nach verschiedenen Probenvorbereitungsprotokollen für das Rückenmark von Nagetieren, einschließlich verschiedener Aldehydfixierungen und Osmium Färbung, eingesetzt. Schließlich wurde X-PCI-CT zur Charakterisierung von Gefäßanomalien in einem Maus-Tiermodell für Bluthochdruck und zur quantitativen Interpretation des ^{18}F -Florbetaben-Amyloid-PET-Signals in einem AD-Mausmodell angewendet.

Insgesamt zeigen diese Fallstudien die möglichen Auswirkungen von X-PCI-CT-Bildgebungsmethoden auf das Gebiet der Bildgebung. Optimierte Versuchsaufbau und Datenverarbeitung, die im Rahmen dieser Arbeit verwendet und implementiert wurden, lieferten markierungs-, sektionsfreie und quantifizierbare anatomisch dichte 3D-Visualisierungen der Struktur, des Gefäßsystems und der Pathologie des ZNS Multiskala-Nervengewebes mit hoher räumlicher und kontrastauflösender Auflösung. Durch die Überbrückung einer entscheidenden Lücke in räumlicher Auflösung wurde festgestellt, dass multiskala X-PCI-CT-Ergebnisse komplementäre 3D-Informationen in Bezug auf andere derzeit verfügbare Methoden der Bildgebung auf dem neuesten Stand der Technik enthalten, und dass sie einzigartige Vorteile anbieten, die sich auf neurowissenschaftliche Forschung und anatomische medizinische Ausbildung auswirken können.

List of Publications

Here is the complete list of publications produced as part of this Thesis work.

First-author Papers:

G.E. Barbone, A. Bravin, A. Mittone, S. Grosu, J. Ricke, G. Cavaletti, V. Djonov, P. Coan. “High-Spatial-Resolution Three-dimensional Imaging of Human Spinal Cord and Column Anatomy with Postmortem X-ray Phase-Contrast Micro-CT”, *Radiology*, Vol. 298, No. 1, pp. 135-146 (2021). <https://doi.org/10.1148/radiol.2020201622>

G.E. Barbone, A. Bravin, A. Mittone, M.J. Kraiger, M. Hrabě de Angelis, M. Bossi, E. Ballarini, V. Rodriguez-Menendez, Cecilia Ceresa, Guido Cavaletti, Paola Coan. “Establishing sample-preparation protocols for X-ray phase-contrast CT of rodent spinal cords: Aldehyde fixations and osmium impregnation”, *Journal of Neuroscience Methods*, Vol. 339, 108744 (2020). <https://doi.org/10.1016/j.jneumeth.2020.108744>

G.E. Barbone, A. Bravin, P. Romanelli, A. Mittone, G. Le Duc, D. Bucci, S. Auweter, M.F. Reiser, M.J. Kraiger, M. Hrabě de Angelis, G. Battaglia, P. Coan, “Micro-imaging of Brain Cancer Radiation Therapy Using Phase-contrast Computed Tomography”, *Int J Radiation Oncol Biol Phys*, Vol. 101, No. 4, pp. 965-984 (2018). <https://doi.org/10.1016/j.ijrobp.2018.03.063>.

[Submitted] G.E. Barbone, A. Bravin, A. Mittone, A. Pacureanu, G. Mascio, P. Di Pietro, M.J. Kraiger, M. Eckermann, M. Romano, M. Hrabě de Angelis, P. Cloetens, V. Bruno, G. Battaglia, P. Coan. “A multiscale 3D method for post-mortem detection and quantification of cellular neurodegeneration in experimental Alzheimer’s disease”, (2020).

Other Papers:

A. Mittone, L. Fardin, F. Di Lillo, M. Fratini, H. Requardt, A. Mauro, R. A. Homs-Regajo, P. A. Douissard, G. E. Barbone, J. Stroebel, M. Romano, L. Massimi, G. Begani-Provinciali, F. Palermo, S. Bayat, A. Cedola, P. Coan and A. Bravin. Multiscale pink beam microCT imaging at the ESRF-ID17 biomedical beamline. *Journal of Synchrotron Radiation* 2020 *J. Synchrotron Rad.* (2020). 27, 1347–1357. DOI: 10.1107/S160057752000911X

E. Fardone, B. Pouyatos, E. Bräuer-Krisch, S. Bartzsch, H. Mathieu, H. Requardt, D. Bucci, G. Barbone, P. Coan, G. Battaglia, G. Le Duc, A. Bravin & P. Romanelli. Synchrotron-generated microbeams induce hippocampal transections in rats. *Sci. Rep.* (2018). DOI: 10.1038/s41598-017-18000-x

Acknowledgements

This Thesis work could not have been possible without the help and support of many, which I would like to wholeheartedly thank here.

First and foremost, I would like to thank my supervisor Prof. Paola Coan for being a great mentor, and for supporting me in every step of this project. I really appreciate how you have inspired this research topic and our group's work, how you manage to keep us students motivated and how you encourage critical thinking. Thank you for your patience, for allowing me to express my creativity, for listening to my point of view, and for believing in this project not only in times of success but even more so in times of struggle.

I also wish to thank Dr. Alberto Bravin for serving as an informal vice-supervisor. As a close collaborator of our research team, you were fundamental in designing and promoting our scientific endeavors, and you have been a valuable sounding board for new ideas and a very appreciated source of constructive criticism and insight. Thank you also for introducing me to the world of synchrotron science at the ESRF, where this whole project got started.

A special thanks goes to Johannes Stroebel, my lab partner and daily companion of our shared PhD life in the group. I feel fortunate to have connected with you and I especially appreciate your willingness to always help out, your patience in listening and your humbleness and maturity in discussing things. Your presence in the office has had a constant tangible positive impact of both our scientific work and in creating a collaborative working atmosphere.

I would also like to thank the Master students of the LMU Medical Physics Chair, which joined our group to work on various parts of this project. Marina Eckermann, Christiane Schmeichel and Laurent Jacques – your diligent and qualitative work brought decisive contributions to this project and was instrumental in the development of various steps in this Thesis. I would also like to thank you specifically for your company during long days and nights of experiments, and for making our group an exciting environment where to work.

I wish to express my gratitude to the ESRF ID17 team – without your help, support and expertise these experiments would not have been possible. I would like to thank especially Dr. Alberto Mittone for all your contributions and tireless support, during all the beam-times, the group meetings and the data analysis. Your experience, knowledge and character were extremely valuable and appreciated! Many thanks go also to Herwig Requardt, Charlene Caloud, Helene Bernard, Benjamin Restaut, Emmanuel Brun and Ludovic Broche – each of you supported me and made substantial contributions to this work!

Many thanks go to the two home institutions, who hosted me and also supported me financially as a student during my PhD: the LMU Chair for Medical Physics and the Max Plank Institute for Quantum Optics, including their brilliant communities of scholars and researchers.

I also would like to express my gratitude to the many collaborators in these multidisciplinary projects. Special thanks go to Dr. Giuseppe Battaglia for sharing with me your expertise in neuroscience – you were fundamental in many of our common projects and contributed to

my growing passion for the study of the nervous system. Thank you also to your team at Neuromed. I would also like to thank Dr. Pantaleo Romanelli and Dr. Guido Cavaletti for your expert feedback and contributions in many of these projects, and Dr. Markus Kraiger and Dr. Alexandra Pacureanu for your time, expertise and dedication during the collection of various key datasets in this thesis work – it was a pleasure getting to know you and working with you!

Last but not least I wish to thank my family and friends for your support during these years. Thank you so much to my parents and sisters for always believing in me, supporting me, rooting for me and loving me. I also really appreciated the support of many friends in France, Italy, the USA and Germany. Thanks to all of you for your friendship, and especially to Perrine, Olivier, Theó, the JOG, Jan-Peter, Achim, Martin, Blaš, Fede, Tex, Ricky, Nick and Caleb, Olympus and the WGang. A very special thank goes to Laura for your tireless support, for standing by my side and for being an irreplaceable source of happiness.

Many other people would deserve to be mentioned and included. To each of you – thanks for supporting me during my doctoral studies, I could not have made it without you in my life!

Thanks, Danke, Merci, Grazie,

Giacomo

Table of Contents

Contents

ABSTRACT	VII
ZUSAMMENFASSUNG	IX
LIST OF PUBLICATIONS	XI
FIRST-AUTHOR PAPERS:.....	XI
OTHER PAPERS:	XI
ACKNOWLEDGEMENTS	XIII
TABLE OF CONTENTS	XV
CHAPTER 1 - INTRODUCTION	1
1.1 DEVELOPMENT OF X-RAY PHASE-CONTRAST IMAGING	2
1.2 BIOMEDICAL APPLICATIONS OF X-RAY PCI	5
1.3 X-PCI-CT FOR NEUROIMAGING	7
1.4 THESIS MOTIVATION AND OUTLINE	14
REFERENCES:	16
CHAPTER 2 - BASICS OF X-RAY PHASE-CONTRAST CT	19
2.1 FUNDAMENTALS IN X-RAY IMAGING	20
2.1.1 X-rays	20
2.1.2 Hard X-rays and Radiography	20
2.1.3 X-rays through matter – the physics of traditional radiography.....	21
2.1.4 Computed Tomography	24
2.2 FUNDAMENTALS IN X-RAY PHASE-CONTRAST IMAGING	25
2.2.1 The complex index of refraction	25
2.2.2 X-ray absorption-contrast imaging and phase-contrast imaging	26
2.2.3 X-ray propagation-based PCI and holo-tomography	27
2.3 X-RAY SOURCES.....	31
REFERENCES:	34
CHAPTER 3 - EXPERIMENTAL METHODS	37
3.1 SAMPLE PREPARATION	38
3.2 X-PCI-CT EXPERIMENTS	39
3.2.1 PB X-PCI-CT setups	39
3.2.2 Nano-holotomography setup	42
3.3 X-PCI-CT IMAGE RECONSTRUCTION AND PROCESSING	43
3.3.1 Phase retrieval and CT reconstruction	43
3.3.2 Post-processing of X-PCI-CT images	48
3.4 PROCEDURES FOR 3D QUANTIFICATION	54
3.4.1 Data masking	54
3.4.2 3D PCI-data segmentation	55
3.4.3 3D object measurements	56
3.4.4 Workflow design for the quantification of X-PCI-CT neuroimages.....	60
3.5 PROCEDURES FOR CNS FEATURE VISUALIZATION	61
3.5.1 MIPs and mipS.....	61
3.5.2 3D rendering	61
3.6 MULTISCALE NEUROIMAGING VIA X-PCI-CT	62

REFERENCES:	66
CHAPTER 4 – X-PCI-CT TO IMAGE BRAIN RADIOTHERAPY	69
MICRO-IMAGING OF BRAIN CANCER RADIATION THERAPY USING PHASE-CONTRAST COMPUTED TOMOGRAPHY	69
4.1 ABSTRACT.....	70
4.2 INTRODUCTION	70
4.3 METHODS.....	73
4.3.1 <i>Animal preparation</i>	73
4.3.2 <i>MRT irradiation</i>	74
4.3.3 <i>Propagation-based Phase Contrast Imaging</i>	75
4.3.4 <i>Vessel network renderings</i>	75
4.3.5 <i>Histology & Immunohistochemistry</i>	75
4.3.6 <i>MRI Experiment</i>	76
4.4 RESULTS	77
4.4.1 <i>Imaging brain anatomy</i>	77
4.4.2 <i>Imaging glioblastoma tumor</i>	78
4.4.3 <i>Imaging brain vasculature</i>	82
4.4.4 <i>Imaging MRT irradiation</i>	84
4.4.5 <i>PCI-CT & Histology</i>	87
4.4.6 <i>PCI-CT & MRI</i>	90
4.5 DISCUSSION.....	91
4.6 CONCLUSIONS.....	95
4.7 SUPPLEMENTARY MATERIAL	96
REFERENCES:	101
CHAPTER 5 – X-PCI-CT TO IMAGE ALZHEIMER’S DISEASE	107
A MULTISCALE 3D METHOD FOR POST-MORTEM DETECTION AND QUANTIFICATION OF CELLULAR NEURODEGENERATION IN EXPERIMENTAL ALZHEIMER’S DISEASE.....	107
5.1 ABSTRACT	108
5.2 INTRODUCTION	108
5.3 RESULTS	111
5.3.1 <i>X-PCI-CT detects intra-cellular hyper-density in aged WT and 3xTgAD mouse brains</i>	111
5.3.2 <i>Multiscale X-PCI-CT maps organ- to cellular-level intra-cellular proteopathy in aged brains</i>	113
5.3.3 <i>ICHD correlates to Aβ and p-tau IHC, i.e. to AD-linked cellular neurodegeneration</i>	118
5.3.4 <i>X-PCI-CT vs. X-ray fluorescence-microscopy, MRI & TEM</i>	119
5.3.5 <i>X-PCI-CT 3D virtual-histology to quantify AD-linked cellular neurodegeneration after pharmacological treatment</i>	124
5.4 DISCUSSION.....	128
5.5 CONCLUSION	130
5.6 METHODS.....	131
5.6.1 <i>Materials</i>	131
5.6.2 <i>Animals</i>	131
5.6.3 <i>Synchrotron X-PCI-CT acquisitions</i>	132
5.6.4 <i>X-PCI-CT data post-processing and analysis</i>	135
5.6.5 <i>XFM measurements</i>	137
5.6.6 <i>High-field MRI measurements</i>	139
5.6.7 <i>TEM measurements</i>	139
5.6.8 <i>Histology and immunohistochemistry</i>	140
5.7 SUPPLEMENTARY MATERIAL	141
5.7.1 <i>SUPPLEMENTARY DISCUSSION</i>	141
5.7.2 <i>SUPPLEMENTARY FIGURES & LEGENDS</i>	145
5.7.3 <i>SUPPLEMENTARY VIDEOS</i>	159
REFERENCES:	167

CHAPTER 6 – X-PCI-CT OF THE HUMAN SPINAL CORD	173
HIGH-SPATIAL-RESOLUTION 3D IMAGING OF HUMAN SPINAL CORD AND COLUMN ANATOMY BY POST-MORTEM X-RAY PHASE-CONTRAST MICRO-CT.....	173
6.1 ABSTRACT	174
6.2 INTRODUCTION	175
6.3 MATERIALS AND METHODS	177
6.3.1 <i>Specimen preparation</i>	177
6.3.2 <i>Propagation-based X-PCI-CT</i>	178
6.3.3 <i>Data processing</i>	178
6.4 RESULTS	180
6.4.1 <i>Thiel-embalmed spinal column imaging</i>	180
6.4.2 <i>Formalin-fixed spinal cord imaging</i>	185
6.4.3 <i>Comparison Thiel vs. Formalin embalming</i>	187
6.5 DISCUSSION.....	189
6.6 CONCLUSIONS.....	191
6.7 SUPPLEMENTARY MATERIAL	192
6.7.1 <i>Supplementary Text</i>	192
6.7.2 <i>Supplementary Figures</i>	195
6.7.3 <i>Supplementary Videos</i>	196
REFERENCES:.....	198
CHAPTER 7 – FIXATIVES FOR RODENT SPINAL CORD X-PCI-CT.....	203
OPTIMIZATION OF RODENT SPINAL CORD SAMPLE PREPARATION FOR SYNCHROTRON X-RAY PHASE-CONTRAST COMPUTED TOMOGRAPHY USING A COMBINATION OF ALDEHYDE FIXATIVES & OSMIUM IMPREGNATION	203
7.1 ABSTRACT	204
7.2 INTRODUCTION	205
7.3 MATERIALS AND METHODS	208
7.3.1 <i>Animals</i>	208
7.3.2 <i>Sample preparation</i>	208
7.3.3 <i>Synchrotron X-PCI-CT imaging acquisitions</i>	209
7.3.4 <i>X-PCI-CT image processing</i>	210
7.3.5 <i>X-PCI-CT image analysis</i>	211
7.3.6 <i>High-field MRI</i>	211
7.3.7 <i>Histological stainings</i>	211
7.4 RESULTS	212
7.4.1 <i>Impact of different fixation protocols</i>	212
7.4.2 <i>X-PCI-CT with osmium</i>	215
7.4.3 <i>Sub-micron X-PCI-CT of the spinal cord</i>	217
7.4.4 <i>Morphological quantifications</i>	219
7.4.5 <i>X-PCI-CT vs. MRI vs. histology</i>	221
7.4.6 <i>Multiscale 3D X-PCI-CT vs. 2D histology & 3D fluorescence-histology</i>	224
7.5 DISCUSSION.....	226
7.5.1 <i>Image contrast in multiscale X-PCI-CT of the spinal cord</i>	226
7.5.2 <i>Sample preparation vs. image quality and microstructure detection</i>	227
7.5.3 <i>3D quantification of CNS microstructure</i>	228
7.5.4 <i>X-PCI-CT vs. established volumetric and histological neuroimaging technologies</i>	229
7.6 CONCLUSIONS.....	231
7.7 SUPPLEMENTARY FIGURES.....	232
REFERENCES:	238
CHAPTER 8 - OTHER PIONEERING STUDIES.....	243
8.1 A LIQUID METAL JET VS. SYNCHROTRON X-RAY SOURCE	244

8.1.1 Project goals.....	244
8.1.2 Methods and Results.....	245
8.1.3 Conclusions	248
8.2 X-PCI-CT TO STUDY AMYLOID-PET SIGNAL	249
8.2.1 Project goals.....	249
8.2.2 Methods.....	250
8.2.3 Results & Conclusions.....	251
8.3 X-PCI-CT TO STUDY HEMORRHAGE.....	255
8.3.1 Project goals.....	255
8.3.2 Methods.....	255
8.3.3 Results.....	257
8.3.4 Conclusions	265
REFERENCES:	266
CONCLUSIONS	269
TAKE-AWAY POINTS, APPLICATIONS & LIMITATIONS	269

Chapter 1 - Introduction

This introductory chapter is intended to motivate working on neuroimaging using X-ray phase-contrast tomography, to present the most salient state-of-the art results of this field of research obtained previously or concurrently to this Thesis work, and to briefly summarize the chapter-by-chapter organization of this Thesis manuscript.

1.1 Development of X-ray phase-contrast imaging

Radiographic and tomographic imaging with hard X-rays represents one of the two main workhorses, alongside magnetic resonance imaging (MRI), of clinical diagnostic imaging. These techniques are also important research tools in biology and material science (Davis *et al.*, 1995). Ever since Röntgen's 1895 discovery of a "new kind of rays" (Röntgen, 1896, 1898), X-rays have been providing doctors and researchers information on internal structures or components of objects, which cannot otherwise be obtained in a non-destructive matter.



FIG. 1.—Photograph of the bones in the fingers of a living human hand.
The third finger has a ring upon it.

Figure 1.1: The first X-ray image, and concurrently the first example of *in-vivo* X-ray use for medical imaging, capturing the ring-bearing hand of Bertha Röntgen. Figure taken from (Röntgen, 1896), reprinted by permission from Springer Nature Customer Service Centre GmbH, Springer Nature, [Nature](#) [COPYRIGHT] (1896).

As the famed radiograph of Bertha Röntgen's hand reproduced in **Fig. 1.1** testifies, X-rays are able to penetrate into most biological tissues and are sensitive to the attenuation properties of tissues. For this reason, conventional absorption-based X-ray radiography and computed tomography (CT), which relies on X-ray absorption processes inside the imaged object as image contrast formation mechanisms, has since been playing a central role in the field of medical imaging. Physically, it is density, thickness and atomic composition variations within a sample, which concur to create differences in X-ray attenuation and lead to differences in intensities captured by a nearby detector. Typical sources of high CT contrast are highly-absorbing high-density and high-Z materials (Z, atomic number). In medical diagnostics, such conditions occur, for example, within bone structure, surgical metal implants, pathological calcium and iron deposits or in contrast-enhanced radiology.

The sensitivity of absorption X-ray tomography, though, drastically decreases for low-absorbing objects, such as the carbon-based soft-matter structures within biological organisms, and generally affords quite poor image contrast within soft tissue. Interestingly, while traversing a samples, X-rays are not only attenuated, but also refracted, introducing small angular deviations to the X-rays, which were first measured by Davis and Slack already in 1926 (Davis and Slack, 1926). This mechanism, if properly detected and decoupled from the absorption signal, has the potential to enhance the contrast obtained in X-ray images of weakly absorbing materials.

Detecting electromagnetic wave phase variations in addition to amplitude variations, though, is an idea first applied to visible light and optical microscopy, with the development of so-called light phase-contrast microscopy by the 1953 Nobel Laureate Fritz Zernike (Nobel Media AB, 1953). Since the deviation of the refractive index from unity for visible light is about 10^5 times larger than for X-rays, visible-light phase effects are much easier to capture and observe than while using X-rays. In 1942, then, Zernike demonstrated a new microscopic method for the conversion of light phase shifts through transparent objects into brightness changes within microscope images (Zernike, 1942, 1955), which involved the exploitation of dark and bright edges, arising from object-provoked wave phase shifts during wave transmission, as an added source of image contrast. This method is used even today for label-free live-cell imaging and for the quantification of cellular structure and components (El-Schich, Leida Mölder and Gjørloff Wingren, 2018) without the need for fluorescent probes. After the conversion of edge-enhanced phase-contrast micrographs into quantitative 2D phase maps, as illustrated in the example in **Fig. 1.2**, visible-light phase-contrast microscopy, in fact, becomes a non-invasive quantitative tool for the density-based analysis of living cells (PHI AB, 2019).

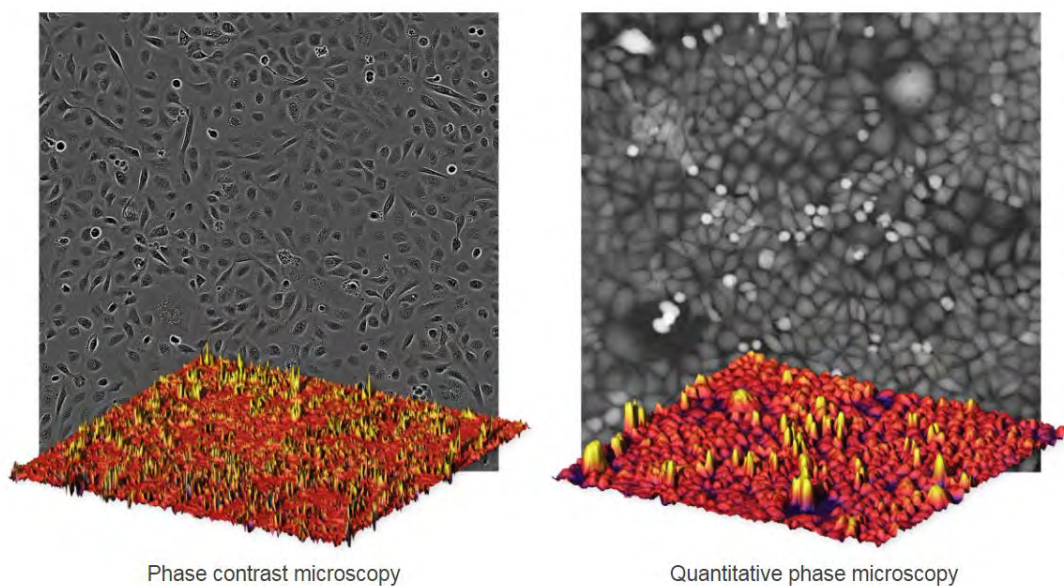


Figure 1.2: visible light phase-contrast microscopy image of live-cells, showing characteristic edge enhancement, vs. quantitative phase microscopy image, where image gray-levels are proportional to local sample thickness and optical density. Figure taken from (PHI AB, 2019).

Phase-modulation effects similar to the ones detected by Zernike phase-contrast light microscopy can be recapitulated also while using X-rays and phase-sensitive X-ray imaging setups (Fitzgerald, 2000). As shown in **Fig 1.3**, an X-ray phase-contrast radiography of a soft-matter object, collected via a so-called propagation-based (or in-line) imaging setup (Cloetens *et al.*, 1996, 1999), resolves interference fringes and edge-enhancement at the contours of both external and internal object features, which are not visible via conventional radiography (**Fig. 1.3**).

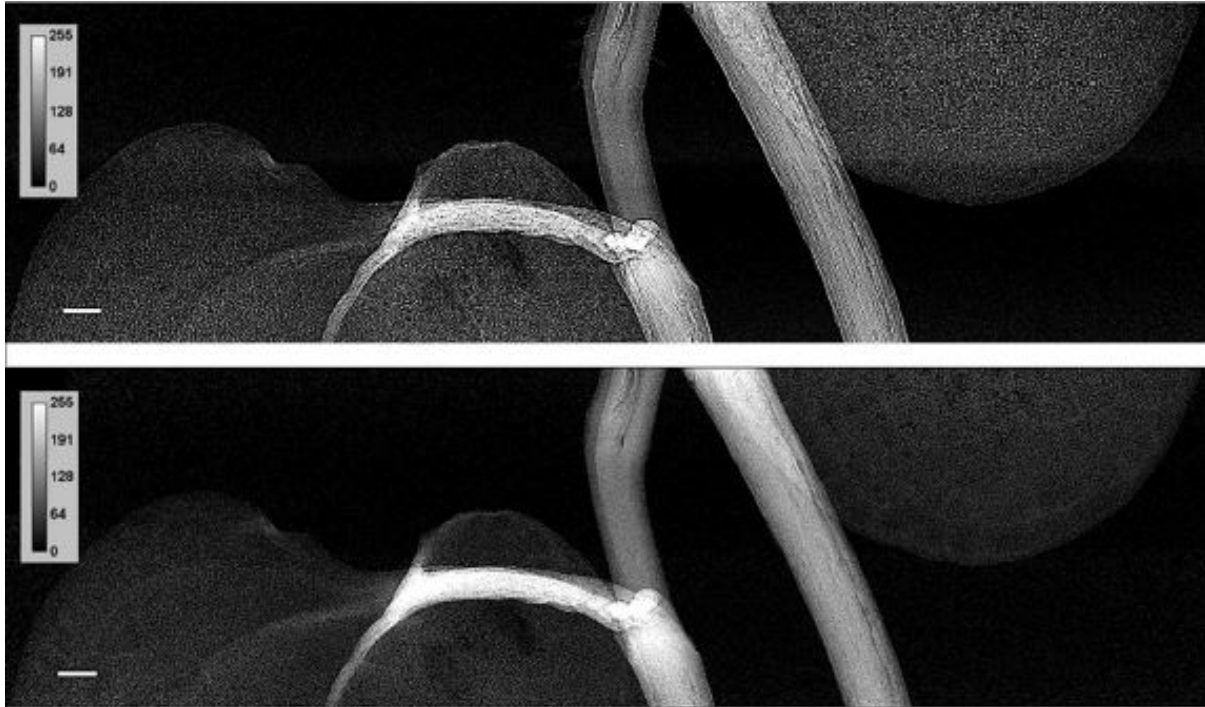


Figure 1.3: Conventional X-ray absorption-contrast (**bottom**) vs. X-ray phase-contrast radiograph (**top**) of a canola plant, obtained using X-rays from a synchrotron-radiation X-ray source using a propagation-based (in-line) setup. **Top** image shows edge-enhancement of both internal and edge structure, resulting in better feature delineation compared to **bottom** image, where no edge-enhancement is present. Figure modified from (Karunakaran *et al.*, 2015).

The X-ray-based phase-contrast imaging (X-PCI) technique (Mayo *et al.*, 2003) was quickly recognized as of great interest to image scientists working with low-absorption biological samples. In fact, theoretical calculations of phase-contrast mechanisms within weakly-absorbing objects in the hard X-ray regime predicted, and experimental evidence confirmed, the possibility to obtain a dramatic image contrast enhancement (Davis *et al.*, 1995) of up to three orders of magnitude compared to absorption mechanisms (Sayre and Chapman, 1995; Cloetens, 1999).

Several X-PCI-CT setups exist, and are named based on the optical elements used to detect X-ray phase modulations. PCI interferometry, for example, involves the generation of interference patterns by perfect crystals; analyzer-based PCI, also called diffraction-enhanced imaging (DEI), instead exploits Bragg diffraction within a single crystal; grating-based PCI uses two periodic gratings to capture phase, amplitude and dark (scattering) signals; edge-illumination (EI) obtains its angular selection and phase sensitivity by means of two specifically-designed coded apertures. The X-PCI technique, though, which implicates the

simplest setup and the least limitations, is the propagation-based (in-line) PCI technique (PB-X-PCI), where free-space wave propagation and Fresnel diffraction lead to detectable phase-driven beam intensity variations without the need for any optical elements along the X-ray beam path. All these so-called coherent X-ray imaging techniques have been first demonstrated using synchrotron X-ray sources, but over the years have been increasingly moving toward more compact table-top settings illuminated by state-of-the-art X-ray tube sources.

1.2 Biomedical applications of X-ray PCI

Coherent X-PCI, owing to its unique characteristics, has shown high potential in a wide variety of imaging fields since its earliest times (Momose *et al.*, 1996). Application range from material science (Olbinado *et al.*, 2017), to papyrus deciphering (Mocella *et al.*, 2015), to evolutionary biology (Qvarnström *et al.*, 2017), to paleontology (Tafforeau *et al.*, 2006), and to medicine (Pisano *et al.*, 2000; Mollenhauer *et al.*, 2002; Pfeiffer *et al.*, 2007). Tomographic X-PCI datasets provide unique high-contrast and high-resolution 3D visualizations of thick complex samples containing features, which are difficult to reproduce via other imaging techniques (e.g. weakly-absorbing features or features with similar absorption properties).

Focusing on biomedical applications only, X-PCI-CT has been successfully employed to image a wide range of biological organs, organ structures, and organ pathological features, in both *post-mortem* and *in-vivo* settings (Bravin, Coan and Suortti, 2013). The possibility to successfully apply X-PCI-CT with current state-of-the-art technology depends, among other things, on an organ's local environment. In the relatively simple case of mammography, for example, where the organ under investigation can be easily imaged in radiographic mode in isolation from the rest of the body, a first clinical *in-vivo* mammography study using synchrotron X-PCI-CT was already pioneered in 2011 (Castelli *et al.*, 2011). Other anatomical body parts with good accessibility are musculoskeletal joints, and X-PCI-CT has been in fact fruitfully applied to the investigation the internal structure of articular cartilage within samples from humans and animal models, both *post-mortem* (Coan, Bamberg, *et al.*, 2010; Horng *et al.*, 2014) and *in-vivo* (Coan, Wagner, *et al.*, 2010). Very interesting PCI work is also possible while imaging lungs, which present a complex multi-compartmental 3D structure ideal for phase-sensitive methodology; lung PCI has already progressed to impact advanced pre-clinical *in-vivo* studies on small animals, e.g. measuring alveolar airspace morphological dynamics during lung injury (Broche *et al.*, 2017) or so-called 'dark' scattering signal abnormalities due to different lung diseases (Bech *et al.*, 2013), and its application to human organs is under evaluation (Willer *et al.*, 2018). Moreover, some of these applications were successfully performed *post-mortem* also while using compact X-ray light sources (Eggl *et al.*, 2015). A few highlights from biomedical applications of X-PCI-CT are shown in **Fig. 1.4**, and many more can be found today in biomedical literature, a sign that this technique is nowadays transitioning from a novel experimental imaging approach to an established tool for 3D soft-tissue explorations.

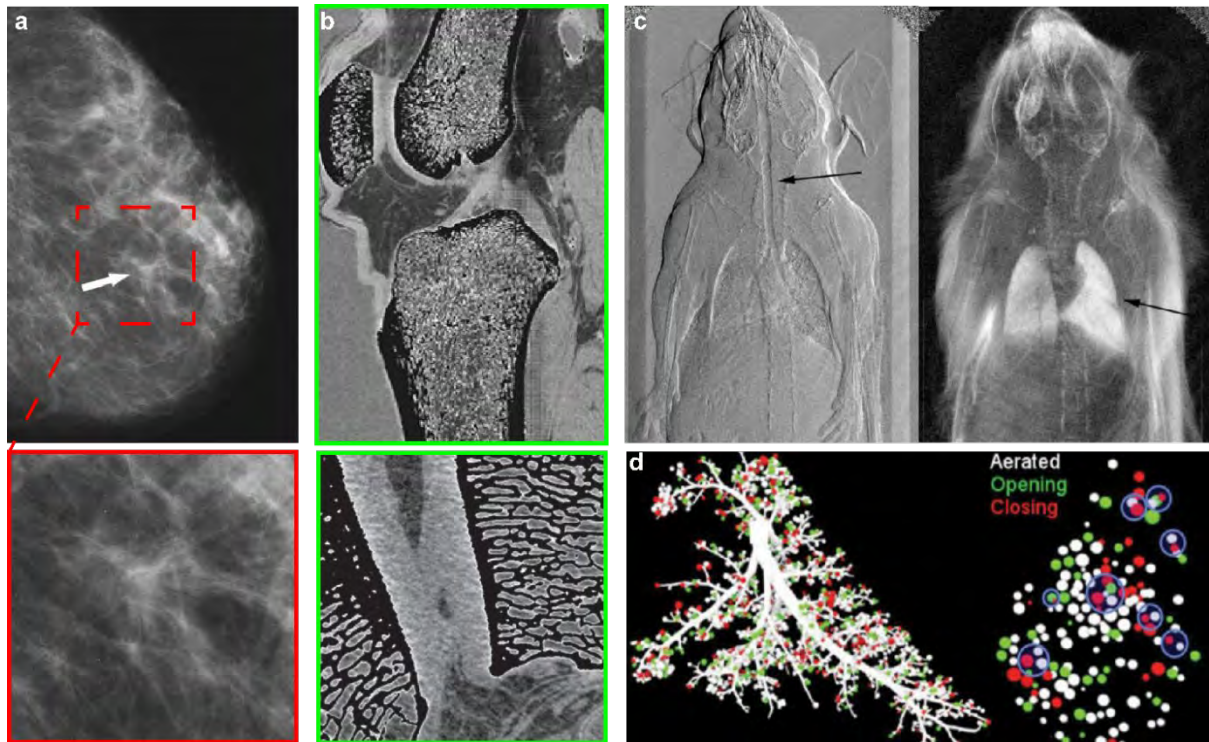


Figure 1.4: (a) example of human *in-vivo* X-PCI mammography, modified from (Castelli *et al.*, 2011) with permission from the [RSNA, Radiology](#) [COPYRIGHT] (2011), within enhanced visualization of a speculated mass. (b) example of human *post-mortem* cartilage imaging, reproduced from (Hornig *et al.*, 2014) with permission from [Wolters Kluwer Health, Inc., Investigative Radiology](#) [COPYRIGHT] (2014), showing good visualization of knee-joint cartilage alongside bone structure. (c) example of rodent *in-vivo* full-body imaging, modified from (Bech *et al.*, 2013), showing phase-contrast (left) and dark field (right) signals. (d) 3D reconstruction of an *in-vivo* rodent lung dataset, reproduced from (Broche *et al.*, 2017) with permission from [Wolters Kluwer Health, Inc., Critical Care Medicine](#) [COPYRIGHT] (2017), showing application of X-PCI to the dynamic morphological study of alveolar compartments.

1.3 X-PCI-CT for Neuroimaging

Central nervous system (CNS) imaging is notoriously challenging due to its intrinsic complex anatomical structure, as well as the complicated environments surrounding the brain and spinal cord. In fact, both the brain and the spinal cord contain complicated multiscale 3D networks of cells, fiber structures, which makes this system impossible to visualize and characterize well with only one neuroimaging technique. As schematically displayed in **Fig. 1.5**, technology for neuroimaging is a growing field in both the spatial and temporal domain. A goal of this Thesis work is to find a well-defined place for X-PCI-CT within such a map, and to determine whether this technique can bridge any of the still-existing technological gaps.

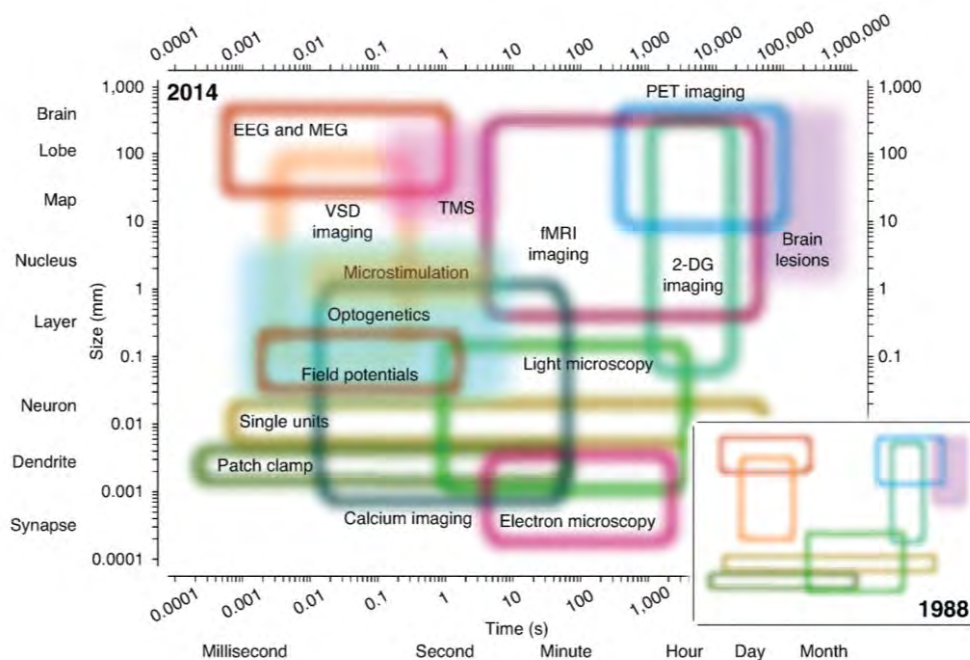


Figure 1.5: Spatiotemporal domain development of neuroimaging technology between 1988 and 2014. Open regions represent measurement techniques; filled regions, perturbation techniques. EEG, electroencephalography; MEG, magnetoencephalography; PET, positron emission tomography; VSD, voltage-sensitive dye; TMS, transcranial magnetic stimulation; 2-DG, 2-deoxyglucose. Figure taken from (Sejnowski, Churchland and Movshon, 2014), reprinted by permission from **Springer Nature Customer Service Centre GmbH: [Springer Nature] [Nature Neuroscience] [COPYRIGHT] (2014)**.

Aside from the inherent complexity of the CNS, skull bones enclose the brain and thick bony vertebral structures surround the spinal cord in humans and small animal models alike. These bulky high-absorption and high-scattering natural organ encasements represent a serious obstacle for many neuroimaging approaches. This is also the case for coherent X-PCI methodology, since high-scattering materials negatively influence coherent X-ray propagation and transmission. What follows is a brief overview of X-PCI-CT neuroimaging applications, which were successfully conducted by other researchers and groups both prior and concurrently to this Thesis work. Notably, all of the work found in the literature is *post-mortem* work, and most of the experiments have been performed after CNS organ dissection and extraction of soft tissues from their protective bone components.

One of the first example of X-PCI-CT neuroimaging involved the *in-vitro* measurement of an extracted tumor-bearing rat brain sample (**Fig. 1.6a**) via a gratings-based PCI setup (Pfeiffer *et al.*, 2007). Without need of contrast agent, the collected PCI CT slices with $\sim 16 \mu\text{m}$ effective pixel size obtained exciting white vs. gray matter and normal- vs. tumor-tissue contrast and demonstrated the ability of the technique to render 3D morphological maps of brain structure macroscopic anatomy. In another study, so-called SAXS-CT imaging (i.e. small-angle X-ray scattering CT) was used to map molecular concentration of cytoskeletal neuro-filaments within myelin sheaths (**Fig. 1.6b**), further establishing proof of X-ray signal differentiation between different deep brain tissues and fibers (Jensen *et al.*, 2011). A multimodal *post-mortem* study on human cerebellar tissue (Schulz *et al.*, 2012), involving gratings-based X-PCI-CT, MRI and histology, showed how PCI can afford image contrast within white vs. gray matter tissues that is complementary to the maps obtained via MRI and histology (**Fig. 1.6c**). However, the acquired X-PCI-CT datasets with $\sim 5 \mu\text{m}$ effective pixel size remain pre-cellular in their visualization of nervous tissue sub-structure, and are thus hard to compare to an intra-cellular neuroimaging technique, such as histology. A much later *post-mortem* 3D micro-CT experiment showed how appropriate iodine-based chemical contrasting protocols can lead to exquisite brain soft tissue contrast (**Fig. 1.6d**) for neurobiological research interested in precise morphological brain visualizations (Zikmund *et al.*, 2018), though at the expense of sample invasiveness. Aside from white-gray matter contrast, X-PCI techniques have been demonstrated to present high sensitivity in the contrast-agent-free detection of vascular features. Via this technique, brain vascular networks of rodent animal models can be measured *post-mortem* and in 3D (**Fig. 1.6e**) down to their microscopic details (Heinzer *et al.*, 2008; Mader *et al.*, 2011), again though only after brain extraction from its skull. It is not until very recently that dissection-free *in-situ* brain PCI has been attempted, and some degree of success in intra-skull brain tissue visualization (**Fig. 1.6f-g**) has been demonstrated *post-mortem* for two different animal models (Zamir *et al.*, 2016; Croton *et al.*, 2018).

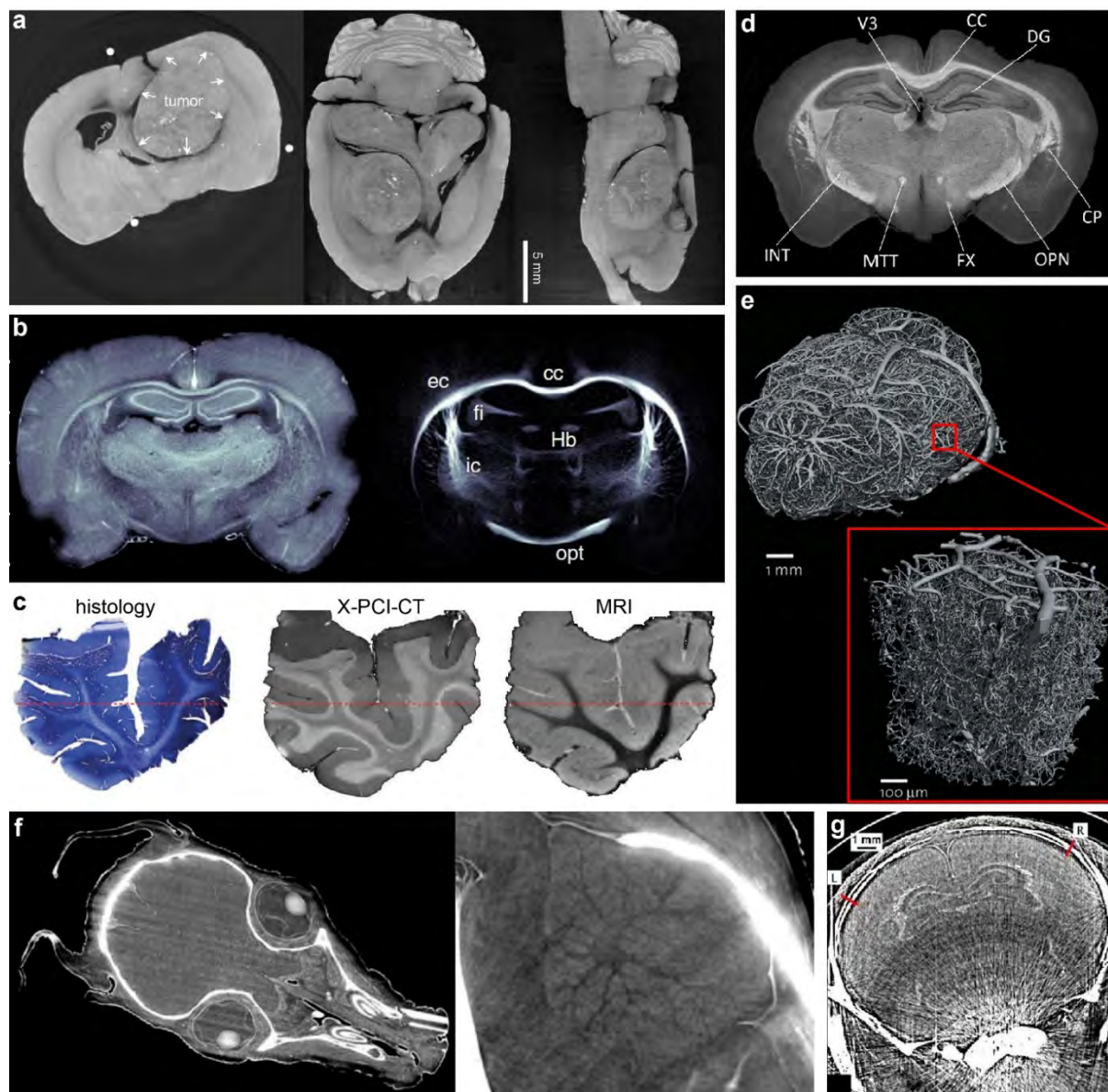


Fig. 1.6: (a) coronal (left), axial (middle) and sagittal (right) slices from an *post-mortem* 3D X-PCI-CT dataset of a tumor-bearing rodent brain; panels modified from (Pfeiffer *et al.*, 2007), reproduced with permission from **IOP Publishing, [Physics in Medicine & Biology](#) [COPYRIGHT]** (2007). (b) coronal view of a SAXS-CT dataset (left) and myelin molecular signal (right) from an extracted rodent brain sample; panels modified from (Jensen *et al.*, 2011), reproduced with permission from **Elsevier, [NeuroImage](#) [COPYRIGHT]** (2011). (c) histology vs. *post-mortem* X-PCI-CT vs. *post-mortem* MRI of a human brain cerebellum; panels modified from (Schulz *et al.*, 2012). (d) iodine-stained coronal-view micro-CT of a rodent brain; panels modified from (Zikmund *et al.*, 2018). (e) 3D rendering of full-brain vascular network, and zoom-in, obtained from an X-PCI-CT dataset of a rodent brain; panels modified from (Mader *et al.*, 2011). (f) *post-mortem* intra-skull X-PCI-CT of a piglet head; panels modified from (Zamir *et al.*, 2016). (g) *post-mortem* intra-skull X-PCI-CT of a kitten head; panel modified from (Croton *et al.*, 2018).

Spinal cord X-PCI-CT has followed a similar development trajectory to that of brain X-PCI-CT, starting with acquisitions of pre-cellular micro-CT datasets focused on both white and gray-matter tissue visualization and embedded vascular network structure. As summarized in **Fig. 1.7**, published X-PCI-CT results demonstrate the possibility for the depiction of medullary anatomy with high soft-tissue contrast (Fratini *et al.*, 2015), of the detailed micro-morphology

within specimens affected by neurodegenerative disease (Cedola *et al.*, 2017), of 3D intra-medullary vascular trees (Cao *et al.*, 2016) and of combined 3D white-matter fiber bundles and vasculature (Hu *et al.*, 2017).

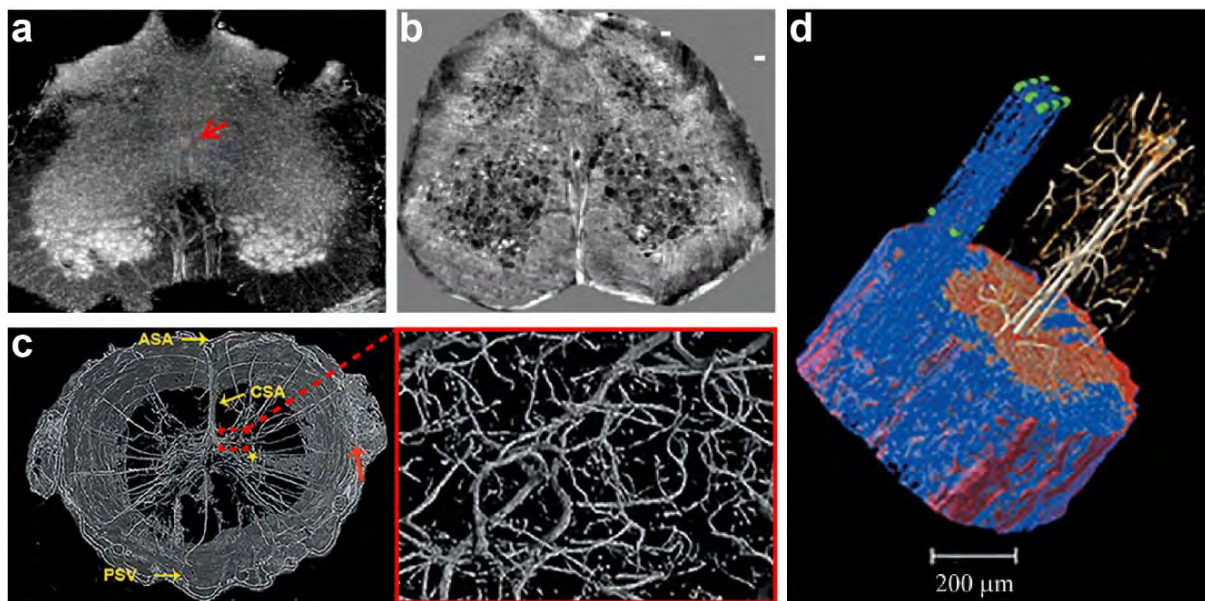


Fig. 1.7: (a) *post-mortem* X-PCI-CT of a rodent spinal cord sample, showing intra-medullary white-gray matter contrast; panel modified from (Fratini *et al.*, 2015). (b) *post-mortem* X-PCI-CT of a rodent spinal cord sample affected by autoimmune encephalomyelitis; panel modified from (Cedola *et al.*, 2017). (c) 3D rendering of segmented X-PCI-CT, showing intramedullary arterial networks in the un-sectioned spinal cord of a rodent; panels modified from (Cao *et al.*, 2016). (d) 3D rendering of vascular (white), white-matter (blue) and gray-matter (orange) rodent spinal cord structure, obtained from an *post-mortem* X-PCI-CT dataset; panels modified from (Hu *et al.*, 2017).

It is only with the advent of sub-micron pixel X-PCI-CT setups, though, that *post-mortem* neuro-PCI has really become a virtual pseudo-histological imaging technique. At these ultra-high CT resolutions, brain cellular structure can be visualized in detail, for example the Purkinje cells (**Fig. 1.8a-b**) lining the interstice between molecular and granular layers of the cerebellum (Hieber *et al.*, 2016). In this way, detailed 3D quantifications of deep cellular and vascular micro-structure (**Fig. 1.8c**) within thick brain samples were made possible (Dyer *et al.*, 2017). Ultra-high-resolution micro-X-PCI-CT was also applied to *post-mortem* spinal cord gray-matter imaging (Bukreeva *et al.*, 2017) demonstrating the potential for single motor-neuron imaging (**Fig. 1.8d**). With the highest-resolution X-PCI-CT setups available worldwide, nano-metric holographic CT *post-mortem* neuro-datasets were recently acquired, which capture the volumetric cyto-architecture of individual neuron cells (**Fig. 1.8e**) in unprecedented detail (Khimchenko *et al.*, 2018). The 3D nano-anatomy of osmium-stained mouse nerves could also be explored via the same approach (Bartels *et al.*, 2015), to render ultra-detailed histology-like visualizations of individual myelin sheaths padding axonal fibers (**Fig. 1.8f**). It is these later applications, which fully establish X-PCI-CT as a 3D virtual histology tool to study soft-mattered nervous-tissue samples.

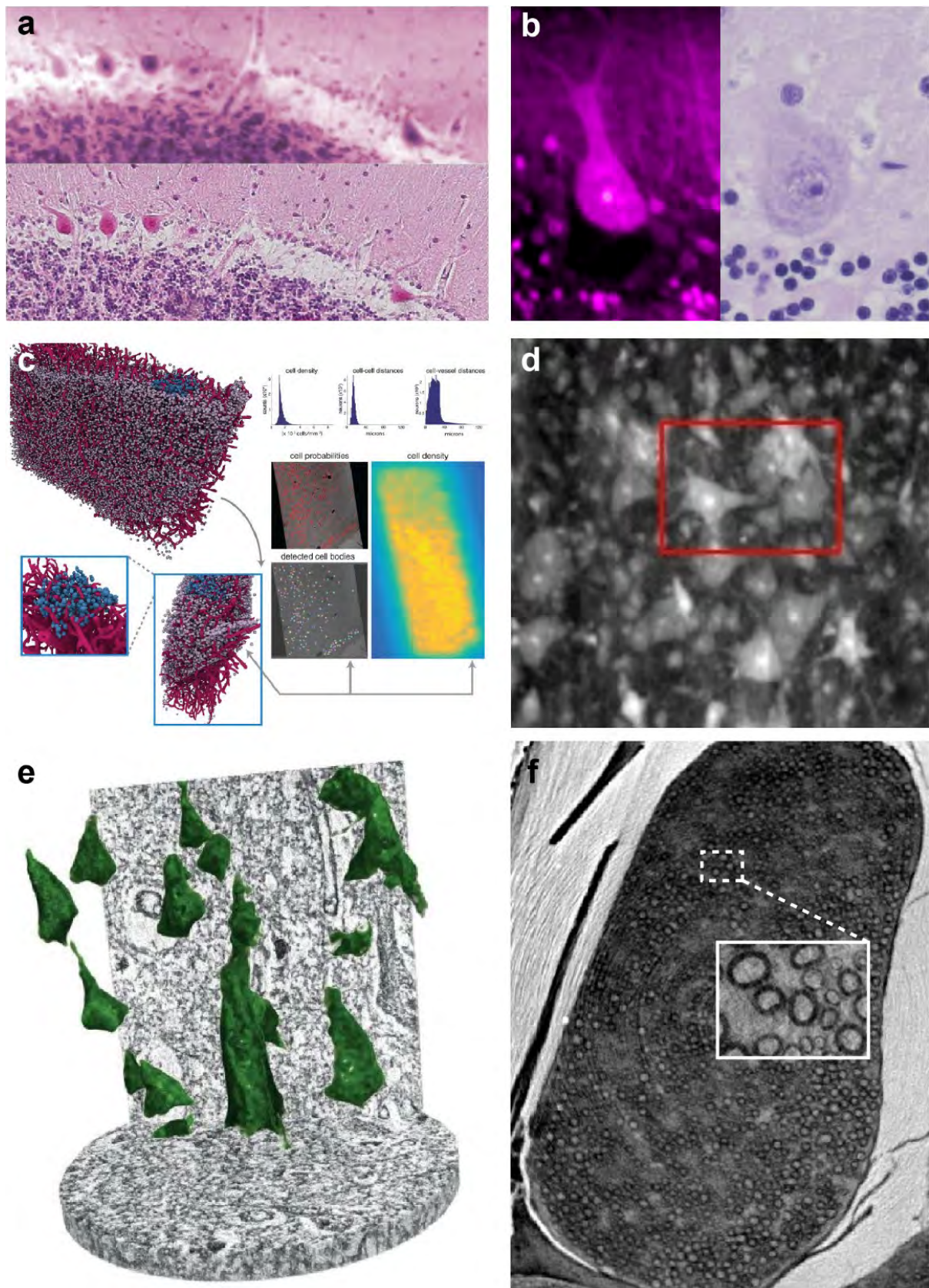


Fig. 1.8: (a-b) recolored cellular-resolution X-PCI-CT slice (top/left) vs. traditional histological slice (bottom/right) of (a) a Purkinje cell layer within cerebellar tissue and (b) an individual Purkinje cell; panels modified from (Hieber *et al.*, 2016). (c) sub-micron resolution CNS X-PCI-CT leading to quantitative evaluations of 3D vascular and cellular structure; panel modified from (Dyer *et al.*, 2017). (d) cellular-resolution spinal cord X-PCI-CT, showing

a deep motor neuron population; panel modified from (Bukreeva *et al.*, 2017). (e) 3D rendering of nano-C data visualizing individual deep neuron cells and their cyto-architecture; panel modified from (Khimchenko *et al.*, 2018). (f) nano-CT of osmium-stained nerve fibers, measuring the detailed myelination of individual nerves; panel modified from (Bartels *et al.*, 2015), reproduced with permission from Elsevier, [Journal of Structural Biology](#) [COPYRIGHT] (2015). Note that all these X-PCI-CT datasets were acquired *post-mortem*, and that nano-CT results involved further sample dissection beyond simple soft-matter excision from bone structure.

The last neuroimaging topic, to which extensive X-PCI-CT work has been dedicated, is the detection of Alzheimer Disease (AD) effects on nervous tissue. **Fig. 1.9** summarizes the main results in this field, which include the correlation of hyper-intense local image spots, detected via X-PCI-CT in the brains of rodent animal models of AD, with immuno-histology (Noda-Saita *et al.*, 2006) and immunofluorescence signals (Pinzer *et al.*, 2012) pertaining to amyloid protein aggregates. This discovery led to the fruitful application of various different X-PCI-CT-based neuroimaging methodologies, including both gratings-based and propagation-based PCI (Astolfo *et al.*, 2016), to the quantification of brain-wide amyloid deposition in rodent animal models. Most recently, nano-holo-tomography was applied to the characterization of the local morphological 3D nano-environment surrounding amyloid deposits (Massimi *et al.*, 2019), as a first step at a 3D study of toxic protein vs. neural cells vs. vasculature interactions in AD-driven neurodegeneration within deep layers of un-sectioned brain-tissue samples. Together, this literature shows the potential impact of X-PCI-CT data in the experimental neuroscientific study of amyloidopathy.

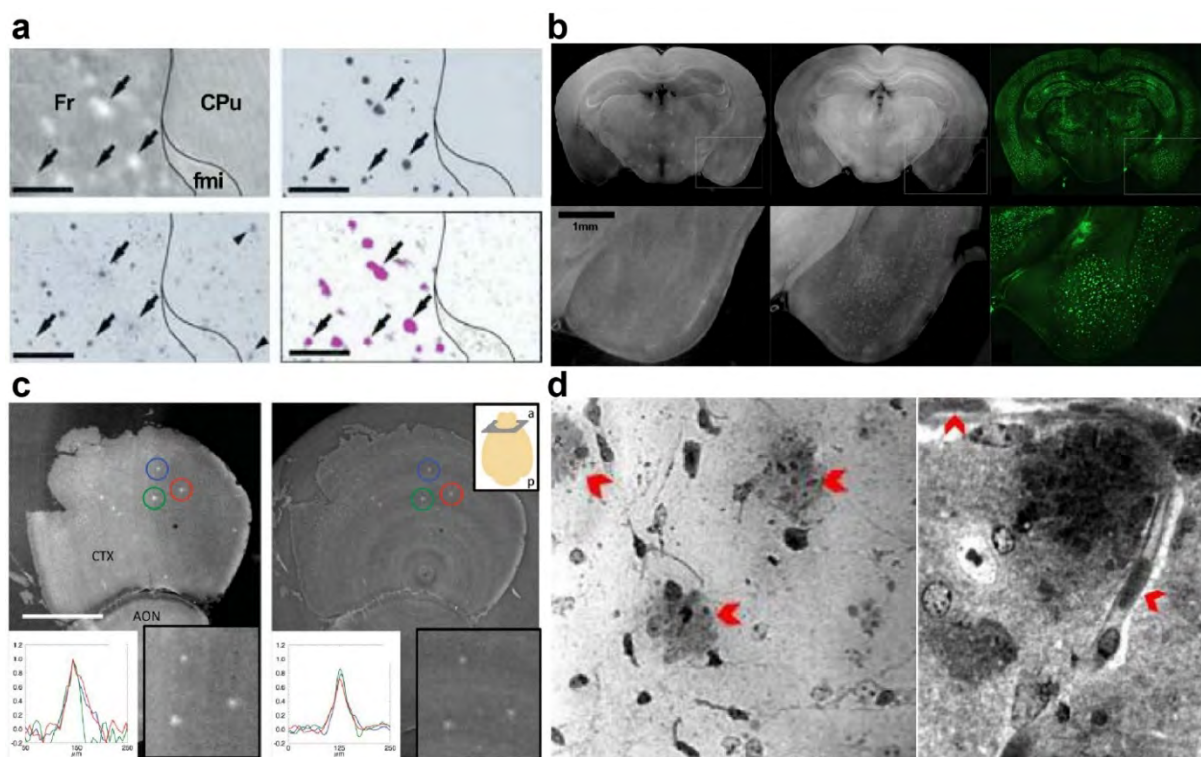


Fig. 1.9: (a) identification by immuno-histology of bright spots in X-PCI-CT data of a PSAPP mouse brain tissue as high-density amyloid protein deposits; panels modified from (Noda-Saita *et al.*, 2006), reproduced with permission from Elsevier, [Neuroscience](#) [COPYRIGHT] (2006). (b) coronal X-PCI-CT slices of a normal (left) vs. 5x FAD (middle) mouse brain, and Thioflavin S fluorescence (right) of the 5x FAD mouse brain tissue, showing spatial correspondence between bright spots in PCI images and Thioflavin S signal; panels modified from (Pinzer *et al.*, 2012), reproduced with permission from Elsevier, [NeuroImage](#) [COPYRIGHT] (2012). (c) amyloid signal

detection in AD rodent brain tissue via gratings-based (left) vs. propagation-based (right) X-PCI-CT; panels modified from (Astolfo *et al.*, 2016). **(d)** nano-CT data showing the nano-morphology of (left) several amyloid deposits alongside local cellular structure, and (right) a single amyloid deposits alongside pathologic vascular features; panels modified from (Massimi *et al.*, 2019), reproduced with permission from Elsevier, [NeuroImage](#) [COPYRIGHT] (2019).

In light of all these published works, the main achievements of X-PCI-CT neuroimaging thus far can be summarized as follows:

1. high soft-tissue contrast within both excised brain and spinal cord samples;
2. *post-mortem* measurement of deep cellular and vascular structure without need for labelling;
3. potential impact of this technique in the experimental study of various CNS pathologies.

1.4 Thesis motivation and outline

This Thesis work has been motivated by the belief that this relatively-novel imaging technique may offer a new and fruitful perspective to experimental neuroscientific inquiry, as the many afore-mentioned experimental works already help show. At the initial stages of this doctoral work, in fact, X-PCI-CT for neuroimaging was still quite a young area of exploration, but has since grown to a more established technique, especially thanks to the technological advancements made by several synchrotron beamlines with the specific aim of tailoring X-PCI-CT setups for pseudo-histological 3D analyses of interest to biology and biomedicine.

In this Thesis work, I present original synchrotron-based *post-mortem* X-PCI-CT neuroimaging results concerning several specific areas of application, and focus on evaluating the relevance and uniqueness of the method compared to other technologies in the fast-growing and fascinating field of research that is neuroimaging. And even though individual experiments included in this manuscript may have even quite different underlying objectives, the overarching purpose of these efforts should be identified in the exploration of the capabilities (and limits) of this imaging approach in the context of experimental neuroimaging.

Overall, this work:

1. **explores new *post-mortem* neuroimaging applications for X-PCI-CT**, such as the effects of radiation therapy on brain tissue and glioblastoma tissue, human spinal cord imaging, and hypertension-mediated vascular remodeling in rodent samples;
2. **further develops already existing application fields**, such as the detection Alzheimer's Disease pathology in the brain of rodents and the characterization of spinal cord vasculature;
3. **employs a multi-scale approach** for full-organ to intra-cellular CNS imaging;
4. **tests and evaluates different sample preparation protocols** for spinal cord imaging;
5. **provides direct comparisons of X-PCI data to other neuroimaging approaches**, by same-sample multi-technique analyses;
6. **carries-out experimental neuroscience studies** on small animals, involving e.g. drug testing and X-ray radiotherapy, using X-PCI-CT for unique quantitative 3D sample analyses.

Briefly, the outline of this Thesis manuscript involves two methodological chapters, **Chapters 2-3**, discussing the technical aspects of this experimental Thesis, and five results chapters, **Chapters 4-8**, presenting the detailed results of independent neuroimaging projects, each including sections devoted to better specify the individual CNS scientific cases, methods, and analyses used, and to brief case-specific discussions.

Methods Chapters:

Chapter 2: provides the fundamental information necessary to understand X-ray phase-contrast tomography as a 3D technique for soft-tissue analysis.

Chapter 3: provides a brief guide to all the main experimental methods recurring in individual imaging experiments.

Results Chapters:

Chapter 4: presents the application of X-PCI-CT to the study of brain cancer radiation therapy.

Chapter 5: presents an X-PCI-CT-based study of Alzheimer Disease (AD) neurodegeneration, using a multiscale analysis approach for the visualization and quantification of intra-cellular protein deposits, within a neuroscience experiment also involving a test AD drug.

Chapter 6: presents a proof-of-principle X-PCI-CT-based autopsy of human spinal cord samples.

Chapter 7: presents a study of the effect of the standard sample-preparation protocols for electron microscopy on rodent spinal cord X-PCI-CT.

Chapter 8: briefly summarizes other minor projects carried out during my doctoral work.

This manuscript terminates with a brief **Conclusions** section, which recapitulates the main results achieved, proposes a few major take-away points and suggests some future perspectives.

REFERENCES:

- Astolfo, A. *et al.* (2016) 'Amyloid- β plaque deposition measured using propagation-based X-ray phase contrast CT imaging', *Journal of Synchrotron Radiation*, 23(3), pp. 813–819. doi: 10.1107/S1600577516004045.
- Bartels, M. *et al.* (2015) 'Myelinated mouse nerves studied by X-ray phase contrast zoom tomography', *Journal of Structural Biology*, 192(3), pp. 561–568. doi: <https://doi.org/10.1016/j.jsb.2015.11.001>.
- Bech, M. *et al.* (2013) 'In-vivo dark-field and phase-contrast x-ray imaging', *Scientific Reports*. The Author(s), 3, p. 3209. Available at: <https://doi.org/10.1038/srep03209>.
- Bravin, A., Coan, P. and Suortti, P. (2013) 'X-ray phase-contrast imaging: from pre-clinical applications towards clinics.', *Physics in Medicine and Biology*, 58(1), pp. R1–R35. doi: 10.1088/0031-9155/58/1/R1.
- Broche, L. *et al.* (2017) 'Dynamic Mechanical Interactions Between Neighboring Airspaces Determine Cyclic Opening and Closure in Injured Lung', *Critical care medicine*, 45(4), pp. 687–694. doi: 10.1097/CCM.0000000000002234.
- Bukreeva, I. *et al.* (2017) 'Quantitative 3D investigation of Neuronal network in mouse spinal cord model', *Scientific reports*. Nature Publishing Group, 7, p. 41054. doi: 10.1038/srep41054.
- Cao, Y. *et al.* (2016) 'Visualization of mouse spinal cord intramedullary arteries using phase- and attenuation-contrast tomographic imaging', *Journal of Synchrotron Radiation*, 23(4), pp. 966–974. doi: 10.1107/S1600577516006482.
- Castelli, E. *et al.* (2011) 'Mammography with Synchrotron Radiation : First Clinical Experience with Phase-Detection Technique', *Radiology*, 259(3). doi: 10.1148/radiol.11100745.
- Cedola, A. *et al.* (2017) 'X-Ray Phase Contrast Tomography Reveals Early Vascular Alterations and Neuronal Loss in a Multiple Sclerosis Model', *Scientific Reports*, 7(1), p. 5890. doi: 10.1038/s41598-017-06251-7.
- Cloetens, P. *et al.* (1996) 'Phase objects in synchrotron radiation hard x-ray imaging', *J. Phys. D: Appl. Phys.*, 29, pp. 133–146. doi: 10.1088/0022-3727/29/1/023.
- Cloetens, P. (1999) *Contribution to Phase Contrast Imaging, Reconstruction and Tomography with Hard Synchrotron Radiation*. Vrije Universiteit Brussel.
- Cloetens, P. *et al.* (1999) 'Hard x-ray phase imaging using simple propagation of a coherent synchrotron radiation beam', *Journal of Physics D: Applied Physics*. IOP Publishing, 32(10A), pp. A145–A151. doi: 10.1088/0022-3727/32/10a/330.
- Coan, P., Bamberg, F., *et al.* (2010) 'Characterization of osteoarthritic and normal human patella cartilage by computed tomography X-ray phase-contrast imaging: a feasibility study.', *Investigative radiology*, 45(7), pp. 437–444. doi: 10.1097/RLI.0b013e3181e193bd.
- Coan, P., Wagner, A., *et al.* (2010) 'In vivo x-ray phase contrast analyzer-based imaging for longitudinal osteoarthritis studies in guinea pigs', *Physics in Medicine and Biology*. IOP Publishing, 55(24), pp. 7649–7662. doi: 10.1088/0031-9155/55/24/017.
- Croton, L. C. P. *et al.* (2018) 'In situ phase contrast X-ray brain CT', *Scientific reports*. Nature Publishing Group UK, 8(1), p. 11412. doi: 10.1038/s41598-018-29841-5.
- Davis, B. and Slack, C. M. (1926) 'Measurement of the Refraction of X-Rays in a Prism by Means of the Double X-Ray Spectrometer', *Physical Review*. American Physical Society, 27(1), pp. 18–22. doi: 10.1103/PhysRev.27.18.
- Davis, T. J. *et al.* (1995) 'Phase-contrast imaging of weakly absorbing materials using hard X-rays', *Nature*, 373(6515), pp. 595–598. doi: 10.1038/373595a0.

- Dyer, E. L. *et al.* (2017) 'Quantifying Mesoscale Neuroanatomy Using X-ray Microtomography', *eNeuro*, 4(5)(e0195-17.2017). doi: 10.1523/ENEURO.0195-17.2017 1.
- Eggl, E. *et al.* (2015) 'X-ray phase-contrast tomography with a compact laser-driven synchrotron source', *PNAS*, 112(18), pp. 5567–5572. doi: 10.1073/pnas.1500938112.
- El-Schich, Z., Leida Mölder, A. and Gjørloff Wingren, A. (2018) 'Quantitative Phase Imaging for Label-Free Analysis of Cancer Cells—Focus on Digital Holographic Microscopy', *Applied Sciences*. Multidisciplinary Digital Publishing Institute, 8(7), p. 1027. doi: 10.3390/app8071027.
- Fitzgerald, R. (2000) 'Phase-Sensitive X-ray Imaging', *Physics Today*, 7(23). doi: 10.1063/1.1292471.
- Fratini, M. *et al.* (2015) 'Simultaneous submicrometric 3D imaging of the micro-vascular network and the neuronal system in a mouse spinal cord.', *Scientific reports*, 5, p. 8514. doi: 10.1038/srep08514.
- Heinzer, S. *et al.* (2008) 'Novel three-dimensional analysis tool for vascular trees indicates complete micro-networks, not single capillaries, as the angiogenic endpoint in mice overexpressing human VEGF165 in the brain', *NeuroImage*, 39(4), pp. 1549–1558. doi: <https://doi.org/10.1016/j.neuroimage.2007.10.054>.
- Hieber, S. E. *et al.* (2016) 'Tomographic brain imaging with nucleolar detail and automatic cell counting', *Scientific Reports*. The Author(s), 6, p. 32156. Available at: <https://doi.org/10.1038/srep32156>.
- Hornig, A. *et al.* (2014) 'Cartilage and Soft Tissue Imaging Using X-rays: Propagation-Based Phase-Contrast Computed Tomography of the Human Knee in Comparison With Clinical Imaging Techniques and Histology', *Invest Radiol*, 49(9), pp. 627–634. doi: 10.1097/RLI.000000000000063.
- Hu, J. *et al.* (2017) 'Nondestructive imaging of the internal micro-structure of vessels and nerve fibers in rat spinal cord using phase-contrast synchrotron radiation microtomography', *Journal of Synchrotron Radiation*, 24(2), pp. 482–489. doi: 10.1107/S1600577517000121.
- Jensen, T. H. *et al.* (2011) 'Molecular X-ray computed tomography of myelin in a rat brain', *NeuroImage*. Elsevier Inc., 57(1), pp. 124–129. doi: 10.1016/j.neuroimage.2011.04.013.
- Karunakaran, C. *et al.* (2015) 'Factors influencing real time internal structural visualization and dynamic process monitoring in plants using synchrotron-based phase contrast X-ray imaging', *Scientific Reports*, 5(1), p. 12119. doi: 10.1038/srep12119.
- Khimchenko, A. *et al.* (2018) 'Hard X-Ray Nanoholotomography: Large-Scale, Label-Free, 3D Neuroimaging beyond Optical Limit', *Advanced Science*, 5, p. 1700694. doi: 10.1002/advs.201700694.
- Mader, K. *et al.* (2011) 'High-throughput full-automatic synchrotron-based tomographic microscopy', *Journal of synchrotron radiation*. 2011/01/20. International Union of Crystallography, 18(Pt 2), pp. 117–124. doi: 10.1107/S0909049510047370.
- Massimi, L. *et al.* (2019) 'Exploring Alzheimer's disease mouse brain through X-ray phase contrast tomography: From the cell to the organ', *NeuroImage*. Elsevier Ltd, 184, pp. 490–495. doi: 10.1016/j.neuroimage.2018.09.044.
- Mayo, S. C. *et al.* (2003) 'X-ray phase-contrast microscopy and microtomography', *Optics Express*. OSA, 11(19), pp. 2289–2302. doi: 10.1364/OE.11.002289.
- Mocella, V. *et al.* (2015) 'Revealing letters in rolled Herculaneum papyri by X-ray phase-contrast imaging', *Nature Communications*, 6(1), p. 5895. doi: 10.1038/ncomms6895.
- Mollenhauer, J. *et al.* (2002) 'Diffraction-enhanced X-ray imaging of articular cartilage', *Osteoarthritis and Cartilage*, 10(3), pp. 163–171. doi: 10.1053/joca.2001.0496.
- Momose, A. *et al.* (1996) 'Phase-contrast X-ray computed tomography for observing biological soft tissues.', *Nature Medicine*, 2(4), pp. 473–475. doi: 10.1038/nm0496-473.
- Nobel Media AB (1953) *The Nobel Prize in Physics 1953*, *NobelPrize.org*. Available at: www.nobelprize.org/prizes/physics/1953/summary/ (Accessed: 10 September 2019).

- Noda-Saita, K. *et al.* (2006) 'Quantitative analysis of amyloid plaques in a mouse model of Alzheimer's disease by phase-contrast X-ray computed tomography', *Neuroscience*, 138(4), pp. 1205–1213. doi: 10.1016/j.neuroscience.2005.12.036.
- Olbinado, M. P. *et al.* (2017) 'MHz frame rate hard X-ray phase-contrast imaging using synchrotron radiation', *Optics Express*. OSA, 25(12), pp. 13857–13871. doi: 10.1364/OE.25.013857.
- Pfeiffer, F. *et al.* (2007) 'High-resolution brain tumor visualization using three-dimensional x-ray phase contrast tomography', *Physics in Medicine and Biology*, 52(23), pp. 6923–6930. doi: 10.1088/0031-9155/52/23/010.
- PHI AB (2019) *quantitative-phase-imaging*, *phiab.com*. Available at: <https://phiab.com/holomonitor/quantitative-phase-imaging/>.
- Pinzer, B. R. *et al.* (2012) 'Imaging brain amyloid deposition using grating-based differential phase contrast tomography', *NeuroImage*. Elsevier Inc., 61(4), pp. 1336–1346. doi: 10.1016/j.neuroimage.2012.03.029.
- Pisano, E. D. *et al.* (2000) 'Human Breast Cancer Specimens: Diffraction-enhanced Imaging with Histologic Correlation—Improved Conspicuity of Lesion Detail Compared with Digital Radiography', *Radiology*, 214(3). doi: 10.1148/radiology.214.3.r00mr26895.
- Qvarnström, M. *et al.* (2017) 'Synchrotron phase-contrast microtomography of coprolites generates novel palaeobiological data', *Scientific reports*, (7), p. 2723. doi: 10.1038/s41598-017-02893-9.
- Röntgen, W. C. (1896) 'On a New Kind of Rays', *Nature*, 53(1369), pp. 274–276. doi: 10.1038/053274b0.
- Röntgen, W. C. (1898) 'Ueber eine neue Art von Strahlen', *Annalen der Physik*. John Wiley & Sons, Ltd, 300(1), pp. 12–17. doi: 10.1002/andp.18983000103.
- Sayre, D. and Chapman, H. N. (1995) 'X-ray microscopy', *Acta Crystallographica Section A*. International Union of Crystallography (IUCr), 51(3), pp. 237–252. doi: 10.1107/S0108767394011803.
- Schulz, G. *et al.* (2012) 'Multimodal imaging of human cerebellum - merging X-ray phase microtomography, magnetic resonance microscopy and histology.', *Scientific Reports*, 2, p. 826. doi: 10.1038/srep00826.
- Sejnowski, T. J., Churchland, P. S. and Movshon, J. A. (2014) 'Putting big data to good use in neuroscience.', *Nature neuroscience*, 17(11), pp. 1440–1441. doi: 10.1038/nn.3839.
- Tafforeau, P. *et al.* (2006) 'Applications of X-ray synchrotron microtomography for non-destructive 3D studies of paleontological specimens', *Applied Physics A*, 83(2), pp. 195–202. doi: 10.1007/s00339-006-3507-2.
- Willer, K. *et al.* (2018) 'X-ray dark-field imaging of the human lung-A feasibility study on a deceased body', *PloS one*. Public Library of Science, 13(9), pp. e0204565–e0204565. doi: 10.1371/journal.pone.0204565.
- Zamir, A. *et al.* (2016) 'X-ray phase contrast tomography; proof of principle for post-mortem imaging', *The British journal of radiology*. 2015/11/27. The British Institute of Radiology., 89(1058), p. 20150565. doi: 10.1259/bjr.20150565.
- Zernike, F. (1942) 'Phase contrast, a new method for the microscopic observation of transparent objects', *Physica*, 9(7), pp. 686–698. doi: [https://doi.org/10.1016/S0031-8914\(42\)80035-X](https://doi.org/10.1016/S0031-8914(42)80035-X).
- Zernike, F. (1955) 'How I Discovered Phase Contrast', *Science*, 121(3141), pp. 345 LP – 349. doi: 10.1126/science.121.3141.345.
- Zikmund, T. *et al.* (2018) 'High-contrast differentiation resolution 3D imaging of rodent brain by X-ray computed microtomography', *Journal of Instrumentation*. IOP Publishing, 13(02), pp. C02039–C02039. doi: 10.1088/1748-0221/13/02/c02039.

Chapter 2 - Basics of X-ray phase-contrast CT

This chapter is intended to provide a brief introduction to X-ray imaging, and specifically X-ray phase-contrast tomography (X-PCI-CT), i.e. the experimental technique of choice for the neuroimaging studies presented in this Thesis. Only a brief overview of the theoretical and practical aspects of X-PCI-CT can be found here, with references indicating more thorough descriptions from literature. Specific methodology related to individual experiments is discussed in **Chapter 3 – Experimental Methods**, and can be also found within the methods sections of individual case-study results in **Chapter 4 - Results**.

2.1 Fundamentals in X-ray imaging

2.1.1 X-rays

As can be observed in **Fig. 2.1**, X-rays (or Röntgen radiations) are a high-energy form of electromagnetic radiation in the 100 eV to 100 keV range, corresponding to wavelengths ranging from 20 nm to 0.01 nm, i.e. much shorter wavelengths than that of visible light. Since smaller resolution-limiting diffraction effects arise when using smaller wavelengths, X-ray-based microscopy should be able, at least in principle, to achieve higher spatial resolutions than that of visible light microscopy. According to the Rayleigh criterion, the minimal resolvable distance R by an imaging system (i.e. minimum separation distance between two light sources that may be resolved into distinct objects) is proportional to the wavelength of the radiation used ($R \propto \lambda$, with R the resolution distance, λ the wavelength). For this reason, the resolving power of X-ray microscopy lies between the resolving power of visible light microscopy and electron microscopy, which in turn uses 10^{-2} to 10^{-3} nm wavelength electron beams enabling sub-angstrom level imaging.

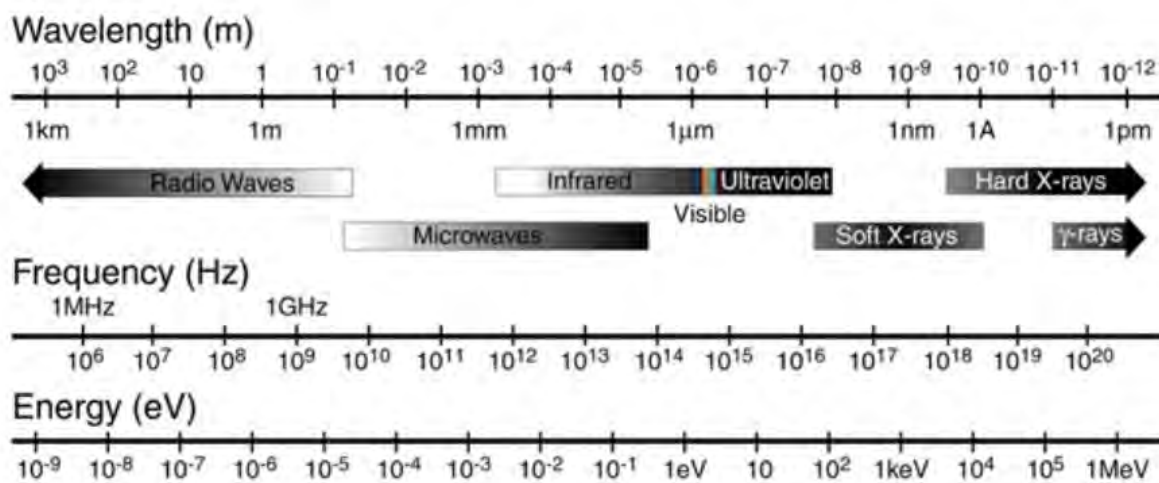


Fig 2.1: Spectrum of electromagnetic radiation. Figure is property of NAU, James H. Wittke [COPYRIGHT] (2016).

X-ray energy and its relation to the binding energy of electrons within an object determines the nature of their interactions with matter. Since X-ray photon energies are much larger than chemical binding energies, it is the density, thickness and elemental composition of a material, and not its chemical bonds, that mainly affects X-ray interactions (Bushberg *et al.*, 2003). In other words, as X-rays traverse an object, their penetration depth and attenuation depends on the photon energy used.

2.1.2 Hard X-rays and Radiography

So-called hard X-rays, i.e. the ones used in this Thesis work, correspond to radiation with energy in the 10-100 keV range, which can penetrate biological tissue for up to tens of centimeters (Russo, 2017). In this way, X-rays can measure the inside of thick visually-opaque

objects and, for this reason, they have found fruitful application as a medical imaging technique, i.e. radiography, permitting the observation of internal parts of a patient without surgical intervention.

Radiography is the oldest imaging modality ever used for medical imaging, and typically involves irradiating an object with X-rays emitted from a radiation source (e.g. a cathode X-ray tube) and recording the modulated intensity of the X-rays after interaction with the materials in the investigated object. The used X-ray spectrum shape and energy depends on the energy of the electrons inside the tube, on the composition of the anode (often molybdenum, rhodium or tungsten), and on the filters intersecting the beam path. The energy choice normally depends on the characteristics (composition and size) of the sample to be imaged and the acceptable radiation doses to be delivered to it.

During a radiographic scan, the X-rays enter the sample and are absorbed, scattered or simply transmitted with different probabilities, and the X-ray sensor detects both primary and scattered photons, creating an image. Un-scattered photons are responsible for forming the image of the scanned object; scattered ones produce a degrading background signal. Different X-ray attenuation properties within different parts of a biological sample will produce variations of the signal intensity at the detector, and thereby give rise to image contrast between different tissues. This is the basic image formation mechanism in conventional medical absorption-based X-ray imaging. High-density materials and high-atomic-number elemental composites, e.g. bone tissue, determining strong X-ray attenuation, are thus clearly visualized.

Summarizing, radiography exploits intra-sample variations in absorption and forward scattering, by measuring via a detector the projection along the X-ray path of the attenuation properties of the sample and recording them in a 2D image, called the radiograph. This is the basis of so-called absorption-contrast X-ray imaging, which can be better understood by looking at the atomic-level properties of X-ray-matter interactions.

2.1.3 X-rays through matter – the physics of traditional radiography

Physically, when X-rays propagate through a biological tissue, both absorption and scattering of photons will occur. As a result, the intensity of monochromatic X-ray radiation will decrease according to the Beer-Lambert law:

$$I(z) = I(0)e^{-\mu x}$$

where $I(z)$ is the transmitted intensity in the propagation direction z , $I(0)$ the incident intensity, x the path length (i.e. the object thickness), and μ the linear attenuation coefficient. The μz dependence of the decreasing exponential means that the intensity of the transmitted X-ray beam will be lower for thicker (large z) and denser (large μ) objects. Instead, since both weakly absorbing (small μ) materials and small objects (small z) will absorb very little, absorption-based imaging will afford low sensitivity for such cases. This realization has historically been the reason for the development of X-ray phase-contrast imaging techniques,

which move beyond the attenuation properties of a sample by being able to probe phase-related X-ray beam diffraction and interference effects.

Interestingly, the linear attenuation coefficient μ in Beer-Lambert's law actually depends on several properties related to the X-rays and the absorbing medium, including the photon energy of the X-ray beam (E), the electron density of the absorber material (ρ_e), and the effective atomic number of the material (Z). Moreover, as can be seen in **Fig. 2.2**, inner orbital transitions can create sharp step-functions in the plots of mass attenuation coefficients $\mu_{mass} = \mu/\rho$, with ρ the material density. For composite materials, such as biological bone, muscle and fat tissues, μ_{mass} is calculated as the mass-weighted sum of coefficients from each composite element. Note how attenuation increases with increasing atomic number of the absorber and decreases with increasing X-ray photon energy (Chen, Rogalski and Anker, 2012). Interestingly, note also how attenuation coefficients from biological materials become increasingly similar at higher X-ray energies.

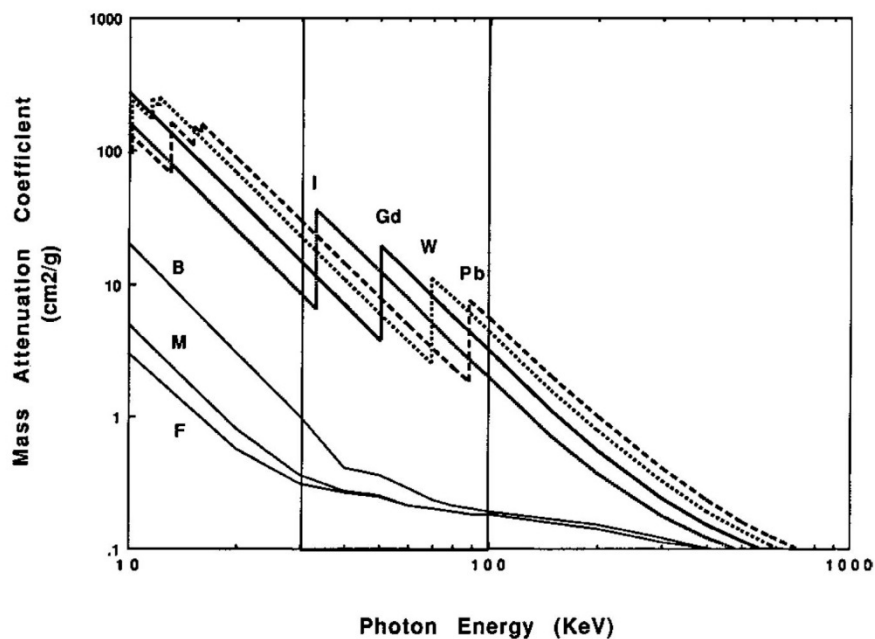


Figure 2.2: Mass attenuation coefficients (μ_{mass}) vs. photon energy for several elements (I, Gd, W, and Pb) and biological composite materials (bone, B; muscle, M; fat, F). Figure reproduced from (Yu and Watson, 1999), reprinted (adapted) with permission from the **American Chemical Society**, [Chemical Reviews](#). [COPYRIGHT] (1999).

In terms of atomic-level physical interactions, X-ray attenuation arises due to **photo-electric absorption** (τ) and non-resonant scattering, both **Compton** (γ) and **coherent** (ω) scattering, and μ can be written as:

$$\mu = \tau + \gamma + \omega$$

Photo-electric τ absorption dominates at low photon energies, since it involves the interaction of X-ray photons with inner-shell electrons: sufficiently energetic photons are absorbed, transferring their energy to the electrons, which are ejected. This leads to so-called free electrons, which are readily reabsorbed, and inner-shell vacancies, which are immediately filled by outer-shell electrons, leading to characteristic lower-energy radiation

emission in a random direction or to Auger electron emission. Since the initial photon absorption is most likely to occur when photon energies are higher but similar to inner-shell electronic binding energies, τ is inversely proportional to E as follows:

$$\tau \propto \frac{1}{E^3}$$

Conversely, inner-shell electrons with high binding energies, such as K-shell electrons of high- Z materials, make a τ photon-electron interaction more likely, so that:

$$\tau \propto Z^3$$

Summarizing, the contribution of the photo-electric absorption to X-ray attenuation is high for low-energy X-ray radiation and for high Z materials. Since most of this energy is being absorbed by the tissue, τ processes expose tissues to a high dose of radiation (Yu and Watson, 1999).

Compton γ scattering involves the interaction of an X-ray photon with an outer-shell electron. Since, in this case, the electron binding energy is relatively small compared to the photon, the electron will be ejected and the photon will be deflected and scattered in a new direction with a different wavelength and lower energy. Compton scattering is thus a partial-absorption process, and the likelihood of γ scattering depends on the total number of outer-shell electrons, independently of atomic number Z , i.e.:

$$\gamma \propto \rho_e \text{ and } \gamma \propto \rho$$

with ρ_e the electron density, ρ the physical (macroscopic mass) density. The photon energy dependence of γ scattering, i.e. a decreasing γ effect with increasing photon energy, is marginal. Compton scattering becomes the dominant process in soft tissue for X-ray energies above 30 keV (Hubbell, 1999), whereas at the low-energy limit it becomes the elastic non-absorptive process called Thompson scattering.

Interestingly, both τ and γ decrease the amount of photons in the primary beam, but γ -scattered electrons still may reach a detector, whereas τ -absorbed photons completely disappear. Therefore, the μ dependences can be summarized as follows:

$$\mu \propto a\rho_e + b\rho_e \frac{Z^3}{E^3}$$

with the first term referring to γ scattering, and the second to τ absorption, with a weakly dependent on photon energy, and b a constant (Chen, Rogalski and Anker, 2012).

Coherent (Rayleigh) ω scattering involves the elastic scattering between X-ray photons and electrons in the absorber material, with no energy transfer and a coherent deflection of the photon in a non-random direction. Thus, no dose-deposition occurs due to coherent scattering. ω scattering varies proportionally with Z and with $1/E^2$. It is described, in general, by complex atomic scattering factors, with the most important components, the forward scattering factors, directly influencing both the real and imaginary components of the complex refractive index n (Attwood, 1999), which it is just slightly below 1 for all materials and hard X-ray wavelengths.

2.1.4 Computed Tomography

Computed tomography (CT) is an X-ray-based imaging method introduced in medical diagnostics in the 1970's to obtain 3D maps of internal sample structure, a technology for which Sir Godfrey N. Hounsfield and Allan M. Cormack shared the 1979 Nobel prize in Physiology or Medicine (Nobel Media AB, 1979). Via CT, internal cross-sectional images of a sample can be computed from many 2D radiographs (i.e. projection images) of the investigated object acquired from different illumination directions around it. The CT slices are mathematical reconstructions of planes parallel to the direction of X-ray propagation, and the 3D dataset is generated by the ordered stacking of multiple consecutive 2D slices. Since its discovery, CT has become one of the two most important workhorses for 3D medical diagnostics, along with MRI.

Several algorithms for CT image reconstruction have been implemented, including both analytical (Fourier) and iterative methods (algebraic and statistical). The most widely used analytical mathematical solution for the CT reconstruction problem is based on the inverse Radon transform and involves a so-called filtered back-projection algorithm. The algorithm involves the collection of projections at different equidistant illumination angles, the convolution of each projection with a filter function, e.g. a ramp filter in Fourier space, the back-projection of filtered projections along the different illumination directions and the summation of attenuation in the CT slice planes parallel to the X-ray propagation. The mathematics of CT is very well described in the literature, e.g. in (Kak and Slaney, 2001).

2.2 Fundamentals in X-ray phase-contrast imaging

2.2.1 The complex index of refraction

For a description of X-ray propagation through matter, which includes both wave phase and amplitude modulations, the complex index of refraction n is generally used, with:

$$n = 1 - \delta + i\beta$$

where the refractive index decrement δ quantifies wave phase shifts induced by the refraction of photons, and the absorption index β represents amplitude shifts linked to absorption (Paganin, 2006). Since the wavenumber in vacuum is $k = 2\pi/\lambda$, the wavenumber in a material with refractive index n becomes $k' = nk$. A plane wave traveling through such a material would then be of the form

$$e^{inkz} = e^{i(1-\delta+i\beta)kz} = e^{i(1-\delta)kz} e^{-\beta kz}$$

with the phase term dependent on δ and the decaying exponential dependent on β (Cloetens, 1999). As discussed, the main contributors to β -related X-ray attenuation in the hard X-ray regime are τ absorption and ν scattering, whereas it is elastic forward photon scattering (i.e. Thompson scattering mainly), which mainly determines δ -related phase shifts.

For hard X-rays away from absorption edges, their influence on a material can be described by the free-electron model (related to Thompson scattering), and the coherent scattering, as already mentioned, by forward-scattering factors. Since in this case the electric susceptibility of the medium χ is proportional to the electron density, the refractive index decrement of a non-composite material can be alternatively rewritten as:

$$\delta = \frac{r_e \lambda^2}{2\pi} \rho_e = \frac{r_e (hc)^2 Z}{2\pi E^2 V}$$

using $\rho_e = Z/V$, with r_e the classical electron radius, and hc respectively Planck's constant and the speed of light. Therefore, **δ is proportional to the electron density (and thus to Z)**, and approximately inversely proportional to E^2 . The relationship of β to the linear absorption coefficient becomes, instead:

$$\beta = \frac{\lambda}{4\pi} \mu \propto \frac{hc}{4\pi E} \rho_e \frac{Z^3}{E^3}$$

using the dependences of μ related to photo-electric absorption. Therefore, **β is proportional to μ (and thus to Z^3)**, and approximately inversely proportional to E^4 .

Notably, δ and β are small ($< 10^{-6}$) for hard X-rays, so that n deviates only very slightly from 1. Even more interestingly, though, is the fact that **δ is much greater than β in this regime, and up to 10^3 times greater**, as illustrated in **Fig. 2.3** for biological materials.

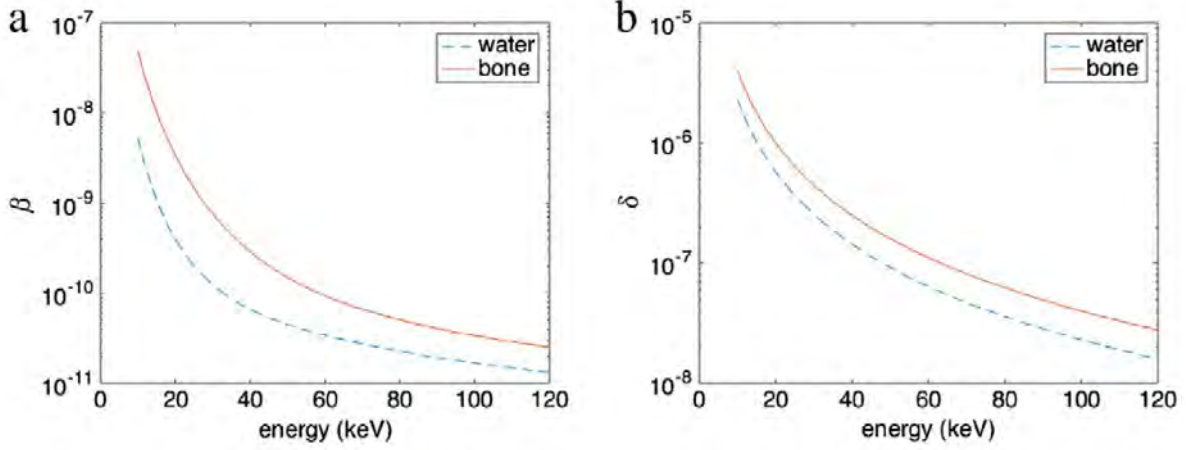


Fig. 2.3: (a) β index and (b) δ index for water and bone irradiated by X-ray photons in the 10-120 keV energy range. Figure taken from (Endrizzi, 2018), reproduced with permission from Elsevier, [Nuclear Instruments and Methods in Physics Research Section A: Accelerators, Spectrometers, Detectors and Associated Equipment \[COPYRIGHT\] \(2018\)](#).

For weakly-absorbing materials, such as biological soft tissues, it may be more advantageous to measure δ -related phase shifts in the X-rays, than their much smaller β -related attenuation. **This notion is at the basis of the potential advantage in the use of X-ray phase-contrast imaging (PCI) for biomedical applications over traditional absorption-based imaging.**

2.2.2 X-ray absorption-contrast imaging and phase-contrast imaging

A treatment of monochromatic X-ray- matter interactions based on the complex index of refraction, as above, allows the introduction of the following expression, valid for thin objects, for the X-ray transmission function $T(x, y)$:

$$T(x, y) = A(x, y)e^{-i\varphi(x, y)} \text{ with } A(x, y) = e^{-B(x, y)}; B(x, y) = \frac{2\pi}{\lambda} \int [\mu(x, y, z)] dz$$

$$\text{and } \varphi(x, y) = \frac{2\pi}{\lambda} \int [1 - \delta(x, y, z)] dz = \varphi_0 - \frac{2\pi}{\lambda} \int \delta(x, y, z) dz$$

with z the X-ray propagation direction, φ_0 the phase modulation in the absence of the object, φ the phase-shift in the x - y plane imparted within the sample to a straight-propagating wave, and $U_{out}(x, y) = T(x, y)U_{inc}(x, y)$ the transmitted wave-field at a distance $z = 0$ behind the object. Note that recording the a beam intensity $I(x, y, 0)$ at $z = 0$, i.e. a 0 distance away from the object, would lead to the following complex square modulus of the complex wave field:

$$I_0 = I(x, y, 0) = |U_{out}(x, y, 0)|^2 = I_{inc}e^{-\int \mu dz}$$

since $|U_{inc}(x, y, 0)|^2 = I_{inc}$ and $|e^{i\varphi(x, y)}|^2 = 1$, i.e. it corresponds to no detectable phase-shifts and all phase information being lost. This intensity corresponds to conventional **absorption-based radiography** (Appel, Anastasio and Brey, 2011) and reduces itself to the Lambert-Beer law.

An imaging system for PCI, instead, allows **phase-contrast effects** to be observed, by further modification of U_{out} by convolution, $*$, with a technique-specific propagator P , so that the detector-measured intensity $I_{det} = |U_{out} * P|^2$ will be dependent on φ . In crystal interferometry PCI, for example, a Bonse-Hart interferometer is used to interfere a reference beam with the beam through the sample (Momose, 1995); in analyzer-based and diffraction-enhanced PCI, an analyzer crystal is used as angular filter (Chapman *et al.*, 1997); in grating-based PCI, two gratings are used to measure object-influenced fringe patterns (Weitkamp *et al.*, 2005), and in edge-illumination PCI, only the edges of detector pixels are illuminated (Olivo *et al.*, 2001). The two phase-contrast methods used in this Thesis, i.e. X-ray propagation-based imaging and X-ray holo-tomography, exploit wave propagation downstream of the sample and concurrent Fresnel diffraction. The way these setups extract the sample-induced phase-shift information from the X-ray beam is described in the following paragraphs.

2.2.3 X-ray propagation-based PCI and holo-tomography

Propagation-based PCI (PB-PCI) is the simplest of PCI techniques, in that it does not require any additional optical elements. This technique exploits the deflections of photons within the scanned object and the occurring Fresnel diffraction of the distorted wave-front during propagation over a certain distance downstream of the sample.

For small phase gradients, the angular deviation $\Delta\alpha$ of the X-ray photons relative to the propagation direction can be expressed, after paraxial approximation ($|\nabla\varphi| \ll 2\pi/\lambda$), as (Davis *et al.*, 1995):

$$\Delta\alpha(x, y) = -\frac{\lambda}{2\pi} \nabla\varphi(x, y, \lambda)$$

Since the refractive index for X-rays is very close to 1, the $\Delta\alpha$ X-ray deviation is very small, in the order of micro-radians. Therefore, to allow the detection of phase-effect related to such small angular deviations, a high resolution of the imaging system as well as long sample-to-detector distances are necessary and crucial requirements for this technique to work.

A standard PB-PCI setup looks like the one depicted in **Fig. 2.4**, in which a planar usually monochromatic X-ray wave-front impinges on the measured object, is perturbed according to the object's refractive index, and then exits the object and is propagated for a variable distance d , until its intensity is measured by a detector. This increased sample to detector distance is the only alteration of the setup otherwise identical to an absorption-based imaging setup, and mono-chromaticity, as discussed later, is not a stringent requirement.

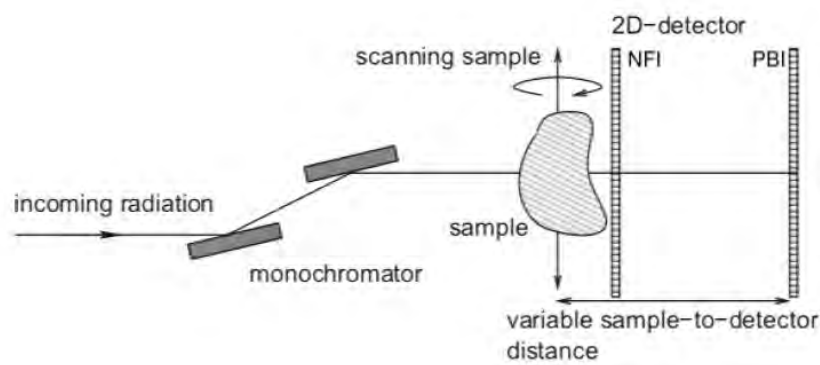


Figure 2.4: a propagation-based imaging (BPI) experimental setup, in which a quasi-monochromatic X-ray beam traverses the sample and propagates in free-space between the sample and a downstream detector a distance d away, placed in the near-field diffraction regime (NFI). Figure taken from (Keyriläinen *et al.*, 2010).

The Fresnel diffraction of the beam during free-space propagation translates object-induced phase shifts into intensity modulation at the detector. Thus, the occurrence of image contrast can be understood as due to interference between parts of the wave-front that have undergone different angular deviations associated to different phase gradients (Cloetens, 1999). Note that measured raw phase-contrast radiographs will contain mixed contrast from both absorption and phase effects.

As **Fig. 2.5** shows, PB-PCI signal depends on the sample-to-detector distance d , and three different imaging regimes can be distinguished (Snigirev *et al.*, 1995):

1. the **absorption** regime: $d \approx 0$, no space-propagation and no Fresnel diffraction occurs.
2. the **(edge-detection)** near-field diffraction regime: $r_f^2 = \lambda d \leq a^2$, i.e. a small propagation distance d . r_f is the radius of the so-called first Fresnel zone in the object plane, and a is the characteristic length scale of the sample object. The sample details with high frequency components of the phase modulation form the contrast. Boundaries are enhanced and show a distinctive edge interference pattern.
3. the **(holographic)** far-field diffraction regime: $r_f^2 = \lambda d > a^2$, i.e. the propagation distance is so large that, even though the interference fringes are very well defined, they cannot be associated to a specific edge in the sample.

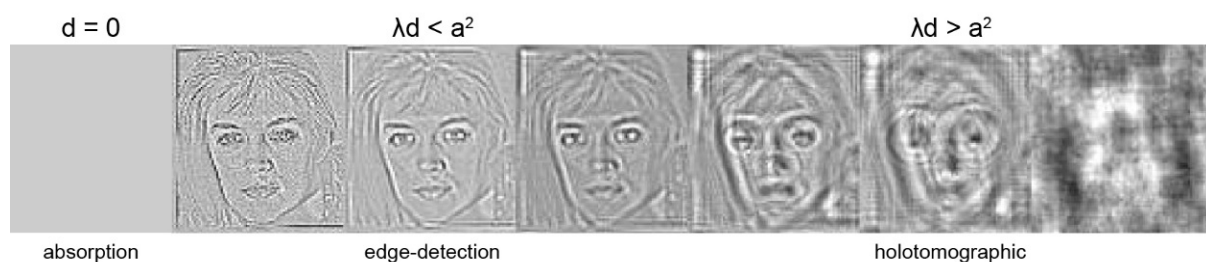


Figure 2.5: radiographs of a theoretical pure phase object detected by a PB-PCI setup, at increasing (left-to-right) sample-to-detector distance d . Three imaging regimes are visible: absorption, edge-detection, and holotomographic. Figure modified from (Mayo *et al.*, 2003).

The fine interference patterns detectable in the edge-detection regime, which highlight phase jumps associated with object discontinuities, are the ones used in **PB-PCI**. The deformed images obtainable in the holographic regime are at the basis of **holo-tomography**, briefly discussed later in this chapter, which combines image recorded at multiple distances with ad-hoc image processing and phase-retrieval algorithms (P Cloetens *et al.*, 1999).

Mathematically, the intensity recorded in near-field PB-PCI images of homogenous samples can be derived in at least two different ways, either using the Australian School approach and the transport of intensity equation (TIE) (Gureyev *et al.*, 1999), or using the Flemish School approach and the transfer function approach (Guigay, 1977). For a slowly-varying phase in the transverse plane and a detector in the near-field regime (i.e. $\sqrt{\lambda d} \ll a$), a PB-PCI setup will measure the following (radiographic) intensity:

$$I_{det}(x, y) = I_0(x, y) \left[1 - \frac{\lambda d}{2\pi} \Delta_{x,y} \varphi(x, y) \right]$$

PB-PCI is therefore a differential phase imaging technique, since it depends on the second-order Laplacian of the phase. This means that homogenous gradients (overall beam deflections) cannot be detected, and instead a non-zero second derivative of the phase is necessary for contrast formation. **Such an effect will readily occur if the X-ray beam is tangential e.g. to object edge structures, internal holes, cracks, etc., and give rise to the edge-enhancement, hallmarks image features, in the collected PB-PCI radiographs.**

Edge-enhanced PB-PCI images do not directly correspond to an object property along the line of X-ray propagation. Instead, to obtain a transmission function or a phase map of the measured object from collected images, a so-called **phase retrieval algorithm** needs to be applied to the raw edge-enhanced radiograph. Due to the Talbot effect (Talbot, 1836), though, PB-PCI imaging based on Fresnel diffraction at a given distance d will be blind to some spatial frequencies in the phase distribution, . A first approach to solve this problem is to impose strong constraints to the object characteristics, i.e. to make certain plausible assumptions and thereby retrieve the object phase from a single collected radiograph, e.g. the low-frequency phase components of a pure phase object (Nugent *et al.*, 1996).

Recently, Paganin and coworkers were able to solve the TIE and retrieve the phase using a single defocused distance and either homogenous (Paganin *et al.*, 2002) or multi-material objects (Beltran *et al.*, 2010). Implementations of Paganin's 2002 phase retrieval algorithm, which enables transformations of edge-enhancement into area contrast as illustrated in **Fig. 2.6**, were used through-out this Thesis work to retrieve phase maps from raw PB-PCI radiographic datasets. 3D CT datasets are then reconstructed from PB-PCI projects in the same way as from standard absorption-based projections.

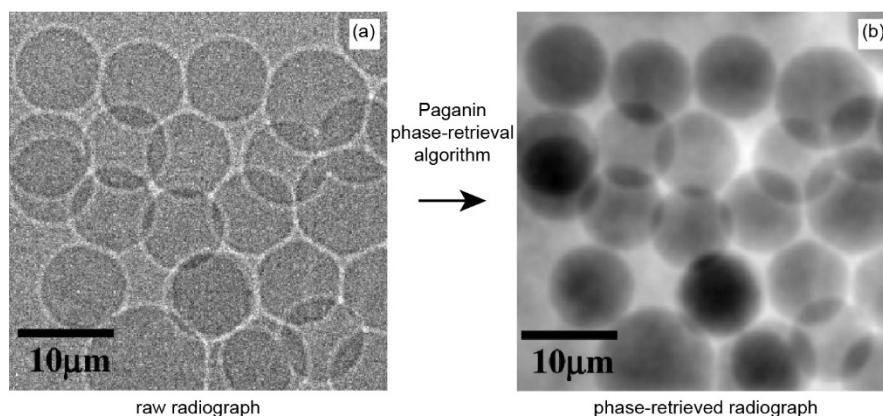


Figure 2.6: (a) a raw PB-PCI radiograph depicting latex spheres. (b) phase-retrieved image in (a), obtained using Paganin's algorithm for single-shot PB-PCI of homogenous samples. Figure modified from (Paganin *et al.*, 2002), reproduced with permission from **John Wiley and Sons**, [Journal of Microscopy](#) [COPYRIGHT] (2002).

Less constrained ways to solve the phase retrieval inverse problem instead involve more cumbersome and prolonged acquisition procedures, such as via multi-image acquisition either with different beam energies (Gureyev *et al.*, 2001) or at different sample-to-detector distances d (P Cloetens *et al.*, 1999). The latter is the basis of so-called holo-tomographic imaging, briefly described below.

Based on a scheme already proposed for electron microscopy (Coene *et al.*, 1992), Cloetens and coworkers developed a procedure to disentangle phase information from X-ray radiographs called in-line X-ray holography (P Cloetens *et al.*, 1999), using multiple radiographs acquired at different sample-to-detector distances d , as illustrated in **Fig. 2.7**.

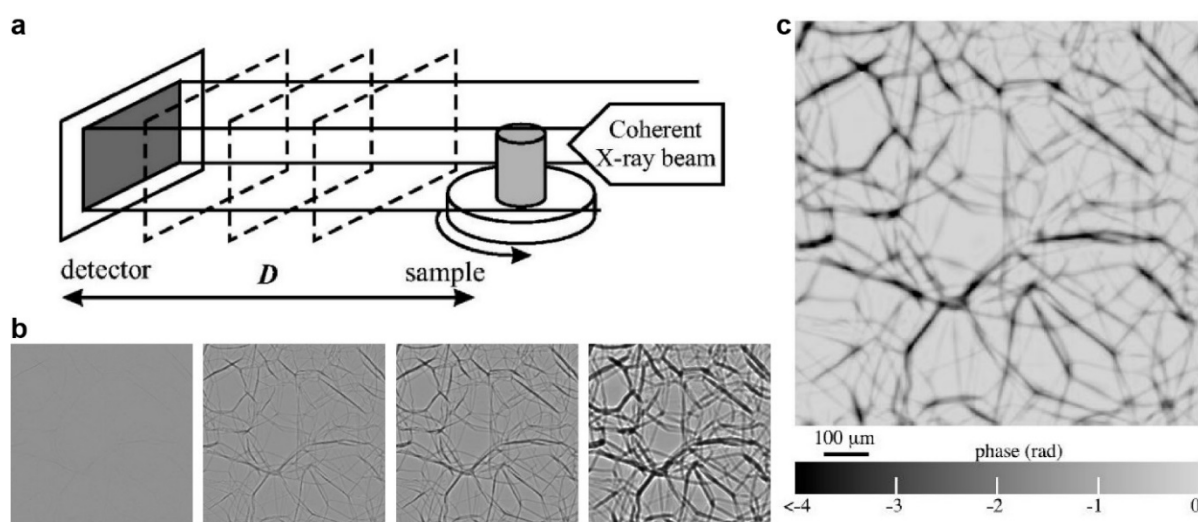


Figure 2.7: (a) setup scheme for in-line X-ray holography, with projection acquisitions at multiple sample-to-detector distances D . (b) 4 Holographic radiographs of polystyrene foam, acquired at increasing (left to right) setup D . Contrast and width of fringes increases with increasing D . (c) Quantitative phase map in radians, computed using 16 different-distance projection images, including those in (b). Panels (a,c) taken from (P Cloetens *et al.*, 1999), reprinted with the permission of **AIP Publishing**, [Applied Physics Letters](#) [COPYRIGHT] (1999), and panel (b) from (P Cloetens *et al.*, 1999), reproduced with permission from **IOP Publishing**, [Journal of Physics D: Applied Physics](#) [COPYRIGHT] (1991).

As already mentioned, this variation of the distance d and the acquisition of multiple projections is introduced to avoid indeterminations in the phase retrieval problem (Peter Cloetens *et al.*, 1999). Then, the phase reconstruction procedure, which combines all projections at different distances, involves either simple filtering (Cloetens *et al.*, 1997) or more complex optimization procedures, as already implemented for electron microscopy (Kirkland, 1984). The reconstructed maps (e.g. **Fig. 2.7c**) represent the quantitative projection of the electron density inside the object. Standard 3D CT reconstruction procedures then combine phase projections to obtain quantitative 3D datasets of internal sample electron density.

2.3 X-ray sources

The historical X-ray source is the X-ray tube, which produces X-rays by shooting electrons onto a metal target. This source is a simple and compact, and therefore robust and inexpensive. X-ray tubes also provide little control over the properties of the X-rays produced. On the contrary, large-scale X-ray source facilities, such as synchrotrons and free-electron lasers, have been constructed to provide X-ray light with advantageous spectral and geometrical properties for broad scientific applications. Accelerator-based sources are, though, quite large, in the order of several buildings, and mostly dedicated to research due to their high cost and difficult accessibility. Both tube-based and synchrotron X-ray source types are briefly discussed below in order to motivate the choice of using synchrotron X-rays for the experimental work presented in this Thesis manuscript.

X-rays for medical diagnostics are routinely produced by **X-rays tubes**, in which accelerated electrons, ejected from a cathode due to current application, hit a metal anode target and decelerate. This abrupt deceleration produces Bremsstrahlung (i.e. breaking) radiation, which has a continuous spectrum ranging up to the energy of the incident free electron. A sufficiently energetic incident electron could also ionize an atom in the target material, knock-off an inner-shell electron, and lead to the atomic emission of characteristic X-ray after vacancy filling by outer-shell electrons. This atomic radiation emission depends of the precise energy levels of the ejected and vacancy-filling electrons, and thus on the atomic composition of the anode material. The two emission processes combined produce the typical X-ray tube emission spectrum depicted in **Fig. 2.8a**, which shows a broad distribution interspersed by a few 'characteristic' emission spikes.

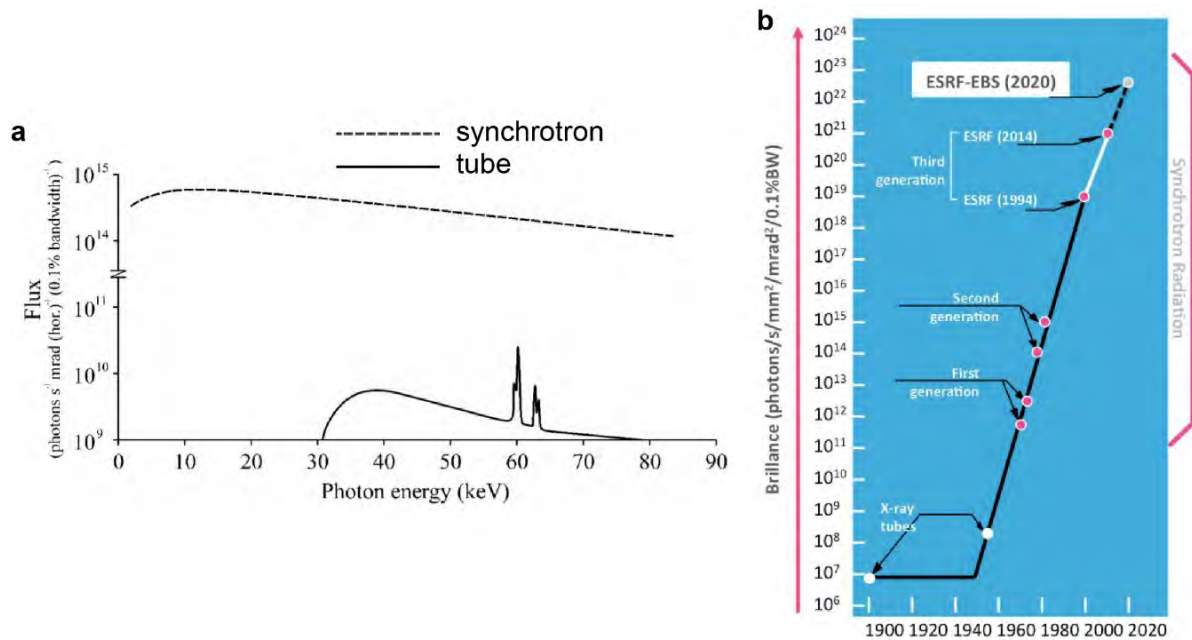


FIG. 2.8: (a) comparison between a wiggler-based synchrotron beam spectrum and an Al X-ray tube (b) advancement in X-ray beam brilliance at the ESRF synchrotron vs. the brilliance of X-ray tubes. Panel (a) taken from (Coan, 2006); panel (b) taken from www.esrf.eu/about/synchrotron-science.

Interestingly, the process of breaking radiation production has an efficiency of only about 1% (Lundström, 2014), and most of the free electron energy in an X-ray tube is deposited on the anode in the form of heat. For this reason, X-ray tubes are designed to limit and remove the heat deposition on the target anode, e.g. via slit sources of electrons, which spread out the target area, or via rotating anodes, which additionally remove heat, or via liquid metal jet anodes, which solve the heat dissipation problem by substituting the traditional static metal anode with a self-regenerating fast-flowing jet of metal (Hemberg, Otendal and Hertz, 2003).

Synchrotron sources, instead, are the most common facility-based X-ray sources. Synchrotron radiation (SR) is produced whenever a beam of relativistic electrons (or positrons) is deviated in a magnetic field: what is generated is a highly collimated, i.e. small-angled, conical X-ray radiation beam tangentially to the curved particle path. In a synchrotron facility, the process of SR generation is obtained by accelerating electrons in the closed ultra-high-vacuum chamber of a large storage ring, in the order of hundreds of meters in diameter, with periodic magnetic elements positioned along the particle orbit. In the curved sections of the orbit, bending magnets (BM) produce a continuous spectrum of SR; in the straight sections, other types of magnetic devices called insertion devices, such as wigglers or undulators, are used to produce SR emission with further tuned geometry and spectra (Coan, 2006; Als-Nielsen and McMorrow, 2011). Considering some of the most important beam properties in X-ray imaging, i.e. the spectrum, the source size and the photon flux, first of all, beams with a much higher brilliance are produced via synchrotron emission than via bremsstrahlung, as **Fig. 2.8b** shows. This high SR brilliance allows much shorter measurement times compared to the use of X-rays from tube sources. Moreover, SR has a tunable spectrum of emission, is polarized and has a pulsed time structure, allowing more diverse applications. Last, SR has a high directionality (small opening angle) and a small source size, which, far away

from the X-ray source, can lead to quasi-parallel spatially-coherent X-rays well-suited for both CT and PCI imaging.

SR imaging beamlines are generally designed to accommodate quite large source-to-object distances. This is because the degree of (lateral) X-ray spatial coherence, defined by a lateral coherence length $l_c = \frac{\lambda L}{2S}$, is proportional to L the source-object distance and inversely proportional to S the source size. Interestingly, l_c determines the maximum distance between spatially-correlated waves in the (transverse) object plane, i.e. between waves, which will lead to observable interference and diffraction effects. Beyond this inter-wave spatial distance, instead, interference fringes will be blurred. Therefore, in the context of PCI imaging spatial coherence will represent an important beam quality, and l_c will determine the minimal size of an internal object detail, which will lead to its characteristic interference- and diffraction-related phase-contrast effects (Keyriläinen *et al.*, 2010). Note instead that for certain PCI techniques, including PB- PCI (Wilkins *et al.*, 1996), beam mono-chromaticity, which influences (longitudinal) temporal coherence, has been found, unlike spatial coherence, not to represent a strict technical requirement. This more-relaxed requirement on the needed X-ray beam represents another advantage, in addition to the simplicity of the setup, of PB-PCI compared e.g. to interferometric, grating- & analyzer-based PCI techniques, which instead require mono-chromaticity.

Overall, SR is very brilliant (high-flux and small source size), quasi-monochromatic, and highly collimated, and thus highly intense and temporally- and spatially-coherent. All these properties of a SR beam make it the optimal radiation for the high resolution X-ray phase-contrast CT (X-PCI-CT) imaging.

REFERENCES:

- Als-Nielsen, J. and McMorrow, D. (2011) *Elements of Modern X-ray Physics*. John Wiley & Sons, Ltd. doi: 10.1002/9781119998365.
- Appel, A., Anastasio, M. A. and Brey, E. M. (2011) 'Potential for imaging engineered tissues with X-ray phase contrast', *Tissue engineering. Part B, Reviews*. 2011/08/02. Mary Ann Liebert, Inc., 17(5), pp. 321–330. doi: 10.1089/ten.TEB.2011.0230.
- Attwood, D. (1999) *Soft X-Rays and Extreme Ultraviolet Radiation: Principles and Applications*. Cambridge: Cambridge University Press. doi: 10.1017/CBO9781139164429.
- Beltran, M. A. *et al.* (2010) '2D and 3D X-ray phase retrieval of multi-material objects using a single defocus distance', *Optics Express*. OSA, 18(7), pp. 6423–6436. doi: 10.1364/OE.18.006423.
- Bushberg, J. T. *et al.* (2003) 'The Essential Physics of Medical Imaging', *Medical Physics*. John Wiley & Sons, Ltd, 30(7), p. 1936. doi: 10.1118/1.1585033.
- Chapman, D. *et al.* (1997) 'Diffraction enhanced x-ray imaging', *Physics in Medicine and Biology*. IOP Publishing, 42(11), pp. 2015–2025. doi: 10.1088/0031-9155/42/11/001.
- Chen, H., Rogalski, M. M. and Anker, J. N. (2012) 'Advances in functional X-ray imaging techniques and contrast agents', *Physical Chemistry Chemical Physics*. The Royal Society of Chemistry, 14(39), pp. 13469–13486. doi: 10.1039/C2CP41858D.
- Cloetens, P. *et al.* (1997) 'Quantitative aspects of coherent hard x-ray imaging: Talbot images and holographic reconstruction', in *Proc.SPIE*. Available at: <https://doi.org/10.1117/12.293359>.
- Cloetens, P. (1999) *Contribution to Phase Contrast Imaging, Reconstruction and Tomography with Hard Synchrotron Radiation*. Vrije Universiteit Brussel.
- Cloetens, Peter *et al.* (1999) 'Hard x-ray phase imaging using simple propagation of a coherent synchrotron radiation beam', *Journal of Physics D: Applied Physics*. IOP Publishing, 32(10A), pp. A145–A151. doi: 10.1088/0022-3727/32/10a/330.
- Cloetens, P *et al.* (1999) 'Holotomography: Quantitative phase tomography with micrometer resolution using hard synchrotron radiation x rays', *Applied Physics Letters*. American Institute of Physics, 75(19), pp. 2912–2914. doi: 10.1063/1.125225.
- Coan, P. (2006) *Development and application of the analyzer-based imaging technique with hard synchrotron radiation*.
- Coene, W. *et al.* (1992) 'Phase retrieval through focus variation for ultra-resolution in field-emission transmission electron microscopy', *Physical Review Letters*. American Physical Society, 69(26), pp. 3743–3746. doi: 10.1103/PhysRevLett.69.3743.
- Davis, T. J. *et al.* (1995) 'Phase-contrast imaging of weakly absorbing materials using hard X-rays', *Nature*, 373(6515), pp. 595–598. doi: 10.1038/373595a0.
- Endrizzi, M. (2018) 'X-ray phase-contrast imaging', *Nuclear Instruments and Methods in Physics Research Section A: Accelerators, Spectrometers, Detectors and Associated Equipment*, 878, pp. 88–98. doi: <https://doi.org/10.1016/j.nima.2017.07.036>.
- Guigay, P. (1977) 'Fourier-transform analysis of Fresnel diffraction patterns and in-line holograms', *Optik*, 49, pp. 121–125. Available at: <https://ci.nii.ac.jp/naid/80014866943/en/>.
- Gureyev, T. E. *et al.* (1999) 'Hard x-ray quantitative non-interferometric phase-contrast microscopy', *Journal of Physics D: Applied Physics*. IOP Publishing, 32(5), pp. 563–567. doi: 10.1088/0022-3727/32/5/010.

- Gureyev, T. E. *et al.* (2001) 'Quantitative In-Line Phase-Contrast Imaging with Multienergy X Rays', *Physical Review Letters*. American Physical Society, 86(25), pp. 5827–5830. doi: 10.1103/PhysRevLett.86.5827.
- Hemberg, O., Otendal, M. and Hertz, H. M. (2003) 'Liquid-metal-jet anode electron-impact x-ray source', *Applied Physics Letters*. American Institute of Physics, 83(7), pp. 1483–1485. doi: 10.1063/1.1602157.
- Hubbell, J. H. (1999) 'Review of photon interaction cross section data in the medical and biological context', *Physics in Medicine and Biology*. IOP Publishing, 44(1), pp. R1–R22. doi: 10.1088/0031-9155/44/1/001.
- Kak, A. C. and Slaney, M. (2001) 'Principles of computerized tomographic imaging'. Philadelphia: Society for Industrial and Applied Mathematics. Available at: <http://www.books24x7.com/marc.asp?bookid=23044>.
- Keyriläinen, J. *et al.* (2010) 'Phase-contrast X-ray imaging of breast', *Acta Radiologica*. SAGE Publications, 51(8), pp. 866–884. doi: 10.3109/02841851.2010.504742.
- Kirkland, E. J. (1984) 'Improved high resolution image processing of bright field electron micrographs: I. Theory', *Ultramicroscopy*, 15(3), pp. 151–172. doi: [https://doi.org/10.1016/0304-3991\(84\)90037-8](https://doi.org/10.1016/0304-3991(84)90037-8).
- Lundström, U. (2014) *Phase-Contrast X-Ray Carbon Dioxide Angiography, TRITA-FYS NV - 2013:70*. KTH Royal Institute of Technology. Available at: <http://kth.diva-portal.org/smash/get/diva2:687022/FULLTEXT01.pdf>.
- Mayo, S. C. *et al.* (2003) 'X-ray phase-contrast microscopy and microtomography', *Optics Express*. OSA, 11(19), pp. 2289–2302. doi: 10.1364/OE.11.002289.
- Momose, A. (1995) 'Demonstration of phase-contrast X-ray computed tomography using an X-ray interferometer', *Nuclear Instruments and Methods in Physics Research Section A: Accelerators, Spectrometers, Detectors and Associated Equipment*, 352(3), pp. 622–628. doi: [https://doi.org/10.1016/0168-9002\(95\)90017-9](https://doi.org/10.1016/0168-9002(95)90017-9).
- Nobel Media AB (1979) *The Nobel Prize in Physiology or Medicine 1979*, *NobelPrize.org*. Available at: www.nobelprize.org/prizes/medicine/1979/summary/.
- Nugent, K. A. *et al.* (1996) 'Quantitative Phase Imaging Using Hard X Rays', *Physical Review Letters*. American Physical Society, 77(14), pp. 2961–2964. doi: 10.1103/PhysRevLett.77.2961.
- Olivo, A. *et al.* (2001) 'An innovative digital imaging set-up allowing a low-dose approach to phase contrast applications in the medical field', *Medical Physics*. John Wiley & Sons, Ltd, 28(8), pp. 1610–1619. doi: 10.1118/1.1388219.
- Paganin, D. *et al.* (2002) 'Simultaneous phase and amplitude extraction from a single defocused image of a homogeneous object', *Journal of Microscopy*, 206(1), pp. 33–40. doi: 10.1046/j.1365-2818.2002.01010.x.
- Paganin, D. M. (2006) 'Coherent X-ray imaging', in *Coherent X-Ray Optics*. Oxford: Oxford University Press. doi: 10.1093/acprof:oso/9780198567288.003.0004.
- Russo, P. (2017) 'Handbook of X-ray Imaging: Physics and Technology'. Available at: <http://www.crcnetbase.com/isbn/9781351228251>.
- Snigirev, A. *et al.* (1995) 'On the possibilities of x-ray phase contrast microimaging by coherent high-energy synchrotron radiation', *Review of Scientific Instruments*. American Institute of Physics, 66(12), pp. 5486–5492. doi: 10.1063/1.1146073.
- Talbot, H. F. (1836) 'LXXVI. Facts relating to optical science. No. IV', *The London, Edinburgh, and Dublin Philosophical Magazine and Journal of Science*. Taylor & Francis, 9(56), pp. 401–407. doi: 10.1080/14786443608649032.
- Weitkamp, T. *et al.* (2005) 'X-ray phase imaging with a grating interferometer', *Optics Express*. OSA, 13(16), pp. 6296–6304. doi: 10.1364/OPEX.13.006296.

Wilkins, S. W. *et al.* (1996) 'Phase-contrast imaging using polychromatic hard X-rays', *Nature*, 384(6607), pp. 335–338. doi: 10.1038/384335a0.

Yu, S.-B. and Watson, A. D. (1999) 'Metal-Based X-ray Contrast Media', *Chemical Reviews*. American Chemical Society, 99(9), pp. 2353–2378. doi: 10.1021/cr980441p.

Chapter 3 - Experimental Methods

This chapter is intended to provide an overview of all the X-PCI methodology used in the experimental neuroimaging work of this Thesis, from sample preparation, to the experimental setups and tomographic scan parameters, image processing and analysis tools. Specific methodology related to individual experiments is discussed within results chapters (**Chapters 4-8**), including other neuroimaging approaches, such as high-field MRI, TEM and immunohistology.

3.1 Sample preparation

All neuroimaging results in this Thesis work have been performed *post-mortem*.

Generally, the CNS samples used have been collected from rodent animal models, after animal sacrifice and extraction of soft-matter organs from within their bone structure. Brain organs were extracted from their protective skull structure, and spinal cord medullas were dissected from their bony vertebral canal. After dissection, the standard first step was a paraformaldehyde 4% fixation by immersion, in order to avoid progressive CNS tissue degradation during storage and imaging experiments. Samples were then either stored immersed in formalin or PBS at 4° C, or embedded in standard histological paraffin blocks. In addition to the small animal organs, human CNS samples were lawfully procured from donors after autopsy and embalmment.

Just before X-PCI-CT measurements, samples were placed vertically and either fit tightly within formalin-filled plastic containers, or embedded within agar-agar gel, in both cases in order to avoid any sample movement during CT rotations. In some cases, paraffin-embedded samples were de-embedded from their paraffin blocks (via heating) and placed in agar or formalin to minimize X-ray absorption and scattering from the embedding material.

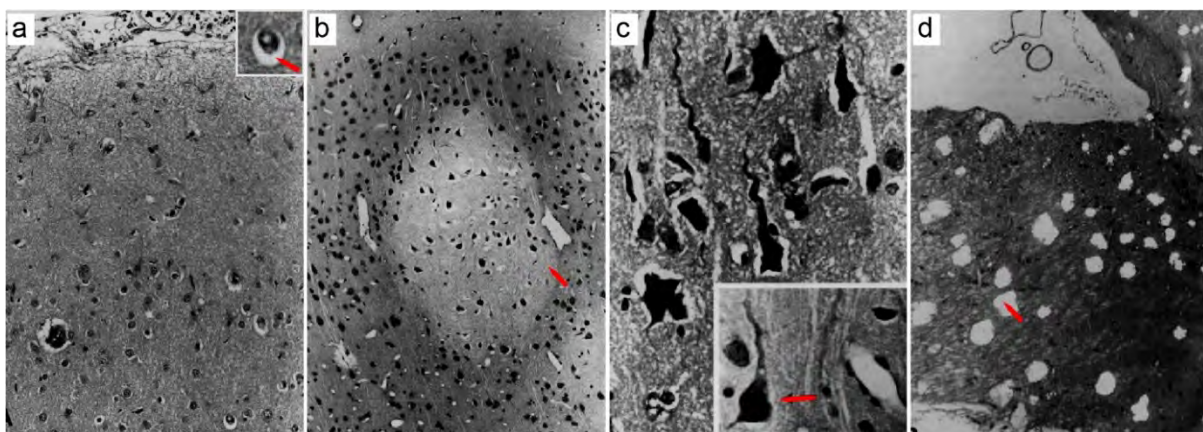


Fig. 3.1: Common CNS artifacts of fixation and paraffin embedment. (a) and its insert show retraction spaces around cells and vessels in a formalin-fixed brain cortex histological slice. (b) shows uneven formalin penetration within cortical tissue. (c) and its insert show artifactual dark neurons with characteristic corkscrew dendrites. (d) shows typical distorted white-matter tracts called mucocytes (or Buscaino bodies) altered by fixation and paraffin blocking. Red arrows point to the CNS tissue artifacts. Panels taken and modified from (Fix and Garman, 2000).

All these sample manipulations procedures have an influence on the soft-tissue of the specimen:

1. **Mechanical forces** during extraction can cause sample deformation or ruptures.
2. **Fixation and embedment** procedures are notoriously sample-invasive, in that they lead to both uniform and differential sample shrinkage, and thus to local intra-tissue deformations and possibly artifactual cyto-architecture.

Example of fixation- and paraffin-embedment-related cellular-level artifacts specific to nervous tissue nervous-tissue include retraction spaces, uneven fixative penetration,

artificial dark neurons with corkscrew-shaped dendrites and white-matter mucocytes (Fix and Garman, 2000), as illustrated in **Fig. 3.1**. These artifacts all influence tissue and cell morphology within samples, and may make result interpretations and evaluations difficult and error-prone. Last, X-PCI-CT measurements themselves can have an effect on the imaged tissues due to heat and/or radiation dose deposition. Both heat-dependent sample movement and shrinkage may occur during CT scans.

In addition to this overview, individual specific sample manipulation procedures are detailed within the experimental sections of individual experiments presented in **Chapters 4-8**.

3.2 X-PCI-CT experiments

All propagation-based (PB) X-PCI-CT experiments reported in this Thesis manuscript were performed in the years using synchrotron X-rays and specifically-designed imaging setups at either the beamline ID17 at the European Synchrotron (ESRF) in Grenoble - France, or at the beamline TOMCAT at the Swiss Light Source (LSL) of the Paul Scherrer Institute (PSI) in Villigen. All nano-holotomography measurements were, instead, carried out using the imaging setup available at the ID16 beamline of the ESRF. Experiments at SLS spanned the years 2017-2019. Experiments at the ESRF spanned the years 2014-2018. In 2019, the ESRF was shut down to install a new X-ray source, the EBS (Extremely Brilliant Source) to become the first 4th generation synchrotron in the world.

What follows is a brief description of specific features within different X-PCI-CT setups. Since the beamline development work has been largely carried out by others and before this Thesis work, references to the relevant literature are provided. Further detail can also be found within the methods sections of the specific X-PCI-CT experiments reported in results **Chapters 4-8**.

3.2.1 PB X-PCI-CT setups

Synchrotron beamline PB-X-PCI-CT setups are equipped with motorized high-precision rotating and translating stages, which permit the 3D movement of sample and detector stages, and thus the alignment of every setup component with respect to the direction of X-ray beam propagation. PB-X-PCI-CT setup components included:

1. **X-ray source:** either highly collimated, quasi-coherent monochromatic 30 to 60 keV synchrotron X-rays, or pink-beam X-rays.
2. **Detector:** either an in-house built 'FReLoN' camera (Coan *et al.*, 2006) with a field of view (FOV) of 2048 x 2048 pixels, or a PCO-Edge 5.5 sCMOS detector (Mittone *et al.*, 2017) with a FOV of 2560 x 2160 pixels. Detectors were coupled to optics systems affording effective pixel sizes between 46 μm and 0.3 μm .

3. **Propagation distance:** sample-to-detector distances ranging between 10 cm and 10 m, depending on the selected imaging system effective pixel size.
4. **Integration time:** X-ray spectrum- and sample-dependent, in the seconds to milliseconds range.

CT acquisitions were performed following two modes:

1. **“full-acquisition” CT mode:** CT angular projections were collected over a 180-degree sample rotation with the center of rotation (COR) placed in the middle of the projection.
2. **“half-acquisition” CT mode:** CT angular projections were collected over a 360-degree sample rotation with the COR placed at the edge of the projection.

Since the “half-acquisition” CT mode can almost double the horizontal dimension of the FOV, it was used when dealing with samples larger than the detector FOV or during local tomography scans. After each CT acquisition, high-resolution vertical-translation motor stages could be used to acquire consecutive spatially contiguous vertical image stacks, and thereby extend the vertical FOV, when required.

ID17 PB-X-PCI-CT setups:

ID17 (**Fig. 3.2**) is a 150m-long ESRF beamline featuring a multipole wiggler magnet with a variable gap (21 poles, period: 15 cm) as its insertion device. A second wiggler magnet (22 poles, period: 12.5 cm) can be used to increase the photon flux. The beamline holds two different end-stations, connected by a 100m-long vacuum pipe in the beam transfer tunnel, in which white radiation can travel.

1. **MRT-hutch:** the first end-station, 40 m downstream of the insertion devices, is the so-called MRT-hutch, an experimental room primarily dedicated to X-ray microbeam radiation therapy (MRT) (Siegbahn *et al.*, 2006), and more-recently also equipped with a pink-beam X-PCI-CT setup. Just upstream of the MRT-hutch, several slits, filters (Al, C, and Cu) and shutters define and tailor the geometry and spectrum of the incoming X-ray beam. The vertical size is here 2.4 mm, due to the limited vertical size of the beam at this station.
2. **Experimental-hutch:** ID17 holds a second experimental end-station 150 m downstream of the wiggler, the so-called “Imaging hutch”. Owing to the long distance between the source and the hutch, high X-ray beam spatial coherence is achieved here. This end-station is thereby suitable for different coherent X-PCI-CT imaging techniques, including analyzer-based X-PCI as well as PB-X-PCI-CT. Just upstream of this hutch, a second set of slits and filters is used to further tailor the beam spectrum. A monochromator hutch stations a double silicon crystal monochromator system in Laue geometry, used for fixed-exit applications to extract quasi-monochromatic X-rays in the 18 to 150 keV range, with a flux in the order of 10^{14} photons/second unfiltered. Other monochromator systems are also available, including a single bent silicon Laue crystal monochromator, and a multilayer monochromator.

Both hutches can be equipped with an end-station for edge-enhanced PB-PCI-CT. There, the detection system includes either GGG:Eu:Ce or LuAg:Ce scintillators, and either the CCD FReLoN or the sCMOS PCO-Edge 5.5 imaging sensors, coupled with indirect conversion optics

(Optique Peter, France) with 1x, 2x, 5x and 10x objectives. The sCMOS chip pixel size is $6.5 \times 6.5 \mu\text{m}^2$ while the CCD one is $11 \times 11 \mu\text{m}^2$. A schematic of the ID17 beamline is displayed in **Fig. 3.2**.

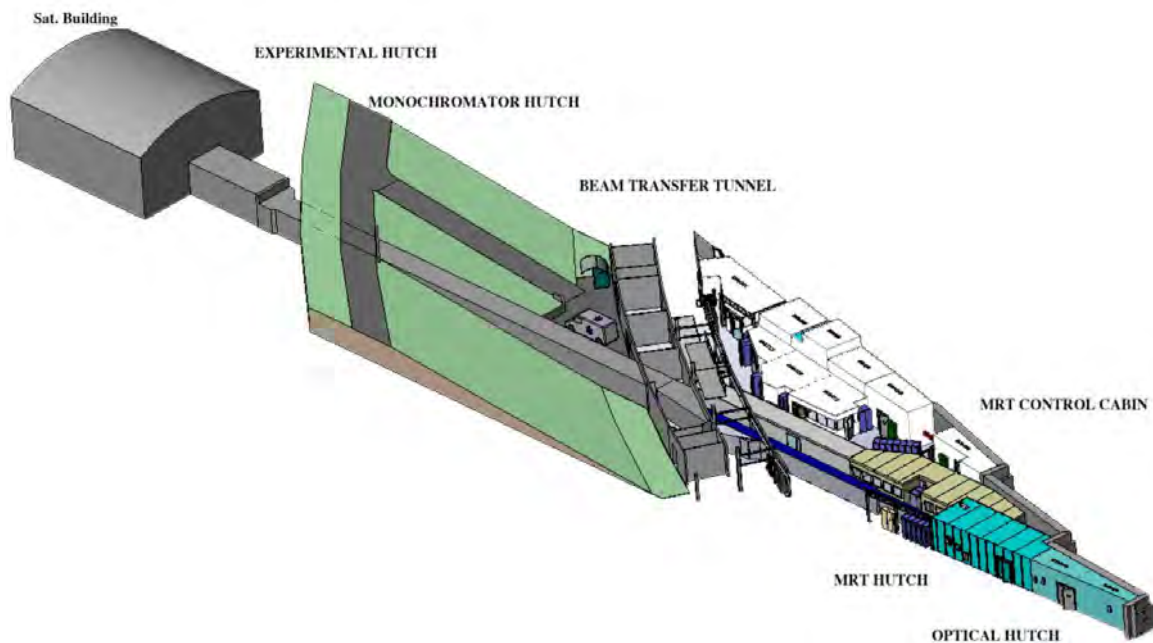


Figure 3.2: beamline schematic of ID17 at the European Synchrotron. Figure taken from: www.esrf.eu/home/UsersAndScience/Experiments/.

0.7 μm pixel size CT datasets in this Thesis work were all acquired in pink-beam mode in the ID17 MRT-hutch, by setting the two wiggler gaps to 70 and 200 mm (the latter thus completely open) respectively and by using as filters 1.5 mm of Al, 0.69 mm of Cu, and 1.15 mm of C. The PCO camera was used for these experiments consisting in the acquisition of 2000- to 3000-projection PB-X-PCI-CT scans, mostly performed in full-acquisition mode.

46, 8, and 3 μm pixel size CT datasets in this Thesis, instead, were all acquired in monochromatic mode in the ID17 imaging hutch, by setting wiggler gaps to 70 and 200 mm (the latter thus completely open) respectively, by adding Al and C beam filters (1.5 mm of Al, 0.8 mm of C), and by selecting (via the double-Si monochromator system) monochromatic beams from 30 keV to about 60 keV. The FReLoN camera was used to collect 46 and 8 μm pixel datasets, the PCO detector for 3 μm pixel ones. CT scans in both half- and full-acquisition mode were acquired, made up of 2000 to 6000 projections.

TOMCAT PB-PCI setup: this beamline of the SLS receives an X-ray beam from a super-bending magnet, which allows much higher flux (Lovric *et al.*, 2014) in the hard X-ray regime compared to normally-bending magnets, and is designed for fast and sub-micron resolution PCI tomography (Stampanoni *et al.*, 2010). Its main optical component is a fixed-exit double crystal multilayer monochromator, covering energies from 8 to about 45 keV, with a flux in the order of 10^{14} photons/second unfiltered. The beamline is equipped with two end-station, one for edge-enhanced PB-PCI-CT, and a second one devoted to differential PCI based on grating interferometry (Weitkamp *et al.*, 2005). Only the first end-station was used in the context of this Thesis work. There, the detection system includes either LuAG:Ce or LSO:Tb

scintillators, an Optique Peter microscope system with 1.25x, 2x, 4x, 10x, 20x and 40x objectives, and a PCO-Edge 5.5 detector with a chip pixel size of 6.5 μm .

0.3 μm pixel size CT datasets in this Thesis work were acquired in monochromatic mode using the TOMCAT PB-PCI setup. Experimental parameters included 21 keV energy, a 100 μm Al filter and a 10 μm Fe filter, a sample-to-detector propagation distance of ~ 50 mm, a 20 μm LuAG:Ce scintillator, 20x optical magnification coupled to the PCO camera, affording 0.33 μm effective pixel sizes. Scan parameters included 3000 projections for CTs in full-acquisition mode, with exposure time in the order of 120 ms.

3.2.2 Nano-holotomography setup

The nano-holotomographic imaging presented in this Thesis, as already mentioned, was all performed at the ID16a beamline of the ESRF. This beamline is designed for nanometric spatial resolution 3D holographic (and thus quantitative) imaging. By combining coherence techniques with X-ray fluorescence microscopy, native-state elemental analysis of specimen can also be performed. The beamline is 185m long, and, via a pair of multilayer-coated Kirkpatrick-Baez mirrors (Mokso *et al.*, 2007), provides nano-focused (spot size $\sim 25 \times 30 \text{ nm}^2$) monochromatic beams at either 17 or 33.6 keV, with flux in the order of 10^{14} photons/s unfiltered, 10^{11} photons/s after filtering. In addition to standard sample fixation, cryogenic sample preservation is also available. The holotomography setup, illustrated in **Fig. 3.3**, includes a cone-beam geometry, usually 4 holographic sample-to-detector distances of CT acquisition, piezo motors for 3D sample movement, and recording of holographic radiographs with a FReLoN CCD camera. The details of this setup are well-described in (Khimchenko *et al.*, 2018), and additional information are reported in this Thesis manuscript in the Methods section of **Chapter 5**.

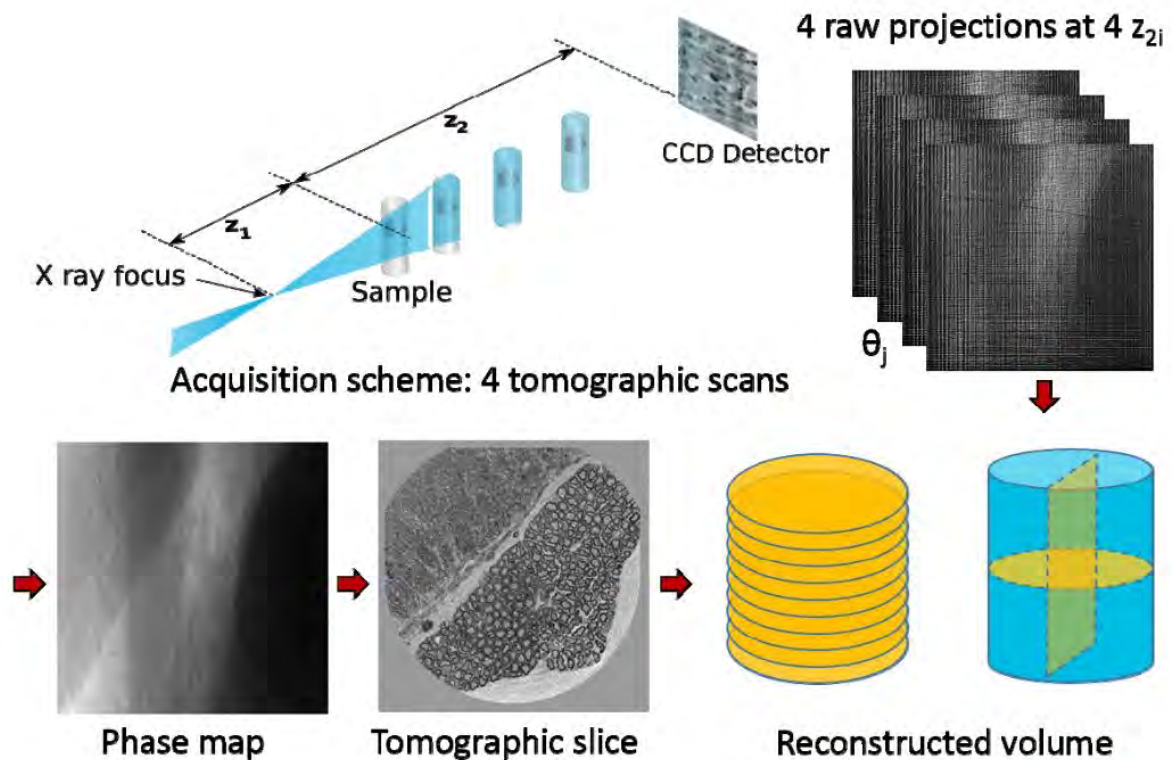


Figure 3.3: 4-distance nano-holography setup at ID16a of the ESRF. Figure taken from (Pacureanu *et al.*, 2018), reproduced with permission from the SPIE, [Proceedings](#) [COPYRIGHT] (2018).

0.1 μm pixel size CT datasets in this Thesis work were all acquired using monochromatic 17 keV X-rays, 4-distance sets of holographic CT projections (phase-maps) over 180 degrees, with propagation distances in the $\sim 40\text{-}60$ mm range. The voxel size, given by the geometrical magnification, was set to $0.1^3 \mu\text{m}^3$ and the corresponding field of view was $0.2 \text{ mm} \times 0.2 \text{ mm}$ (H x V). Scan parameters included 2000 projections for CTs in full-acquisition mode, with exposure time in the order of 250 ms.

3.3 X-PCI-CT image reconstruction and processing

All image processing steps used in this Thesis work are described in this chapter. Image processing is intended as all the operations applied to the acquired raw CT projection radiographs in order to obtain the results presented in **Chapters 4-8**. A workflow diagram summarizing the most relevant image-processing steps can be found in section **3.4.4**.

3.3.1 Phase retrieval and CT reconstruction

The first step after acquisition of X-PCI-CT datasets is the so-called phase retrieval process, which is slightly different for PB X-PCI-CT datasets compared to holotomographic ones.

Propagation-based PCI:

In the case of PB-PCI, radiographs were first normalized against the incoming X-ray beam and against background noise after collection of so-called flat-field and dark-field images. Paganin's phase retrieval (Paganin *et al.*, 2002), specific for single-distance PB-PCI of a homogenous object, was then used to extract simultaneously phase and amplitude maps from single-distance defocused radiographs. As already mentioned, this algorithm, based on the transport of intensity equation (TIE), assumes an infinitely-far source of planar X-rays, and a beam intensity at the exit of the measured object governed the by Beer-Lambert law.

In practice, at the ESRF the phase-retrieval algorithm is implemented within the PyHST2 software platform (Mirone *et al.*, 2014), which assumes uniform spatially-coherent monochromatic SR X-rays, small beam divergence, and kinematic propagation. This algorithm can be used also in the case of non-homogenous objects, and becomes increasingly less quantitative the more the experimental conditions differ from the algorithm's assumptions.

The main input for this phase retrieval algorithm is the so-called Paganin Length L , s.t

$$L^2 = 4\pi^2 d \frac{\delta}{\mu} = \pi\lambda d \frac{\delta}{\beta}$$

with d the sample-to-detector distance, δ and β the real and imaginary components of the complex index of refraction n , using $\mu = \frac{4\pi\beta}{\lambda}$ in the last step. Note how, for a given sample-to-detector distance, L depends on the δ/β ratio and on the X-ray beam wavelength λ . Values of L as a function of the X-ray energy, for several different bio-materials, including brain tissue, and two different sample-to-detector distances, 2.3 and 11 m, are plotted in **Fig. 3.4** below.

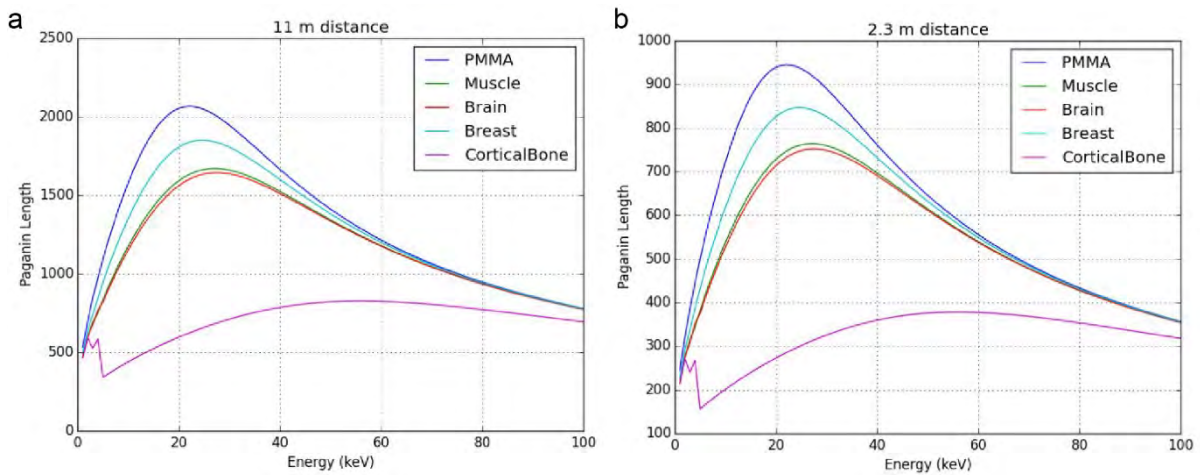


Figure 3.4: Paganin Length, plotted as a function of incoming X-ray beam energy, of different bio-materials and for PB-PCI setups with a sample-to-detector propagation distance of (a) 11 m and (b) 2.3 m. Figure adapted from the ID17 wiki of the ESRF website.

In addition to using the plots in **Fig. 3.4**, in this Thesis work the Paganin-Length L parameter was often determined experimentally by testing several values, and then qualitatively choosing the one, which best seemed to transform edge-enhanced images into phase-based area-contrast maps. An example test is illustrated in **Fig. 3.5**, where the PB X-PCI-CT image of a rodent embryo was computed using several different L values.

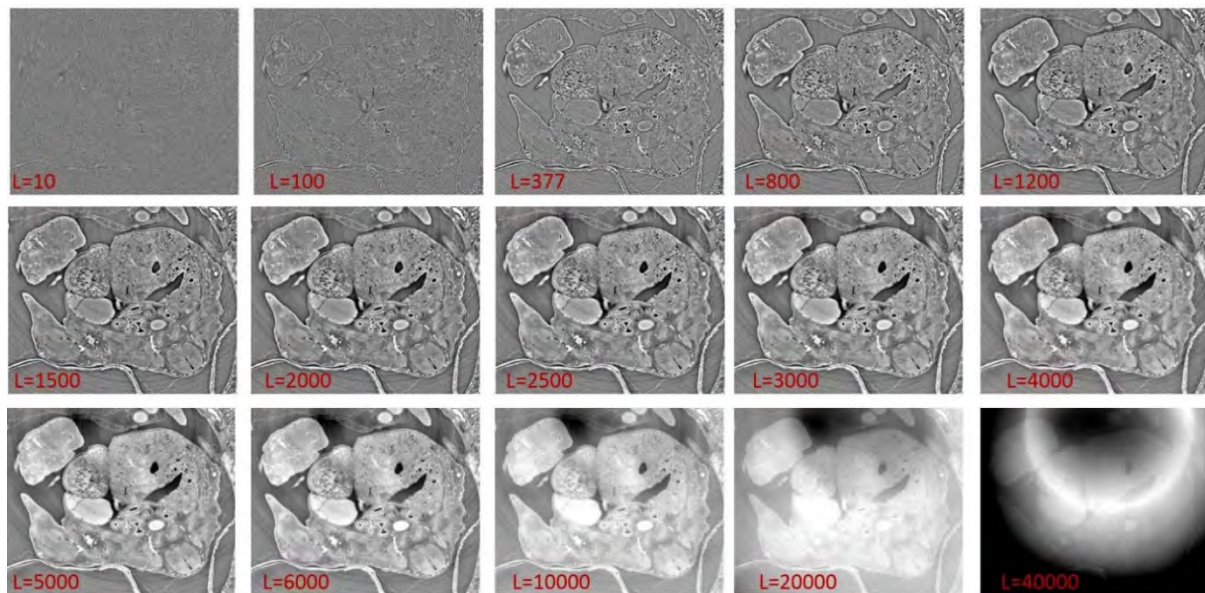


Figure 3.5: PB X-PCI-CT data of a rodent embryo at $46^3 \mu\text{m}^3$ voxel size, computed using PyHST2 and different input Paganin Lengths (L in red). Note a progressive transformation of edge-enhancement into phase-contrast.

Note how increasing values of L lead to the disappearance of the characteristic edge-contrast within PB-PCI images, and the appearance of an area-contrast proportional to the local electron density. Note also how a too high choice in the value of L can lead to blurring, cupping and other image artifacts of the phase-retrieval algorithm. This effect becomes even more evident by plotting the profiles of the edge of the image details in the zoomed panels of **Fig. 3.6**. With increasing values of L , the sinusoidal black-white shapes characteristic of edges in an edge-enhanced un-retrieved image leave space to step-functions at the edges, distractive of well-retrieved phase-contrast images.

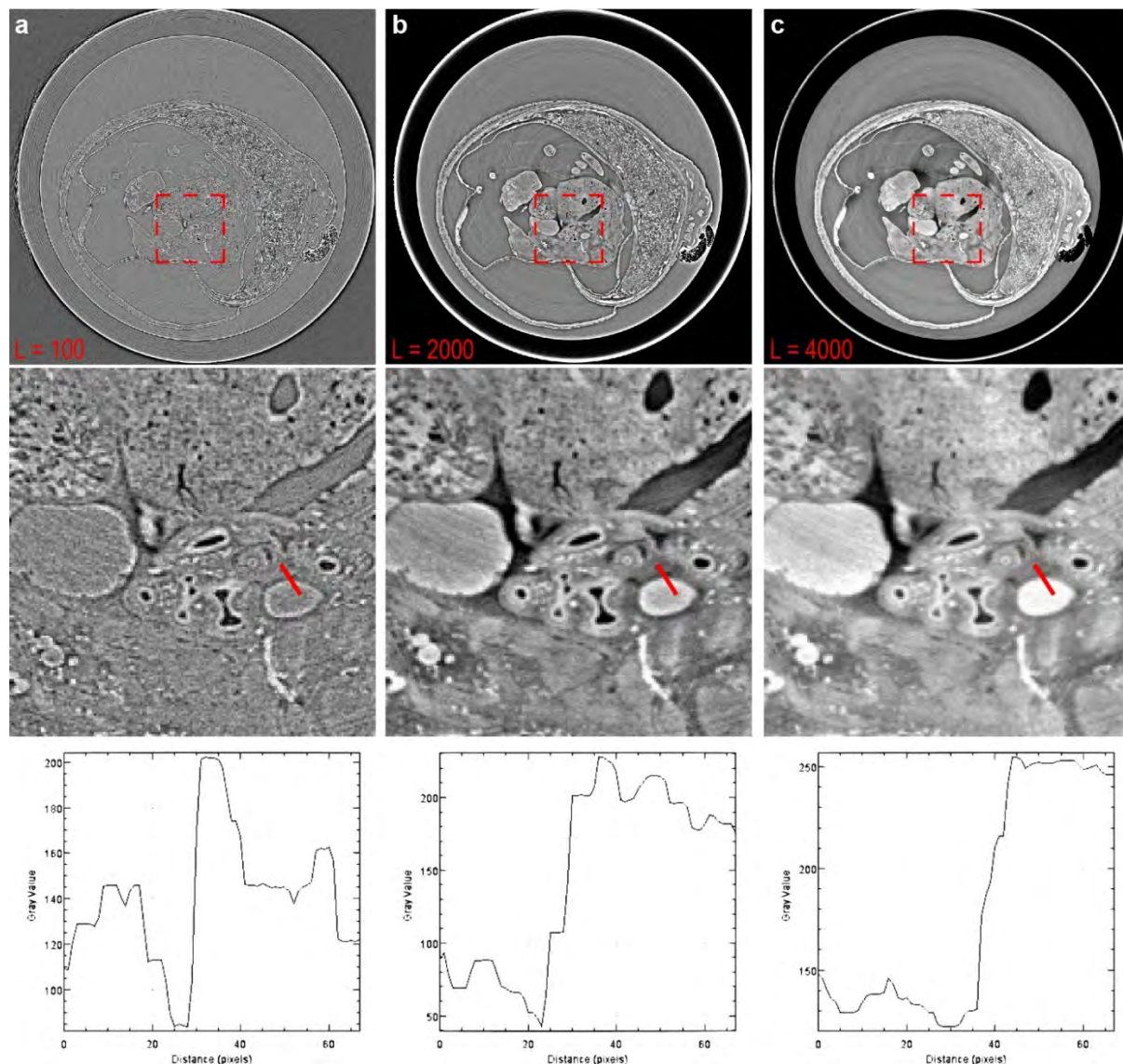


Figure 3.6: Full views of the PB X-PCI-CT data from the same samples as in **Fig. 3.5**, computed in PyHST2 using (a) 100, (b) 2000 and (c) 4000 as input Paganin Lengths. Zoom-ins, extracted from the dashed squares in the CT images, better visualize the transformation of white/black edge-enhancement into area phase-contrast. Plots demonstrate the changes in gray-levels arising at the edge of the feature profiled under the red lines within the zoomed-panels. Note how the edge profile transitions from a sinusoidal shape, characteristic of edge-enhancement regime PCI, to a step function, characteristic of a phase-retrieved image.

For the work in this Thesis, similar sets of images to the ones in **Fig. 3.5** were produced to qualitatively choose the optimal L value to use for the reconstruction of the data of each experimental session at ID17. Establishing a quantitative method to choose L is challenging in practice due to the presence of different image artifacts and the application of this phase-retrieval procedure to measurements of multi-material non-homogenous objects. At TOMCAT, instead, for every 20x magnified dataset, a fixed δ/β ratio of ~ 200 was used as input to an in-house designed phase-retrieval software tool (Marone and Stampanoni, 2012).

Nano-holotomography:

In the case of holotomography, the processing workflow implemented at ID16a was used, i.e. radiographs were also normalized with respect to the incoming X-ray beam, different-

distance sets in cone-beam geometry were brought to the same image magnification and aligned, and then an adapted contrast transfer function was used to retrieve the phase shift in the object plane (P Cloetens *et al.*, 1999; Peter Cloetens *et al.*, 1999; Bleuet *et al.*, 2009). This workflow, which brings raw projections from 4 different CT sets to one 3D phase-contrast volume is also illustrated in **Fig. 3.3**.

CT reconstruction:

CT reconstruction was always performed using the filtered back-projection algorithm (FBP), based on the Radon transform and the Fourier slice theorem (Russo, 2017). At ID17 and ID16a beamlines, PyHST2 software was also used for CT reconstruction purposes. At TOMCAT, instead, a similar in-house platform (Marone and Stampanoni, 2012; Marone *et al.*, 2017), available to users, was used for the same purpose, again based on FBP.

An important part of the CT reconstruction procedure involves the input of a center of rotation (COR) parameter, which defines the horizontal pixel value within collected projections at which the CT rotation axis lies (i.e. projection onto the detector pixel matrix of the sample rotation axis). As can be seen in **Fig. 3.7**, incorrect values for the COR can lead to distinctive half-circle image artifacts. These artifacts can be used to determine the correct value iteratively. Moreover, if these artifacts arise only in certain portions of a reconstructed CT image, they may signify object movement during the CT scan.

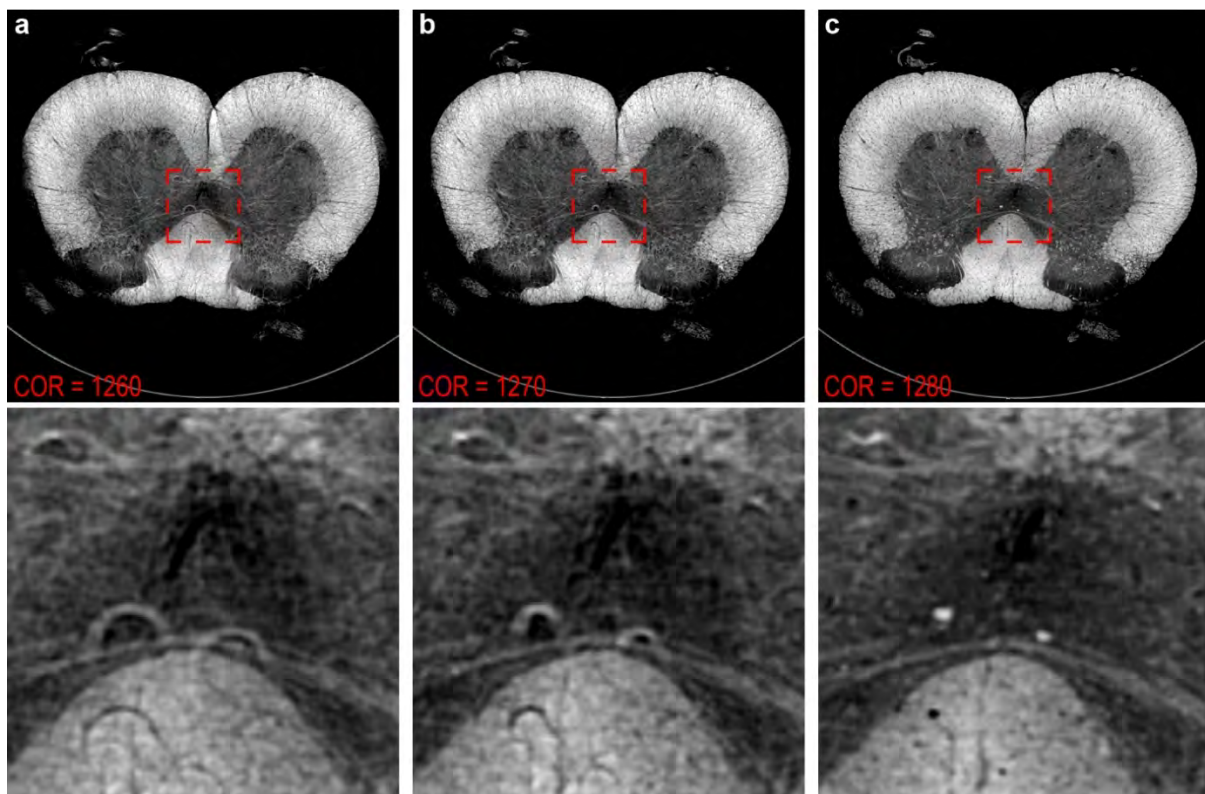


Figure 3.7: 3 μm pixel CT slice of an osmicated rodent spinal cord, computed with increasingly more correct reconstruction centers-of-rotation (COR), (a) to (c). Zoom-ins show typical half-circled COR artifacts, which diminish for better COR input values, and disappear with a correct COR (c), leaving space to well-visualized object internal microstructure.

Overall, the obtained reconstructed images represent 3D maps dependent on the real part of the complex index of refraction, and thus represent 3D datasets proportional to the local electron density ρ_e . Such data served in this Thesis work as a basis for both qualitative and quantitative studies of CNS anatomy and pathology, but often only after several further post-processing steps, required to reduce/remove image artifacts and thereby optimize the visualization of the underlying structures within analyzed samples.

3.3.2 Post-processing of X-PCI-CT images

Various types of image artifacts can arise within X-PCI-CT images of soft tissue, either due to setup imperfections or specific sample properties. Either way, image artifacts should be minimized with a careful setup and sample preparation, if possible, and then should be removed during post-processing, in order to avoid image misinterpretation and biasing of image-based quantifications.

CT image artifacts removal technology is a vast and growing field, and many artifact-specific strategies are readily available today. What follows is a brief description of the most common image artifacts encountered in the X-PCI-CT datasets acquired in this Thesis, and the ways adopted to limit or remove them.

Motion artifacts: synchrotron-based X-PCI-CT datasets are acquired by sample rotation within a fixed planar or conical X-ray beam. These angular movements, even if performed by precise motor stages, may induce unwanted sample movements and lead to artifacts, especially if the sample is not properly fixed within its container and onto the rotating plate. Sample movement may also arise due to X-ray absorption-based sample heating and because of consequent sample deformation. In both cases, the typical artifact consists in half-circle structures similar to the ones, which arise by inputting an incorrect COR in the reconstruction algorithm (**Fig. 3.7**), but in this case limited to a portion of the image and not its entirety. To limit these artifacts, sample preparation for the experiments reported in this Thesis often involved the inclusion of samples in agar-agar gel or paraffin, to avoid mechanical sample motion; moreover, detector integration time and beam filtering were chosen to minimize the deposited radiation dose, especially when evident motion artifacts would arise during test scans. An example of motion artifacts is presented in **Fig. 3.8a**.

Streak artifacts: streaks in CT images may arise due to intra-sample sources of high density gradients, and because of beam hardening and scatter, e.g. when external or internal sharp sample edges, or highly-dense materials, are present within the sample. These sample features lead to discontinuities in the index of refraction, and to mild to strong X-ray deviations and scattering (Hsieh, 2015). This may occur due to air bubbles with sharp density gradients, paraffin edges, and other internal edges within both brain and spinal cord samples. Within images, bright streaks can be observed adjacent to dark streaks, which generally occur in the direction of highest attenuation features. In the experiments in this Thesis work, the main contributors of streak artifacts are air bubbles trapped within brain samples, which can be minimized during samples preparation. Examples of both dark and bright streak artifacts can be seen in **Fig. 3.8b**.

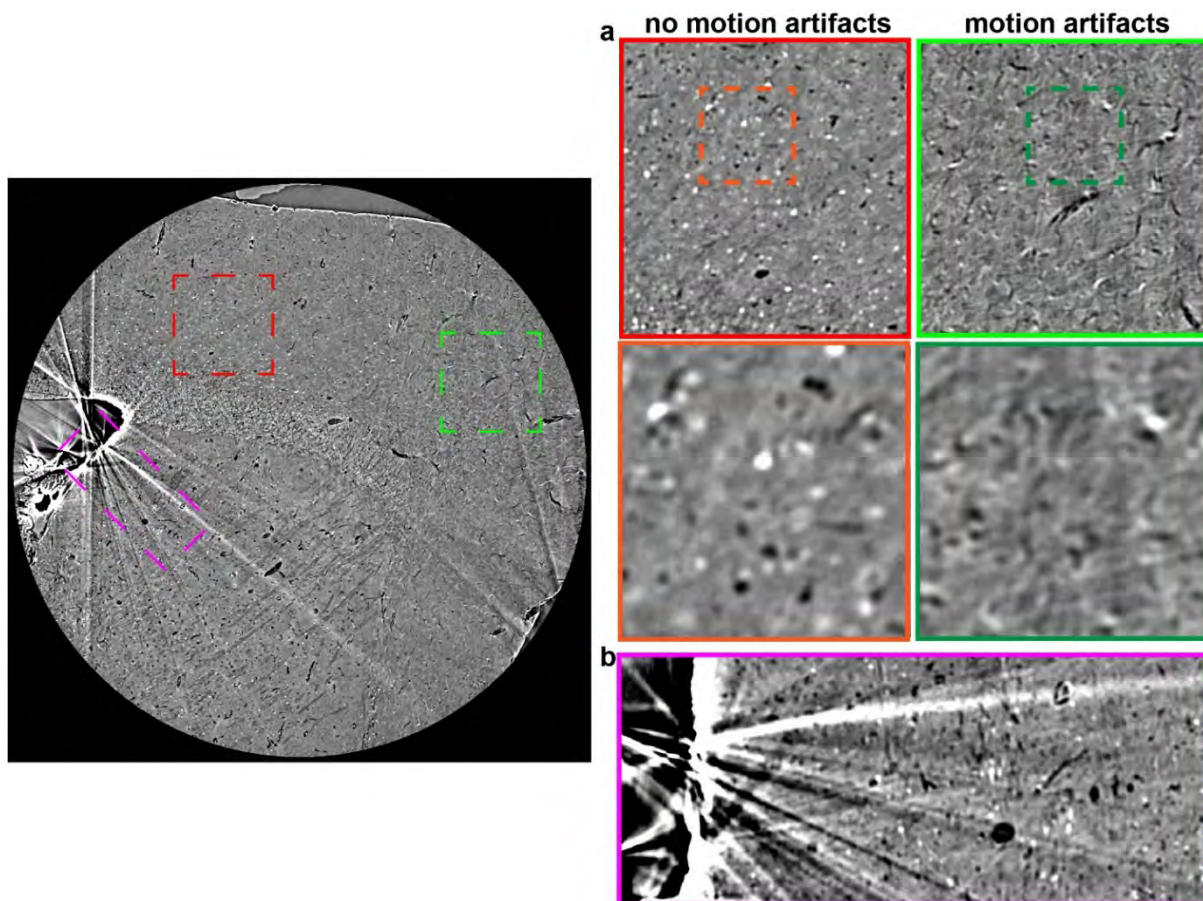


Figure 3.8: a local X-PCI-CT of a rodent brain embedded in paraffin. (a) shows areas of the CT image with no motion artifacts, compared to other areas with small half-circle artifacts, typical signs of an incorrect COR, and thus to sample movement or internal deformation during the scan. (b) shows dark & bright streak artifacts, arising from areas of drastic density gradients, i.e. the sharp edges of air bubbles trapped in a paraffin-filled brain ventricle.

Ring artifacts: maybe the most common of all CT artifacts, ring artifacts consist in the appearance of concentric rings centered at the center of the reconstructed CT image. These artifacts arise due to an aberrant response of individual detector pixels, which is not corrected by flat-field normalization (Vidal *et al.*, 2005). They can be caused by detector defects, but also by defects in other setup optical components, and lead to vertical line artifacts in CT sinograms. In CT, a sinogram is a representation of a set of CT projections on the detector plane, in which each projection line, for each acquisition angle, is stacked into a single image. A point of a scanned object traces, as the object rotates, a sinusoidal path in projection space, and thus in the sinogram. Therefore, the sinogram can be recognized as the superposition of all sinusoids, and a vertical line in the sinogram (i.e. in projection space), after radon transformation, will lead to a ring in the CT reconstruction. In practice, these ring artifacts consist in concentric sharp round waves of image intensity distortion within CTs and can cover image details. In order to be able to use CT datasets for both qualitative evaluations and also for quantification, these artifacts need to be removed. In this Thesis work, a published post-processing ring-correction MATLAB tool implemented in the CT workflow at the ID19 beamline (Lyckegaard, Johnson and Tafforeau, 2011) was used to successfully remove most of the rings produced during experimental sessions both at the ESRF and at SLS. An example

CT filled with unwanted ring artifacts, as well as its corrected version after application of the algorithm by Lyckegaard and coworkers, is displayed in **Fig. 3.9**.

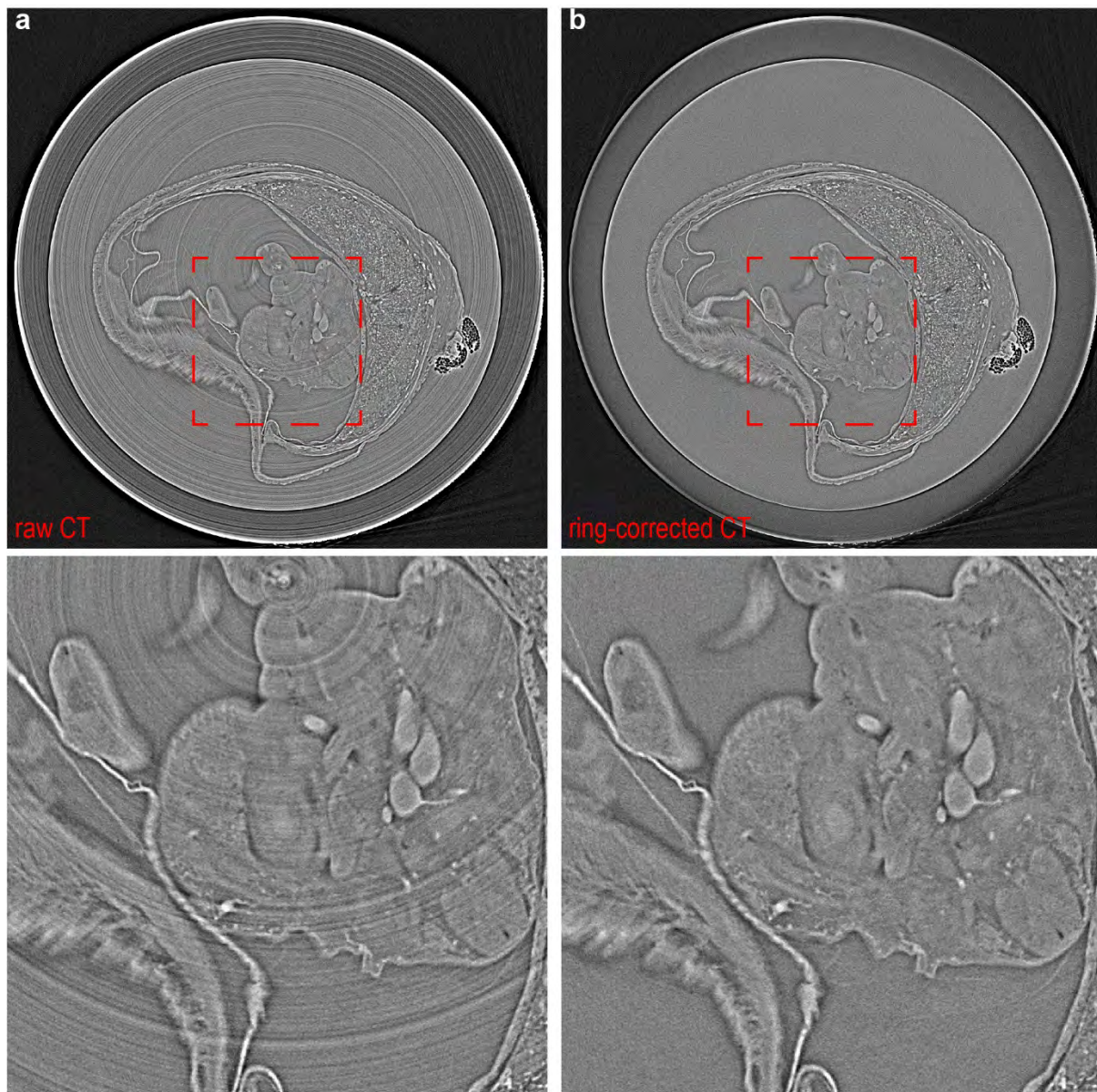


Figure 3.9: (a) un-corrected CT image, with 46 μm effective pixel size, of a rodent embryo, showing abundant ring artifacts. (b) the same CT image as in (a), but after ring-correction with the algorithm described in (Lyckegaard, Johnson and Tafforeau, 2011).

Cupping artifacts: in standard CT, these artifacts are normally related to radial intensity gradients arising artifactually, due to beam hardening (Vidal *et al.*, 2005). Beam hardening names as the effect, which occurs in matter while low-energy photons are absorbed with higher probability than high-energy ones. This effect leads to a differential attenuation of different parts of an X-ray beam spectrum. During the CT imaging of thick samples with a polychromatic or pink beam, this leads to an underestimation of object thickness, and to bowl-shaped radial CT image profiles. Interestingly, similar artifacts arise also with monochromatic X-ray beams, due to acquisitions in local tomography mode (Kilegran, 2019), as illustrated in **Fig. 3.10**. Local tomography can in fact be defined as a CT scan, in which the sample is horizontally larger than the FOW of the setup. Since, in this case, data is missing

within projection images, the reconstruction algorithm itself generates the cupping. Local CT images, in fact, become “contaminated” by the (unknown) attenuations by parts of the object outside of the FOV, and artifacts due to local-CTs can increase in severity the smaller the FOV is with respect to the object size, and in the presence of highly-absorbing materials outside of the FOV (Gompel *et al.*, 2004). Also in this case, their radial shape resembles that of a cup.

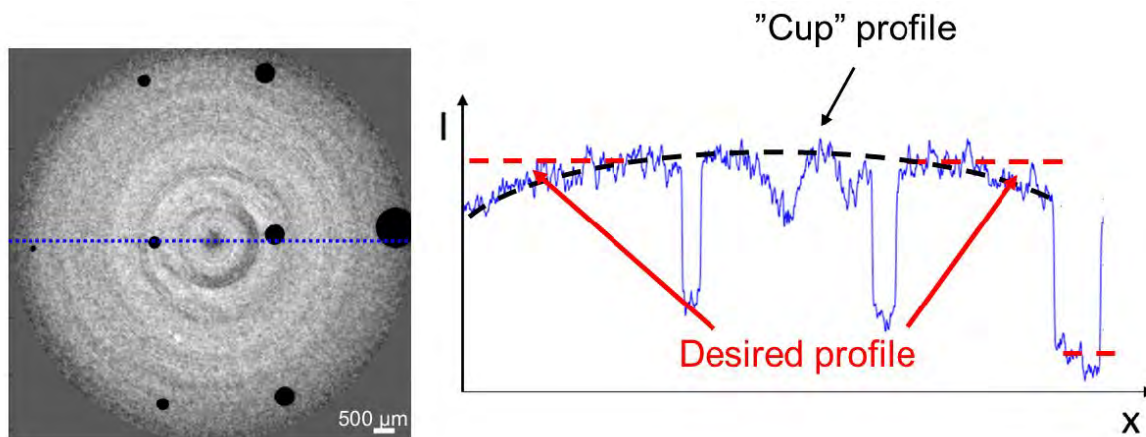


Figure 3.10: demonstration of cupping artifact arising in a CT with monochromatic X-ray beam in local tomographic mode. Within a homogenous material, the blue intensity profile shows a curved “cup” shape, instead of the expected flat profile shape (red). Figure taken from (Kilegran, 2019).

In the neuroimaging X-PCI-CT datasets acquired in this Thesis work, some cupping effects, similar to the one in **Fig. 3.10**, could be recognized, and at times appeared quite prominent. Since CNS tissues are relatively low-absorption samples, when working with polychromatic/pink beams cupping artifacts arose only up to some degree due to beam hardening. Instead, they appeared most prominently in cases of local tomography and monochromatic beams. A few examples from CNS datasets in local tomography, from monochromatic-beam CT with both 3 and 0.3 μm effective pixel sizes, can be found in **Fig. 3.11**.

In order to get rid of these marked cup-shaped intensity gradients, a simple image-dependent normalization procedure was designed and implemented as part of this Thesis work. Mathematically, the normalization consisted in the spatial filtering of the raw CT image I_{raw} via a convolution with the smoothing low-pass Gaussian kernel G , to create a map of the unwanted low-frequency cup-like intensity variations. G blurs the image in a circularly symmetric way. Moreover, it represents a separable kernel (Gonzalez and Woods, 2018), which therefore can be applied on a 2D image as a sequence of 1D convolution filters. The 1D kernel is of the form:

$$G(x) = \frac{1}{\sqrt{2\pi}\sigma} e^{-\frac{x^2}{2\sigma^2}}$$

with σ the standard deviation of the Gaussian distribution, and σ^2 the Gaussian blur radius. Applied to an image, it smooths its gray-levels by computing for each source pixel the Gaussian-weighted average over its neighbor pixels. The larger σ is, the wider is the Gaussian function and the more further-away pixels are involved in the averaging, so than a selection

of a very large value of σ will completely blur-out small local features and only maintain very broad image trends. In order to correct the cupping artifacts, the raw CT images were normalized against their Gaussian-blurred version (with large σ), and thereby highlight high-frequency image components and flatten the low-frequency ones (suppressed in the division by the low-frequency Gaussian-blurred images). Mathematically the normalized image I_{norm} was computed as:

$$I_{norm} = \frac{I_{raw}}{G(I_{raw})}$$

In practice, the implementation of this procedure was done via a python script, which for G uses a multidimensional Gaussian filter, taking as input parameters I_{raw} , as input array, and the desired value for the Gaussian blur radius (σ^2), as input filter size. The values of σ^2 , which proved effective to flatten the cup-shaped local-tomography CNS X-PCI-CT images in this Thesis, were generally in the 20-60 range. **Figure 3.11** shows the effects of this normalization procedure for two X-PCI-CT neuroimaging examples at different spatial resolutions.

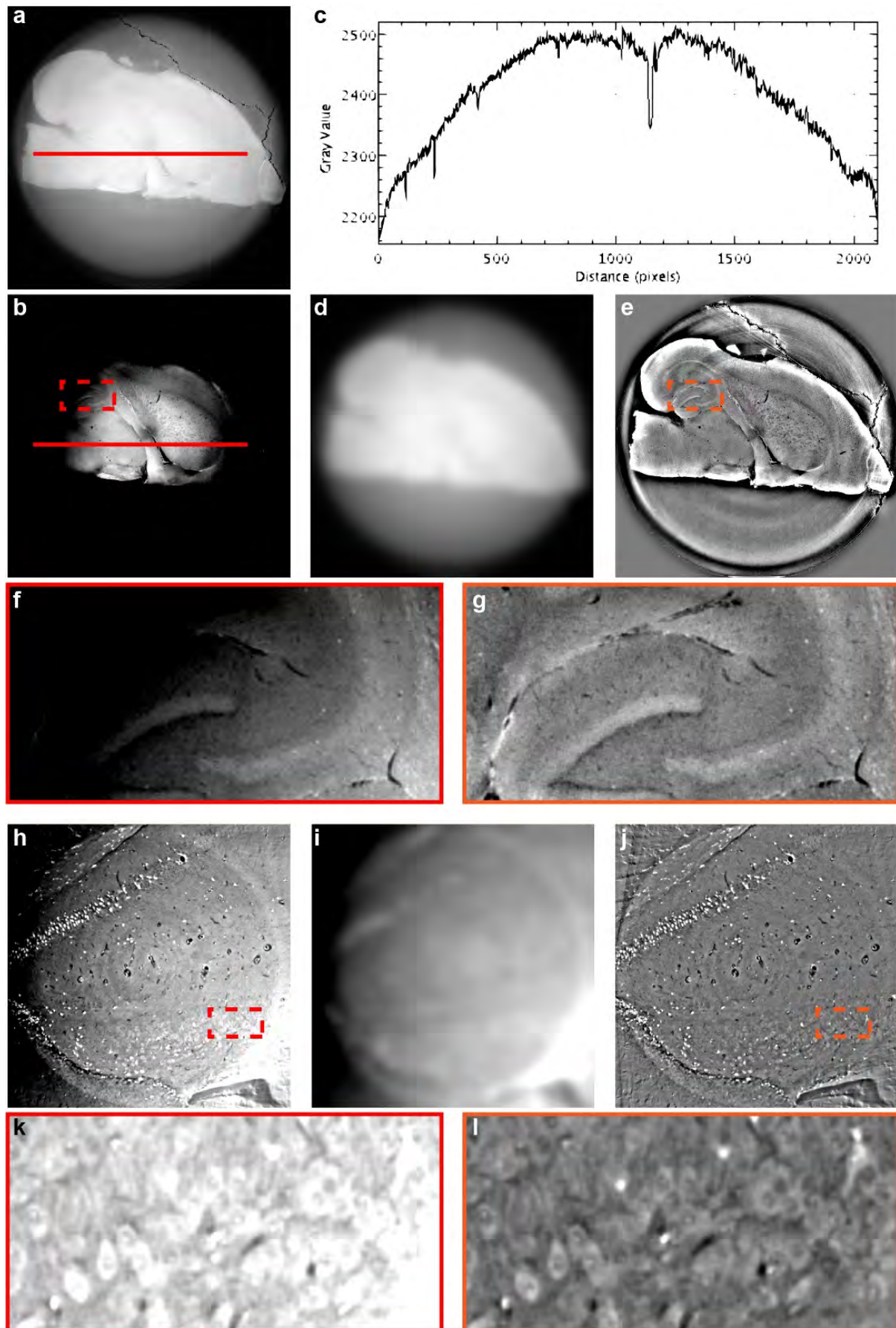


Figure 3.11: (a) local X-PCI-CT, with $3\ \mu\text{m}$ effective pixel size, of a paraffin-embedded mouse brain sample. (b) the same image as in (a), but with gray-level image windowing adapted to the central part of the image. (c) cup-

shaped gray-level profile obtained from the red-traced line in (a-b). (d) Gaussian-filtered version of image in (a-b). (e) G-normalized version of image in (a-b), obtained by division with image in (d). (f) raw vs. (g) G-normalized image detail taken from (b) vs. (e) images respectively. (h) local X-PCI-CT, with 0.3 μm effective pixel size, of a paraffin-embedded mouse brain sample, centered at the hippocampal layers. (i) Gaussian-filtered version of image in (h). (j) G-normalized version of image in (h), obtained by division with image in (i). (k) raw vs. (l) G-normalized image detail taken from (h) vs. (j) images respectively.

Noticeably, normalized results in **Fig. 3.11 (Fig. 3.11e,j)** lack the artifactual bowl-shaped intensity variations of input datasets (**Fig. 3.11a-b,h**), and achieve a homogeneity of gray-levels within same-material object components, especially within the central parts of objects. The goodness of the normalization is especially well visible in the detail views (**Fig. 3.11f vs g** and **k vs l**), which visualize tissue and cellular anatomy previously obscured/saturated by the artifactual intensity gradients. All the same, other artifacts are introduced, including an overall flattening of true local area contrasts (**Fig. 3.11e,j**), which were present in raw images between neighboring tissue structures before normalization, as well as a strong aberrant enhancement of bright and dark bands at object edges (**Fig. 3.11e**). The bright/dark bands arise, since this Gaussian-normalization procedure enhances high-frequency components, both within and around the sample. To limit the impact of these new edge artifacts, G-normalized CT images were often masked to exclude background and edges of a sample, and isolate only the flattened internal parts of organs of interest.

3.4 Procedures for 3D quantification

Even more so than during post-processing, analysis steps very much depend on the sample under investigation and the underlying research questions of a specific scientific case. For this reason, the specifics regarding analysis objectives of individual experiments are detailed in **Chapters 4-8**. Overall, though, a few key processes can be identified as common analytical steps useful to most of the experiments presented in this work. For this reason, they are briefly outlined below.

3.4.1 Data masking

CT images, and brain images especially, were often masked during analysis to remove the unwanted background (paraffin, formalin etc.) from the sample. And even more important that sample visualization, background removal was useful to simplify segmentation and quantification procedures, and make image analysis more precise. For this purpose, the Segmentation Editor plugin of the open-source software platform FIJI (Schindelin *et al.*, 2012) was used. Via the plugin, individual slices can be manually masked. In this Thesis, to correctly mask an entire 3D CT dataset, about 10% of the slices, evenly distributed throughout the stack, were manually masked, and interpolation was then used to connect the 2D and achieve an acceptable 3D mask of the full sample. Simple multiplication of the 3D CT dataset with the

3D mask then afforded a masked 3D dataset of the sample stripped of its (unwanted) background. An example of the result of a 2D brain masking is displayed in **Fig. 3.12**.

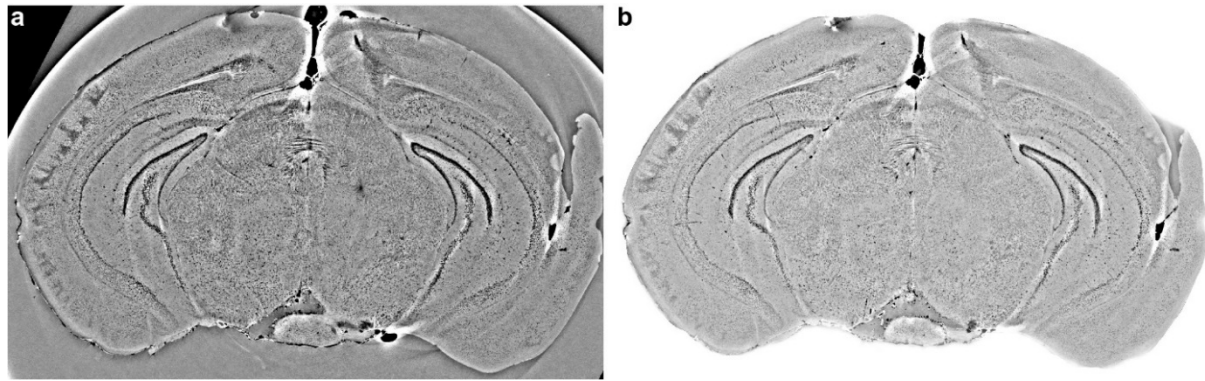


Figure 3.12: manual masking procedure of a rodent brain 2D slice, using the Segmentation Editor plugin in FIJI. (a) unmasked slice. (b) masked background-free brain sample.

3.4.2 3D PCI-data segmentation

The separation of different key neuroanatomical and pathological features within images of CNS system samples is a broad methodological task, which generally involves the application of different segmentation strategies. In neuroimaging, some of the most common features of interest are e.g. different brain tissue regions, such as the amygdala or hippocampal layers, vasculature and micro-vasculature, cellular structure, such as cell somas or axonal matter, and pathological features, such as tumors or calcifications. Since each feature often involves a different strategy tailored to best suit its image properties, only a brief overview of methodological options is presented here. The specific strategies used in this Thesis to obtain the presented experimental results are described in the methodological sections of individual experiments (**Chapters 4-8**).

The simplest way to extract features of interest is a threshold-based segmentation. Given a gray-level threshold value T and an input image $I(x,y)$, the binary threshold-based segmentation mask $S(x,y)$ can be constructed, pixel by pixel, as $S(x,y) = 1$ if $I(x,y) > T$, $S(x,y) = 0$ otherwise. This is often also referred to as a global thresholding method (Gonzalez and Woods, 2018). The ‘art’ in a threshold-based segmentation procedure is the method for selection of the threshold value T . Especially when the segmentation serves as a basis for quantification of image features in different experimental groups, an unbiased possibly-automated threshold selection method is of paramount importance. For this reason, many different gray-level-based algorithms for automatic image segmentation have been implemented by the imaging and image analysis research communities.

In this Thesis work, auto-threshold segmentation procedures have been performed using different algorithms available in the open-source ImageJ software package (Schneider, Rasband and Eliceiri, 2012), and are all based on the shape of image intensity histograms. As already evident in X-PCI-CT neuroimaging literature (Pinzer *et al.*, 2012), especially useful for the automated extraction of hyper-dense particle-like image features is the Maximum Entropy algorithm (Kapur, Sahoo and Wong, 1985). Other algorithms, which worked well for different neuroimaging applications, were the Triangle algorithm (Zack, Rogers and Latt,

1977) and Otsu's algorithm (Otsu, 1979). As an example, **Figure 3.13** shows the effect of the Max Entropy auto-threshold algorithm on a nano-CT slice of cortical brain tissue affected by Alzheimer's Disease (AD), i.e. the extraction of hyper-dense globular intra-cellular hyper-dense deposits from low-density healthy brain parenchyma.

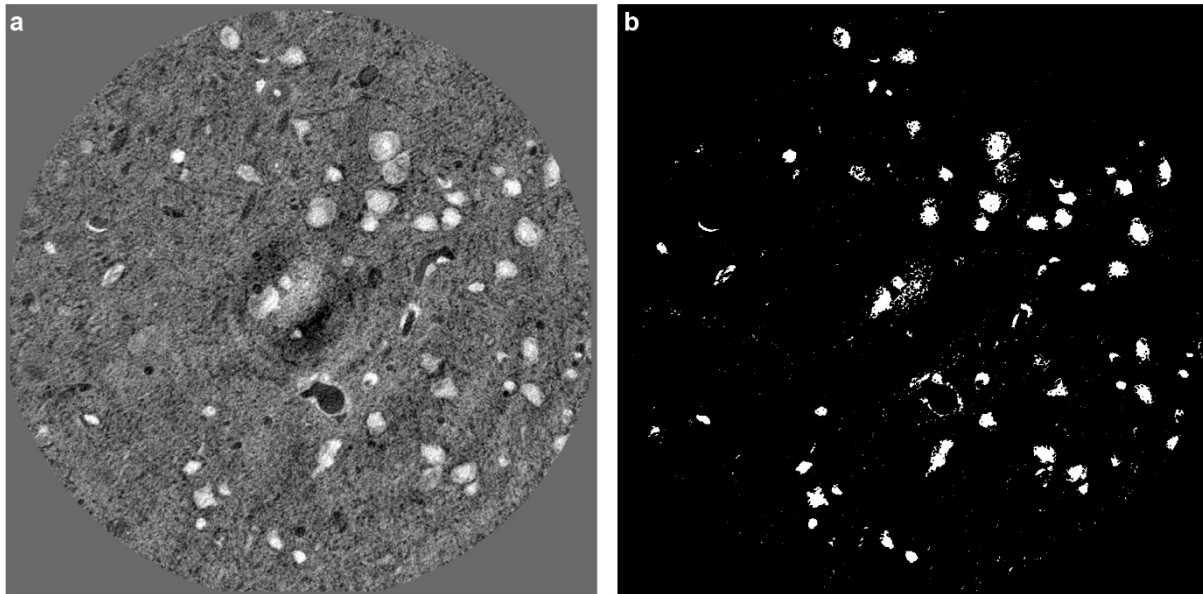


Figure 3.13: (a) a nano-X-PCI-CT of a cortex tissue affected by AD pathology. The globular hyper-dense image features in (a), mainly hosted within neuronal cells, are segmented to create the binary mask in (b) via the Max Entropy auto-threshold segmentation algorithm (Kapur, Sahoo and Wong, 1985) implemented in ImageJ.

Multiple other segmentation techniques, different from threshold-based ones, were also employed in this Thesis for certain specific purposes. The semi-manual implementation of region-growing algorithms in the commercially-available software VG Studio MAX (Volume Graphics GmbH., 2001), was often used, for example, to extract individual objects, e.g. large AD plaques, single vessels, tumor tissues or deposits of calcium and iron. Last, watershed algorithms (Brun *et al.*, 2014) were also occasionally employed to extract broad tissue structures.

3.4.3 3D object measurements

After segmentation-based feature extraction from 3D CT datasets, the obtained feature-specific (masked) 3D datasets can be analyzed to extract various morphological parameters. A summary of the main tools used in this thesis can be found in **Table 3.1**.

Computational Tool in ImageJ	Input Dataset	Output Morphological Parameter	Anatomical Feature
3D Object Counter plugin	16bit gray-valued image stack	volumes of unconnected particles	Volumetric cell size
Local Thickness plugin	binary image stack	tubular structure thickness	thickness of blood vessels
Skeletonization & AnalyzeSkeleton plugin	binary images	skeleton branching parameters (e.g. branch lengths)	vascular network branching

Table 3.1: Summary of the ImageJ computational tools used in this Thesis work to extract different morphological image parameters. These parameters enabled the quantification of different CNS anatomical features.

In neuroimaging, parameters of interest are usually related to anatomical properties of nervous tissue, e.g. cell counts and cellular population densities, cell sizes, vascular thickness, brain region volumes, white matter orientation.

The main tool employed to measure 3D morphological properties of unconnected populations of objects has been the 3D Object Counter plugin (Bolte and Cordelières, 2006) of ImageJ, which provides a computation platform for the separation of unconnected pixel groups within binary masks and the measurement of the volume and surface of each individual pixel group. A built-in threshold segmentation tool permits here the use directly of unsegmented 16bit gray-valued image stacks. The analysis of populations of objects within extended 3D datasets, then, permits the extraction of size distributions, which can characterize the objects themselves. This tool proved especially well suited, for example, for the extraction of size distributions of different cellular populations co-inhabiting the same nervous tissue specimen, as illustrated in **Fig. 3.14**. In this case, 3D object volume counting within a tissue sample affected by AD permitted the distinction, based on size, of three cellular populations, i.e. small nucleoli of normal amyloid-negative neurons, large amyloid-positive neurons, and intermediate-size neuro-glial cells.

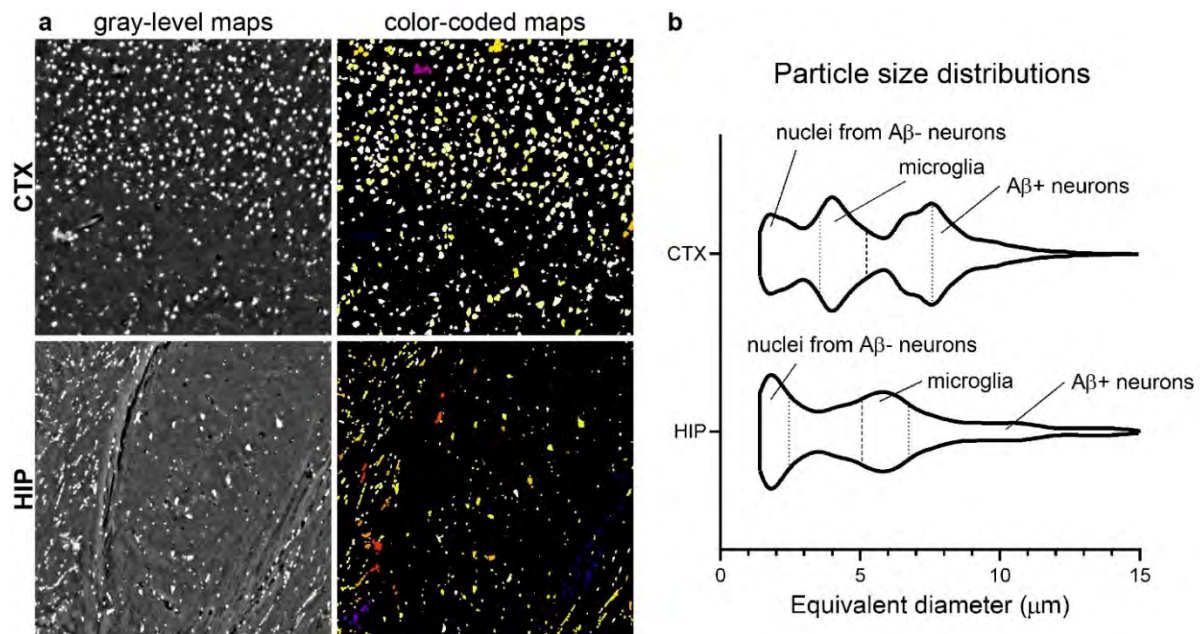


Figure 3.14: (a) measurement of individual object volumes of cell-like object populations within a cortical and a hippocampal brain slice of a rodent brain affected by AD, using the 3D Object Counter ImageJ plugin. The inputs to the plugin are the gray-level X-PCI-CT maps. The outputs of the plugin are color-coated maps, which measure and label individual unconnected objects, and correlated data tables filled with the results of the measurements (not shown). Using the output data tables, size distributions as in (b) can be extracted, with the size parameter here expressed as an equivalent diameter, computed from volume data after the assumption of spherical object shapes. (b) shows tri-modal size distributions, sign that at least three size-based different object populations are present in the input gray-valued maps in (a). Further analysis (see Results) could in this case identify these objects as either large amyloid-positive neurons, small nucleoli in normal amyloid-negative neurons, or intermediate-size microglia.

Other types of parameters of interest, different from object size, instead, may better characterize extended multi-part structures such as vascular networks. In fact, since vessels are interconnected tubular features, they are often quantified in terms of their local thickness and branch length. In this Thesis, two other ImageJ tools, i.e. the Local Thickness plugin (Hildebrand and Rügsegger, 1997) and the Skeletonization & AnalyzeSkeleton plugin (Arganda-Carreras *et al.*, 2010), were successfully applied for such purposes, e.g. in the quantification of vasculature thickness and branching within micro-X-PCI-CT datasets containing spinal cord vasculature, as illustrated in **Fig. 3.15**. Local thickness measurements (**Fig. 3.15b**) are computed on binary masks, in turn obtained, once again, via threshold-based segmentations of original gray-level maps (**Fig. 3.15a**). Skeleton parametrizations (**Fig. 3.15c**), instead, were computed directly on the gray-level maps.

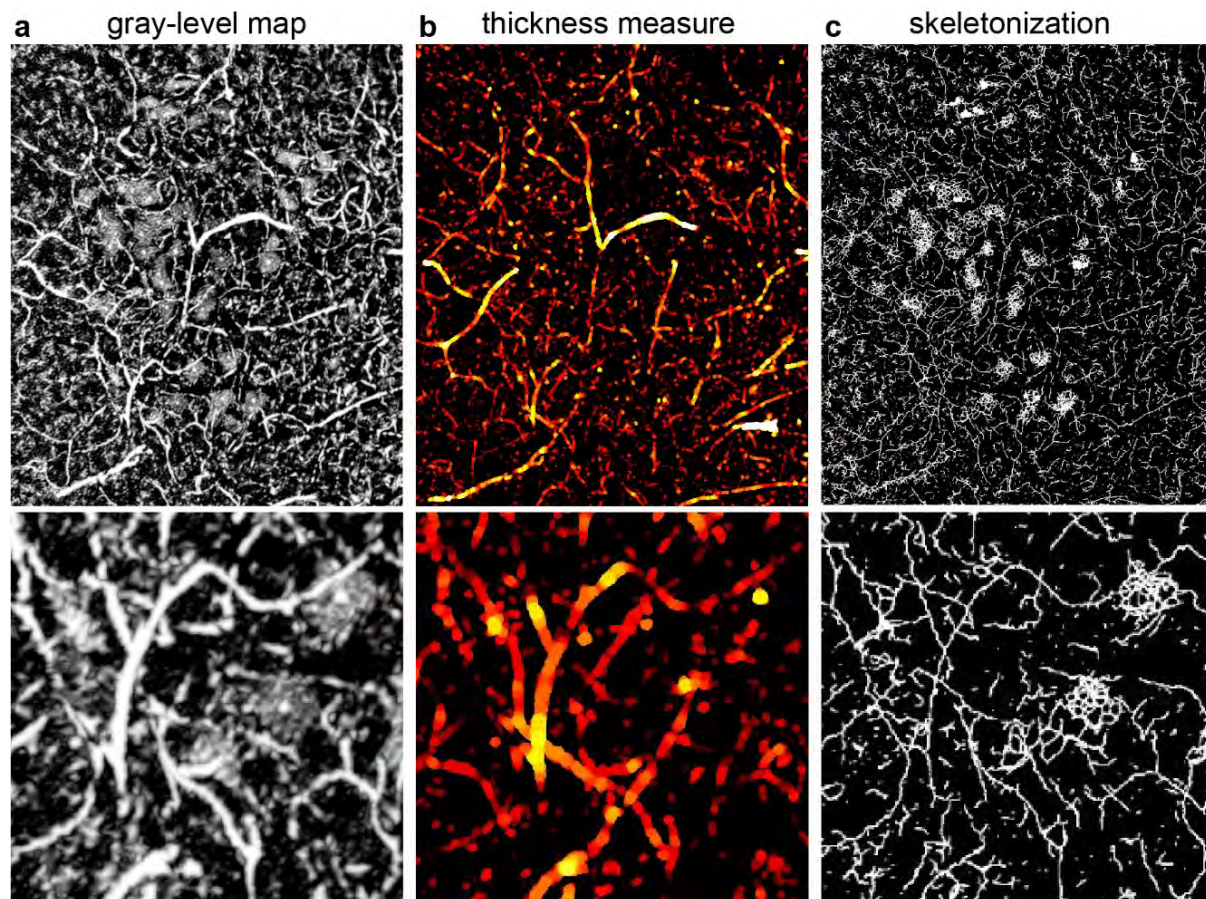


Figure 3.15: (a) gray-level map of local spinal-cord tissue, showing tubular vascular-network features and several neuron cells. (b) quantification of the thickness of local vascular structures, obtained via the Local Threshold plugin (Hildebrand and Rügsegger, 1997) applied to a threshold-based mask of (a), tailored to extract local vasculature. (c) skeletonization of hyper-dense features in (a), obtained via application of the Skeletonization plugin (Arganda-Carreras *et al.*, 2010) directly to (a). Note how cellular features may influence the obtained skeleton.

The obtained color-coded local vasculature thickness distributions are easily interpretable, since the obtained colors encode the local thickness value of each pixel between borders of tubular structures, and can be transformed in quantitative thickness distributions in a straight-forward way, i.e. by collecting all image pixel values in a histogram. After skeletonization, the analysis of branching patterns, instead, is complex, and results are more prone to error, especially when the image contrast of vascular features is not high enough to avoid artifactual interruptions in the local networks, or when unwanted cellular features influence the extracted skeleton itself. The latter case can occur, for example, when cell bodies, cell nuclei, or nucleoli hold the same gray levels as their surrounding (supplying) vasculature. For these reasons, in the end, only local thickness maps were used in this Thesis for vascular feature quantification purposes.

Overall, since further and more original technical development of quantification technology for morphometric CNS studies was deemed beyond the scope of this Thesis work, the two main tools for quantitative analysis included the aforementioned 3D Object Counter and Local Thickness plugins. Certainly, these tools have limitations in both scope, and especially speed, with long computation times, in the order of days, needed to analyze binary 3D datasets in

the order of 10^9 voxels large. Other, faster and more flexible solutions may be possible, both via more advanced open-source tool-kits or even via other commercial metrology software solutions.

3.4.4 Workflow design for the quantification of X-PCI-CT neuroimages

To summarize all image post-processing & analysis procedures routinely applied to the CNS X-PCI-CT images presented in this Thesis, **Fig. 3.16** provides a schematic step-wise view of the standard workflow, designed (here) to take raw X-PCI-CT radiographs, collected during experimental sessions, and from them obtain volumetric analyses of key neuro-structures.

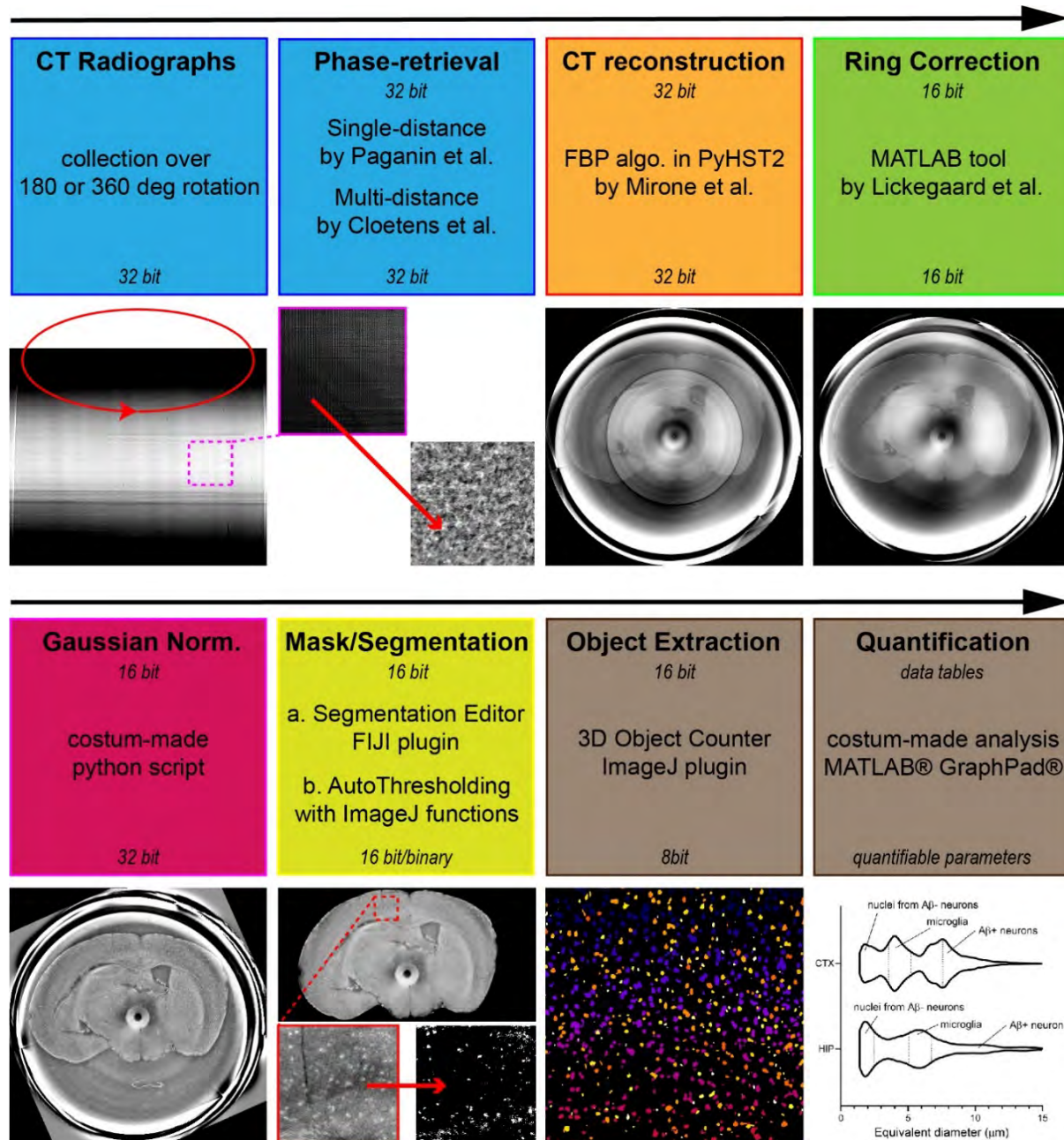


Figure 3.16: Schematic view of the standard workflow adopted in this Thesis to process and analyze X-PCI-CT neuroimaging datasets. Bit size of input and output images after each key step is reported, along with key contributions from the literature or from various publically-available computing tools.

3.5 Procedures for CNS feature visualization

Before presenting experimental results, a brief overview of common feature visualization procedures is summarized here. In fact, while 3D X-PCI-CT datasets, and image features within them, may be viewed most simply by scrolling through the thousands of slices of each dataset, other methods are more effective and powerful in extracting and visualizing the CNS structure captured within them, and are thus worthy of a brief dedicated methodological discussion.

3.5.1 MIPs and mIPs

Maximum intensity projections (MIPs) and minimum intensity projections (mIPs) functions (available in ImageJ software, for example) can be used to highlight respectively hyper-intense (MIPs) and hypo-intense (mIPs) image features within a stack of CT slices. These functions project each 3D stack's brightest (darkest) pixels onto the common 2D plane in the stack direction, mimicking in some ways a radiographic projection image. The resulting image is basically a collapse of volumetric image features onto a flat image, thereby rendering inter-slice information, which was difficult to observe on individual slices. As illustrated in **Fig. 3.17**, MIPs and mIPs can be used, for example, to better characterize vascular network development within nervous tissue or make specific cell-structure within certain neural layers more evident.

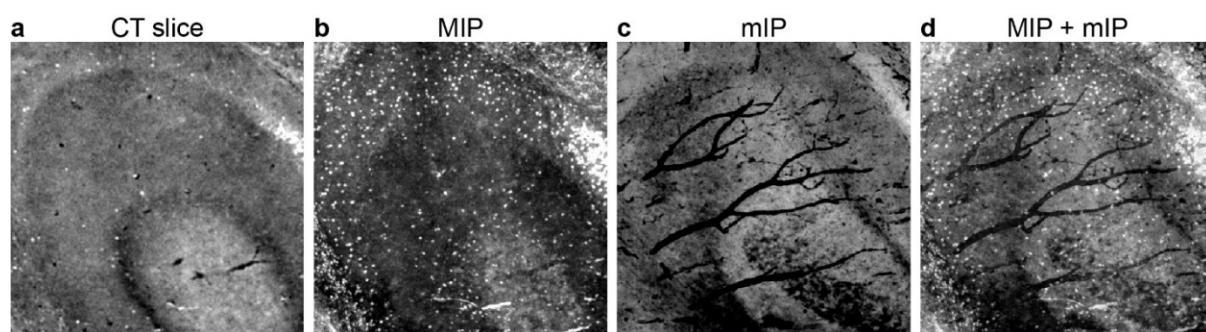


Figure 3.17: (a) local crop of a single CT slice of rodent brain hippocampus structure. (b) MIP map computed from the 50 CT slices consecutive to (a). (c) mIP map computed with the same slices as in (b). (d) Sum of (b) and (c).

Interestingly, by summing MIPs and mIPs of the same stack together (**Fig. 3.17d**), the simultaneous representation of hyper-dense and hypo-dense structure enables the concurrent study of diverse anatomical and pathological structures within the same dataset, as well as their volumetric morphological interplay.

3.5.2 3D rendering

A 3D virtual visualization of CT datasets can be achieved via various methods of 3D rendering of volumetric image data. In this Thesis work, the main tool used for this purpose has been the commercial software tool for pixel solutions called VG Studio MAX (Volume Graphics GmbH., 2001). Within the software, various segmentation routines as well as rendering

algorithms permit the production of volumetric representations from any input CT stack. In the same way as before quantification, CNS system CT data needs to be segmented into its mayor anatomical and tissue components, before meaningful 3D renderings can be produced. For this purpose, the same (already discussed) segmentation procedures were performed to obtain 3D gray-level masks either before data upload on VG Studio, or also within the software itself. Typical extracted 3D features were vascular networks and cellular populations, as illustrated in **Fig. 3.18**.

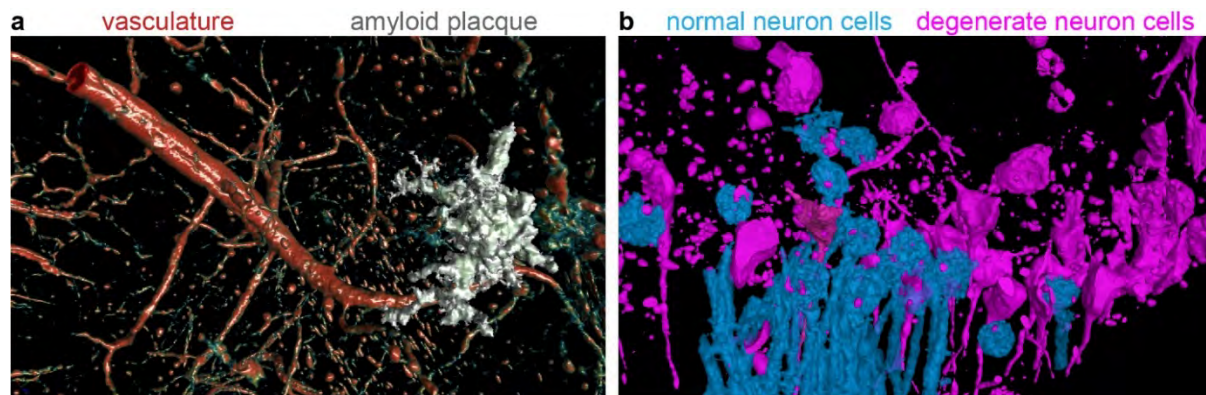


Figure 3.18: (a) 3D rendering of a $3^3 \mu\text{m}^3$ voxel X-PCI-CT dataset containing local nervous-tissue vasculature (red) and an extra-cellular amyloid deposit (amyloid plaque, white/silver). (b) 3D rendering of a $0.1^3 \mu\text{m}^3$ voxel X-PCI-CT dataset containing a hippocampal cell population, in which both normal (healthy) neuron cells (azure) and degenerate neurons (magenta) are present.

After segmentation, features can be recolored to artificial pigments in order to better distinguish different anatomical components within a rendering, e.g. differentiate nervous-tissue vasculature from nervous-tissue amyloid pathology (Fig. 3.18a) or normal neurons from degenerating ones (**Fig. 3.18b**). 3D rendering proved useful in the majority of the experimental neuroimaging applications presented in this Thesis work, especially to help substantiate the added-value of a volumetric virtual X-PCI-CT-based neuroimaging approach compared to 2D histology-based methods.

3.6 Multiscale neuroimaging via X-PCI-CT

The last methodology, central in this Thesis work, has been the design of a multi-scale approach to 3D X-PCI-CT-based neuroimaging of rodent brain samples. In fact, by successive imaging session at different synchrotron facilities and at different experimental X-PCI-CT setups, the same brain samples could be progressively characterized at higher resolution, and thereby analyzed at different physical and biological scales.

The approach involved the collection of the following datasets:

1. 3^3 and $0.7^3 \mu\text{m}^3$ voxel PB-PCI data at the ID17 beamline of the ESRF.
2. $0.3^3 \mu\text{m}^3$ voxel PB-PCI data at the TOMCAT beamline of the SLS.
3. $0.1^3 \mu\text{m}^3$ voxel nano-holotomography data at the ID16a beamline of the ESRF.

In terms of rodent animal-model brain biology, the 3^3 - $0.7^3 \mu\text{m}^3$ voxel imaging spatial regime allowed full-organ to partial organ scanning, without stitching of projections and without further sample dissection, and the visualization of pre-cellular 3D nervous tissue detail. The 0.3^3 voxel spatial regime enabled better spatial resolution, and thereby the acquisition of cellular-level deep tissue maps without need for sample dissection. Without projection stitching, though, these acquisition could capture only more limited sub-regional brain areas. The 0.1^3 voxel imaging data permitted intra-cellular 3D investigations of deep neuron populations, but only after the further dissection of rodent brain samples into $\sim 1 \times 0.5 \times 0.5 \text{ mm}^3$ rods of tissue. Sample images of the same brain sample images with all four different available voxel sizes are presented in **Fig. 3.19**, proving the potential of this multiscale approach to CNS imaging for pre-cellular to intra-cellular visualization of neuronal morphology.

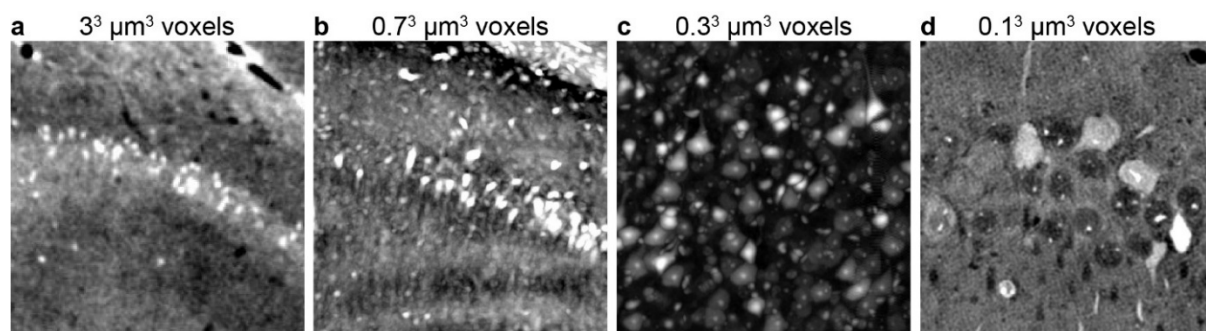


Figure 3.19: multiscale imaging of rodent brain neuronal layers obtained with imaging systems having (a) $3^3 \mu\text{m}^3$, (b) $0.7^3 \mu\text{m}^3$, (c) $0.3^3 \mu\text{m}^3$ and (d) $0.1^3 \mu\text{m}^3$ effective voxel sizes. Increasing resolution enables the visualization of pre-cellular to intra-cellular detail.

Overall, being performed in succession, these acquisitions afforded a platform for label-free 3D microscopy of the CNS with the unprecedented ability to analyze volumetric tissue anatomy and pathology within extended samples, from the broad overall morphology of macroscopic brain areas to the small details of intracellular neuron components. An example of the results obtainable via this multiscale platform for CNS imaging is presented in **Fig. 3.20**, within 2D and 3D renderings of X-PCI-CT data of a rodent brains from an Alzheimer Disease animal model, and more multiscale neuroimaging results can be found in the Results sections of this Thesis.

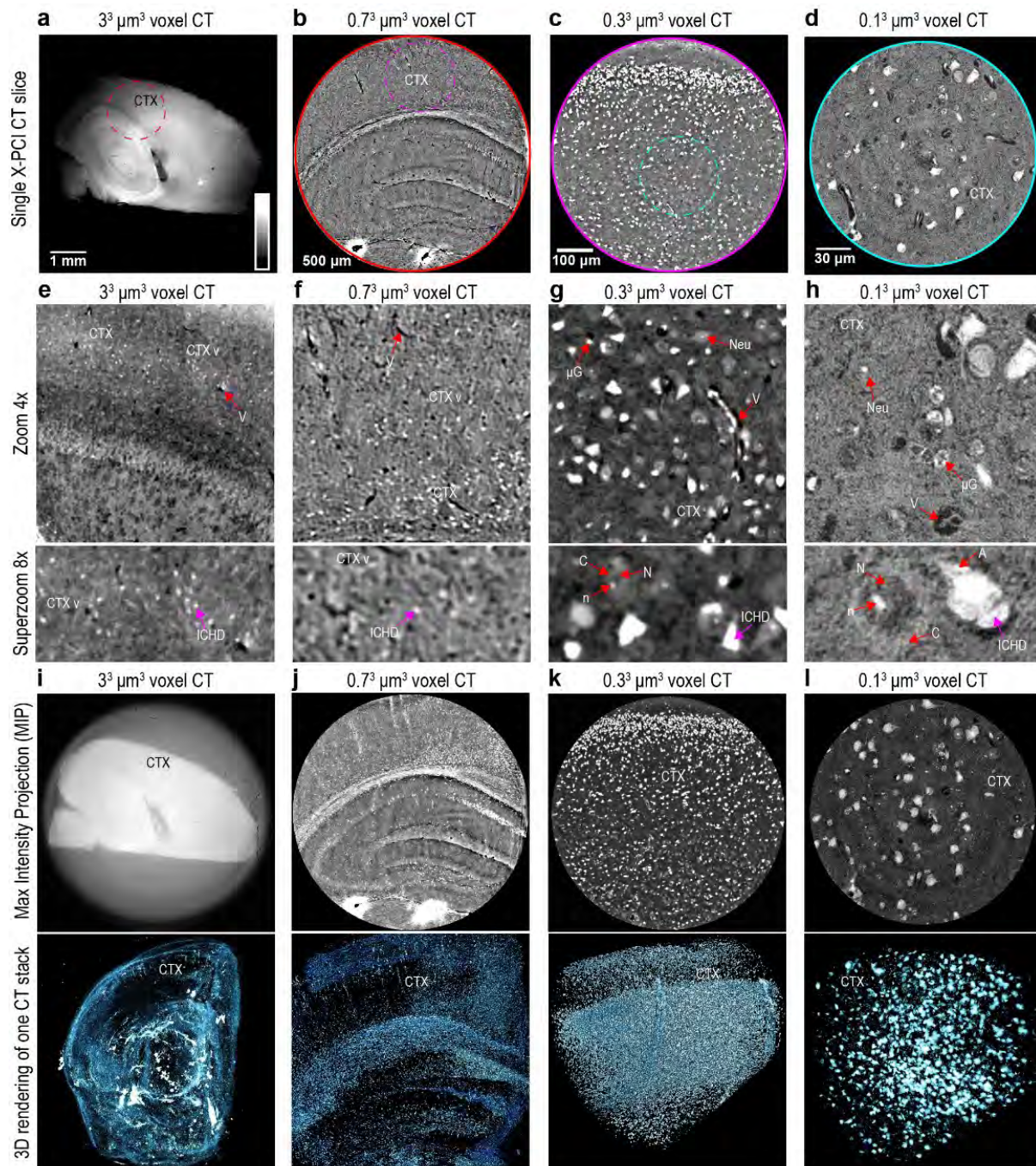


Figure 3.19: the. **a-d**, Illustrative *post-mortem* single X-PCI-CT slices of a paraffin-embedded rodent brain from an Alzheimer's Disease animal model, showing PB micro-X-PCI-CT and nano-holotomography datasets with effective voxel sizes respectively of **(a)** $3^3 \mu\text{m}^3$, **(b)** $0.7^3 \mu\text{m}^3$, **(c)** $0.3^3 \mu\text{m}^3$ and **(d)** $0.1^3 \mu\text{m}^3$. Samples were dissected into $1 \times 1 \times 3 \text{ mm}^3$ rods before nano-holotomography **(d)**. The full-brain maps **(a)** are suitable for complete pre-cellular organ analysis, and can be used to aim successive same-sample local micro-CTs **(b-c)**. This multi-scan approach allows a multiscale neuroanatomical exploration of selected brain regions, e.g the cortex (CTX), and of specific layers, e.g. pyramidal neurons of the v^{th} cortical layer (CTX v), and the probing of angio- & cyto-architecture at the intra-cellular level. **e-h**, Zooms (4x **a-d**) show non-sparse representations of **(e-f)** deep vasculature (V, hypo-dense since empty) and neuronal layers (e.g. CTX IV), and of **(g-h)** single neurons (Neu) and microglial (μG) cells. Superzooms (8x **a-d**) highlight pre-cellular **(e-f)**, CTX IV layers) to intra-cellular detail **(g-h)**, dense cytoplasm (C), hypo-dense nucleus (N), hyper-dense nucleolus (n), hypo-dense axons (A) within CTX cell layers. Note presence of cells (violet arrows) exhibiting abnormal intra-cellular hyper-density (ICHD). **i-l**, Max intensity projections (MIP) of 50 consecutive CT slices enhance hyper-dense features in pseudo-3D. 3D

renderings, after threshold-based gray-level segmentations, visualize the volumetric development of full-organ to intra-cellular hyper-dense morphology.

REFERENCES:

- Arganda-Carreras, I. *et al.* (2010) '3D reconstruction of histological sections: Application to mammary gland tissue', *Microscopy Research and Technique*. John Wiley & Sons, Ltd, 73(11), pp. 1019–1029. doi: 10.1002/jemt.20829.
- Bleuet, P. *et al.* (2009) 'A hard x-ray nanoprobe for scanning and projection nanotomography', *Review of Scientific Instruments*. American Institute of Physics, 80(5), p. 56101. doi: 10.1063/1.3117489.
- Bolte, S. and Cordelières, F. P. (2006) 'A guided tour into subcellular colocalization analysis in light microscopy', *Journal of Microscopy*. John Wiley & Sons, Ltd (10.1111), 224(3), pp. 213–232. doi: 10.1111/j.1365-2818.2006.01706.x.
- Brun, E. *et al.* (2014) 'Breast tumor segmentation in high resolution x-ray phase contrast analyzer based computed tomography.', *Medical Physics*, 41(11), p. 111902. Available at: <http://scitation.aip.org/content/aapm/journal/medphys/41/11/10.1118/1.4896124>.
- Cloetens, Peter *et al.* (1999) 'Hard x-ray phase imaging using simple propagation of a coherent synchrotron radiation beam', *Journal of Physics D: Applied Physics*. IOP Publishing, 32(10A), pp. A145–A151. doi: 10.1088/0022-3727/32/10a/330.
- Cloetens, P *et al.* (1999) 'Holotomography: Quantitative phase tomography with micrometer resolution using hard synchrotron radiation x rays', *Applied Physics Letters*. American Institute of Physics, 75(19), pp. 2912–2914. doi: 10.1063/1.125225.
- Coan, P. *et al.* (2006) 'Evaluation of imaging performance of a taper optics CCD 'FRELoN' camera designed for medical imaging', *Journal of Synchrotron Radiation*, 13(3), pp. 260–270. doi: 10.1107/S0909049506008983.
- Fix, A. S. and Garman, R. H. (2000) 'Practical Aspects of Neuropathology: A Technical Guide for Working with the Nervous System', *Toxicologic Pathology*. SAGE Publications Inc, 28(1), pp. 122–131. doi: 10.1177/019262330002800115.
- Gompel, G. Van *et al.* (2004) 'A new algorithm for 2D region of interest tomography', in *Proc.SPIE*. Available at: <https://doi.org/10.1117/12.536685>.
- Gonzalez, R. C. and Woods, R. E. (2018) *Digital Image Processing*. 4th Editio. New York, NY: Pearson.
- Hildebrand, T. and Rügsegger, P. (1997) 'A new method for the model-independent assessment of thickness in three-dimensional images', *Journal of Microscopy*. John Wiley & Sons, Ltd (10.1111), 185(1), pp. 67–75. doi: 10.1046/j.1365-2818.1997.1340694.x.
- Hsieh, J. (2015) *Computed Tomography: Principles, Design, Artifacts, and Recent Advances*. 3rd edn. SPIE Press.
- Kapur, J. N., Sahoo, P. K. and Wong, A. K. C. (1985) 'A new method for gray-level picture thresholding using the entropy of the histogram', *Computer Vision, Graphics, and Image Processing*, 29(3), pp. 273–285. doi: [https://doi.org/10.1016/0734-189X\(85\)90125-2](https://doi.org/10.1016/0734-189X(85)90125-2).
- Khimchenko, A. *et al.* (2018) 'Hard X-Ray Nanoholotomography: Large-Scale , Label-Free , 3D Neuroimaging beyond Optical Limit', *Advanced Science*, 5(1700694). doi: 10.1002/adv.201700694.
- Kilegran, J. (2019) *Correction of cupping artifacts in localized laboratory phase-contrast CT*. KTH - Royal Institute of Technology. doi: TRITA-SCI-GRU 2019:034.
- Lovic, G. *et al.* (2014) 'A robust tool for photon source geometry measurements using the fractional Talbot effect', *Optics Express*. OSA, 22(3), pp. 2745–2760. doi: 10.1364/OE.22.002745.
- Lyckegaard, A., Johnson, G. and Tafforeau, P. (2011) 'Correction of ring artifacts in X-ray tomographic images', *International Journal of Tomography and Statistics*, 18(F11), pp. 1–9.
- Marone, F. *et al.* (2017) 'Towards on-the-fly data post-processing for real-time tomographic imaging at TOMCAT', *Advanced Structural and Chemical Imaging*, 3(1), p. 1. doi: 10.1186/s40679-016-0035-9.

- Marone, F. and Stampanoni, M. (2012) 'Regridding reconstruction algorithm for real-time tomographic imaging', *Journal of synchrotron radiation*. 2012/09/01. International Union of Crystallography, 19(Pt 6), pp. 1029–1037. doi: 10.1107/S0909049512032864.
- Mirone, A. *et al.* (2014) 'The PyHST2 hybrid distributed code for high speed tomographic reconstruction with iterative reconstruction and a priori knowledge capabilities', *Nuclear Instruments and Methods in Physics Research Section B: Beam Interactions with Materials and Atoms*, 324, pp. 41–48. doi: <https://doi.org/10.1016/j.nimb.2013.09.030>.
- Mittone, A. *et al.* (2017) 'Characterization of a sCMOS-based high-resolution imaging system', *Journal of Synchrotron Radiation*, 24(6), pp. 1226–1236. doi: 10.1107/S160057751701222X.
- Mokso, R. *et al.* (2007) 'Nanoscale zoom tomography with hard x rays using Kirkpatrick-Baez optics', *Appl. Phys. Lett.*, 90(144104). doi: 10.1063/1.2719653.
- Otsu, N. (1979) 'A Threshold Selection Method from Gray-Level Histograms', *IEEE Transactions on Systems, Man, and Cybernetics*, 9(1), pp. 62–66. doi: 10.1109/TSMC.1979.4310076.
- Pacureanu, A. *et al.* (2018) 'Nanoscale three-dimensional imaging of biological tissue with x-ray holographic tomography', *Proc. SPIE 10711, Biomedical Imaging and Sensing Conference*, (107112B). doi: 10.1117/12.2319477.
- Paganin, D. *et al.* (2002) 'Simultaneous phase and amplitude extraction from a single defocused image of a homogeneous object', *Journal of Microscopy*, 206(1), pp. 33–40. doi: 10.1046/j.1365-2818.2002.01010.x.
- Pinzer, B. R. *et al.* (2012) 'Imaging brain amyloid deposition using grating-based differential phase contrast tomography', *NeuroImage*. Elsevier Inc., 61(4), pp. 1336–1346. doi: 10.1016/j.neuroimage.2012.03.029.
- Russo, P. (2017) 'Handbook of X-ray Imaging: Physics and Technology'. Available at: <http://www.crcnetbase.com/isbn/9781351228251>.
- Schindelin, J. *et al.* (2012) 'Fiji: an open-source platform for biological-image analysis', *Nature Methods*. Nature Publishing Group, a division of Macmillan Publishers Limited. All Rights Reserved., 9, p. 676. Available at: <https://doi.org/10.1038/nmeth.2019>.
- Schneider, C. A., Rasband, W. S. and Eliceiri, K. W. (2012) 'NIH Image to ImageJ: 25 years of image analysis', *Nature methods*, 9(7), pp. 671–675. Available at: <https://www.ncbi.nlm.nih.gov/pubmed/22930834>.
- Siegbahn, E. A. *et al.* (2006) 'Determination of dosimetric quantities used in microbeam radiation therapy (MRT) with Monte Carlo simulations', *Medical Physics*, 33(9), p. 3248. doi: 10.1118/1.2229422.
- Stampanoni, M. *et al.* (2010) 'Phase-contrast tomography at the nanoscale using hard x rays', *Physical Review B*. American Physical Society, 81(14), p. 140105. doi: 10.1103/PhysRevB.81.140105.
- Vidal, F. *et al.* (2005) 'Investigation of artefact sources in synchrotron microtomography via virtual X-ray imaging', *Nuclear Instruments & Methods in Physics Research Section B-beam Interactions With Materials and Atoms - NUCL INSTRUM METH PHYS RES B*, 234, pp. 333–348. doi: 10.1016/j.nimb.2005.02.003.
- Volume Graphics GmbH. (2001) 'VGStudio MAX 2.2'. doi: www.volumegraphics.com.
- Weitkamp, T. *et al.* (2005) 'X-ray phase imaging with a grating interferometer', *Optics Express*. OSA, 13(16), pp. 6296–6304. doi: 10.1364/OPEX.13.006296.
- Zack, G. W., Rogers, W. E. and Latt, S. A. (1977) 'Automatic measurement of sister chromatid exchange frequency.', *Journal of Histochemistry & Cytochemistry*. Journal of Histochemistry & Cytochemistry, 25(7), pp. 741–753. doi: 10.1177/25.7.70454.

Chapter 4 – X-PCI-CT to image brain radiotherapy

Micro-imaging of brain cancer radiation therapy using phase-contrast computed tomography

This chapter reports on the first neuroimaging project of this Thesis work, and explored for the first time the use of X-PCI-CT for the investigation a novel brain radiosurgery approach based on spatial fractionation of dose delivery, called Microbeam Radiation Therapy (MRT). This technique administers synchrotron X-rays spatially-reshaped into highly collimated micrometer-thick arrays of ultra-high-dose (>100 Gy) beams (so-called microbeams). To better understand the bio-mechanisms of this protocol, current biomedical research is studying the effects of MRT irradiations on nervous tissue, tumor tissue and brain vasculature. In order to overcome some of the current limitations in neuro-imaging, we thought of applying X-PCI-CT to obtain high-resolution soft-tissue data, to non-invasively detect MRT microbeams, and to discriminate at the micrometer level between normal brain tissue morphology and tumor tissue and vasculature post-treatment.

This pioneering project has been a collaborative effort between our LMU group, the group of Dr. Bravin at the ESRF in Grenoble –France and the group of Dr. Battaglia at the Neuromed Institute in Pozzilli – Italy. This work has been published in 2018 in the [Red Journal](#) (International Journal of Radiation Oncology*Biography*Physics), [COPYRIGHT] (2018), as follows:

G.E. Barbone, A. Bravin, P. Romanelli, A. Mittone, G. Le Duc, D. Bucci, S. Auweter, M.F. Reiser, M.J. Kraiger, M. Hrabe de Angelis, G. Battaglia, P. Coan, “Micro-imaging of Brain Cancer Radiation Therapy Using Phase-contrast Computed Tomography”, Int J Radiation Oncol Biol Phys, Vol. 101, No. 4, pp. 965-984 (2018). <https://doi.org/10.1016/j.ijrobp.2018.03.063>.

This work was presented orally at the European Congress of Radiology 2017 (ECR 2017), where it received the “Best Scientific Paper Presentation” Award within the topic “Neuro”.

Summary: Experimental X-ray Phase Contrast micro-CT provides *post-mortem* 3D representations of post-mortem brain tissue and glioblastoma tumor anatomy of high sensitivity and resolution without the need for extensive sample preparation. This imaging technique proved suitable for a follow-up study of a spatially fractionated radiotherapy technique, X-ray Microbeam Radiation Therapy. We detect 50µm-thick ablations on healthy and tumor tissue, arising from locally-delivered ultra-high-dose X-ray microbeams, as well as calcium and iron accumulation within necrotic tumor tissue.

4.1 Abstract

Purpose: Experimental neuroimaging provides a wide range of methods for the visualization of brain anatomical morphology down to sub-cellular detail. Still, each technique-specific detection mechanism presents compromises between achievable field-of-view size, spatial resolution or nervous-tissue sensitivity, leading e.g. to partial sample coverage, unresolved morphological structure or sparse labeling of neuronal populations, and often also to obligatory sample dissections or other sample-invasive manipulations. X-ray Phase Contrast CT (PCI-CT) is an experimental imaging methodology, which simultaneously provides micrometric spatial resolution, high soft-tissue sensitivity and *post-mortem* full-organ rodent brain coverage without any need for sample dissection, staining/labeling or contrast agent injection. In this work, we explore the benefits and limitations of PCI-CT use for the *in-vitro* imaging of normal and cancerous brain neuro-morphology after *in-vivo* treatment with synchrotron-generated X-ray Microbeam Radiation Therapy (MRT), a spatially fractionated experimental high-dose radiosurgery. The goals are the visualization of MRT treatment effects on nervous tissue, and qualitative comparison of results to histology and high-field MRI.

Methods: MRT was administered *in-vivo* to the brain of both healthy and cancer-bearing rats. Forty-five days post-treatment, brain organs were dissected out and imaged *post-mortem* via propagation-based PCI-CT.

Results: PCI-CT visualizes brain anatomy and micro-vasculature in 3D, and distinguishes cancerous tissue morphology, necrosis, and intra-tumor accumulation of iron and calcium deposits. Moreover, PCI-CT detects the effects of MRT throughout treatment target areas, e.g. the formation of micrometer-thick radiation-induced tissue ablations. Observed neuro-structures were confirmed by histology and immunohistochemistry, and related to micro-MRI data.

Conclusions: PCI-CT enables a unique 3D neuroimaging approach for *post-mortem* studies on small animal models, in that it concurrently delivers high-resolution insight on local brain tissue morphology in both normal and cancerous micro-milieu, localizes radiosurgical damage, and highlights deep micro-vasculature. This method could assist experimental small-animal neurology studies in the *post-mortem* evaluation of neuropathology or treatment effects.

4.2 Introduction

Spatial fractionation of radiation dose delivery, by relying on the so-called tissue-sparing dose-volume effect, is an emerging issue in neuro-radiosurgery and might represent a new avenue for effective and less invasive brain cancer radiotherapy (Girst *et al.*, 2016). X-ray Microbeam Radiation Therapy (MRT) (Smyth *et al.*, 2016) features the reshaping of a laminar synchrotron beam into arrays of highly collimated quasi-parallel micrometer-thick microbeams. This technique administers spatially-restricted peak doses of many hundreds of Grays

indiscriminately to healthy and tumor tissues alike, and was proven to selectively disrupt tumor tissues, while being well tolerated by healthy ones (Bräuer-Krisch *et al.*, 2010). Its success in tumor treatment has been attributed to differences in tissue radio-resistance (Dilmanian *et al.*, 2003) and a diminished reorganization and repair capability of tumor vessel networks with respect to healthy ones (Bouchet *et al.*, 2010; Sabatasso *et al.*, 2011). The reported efficacy of MRT, though, remains a complex and partly-unanswered question, and neuroimaging methodologies able to perform rigorous follow-ups of this pre-clinical technique's effects would be of paramount importance to gain a better understanding of MRT's tissue-dependent dose response.

Modern neuroimaging is a fast-growing field, today able to provide high-quality anatomical and functional maps of the Central Nervous System (CNS) from full organs down to sub-cellular structure. MRI and CT can both attain 3D micrometric resolution via small-animal micro-MRI and micro-CT scanners. Recent *in-vivo* advances include ultra-high-field small animal brain imaging (Benveniste and Blackband, 2002). Brain tumor angiogenesis can also be studied via micro-MR angiography, at spatial resolutions of 60 μm and after contrast agent administration (Lin *et al.*, 2013). Conventional X-ray micro-CT, for its part, is able to assess the presence of tumors in small animals *in-vivo* (Engelhorn *et al.*, 2009) after contrast media injection, but otherwise affords soft-tissue sensitivity that is, in absence of contrast agents, rather low.

Post-mortem high-resolution MRI after active staining (Johnson *et al.*, 2002) allows the study of full-organ brain tissue microstructure down to 10-25 μm isotropic resolution, quantitative regional volumetric measurements, and the elaboration of several distinct image contrasts, so-called *proton stains*, highlighting specific anatomical features. When applied *post-mortem*, these imaging methods are referred to as MR-histologies, even though they do not fully discriminate single cells. MRI-based morphologic phenotyping of neuroanatomy has been instrumental in non-destructively creating 3D full-organ atlases of a number of animal models (Chuang *et al.*, 2011; Johnson *et al.*, 2012), and is used for the full-organ study of neuropathologies and of neuro-development (Calabrese *et al.*, 2013). Moreover, by imaging local molecular water diffusion to detect microstructural differences in bio-tissues, MRI permits the calculation of 3D axonal inter-voxel connectivity via diffusion tensor imaging (DTI) and fiber tractography (Mukherjee *et al.*, 2008), giving access to a unique full-organ view of (white-matter) brain organization (Jiang and Johnson, 2011; Veraart *et al.*, 2011). Interestingly, cutting-edge micro-MRIs, combining different kinds of MR contrasts, are able to resolve the laminar anatomy and underlying cyto-architecture of the hippocampus (e.g. using DTI and 60 microns in-plane resolution) (Shepherd *et al.*, 2007), are sensitive to brain tumor cell density (Chenevert *et al.*, 2000), detect tumor invasion (Bennett *et al.*, 2004), recover complex 3D maps of vascular micro-architecture and can measure vascular angiogenesis (Kim *et al.*, 2011). Functional small-animal positron emission tomography (PET), for its part, provides dynamic images of the bio-distributions of radioactive tracers and allows a wide range of full-organ and *in-vivo* longitudinal follow-up studies for neuro-pharmacological testing and neurodegenerative disease characterization (Virdee *et al.*, 2012). PET, though, is a relatively low-resolution imaging tool, and offers indirect-only morphological imaging.

Histology and immunohistochemistry, gold standard methodologies in neuroscience, instead, offer both sub-cellular resolution and tailored stain-dependent tissue contrasts. Still, they remain highly sample-invasive techniques (the specimen being sectioned by a microtome to produce planar histological slices), are often time consuming and mostly still lack the capability to directly render complex neuron and vessel networks developing in 3D space. The gap between histology and MRI/CT-based approaches has been filled by other powerful ultra-high resolution neuroimaging research methodologies, having varying degree of sample-invasiveness, resolution and fields of view: two-photon microscopy, for example, detects deep-brain calcium dynamics by using fluorescent indicators, reveals large-scale neuronal activity *in-vivo*, and renders a functional and structural image of single neurons within localized neural populations (Birkner, Tischbirek and Konnerth, 2016; Song *et al.*, 2017) at the cellular and subcellular level. This method can also be combined with electrical recordings of neuronal activity (Yashiro *et al.*, 2017) to obtain precious morphological and functional information simultaneously. *Post-mortem* local 3D properties of single glial, astrocytic and neuronal cyto-architecture, as well as subcellular detail and synaptic organization, can also be rendered today by combining 3D light microscopic methodology with deep and uniform antibody labeling procedures (Bouvier *et al.*, 2016) even after long-term sample storage. On the other hand, novel optical tissue-clearing (TC) methods enable full-organ 3D fluorescence imaging (Ertürk *et al.*, 2012; Hama *et al.*, 2015) and the *post-mortem* study of cellular and vascular organization throughout entire organisms (Pan *et al.*, 2016). Finally, optical coherence tomography (OCT), which is an ultra-fast technique applied *in-vivo*, permits minimally-invasive local endoscopic optical biopsies (Tearney *et al.*, 1997), revealing both brain (Xie *et al.*, 2013) and tumor morphology (Xie *et al.*, 2014). Furthermore, swept-source optical coherence Doppler tomography (SS-ODT), sensitive to dynamic and transient changes in 3D cerebral blood-flow, enables *in-vivo* functional micro-circulatory imaging of deep brain vasculature at depths down to 3.2mm (Chen *et al.*, 2016).

Overall, the great diversification of novel neuroimaging technology gives neuroscientists a much-expanded tool-kit with which to tackle the complexity of the CNS. Still, all these methods have evident limitations, which are more or less critical depending on the desired application: some struggle to achieve sample-coverage of more than a few millimeters (OCT, SS-ODT) or present spatial restrictions of the neuronal area of visualization (e.g. cellular visualizations are limited to the staining-area covered by calcium indicator dyes or by the antibody-label penetration depth). Others afford an only partial labelling of cell populations (fluorescence-based methodologies), or have very sample-invasive procedures (TC and deep antibody labeling, for example), which hamper any prospects of future *in-vivo* application. Full-organ rodent brain coverage, a non-specific both nervous- and tumor-tissue-sensitive contrast mechanism, and micrometric resolution are instead concurrent requirements to reliably study local effects in the brain of fractionated high-dose radiosurgery on both normal and cancerous neuro-morphology.

X-ray Phase Contrast CT (PCI-CT) is an experimental high-resolution imaging technique of interest to biomedical research for its ability to visualize soft-matter biological tissues (Donath *et al.*, 2010; Sztrókay *et al.*, 2012; Zhao *et al.*, 2012; Bravin, Coan and Suortti, 2013), providing a sensitivity 2 to 3 order of magnitudes higher than that of absorption CT (Horng *et al.*, 2014;

Yoneyama *et al.*, 2015) in the hard X-ray regime. We presume that PCI-CT might be able to contribute to the study of X-ray irradiation effects on brain tissue, since the technique was reported to provide high nervous-tissue contrast complementary to MRI (Schulz *et al.*, 2012). Various PCI techniques have already been applied to neuroimaging: grating interferometry enables high-resolution depictions of tumor tissues, the hippocampus and cerebellum regions (Pfeiffer *et al.*, 2007), white and gray matter (Rutishauser *et al.*, 2011), the *substantia nigra* structure (McDonald *et al.*, 2009) and brain myelin sheaths (Jensen *et al.*, 2011). More localized brain tissue studies, using crystal interferometry, single-shot propagation-based phase-contrast imaging or other PCI-CT techniques, have identified blood micro-vessels (Zhang *et al.*, 2015), the molecular layer and the granular layer in the cerebellum, and have shown how multimodal brain imaging can lead to deeper insight compared to single-technique studies (Schulz *et al.*, 2012). Finally, PCI techniques were able to effectively localize cancer masses within the brain (Pfeiffer *et al.*, 2007), to demarcate tumor vs. healthy tissue boundaries (Beltran *et al.*, 2011), to visualize cancerous tissue morphology (Takeda *et al.*, 2000; Lwin *et al.*, 2016) and to identify cancer-driven tissue degeneration (Momose *et al.*, 1996; Huang *et al.*, 2015) without addition of contrast-agent.

All of these results together show that PCI-CT is a unique *post-mortem* high-resolution neuroimaging technique, providing high degrees of morphological precision, full-organ rodent brain coverage and sensitivity in the 3D visualization of both healthy and pathological CNS tissues. Moreover, PCI-CT overcomes some of the burdens and limitations of histological work-up, by allowing a dissection-free 3D virtual direct measurement of deep morphology within large samples (several cm in both width and height). Thus, PCI-CT-based high-resolution structural neuroimaging could provide new insight to ongoing oncology research on small-animals involving micrometric dose-fractionation in radiotherapy. Here we investigate the possibility of visualizing the biological marks of an X-ray microbeam irradiation protocol, by evaluating rat brain PCI-CT images and comparing them to histology and MRI, with the goal of validating PCI-CT as a viable imaging technique for *post-mortem* MRT-treatment evaluation.

4.3 Methods

4.3.1 Animal preparation

Six eight-week-old male Fisher (Charles-River Laboratories - France, no date) rats were implanted with the 9L glioblastoma (GBM) cell line (Barth and Kaur, 2009) in the right hemisphere, following published protocols (Régnard, Bräuer-Krisch, *et al.*, 2008; Régnard, Le Duc, *et al.*, 2008). Three rats, used as controls, were not implanted with tumors. Fifteen days after tumor cell inoculation, all animals (9 in total) were treated with different MRT protocols (see MRT irradiation protocols in the following section of the Methods), and then sacrificed 1.5 months post-treatment. After animal sacrifice, all 9 brain samples were dissected out, fixed in 10% formalin solution (no negative influence in PCI experiments (Mollenhauer *et al.*,

2002)) and stored in plastic tubes until imaging analysis. All operative procedures related to animal care strictly conformed to guidelines of the French Government and were approved by the ethical committee of the European Synchrotron (ESRF).

4.3.2 MRT irradiation

Both radiotherapy and imaging were performed at the Biomedical Beamline ID17 of the ESRF. The first beamline hutch, stationed 42 m away from a wiggler-based synchrotron X-ray source and devoted to MRT treatment, receives filtered X-rays of wide spectral range (median energy: 90 keV; spectral range: 50-350 keV) and of high dose rates (Siegbahn *et al.*, 2006) (>14 kGy/s). Via a specifically engineered tungsten multi-slit collimator (Bräuer-Krisch *et al.*, 2009), the beam is spatially fractionated into a comb-like dose profile, producing 25-75 μm -thick high-dose microbeams (peak doses > 100 Gy) interspersed by much wider valleys, where lower well-tolerated doses are delivered to biological samples (Laissue *et al.*, 2007). Animals were anesthetized (4% isoflurane inhalation, for induction, and ketamine, 100 mg/kg, + xylazine, 10 mg/kg, i.p., for maintenance) and positioned on a stereotactic frame (Régnard, Le Duc, *et al.*, 2008). Rat brains were then irradiated with microbeams 50 μm in width and 1 cm in height, both uni-directionally and by 90 degree cross-firing (Dilmanian *et al.*, 2006). Inter-microbeam spacing was varied between different sample irradiations, determining center-to-center (c-t-c) inter-microbeam distances of 200 or 400 μm . Moreover, three microbeam peak entrance doses were selected (250, 400 and 600 Gy, measured at 2 mm depth). A total 1 cm^2 square-shaped irradiation area was delivered posteriorly and laterally to the cranium bregma point. MRT valley doses for 50 μm thick microbeams with 200 μm c-t-c distance are reported (Serduc *et al.*, 2009) to scale the peak dose by a factor of $\sim 1/27$, leading to estimated valley doses of around 9, 15 and 22 Gy (for the MRT treatments with peak doses respectively at 250, 400 and 600 Gy). In the 400 μm c-t-c distance case, the scaling factor is reported (Martínez-Rovira, Sempau and Prezado, 2012) to be $\sim 1/57$, leading, as expected, to lower valley doses, respectively of 4, 7 and 11 Gy. Since dose scales linearly, 2-direction cross-firing irradiations lead to a doubling of the dose in the valleys.

Sample-specific irradiation parameters:

sample 1: tumor-bearing, unidirectional 600 Gy 400 μm c-t-c MRT, valley dose ~ 11 Gy;

sample 2: tumor-bearing, unidirectional 400 Gy 400 μm c-t-c MRT, valley dose ~ 7 Gy;

sample 3: tumor-bearing, unidirectional 600 Gy 200 μm c-t-c MRT, valley dose ~ 22 Gy;

sample 4: tumor-bearing, unidirectional 400 Gy 200 μm c-t-c MRT, valley dose ~ 15 Gy;

sample 5: tumor-bearing, cross-firing 400*2 Gy 400 μm c-t-c MRT, valley dose ~ 14 Gy;

sample 6: tumor-bearing, cross-firing 250*2 Gy 400 μm c-t-c MRT, valley dose ~ 8 Gy;

sample 7: healthy, cross-firing 400*2 Gy 400 μm c-t-c MRT, valley dose ~ 14 Gy;

sample 8: healthy, cross-firing 250*2 Gy 400 μm c-t-c MRT, valley dose ~ 8 Gy;

sample 9: healthy and untreated.

4.3.3 Propagation-based Phase Contrast Imaging

Post-mortem imaging was performed in the ID17 imaging hutch (150 m away from the source), using a standard propagation-based PCI (PBI) experimental setup (Cloetens *et al.*, 1996; Wilkins *et al.*, 1996; Bidola *et al.*, 2015). The 9 extracted brain samples were placed in a formalin-filled Falcon tube and illuminated with highly-collimated quasi-coherent monochromatic 26 keV X-rays. A low-noise 2k CCD FReLoN camera (Coan *et al.*, 2006) was selected as imaging detector, in turn coupled to an 8 μm lens-based optics (sample-to-detector distance: 7 m; detector field-of-view (FoV): 16 mm; voxel size: $8 \times 8 \times 8 \mu\text{m}^3$). We acquired PCI-CT image-datasets with 3000 projections over 360 degrees in half acquisition (Sztrókay *et al.*, 2012) (total acquisition time: ~ 2.5 h per sample), achieving an overall horizontal FoV of 30 mm. Vertically, motorized sample translation of sub-pixel precision enables subsequent CT scans at different heights, and an overall vertical FoV of up to 100 mm. The combined FoV of $30 \times 100 \text{ mm}^2$ is suitable for full-organ rodent brain imaging. PCI-CT images were reconstructed using standard filtered back-projection algorithms for CT, and a phase retrieval algorithm (Paganin *et al.*, 2002; Beltran *et al.*, 2011) specific for single distance PBI was used to extract the sample phase-contrast map. Arising CT ring artefacts were in large part removed from reconstructed CT slices using a published correction tool (Lyckegaard, Johnson and Tafforeau, 2011).

4.3.4 Vessel network renderings

Brain vessel-network segmentations were obtained using a region growing algorithm (applied to sample 9 datasets), and the 3D renderings were produced using the commercial software VG Studio MAX (Volume Graphics GmbH, 2001). Moreover, brain vessel 2D maximum intensity projection maps were computed over 200 consecutive slices (from sample 2 and 4 data) by awarding to each particular pixel location its maximum value over all images in the stack (i.e. the maximum intensity z-projection function in ImageJ software (NIH, USA), a method which highlights bright 3D features and maps them onto a 2D plane).

4.3.5 Histology & Immunohistochemistry

Hematoxylin/eosin (H&E) histology was performed on samples 2-9. Nissl staining, Perls' Prussian Blue staining, specific for iron deposits, and Alizarin Red S staining, specific for calcium deposits, were performed after imaging on two MRT-irradiated and tumor-bearing brain samples (sample 2 and 6). Formalin-fixed brains were included in paraffin and 15 μm sections were cut on a microtome. The Perls' Prussian Blue consists of potassium ferrocyanide, which reacts with ferritin to yield a blue-colored compound. For Alizarin Red S

staining, sections were hydrated in descending series of ethanol and immersed in 2% Alizarin red S (2% in distilled water pH 4.3) for 45 sec. For immunohistochemistry deparaffinised sections from sample 6 were soaked in 3% hydrogen peroxide, to block endogenous peroxidase activity, and incubated overnight with polyclonal goat anti-ionized calcium binding adaptor molecule-1 (Iba-1) (1:1000, ab-107159, Abcam, Cambridge, United Kingdom), monoclonal mouse anti-gial fibrillary acidic protein (GFAP) (1:100, G-3893, Sigma-Aldrich, St. Louis, MO), with polyclonal rabbit anti-Ki-67 (1:20, RM-9106, Thermo Fisher Scientific, Fremont, CA), and with rabbit anti-laminin (1:100, NB300-144, Novus Biological, Littleton, CO), and then for 1h with secondary biotinylated anti-goat, anti-mouse and anti-rabbit antibodies, respectively (1:200; Vector Laboratories, Burlingame, CA). Sections were treated with 10 mM, pH 6.0, citrate buffer, and heated in a microwave for 30 min for antigen retrieval. Control staining was performed without the primary antibodies. The immunoreaction was performed with 3,3-diaminobenzidine tetrachloride (ABC Elite kit; Vector Laboratories).

4.3.6 MRI Experiment

One MRT-irradiated tumor-bearing brain sample (sample 1) was additionally *post-mortem* imaged inside a formalin-filled Falcon tube with a pre-clinical 9.4 T MRI scanner (BioSpec 94/20 USR, Bruker). Since all PCI neuro-images in this work were taken *post-mortem*, the specimen was also MRI-imaged *post-mortem* in exactly the same sample conditions and environment as for PCI-CT, in order to obtain a comparable MRI dataset. Axial brain images were taken using the manufacture's two channel array RX/TX cryo probe (Z125365). Coronal brain images were acquired using an eight channel RX array volume coil (T20030V3) optimized for rat brain imaging in combination with a quadrature TX volume resonator (T12054V3). We acquired both T1- and T2-weighted sequences optimized for brain anatomical high-resolution imaging.

Axial MRI sequences specifications:

2D-T2 MSME: Bruker Biospin 2D-T2map-MSME sequence; echo images: 8; echo spacing: 8.63 ms; TR: 4000 ms; N-averages: 8; FOV: 20*15 mm²; slice thickness: 0.8 mm; pixel size: 63*59 μm²; acquisition matrix size: 320*256; bandwidth: 78125 Hz; duration: 2 h 16 m 32 s.

3D-T1 FLASH: Bruker Biospin T1_FLASH_3D_SWI sequence; flip angle: 25°; TE: 4.74 ms; TR: 100 ms; N-averages: 6; FOV: 25*15*5 mm³; pixel size: 48.8*46.9*78 μm³; acquisition matrix size: 512*320*64; Anti-alias in slice direction: 1.313; bandwidth: 100000 Hz; duration: 4 h 28 m 48 s.

Coronal MRI sequences specifications:

2D-DTI: Bruker Biospin DTI_EPI sequence; diffusion directions: 30; A0 reference images: 5; max. b-value: 1634.03 s/mm²; TE: 19.96 ms; TR: 3000 ms; N-averages: 35; FOV: 15*15 mm²; pixel size: 138.9*156.3 μm²; slice thickness: 0.8 mm; acquisition matrix size: 108*60; reconstruction matrix size: 108*96; Partial FT: 1.6; bandwidth: 340909.1 Hz; duration: 1 h 1 m 15 s.

3D-T1 RARE: Bruker Biospin T1_RARE sequence; TE: 8.35 ms; RareFactor: 2; TR: 1000 ms; inversion delay: 400 ms; N-averages: 8; FOV: 15x15x16 mm³; pixel size: 53.6*53.6*250 μm³; acquisition matrix size: 256*256*64; bandwidth: 50000 Hz; duration: 9 h 57 m 20 s.

3D-T2* MGE: Bruker Biospin T2_star_MGE sequence; flip angle: 30°; TE: 3.46 ms; TR: 150 ms; N-averages: 10; FOV: 15*15*4 mm³; pixel size: 58.6*58.6*250 μm³; acquisition matrix size: 256*192*16; reconstruction matrix size: 256*256*16; Partial FT: 1.33; bandwidth: 69444.4 Hz; duration: 1 h 16 m 48 s.

4.4 Results

4.4.1 Imaging brain anatomy

High resolution X-ray PCI images (**Fig. 1**) of an excised control rat brain sample (sample 9) showcase the achievable sensitivity to brain anatomical detail of this imaging method, which measures small differences in local tissue density and refractivity. Sagittal (**Fig. 1a**) and coronal (**Fig. 1b-d**) slices exhibit full-organ brain structural images, including cerebellar, cortical, thalamic and hypo-thalamic areas. Brain sub-region anatomy is visualized in the coronal slices, e.g. the striatum region and lateral ventricles filled with choroid plexi (**1b**), the hippocampus and the cell layers within Ammon's Horn and the Dentate Gyrus (**1c**), cerebellar granular and molecular layers of gray matter and the white matter of the arbor vitae (**1d**). Phase-contrast signal (**1e**) in the granular cell layer (*stratum granulosum*) of the hippocampal Dentate Gyrus is compared (**1f**) and superimposed (**1g**) to H&E histological staining. A formalin-filled third ventricle is also visible in the PCI image, corresponding in the histological slice to an area empty of tissues. Zoom-ins of the striated architecture of the caudate-putamen, of the ventricles, of the layers of the hippocampal formation and of the cerebellar arbor vitae can be found in **Suppl. Figure 7**.

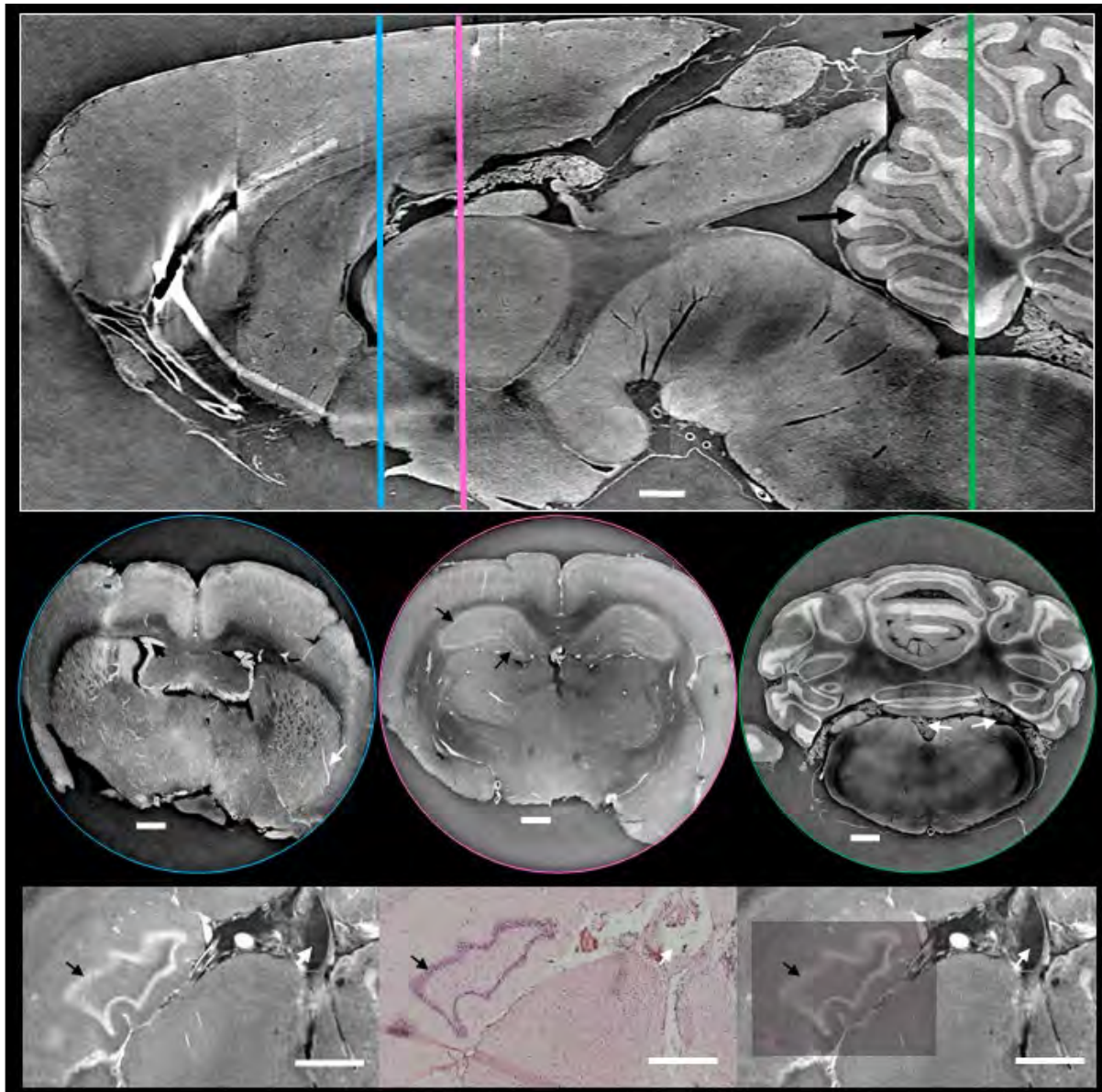


Figure 1 | X-ray phase-contrast CT of rat brain anatomy. (a) sagittal slice displaying somatosensory and visual areas of the cortex (CTX), the thalamus (TH), hypothalamus (HY) and midbrain (MB), the lobules of the cerebellum (CB) with distinct molecular (mo) and granular (gr) layers, and large portions of the medulla (MY) and pons (P) regions. (b) coronal section of cortical (CTX), thalamic (TH) and hypothalamic (HY) regions, with view of the third ventricle (V3) and lateral ventricles (LV) filled with choroid plexi (cp), and of the striated architecture of the caudate-putamen of the dorsal striatum (dSRT) perfused by long bright blood-vessels (BV). (c) coronal view of the dorsal hippocampus, divided in the layers within Hammon's Horn (CA) and in the Dentate Gyrus (DG). (d) cerebellar (CB) slice, showing the arbor vitae (arb) and lobules (lob) and contrast in both the granular (gr) and molecular (mo) layers of gray matter, part of the fourth ventricle system (V4) and a large section of the medulla region (MY). PCI (e), H&E histology (f) and superposition of the two techniques (g) illustrate the structure of the granular cell layer (*stratum granulosum*, sg) of the hippocampal Dentate Gyrus. The third ventricle (V3) is filled with low-signal formalin in PCI (e) and is empty in the histology slice (g).

4.4.2 Imaging glioblastoma tumor

Fig. 2 shows how the PCI contrast mechanism enables the detection of GBM tumor tissue morphology. Cancerous tissue from implanted 9L glioblastoma cells (marked as GBM in **Fig. 2**, data from samples 1-5) was observed via PCI within brain striatum, thalamic (**2a, 2e**) and

hypothalamic regions (**Fig. 2c-d**), as well as partly growing inside lateral ventricles (**Fig. 2a**). GBM neoplasms can be recognized as regions of higher phase-contrast relatively to surrounding normal brain parenchyma and to contralateral non-implanted brain hemispheres (**Fig. 2a, 2c-f**). Core GBM lesions feature hyper-cellularity, comprised of a mix of densely-packed astrocytes, blood vessels and other cells, an abnormal hyper-dense cellular microenvironment, which modifies local refractive properties and densities compared to those within normal nervous tissue, thereby influences PCI signal and seems to lead to local hyper-intensity within GBMs (**Fig. 2a, 2c-f**).

Figures 2a-b highlight PCI intensity differences within one selected tumor-bearing brain sample: some of the lowest gray-levels pertain to the low-density formalin environment surrounding the sample and within formalin-filled ventricles and blood vessels (samples were formalin-fixed and vasculature was at least partially perfused). Normal nervous tissue presents average gray-levels slightly above those pertaining to formalin (see cortex and amygdalar gray-levels in **Fig. 2a-b**). Peaks in the gray-value profile seem instead to correspond to local vasculature, which was not completely washed during perfusion: vessels partially filled with densely-packed blood cells or with collapsed endothelial membranes, create local hyper-density areas detected by the PCI technique. PCI signal within GBM tissue was found on average higher than nervous tissue in all inoculated cerebra, with signal contributions coming from all sources of hyper-density: notably the typical densely-packed cancerous cellularity and the increased and aberrant vascularization (**Fig. 2 c-e**), and even localized tumor-driven blood extravasations or tissue calcification (**Fig. 2e**), all contribute to give rise respectively to the highest average gray-levels and to intra-GBM signal peaks. Other areas of low PCI signal arise from necrotic areas at the center of tumor masses, affording troughs within GBM gray-value profiles (**Fig. 2a-c, 2e**): cell death causes decreased cellularity and even the formation of empty cystic cavities, which diminishes the local density and local refraction effects and affords a PCI signal similar (or even lower) to that of formalin-filled brain ventricles (see trough within the GMB gray-level profile in **Fig. 2b**, marked as necrotic in origin). PCI signal is admittedly non-specific in nature, in that different features can give rise to similar PCI intensity levels. **Fig. 2a-b** show that it is indeed difficult to differentiate formalin from an empty vessel from a cyst in a necrotic area (all hypo-intense features) based on PCI signal alone, as is difficult differentiating between filled vessels and tumor tissue (both hyper-intense features). In these cases, gray-level-based structure differentiation must be complemented by morphological observations. What is though possible with PCI, is to differentiate between low-intensity and high-intensity features, and, most importantly, to recognize these structures within normal nervous tissue.

The high phase-contrast between areas of tumor-driven parenchymal cell destruction and surrounding normal tissues enables the visualization of tumor micro-morphology: broad anatomical deformation and compression, caused by neoplasm growth, are visualized in all tumor-bearing samples (e.g. deformed lateral ventricle above the tumor mass in **Fig. 2f-g**). In **Fig. 2c** and **2d**, we observe the invasion by infiltrating malignant tissue of areas neighboring core lesions (tentacle-like tissue morphology and high PCI-signal areas at the periphery of and beyond the main tumor mass). Thorough identification of GBM tissue composition (and of microglial infiltrating cells) by immunohistochemical analysis can be found in **Fig. 5. Figures**

2e and **2e'** show a typical pathologic feature of GBM, i.e. tumor cells forming pseudopalisades (Rong *et al.*, 2006), characterized by interconnected hyper-dense layers of tumor-cell accumulation surrounding a central clear zone of hypoxia-driven necrosis. Tissue apoptosis and necrosis are, in fact, caused by the malfunction of the vessel at the center of the pseudopalisade after tumor-growth-driven endothelial injury, vaso-occlusion and intravascular thrombosis (a central bright vessel is visible within all pseudopalisades in **2e**). The pseudopalisades successively also secrete angiogenic factors leading to microvascular proliferation and hyperplasia in adjacent regions (Rong *et al.*, 2006) (hyperplasia is visible in **Fig. 2e**). All the morphologic features of pseudopalisades observed via PCI in **2e** were confirmed by the H&E histology in **2e'**.

A comparison of phase-contrast vs. histological tumor tissue characterization can be observed in **Fig. 2f** vs. **2g**: cortical and hypothalamic tissue, a formalin-filled ventricle and blood-filled vasculature, and, most importantly, GBM tissue are visualized via both techniques. A PCI zoom-in on GBM morphology (**Fig. 2h**) highlights, by comparison (**2j**) and superposition (**2i**) to the corresponding histological slice, how PCI signal differences are closely related to the cellularity differences between normal and cancerous tissues present in the histology. Further immunohistochemical characterization of PCI signal within tumor tissue and within blood vessels is carried out respectively in **Fig. 5** and in **Fig. 3**.

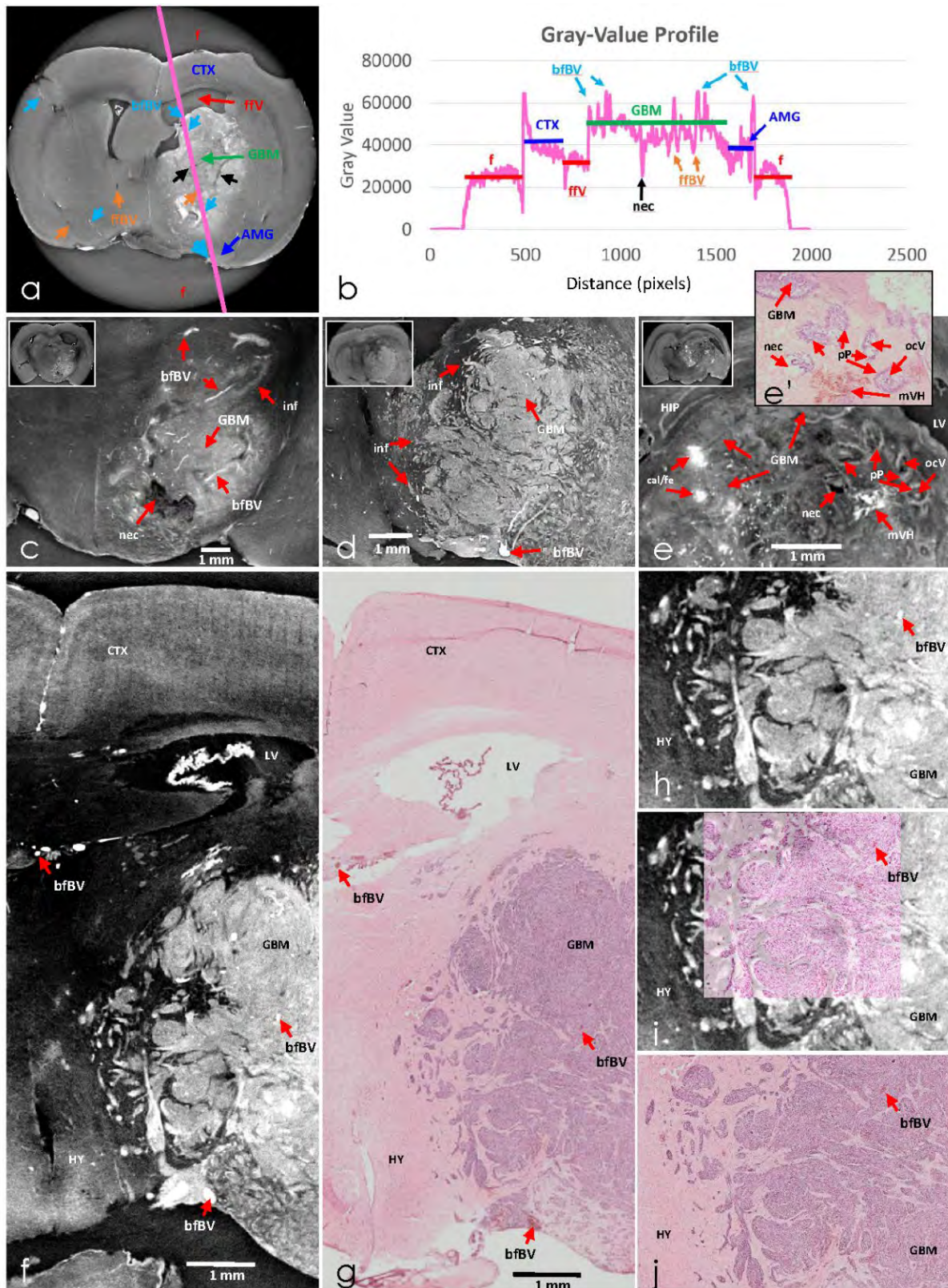


Figure 2 | X-ray phase-contrast CT of tumor anatomy. (a) a GBM-bearing PCI slice and its corresponding 16-bit gray-value profile (b), measured along the pink line in (a), illustrates PCI contrast between different brain anatomical features: surrounding formalin and a formalin-filled ventricle (f and ffV, red), formalin-filled blood vessels (ffbV, orange), cortical and amygdalar normal tissue (CTX and AMG, blue), blood-filled blood vessels (bfBV, turquoise), glioblastoma tumor tissue (GBM, green) and necrotic tissue (nec, black). Colored arrows point to features in (a) and to corresponding gray-value levels in (b). (c) GBM tissue appears as an asymmetric bright

area within the thalamus and hypothalamus. The tumor is necrotizing at the core (nec, dark-pixels area) and infiltrating surrounding tissues (inf). **(d)** GBM tissue infiltration (inf), with islets of tumor cells and tentacular cancer regions invading normal tissue. **(e)** a large necrotizing (nec) GBM growing near a deformed hippocampus (HIP) and lateral ventricle (LV). PCI shows sign of potential tissue calcification and tumor-driven iron-rich blood extravasation (cal/fe) leading to the agglomeration of hyper-dense intra-tumoral clusters (very bright areas in PCI). PCI also shows pseudopalisading (pP) tumor cell hyper-dense accumulation surrounding a hypo-dense hypoxia-driven necrotic region and an occluded central vessel (ocV). Nearby microvascular hyperplasia (mVH) is caused by proangiogenic factor secretion by the hypoxic pseudopalisades. **(e')** H&E histology confirms the morphology of GBM pseudopalisades seen in **(e)**. **(f-g)** comparison between PCI **(f)** and H&E histology **(g)** of cortex (CTX), lateral ventricle (LV), hypothalamus (HY) and GBM morphology. Zoom-in of PCI **(h)**, histology **(l)** and superposition of the two **(i)** illustrate the local structure of GBM tissue invading surrounding hypothalamic (HY) tissue. Blood-filled blood vessels (bfBV) are annotated throughout the figure.

4.4.3 Imaging brain vasculature

Brain blood vessels, which irrigate the encephalon both superficially and internally, can be recognized throughout PCI data of normal and tumor-bearing tissues as both low-density (hypo-intense) and high-density (hyper-intense) interconnected tubular structures of size down to a few tens of μm (**Fig. 3a**). The hyper-dense features can be segmented, to provide 3D vessel-network trees, or superimposed by addition of several consecutive image-slices, to provide 2D maximum intensity projection maps (2D MIP, see Methods section), with the tree-shaped volumetric morphology of these tubular features (**Fig. 3f-k**) suggesting their vascular nature. Immunohistochemistry of laminin, a marker for blood vessels, confirmed their presence, and helped characterize the meaning of the PCI gray-levels: hyper-dense structures consisting of collapsed or blood-filled blood vessels correspond to bright tubules in PCI (**Fig. 3b-d** vs. **3b'-d'**), and hypo-dense empty vessels correspond to dark formalin-filled tubules in PCI (**Fig. 3e** vs. **3e'**). H&E staining confirmed the presence of collapsed blood vessels (**Fig. 3b''**), of vessels half-filled with blood red cells (**3c''**), of collapsed vessel with packed red blood cells (**3d''**), and of empty blood vessel (**3e''**). The full laminin histology vs. the corresponding PCI image can be found in **Suppl. Fig. 8**.

Larger superficial blood vessels with thick hyper-dense endothelial membranes, residing in the subarachnoid space, are visualized as bright tubes covering most of the external organ (**Fig. 3i**). Intra-cortical vasculature and capillaries, branching radially inwards from the outer layers toward the inner brain (**Fig. 3a, 3f-g**), are visible as bright tubules, when collapsed or when filled or half-filled with red blood cells, or as dark tubules, when non-collapsed and formalin-filled. The full-organ angio-architecture, comprised of anterior (ACA), middle (MCA) and posterior cerebral arteries (PCA) can be followed on 2D MIPs both in healthy samples (**Fig. 3f-h**), where it is notably hierarchically organized and evenly distributed, and in tumor-bearing samples (**Fig. 3i-k**), which, as is well-known (Siemann, 2011), features densely-packed immature, tortuous and disorganized tumor vasculature in and around the malignant lesions (data from sample 2, 4 and 9). Deep hyper-dense micro-vascularization was detected extending to the center of the organ as an organized and tidy network in a healthy brain (**Fig. 3h**), or as a chaotic bundle wrapping around the GBM in a tumor-bearing cerebrum (**Fig. 3j**). Undeniably, it is difficult to differentiate between signals from local aberrant vessel anatomy and GBM tissue hyper-cellularity within the core of neoplasms in 2D, as both anatomical

components are present at the same time: a close-reading of local 3D morphology and of relative gray-level differences is needed in this case (**Fig. 3i-k**). Vasculature within healthy parenchyma, as the tumor-free vasculature imaging in **Fig. 3f-h** demonstrates, is instead much easier to recognize. Further 2D and 3D PCI-based renderings of tumor and vascular anatomy can be found in **Suppl. Fig. 9**.

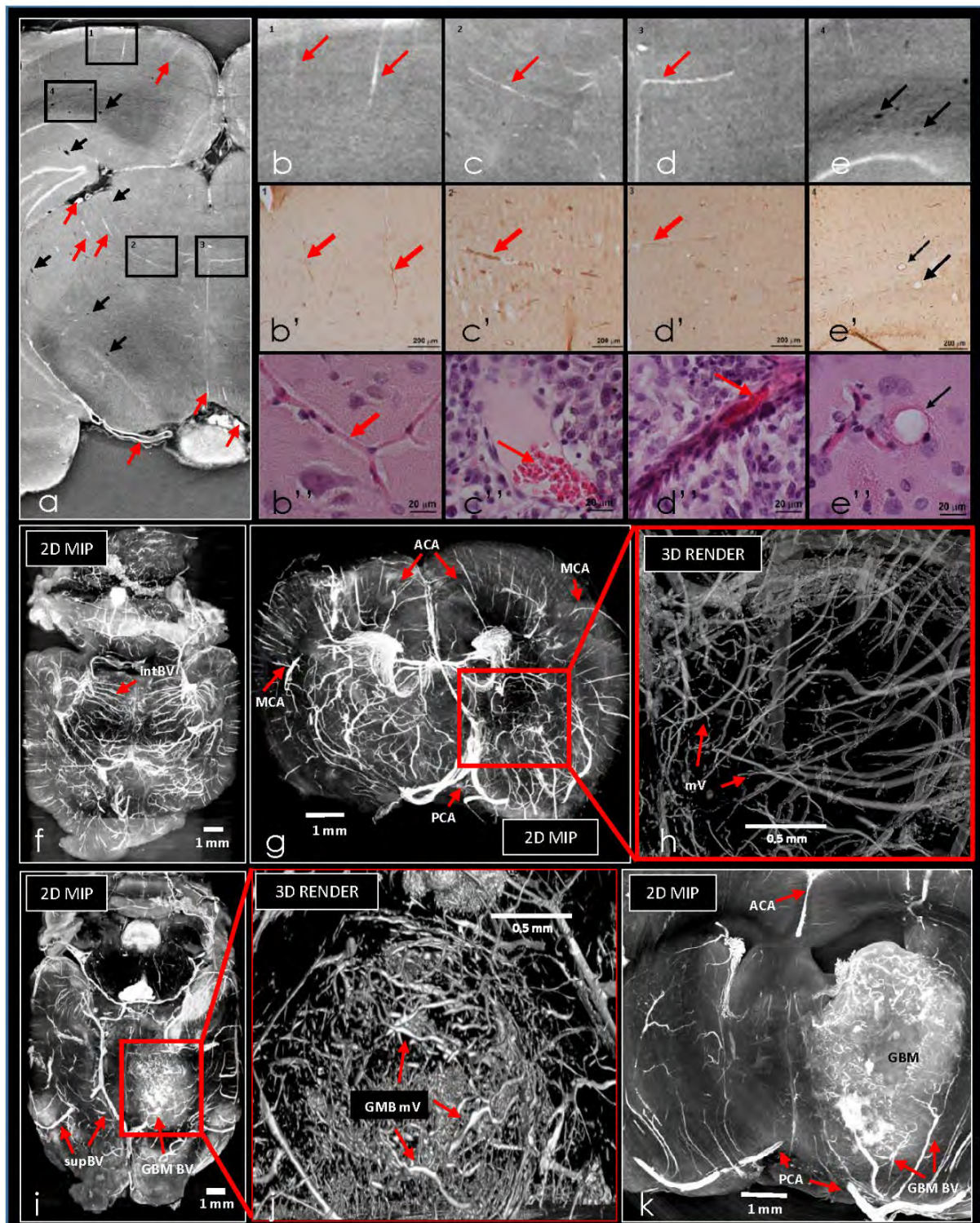


Figure 3 | X-ray PCI-CT, immunohistochemistry and H&E staining of blood vessel anatomy. (a) Coronal PCI slice at the -5.4 mm from bregma level of a rat brain bearing a GBM shows both low-density (black arrows) and high-density (red arrows) tubular interconnected structures. **(b,c,d,e)** details of PCI vascular imaging taken from the

squares 1, 2, 3 and 4 highlighted in **(a)**. **(b',c',d',e')** details from the immunohistochemistry of laminin, a marker of blood vessels performed at the same bregma level as the PCI in **(a)** and taken from the same 1 to 4 squares (a full laminin histology slice can be found in **Suppl. Fig. 8**). Note the presence of collapsed or blood-filled blood vessels **(b', c', d')**, corresponding to bright high-density tubular structures (red arrows) in **(a)**, and empty blood vessels **(e')**, corresponding to dark low-density formalin-filled tubular structures (black arrows) in **(a)**. H&E staining at the same bregma level as the PCI in **(a)** showing a collapsed capillary **(b'')**, a half-empty vessel with few red blood cells **(c'')**, a vessel filled with packed red blood cells and an empty blood vessel **(e'')**. Red arrows indicate vessels corresponding to bright PCI signal and black arrows indicate vessels corresponding to dark PCI signal. Axial **(f, i)** and coronal **(g,k)** 2D maximum intensity projection maps (MIP, see Methods on vessel network renderings) highlight blood-filled, collapsed and thick-walled vascular anatomy: large superficial (supBV) and microscopic ($> 16 \mu\text{m}$ -thick) intra-cortical blood vessels (intBV) appear as intense tubular structures (red arrows point towards them), i.e. anterior (ACA), middle (MCA) and posterior cerebral arteries (PCA) and related microvasculature, in both healthy **(f,g)** and tumor-bearing **(i,k)** brain samples. **(h,j)** 3D render zoom-ins of deep microvasculature: tumor blood vessels (GBM mV) appear aberrant, while healthy ones (mV) more orderly.

4.4.4 Imaging MRT irradiation

After imaging healthy and cancerous brain micro-morphology, we investigated PCI's ability to visualize fractionated radiation effects on nervous tissue, with results summarized in Fig. 4 (data from samples 2-4, 5 and 8). Brain samples from MRT-treated animals bear the typical signatures of this radiosurgery methodology: the spatially-fractionated high-dose microbeams mark brain tissue with $50 \mu\text{m}$ parallel lines of tissue ablation, interspersed by valley regions of low dose delivery. Hypo-dense (and thus hypo-intense in PCI) comb-like patterns are visible in *post-mortem* PCI images (**Fig. 4a-e**) and were confirmed by comparison to histology (**Fig. 4a'-e'** vs. **4a''-e''**). Finally, the ablations were related to similar patterns appearing also in MRI images (**Fig. 6**).

Via PCI, different modes of irradiation can be recognized, differentiated and verified post-treatment: cross-firing modes (**Fig. 4b** and **4d**) feature a checkered irradiation signature, as opposed to the striated patterns typical of unidirectional treatment (**Fig. 4a, 4c, 4e**). Post-irradiation tumor growth and *post-mortem* sample preparation play a role in making the micrometric hypo-dense striations appear only quasi-parallel or even curved. Still, relative spacing in-between ablations is preserved. Radiation-driven tissue ablations are likewise detected by PCI as they target cancerous masses (**Fig. 4c, 4d**). We observe MRT beam-paths transect distorted hippocampal cell layers, hyperplastic vessels (**Fig. 4c, 4c'**), or cortical brain tissue (**Fig. 4d, 4d'**) and hit implanted tumors, which are calcifying, present extravasations (**Fig. 4c**), or are infiltrating adjacent regions (**Fig. 4d**). Microbeams slice the target region into parallel micro-planes, and blood vessels within nervous tissue are also traversed by the radiation. Despite the high doses delivered ($> 250 \text{ Gy}$), we observe preservation of vascular anatomic continuity post-treatment of both large and microscopic vessels: vasculature can be followed branching across microbeam-ablated areas, resist microbeam erosion and connect to valley-dose tissue regions (**Fig. 4e, 4e'**). By comparison to H&E histology, microbeams appear well resolved by PCI within the layers of denser cellularity and with abundant cell bodies, such as the cerebellar granular layer (**Fig. 4a'-a''**), areas within the cortex and midbrain regions (**Fig. 4b', 4b''**) or the packed pyramidal and granular layers of the hippocampus (**Fig. 4c', 4c''**). Less image contrast is achieved when the ablations cross the

cerebellar molecular layer and white matter regions (**Fig. 4a'-a''**), or the sparser-in-cell-bodies and more fiber-rich hippocampal strata (**Fig. 4c', 4c''**), though a glimpse of their presence and directionality can be in most cases still recognized by the expert eye. Signs of intra-microbeam reactive gliosis are revealed by GFAP (**Fig. 4d''**) and compared to PCI (**Fig. 4d'**): in both panels we observe right hemispheres with crossed microbeam paths, and contralateral hemispheres with unidirectional microbeams. Additionally, Iba-1 immunohistochemistry in **Suppl. Fig. 10** shows signs of microglial infiltration (Iba-1-positive cells) along microbeam paths. Finally, the preserved morphology of MRT-targeted local vasculature and microvasculature recognized by PCI was confirmed by comparison to H&E histology in **Fig. 4e'-4e''**.

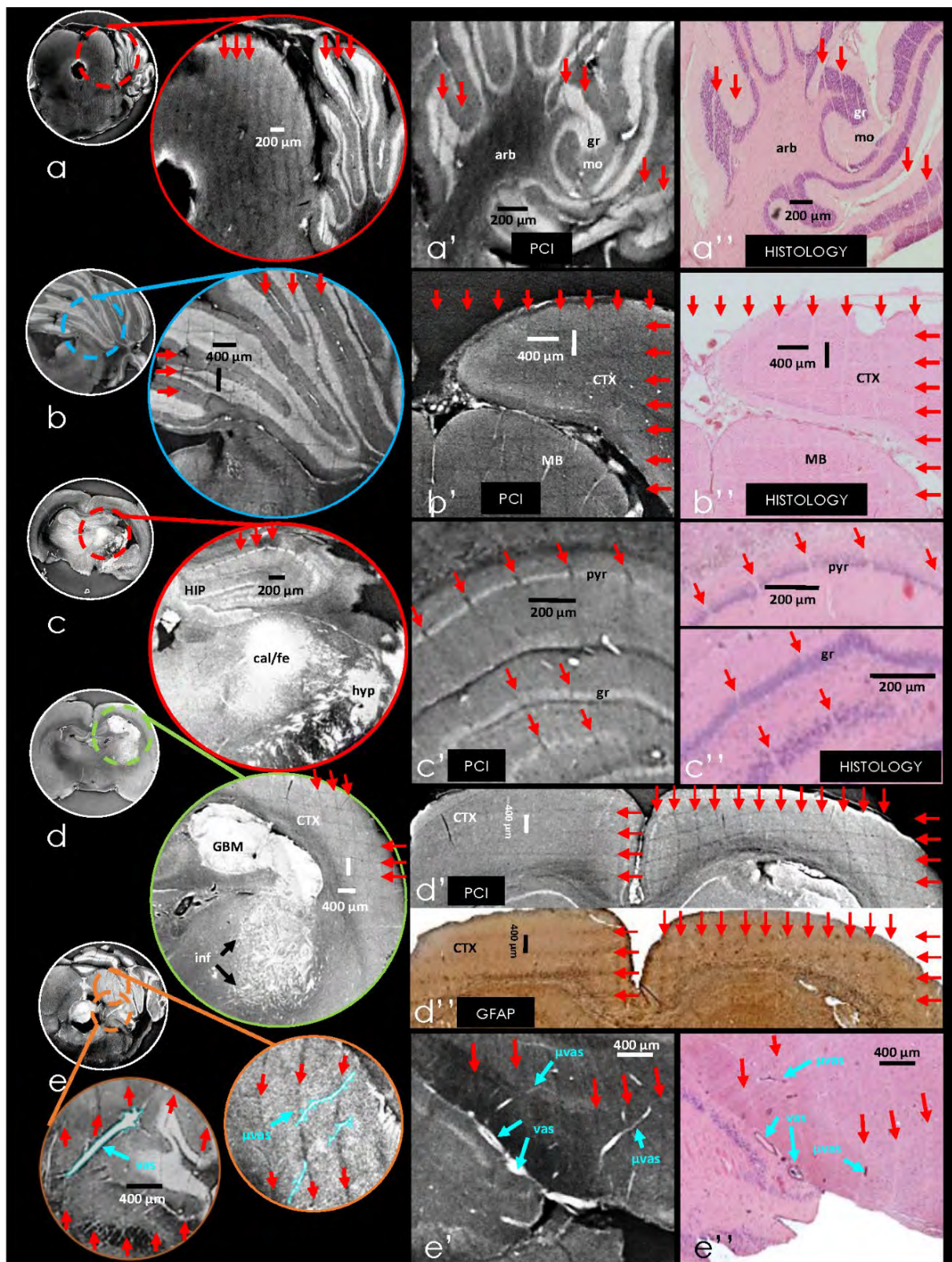


Figure 4 | Phase-contrast CT of MRT treatment on normal tissue, tumor tissue and vessels. 1.5 months after irradiation collimated X-ray planes administered during MRT treatment appear on brain tissue as comb-like traces of tissue ablation. Red arrows point in the direction of incoming microbeams (width 50 μm). Coronal slices of: **(a)** unidirectional MRT irradiation with peak entrance-dose at 400 Gy and 200 μm c-t-c inter-microbeam distance. Zoom-in of microbeam ablations within cerebellar granular (gr) and molecular (mo) layers, and the *arbor vitae*, resolved by PCI **(a')** and confirmed by H&E histology **(a'')**. **(b)** cross-firing MRT irradiation at 2x400 Gy and 400 μm c-t-c distance. **(b'')** histology confirms presence of the checkered ablations seen via PCI **(b')** in

both the cortex (CTX) and midbrain regions (MB). **(c)** unidirectional MRT irradiation, with peak entrance-dose at 600 Gy and 200 μm c-t-c inter-microbeam distance, crossing inner layers of a dorsal hippocampus (HIP) distorted by nearby tumor growth. Presence of local high-Z material accumulation is observed (cal/fe, confirmed as calcium and iron deposits in Fig. 5), and vasculature shows signs of tumor-induced endothelial-cell hyperplasia (hyp). MRT-driven transection of hippocampal layers is detected by PCI **(c')** and confirmed by H&E histology **(c'')**. MRT ablation contrast is relatively strong in pyramidal (pyr) and granular (gr) layers, feeble in the other layers. **(d)** cross-firing MRT irradiation at 400x2 Gy and 200 μm c-t-c distance crossing the brain cortex (CTX) and targeting a glioblastoma tumor (GBM) in the lateral ventricle, showing microscopic cancerous infiltration (inf) toward the diencephalon. Intra-microbeam cells are positive for GFAP immunostaining **(d'')**, revealing signs of reactive gliosis along beam paths, which are visible in both PCI **(d')** and GFAP **(d'')** as crossed ablations in the right brain hemisphere, and as feeble uni-directional ones in the contralateral hemisphere further away from incoming MRT radiation. **(e, e')** brain vasculature and microvasculature (vas and μvas , in turquoise) resist microbeam erosion, bridging across microbeam-generated gaps, as confirmed by histology **(e'')**.

4.4.5 PCI-CT & Histology

PCI as an anatomical neuroimaging modality was compared to histology and to immunohistochemistry in **Fig. 5**, by analyzing a brain sample featuring a GBM tumor growing in the striatum, in the lateral ventricle and massively infiltrating the nearby thalamus (data from sample 6). Overall, as already observed in **Figures 1 to 4**, here too PCI image contrast (**Fig. 5a-a'-a''**) matches the morphological histology of normal and tumor tissues afforded by both H&E stain (**Fig. 5b-b'-b''**) and Nissl stain (**Fig. 5c-c'**). MRT-driven ablations are also visible via all three techniques (**Fig. 5a,b,c**). Broad pathologic hyper-intense regions in PCI, attributed to GBM cancerous tissues already in **Fig. 2**, are visible in the PCI coronal slice in **Fig. 5a**. Again, GBM hyper-intense signal and altered morphology in PCI finds histological match in the signal and morphology of the most strongly marked tissues of both Nissl and H&E histology data (**Fig. 5a,a''** vs. **5b,b''** and **5c,c'**): denser and altered GBM cancerous cellularity seen via histology (**5b'', 5c'**) leads to macroscopic tumor-driven morphological tissue modifications and to cellular hyper-density, both of which increase PCI signal (**5a''**). Normal striatal tissue cellularity (**5b'**), in comparison, leads to a lower more homogeneous PCI signal (**5a'**). Though the cellular level reached via histology is not fully resolved in PCI at this imaging resolution, we observe once again how tissue cellular micro-milieu and macroscopic morphological differences between normal and cancerous tissues together play an important role in determining PCI signal differences.

Immunohistochemical analysis (**Fig. 5d-f**) of GFAP, a marker of reactive gliosis, Iba-1, a microgliosis marker, and Ki-67 protein, a marker of proliferating cells, shows the altered cellularity in the tumor mass detected via PCI, and additionally allows the identification of different cellular types in the tumor. Analysis of GFAP (**Fig. 5d, 5d'**) shows the presence of reactive astrocytes within cancerous tissues, and few reactive astrocytes also along MRT microbeam paths (see MRT tissue ablations and immunohistochemistry also in **Fig. 4d'-d''**). Analysis of Iba-1 (**Fig. 5e, 5e'**) shows the presence of a massive microglial inflammatory infiltration within cancerous tissues, and very few microglial cells along MRT microbeam paths. Finally, analysis of the expression of the Ki-67 protein (**Fig. 5f, 5f'**) shows the presence of dividing cells within cancerous tissues only.

Next, PCI images of MRT-treated tumor-bearing samples were often observed to present areas of bright globular agglomerates (**Fig. 5g**) within and surrounding tumor tissues. Due to image windowing, these ultra-dense areas (most likely pertaining to an absorbing high-Z material) appear as extended bright saturated patches in PCI (**Fig 5g'**), though they are actually grainy in morphology, as visible when gray-levels are better adjusted to visualize these features alone (**Fig. 5g''**). In **Fig. 5h-h'**, obtained by multiplication of **5g'** and the inverse of **5g''**, we can create artificial intra-agglomerate image contrast, which enables the visualization of the correct agglomerate local morphology via PCI. In fact, by substituting to the original image the ultra-dense patches in **Fig. 5g''**, this time with inverted pixel gray-levels, we form central dark/black ultra-dense clusters, which highlight the proper local shape of the ultra-bright region in the original unaltered PCI image in **Fig. 5g**. Histological analysis characterized the ultra-dense PCI-detected features in **Fig. 5g-h** as regions of altered cellular composition (**Fig. i,i'**), where accumulation of calcium (**Fig. 5j,j'**) and iron deposits (**Fig. 5k,k'**) is present. In fact, the ultra-dense agglomerates in PCI (dark pixels in **Fig. 5h**) correspond to large areas of altered tissue cellularity and possible calcification in H&E histology (**Fig. 5i**). Moreover, these same areas are positive to Alizarin red S staining (**Fig. 5j**), specific for calcium deposits, and to Perls' Prussian Blue staining (**Fig. 5k**), specific for the detection of iron. The broad shapes of the deposits are closely matching in all four methodologies (**Fig. h-i-j-k**). Moreover, by zooming in and viewing the agglomerates at the supra-cellular level (**Fig. h'-i'-j'-k'**), we observe how the deposits are composed of many localized round grains in both PCI (**Fig. 5h'**, dark/black grains), H&E histology (**Fig. 5i'**, dark-pink grains), after Alizarin red S staining (**Fig. 5j'**, red grains) and after Perls' Prussian Blue staining (**Fig. 5k'**). Again the methods all afford similar morphological results and complement each other in terms of functional information. The presence of calcium and iron accumulation within degenerating cancerous tissues, either radiation-induced, as already reported in literature (Flament-Durand *et al.*, 1975; Shanley, 1995; Suzuki *et al.*, 2000), or from intra-tumor calcification or blood extravasation, leads to very intense bright signals in PCI. We can conclude that highly dense materials (such as iron and calcium) strongly affect PCI imaging and could be involved in the formation of the PCI signal hyper-intensities observed within vasculature (from iron-rich blood aggregates) or within GBM tissues (again from the high blood volumes likely present). These results, supported by the immunohistochemistry in **Fig. 5**, are in line with the characterization of both GBM and vasculature morphology made in **Fig. 2** and **3**. Full histological and immunohistochemical datasets are included in **Suppl. Fig. 10**.

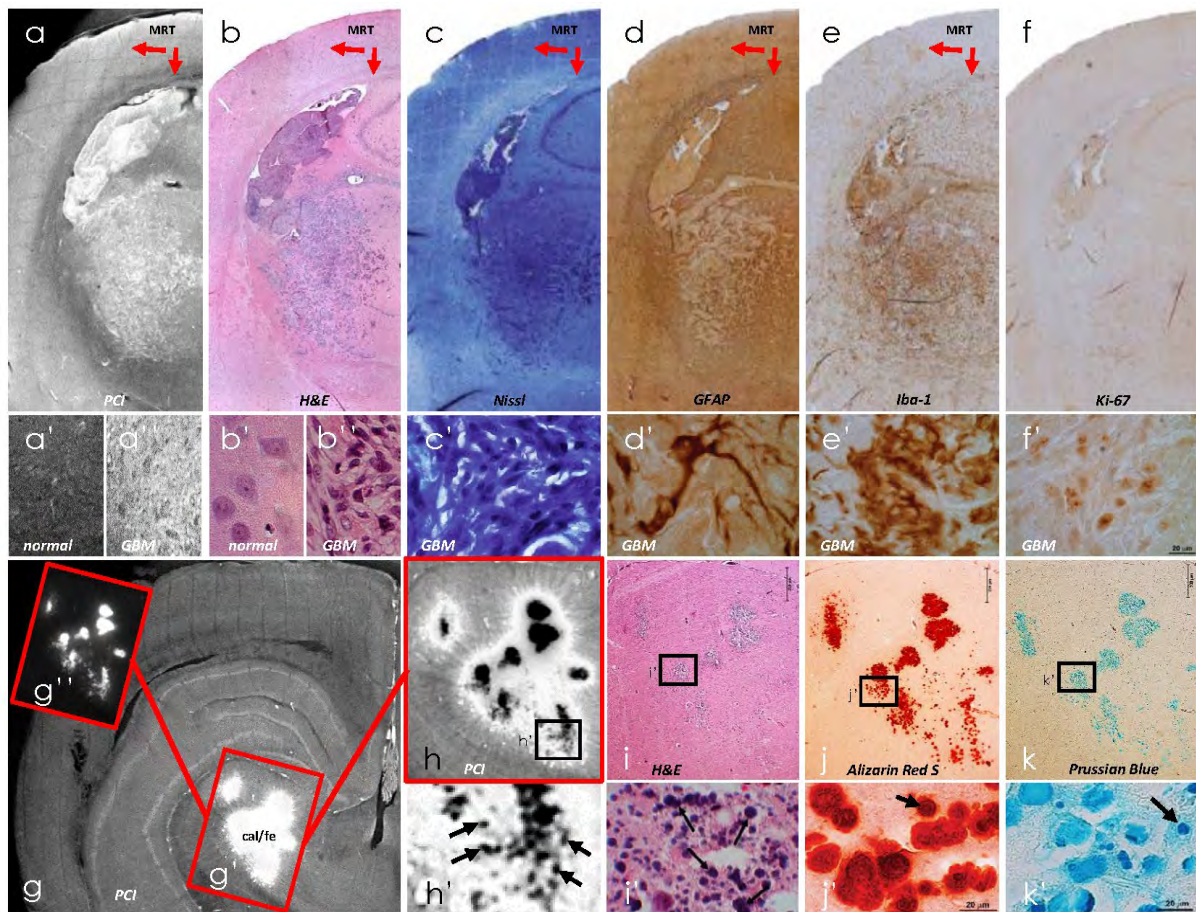


Figure 5 | Histological and immunohistochemical confirmation of X-ray phase-contrast CT imaging. (a) Coronal PCI at the -2.4 mm from bregma level of a rat brain bearing a GBM. (b) Corresponding hematoxylin/eosin (H&E) staining at the same bregma level. (c) Coronal Nissl staining at the -2.5 mm from bregma level of a rat brain bearing a GBM. (d) Immunohistochemistry for GFAP of an adjacent coronal section of a rat bearing GBM. Note the presence of GFAP-positive cells in the tumor tissues and along MRT microbeam paths. (e) Immunohistochemistry for Iba-1 in an adjacent coronal section of a rat bearing GBM. Note the presence of Iba-1-positive cells in the tumor tissues and along MRT microbeam paths. (f) Immunohistochemistry for Ki-67 in an adjacent coronal section of a rat bearing GBM. Note the presence of Ki-67-positive cells in the tumor tissues. (a', b') Details of PCI and H&E staining taken in the normal contralateral striatum, showing respectively smooth local morphology and normally-appearing cells. (a'', b'') Details of PCI and H&E staining taken within GBM tissue, showing respectively altered morphology and cancer cells. (c') Higher magnification of Nissl staining taken within GBM tissue, showing altered cellularity. (d') Higher magnification of GFAP-positive cells taken within GBM tissue. (e') Higher magnification of Iba-1-positive cells taken within GBM tissue. (f') Higher magnification of K-67-positive cells taken within GBM tissue. (g) Coronal PCI at the -4.8 mm from bregma level of a rat brain bearing a GBM, showing an extended area of accumulation of bright high-Z material (cal/fe) within cancerous tissue in (g'). (g'') readjusted image windowing of (g') to show the grainy morphology of the high-Z material accumulations. (h) PCI Zoom-in obtained by multiplication of (g') and the inverse of (g''). The artificial gray-levels enable the visualization of correct agglomerate local morphology. Note the *sui generis* meaning of the inverted dark pixels in (h) after the image processing, unconventionally standing for ultra-density instead of for low-density. (h') Magnification of (h): note the granular morphology of the ultra-dense particles (arrows in h'). (i, i') Different magnifications of H&E histology show calcifications within altered cancerous tissue corresponding to the hyper-dense agglomeration area in (h, h') and (g). These calcifications (large dark pink grains, arrows in i') appear as areas of high-intensity signal in (g'-g''-h) as a likely result of tumor-driven tissue degeneration. (j, j') Different magnifications of Alizarin Red S staining, specific for calcium deposits, within the tissue corresponding to the PCI image in (h). Note the granular morphology of the red-stained particles (arrow in j'). (k, k') Different

magnifications of Perls' Prussian Blue staining, specific for iron deposits, within the tissue corresponding to the PCI image in **(h)**. Note the granular morphology of the blue-stained particles (arrow in **k'**).

4.4.6 PCI-CT & MRI

Various both T1- and T2-weighted ultra-high-field 9.4 T MRI measurements were performed on one brain sample (sample 1), and compared to the X-ray PCI-CT datasets. The MRI sequences, optimized for high-resolution brain anatomical imaging, were selected to serve as an additional established basis for the validation of PCI as a morphological neuroimaging technique. Selected best results are included in Figure 6 (with sequence specifications in the Methods), and a complete dataset, showing the comparison of PCI signal to 10 different MRI sequences and related sequence specifications, can be found in **Suppl. Fig. 11** (axial images) and **Suppl. Fig. 12** (coronal images). As a note, the sample faced long-term storage immersed in formalin. As previously reported in literature (Shepherd *et al.*, 2005), formalin fixation permanently alters relaxation and diffusion properties of CNS tissues, with resulting both T1 and T2 times being reduced with respect to standard fresh unfixed slices or compared to *in-vivo* imaging. In fact, the measured T1 and T2 maps (**Suppl. Fig. 13**) show reduced T1/T2 times compared to standard literature values (**Suppl. Table 1** and **Suppl. Table 2**). In light of this, the MRI data presented here (**Fig. 6**), though it can still serve as an established platform for the validation of PCI neuro-contrast, it is not appropriate for a quantitative contrast comparison, which would need specific *post-mortem* MRI sample fixation, washing and staining procedures (Johnson *et al.*, 2002) in order to fully exploit the technique's potential.

Full-organ gross brain anatomical features are visible in axial images from both T1-weighted (**Fig. 6a**) and T2-weighted (**Fig. 6b**) MRI. Furthermore, we observe that the corresponding PCI-CT dataset slice (**Fig. 6c**) renders a matching sample brain local morphology, for example, in the layers of hippocampal tissue, in brain ventricles, in the striatum region and for large fiber tracts. The DTI metric D_{zz} tensor symmetric component (a diffusion map) and RARE imaging (**Fig. 6d-e**) both show high fiber-tract contrast (forebrain bundles especially) compared to corresponding PCI-CT (**Fig. 6f**), which instead seems more sensitive to the densely-packed micro-environment of neuron cell-bodies in the hippocampal pyramidal and granular layers. MSME (**Fig. 6a**), MGE (**Fig. 6g**), FLASH (**Fig. 6b**) and RARE (**Fig. 6e,h**) sequences all detect the microbeam-induced tissue ablations visible in PCI-CT images (**Fig. 6c,f,i**). Microbeams appear as hyper-intense parallel lines in the MSME and FLASH scans, and instead as hypo-intense in both MGE and RARE maps. MRT tissue ablations feature local hypo-density, and thus appear hypo-intense in PCI maps, as already shown in **Fig. 4**. Both imaging techniques well describe intra-cerebral calcifications and iron deposits (see also **Fig. 5**), which are hypo-intense in MRI and hyper-intense in PCI-CT (**Fig. 6a,b** vs. **6c** and **6d,e** vs. **6f**). Finally, overall tumor morphology can be appreciated in both imaging modalities (**Fig. 6a** vs. **6c**, and **6e** vs. **6f**). PCI-CT's higher resolution benefits the visualization of local intra-tumor details from pathological GBM cellularity and vasculature (**Fig. 6c,f**).

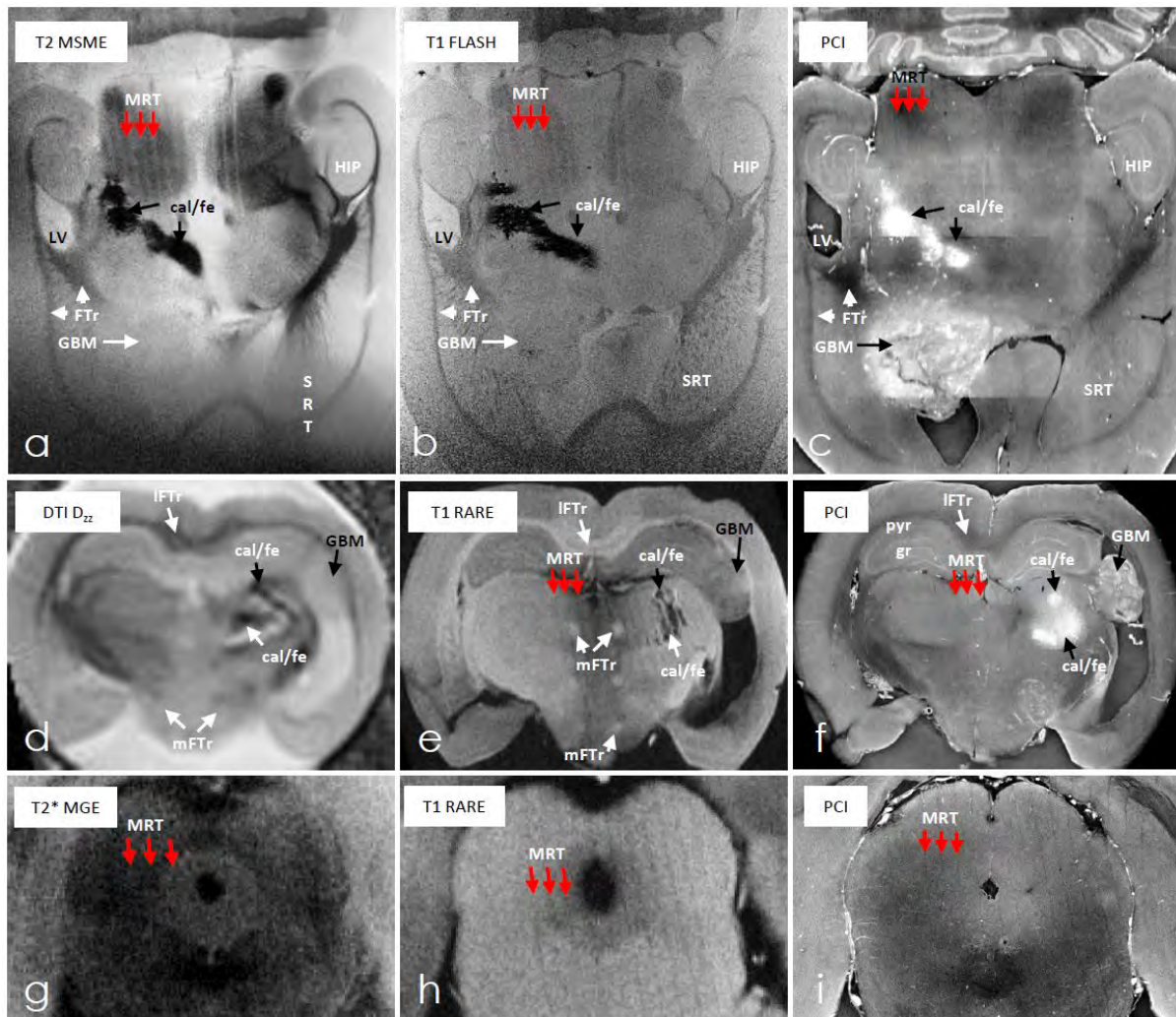


Figure 6 | X-ray phase contrast CT vs. MRI. Corresponding axial images of a tumor-bearing MRT-irradiated brain, from (a) a T2-weighted MSME sequence, (b) a T1-weighted FLASH sequence and (c) PCI-CT, compare local anatomy of the hippocampus (HIP), lateral ventricles (LV), striatum (STR) and cerebral fiber tracts (FTr). Corresponding coronal images of the same sample, at a first slice-level from (d) the DTI metric D_{zz} symmetric tensor component (a diffusion image), (e) a T1-weighted RARE sequence and (f) PCI-CT, and at a second slice-level from (g) a T2*-weighted MGE sequence, (h) a T1-weighted RARE sequence and (i) PCI-CT: medial forebrain bundles of fiber tracts (mFTr) show strong RARE signal (e) and some diffusion signal in the D_{zz} DTI metric (d), whereas lateral forebrain bundles (IFTr) are visible also in PCI-CT (f); pyramidal (pyr) and granular (gr) layers of the hippocampus in (f) can be resolved at high resolution. Finally, both MRI and PCI images show sensitivity to deposits of iron and calcium (cal/fe), to MRT-induced tissue ablations (MRT) and to glioblastoma tissue (GBM) (a-i). Red arrows point in the direction of incoming microbeams.

4.5 Discussion

This experimental neuroimaging study evaluates how well PCI-CT imaging can visualize the effects of MRT on normal and tumor tissue in the brain of an animal model. Our results show micrometric histological precision and high soft-tissue contrast without addition of contrast

agent (**Fig.1-4**, **Suppl. Fig. 7**), enabling effective 3D full-organ segmentations and renderings of complex anatomical and pathological brain structure (**Fig. 2**, **Suppl. Fig. 9**).

Being sensitive to the refraction of X-rays in matter, PCI-CT is particularly adapted to visualize weakly absorbing details, like those often encountered in biology and medicine. In fact, this imaging method has already been demonstrated to enable the *post-mortem* analysis of a broad range of biological tissues, and has been recognized as interesting for biomedical applications and experimental studies (Bravin, Coan and Suortti, 2013). Of note in the result presented in this work is the variety of concurrent anatomical detail PCI is sensitive to: intra-cortical micro-vasculature and cancerous lesions are well depicted alongside MRT-driven tissue ablations and minute cerebral structures, such as the dentate gyrus within the dorsal hippocampus or the choroid plexi within lateral ventricles (**Fig. 1-3**). Moreover, worth mentioning, and of interest to preclinical studies, beyond a delineation of *post-mortem* CNS gross anatomy comparable to that of MRI (**Fig. 6**), is the achievable degree of precision in the rendering of brain and brain tumor micro-anatomy, even after sample storage in formalin fixative. For example, phase-contrast within several neuronal microscopic strata, such as the pyramidal and granular layers of the hippocampal formation, was observed both in healthy layers and after transection by MRT radiation (**Fig. 1e**, **Fig. 4c'**). Micrometric striated tissue ablations, traced by high-dose parallel X-ray microbeams, forming comb-like hypo-dense patterns, were visible via PCI imaging also in cerebellar and cerebral regions of the brain organ (**Fig. 3**). Last, we observed diverse of local tissue effects due to both MRT treatment and GBM tumor growth, from pseudopalisading (**Fig. 2e**) and to necrosis (**Fig. 2c,e**), to intra-tumor deposition of iron and calcium granular aggregates (**Fig. 2e**, **Fig. 4c**, **Fig. 5g-h-h'**) and to tumor infiltration (**Fig. 4d** and **5**).

As already mentioned, in terms of contrast mechanism, the X-ray PCI-CT technique exploits the phase effects of an X-ray wave within a material (Momose *et al.*, 1996), a process governed by its index of refraction. In simple terms, the technique produces a 3D spatial distribution of phase shifts, which depend on local material properties including the local electronic density. Macroscopically, this signal can be understood as a map of the local density and refraction-related properties of a material, with PCI image contrast arising from local relative differences in these properties. This fact holds true also for biological materials, such as the nervous tissue in the brain, where absorption effects are generally quite small. High PCI contrast can be observed in **Fig.1**, for example, between the two (granular and molecular) layers of gray matter in the cerebellum (**Fig. 1a**, **1d**). The granular layer contains a high number of small but densely-packed neuron cells (granule cells) and is reported to make up a disproportionate amount of the brain's mass compared to its volume, thus forming a peculiarly dense layer (Shepherd, 2004). Instead, the cells present in the nearby molecular layer, are much sparser. This difference in cellular composition is well-described by H&E-stained histological cerebellar slices, where the abundant cell-bodies in the granular layer stain dark violet (hematoxylin attaches to intra-soma DNA/RNA), whereas the molecular layer, where fewer cell nuclei are present, stains mainly pink (from the eosin). Interestingly, the two layers show distinctly different PCI signals (see **Fig. 1a** and **1d**, labeled *mo* and *gr*) and give rise to high phase-contrast. MRI contrast between granular and molecular layers, instead, is reported (Schulz *et al.*, 2012) to be low, suggesting that similar tissue environments for

water molecules and low differences in local vasculature and blood volumes are present. Since the key tissue feature discriminating between the cerebellar gray matter layers is the difference in cellular density and composition (and thus of tissue cellularity, intended as number and type of cells present), the observed high PCI contrast within these layers points toward a link between PCI signal and local brain tissue cellularity. This connection seems to hold also in the white matter layer of the cerebellum. Central to the granular layer and formed mainly by input and output nerve-fiber systems, it is also poor in cell somas (being mainly composed of climbing and mossy fibers) and it typically stains mostly pink in H&E histology. As expected from its cellularity (low cell-soma densities), its PCI signal (see **Fig. 1d**, labeled *arb*) is also relatively hypo-intense relatively to the granular layer. Finally, the same relationship can also be seen in the granular vs. molecular layers of the hippocampus in **Figures 1e-f-g**: the H&E histology stains the granular layer mostly violet and the molecular layer mostly pink (**Fig. 1f**), highlighting cellularity differences. And the PCI too exhibits hyper-intensity in the granular layer compared to the molecular one (**Fig. 1e**). Several other figure panels (in **Fig. 2, 4** and **5**) compare brain tissue cellularity highlighted by H&E staining to corresponding PCI contrast. What we observe overall is a representation of local brain morphology (how tissue shapes are visualized), which is quite similar in both techniques (PCI vs. H&E). Moreover, histological cellular staining levels seem to relate to PCI signal intensities as well (with areas of hyper-intense PCI matching histological areas of hyper-cellularity). In light of the type of PCI contrast observed in all these tissues, a link between PCI signal and local tissue cellularity seems plausible to us. Moreover, this link seems reasonable, because for biological tissues it is their composition (and thus also their cellularity) that influences local density and refractive properties, and thus PCI measurements.

A similar relationship between overall tissue composition, cellularity and PCI contrast should hold also in the case of GBM tissue. At the cellular level, the abnormal biology of GBM tissue, e.g. local parenchymal destruction, hyper-cellularity, metastatic cell infiltration, high-rates of cell reactive gliosis, proliferation, high blood local volumes, aberrant hyperplastic microvasculature as well as blood extravasation are all factors, which concur to generate densely-packed, blood-rich and chaotic intra-tumoral environments. This exotic tissue micro-milieu must influence local density and refraction properties, and thus should reasonably also play a role in PCI contrast formation. In panels **2f-g, 2h-i-j**, and even **2e-e'**, we observe GBM tissues, which stain dark-violet in H&E histology. PCI shows GBM tissues, which morphologically follow the histological GBM shapes, and an overall local increase in PCI signal in all datasets acquired (**Fig. 2a** and **2b**). In addition, PCI-based panels **3i-j-k** showcase the rich presence of local aberrant GBM vasculature and micro-vasculature. Overall, the imaging method seems to provide cancer-tissue morphological visualizations that are related to local malignant cellularity and to malignant tissue and vasculature anatomy. And, in light of the PCI contrast mechanism already noted for normal brain layers, the observed link between PCI hyper-signal, GBM density, hyper-cellularity, high blood contents and local aberrant micro-vasculature does indeed seem reasonable. This biological interpretation of the detected PCI signal seems also supported by the immunohistochemical analysis in **Fig. 3** and **5**. Admittedly, though, PCI is a morphological experimental imaging modality but not a functional imaging tool, and for this reason any differentiation of brain structure based on PCI intensity

information should best be complemented at least partially by the recognition of specific morphological features.

As already discussed, other cutting-edge technologies used in neuroimaging have their strengths and limits: brain micro-MRI can routinely be applied *in-vivo* at increasing resolution for both morphological and functional imaging, but for the highest *post-mortem* resolutions needs tailored 'staining' protocols and struggles to achieve sub-micrometric resolution. Most other high-resolution preclinical neuroimaging techniques instead can clearly observe cellular and subcellular detail, but offer only a partial or localized (often stain-dependent) anatomical visualization, including traditional 2D imaging approaches like histology or scanning electron microscopy. To the best of our knowledge, PCI is the only imaging technique providing rodent full-organ micrometric resolution in neuroimaging and high-contrast tumor imaging without extensive sample-preparation (e.g. without injection of intra-venous contrast, mechanical alterations or dissection). For its part, a current clear limitation of PCI-CT in neuroimaging is the difficulty arising when the method is applied *in-vivo* in the CNS: the negative influence of high-scattering and porous materials, such as those within the skull and vertebral bones, on the detectable X-ray phase-contrast drastically reduces the quality of intra-skull and intra-vertebral nervous tissue visualizations. PCI resolution limits are related to detector, optics and X-ray source technologies, and ongoing technological efforts aim to obtain even sub-micron resolution datasets (i.e. cellular level datasets) at fields-of-view interesting for brain soft-tissue small animal studies. Other limitations for *in-vivo* experimental applications are due to the high doses delivered in CT mode in combination with motion-artifact reduction algorithms, and to the high current acquisition times needed by laboratory setups, where the available photon fluxes are much lower compared to those available at synchrotron sources. Ongoing new developments in both dose-reduction algorithms (Zhao *et al.*, 2012) and compact high-flux X-ray light sources (Variola, 2011) are aimed at mitigating these challenges. Moreover, PCI-CT today can be applied also in the laboratory with several novel advanced X-ray-tube technologies (Larsson *et al.*, 2013; Eggl *et al.*, 2015; Bidola *et al.*, 2017), freeing this imaging technique from a synchrotron-only setting.

The results presented here explore a young and challenging field of application for PCI, experimental neuroimaging. Though a full biological and functional characterization in many cases will still necessitate immunohistochemical analysis, the methods used here appear well-suited for *post-mortem* morphological brain analyses, which need to avoid any sample dissection. In fact, complex full-organ vascular and cancerous pathologies arising from GBM tumor were visualized within an excised rodent encephalon. Moreover, the morphology of biological and physical effects on nervous tissue after brain cancer radiotherapy were also faithfully depicted. The microbeam configuration, geometry and dose distributions used within this study (peak and valley doses, microbeam size, center-to-center distances and irradiation area) are all in line with the values used in the literature of MRT preclinical research on rodents (Bartzsch *et al.*, 2013; Bouchet *et al.*, 2013, 2016; Dufort *et al.*, 2016). In addition, following published Monte Carlo calculations, the doses used are relevant also in view of the clinical translation of MRT (Martínez-Rovira, Sempau and Prezado, 2012). In light of this, the presented results, by setting the groundwork for the identification of GBM tissue, of MRT-driven tissue ablations and of both normal and pathologic vascularization, can serve as a guide

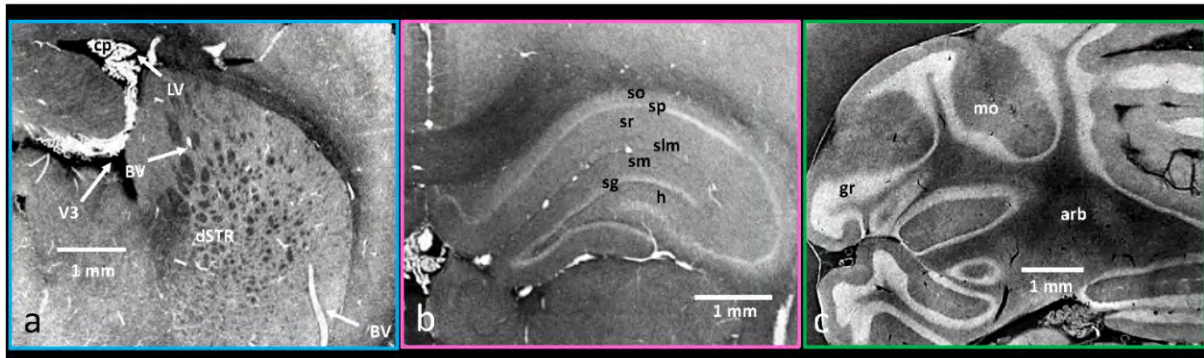
for image interpretation of future PCI-based *post-mortem* imaging studies of MRT treatment using standard irradiation parameters. Tumor radio-resistance and drug efficacy studies could also benefit from the volumetric quantifications of tissue volume modifications, which PCI can provide. Finally, and most importantly, this manuscript shows how the PCI technique can precede and guide localized histological analyses (e.g. immunohistochemistry, as shown in **Fig. 5**), and how it can be used for multimodal biomedical imaging in combination with, before or after other experimental neuroimaging methodologies (e.g. before MRI, as shown in **Fig. 6**).

4.6 Conclusions

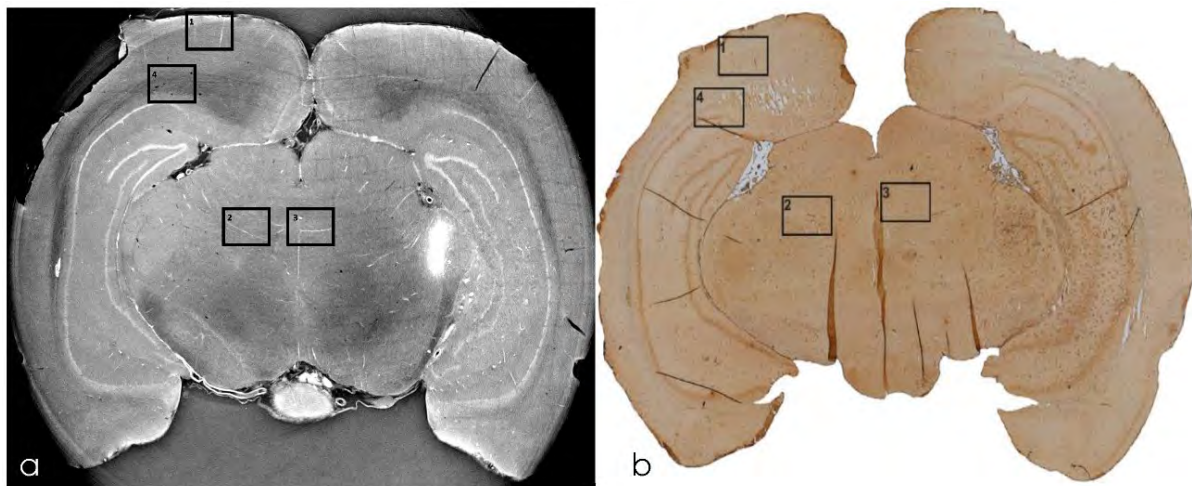
Our results demonstrate that PCI-CT is an experimental imaging technique viable for *post-mortem* follow-up studies of X-ray radiotherapy techniques, e.g. MRT, on small animal models. In fact, PCI-CT, sensitive to soft tissue morphology and composition, provided high-contrast microscale representations of 3D full-organ rodent brain anatomy. PCI images concurrently visualized deep encephalic tumor tissues, healthy tissues, micrometric angio-structure and the effects of high-dose ionizing radiation, all within a one-shot image and without the need to dissect the sample. Moreover, PCI-CT signals were shown to match histological and immunohistochemical data, and to find a counterpart also in experimental high-field MRI. In conclusion, the deep insight into brain and cancer anatomy, which this imaging technique was able to provide *post-mortem*, make it an interesting tool for neurological studies. PCI-based morphological representations of complex vascular and cancerous pathologies, and of biological effects after brain cancer radiotherapy could provide new insight, among others, to studies on local brain tumor tissue radio-resistance, or on drug efficacy in experimental models of neurodegeneration. This technique can precede and guide histological analysis, and can be used for multimodal biomedical imaging in combination with or after other experimental neuroimaging methodologies.

Acknowledgements: Authors would like to acknowledge the financial support from the Deutsche Forschungsgemeinschaft (cluster of excellence) - Munich Center for Advanced Photonics (EXE158) and of the European SYRA3 COST Action TD1205 for networking and financing scientific missions within this project. Authors also thank the ESRF for provision of beamtime and laboratory facilities, Dr H. Requardt for the technical support, Dr. E. Brun for the help in the initial phase of this work, as well as the electronic, computing, and software assistance of the ESRF. Finally, authors thank Prof. B. Ertl-Wagner from the LMU Klinikum Grosshadern for supporting this collaboration, the German Mouse Clinic of the Helmholtz Zentrum München for allowing us to use their 9.4T MRI scanner, and the German Federal Ministry of Education and Research (Infrafrontier grant 01KX1012) (MHdA).

4.7 Supplementary Material



Suppl. Figure 7 | Zoom-ins of local rat brain anatomy. (a) zoom-in of the striated architecture of the caudate-putamen of the dorsal striatum (dSTR) perfused by long bright blood-vessels (BV), and of third ventricle (V3) and lateral ventricles (LV) filled with choroid plexi (cp). **(b)** zoom-in of the dorsal hippocampus divided in Hammon's Horn (stratum oriens (so), str. pyramidale (sp), radiatum (sr), lacunosum-moleculare (slm)) and Dentate Gyrus (str. moleculare (sm), granulosum (sg), hilus (h)). **(c)** zoom-in of the cerebellar arbor vitae (arb), granular (gr) and molecular layers (mo).



Suppl. Figure 8 | Vessel X-ray phase-contrast CT vs. laminin immunohistochemistry. (a) Coronal slice of a rat brain bearing a GBM at the -5.4 mm bregma level. **(b)** Corresponding immunohistochemistry of laminin, a marker of blood vessels, at the same bregma level. Squares 1, 2, 3 and 4 highlight details of PCI and immunohistochemistry used in Fig. 3b-3e and Fig. 3b'-3e'.

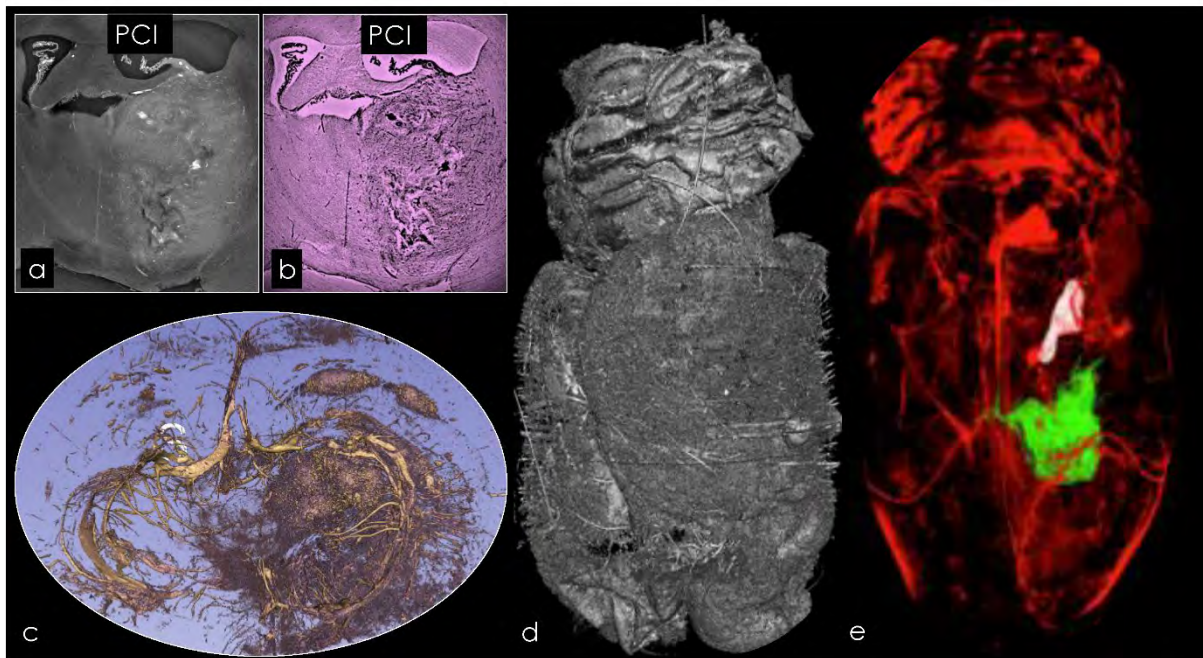


Figure 9 | Phase contrast CT – a tool for 3D virtual histology. (a) 2D PCI image of a tumor-bearing rat brain vs. (b) the same 2D PCI image with histology-like recoloring; (c) 3D region-growing segmentation of a tumor mass and surrounding blood vessel network; (d) full rat brain 3D surface rendering; (e) combined render of a segmented tumor mass (green), a calcium and iron agglomerate (white) and blood vessels or other features (red).

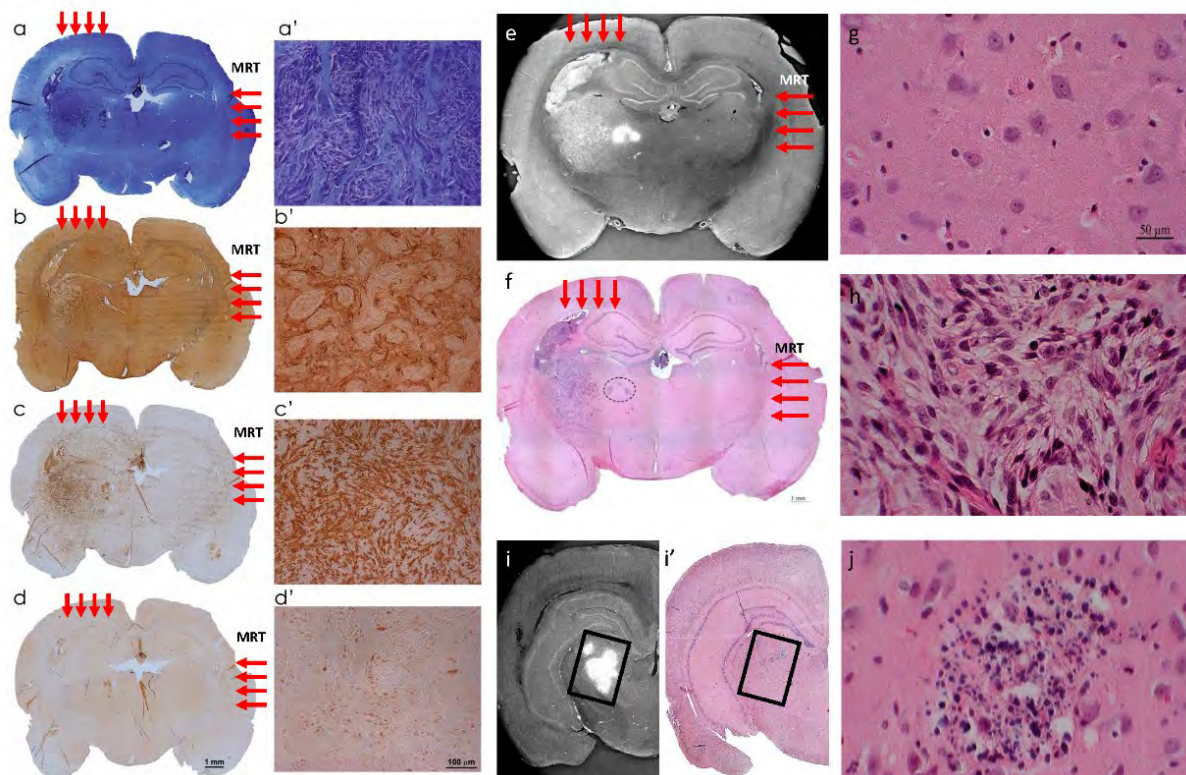


Figure 10 | Full Histological and immunohistochemical (IHC) confirmation of X-ray PCI-CT imaging. Full left-hemisphere coronal images of a GBM-bearing rat brain: (a) Nissl staining at the -2.5 mm bregma level. Adjacent sections: (b) IHC for GFAP. GFAP-positive cells are visible in the GBM tumor mass and along the irradiation path of microbeams. (c) IHC for Iba-1. Like for GFAP, Iba-1-positive cells are present in the GBM tumor mass and along the irradiation path of microbeams. (d) IHC for Ki-67. Ki-67-positive cells are present in the GBM tumor mass. (e,

i) Coronal PCI-CT. **(f, i')** H&E staining. High-magnification images: **(a')** Nissl staining taken in the center of striatum bearing a GBM showing altered cellularity. **(b')** GFAP-positive cells taken the center of striatum bearing a GBM. **(c', c'')** Iba-1-positive cells taken the center of striatum bearing a GBM. **(d')** K-67-positive cells taken the center of striatum bearing a GBM. **(g)** Details of H&E staining taken in the intact striatum showing normal cells. **(h)** Details of H&E staining taken in the center of striatum bearing a GBM showing cancer cells. **(j)** Higher magnification of calcium and iron aggregation corresponding to the squared area in **(i')**. These calcium and iron deposits appear as areas of high-intensity signal in the PCI slice in **(i)**.

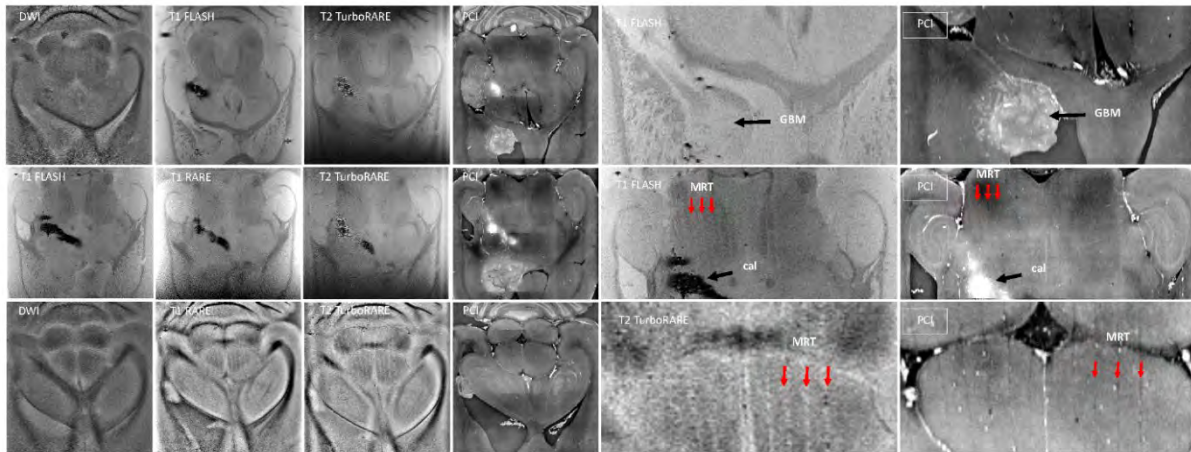


Figure 11 | Axial MRI vs. PCI-CT. Dataset acquired using a two channel array RX/TX cryo-probe (Bruker Z125365).

Sequences specifications for **Figure 11**:

3D-T1 FLASH: Bruker Biospin T1_FLASH_3D_SWI sequence; flip angle: 25°; TE: 4.74ms; TR: 100ms; N-averages: 6; FOV: 25x15x5mm³; pixel size: 48.8x46.9x78μm³; bandwidth: 100000 Hz; duration: 4h 28m 48s.

2D-T1 RARE: Bruker Biospin RAREVTR sequence; TE: 8.75ms; RareFactor: 2; TR-range: 867.5-5000ms; N-T1 experiments: 6; N-averages: 7; FOV: 18x15mm²; slice thickness: 0.8mm; pixel size: 47.3x46.9μm²; bandwidth: 81521.7 Hz; duration: 3h 53m 16s.

3D-T2 TurboRARE: Bruker Biospin T2_TurboRare_3D sequence; TE: 7.32ms; RareFactor: 2; TR: 1800ms; N-averages: 1; FOV: 18x15x8mm³; pixel size: 47.3x46.9x500μm³; bandwidth: 98684.2 Hz; duration: 1h 26m 24s.

2D-DWI: Bruker Biospin DWI_SE sequence; 3 diffusion directions; TE: 20.00ms; TR: 2500ms; N-averages: 1; FOV: 18x15mm²; slice thickness: 0.8mm; pixel size: 56.3x58.6μm²; bandwidth: 45454.5 Hz; duration: 0h 32m 0s.

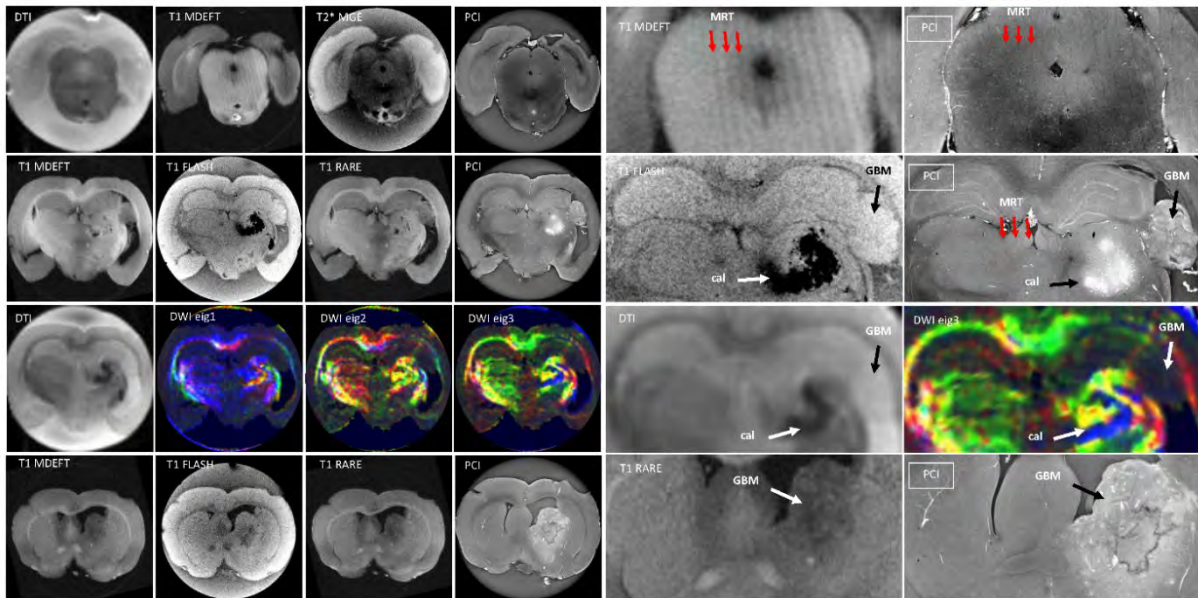


Figure 12| Coronal MRI vs. PCI-CT. Dataset acquired using an eight channel RX array volume coil (Bruker T20030V3) optimized for rat brain imaging in combination with a quadrature TX volume resonator (Bruker T12054V3).

Sequences specifications for **Figure 12**:

2D-DTI: Bruker Biospin DTI_EPI sequence; 30 diffusion directions; max. b-value: 1634.03 s/mm²; TE: 19.96ms; TR: 3000ms; N-averages: 35; FOV: 15x15mm²; pixel size: 138.9x156.3μm²; slice thickness:0.8mm; bandwidth: 340909.1Hz; duration: 1h 1m 15s.

3D-T1 RARE: Bruker Biospin T1_RARE sequence; TE: 8.35ms; RareFactor: 2; TR: 1000ms; inversion delay: 400ms; N-averages: 8; FOV: 15x15x16mm³; pixel size: 53.6x53.6x250μm³; bandwidth: 50000 Hz; duration: 9h 57m 20s.

3D-T2* MGE: Bruker Biospin T2_star_MGE sequence; flip angle: 30°; TE: 3.46ms; TR: 150ms; N-averages: 10; FOV: 15x15x4mm³; pixel size: 58.6x58.6x250μm³; bandwidth: 69444.4 Hz; duration: 1h 16m 48s.

3D-T1 MDEFT: Bruker Biospin T1_MDEFT sequence; flip angle: 30°; N-segments: 5; segment duration: 560ms; TE: 2.40ms; segment TR: 1161ms; inversion delay: 300ms; N-averages: 20; FOV: 15x15x16mm³; pixel size: 53.4x53.4x250μm³; bandwidth: 69444.4Hz; duration: 4h 10m 48s.

3D-T1 FLASH: Bruker Biospin T1_FLASH_3D_SWI sequence; flip angle: 25°; TE: 6.11ms; TR: 100ms; N-averages: 4; FOV: 15x15x16mm³; pixel size: 39.5x39.5x125μm³; bandwidth: 50000Hz; duration: 7h 5m 36s.

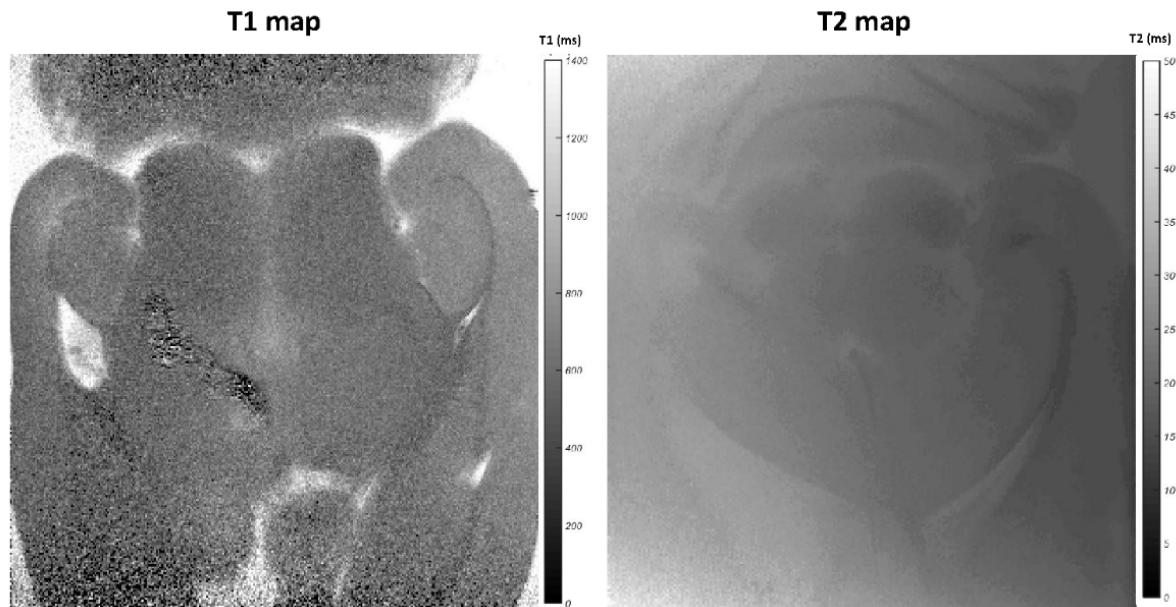


Figure 13 | Quantitative T1 and T2 relaxation maps. Sample T1 and T2 maps showing reduced relaxation times, compared to fresh sample values from literature (Guilfoyle *et al.*, 2003) and measurements reported on the scanner Bruker manual. See also the quantitative comparison of T1 and T2 values as extra material, respectively in the supplementary material Table 1 and Table 2.

Table 1: quantitative comparison T1-times. T1-times measured in our formalin-fixed samples (Measured T1) vs. T1-times on fresh tissue reported in the Bruker manual (Literature T1), both measured with a RAREVTR sequence from Bruker.

Brain areas	Measured T1 (ms)	Literature T1 (ms)
Cortex	780	1842
Hippocampus	810	1867
Corpus Callosum	730	1642
Cerebellar gray matter	800	1846

Table 2: quantitative comparison of T2-times. T2-time measured in our formalin-fixed samples (Measured T1) vs. T2-times on fresh tissue reported in the Bruker manual (Literature T2), both measured with a MSME sequence from Bruker.

Brain areas	Measured T1 (ms)	Literature T1 (ms)
Cortex	15	38.6
Hippocampus	17	39.5
Corpus Callosum	14	32.8
Cerebellar gray matter	24	39.7

REFERENCES:

- Barth, R. F. and Kaur, B. (2009) 'Rat brain tumor models in experimental neuro-oncology: the C6, 9L, T9, RG2, F98, BT4C, RT-2 and CNS-1 gliomas', *J Neurooncol.*, 94(3), pp. 299–312. doi: 10.1007/s11060-009-9875-7.
- Bartzsch, S. *et al.* (2013) 'Response of the rat spinal cord to X - ray microbeams', *Radiotherapy and Oncology*, 106(1), pp. 106–111. doi: 10.1016/j.radonc.2012.12.007.
- Beltran, M. a *et al.* (2011) 'Interface-specific x-ray phase retrieval tomography of complex biological organs', *Physics in Medicine and Biology*, 56, pp. 7353–7369. doi: 10.1088/0031-9155/56/23/002.
- Bennett, K. M. *et al.* (2004) 'Intravoxel Distribution of DWI Decay Rates Reveals C6 Glioma Invasion in Rat Brain', 1004, pp. 994–1004. doi: 10.1002/mrm.20286.
- Benveniste, H. and Blackband, S. (2002) 'MR microscopy and high resolution small animal MRI: Applications in neuroscience research', *Progress in Neurobiology*, 67(5), pp. 393–420. doi: 10.1016/S0301-0082(02)00020-5.
- Bidola, P. *et al.* (2017) 'Application of sensitive , high-resolution imaging at a commercial lab-based X-ray micro-CT system using propagation-based phase retrieval', *Journal of Microscopy*, 266(2), pp. 211–220. doi: 10.1111/jmi.12530.
- Bidola, P. M. *et al.* (2015) 'Optimization of propagation-based phase-contrast imaging at a laboratory setup', *Optics Express*, 23(23), pp. 30000–30013. doi: 10.1364/OE.23.030000.
- Birkner, A., Tischbirek, C. H. and Konnerth, A. (2016) 'Improved deep two-photon calcium imaging in vivo', *Cell Calcium*. Elsevier Ltd, pp. 1–7. doi: 10.1016/j.ceca.2016.12.005.
- Bouchet, A. *et al.* (2010) 'Preferential effect of synchrotron microbeam radiation therapy on intracerebral 9l gliosarcoma vascular networks', *International Journal of Radiation Oncology Biology Physics*, 78(5), pp. 1503–1512. doi: 10.1016/j.ijrobp.2010.06.021.
- Bouchet, A. *et al.* (2013) 'Synchrotron microbeam radiation therapy induces hypoxia in intracerebral gliosarcoma but not in the normal brain', *Radiotherapy and Oncology*, 108(1), pp. 143–148. doi: 10.1016/j.radonc.2013.05.013.
- Bouchet, A. *et al.* (2016) 'Better Efficacy of Synchrotron Spatially Microfractionated Radiation Therapy Than Uniform Radiation Therapy on Glioma', *International Journal of Radiation Oncology Biology Physics*, 95(5), pp. 1485–1494. doi: 10.1016/j.ijrobp.2016.03.040.
- Bouvier, D. S. *et al.* (2016) 'High Resolution Dissection of Reactive Glial Nets in Alzheimer ' s Disease', *Scientific Reports*. Nature Publishing Group, (6), p. 24544. doi: 10.1038/srep24544.
- Bräuer-Krisch, E. *et al.* (2009) 'New technology enables high precision multislit collimators for microbeam radiation therapy', *Review of Scientific Instruments*, 80(074301), pp. 1–6. doi: 10.1063/1.3170035.
- Bräuer-Krisch, E. *et al.* (2010) 'Effects of pulsed, spatially fractionated, microscopic synchrotron X-ray beams on normal and tumoral brain tissue', *Mutation Research - Reviews in Mutation Research*, 704(1–3), pp. 160–166. doi: 10.1016/j.mrrev.2009.12.003.
- Bravin, A., Coan, P. and Suortti, P. (2013) 'X-ray phase-contrast imaging: from pre-clinical applications towards clinics.', *Physics in Medicine and Biology*, 58(1), pp. R1–R35. doi: 10.1088/0031-9155/58/1/R1.
- Calabrese, E. *et al.* (2013) 'A quantitative magnetic resonance histology atlas of postnatal rat brain development with regional estimates of growth and variability', *NeuroImage*, 71, pp. 196–206.
- Charles-River Laboratories - France (no date) 'Fischer Rat (F344/DuCrI, strain code 002)'.
- Chen, W. *et al.* (2016) 'High-speed swept source optical coherence Doppler tomography for deep brain microvascular imaging', *Scientific Reports*. Nature Publishing Group, 6, p. 38786. doi: 10.1038/srep38786.
- Chenevert, T. L. *et al.* (2000) 'Diffusion Magnetic Resonance Imaging : an Early Surrogate Marker of Therapeutic Efficacy in Brain Tumors', *Journal of the National Cancer Institute*, 92(24), pp. 2029–2036. doi:

10.1093/jnci/92.24.2029.

Chuang, N. *et al.* (2011) 'An MRI-based Atlas and Database of the Developing Mouse Brain', *NeuroImage*, 54(1), pp. 80–89. doi: 10.1016/j.neuroimage.2010.07.043.An.

Cloetens, P. *et al.* (1996) 'Phase objects in synchrotron radiation hard x-ray imaging', *Journal of Physics D: Applied Physics*, 29(1), pp. 133–146. doi: 10.1088/0022-3727/29/1/023.

Coan, P. *et al.* (2006) 'Evaluation of imaging performance of a taper optics CCD "FReLoN" camera designed for medical imaging', *Journal of Synchrotron Radiation*, 13(3), pp. 260–270. doi: 10.1107/S0909049506008983.

Dilmanian, F. A. *et al.* (2003) 'Murine EMT-6 carcinoma: high therapeutic efficacy of microbeam radiation therapy.', *Radiation research*, 159(5), pp. 632–641. doi: 10.1667/0033-7587(2003)159[0632:MECHTE]2.0.CO;2.

Dilmanian, F. A. *et al.* (2006) 'Interlaced x-ray microplanar beams: a radiosurgery approach with clinical potential.', *Proceedings of the National Academy of Sciences of the United States of America*, 103(25), pp. 9709–14. doi: 10.1073/pnas.0603567103.

Donath, T. *et al.* (2010) 'Toward clinical X-ray phase-contrast CT: demonstration of enhanced soft-tissue contrast in human specimen.', *Investigative radiology*, 45(7), pp. 445–52. doi: 10.1097/RLI.0b013e3181e21866.

Dufort, S. *et al.* (2016) 'The High Radiosensitizing Efficiency of a Trace of Gadolinium-Based Nanoparticles in Tumors', *Scientific Reports*, 6, p. 29678. doi: 10.1038/srep29678.

Eggl, E. *et al.* (2015) 'X-ray phase-contrast tomography with a compact laser-driven synchrotron source', *Proceedings of the National Academy of Sciences of the United States of America*, 112(18), pp. 5567–5572. doi: 10.1073/pnas.1500938112.

Engelhorn, T. *et al.* (2009) 'In vivo micro-CT imaging of rat brain glioma: A comparison with 3 T MRI and histology', *Neuroscience Letters*, 458(1), pp. 28–31. doi: 10.1016/j.neulet.2009.04.033.

Ertürk, A. *et al.* (2012) 'Three-dimensional imaging of the unsectioned adult spinal cord to assess axon regeneration and glial responses after injury', *Nature Medicine*, 18(1), pp. 166–172. doi: 10.1038/nm.2600.

Flament-Durand, J. *et al.* (1975) 'Intracerebral calcifications appearing during the course of acute lymphocytic leukemia treated with methotrexate and x-rays', *Cancer*, 35, pp. 319–325.

Girst, S. *et al.* (2016) 'Proton Minibeam Radiation Therapy Reduces Side Effects in an in Vivo Mouse Ear Model', *International Journal of Radiation Oncology Biology Physics*, 95(1), pp. 234–241. doi: 10.1016/j.ijrobp.2015.10.020.

Guilfoyle, D. N. *et al.* (2003) 'Quantitative measurements of proton spin-lattice (T1) and spin-spin (T2) relaxation times in the mouse brain at 7.0 T', *Magnetic Resonance in Medicine*. John Wiley & Sons, Ltd, 49(3), pp. 576–580. doi: 10.1002/mrm.10371.

Hama, H. *et al.* (2015) 'Sca/eS : an optical clearing palette for biological imaging', *Nature Neuroscience*, 18(10), pp. 1518–1529. doi: 10.1038/nn.4107.

Hornig, A. *et al.* (2014) 'Cartilage and Soft Tissue Imaging Using X-rays: Propagation-Based Phase-Contrast Computed Tomography of the Human Knee in Comparison With Clinical Imaging Techniques and Histology', *Invest Radiol*, 49(9), pp. 627–634. doi: 10.1097/RLI.000000000000063.

Huang, S. *et al.* (2015) 'In-line phase-contrast and grating-based phase-contrast synchrotron imaging study of brain micrometastasis of breast cancer.', *Scientific Reports*, 5, p. 9418. doi: 10.1038/srep09418.

Jensen, T. H. *et al.* (2011) 'Molecular X-ray computed tomography of myelin in a rat brain', *NeuroImage*. Elsevier Inc., 57(1), pp. 124–129. doi: 10.1016/j.neuroimage.2011.04.013.

Jiang, Y. and Johnson, G. A. (2011) 'Microscopic diffusion tensor atlas of the mouse brain', *NeuroImage*, 56, pp. 1235–1243. doi: 10.1016/j.neuroimage.2011.03.031.

Johnson, G. A. *et al.* (2002) 'Morphologic Phenotyping with MR Microscopy: The Visible Mouse', *Radiology*, 222, pp. 789–793.

- Johnson, G. A. *et al.* (2012) 'A Multidimensional Magnetic Resonance Histology Atlas of the Wistar Rat Brain', *62*(3), pp. 1848–1856. doi: 10.1016/j.neuroimage.2012.05.041.A.
- Kim, E. *et al.* (2011) 'Vascular phenotyping of brain tumors using magnetic resonance microscopy (μ MRI)', *Journal of Cerebral Blood Flow & Metabolism*, *31*, pp. 1623–1636. doi: 10.1038/jcbfm.2011.17.
- Laissue, J. A. *et al.* (2007) 'Prospects for microbeam radiation therapy of brain tumours in children to reduce neurological sequelae', *Developmental Medicine and Child Neurology*, (*49*), pp. 577–581.
- Larsson, D. H. *et al.* (2013) 'First application of liquid-metal-jet sources for small-animal imaging: high-resolution CT and phase-contrast tumor demarcation.', *Medical physics*, *40*(2), p. 021909. doi: 10.1118/1.4788661.
- Lin, C. Y. *et al.* (2013) 'Visualization of rodent brain tumor angiogenesis and effects of antiangiogenic treatment using 3D ΔR_2 - μ RA', *Angiogenesis*, *16*(4), pp. 785–793. doi: 10.1007/s10456-013-9355-8.
- Lwin, T.-T. *et al.* (2016) 'Spontaneous brain tumor imaging of aged rat by crystal X-ray interferometer-based phase-contrast X-ray CT', *Acta Radiologica Open*, *5*(2), pp. 1–6. doi: 10.1177/2058460115626958.
- Lyckegaard, A., Johnson, G. and Tafforeau, P. (2011) 'Correction of ring artifacts in X-ray tomographic images', *International Journal of Tomography and Statistics*, *18*(F11), pp. 1–9.
- Martínez-Rovira, I., Sempau, J. and Prezado, Y. (2012) 'Development and commissioning of a Monte Carlo photon beam model for the forthcoming clinical trials in microbeam radiation therapy', *Medical Physics*, *39*(1), pp. 119–131. doi: 10.1118/1.3665768.
- McDonald, S. A. *et al.* (2009) 'Advanced phase-contrast imaging using a grating interferometer', *Journal of Synchrotron Radiation*, *16*(4), pp. 562–572. doi: 10.1107/S0909049509017920.
- Mollenhauer, J. *et al.* (2002) 'Diffraction-enhanced X-ray imaging of articular cartilage', *Osteoarthritis and Cartilage*, *10*(3), pp. 163–171. doi: 10.1053/joca.2001.0496.
- Momose, A. *et al.* (1996) 'Phase-contrast X-ray computed tomography for observing biological soft tissues.', *Nature Medicine*, *2*(4), pp. 473–475. doi: 10.1038/nm0496-473.
- Mukherjee, P. *et al.* (2008) 'Diffusion Tensor MR Imaging and Fiber Tractography : Theoretic Underpinnings', *AJNR*. doi: 10.3174/ajnr.A1051.
- Paganin, D. *et al.* (2002) 'Simultaneous phase and amplitude extraction from a single defocused image of a homogeneous object', *Journal of Microscopy*, *206*(1), pp. 33–40. doi: 10.1046/j.1365-2818.2002.01010.x.
- Pan, C. *et al.* (2016) 'Shrinkage-mediated imaging of entire organs and organisms using uDISCO', *Nature Methods*, *13*, pp. 859–867. doi: 10.1038/nmeth.3964.
- Pfeiffer, F. *et al.* (2007) 'High-resolution brain tumor visualization using three-dimensional x-ray phase contrast tomography', *Physics in Medicine and Biology*, *52*(23), pp. 6923–6930. doi: 10.1088/0031-9155/52/23/010.
- Régnard, P., Bräuer-Krisch, E., *et al.* (2008) 'Enhancement of survival of 9L gliosarcoma bearing rats following intracerebral delivery of drugs in combination with microbeam radiation therapy', *European Journal of Radiology*, *68*(3 Supplement), pp. 151–155. doi: 10.1016/j.ejrad.2008.04.049.
- Régnard, P., Le Duc, G., *et al.* (2008) 'Irradiation of intracerebral 9L gliosarcoma by a single array of microplanar x-ray beams from a synchrotron : balance between curing and sparing', *Phys. Med. Biol.*, *53*, pp. 861–878. doi: 10.1088/0031-9155/53/4/003.
- Rong, Y. *et al.* (2006) 'Pseudopalisading ` Necrosis in Glioblastoma : A Familiar Morphologic Feature That Links Vascular Pathology , Hypoxia , and Angiogenesis', *J Neuropathol Exp Neurol*, *65*(6), pp. 529–539.
- Rutishauser, S. *et al.* (2011) 'A tilted grating interferometer for full vector field differential x-ray phase contrast tomography.', *Optics Express*, *19*(25), pp. 24890–6. doi: 10.1364/OE.19.024890.
- Sabatasso, S. *et al.* (2011) 'Microbeam radiation-induced tissue damage depends on the stage of vascular maturation', *International Journal of Radiation Oncology Biology Physics*, *80*(5), pp. 1522–1532. doi: 10.1016/j.ijrobp.2011.03.018.

- Schulz, G. *et al.* (2012) 'Multimodal imaging of human cerebellum - merging X-ray phase microtomography, magnetic resonance microscopy and histology.', *Scientific Reports*, 2, p. 826. doi: 10.1038/srep00826.
- Serduc, R. *et al.* (2009) 'First trial of spatial and temporal fractionations of the delivered dose using synchrotron microbeam radiation therapy', *Journal of Synchrotron Radiation*, (16), pp. 587–590. doi: 10.1107/S0909049509012485.
- Shanley, D. J. (1995) 'Mineralizing microangiopathy: CT and MRI', *Neuroradiology*, 37(4), pp. 331–333. doi: 10.1007/s002340050104.
- Shepherd, G. (2004) 'The Synaptic Organization of the Brain', *Oxford University Press*, Ch. 7. doi: 10.1093/acprof:oso/9780195159561.003.0007.
- Shepherd, T. M. *et al.* (2005) 'Chemical Fixation Alters the Water Microenvironment in Rat Cortical Brain Slices - Implications for MRI Contrast', *Proc Int Soc Magn Reson Med*, 13, p. 619.
- Shepherd, T. M. *et al.* (2007) 'Diffusion Tensor Microscopy Indicates the Cytoarchitectural Basis for Diffusion Anisotropy in the Human Hippocampus', *Am J Neuroradiol*, 28, pp. 958–64.
- Siegbahn, E. A. *et al.* (2006) 'Determination of dosimetrical quantities used in microbeam radiation therapy (MRT) with Monte Carlo simulations', *Medical Physics*, 33(9), p. 3248. doi: 10.1118/1.2229422.
- Siemann, D. W. (2011) 'The Unique Characteristics of Tumor Vasculature and Preclinical Evidence for its Selective Disruption by Tumor-Vascular Disrupting Agents', *Cancer Treat Rev.*, 37(1), pp. 63–74. doi: 10.1016/j.ctrv.2010.05.001.
- Smyth, L. M. L. *et al.* (2016) 'The normal tissue effects of microbeam radiotherapy : What do we know , and what do we need to know to plan a human clinical trial?', *International Journal of Radiation Biology*, 92(6), pp. 302–311. doi: 10.3109/09553002.2016.1154217.
- Song, A. *et al.* (2017) 'Volumetric two-photon imaging of neurons using stereoscopy (vTwINS)', *Nature Methods*, 14(4). doi: 10.1038/nmeth.4226.
- Suzuki, S. *et al.* (2000) 'Radiation-induced brain calcification: Paradoxical high signal intensity in T1-weighted MR images', *Acta Neurochirurgica*, 142(7), pp. 801–804. doi: 10.1007/s007010070095.
- Sztrókay, A. *et al.* (2012) 'High-resolution breast tomography at high energy: a feasibility study of phase contrast imaging on a whole breast.', *Physics Med. Biol.*, 57(10), pp. 2931–2942. doi: 10.1088/0031-9155/57/10/2931.
- Takeda, T. *et al.* (2000) 'Human carcinoma: early experience with phase-contrast X-ray CT with synchrotron radiation--comparative specimen study with optical microscopy.', *Radiology*, 214(1), pp. 298–301. doi: 10.1148/radiology.214.1.r00ja08298.
- Tearney, G. J. *et al.* (1997) 'In Vivo Endoscopic Optical Biopsy with Optical Coherence Tomography', *SCIENCE*, 276(June), pp. 2037–2040.
- Variola, A. (2011) 'The ThomX Project', *2nd International Particle Accelerator Conference*, WEOAA01, pp. 1903–1905.
- Veraart, J. *et al.* (2011) 'Population-averaged diffusion tensor imaging atlas of the Sprague Dawley rat brain', *NeuroImage*, 58, pp. 975–983. doi: 10.1016/j.neuroimage.2011.06.063.
- Virdee, K. *et al.* (2012) 'Applications of positron emission tomography in animal models of neurological and neuropsychiatric disorders', *Neuroscience and Biobehavioral Reviews*. Elsevier Ltd, 36(4), pp. 1188–1216. doi: 10.1016/j.neubiorev.2012.01.009.
- Volume Graphics GmbH. (2001) 'VGStudio MAX 2.2'. doi: www.volumegraphics.com.
- Wilkins, S. W. *et al.* (1996) 'Phase-contrast imaging using polychromatic hard X-rays', *Nature*, 384(6607), pp. 335–338. doi: 10.1038/384335a0.
- Xie, Y. *et al.* (2013) 'Coronal in vivo forward-imaging of rat brain morphology with an ultra-small optical coherence tomography fiber probe', *Phys. Med. Biol.*, 58, pp. 555–568. doi: 10.1088/0031-9155/58/3/555.

Xie, Y. *et al.* (2014) 'In vivo monitoring of glial scar proliferation on chronically implanted neural electrodes by fiber optical coherence tomography', *Frontiers in Neuroengineering*, 7(34). doi: 10.3389/fneng.2014.00034.

Yashiro, H. *et al.* (2017) 'Micro-endoscopic system for functional assessment of neural circuits in deep brain regions: Simultaneous optical and electrical recordings of auditory responses in mouse's inferior colliculus', *Neuroscience Research*. Elsevier Ireland Ltd and Japan Neuroscience Society, pp. 1–9. doi: 10.1016/j.neures.2017.01.002.

Yoneyama, A. *et al.* (2015) 'Quantitative comparison of performance of absorption , Talbot interferometric , and crystal x-ray interferometric imaging', *EPOSTM, ECR*, (C–0531). doi: 10.1594/recr2015/C-0531.

Zhang, M.-Q. *et al.* (2015) 'Ultra-high-resolution 3D digitalized imaging of the cerebral angioarchitecture in rats using synchrotron radiation.', *Scientific reports*. Nature Publishing Group, 5, p. 14982. doi: 10.1038/srep14982.

Zhao, Y. *et al.* (2012) 'High resolution, low-dose phase contrast x-ray tomography for 3D diagnosis of human breast cancers', *Proceedings of the National Academy of Sciences of the United States of America*, 109(45), pp. 18290–18294. doi: 10.1073/pnas.1204460109/
/DCSupplemental.www.pnas.org/cgi/doi/10.1073/pnas.1204460109.

Chapter 5 – X-PCI-CT to image Alzheimer’s Disease

A multiscale 3D method for post-mortem detection and quantification of cellular neurodegeneration in experimental Alzheimer’s disease

This chapter presents a study on the potential application of X-PCI-CT as a technique for full-organ to intra-cellular detection of the neurodegenerative protein agglomeration occurring in Alzheimer’s Disease within rodent brains. Post-mortem MRI-based imaging of AD still lacks the spatial resolution necessary to discriminate nervous tissue complexity at the cellular level, and other pre-clinical techniques for imaging neuronal populations, such as deep two-photon calcium imaging, 3D light microscopy or tissue-cleared full-organ fluorescence microscopy are limited, respectively by the spatial restriction of neuronal staining with calcium indicator dyes, the size of dissected sample sections, or by an only partial labelling of cell populations. X-PCI-CT, instead, provides soft-tissue sensitivity without any application of stains, labels or contrast agents. Moreover, X-PCI-CT can interestingly visualize nervous tissue structure at multiple scales, from full-organ anatomy to single cells without the need for sample dissection. We used here PCI-CT for a unique analysis of AD pathology in the brain of 3xTgAD mice expressing three mutant alleles *Psen1*, *APP* and *tau*, which display both amyloid- β plaque and tangle pathology and represent an experimental model of AD. Moreover, we performed a proof-of-principle study on the effects of a potential AD drug as measured by X-PCI-CT.

This work was performed in collaboration with the group of Dr. Battaglia at the Neuromed Institute in Pozzilli – Italy, who designed the neuro-pharmacological components of the study, provided the samples and performed all the histological and immunohistological work, of Dr. Bravin at the ESRF in Grenoble –France, who helped in experimental design and supported the micro-X-PCI-CT measurements performed at ID17, and Dr. Pacureanu at the ESRF in Grenoble –France, who supported and guided the X-ray nano-holotomography and X-ray fluorescence microscopy measurements performed at ID16A.

This work has been submitted in 2020 for publication as:

G.E. Barbone, A. Bravin, A. Mittone, A. Pacureanu, G. Mascio, P. Di Pietro, M.J. Kraiger, M. Eckermann, M. Romano, M. Hrabe de Angelis, P. Cloetens, V. Bruno, G. Battaglia, P. Coan. “A multiscale 3D method for post-mortem detection and quantification of cellular neurodegeneration in experimental Alzheimer’s disease”, (2020).

This work was presented orally at the Radiological Society of North America meeting in 2017 (RSNA 2017), and at the European Congress of Radiology 2018 (ECR 2018), where it received the “Best Scientific Paper Presentation” Award within the topic “Neuro”.

5.1 Abstract

Anatomically dense and volumetric visualization of neural tissue, unbiased detection of extra- and intra-cellular proteopathy and brain-wide quantification of neuronal damage, all key aspects of an ideal histopathological evaluation of neurodegenerative diseases, remain elusive goals for modern experimental neuroimaging. Here, we report on the *post-mortem* application of multiscale X-ray phase-contrast computed tomography (X-PCI-CT) for the label- and dissection-free organ- to intra-cellular-level 3D-screening of extracted rodent-brain samples. This virtual-histological approach allowed the multiscale visualization of distinct single neurons and glia, and the detection and quantification of abnormal intra-cellular hyper-density (ICHD) in deep cortical and hippocampal neuronal populations in the brain of aged wild-type and 3xTgAD mice, a transgenic animal model of Alzheimer's Disease (AD). The observed ICHD was identified as amyloid- β and hyper-phosphorylated tau protein deposits with calcium- and iron-metal involvement, hallmarks of AD, by correlating the X-PCI-CT data to immunohistochemistry, X-ray fluorescence microscopy, high-field MRI and TEM. As a proof-of-concept, X-PCI-CT was used to analyze hippocampal and cortical regions in the brains of 3xTgAD mice chronically treated with LY379268, the selective agonist of group II metabotropic glutamate receptors classically involved in neurodegeneration/neuroprotection mechanisms. This approach enabled the observation of reduced ICHD, and thus neurodegeneration, in the ventral cerebral cortex, suggesting a local protective effect of LY379268. These results showcase the possible role of multiscale X-PCI-CT as a versatile tool for the detailed study of volumetric neuroanatomy, for the brain-wide quantitative detection of neuropathology associated with brain disorders, and for insightful in-depth evaluations of neuroprotective strategies.

5.2 Introduction

Alzheimer's disease (AD), the leading cause of age-related dementia in humans, occurs due to the convergence of diverse and still ill-understood pathological processes (Selkoe, 2011; Musiek and Holtzman, 2015), including toxic protein deposition, synapse loss and microglial infiltration, which trigger neuronal death and lead to progressive cognitive decline and ultimately to dementia. As for many other neurodegenerative diseases, central in AD etiology is the manifestation of specific forms of neuronal proteopathy: first, prion-like aggregates of misfolded oligomerized amyloid- β ($A\beta$) protein accumulate in both dense mesoscale extra-cellular plaques and intra-cellular fibrils; second, a hyper-phosphorylated microtubule-associated tau (p-tau) cytoskeletal protein fibrillizes in dense intra-neuronal neurofibrillary tangles (NFTs).

While a rather in-depth characterization of AD neurodegeneration has long been achieved using established immunohistochemistry (IHC) approaches (Braak and Braak, 1991), and while extensive PET-tracer development is helping effective differential diagnosis (Nordberg *et al.*, 2010), modern imaging tools still come short of delivering the volumetric cellular-level

visualizations, which would be necessary to reliably detect and differentiate individual subtle protein-based cellular lesions *in-vivo*, especially in the likely-crucial pre-symptomatic early phases of AD. Brain-wide cellular-level monitoring of AD-neurodegeneration progression is especially challenging for neuroimaging and, for this reason, an unequivocal clinical AD diagnosis is still today only reached *post-mortem* by a histopathological workup of nervous-tissue biopsies, which demonstrate the presence of the two hallmark protein-based lesions (A β and p-tau). This limited diagnostic power significantly hinders both our understanding of early-stage AD etiology and our ability to discover disease-modifying drugs for AD, which remains today a disease without a cure.

Even in the context of *post-mortem* small-animal imaging, current cutting-edge experimental neuroimaging methods lack an unbiased high-throughput 3D imaging technology sensitive to neuronal proteopathy, that allows cellular resolution, full-organ brain coverage and unbiased detection mechanisms. State-of-the-art IHC approaches to study brain neuroanatomy permit rather cumbersome 3D cellular imaging, but are limited in terms of organ-coverage, involve sample sectioning and complicated reconstructions with stitching and aligning issues, and require the use of various intrinsically-biased labels (histologic stains, immuno-labels, contrast agents). Recently-emerging super-resolution 3D neuroimaging technologies, mainly based on tissue-clearing(Pan *et al.*, 2016) and expansion-(Murakami *et al.*, 2018) or two-photon-microscopy(Economo *et al.*, 2016), enable brain-wide cellular-resolution structural and functional investigations of entire cell-populations(Kim *et al.*, 2017), and down to single cells(Moffitt *et al.*, 2018) and single intra-cellular molecules(Bon *et al.*, 2018). These methods can be used for organ-level transcriptomics & connectomics, and to investigate complex biological processes such as aging and neurodegeneration(Masuda *et al.*, 2019). Still, they are based on fluorescence light-microscopy, thereby falling short of delivering completely unbiased and anatomically dense visualizations of neural tissue(Venkataramani *et al.*, 2018), due to the notorious issue of sparse labeling(Lichtman and Denk, 2011) by means of antibodies or small molecule tags. Super-resolution electron microscopy (EM) techniques, such as transmission EM (TEM), serial block-face scanning EM (SBEM), or focused ion beam scanning EM (FIB-SEM), are based on label-free cyto-architecture-detection mechanisms and therefore enable anatomically dense characterization of both intra-neuronal amyloid and tau pathology at synaptic resolution by using heavy metal staining. However, these techniques rely on ultrathin sectioning and ablation, generate very large data sets(Mikula and Denk, 2015) requiring alignment and stitching, are hurdled by long acquisition times(Eberle *et al.*, 2015), and are limited to very small tissue volumes, far from rodent 3D whole-brain throughput capabilities.

Amongst novel neuroimaging techniques, X-ray phase-contrast computed tomography(Fitzgerald, 2000) (X-PCI-CT) represents a set of 3D microscopy techniques, which offer enhanced image-contrast compared to traditional absorption CT(Beltran *et al.*, 2011) and thereby enable label-free soft-tissue imaging for diverse biomedical investigations(Bravin, Coan and Suortti, 2013). Its simplest implementation, propagation-based X-PCI-CT(Snigirev *et al.*, 1995; Cloetens *et al.*, 1996), exploits the physical mechanisms of coherent X-ray refraction, propagation and Fresnel diffraction to determine local electron

density within probed samples. Applied *post-mortem*, different X-PCI-CT methods deliver semi- to fully-quantitative label- and dissection-free density-based 3D morphological neuroimaging complementary to other brain mapping techniques(Pfeiffer *et al.*, 2007; Barbone *et al.*, 2018; Khimchenko *et al.*, 2018). Modern synchrotron-radiation setups reach the spatial resolution needed to impact mesoscale neuroimaging(Mokso *et al.*, 2007; Mader *et al.*, 2011; Da Silva *et al.*, 2017; Mittone *et al.*, 2017), permit the volumetric exploration of intra-cellular cyto-architecture within single neurons in deep rodent brain regions(Lathuilière *et al.*, 2016; Cedola *et al.*, 2017; Khimchenko *et al.*, 2018), and can be used to carry out unbiased anatomically dense high-throughput quantifications of cellular and vascular structure within large nervous-tissue samples at histological resolution(Dyer *et al.*, 2017; Töpperwien *et al.*, 2017, 2018).

With regard to the detection of neurodegeneration, this method was shown to be sensitive to extra-cellular A β build-up in several AD animal models *post-mortem*(Noda-Saita *et al.*, 2006; Connor *et al.*, 2009; Pinzer *et al.*, 2012; Astolfo *et al.*, 2016; Okamura *et al.*, 2016; Massimi *et al.*, 2019; Töpperwien *et al.*, 2020). Extra-cellular amyloid plaques lead to local X-PCI-CT signal hyper-intensity, which could be correlated to Thioflavin-S fluorescence(Pinzer *et al.*, 2012), to hyper-density signal in transmission electron microscopy (TEM)(Massimi *et al.*, 2019), and to IHC for A β (Noda-Saita *et al.*, 2006) and tau(Töpperwien *et al.*, 2020). Still, previous studies have come short of a multiscale and multimodal characterization of early-stage A β & p-tau-driven NFT build-up in intra-cellular compartments of animal-model brains, as well as of an investigation of other intra-cellular processes, e.g. cell-body mineralization, which may concurrently contribute to the formation of the abnormal signal hyper-intensity consistently observed in X-PCI-CT data. Application of this imaging approach to experimental neuroscience research on intra-cellular neurodegeneration has thus far also been scarce.

Here, we present a *post-mortem* X-PCI-CT-based multiscale organ- to cellular-level analysis of brain neurodegeneration focusing on intra-cellular abnormal protein and metal accumulation in AD. We performed micro- to nano-X-PCI-CT and X-ray fluorescence microscopy on extracted brain samples from aged wild-type (WT) and triple-transgenic 3xTgAD mice(Oddo, Caccamo, Shepherd, *et al.*, 2003), an experimental AD model, which develops both amyloid and tau pathology(Oddo, Caccamo, Kitazawa, *et al.*, 2003). After analyzing multiscale X-PCI-CT results by comparison to more-established neuroimaging modalities, we used this methodology to quantify differences in intra-cellular A β and p-tau content within key AD-linked hippocampal and cortical brain cell layers. By collecting data from aged WT and 3xTgAD animals, either kept under control conditions or systemically treated with LY379268 – a selective agonist of the metabotropic glutamate receptor mGlu2/3 and potential disease-modifying drug(Bruno *et al.*, 2001) – we demonstrated a first proof-of-principle application of X-PCI-CT to the evaluation of intra-cellular neurodegeneration in an experimental AD drug test.

5.3 Results

5.3.1 X-PCI-CT detects intra-cellular hyper-density in aged WT and 3xTgAD mouse brains

Using un-sectioned paraffin-embedded half-brain samples and a $0.3^3 \mu\text{m}^3$ voxel single-distance propagation-based X-PCI-CT setup (Mader *et al.*, 2011), we analyzed cortical (CTX) and hippocampal (HIP) regions in the brains of one 4-month-old WT mouse, of two 13-month-old WT mice and of two 13-month-old transgenic 3xTgAD mice (**Fig. 1, Suppl. Fig. 1**). Interestingly, the 3D imaging data presented abnormal cell-shaped hyper-dense (HD) particles within CTX and HIP layers only in the brains of the 13-month-old animals (**Fig. 1a, Suppl. Fig. 1**). HD-particles populated the same neuronal layers of adjacent much more hypo-dense neuron-like structures, and their prevalence varied greatly between different tissue locations (**Suppl. Fig. 2**). No HD-particles, instead, were observed in the brain of the young 4-month-old WT mouse. To better access intra-cellular detail, $\sim 2 \times 2 \times 4 \text{ mm}^3$ brain-tissue biopsies, cut out from the original half-brain samples, were analyzed with a $0.1^3 \mu\text{m}^3$ voxel synchrotron-radiation X-ray nano-holotomography setup (Pacureanu *et al.*, 2018). These acquisitions confirmed the presence of cell-shaped HD-particles within CTX and HIP tissues from both WT and 3xTgAD mouse brains at 13 months (**Fig. 1c-d**).

Preliminary characterization of the biological content within HD-particles was obtained by side-by-side comparison of X-PCI-CT data (**Fig. 1a,c-d**) with fluorescence-microscopy of Thioflavin S (ThioS)-stained tissue-sections collected from contralateral hemispheres (**Fig. 1b,c-d**). ThioS-fluorescence, which highlights cross- β -sheet architecture within both amyloid and p-tau protein lesions (Vallet *et al.*, 1992; Honson *et al.*, 2007; Rauch, Olson and Gestwicki, 2017), showed strongly ThioS-positive cell-shaped clusters within sections from 13-month-old mice, whereas only very-low to no ThioS-signal in sections from 4-month-old WT and 3xTgAD mice (**Fig. 1b, Suppl. Fig1**). Patterns of ThioS-fluorescence tissue-marking seemed analogous to HD-particle distributions in X-PCI-CT density-maps, suggesting that HD-particles may contain A β and p-tau protein deposits (**Fig. 1a, Suppl. Fig. 1**). By noticing the spatial co-localization of ThioS- and DAPI-fluorescence within the same cells (**Fig. 1c-d, Suppl. Fig. 1**), we established that the ThioS signal, and thus likely also the HD signal in the X-PCI-CT data, be intra-cellular.

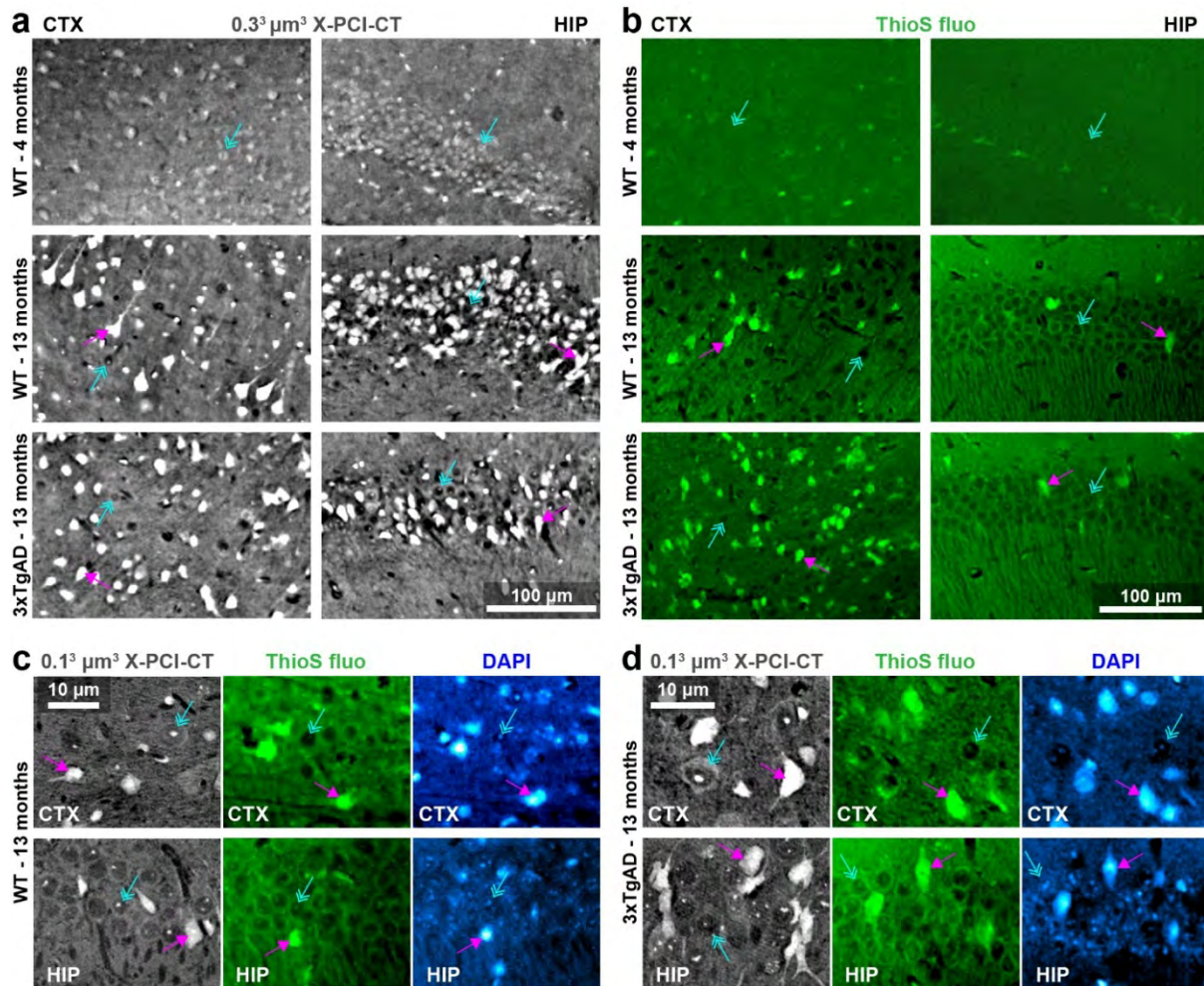


Figure 1 | X-PCI-CT-detected hyper-density matches intra-cellular Thioflavin-S fluorescence. **a**, 0.3³ μm³ voxel X-PCI-CT of deep cortical (CTX) and hippocampal (HIP) layers within extracted paraffin-embedded brain samples from a 4-month-old WT mouse vs. a 13-month-old WT vs. a 13-month-old 3xTgAD mouse. Bright image gray-levels represent hyper-dense tissue areas, dark gray-levels hypo-dense ones. Compared to normal nearby neurons (azure arrows), abnormally hyper-dense (HD) cell-shaped particles (magenta arrows) are present in the 13-month-old WT and 3xTGAD samples. Few to no HD-particles are visible in tissues at 4 months. **b**, Thioflavin S fluorescence microscopy (ThioS fluo) data of CTX and HIP tissues comparable to the ones in **(a)**, collected from contralateral brains hemispheres. **c-d**, 0.1³ μm³ voxel CTX and HIP X-PCI-CT data vs. ThioS and DAPI fluorescence data from contralateral CTX and HIP tissue samples, collected from 13-month-old **(c)** WT and **(d)** 3xTgAD animals. In **(c-d)**, same-cell co-localization of ThioS and DAPI fluorescence can be clearly observed, suggesting intra-cellular localization of the ThioS-positive deposits. In **(a)** vs. **(b)** and in **(c-d)**, ThioS-positive deposits (magenta arrows) in fluorescence datasets show morphological traits and distribution patterns similar to the patterns of HD-particles (magenta arrows) in X-PCI-CT images, whereas ThioS-negative cellularity (azure arrows) in fluorescence datasets matches normal hypo-dense cellularity (azure arrows) in X-PCI-CT images. Small intra-cellular nucleoli are marked by the ThioS dye and appear as intra-nuclear hyper-dense features in X-PCI-CT maps.

5.3.2 Multiscale X-PCI-CT maps organ- to cellular-level intra-cellular proteopathy in aged brains

To systematically localize and characterize intra-cellular hyper-density (ICHHD) within mouse half-brain samples, we applied a multiscale approach to X-PCI-CT-based neuroimaging: consecutive same-sample X-PCI-CT experiments at increasing spatial resolution were performed using different synchrotron-radiation setups. We acquired datasets with effective voxel sizes of 3^3 , 0.7^3 , 0.3^3 and $0.1^3 \mu\text{m}^3$ (see **Methods**), a sequence of measurements, which permitted organ-level inspection of tissue-level 3D-structure followed-up by local cellular-level examinations of single-neuron 3D-morphology (**Fig. 2, Suppl. Fig. 2-3, Suppl. Videos 1-4**).

Overall, we obtained multiscale neuroimaging datasets on fifteen brain hemispheres extracted respectively from eight WT (selected results in **Fig. 2**) and seven 3xTgAD mice (selected results in **Fig. 3**), all aged to 13-months either under control conditions or after treatment with LY379268. The $3^3 \mu\text{m}^3$ voxel maps were used to measure gross pre-cellular neuroanatomy within entire half-brain samples without sectioning of tissue (**Fig. 2a, 3a**), and were essential to aim successive higher-resolution CT acquisitions. Local-tomography 0.7^3 and $0.3^3 \mu\text{m}^3$ voxel scans (**Fig. 2b-c, 3b-d**), also performed dissection-free, were used to bridge the spatial resolution gap between pre-cellular and cellular-level investigations. After a sample dissection step, $0.1^3 \mu\text{m}^3$ voxel nano-holotomography was performed on tissue biopsies to probe sub-cellular-scale data in dorsal CTX and HIP layers (**Fig. 2d, 3e-f**). Higher-resolution acquisitions led to increasingly smaller volumes of brain-tissue being measured, but also to increasingly detailed visualizations of the 3D cyto-architecture of deep pyramidal and granular neurons supplied by their local microvasculature, of bipolar HIP interneurons (Cammalleri, Bagnoli and Bigiani, 2019), and of different glial populations.

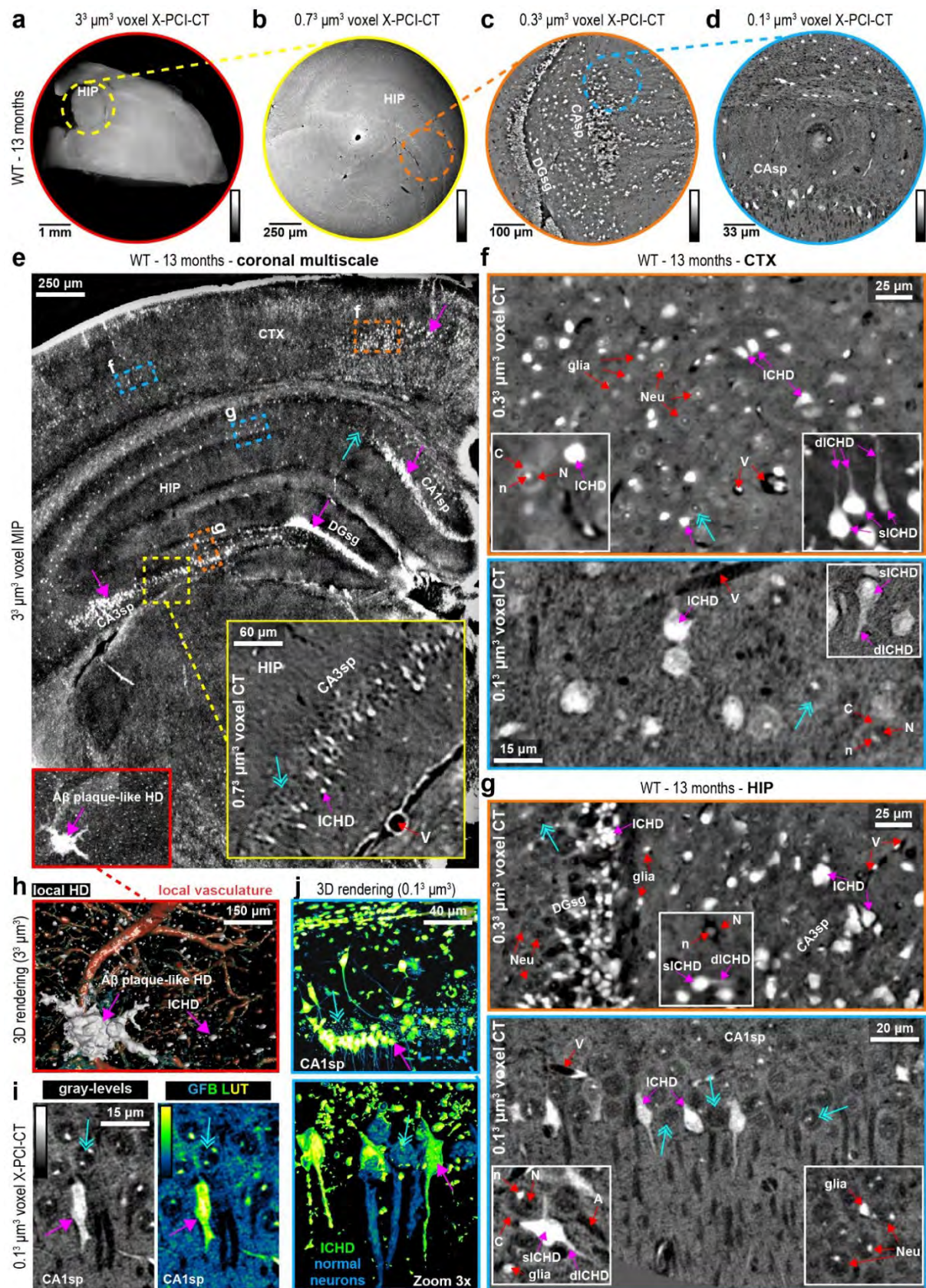


Figure 2 | Multiscale X-PCI-CT of brains from aged WT mice. a-d, organ- to cellular-level X-PCI-CT neuroimaging of the brains of 13-month-old WT mice, at increasingly smaller effective voxel sizes: (a) 3^3 , (b) 0.7^3 , (c) 0.3^3 and (d) $0.1^3 \mu\text{m}^3$. Lower pre-cellular-resolution CTs were used to aim the higher-resolution ones. The latter allowed cellular-level explorations of angio- and cyto-architecture within selected deep brain regions. Calibration bars

specify low-to-high gray-level encoding of tissue density. Brain samples underwent dissection into $1 \times 1 \times 3 \text{ mm}^3$ rods before $0.1^3 \mu\text{m}^3$ voxel X-PCI-CTs in **(d, f-g)**. **e**, $3^3 \mu\text{m}^3$ voxel coronal maximal intensity projection (MIP), enhancing the visibility of intra-cellular hyper-density (ICHD) within neuronal populations in CTX, HIP CA1sp/CA3sp and DGsg layers. **f-g**, 0.3^3 and $0.1^3 \mu\text{m}^3$ voxel X-PCI-CTs of **(f)** CTX and **(g)** HIP layers visualize deep vasculature (V, hypo-dense), individual normal neurons (Neu), non-neuronal glial cells (glia), and intra-neuronal structure (cytoplasm (C), hypo-dense nuclei (N), hyper-dense nucleoli (n), hypo-dense axons (A)). ICHD-bearing neurons contain somatic (sICHD) and dendritic/axonal (dICHD) ICHD. **h**, 3D rendering of a macroscopic HD-object with amyloid ($\text{A}\beta$) plaque-like morphology from **(e)**, alongside ICHD (white) and vasculature (red). **i**, Gray-level coloring vs. fluorescence-like Green-Fire-Blue (GFB) LUT recoloring of $0.1^3 \mu\text{m}^3$ voxel X-PCI-CT data, highlighting a single ICHD-bearing CA1sp neuron within a population of normal neurons. **j**, GFB-recolored 3D rendering of CA1sp ICHD-bearing neurons. Zoom 3x portrays individual ICHD-bearing (green) vs. normal (blue) neurons. In **e-j**, magenta arrows point to example of ICHD, azure arrows to normal neurons.

Via this multiscale approach we could target key brain regions in AD pathology (Yankner, Lu and Loerch, 2008), e.g. the CTX (**Fig. 2e-f, 3c, 3e, Suppl. Video 5-6**) and HIP (**Fig. 2e, 2g, 3d, 3f, Suppl. Video 7-8**), as well as specific layers, e.g. pyramidal-neuron layers within Ammon’s horn (CA1sp/CA3sp) and granulate-neuron layers within the dentate gyrus (DGsg). Widespread cell-shaped ICHD was observed in specific brain layers of all 13-month-old WT mice, and a few macroscopic extra-cellular HD deposits with plaque-like morphology could also be located (**Fig. 2e,h**). By computing maximal intensity projections (MIP) of consecutive CT slices, we observed noticeable preferential deposition of the intra-cellular HD lesions within CA1sp/CA3sp HIP, DGsg HIP and various CTX layers, including the ENT layer 2 (**Fig. 2e, Suppl. Fig. 4**), all AD-linked locations. Importantly, the acquired cellular resolution data allowed the visualization of individual hyper-dense cells and the recognition of sub-cellular density variations (**Fig. 2f-g**): ICHD-bearing neurons appeared completely filled with – likely protein-rich – condensation products, and HD was located in both cell-somas (sICHD), and dendritic/axonal compartments (dICHD). Nearby normal neurons were instead distinguishable due to their comparatively average-density cytoplasm, spherical hypo-dense – likely euchromatin-rich – nuclei, small hyper-dense nucleoli and hypo-dense axons. By pseudo-fluorescent recoloring of 2D X-PCI-CT slices (**Fig. 2i**) and 3D renderings (**Fig. 2j**) of ICHD-bearing cell-layers, we emphasized the similarity between an X-PCI-CT-based nonspecific detection of ICHD bio-deposits to ThioS-fluorescence-based nonspecific detection of protein clumping. To exploit the volumetric nature of the collected data, easy-to-implement mixed semi-automatic threshold-based and manual region-growing segmentation approaches (**Suppl. Fig. 5**) were applied to selectively extract and 3D-visualize ICHD-bearing cells, normal neurons, and hypo-dense vasculature within extended tissue volumes (**Fig. 2h,j, Suppl. Fig. 3,5**).

In all 3xTgAD brains, sparse macroscopic extra-cellular HD aggregates with 3D-morphology reminiscent of $\text{A}\beta$ -plaques (**Fig. 3a**) could be recognized alongside much smaller and more widespread cell-shaped HD. The detected HD was predominantly intra-cellular (ICHD) and presented spatial patterns and morphology typical of AD-linked intra-cellular protein accumulations: ICHD was, in fact, measured preferentially within neurons in notoriously AD-linked HIP and CTX locations (**Fig. 3b**), including CTX’s ii^{nd} - iii^{rd} and iv^{th} - v^{th} layers (**Fig. 3c**), HIP’s CA1sp, CA3sp and DGsg layers (**Fig. 3d**). In the $0.1^3 \mu\text{m}^3$ voxel datasets (**Fig. 3e-f, Suppl. Fig. 6**), we observed the presence also of different glial populations: high-density glial cells likely

pertain to oligodendrocytes and microglia, denser due to their characteristic nuclear chromatin clumps, and the low-density ones are likely astrocytes with pale irregularly-shaped somas, matching known glia density-based contrast patterns traditionally visible via light-microscopy in toluidine-blue-stained semi-thin sections(Landfield *et al.*, 1981; Landfield, Baskin and Pitler, 1981).

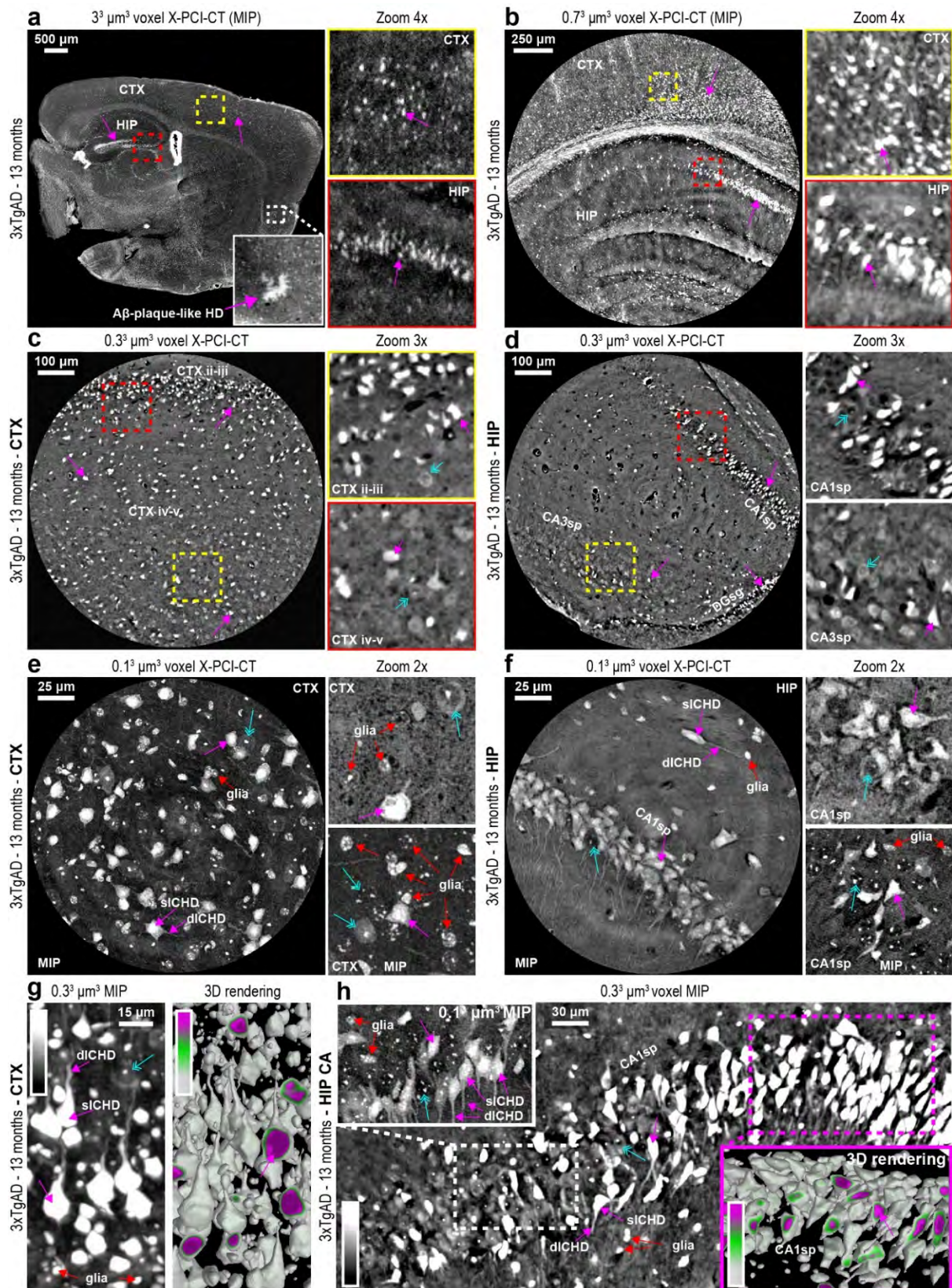


Figure 3 | Multiscale X-PCI-CT of brains from aged 3xTgAD mice. a-f, organ- to cellular-level X-PCI-CT neuroimaging of the brains of 13-month-old 3xTgAD mice, at increasingly smaller effective voxel sizes: (a) 3^3 , (b) 0.7^3 , (c-d) 0.3^3 and (e-f) $0.1^3 \mu\text{m}^3$. Note widespread ICHD within (a-b) cortical (CTX) and hippocampal (HIP) layers, preferential deposition in (c-d) $\text{ii}^{\text{nd}}\text{-iii}^{\text{rd}}$ and $\text{iv}^{\text{th}}\text{-v}^{\text{th}}$ CTX and CA1sp layers, and some deposition in HIP DGsg and CA3sp layers. Sub-cellular datasets (e-f) visualize individual ICHD-bearing cells with bright possibly-condensed

somas (sICHD), and bright dendritic/axonal components (dICHD), compared to more hypo-dense somas and small very-dense intra-nuclear particles (nucleoli) within normal neurons. Intermediate-size mildly-HD glial cellular populations (glia) are also visible. **g-h**, 0.3^3 and $0.1^3 \mu\text{m}^3$ voxel MIP maps and $0.3^3 \mu\text{m}^3$ voxel 3D renderings, obtained after threshold-based gray-level segmentation, of (**g**) CTX and (**h**) HIP CA1sp layers. Note evident dendritic and axonal ICHD involvement in hyper-intense branch-like extensions (dICHD) of ICHD somas (sICHD). 3D renderings demonstrate that the highest gray-level voxel values (rendered magenta, see Calibration Bars), and thus the highest local densities, can be found within internal cellular compartments of ICHD-bearing neurons, and especially cytoplasmic and nuclear one. Normal neuron somas, having intra-cellular gray-levels lower than the chosen threshold, are not rendered in 3Ds in (**g-h**). In (**a-h**), differently-shaped ICHD-bearing pyramidal and bipolar neurons can be recognized, magenta arrows point to example of ICHD, and azure arrows to normal neurons.

Compared to hypo-dense nearby normal neuron parenchyma, 3D renderings of ICHD-bearing multi-polar (pyramidal) neurons in HIP (**Fig. 3g**) and CTX (**Fig. 3h**) layers portray near-nuclear and cytoplasmic somatic compartments as the densest intra-cellular locations, and evident involvement also of dendritic, axon-hillock and axonal compartments. Overall, we observed neurons affected by intra-cellular HD in both aged WT and aged 3xTgAD brain samples (**Fig. 1 vs. Fig. 2**). A qualitative morphological comparison of equivalent CA1sp-layer neurons in one WT vs. one 3xTgAD brain sample (**Suppl. Fig. 7**), though, showed widespread cyto-structural signs typical of cellular neurodegeneration, e.g. somatic cell-blebbing and shrinkage, only in the data pertaining to the 3xTgAD mouse.

5.3.3 ICHD correlates to A β and p-tau IHC, i.e. to AD-linked cellular neurodegeneration

To biologically characterize the content of ICHD-neurons detected via X-PCI-CT, we compared the CT data to A β and p-tau IHC, collected on CTX and HIP tissues of contralateral hemispheres (**Fig. 4**). Double IHC for A β and NeuN showed intra-neuronal somatic amyloid deposition (co-localized A β and NeuN fluorescence) in both 13-month-old WT and 3xTgAD mouse brains (**Fig. 4b**) and no sign of axonal A β fluorescence (**Fig. 4f**). Intra-cellular A β fluorescence was mostly limited to neuron cytoplasm and formed distinctive ring-like patterns around neuron nuclei, which match reported IHC work on 3xTgAD mice (Iulita *et al.*, 2014; Hussain *et al.*, 2017; Rosenberg, Fu and Lambracht-Washington, 2018). These patterns of somatic A β fluorescence resembled X-PCI-CT-detected somatic ICHD in both aged WT and 3xTgAD cells (**Fig. 4a**). Similarly to other IHC studies on the 3xTgAD mouse (Boche *et al.*, 2010; Iulita *et al.*, 2014; Castillo-Carranza *et al.*, 2015; Rosenberg, Fu and Lambracht-Washington, 2018), the double IHC for p-tau and NeuN (**Fig. 4d**) we collected, instead, displayed little somatic p-tau involvement (mild co-localization of p-tau and NeuN signals), whereas strong p-tau-positivity within neuron dendrites and axons. Here too, p-tau IHC patterns matched the ICHD observed in dendritic and axonal compartments of somatically-dense neurons (**Fig. 4c-f**). Overall, A β -positive deposits seemed to correlate to somatic ICHD, p-tau-positive deposits to dendritic/axonal ICHD.

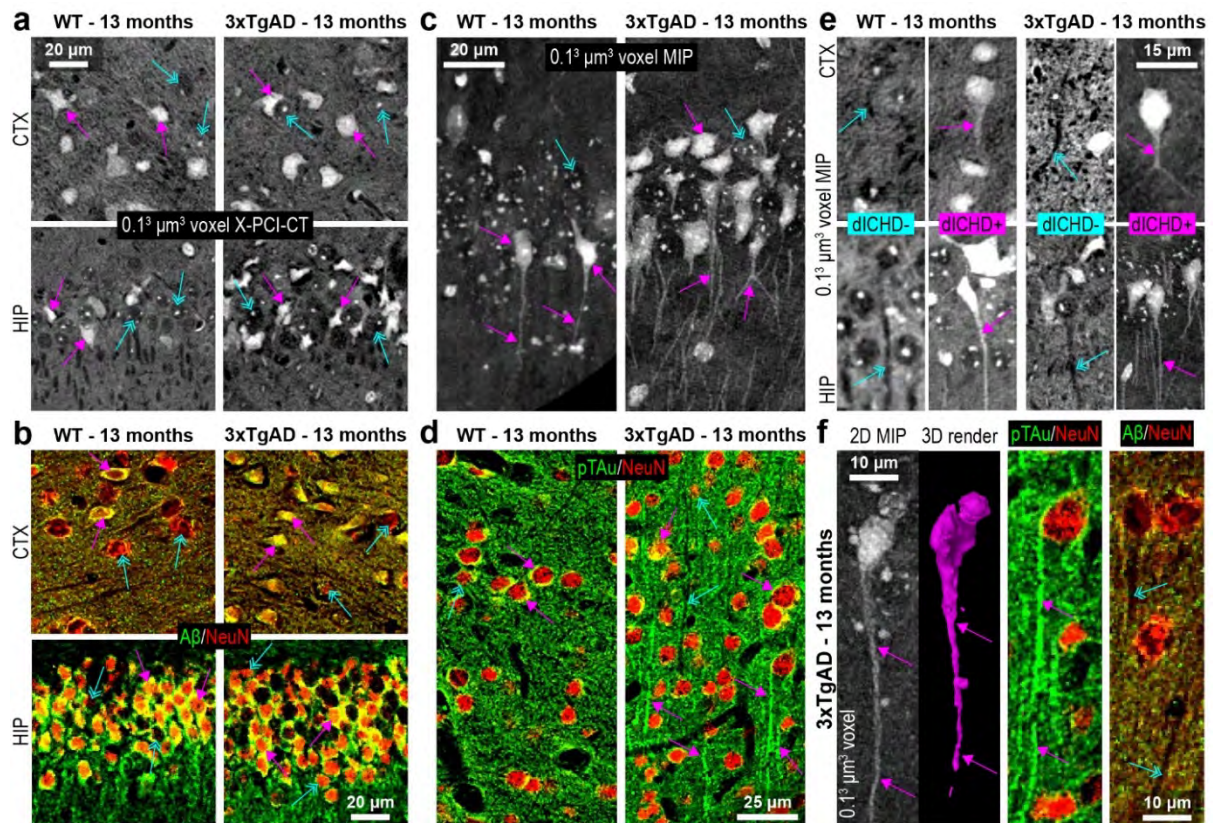


Figure 4 | Label-free X-PCI-CT detection of ICHD vs. IHC for A β and p-tau. **a-b**, Representative (a) X-PCI-CT data vs. (b) contralateral-hemisphere doubly stained A β /NeuN IHC (anti- β -Amyloid 4G8 fluorescence in green, anti-NeuN in red), of comparable CTX/HIP tissues from 13-month-old WT/3xTgAD mice. Note somatic co-localization of A β - and NeuN-positive signals (yellow pixels in b), forming cytoplasmic ring-like patterns, but no dendritic/axonal A β -positive signal. Somatic A β deposition (in b) resembles X-PCI-CT-detected somatic IHCD (in a). Non-ICHD-bearing normal cells in (a) are similar to A β -negative cell-somas in (b). **c-d**, Representative (c) X-PCI-CT MIPs vs. (d) contralateral-hemisphere doubly stained p-tau/NeuN IHC (anti-p-tau pSer404 fluorescence in green, anti-NeuN in red), of comparable tissues from 13-month-old WT/3xTgAD mice. Note mild somatic co-localization of p-tau- and NeuN-positive signals (yellow pixels in d), and high dendritic/axonal p-tau-positive (green) fluorescent signal in long branch-like structures extending from the mildly p-tau- and NeuN-positive cell-somas. Axonal p-tau deposition resembles X-PCI-CT-detected axonal ICHD out-branching from somatically ICHD-bearing cells. **e**, Hyper-dense (dICHD⁺) vs. hypo-dense (dICHD⁻) dendritic/axonal processes observed via nano-X-PCI-CT in 13-month-old WT and 3xTgAD CTX and HIP tissues. dICHD⁺ processes connect to somatically ICHD-bearing cells, dICHD⁻ processes to normal hypo-dense cell-somas. **f**, 2D MIP vs. 3D rendering of a neuron bearing a dICHD⁺ axon extending from its ICHD⁺ cell soma. IHCs show respectively examples of p-tau-positive and A β -negative axons. In **a-j**, magenta arrows point to example of either ICHD-bearing or A β /p-tau-positive somatic and axonal cell compartments, azure arrows to either normally-dense non-ICHD-bearing or A β /p-tau-negative somatic and axonal cell compartments.

5.3.4 X-PCI-CT vs. X-ray fluorescence-microscopy, MRI & TEM

To evaluate the elemental composition of the intra-neuronal ICHD deposits detected via X-PCI-CT, we performed nano-scale X-ray fluorescence microscopy (Gramaccioni *et al.*, 2020) (nano-XFM) on 6- μ m-thick histological sections from one WT and one 3xTgAD brain sample. Using a synchrotron setup with sub-cellular resolution (Ortega *et al.*, 2007; Que *et al.*, 2014; Sanchez-Cano *et al.*, 2017; De Samber *et al.*, 2018) (see **Methods**), we collected 2D phase-

maps and 2D trace-element distribution maps within cells, quantifying several key bio-elements, including phosphorus, sulfur, calcium and iron. These measurements covered tens of individual neurons, and their sub-cellular compartments, in CTX and HIP cell-layers (representative data in **Fig. 5a-b**).

Much like the ICHD-bearing vs. normal neuron dichotomy observed via X-PCI-CT in similar cell populations (**Fig. 5c**), the XFM data too showed presence on one side of normal neurons with limited somatic involvement of the measured elements, and on the other side of neurons abnormally filled with P, S, Ca and even Fe, especially well visible when superimposed in co-localization XFM maps (**Fig. 5b**). Moreover, compared to the smooth-rounded morphology of normal cell-somas, ICHD-bearing cells show signs of altered morphology, e.g. somatic shrinkage/distortion, also in XFM maps.

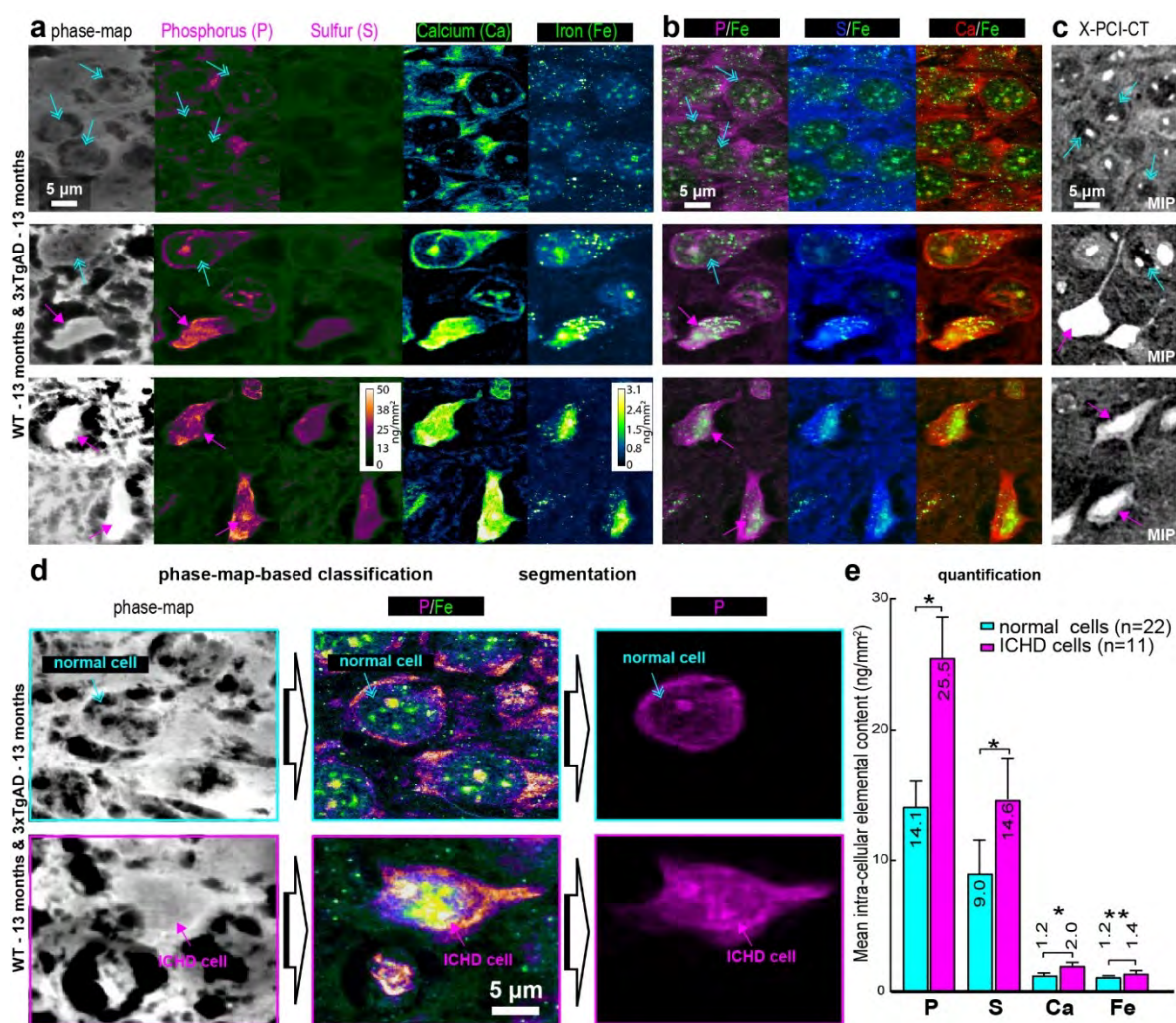


Figure 5 | X-PCI-CT vs. XFM. **a**, recolored cellular XFM data pertaining to 6- μm -thick CTX and HIP brain sections from 13-month-old WT/3xTgAD mice (Calibration Bars in ng/mm²). Maps visualize intra-cellular phase and elemental distributions for phosphorus (P) and sulfur (S), calcium (Ca) and iron (Fe). **b**, co-localization XFM maps of the same cells as in **(a)**, with P, S, or Ca distributions alternatively superimposed to Fe distributions. **c**, MIPs of 0.1³ μm^3 voxel X-PCI-CTs, showing deep neuronal cell-groups, with intra-cellular morphology and density patterns, which match intra-cellular patterns in the XFM-measured cell-groups (**a-b**). In **(a-b vs. c)**, magenta arrows point respectively to elemental hyper-accumulation or ICHD-bearing neurons, azure arrows to normally-compartmentalized low-density elemental accumulations or normal non-ICHD-bearing neurons. **d**, 33 neurons

within the XFM maps were manually classified, based on the morphology and intensity visible in their phase maps, as either ICHD-bearing (n=11, magenta arrows) or normal (n=22, azure arrows) neurons. Representative phase-, P/Fe co-localization-XFM-, and segmented P XFM-maps of two cells are shown here as demonstration. Each classified cell was manually segmented, and masks were used to measure average intra-cellular elemental content within each cell. **e**, Quantification of XFM-measured intra-cellular elemental content in ICHD-bearing (magenta) vs. normal (azure) neurons. Graph shows group mean \pm SD. All elemental distributions (P, S, Ca, Fe) show significant differences in mean intra-cellular elemental content (* $p < .001$, ** $p < .005$) between the two groups, compared by unpaired two-sided two-sample Wilcoxon Testing.

Based on the average intensity of their phase maps, we classified all XFM-measured cells as either ICHD-bearing or normal and segmented them (**Fig. 5d**), and finally quantified their mean intra-cellular elemental content (**Fig. 5e**). Cells classified as ICHD-bearing showed patterns of diffuse hyper-accumulation of P (peaks up to ~ 40 ng/mm²), S (up to ~ 20 ng/mm²) and Ca deposition (peaks > 2.5 ng/mm²) in cytoplasmic, nuclear and even dendritic/axonal compartments, compared to normal cell somas, which presented milder cytoplasmic and dendritic/axonal levels of P (up to ~ 20 ng/mm²), S (up to ~ 10 ng/mm²) and Ca (~ 1 ng/mm²), and relatively little nuclear involvement. Diffuse excess Fe deposition (peaks > 2.5 ng/mm²) was also noticeable in somatic compartments of ICHD-bearing cells, whereas both ICHD-bearing and normal neurons XFM maps contained small globular deposits in near-nuclear regions, likely contained within nucleoli, cell organelles or neurovesicles (Ortega *et al.*, 2007). Trace quantities (< 0.5 ng/mm²) of K, Zn, Cu and Br were also detected. Notably, the mean level of intra-cellular elemental content was found to be significantly higher within ICHD-cells (n=11) than within normal non-ICHD-bearing cells (n=22) for all measured elements except Br (**Fig. 5d**).

Overall, the XFM-detected significant excess of P and S, Ca and Fe within ICHD-bearing cells suggests an intra-cellular accumulation of either protein aggregates (e.g. hyper-phosphorylated p-tau fibrils, Fe-trapping A β oligomers, or others) or the occurrence of other downstream cellular neurodegenerative processes possibly elicited by the toxic-protein-build-up itself (e.g. cell condensation, apoptosis, necrosis, dystrophic mineralization of cell bodies or ferrugination). Interestingly, excess P deposition was detected also in axonal compartments, a likely sign of hyper-phosphorylated NFT abundance driving axonal cytoskeletal degeneration. These significantly higher mean and peak cellular elemental density values found in certain CTX and HIP neurons, as well as their intra-cellular spatial distribution, are in tune with an interpretation of the neuronal ICHD measured via X-PCI-CT as intra-cellular protein and metal accumulations, i.e. typical signs of age-related AD-linked cellular processes of cellular neurodegeneration.

The observed sensitivity of X-PCI-CT to intra-cellular protein and metal depositions was compared to that of a complementary morphological 3D neuroimaging technique, namely high-field MRI, known to permit whole-brain mapping, from which cellular-level microstructures can be inferred (Wei *et al.*, 2016). Here, we collected 9.4 T MRI data with $\sim 20^3$ μm^3 voxel size from one 13-month-old 3xTgAD brain sample, before (**Suppl. Fig. 8**) and after post-mortem application of a gadolinium-based MRI contrast agent (**Fig. 6a-b**), and compared them to 3^3 μm^3 voxel X-PCI-CT data (**Fig. 6c**). The higher spatial resolution of X-PCI-CT permitted a more precise rendition of the sub-cellular lesions: in CTX layers, sparse individual

ICHHD particles, visible via X-PCI-CT, were hardly recognizable as isolated hypo-dense voxels in MR images at similar locations (**Fig. 6a**). Instead, extended abnormal layer-like hypo-density regions were observed within key hippocampal layers (e.g. CA_{sp}) by MRI, matching well X-PCI-CT-based measurements of layer-like HD at similar locations (**Fig. 6b-c**). MRI signal hypo-intensity is known to correlate within amyloid agglomerates, reportedly due to localized Fe trapped within the protein aggregates, and is used both *post-mortem* and *in-vivo* (Vanhouette *et al.*, 2005; Meadowcroft *et al.*, 2009) as morpho-functional marker for AD-linked neurodegenerative processes in the brain of animal models (Delatour *et al.*, 2010) (including the 3xTgAD mouse (Tafoya, Madi and Sillerud, 2017)) and in humans (Atrophy, 2015). Given the known correlation between MRI hypo-intensity, A β and Fe deposition, the good agreement we observed here between MRI hypo-intensity and X-PCI-CT ICHD signal further ties the biological origin of the pathological ICHD lesions to a known process of cellular neurodegeneration: intra-cellular proteopathy with metal co-localization (Honda *et al.*, 2004).

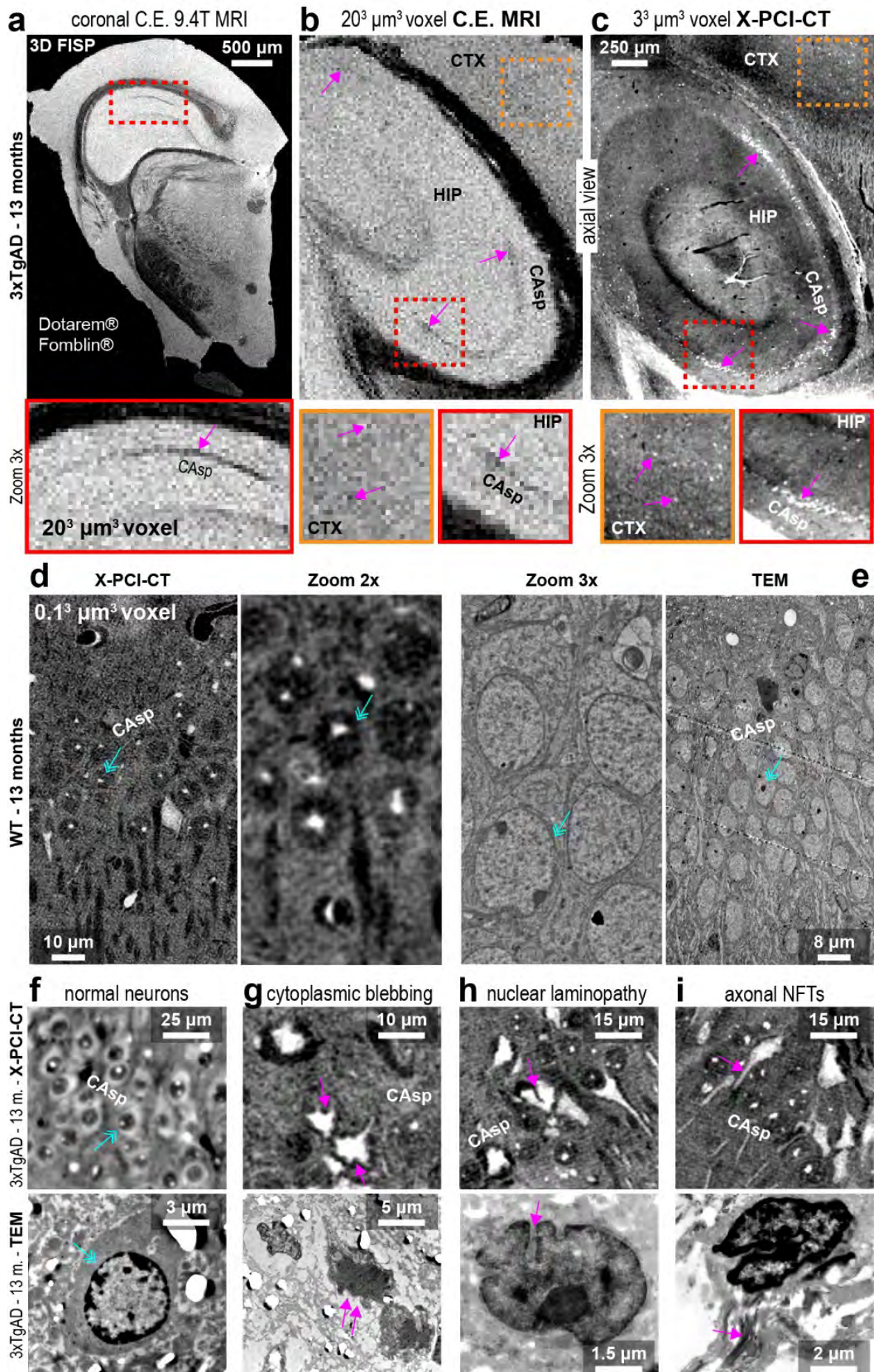


Figure 6 | X-PCI-CT vs. MRI and TEM. **a-c**, $20^3 \mu\text{m}^3$ voxel contrast-enhanced (C.E.) **(a)** coronal and **(b)** axial 9.4 T *post-mortem* MRI vs. **(c)** axial $3^3 \mu\text{m}^3$ voxel *post-mortem* X-PCI-CT of comparable CTX and HIP layers within 3xTgAD half-brain samples. Intra-layer hypo-density (magenta arrows) is visible via MRI in HIP CAsp (see Zooms 3x) and matches layer-like HD-signal in the X-PCI-CT of HIP CAsp. Sparse CTX ICHD-bearing cells are well-resolved via X-PCI-CT, only barely visible via MRI. In the MRI acquisitions, Dotarem® was used as contrast-agent, Fomblin® for artifact reduction. **d-e**, $0.1^3 \mu\text{m}^3$ voxel **(d)** X-PCI-CT vs. **(e)** TEM visualizations (and Zooms) of normal-morphology HIP CAsp pyramidal neurons (azure arrows) within comparable WT brain tissues. **f-i**, cellular-level X-PCI-CT vs. TEM brain-tissue data from 13-month-old 3xTgAD mice. Both techniques visualize **(f)** normal neurons (azure arrows) with spherical cytoplasm, intact nuclear envelopes, and low-density axons; ICHD-bearing cells (magenta arrows) morphologically match TEM-based visualizations of likely-neurodegenerating neurons, bearing signs of cytoplasmic blebbing **(g)**, nuclear-envelope laminopathy **(h)**, and abnormal hyperdense axonal cyto-architecture (probable NFTs) **(i)**.

We also compared X-PCI-CT to TEM (**Fig. 6d-i**), a gold-standard technology for morphological studies of sub-cellular structure sensitive, much like X-PCI-CT, to local differences in electron density. Differently from X-PCI-CT, TEM involved use of heavy metal salt staining, embedding in Epon and sectioning of brain-tissue in 100-200 nm thick slices. Intra-cellular area-contrast in X-PCI-CT imaging of normal HIP CAsp neurons (**Fig. 6d**) correlated very well with rodent brain TEM imaging of similar cell groups (**Fig. 6e**), though the TEM results featured much higher (sub-nanometric) resolving power compared to that of nano-X-PCI-CT. In tissues from both WT (**Fig. 6d-e**) and aged 3xTgAD animals (**Fig. 6f**), both techniques visualize euchromatin-rich hypo-dense nuclei with smooth spherical nuclear envelopes and dense nucleoli. In neurons bearing somato-dendritic ICHD, pathological cell morphology was visible via X-PCI-CT and via TEM (**Fig. 6g-i**): both structural measurements indicated ill-shaped cell-membrane outlines and cytoplasmic blebbing (**Fig. 6g**), disrupted nuclear lamina with tubular invaginations (**Fig. 6h**), and dense fibrillary lesions within dendritic and axonal compartments (**Fig. 6i**). These X-PCI-CT- and TEM-based ultrastructural observations suggest that ICHD-bearing neurons were accumulating intra-cellular toxic protein deposits and undergoing cell death, since nuclear membrane laminopathy is a known effect of tauopathy-induced neurodegeneration (Frost, Bardai and Feany, 2016) and brain ageing (Honavar and Lantos, 1987), and since cytoplasmic blebbing is a typical morphological sign of cellular apoptosis (Wang *et al.*, 2017).

Overall, the presented multi-technique comparative analysis established a clear correlation between the ICHD signal, detected via X-PCI-CT, and known intra-cellular processes related to amyloid and tau proteopathy, ageing and AD-linked cellular neurodegeneration.

5.3.5 X-PCI-CT 3D virtual-histology to quantify AD-linked cellular neurodegeneration after pharmacological treatment

After establishing X-PCI-CT-detected ICHD in aged rodent brains as a *post-mortem* biomarker of cellular neurodegeneration, we could apply the X-PCI-CT technique in a proof-of-principle study on AD neurodegeneration, using this technique as a *de-facto* density-based 3D virtual histology of deep neuronal cell populations and for the quantification of brain-wide volumetric levels of tissue neurodegeneration. Therefore, we chronically treated, for 1 month, both aged WT and aged 3xTgAD mice with LY379268, a group-II metabotropic

glutamate receptor agonist known to induce neuroprotection in experimental models (Bruno *et al.*, 2001, 2017). The collected X-PCI-CT data could serve as the basis for a preliminary evaluation of this experimental pharmacological treatment.

First, to quantitatively measure label-free tissue neurodegeneration, HD particles were extracted from 3^3 - $0.1^3 \mu\text{m}^3$ voxel X-PCI-CT 3D-datasets of CTX and HIP layers (Fig. 7a-d, Suppl. Fig. 9) via an automatic threshold-based segmentation algorithm (see Methods). Annotations of X-PCI-CT-based MIP maps and segmentation-masks (Suppl. Fig. 8,9, Fig. 7a-d) made clear that extracted cell-sized HD particles could be divided, based on size, in three main cellular populations: ICHD-bearing neurons (the largest HD particles), hyper-dense glial cells (particles of intermediate size), and nucleoli (the smallest HD particles) within hypo-dense normal neurons. A small amount (<10 per half-brain sample) of larger extra-cellular HD clusters with senile plaque-like morphology (diameter $\sim 100 \mu\text{m}$, mostly thalamic and brain-stem origins, Suppl. Fig. 9) were also extracted by the auto-threshold algorithm. To focus on intra-cellular pathology, though, plaque-like HD was omitted from the main analysis. Finally, quantification of the data was achieved by application of 3D object-counting particle-size-measuring algorithms to the segmented HD-particle volumes. This approach, applied to 0.7^3 , 0.3^3 and $0.1^3 \mu\text{m}^3$ voxel-size X-PCI-CT data, afforded tri-modal particle size distributions (Fig. 7e), in good agreement with a 3-population model for HD particles (ICHD-bearing neurons, glia & nucleoli of normal neurons). $3^3 \mu\text{m}^3$ voxel-size X-PCI-CT data instead produced only bimodal distributions, with the optical system unable to resolve HD nucleoli.

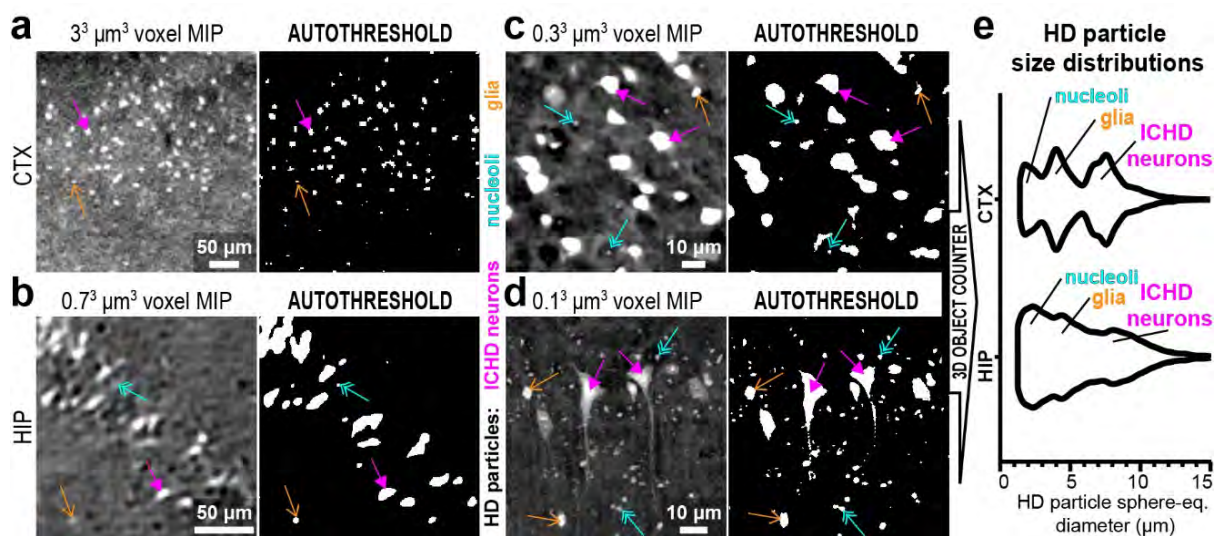


Figure 7 | 3D Segmentation & quantification of HD particles. a-d, Representative results of systematic auto-threshold segmentations of HD particles in (a) $3^3 \mu\text{m}^3$, (b) $0.7^3 \mu\text{m}^3$, (c) $0.3^3 \mu\text{m}^3$ and (d) $0.1^3 \mu\text{m}^3$ CTX and HIP X-PCI-CT volumes of interest (Vol). Segmented HD-particles correspond to three cell-populations: ICHD-bearing neurons (largest particles, magenta arrows), HD glia (intermediate-size, brown arrows) and nucleoli of normal neurons (smallest, azure arrows). Nucleoli are not resolved in (a). e, Computation of HD-particle volumes within the auto-segmented 3D-masks (a-d), using the ImageJ 3D Object Counter plug-in, resulted in the extraction of HD particle size distributions (size expressed as equivalent-sphere diameter). Distributions exhibit tri-modal shapes, in good agreement with a three-population HD particle model.

The drug-test included multiscale X-PCI-CT brain data from fifteen 13-month-old mice, seven WT and eight 3xTgAD, chronically treated with either saline or LY379268, and thus divisible

into four experimental groups (**Fig. 8a**). Quantifications were performed after the sampling of tissue-volumes (66 in total, see **Methods**) within four AD-linked brain regions (dorsal and ventral CTX and HIP, **Fig. 8a**). Examined sample-volumes ranged between 30 mm³ in size, using the largest-field-of-view 3 μm³ voxel data, and 8000 μm³ in size, using the smallest-field-of-view 0.1 μm³ voxel data (**Fig. 8b**). Gaussian Mixture Model (GMM) analysis of the tri-modal particle size distributions (**Fig. 8c**), obtained as in **Fig. 7** after HD-particle segmentation and quantification within each sample-volume, led to the demonstrative extraction of one population-, one morphological- and one neurodegeneration- parameter, respectively proportions of HD-particle populations, HD-particle sizes and 3D HD-particle tissue load, all relevant to the study of AD lesions. Merging results from all sample-volumes, we obtained distributions of each parameter for each experimental group (respectively **Fig 8d, 8e, 8f-g**). The volumetric load of ICHD-particles was studied both overall between animal groups (**Suppl. Fig. 10**), as well as regionally (in CTX and HIP layers, **Fig. 8f**) and sub-regionally (in dorsal and ventral CTX layers, **Fig. 8g**).

The average equivalent-sphere diameter of ICHD-bearing neurons was quantified to almost 8 μm, that of HD-glial cells to almost 4 μm and that of nucleoli to almost 2 μm (**Fig. 8e**), with no significant difference between animal groups. Differences in HD-populations proportions were also found not to be significant (**Fig. 8d**). The quantification of HD-particle load showed conspicuous load variability already between different sample-volumes of the same animal (**Suppl. Fig. 10**). More HD-particle load was found, on average, within CTX layers of saline-treated 3xTgAD mice, but this difference was not significant (**Suppl. Fig. 10**), even after limiting calculations to individual layers (CTX and HIP, **Fig. 8f**). After further constricting of the analysis to cortical areas only (**Fig. 8g**), though, the load within tissue samples from ventral CTX regions in untreated 3xTgAD mice was found to be significantly higher than that within tissue samples from ventral CTX regions in 3xTgAD mice and WT mice treated with LY379268. Finally, the influence of different image voxel sizes in the dataset of this multiscale analysis was found to, naturally, affect object-density calculations (higher resolving powers allowed the detection of smaller, and thus of more objects per unit-volume), but not invalidate the calculations of morphological (particle size) and histopathological (3D load) parameters, which afforded similar results at all imaging-system resolutions (**Suppl. Fig. 10**). In good agreement with previous observations on neuronal cultures (Caraci *et al.*, 2011), these proof-of-principle findings suggest possible mild LY379268-ligand-driven neuro-protective effects with sub-regional efficacy on the ageing AD rodent brain and call for a larger-scale study.

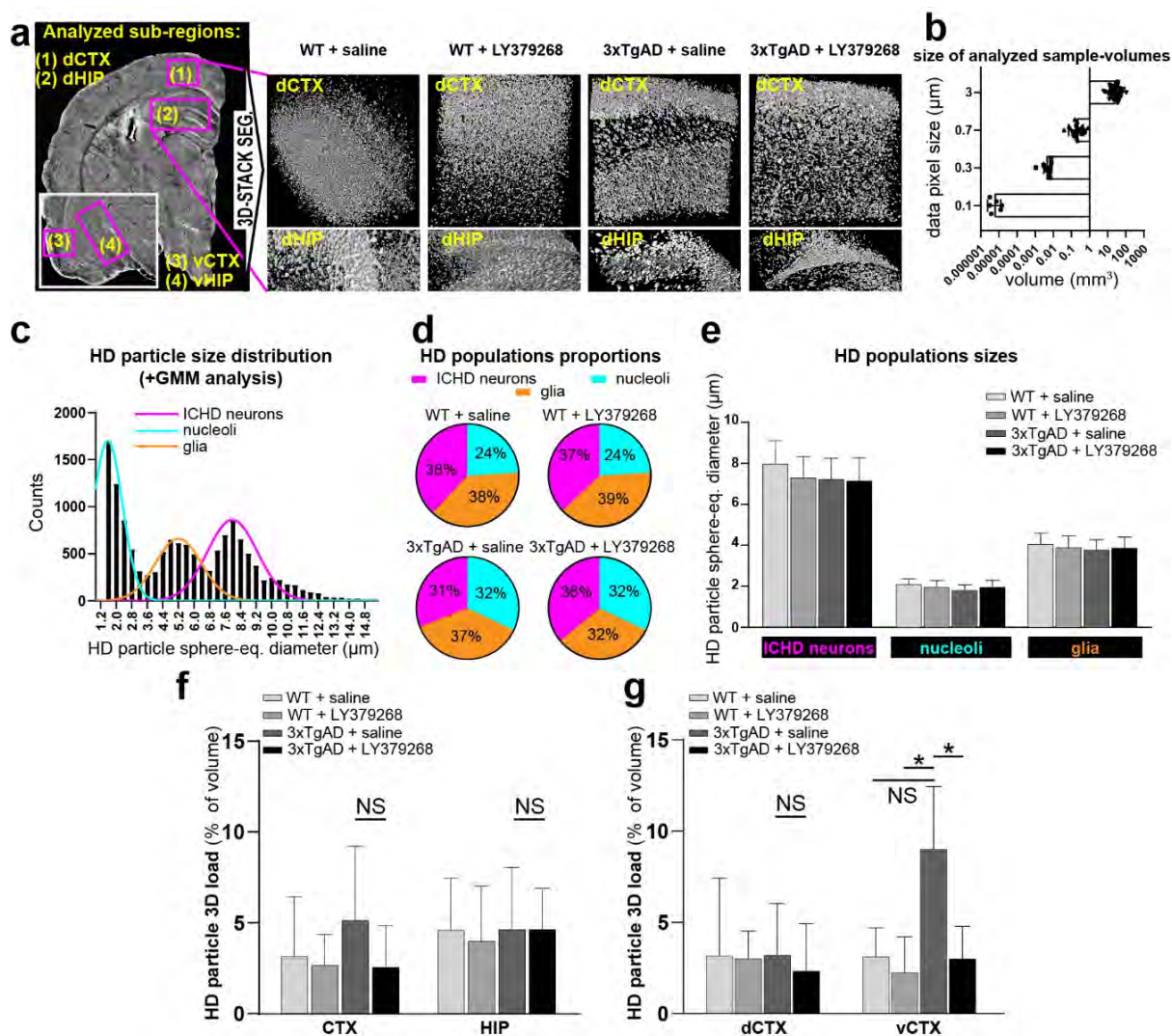


Figure 8 | Proof-of-principle drug-test with the group II metabotropic glutamate receptor agonist LY379268.

a, Experimental animal groups (13-month-old mice): WT treated with saline ($n = 4$), WT treated with LY379268 ($n = 4$), 3xTgAD treated with saline ($n = 3$), 3xTgAD treated with LY379268 ($n=4$). Virtual-histological method: collection of $3^3 \mu\text{m}^3$ to $0.1^3 \mu\text{m}^3$ voxel multiscale X-PCI-CT, and detection, segmentation and quantification of HD-particles (as in Fig. 7), treated as markers of AD-linked cellular neurodegeneration. Analysis limited to 66 total sample-volumes (representative 3D renderings in **a**) within four brain regions: (1) dorsal CTX (dCTX), (2) dorsal HIP (dHIP), (3) ventral CTX (vCTX) and (4) ventral HIP (vHIP). **b**, sizes of analyzed brain-tissue sample-volumes at each imaging resolution. Data show size of individual **sample-volumes**, and group mean \pm SD. **c**, Representative tri-modal HD-particle size distribution, extracted from a $0.3^3 \mu\text{m}^3$ voxel sample-volume, and Gaussian-Mixture Model (GMM) fit, used to separate three HD-particle populations based on size (ICND-bearing vs. glia vs. normal-neuron nucleoli). GMM analysis on all sample-volumes extracted (**d**) group HD-population proportions (pie-charts show group mean % of total HD-particles) and (**e**) group mean particle size for each HD-population (bar-graph shows group mean HD-particle size \pm SD), group mean HD-particle 3D load (bar-graphs show group mean total HD-particle volume % of total sample-volume) in (**f**) CTX vs. HIP and (**g**) dCTX vs. vCTX sample-volumes, for all four animal groups. No significant differences between animal groups were found in (**d-f** and **g**, dCTX), whereas significant differences in 3D-load between animal groups were found in (**g**) vCTX sample-volumes. P-values in (**d-g**) calculated by one-way ANOVA testing with Turkey-Kramer’s multiple comparison post-hoc test. * $P < 0.05$. NS, not significant.

5.4 Discussion

We developed a mesoscale (organ- to cellular-scale) probing system for volumetric *post-mortem* morphological neuroimaging based on state-of-the-art, multiscale synchrotron-based X-PCI-CT. This 3D imaging tool was applied to the brain-wide study of AD-linked cellular neurodegeneration in an experimental AD mouse model. It was shown that X-PCI-CT provides micro- to nano-resolution 3D neuroanatomical representations of deep neuronal populations within extended rodent brain-tissue samples after little manipulation beyond standard sample fixation and paraffin-embedding, affording 3D-morphological measurements comparable to what light-microscopy and TEM approaches can provide on 2D thin sections. Based on morphology, we were able to discriminate different neuron types and different glial populations. X-PCI-CT image contrast is generated via a label- and dissection-free mechanism and quantitatively describes intra-sample X-ray phase variations proportional to local electron density. Therefore, high-resolution X-PCI-CT maps represent a sort of virtual 3D brain histology featuring an electron-density-based coloring. Their freedom from labels and stains qualifies these images as anatomically dense and unbiased direct measurements of nervous-tissue structure. Moreover, X-PCI-CT maps in conjunction with morphological observations enabled discrimination between different neuron types and different glial populations.

Here, the X-PCI-CT technique was proven sensitive to abnormal intra-neuronal proteopathy, establishing it as a method for the full-organ mapping of AD-associated intra-cellular neurodegeneration. X-PCI-CT-based brain density-maps collected from aged WT and 3xTgAD brains showed widespread presence of intra-cellular hyper-density (ICHD) in somatic, nuclear and dendritic/axonal cellular compartments of neurons, especially evident after computation of MIP maps. The presence of these lesions not only in the aged AD-model mice but also in the WT aged brains is unsurprising and a testimony of the known link between brain ageing and neurodegeneration(Wyss-Coray, 2015).

Since X-PCI-CT signal is biologically nonspecific, ICHD-bearing cells could represent a mixture of degenerated cell-types. A biological characterization of the ICHD particles was achieved here *via* extensive multi-technique comparative analysis, involving fluorescence histology, IHC, XFM, MRI, and TEM. All results confirmed that the ICHD signal is highly representative of age-related AD-associated neurodegenerative processes of toxic co-localized A β and p-tau intracellular deposition. Notably, both tissue- and cellular-level patterns of ICHD-positivity matched cellular markings in collected ThioS-dyed sections and patterns of amyloid- and tau-immunoreactivity in collected IHC sections. The somatic compartmentalization of A β , and dendritic and axonal localization of p-tau fluorescent signal in IHC-section suggests that a spatially-differentiated multi-peptidic agglomeration of AD-linked toxic proteins is involved in the increase in density within the ICHD-bearing cells.

The X-PCI-CT-detected ICHD lesions were also detected by the most popular technologies for *post-mortem* morphological neuroimaging, namely high-field MRI and TEM, respectively as hypo-intense clusters and as hyper-dense intra-cellular fibrillary structures. Compared to high-field MRI (pre-cellular spatial resolution(Wei *et al.*, 2016) and tens of hours of scanning-

time in the absence of contrast-agent), X-PCI-CT with brilliant synchrotron-radiation X-rays presents clear advantages in terms of spatial resolution (sub-cellular) and measurement durations (minutes to a few hours (Pacureanu *et al.*, 2018), label-free). The subtlest sub-cellular lesions of early AD-phases, such as axonal p-tau NFT lesions, are, in fact, especially elusive to high-field MRI (Johnson *et al.*, 2007). Compared to TEM, in practice a 2D imaging method for ultra-thin sections, X-PCI captures 3D cellular neuroanatomy within extended un-sliced brain samples.

For its part, the collected XFM data showed significant excess P and S in both somatic and dendritic compartments of ICHD-bearing cells, another observation indicative of intra-cellular agglomeration of dense protein deposits. The highest absolute mean elemental densities found in P distributions of ICHD-bearing cells suggest intra-cellular hyper-phosphorylated tau NFT formation. Even though a contributing factor to these higher concentrations may also be the redistribution of the elements within smaller cell volumes due to pathologic cell-shrinkage of degenerated cells, what certainly stands out is Fe excess in or near nuclei of degenerated cells. And while observed low levels of maculated nuclear Fe involvement in normal cells are consistent with reported anti-fibrillar IHC nuclear staining of normal neurons (Farley *et al.*, 2015), diffuse somatic hyper-accumulation of Ca and Fe metals (high atomic number elements) within abnormal-looking ICHD-labelled neurons represents a sign of cellular dysfunction, likely arising either in direct connection to toxic protein clumping (by protein chelation) or due to other downstream cell-death processes, and can be recognized as another evident link to AD proteopathy. Indeed, iron, either directly bound to amyloid and tau lesions (Smith *et al.*, 1997) or associated to cytoplasmic RNA (Nunomura *et al.*, 1999), is known to play a toxic role in AD pathology (Honda *et al.*, 2004), and to cause oxidative damage and neurodegeneration. A β aggregates, in turn, can induce Ca dyshomeostasis (Kuchibhotla *et al.*, 2008) and lead to cellular synaptic dysfunction, neurodegeneration (Mattson, 2007) and cell death (apoptosis (Loo *et al.*, 1993), necrosis or autophagy (Pinton *et al.*, 2008)). Overall, the XFM data suggest that both non-metallic and metallic intra-cellular elemental deposits are contributing to the increase in intra-cellular electron density measured within ICHD-bearing cells via X-PCI-CTs. Moreover, measured elemental compositions directly imply that multiple concurrent and possibly co-localizing processes of neurodegeneration, linked to AD amyloid and tau pathology, are at play in the aged brains of WT and 3xTgAD mice.

The attained characterization of the ICHD signal as a (nonspecific) cellular biomarker of neuronal degeneration signified that we could apply multiscale X-PCI-CT for the *post-mortem* brain-wide 3D detection and quantification of AD-associated age-related neuropathology within small-animal brain samples. As a proof of concept, we studied the response of aged WT and 3xTgAD mice to a systemic chronic treatment with LY379268, a potential neuroprotective drug. The analysis of *post-mortem* X-PCI-CT data pointed out regional differences in cellular neurodegeneration and, most notably, significant lower levels of lesions in ventral CTX layers of 3xTgAD mice treated with the drug. Our estimates of lesion tissue load, in the 1-5% range, are in good agreement with a similar X-PCI-based AD-lesion quantification performed on the 5xFAD genetic animal model, which reported neocortical amyloid load levels of around 2% in similarly-aged animals (Pinzer *et al.*, 2012). Also the

measurements of HD-particle sizes matched literature values for cellular sizes in the mouse brain: diameters of nucleoli, glia and normal neuron somas are reportedly around 2 μm (Singleton *et al.*, 2011), 4-8 μm (Landfield *et al.*, 1981; Davis *et al.*, 2017), and 12-18(Flood and Coleman, 1988; Benavides-Piccione *et al.*, 2005; Komulainen *et al.*, 2014) μm in size respectively, compared to our X-PCI-CT measurements of about 2, 4 and 8 μm diameters. Overall, the experimental drug-test results reported here provide some preliminary trends and a basis for a future larger-scale study. Further discussion of the main themes of this study is included as supplementary material for the interested reader (see **Suppl. Discussion**).

5.5 Conclusion

In conclusion, the complexity of biological systems, such as the brain, and of biological processes, such as ageing and neurodegeneration, requires a multi-perspective and multi-technique approach to data acquisition. Alternative and new imaging approaches, such as multiscale X-PCI-CT, if applied in synergy with established ones, might help us move one step forward in the quest for a better understanding of these intricate bio-mechanisms. The results presented here demonstrate that high-resolution X-PCI-CT imaging allows multiscale 3D morphological analyses on extended deep label-free neuronal populations. This method enables brain-wide quantitative detection of cellular neuropathology associated with brain disorders and offers a versatile tool for unbiased in-depth evaluations of experimental neuroprotective strategies.

5.6 Methods

Acronyms: X-ray phase-contrast computed tomography (X-PCI-CT); cortex (CTX); hippocampus (HIP); hyper-density (HD); intra-cellular hyper-density (ICHHD); X-ray fluorescence microscopy (XFM); magnetic resonance imaging (MRI); transmission electron microscopy (TEM).

Ethical compliance: Experiments were performed following the Guidelines for Animal Care and Use of the National Institutes of Health (Authorization number: 93/2011-B).

5.6.1 Materials

LY379268, i.e. (-)-2-oxa-4-aminocyclo[3.1.0]hexane-4,6-dicarboxylic acid, was purchased from Tocris Cookson Ltd (Bristol, U.K). All other chemicals were purchased from Sigma (Milano, Italy).

5.6.2 Animals

B6/129 wild-type control mice (Charles-River, Calco, Italy) and transgenic 3xTgAD(Oddo, Caccamo, Shepherd, *et al.*, 2003) mice (B6;129-Tg(APP^{Swe},tauP301L)1Lfa *Psen1*^{tm1Mpm}/Mmjax, Stock No: 34830-JAX) were purchased from the Jackson Laboratories (Bar Harbour, ME). All mice were housed in a controlled-temperature room (21-23 °C, humidity 40-50%) and maintained on a 12-h light/dark cycle with food and water *ad libitum*. All efforts were made to minimize the number of animals used and to alleviate their discomfort. Experimental procedures were approved by the local institute Ethical Committee and the Italian Ministry of Health and performed according to the Italian (D.L. 26/2014) and European Union Directive (2010/63/EU) on the protection of animals used for scientific purposes. Eight symptomatic 11-month old male B6/129 wild-type (WT) mice and seven male 3xTgAD mutant mice (for a total of 15 mice) were treated either with saline or the selective agonist of group II metabotropic glutamate receptors LY379268 by means of subcutaneously implanted osmotic mini-pumps (Alzet, Cupertino, CA), which deliver the drug continuously at the rate of 1 mg/kg/day for 28 days, starting at the symptomatic phase. The nominal delivery of the pump was 250 nl/h, corresponding to a cumulative dose of 1 mg/kg/day of LY379268. Control mice received an equivalent volume of saline. One month after treatment, at the age of 13 months, all mice were sacrificed, brains were dissected out, fixed in Carnoy solution overnight, and finally embedded in paraffin blocks. We used one brain hemisphere for MRI, X-PCI-CT, XFM and TEM, the other hemisphere for histology and immunohistochemistry. In addition to the 13-month-old WT and 3xTgAD mice, one asymptomatic 2-month-old WT mouse was purchased from Charles-River Laboratories (Les Oncins, France), and included to the study as young-animal control in the preliminary imaging vs. Thioflavin S histological study. This animal was not subject to any drug treatment before its sacrifice at 120 days (~ 4

months) of age (same brain extraction, fixation and embedding procedures as for the aged animals).

Experimental treatment groups:

The aged WT and 3xTgAD mice were treated with saline or LY379268 (1 mg/kg) to obtain four experimental groups: 1. WT mice treated with saline (n = 4), 2. WT mice treated with LY379268 (n = 4), 3. 3xTgAD mice treated with saline (n = 3), 4. 3xTgAD mice treated with LY379268 (n=4).

5.6.3 Synchrotron X-PCI-CT acquisitions

3D *post-mortem* multiscale X-PCI-CT was performed (on the collected mouse half-brain samples) using several imaging setups available at beamlines of synchrotron-radiation facilities. There, CT scans were performed by rotation of the sample in front of an either quasi-parallel or conic X-ray beam and by continuous acquisition of CT projection images at different angles. For micrometric scans with 3^3 to $0.3^3 \mu\text{m}^3$ effective voxel size, no sectioning of tissue was necessary, and imaging was performed within the intact mouse half-brains. $3^3 \mu\text{m}^3$ voxel full-organ CT scans were performed with the samples kept within paraffin blocks. For 0.7^3 and $0.3^3 \mu\text{m}^3$ voxel micro-CT imaging, most of the paraffin embedding was removed from samples via heating, and brain samples were de-embedded from paraffin blocks and put in a PBS or ethanol bath within sealed cylindrical Eppendorf plastic tubes. Nanometric $0.1^3 \mu\text{m}^3$ voxel scans were performed in air within a vacuum chamber on $\sim 2 \times 2 \times 4 \text{ mm}^3$ -volume tissue biopsies manually excised and containing dorsal CTX and HIP areas.

X-PCI-CT data collection: one half-brain X-PCI-CT dataset per animal was measured with the $3^3 \mu\text{m}^3$ voxel setup (for a total of 15 half-organ 3D datasets). In addition, local tomographic scans aiming CTX and HIP layers were performed with the 0.7^3 , 0.3^3 and $0.1^3 \mu\text{m}^3$ voxel setups, respectively on 7, 4 and 3 animals. The limited beam-time available at high-resolution synchrotron X-PCI-CT imaging setups was the limiting factor in the collection of the higher-resolution data.

Setup descriptions:

- 1. 3^3 and $0.7^3 \mu\text{m}^3$ voxel micro-X-PCI-CT data collection:** the single-distance propagation-based (PBI) X-ray phase-contrast CT imaging setup of the ID17 Biomedical beamline (Mittone *et al.*, 2017) of the European Synchrotron (ESRF - Grenoble, France) was used to collect full-organ mouse brain X-PCI-CT data with effective voxel size of $3^3 \mu\text{m}^3$, as well as subsequent partial-organ maps with the $0.7^3 \mu\text{m}^3$ voxel optics system. All 15 half-brain samples from aged animals (7 3xTgAD and 8 B6/129 WT mice) were imaged in their entirety with the $3^3 \mu\text{m}^3$ setup, and 7 of those samples were imaged with the $0.7^3 \mu\text{m}^3$ setup, aiming local CT scans to dorsal and ventral CTX and HIP brain regions. $3^3 \mu\text{m}^3$ voxel micro-X-PCI-CTs were performed in the imaging hutch of the ID17 beamline, around 150 m away from a wiggler X-ray source, using a quasi-parallel, quasi-monochromatic 30 keV X-ray beam, obtained from a Si double Laue crystal

monochromator system(Suortti *et al.*, 2000), and 1 mm Al and 0.8 mm Cu as absorption filters. $0.7^3 \mu\text{m}^3$ voxel micro-X-PCI-CTs were instead performed in the so-called MRT hutch of the ID17 beamline, 45 m away from the wiggler, using a pink X-ray beam with peak at 40 keV and a ~ 20 keV broad spectrum. In this case, movable absorber filters included aluminum (1 mm), copper (0.7 mm) and carbon (1.15 mm). Both setups use a sCMOS PCO.Edge 5.5 (PCO AG, Germany) detector camera and a YAG-based scintillator, coupled to a x1:2 optic system to obtain the $3.0^3 \mu\text{m}^3$ effective voxel size (sample-to-detector distance set to 180 cm), and to a x1:10 optic system to obtain the $0.7^3 \mu\text{m}^3$ effective voxel size (sample-to-detector distance set to 50 cm). The 2560×2160 2D pixel array of the detector allow a field-of-view (FoV) at $3.0^3 \mu\text{m}^3$ of about 7.7 mm x 6.5 mm (H x V), at $0.7^3 \mu\text{m}^3$ of about 1.9 mm x 1.5 mm (H x V).

$3^3 \mu\text{m}^3$ voxel CT scan parameters: 300 ms detector exposure time, 2500 projections, standard 180-degree full-tomography with a position of the axis of rotation at the center of the projection images. Two consecutive partially-overlapping CT acquisitions, after vertical displacement of the sample with respect to the X-ray beam, were sufficient to measure the mouse half-brains in their entirety. CT scan time: ~ 12 min.

$0.7^3 \mu\text{m}^3$ voxel CT scan parameters: 100 ms detector exposure time, 3000 projections, 360-degree tomography in half-acquisition mode, with a rotation axis position displaced to near the edge of the projection, almost doubling the horizontal effective CT FoV to $\sim 3.5\text{mm} \times 1.5\text{mm}$ (H x V). Several local-CT scans were performed for each sample. CT scan time: ~ 5 min.

ID17 data CT reconstruction: tomographic reconstructions were performed using the ESRF PyHST2(Mirone *et al.*, 2014) software package via a standard filtered-back projection after application of the single-distance Paganin(Paganin *et al.*, 2002) phase-retrieval algorithm (PyHST2 Paganin-length parameter: 300).

2. 0.3^3 micro-X-PCI-CT data collection: the single-distance PBI X-PCI-CT imaging setup of the TOMCAT beamline(Stampanoni *et al.*, 2007; Mader *et al.*, 2011) of the Swiss Light Source (SLS, Paul Scherrer Institute, Villigen, Switzerland) was used to collect cellular-resolution local brain-tissue X-PCI-CT data using an optical system affording an effective voxel size of $0.3^3 \mu\text{m}^3$. Four aged brain samples (2 3xTgAD and 2 WT mice) plus the 1 young brain sample (WT mouse), were imaged by aiming local CT scans at dorsal and ventral CTX and HIP layers. Acquisitions were performed with a 5 cm sample-detector distance, using a quasi-parallel quasi-monochromatic 21 keV X-ray beam, obtained with a W/Si multilayer monochromator, and $100 \mu\text{m}$ Al and $10 \mu\text{m}$ Fe filters. A sCMOS PCO.Edge 5.5 detector camera, coupled to an Optique Peter microscope at 20x magnification and a $20 \mu\text{m}$ -thick LuAG:Ce scintillator, was used to obtain an effective voxel size of $0.325^3 \mu\text{m}^3$. The 2560×2160 2D pixel array of the detector affords a FoV of $\sim 0.86 \text{ mm} \times 0.70 \text{ mm}$ (H x V).

0.3³ μm³ voxel CT scan parameters: 120 ms detector exposure time, 3000 projections, standard 180 degree full-tomography with central rotation axis position. CT scan time: ~ 6 min.

TOMCAT data CT reconstruction: tomographic reconstructions were performed via filtered-back projection after application of Paganin's single-distance phase-retrieval algorithm, using in-house computing resources available at TOMCAT.

- 3. 0.1³ nano-X-PCI-CT data collection:** the X-ray nanoholotomography (XNH) imaging setup of the ID16A nano-imaging beamline(Mokso *et al.*, 2007; Da Silva *et al.*, 2017; Khimchenko *et al.*, 2018; Pacureanu *et al.*, 2018) of the ESRF was used to collect local brain-tissue X-PCI-CT data with effective voxel sizes of 0.1³ μm³. 3 aged brain samples (2 3xTgAD and 1 WT animals), were imaged by aiming local CT scans at dorsal CTX and HIP layers within dissected 2 x 2 x 4 mm³-volume tissue biopsies. The ID16A XNH setup^{13,14} uses multilayer-coated Kirkpatrick–Baez mirrors to focus the beam to a high-brilliance ~ 30 x 30 nm spot, which enables imaging with sub-100 nm spatial resolution. The beam energy was set to 17 keV, with a monochromaticity of 1%. At a fixed focal-plane-to-detector distance of ~1.2 m, projections images were recorded with a 4Kx4K fast readout and low noise CCD camera (FReLoN, ESRF), binned to 2048 x 2048 pixels and coupled to magnifying optics and a 23 μm thick GGG:Eu scintillator. The voxel size, given by the geometrical magnification, was set to 0.1³ μm³ and the corresponding field of view was 0.2 mm x 0.2 mm (H x V). Samples were placed in vacuum (~10⁻⁷ mbar) on a rotating stage downstream of the focal plane. Single-distance low-resolution CT overview-scans with a voxel size of ~200³ μm³ helped locate the most relevant CTX and HIP regions, within the extended rod-like samples, which were then further imaged at 0.1³ μm³ voxel size.

0.1³ μm³ voxel CT scan parameters: sets of angular holograms(Cloetens *et al.*, 1996) were recorded at 4 different (pre-defined) propagation distances(Bleuet *et al.*, 2009; Bartels *et al.*, 2015; Khimchenko *et al.*, 2018) (starting with a 40 mm focal-plane-to-sample distance, and then moving the sample progressively closer to the detector) by rotating the sample over 180 degrees. Exposure time for each projection was 250 ms and 2000 projections were recorded for each tomographic sub-scan. Total scan duration was around 4 h.

ID16A data CT reconstruction: projections were normalized, rescaled to the smallest pixel size, and registered via an in-house algorithm based on cross-correlation. Assuming pure phase object samples, a 4-distance contrast-transfer-function-based algorithm for phase-retrieval was applied(Cloetens *et al.*, 1999; Bartels *et al.*, 2015), including Wiener regularization(Zabler *et al.*, 2005) to improve low frequencies, using GNU Octave software. The final 3D datasets were obtained from angular phase-maps through filtered-back projection CT reconstruction, using PyHST2(Mirone *et al.*, 2014) software.

5.6.4 X-PCI-CT data post-processing and analysis

CT artefacts: CT cupping artefacts related to local-tomography acquisitions were removed by flattening reconstructed CT images via normalization against their Gaussian-blurred version (filter sigma size: 50). CT ring artifacts were in large part removed from reconstructed CT images with an ESRF in-house post-processing tool (Lyckegaard, Johnson and Tafforeau, 2011).

MIPs: maximum intensity projections (MIPs) were computed by summing 20-100 consecutive CT images via the maximum intensity z-projection function in ImageJ (Schneider, Rasband and Eliceiri, 2012). This approach highlights hyper-intense image features and creates a pseudo-volumetric rendering by projecting the brightest voxels within a 3D stack onto a 2D image.

LUT-recoloring of X-PCI-CT data: different look-up tables (LUTs) available in ImageJ were used in the recoloring of X-PCI-CT images (e.g. 6-shades, Orange Hot, Viridis LUTs).

3D renders: all 3D renderings were obtained using the commercial software VG Studio Max 3.2 (Volume Graphics GmbH, Heidelberg, Germany). Volumetric extraction and segmentation of different tissue features (e.g. hyper-dense particles, vasculature, normal parenchyma) were performed with the threshold-based gray-value-range voxel selection option or the region-growing voxel selection option. The threshold-based tool was used for hyper-dense (HD) particle features and hypo-dense vasculature features. Normal brain cells and plaque-like deposits were instead extracted from inverted-gray-level X-PCI-CT maps via manual selection and the region-growing tool. Color-coding was achieved with customized color presets, generally rendering HD particles in white, vasculature in red and normal parenchyma in azure. 3D renderings were then obtained via either the non-transparent ‘Isosurface’ or the semi-transparent ‘X-ray’ rendering algorithms.

Automated 3D segmentation of hyper-density (HD) within X-PCI-CT data: threshold-based segmentations of HD particles were made automatic by using the auto-thresholding tool in ImageJ and by applying the maximum entropy auto-threshold algorithm (Kapur, Sahoo and Wong, 1985) (MaxEntropy AutoT), which has already been shown to work on X-PCI-CT data for the segmentation of macroscopic amyloid deposits (Pinzer *et al.*, 2012). We computed the MaxEntropy AutoT algorithm slice-by-slice on every 10th CT image in a volume of interest, and averaged the obtained oscillating threshold values to choose a single threshold level for the entire volume. In this way, differently-sized HD particles could be extracted.

Quantification of hyper-density (HD) within X-PCI-CT data:

- a. **Macroscopic plaque-like deposits:** to obtain a one-off proof-of-principle X-PCI-C-based A β plaque quantification, macroscopic senile plaque-like HD objects (n=27) were segmented-out of X-PCI-CT datasets from one WT and two 3xTgAD mice, using the manual region-growing tool in VG Studio Max. The volume of each extracted plaque-like HD objects, obtained by counting the voxels within each object mask, was used to compute the object’s equivalent-sphere diameter. Diameter values from different objects were combined to obtain a distribution and calculate a mean size for these plaque-like HD objects.

b. HD cell-like particles: to obtain a systematic quantification of particle-like HD within HIP and CTX layers in 3-0.1 μm pixel X-PCI-CT data, every volume-of-interest (Vol) was segmented via the automatic threshold-based approach described above, and the automatically-computed threshold value was used as lower limit to compute a volumetric mask of the data. The segmented mask was then analyzed via the '3D Object Counter' ImageJ plugin (Bolte and Cordelières, 2006), which extracts individual unconnected 3D particles and computes their volumes. Just as for macroscopic plaques, the equivalent-sphere diameter was calculated from the volume of each individual HD particle as a way to express object sizes, and all computed diameters were combined to obtain the distribution of particle-like HD 3D objects within the Vol. Objects with diameters smaller than twice the pixel size (i.e. non-resolved objects) were excluded from distributions. Moreover, the few outlier objects with diameters greater than 30 μm were also excluded from distributions, because deemed to arise from non-cell-like objects (possibly image artefacts, or larger anatomical brain features unrelated to cellular neurodegeneration). Three different quantitative parameters were extracted from HD particle size distributions:

- i. HD particle 3D load: the proportion of brain tissue within a Vol pertaining to HD particles, computed by summing the volumes of all extracted individual particles and then normalizing with respect to the total volume of the Vol. Load was then expressed as the percentage of the total volume occupied by the HD particles.

Tri-modal HD-particle size distributions from 0.7³, 0.3³ and 0.1³ μm^3 voxel-size X-PCI-CT data were further analyzed, by fitting to them a 3-component Gaussian mixture model (GMM) and by using the 'fitgmdist' function in Matlab (MATLAB R2018a, The MathWorks, Inc., Natick, Massachusetts, United States), a function that implements an iterative Expectation-Maximization (EM) algorithm (McLachlan and Peel, 2000). A 2-component GMM was instead fitted to the bimodal distributions obtained from the 3³ μm^3 voxel-size X-PCI-CT data. In this way, two additional HD-particle parameters could be obtained:

- ii. HD particle populations mean sizes: the 3-component (2-component) GMM fit of the HD-particle diameter distributions returns three (two) Gaussian means (μ parameters), which express the mean sizes of each of the three (two) cell populations.
- iii. HD particle population proportions: the 3 (2) mixing proportions returned from the 3 (2)-component GMM fit of HD-particle diameter distributions, which express the proportion of each HD particle cell population within a Vol.

3D virtual tissue sample collection: sub-volumes of interest (sVol) were collected from each 3D brain X-PCI-CT dataset, in order to sample four specific brain regions, i.e. dorsal CTX (dCTX), dorsal HIP (dHIP), ventral CTX (vCTX) and ventral HIP (vHIP). sVol centers were positioned at the following bregma-based stereotactic coordinates (in mm), ML being medial-lateral, AP

anterior-posterior, and DV dorsal-ventral, as annotated in the Paxinos Atlas (Paxinos and Franklin, 2001):

- a. dCTX: center ~ ML +0.7, AP -2, DV +0.7
- b. dHIP: center ~ ML +0.7, AP -2, DV +1.5 (HIP CA1sp)
- c. vCTX: center ~ ML +4, AP -3, DV +4
- d. vHIP: center ~ ML +2.9, AP -3, DV +4 (HIP CA1sp).

sVols were sampled from all mice involved in the study and from all the different resolution datasets, affording a total of 90 virtual-histological 3D tissue volumes. The analysis included 60 sVols extracted from $3^3 \mu\text{m}^3$ voxel X-PCI-CTs (all 15 mice were measured at this resolution, so that all 4 regions per animal could be sampled), 16 sVols from $0.7^3 \mu\text{m}^3$ voxel CTs (7/15 mice measured, dorsal and ventral regions sampled), 8 sVols from $0.3^3 \mu\text{m}^3$ voxel CTs (4/15 mice measured, dorsal regions sampled) and 6 samples from $0.1 \mu\text{m}$ pixel CTs (3/15 mice, dorsal regions sampled).

3D Quantification: volumetric HD particle masks were automatically segmented from each of the (90) sampled sVols. As discussed above, individual 3D masks (from each sVol) were analyzed to extract several sample parameters: HD-particle load, mean HD-particle sizes for three different cellular populations, and HD-particle population proportions.

Quantitative group comparisons: Region-based and animal-group-based averaging of the 3 extracted parameters (load, particle sizes, particle proportions) were performed to study potential differences in the quantified levels of HD-based tissue neurodegeneration between different animal types, different treatment types and different brain regions. Group distributions (and group averages) were obtained by combining the individual parameters of all sVols pertaining to a specific group. Possible significant differences in parameters between animal groups were tested by one-way ANOVA testing, with Turkey-Kramer’s multiple comparison post hoc test for unequal sample sizes, or by unpaired two-sided two-sample T-test, using SAS software (SAS Studio, SAS University Edition 2.7, SAS Institute Inc., Cary, NC, USA). Group differences related to calculated P-values of less than 0.05 were deemed significant. In addition, differences between samples of data with different voxel-sizes were explored qualitatively (no ANOVA testing performed).

Data displays: Quantification displays (histograms, bar graphs, pie charts) were all produced with the commercially available software GraphPad Prism (GraphPad Prism 8.0.0, GraphPad Software Inc., San Diego, CA, USA).

5.6.5 XFM measurements

Sample preparation: half-brains from one 13-month-old WT and one 13-month-old 3xTgAD were sliced with a Leica RM2265/LN22 ultra-microtome (Leica Microsystems), using diamond blades, into $6\text{-}\mu\text{m}$ -thick coronal sections. The vertical sample holders consisted of $7 \times 7 \text{ mm}^2$ -

wide, 200 μm -thick silicon frames with $3 \times 3 \text{ mm}^2$ -wide, 500 nm-thick silicon nitride (Si_3N_4) windows (Silson Ltd). Sectioned brain slices were loaded onto the windows after brief soaking of the slices in water.

XFM data collection: 2D scanning nano-XFM measurements were performed in vacuum room-temperature conditions using the setup available at the ID16A beamline (Da Silva *et al.*, 2017; Sanchez-Cano *et al.*, 2017; De Samber *et al.*, 2018) of the ESRF. The samples were raster scanned with a beam of 17 keV X-ray excitation energy (1% bandwidth), focused to $\sim 30 \times 30 \text{ nm}^2$ (H x V). Detected spectra were recorded with a pair of six element silicon drift diode X-ray fluorescence detectors (SDDs, SGX Sortech, UK). This high-brilliance nanoscopic XFM setup can map trace elemental distributions quantitatively in single cells and intra-cellular compartments, within tissue slices, in close to native state. It was also possible to follow-up XFM measurements with coherent X-PCI radiographic imaging of the same sample areas, to obtain additional information on cellular density. A visible-light microscope was used to aim XFM scans toward cells within HIP and CTX layers, and a quantitative calibration of elemental area density was performed with a thin film reference sample (AXO Dresden GmbH) containing mass depositions in the range of ng/mm^2 (1-3 atomic layers).

Coarse XFM raster-scans, acquired to further perfect scan aiming, were performed with a $400 \times 400 \text{ nm}^2$ step size and 100 ms dwell time. Definitive 2D fine raster-scans instead were performed with a $120 \times 120 \text{ nm}^2$ step size and 50 ms dwell time. FoVs of the fine-scans were in the order of $\sim 35 \times 35 \mu\text{m}^2$, obtained from $\sim 85\text{k}$ individual XFM point spectra. Ten 2D fine scans were collected per brain sample, and approximately equal amounts of cortical and hippocampal cells were measured. For each scan, local intra-cellular K, S, P, Zn, Fe, Cu, Ca and Br elemental content maps (in ng/mm^2) were obtained in addition to one 2D X-ray phase-map of the same area.

XFM data post-processing: The quantitative elemental area density maps were obtained from individual point spectra, by fitting and normalizing the data using the PyMCA-software for XFM spectral analysis (Solé *et al.*, 2007) available at the ESRF, including an attenuation correction (significant for low Z elements), which assumed a 500 nm-thick silicon nitride sample matrix. LUT-based recoloring of the quantitative elemental XFM maps was performed with ImageJ, using the Magenta Hot LUT for P & S and the Green-Fire-Blue LUT for Ca/Fe maps. Co-localization XFM maps were recolored with the Magenta (for P), Yellow (for S), Red (for Ca), and Green (for Fe only) LUTs.

XFM image analysis and quantification: Normalized and calibrated XFM elemental density data were used to extract individual 2D cell masks, by manual selection of intra-cellular areas in ImageJ of 22 normal cells and 11 ICHD-bearing cells. The same 2D mask was used for all the different elemental density maps, and the phase-map, pertaining to a specific cell. The labels 'normal' vs. 'ICHD-bearing' were assigned to cells by manual reader inspection of the gray-levels and morphology visualized in the phase maps. For each masked cell and for each interrogated element, the mean intra-cellular 2D elemental density was computed using ImageJ. By combining measurements from all cells in each of the two groups, we obtained distributions of intra-cellular elemental content for each interrogated element. Possible

significant differences in the average elemental density between the two cell groups were tested by unpaired two-sided two-sample Wilcoxon Test, using SAS software (SAS Studio, SAS University Edition 2.7, SAS Institute Inc., Cary, NC, USA). Group differences related to calculated P-values less than 0.05 were deemed significant. Bar graphs were produced with commercially available software GraphPad Prism (GraphPad Prism 8.0.0, GraphPad Software Inc., San Diego, CA, USA).

5.6.6 High-field MRI measurements

Sample preparation: PBS-stored hydrated half-brains from one 13-month-old WT and one 13-month-old 3xTgAD were embedded in 2% agarose gel in PBS and each placed in a 2 ml Eppendorf Safe-Lock tube. After an initial non-contrast-enhanced (non-CE) high-field MRI-imaging session, the agarose gel was removed and the samples were prepared for contrast-enhanced (CE) MRI (following a reported contrast-enhancement approach(Ullmann *et al.*, 2012)). Briefly, samples were first incubated for 24 hrs in PBS containing 0.1% gadoterate meglumine (Dotarem, 0.5 mmol Gd/mL; Guerbet, Aulnay-sous-Bois, France); then, the buffer was replaced and the incubation continued for another 72 hrs. Finally, the brains were placed again in 2 ml Eppendorf Safe-Lock tubes filled with Fomblin (Fomblin® Y; Sigma-Aldrich, Munich, Germany).

MRI data acquisition: a preclinical 9.4 T MRI scanner (BioSpec 94/21 USR; Bruker, Ettlingen, Germany) was used for data collection. Coronal brain images were collected using the manufacturer’s transceiver cryogenic quadrature RF surface probe (CryoProbe, catalog number Z125365, Bruker Biospin, Ettlingen, Germany). The images were acquired with the following parameters:

- A. Non-CE MRI: 3D FISP sequence; repetition time (TR), 29 ms; echo time (TE), 12 ms; excitation pulse angle 20°; FOV, 8 x 8 x 8 mm³; acquisition matrix, 440 x 440 x 440; spatial resolution, 18.2 x 18.2 x 18.2 μm³; number of averages, 22; oversampling slice direction, 30%; bandwidth, 35714 Hz; scan time, 44 hrs 36 min.
- B. CE MRI: 3D FISP sequence; repetition time (TR), 28 ms; echo time (TE), 11 ms; excitation pulse angle 40°; FOV, 6 x 7 x 10 mm³; acquisition matrix, 307 x 358 x 512; spatial resolution, 20 x 20 x 20 μm³; number of averages, 9; bandwidth, 32467 Hz; scan time, 15 hrs 22 min.

5.6.7 TEM measurements

2 x 2 x 4 mm³ biopsies of CTX and HIP layers, already used for 0.1³ voxel X-PCI-CT, were dehydrated through a graded ethanol series (50/70/90/100%), substituted with a mixture of resin and 100% ethanol (50/50 vol/vol), embedded in Embed 812 resin (EPON substitute, EMS) overnight at RT, and then put for 2 days at 65°C for polymerization. Ultrathin sections (100 nm or 200 nm) were cut with a Leica EM UC7 ultra-microtome (Leica Microsystems), collected on formvar-coated copper grids and counterstained with uranyl acetate 2% and lead

citrate 2%. Sections were observed using a Tecnai12 G2 Spirit Bio Twin (ThermoFischer) microscope operating at 120 kV using an Orius SC1000 CCD camera (Gatan).

5.6.8 Histology and immunohistochemistry

Coronal sections (10 μm) were cut on a microtome and processed for Thioflavin-S staining. Briefly, sections were washed in PBS and stained with Thioflavin-S (Sigma-Aldrich, St. Louis, MO) at 1% (w/vol) in 70% ethanol for 10 min. Finally, sections were washed in 50% ethanol and in water, then dried and cover-slipped with Anti-fade mounting media with Dapi for nuclear staining. For immunohistochemistry, sections were deparaffinized and rehydrated by standard procedures. After antigen retrieval in citrate buffer (10 mM, pH 6.0) for 15 min, samples were pretreated with 3% H_2O_2 /3% methanol for 10 min to block endogenous peroxidase activity, and then blocked in 5% normal serum and 0.1% Triton-X100 in PBS for 2 hrs. Sections were incubated with the following primary antibodies: anti- β -Amyloid 17-24 clone 4G8 made in mouse (1:100; Biolegend, S. Diego, CA; RRID: AB_2564633), anti-phospho-tau pSer404 made in rabbit (1:100, Sigma-Aldrich, S. Louis, MO; RRID: AB_261759), anti-NeuN made in rabbit (1:200, Millipore, Darmstadt, Germany; RRID: AB_10807945) and anti-Neu made in mouse (1:200, Millipore, Darmstadt, Germany; RRID: AB_2298772) for double immuno-labeling. Sections were then rinsed and incubated for 2 hrs at room temperature with secondary antibodies: Cy3-conjugated donkey anti-mouse IgG (1:200, Jackson ImmunoResearch, West Grove, PA; RRID: AB_2340818) or donkey anti-rabbit (1:200, Jackson ImmunoResearch, West Grove, PA; RRID: AB_2307443); biotinylated horse anti-mouse IgG (1:200, Vector Laboratories, Burlingame, CA; RRID: AB_2313581), or biotinylated horse anti-rabbit IgG (1:200, Vector Laboratories, Burlingame, CA; RRID: AB_2336201) followed by Streptavidin Alexa Fluor 488 (1:200, Molecular Probes, the Netherlands). Finally, samples were mounted with Vectashield with Dapi (Vector Laboratories, Burlingame, CA) and examined under a Zeiss 780 confocal laser scanning microscope. We used a 488 nm argon laser to excite Alexa 488, and 543 HeNe laser to excite Cy3.

5.7 Supplementary Material

5.7.1 SUPPLEMENTARY DISCUSSION

Benefits of X-PCI-CT neuroimaging:

An evident benefit of a dissection-free multiscale imaging methodology is its ability to collect pre-cellular to cellular-level maps at variable spatial resolutions and from different deep brain regions without having to go through a series of error-prone mechanical sample slicing operations, simply by running an appropriately-aimed sequence of much less invasive local CT scans. Furthermore, while one-shot histological workup requires strategic pre-planning before data collection, X-PCI-CT allows for repeated samples interrogations, admits unexpected observations and can provide a morphological database on which to plan further data-collection. Sample-preserving X-PCI-CT-imaging in fact is conveniently compatible with most other *post-mortem* neuroimaging analyses. Both the XFM and TEM analyses presented in our work, for example, were carried out on the same brain samples previously imaged via X-PCI-CT. In addition, though our histological and IHC analyses were performed on contralateral hemispheres for practical and time sparing reasons contingent to this multi-institutional study, X-PCI-CT is also compatible with post-imaging same-sample histological and IHC work^{1,2}. The only *post-mortem* imaging technique that needs to precede X-PCI-CT is MRI, for which a fully-hydrated sample is necessary.

Possible artifacts in the X-PCI-CT data:

X-PCI-CT scans, especially at the highest spatial resolutions, deposit conspicuous energy locally (from hundreds to thousands of milligrays, depending on the used pixel size), which may lead to sample heating, local dehydration and shrinkage. Moreover, X-PCI-CT data of fixed paraffin-embedded samples may suffer the same differential neuropil shrinkage artifacts typical of histological work.

Non-specificity of the ICHD signal in X-PCI-CT maps vs. other techniques:

Image-contrast in most of the phase-retrieved X-PCI-CT datasets presented here, after application of the Paganin phase-retrieval algorithm³, is only semi-quantitative. In terms of relative density levels, the ICHD-bearing particles appeared as denser than adjacent normal brain parenchyma, but also as less dense than typical high-Z bio-materials (e.g. bones, iron-rich blood-filled vessels, or calcifications¹), and of a comparable density to that of neuron nucleoli. This signal intensity suggests a likely DNA- or protein-based composition for the abnormal aggregates along with possible mild metal involvement (e.g. protein-bound Ca or Fe), all intra-cellular contents expected in neuro-degenerating brains.

X-PCI-CT-measured signal within ICHD neurons is non-specific and could be a reporter of different neurodegenerative cellular conditions, both AD-linked and non-AD-linked⁴. This is not dissimilar to the signal aspecificity of other known histological markers of acute cellular neurodegeneration, e.g. ‘dark’ argyrophilic Gallyas-silver-positive neurons, which aspecifically report cellular neurotoxicity^{5,6}, or Fluoro-Jade-positive, which aspecifically report

degenerating neurons^{7,8}, or even dark-stained neurons in toluidine blue histological sections, which specifically report likely cellular condensation⁹⁻¹¹. Overall, the ICHD tissue markings in our data closely resemble tissues stained with a Campbell-Switzer impregnation, a semi-specific dye for AD neuropathology¹¹.

Morphology of ICHD vs. biological considerations:

The correlation of morphological observations to known AD micro-biology enables the association of different ICHD traits with different expressions of ageing-related AD neurodegeneration: the ring-like patterns of cytoplasmic ICHD accumulations match immunolabeling patterns typical of cellular amyloidopathy¹²; dendritic and axonal ICHD, instead, resemble classic patterns of cytoskeletal tauopathy¹³, which predominantly feature the fibrillization of axonal microtubules (NFT formations). Observed cell-shrinkage, blebbing, and nuclear laminopathy, for their part, are likely linked to protein-induced downstream mechanisms of cell death, which involve somatic condensation, e.g. cell pyknosis during apoptosis or dystrophic mineralization (calcification and ferrugination) during cell necrosis. Glial involvement, for its part, suggests occurred local gliosis, i.e. another process typically present in ageing and degenerating brains. In sum, most of the distinctive morphological features of ICHD-bearing cells can be connected to known mechanisms of A β and p-tau toxic protein clumping during AD neurodegeneration.

Interest of cellular-level AD imaging in animal models:

Cellular-level visualizations of the smallest micrometric intra-cellular lesions in early stages of AD, even in animal models, are valuable to both studies on mechanism and on pharmacological treatment of AD. As it pertains to disease mechanism, AD animal models have long been used to help characterize early disease phases, even though e.g. mice have a short lifespan without a clear-cut neurodegenerative phenotype. As it pertains to AD-drug discovery, preclinical research on mouse models has highlighted how beneficial effects can arise with early treatment¹⁴, a realization which has shifted the focus of some new drug tests toward the pre-symptomatic disease phase and on patients at risk for AD (e.g. solanezumab¹⁵ drug-trial programs).

A β and p-tau IHC in the 3xTgAD mouse:

The patterns of protein deposition observed in the collected IHC are unsurprising, since the 3xTgAD mouse model is known¹⁶ to present co-localized intra-cellular p-tau and A β toxic fibrils. Extra- and intra-cellular A β deposits are reported to arise first, starting in CTX layers and then spreading to HIP ones. P-tau fibrillary buildup, instead, was proved successive to the amyloidopathy, accumulating intracellularly, first in HIP and then in CTX, and often co-localizing with the A β -positive cells. More generally, tauopathy and amyloidopathy are known to coexist in age-related processes of neurodegeneration in many animal models.

More on the XFM data:

Significant excess in cytoplasmic P and S content leads to an increase in local intra-cellular density, to which X-PCI-CT is sensitive¹⁷, and is indicative of intra-cellular agglomeration of

dense AD-linked protein deposits, and especially of hyper-phosphorylated microtubule-associated tau protein. The intra-cellular hyper-accumulation of high-Z elements, such as Ca and especially Fe metal, will also contribute to an increase in local intra-cellular electron density and concur to produce the observed ICHD.

Within normal cells, *post-mortem* XFM detects mostly Ca and Fe that is bound to protein (eg. Ca to calbindin, Fe to ferritin) or other biomolecules (e.g. Fe to dopamine)^{18,19}, since Ca²⁺ ions mostly leak out of cells post-fixation and redox metals (such as Fe) do not appear free in solution within normal cells (this would cause toxic oxidative stress). Within abnormal ICHD-bearing cells, instead, *post-mortem* XFM could detect both free Fe or Fe trapped within larger protein clumps, and is a clear indication of the occurrence of intra-cellular neurodegeneration.

Of note is how nucleoli, regulation centers of ribosomal neurogenesis, neuronal growth and stress response²⁰, and recognizable as single dense and rounded intra-nuclear structures, feature P, Ca and Fe elemental hyper-density in both ICHD-bearing cells and normal cells (**Fig. 4**). The smaller round-shaped deposits are normal and physiological, since P is a constituent of ribosomal DNA, Ca signals regulate normal gene transcription²¹ and Fe reveals itself in the nucleoli of many normal CAsp neurons²². The more extended and diffuse intra-nuclear and near-nucleolar P, Ca and Fe areas within ICHD-bearing cells (**Fig. 4**), instead, seem pathologic, likely driven by nuclear or nucleolar dysfunction and leading to neurodegeneration²⁰.

More on TEM results:

The observed nuclear membrane infoldings, in literature referred to as 'nucleoplasmic reticula', can occur either in certain types of healthy cells²³, or in cells suffering from neurodegenerative laminopathy, which leads to aberrant forms of nucleoskeletal invagination, to heterochromatin relaxation and to neuronal death. Interestingly, tau-induced nuclear envelope invagination²⁴ and lamin dysfunction have been observed in several tauopathy models²⁵, including AD models^{26,27}.

Role of group II metabotropic glutamate receptors:

The role of group-II metabotropic glutamate receptors (mGlu2 and mGlu3 receptors) in influencing mechanisms of neurodegeneration is debated, since activation of mGlu2/3 receptors by selective ligand agonists (e.g. LY379268 or LY354740) has downstream effects that could lead both to deceleration and to acceleration of neurodegeneration. mGlu3 receptors, for instance, have the potential to trigger neuroprotective effects and possibly decelerate neurodegeneration, since they can mediate the production of neurotrophic factors (e.g. transforming growth factor- β (TGF- β) and glial cell line-derived neurotrophic factor (GDNF)²⁸⁻³⁴) and limit the production of A β peptide by stimulating α -secretase activity³⁵. Instead, selective activation of mGlu2 receptors has been shown to amplify neuron death processes in culture^{30,34} and in experimental models of transient global ischemia³⁶. Within microglial cells, mGlu2 receptors are known to activate the release of neurotoxic cytokines^{37,38}.

ICHD signal intensity and interpretation:

ICHD deposits exhibit levels of X-PCI-CT image gray-level hyper-intensity, at which normal cyto-architecture is still well visible. This observation implies that the two different density levels are somewhat comparable, and suggests an endogenous near-to-normal biological origin for the ICHD. More extreme levels of hyper-density, e.g. within metals, would instead likely overpower X-PCI-based image contrast and hide the relatively-hypo-dense neuroanatomy of a normal nervous tissue. This is not the case, though, for the ICHD observed here. Therefore, an interpretation of the ICHD signal as protein aggregation seems fitting to its signal-level.

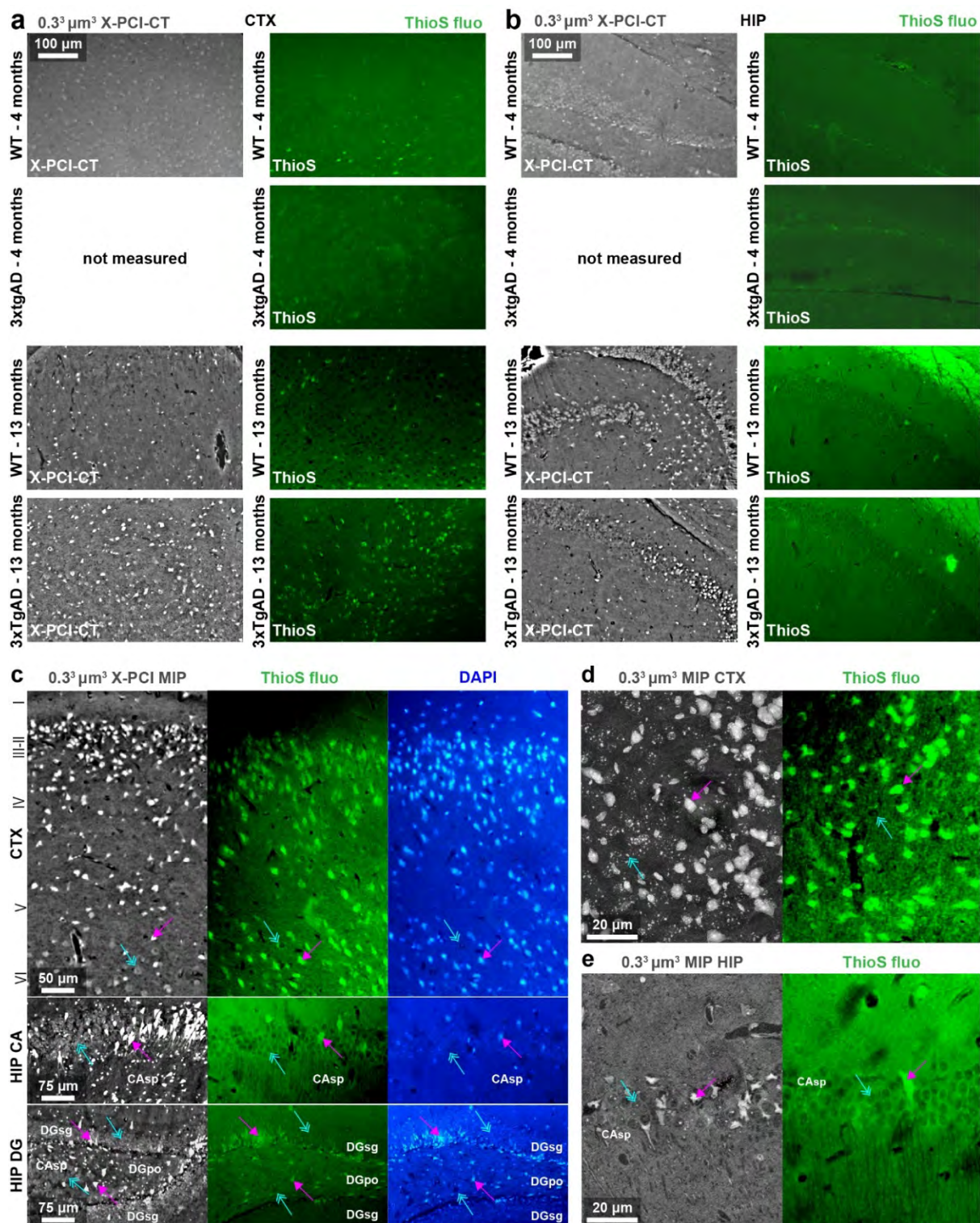
P vs. Fe contributions to X-PCI-CT signal:

Quantitatively, a higher value of the mean P intra-cellular area density ($\sim 25 \text{ ng/mm}^2$) was observed within ICHD-bearing cells, compared to the value of the mean Fe intra-cellular area density ($\sim 1.4 \text{ ng/mm}^2$). This observation may seem to point to a stronger link between X-PCI-CT-detected ICHD and P accumulation, than between ICHD and Fe deposition, and therefore to strengthen an interpretation of the ICHD signal as of peptidic over metallic origin. Nevertheless, since X-PCI-CT phase maps are directly related to δ , i.e. the refractive index decrement in the X-ray complex index of refraction formula $n = 1 - \delta + i\beta$, with δ proportional to the local electron density ρ_e , and $\rho_e = Z/V = Z * \rho * N_A/A$ (Z atomic number, V volume of reference, ρ macroscopic mass density, N_A Avogadro's number and A atomic weight), an equivalent volumetric amount of a high- Z material, such as Fe, will contribute almost twice to X-PCI hyper-intensity compared to a low- Z material such as P ($Z_{\text{Fe}}/Z_{\text{P}}=1.73$). For this reason, the atomic properties of Fe likely make it also a key player in the generation of the X-PCI-CT-observed ICHD signals.

Impact of sample shrinkage on data quantification:

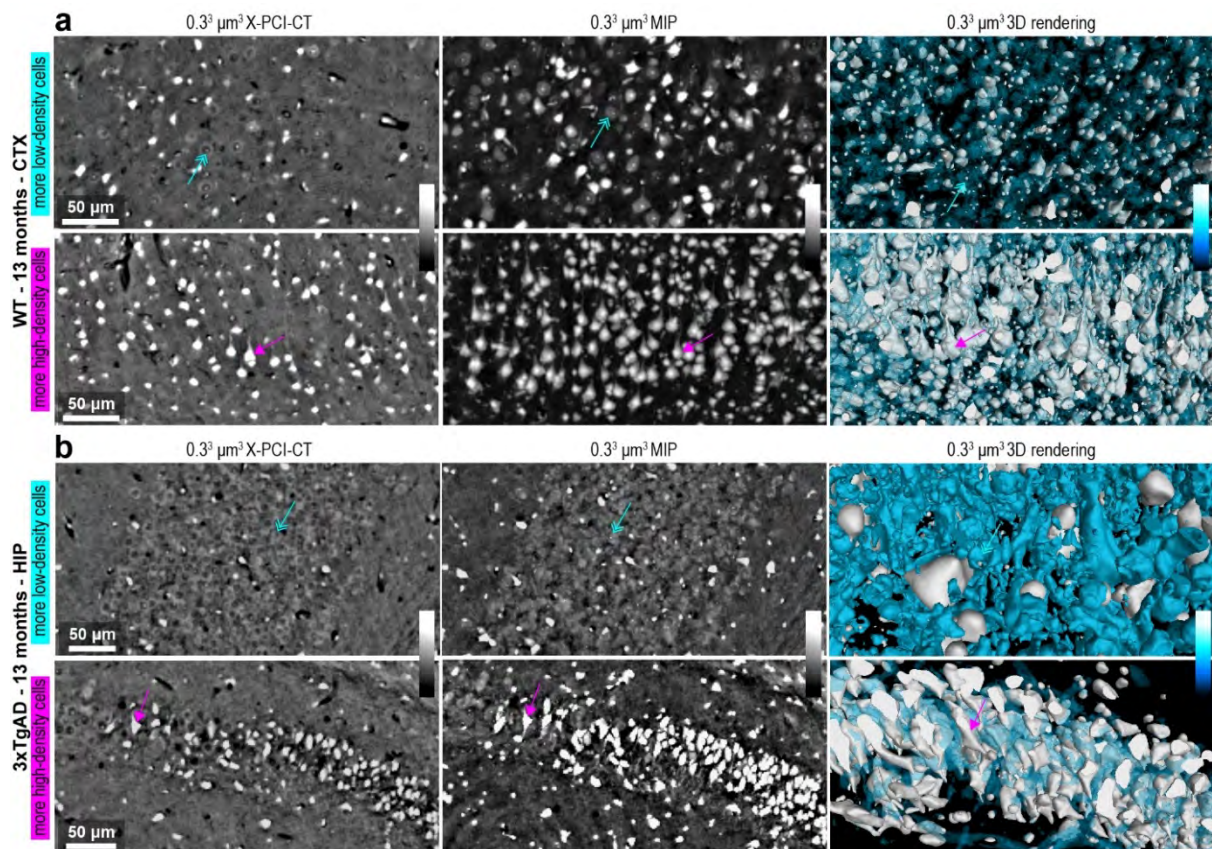
Moderate systematic dehydration-related sample shrinkage, either due to sample-preparation (fixation, paraffination) or during X-PCI-CT acquisitions, may account for the slight discrepancy between literature and measured HD-particle sizes. Since all extracted brains were subject to the same sample-preparation workflow and X-ray irradiation imaging protocols, the comparative analysis of particle size between different animal groups still holds. Actually, 3D tissue virtual analyses (such as the X-PCI-CT-based one applied here), which avoid the lossy traditional histological approach (often leading to partial section analysis and interpolation) hold the promise of more complete and trustworthy neuropathological evaluations compared to more traditional approaches.

5.7.2 SUPPLEMENTARY FIGURES & LEGENDS

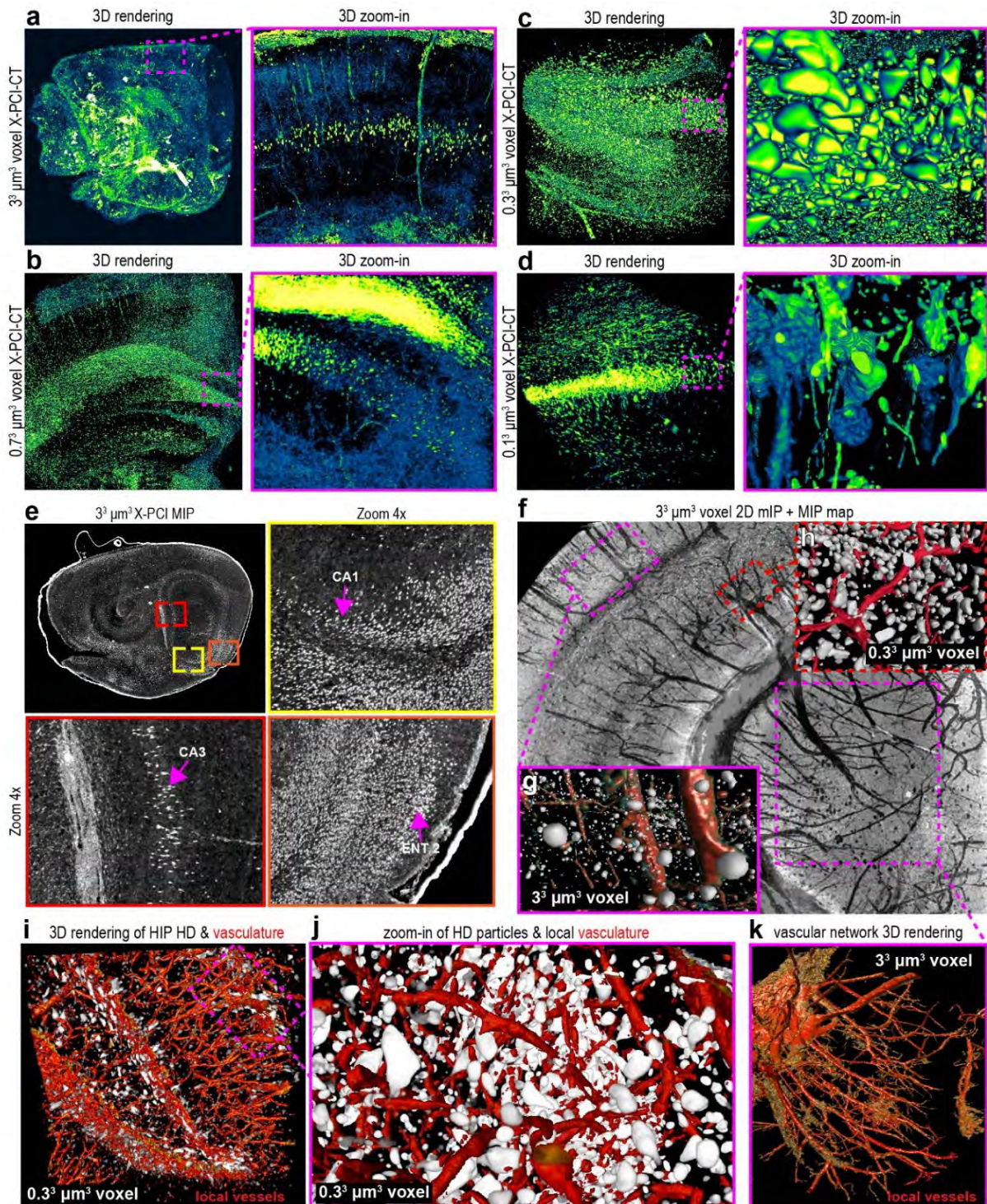


Suppl. Fig. 1 | Extended X-PCI-CT vs. ThioS fluorescence comparison. **a-b**, 0.3³ μm³ voxel X-PCI-CT vs. Thioflavin-S fluorescence (ThioS fluo) of comparable **(a)** CTX and **(b)** HIP cell layers in brain samples extracted from 4-month-old WT and 3xTgAD mice, and from 13-month-old WT and 3xTgAD mice. Patterns of HD-particles and ThioS-positivity are similar. **c**, 0.3³ μm³ voxel X-PCI-CT vs. ThioS and DAPI fluo within comparable CTX, HIP CA and HIP DG cell layers from a 13-month-old 3xTgAD mouse brain. **d-e**, 0.1³ μm³ voxel X-PCI-CT vs. ThioS fluo within comparable **(d)** CTX and **(e)** HIP cell layers from a 13-month-old 3xTgAD mouse brain. In **c-e**, individual ICHD-bearing CTX I to VI neurons, and ICHD-bearing neurons populating CAsp and DGsg layers (magenta arrows)

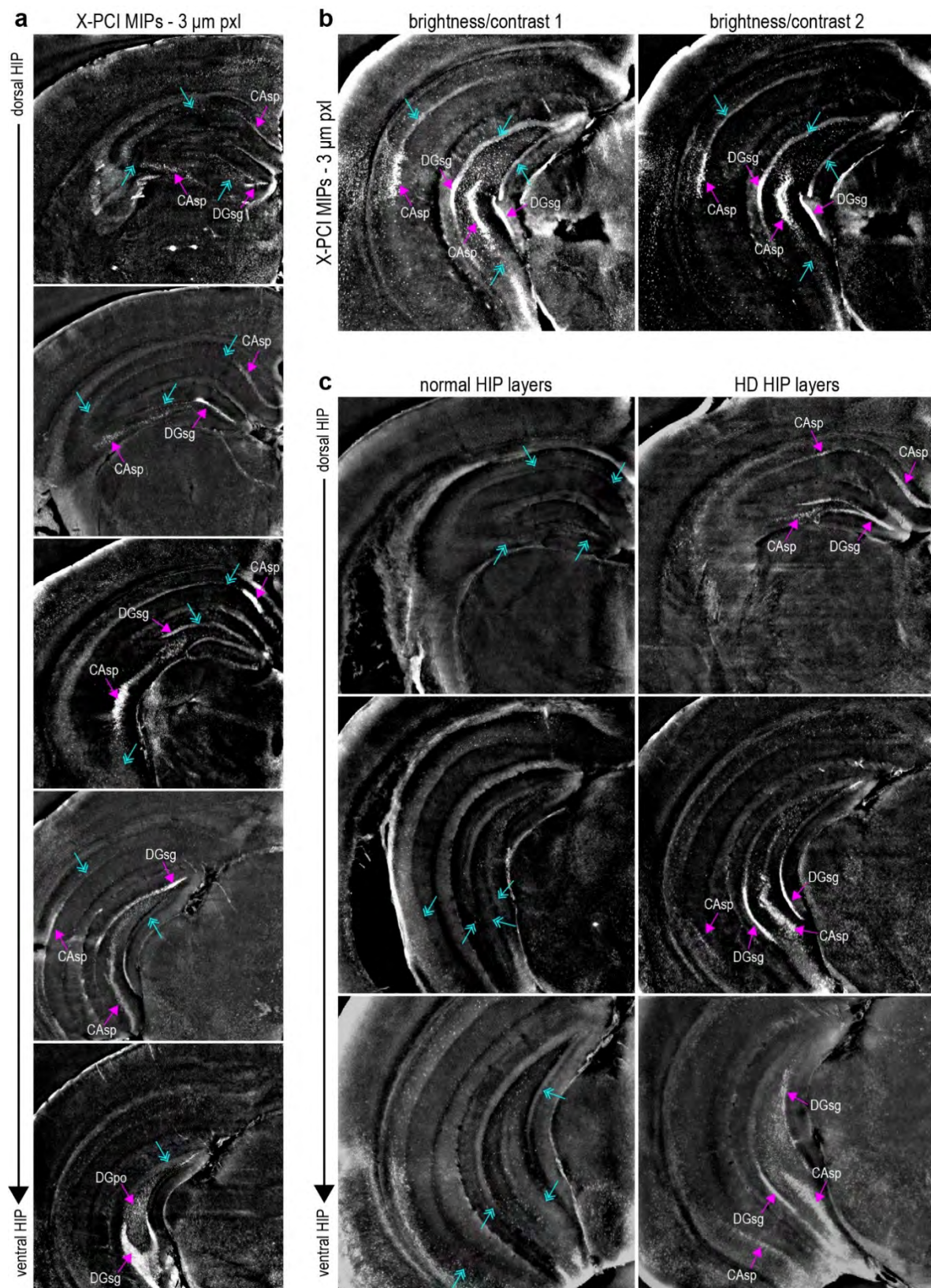
correlate well with ThioS-positive neuron populations, which strongly co-localize with (c) the DAPI nuclear counterstain. Normal hypo-dense neurons correlate well to ThioS-negative cells (azure arrows).



Suppl. Fig. 2 | X-PCI-CT-detected ICHD vs. normal cells. a-b, $0.3^3 \mu\text{m}^3$ voxel X-PCI-CT maps, MIP maps, and 3D renderings of (a) CTX layers within the extracted brain of a 13-month-old WT mouse and of (b) HIP layers within the extracted brain of a 13-month-old 3xTgAD mouse. The presented layers highlight different levels of ICHD abundance (low to high ICHD prevalence over normal low-density neurons). The gray-scale calibration bars specify low-to-high (physical) tissue density. In the 3D renderings, the high gray-levels pertaining to ICHD-bearing cells are recolored as white, lower gray-levels pertaining to normal neuron somas as azure/blue (see Calibration Bar). Magenta and azure arrows point respectively to ICHD-bearing and normal pyramidal neurons.

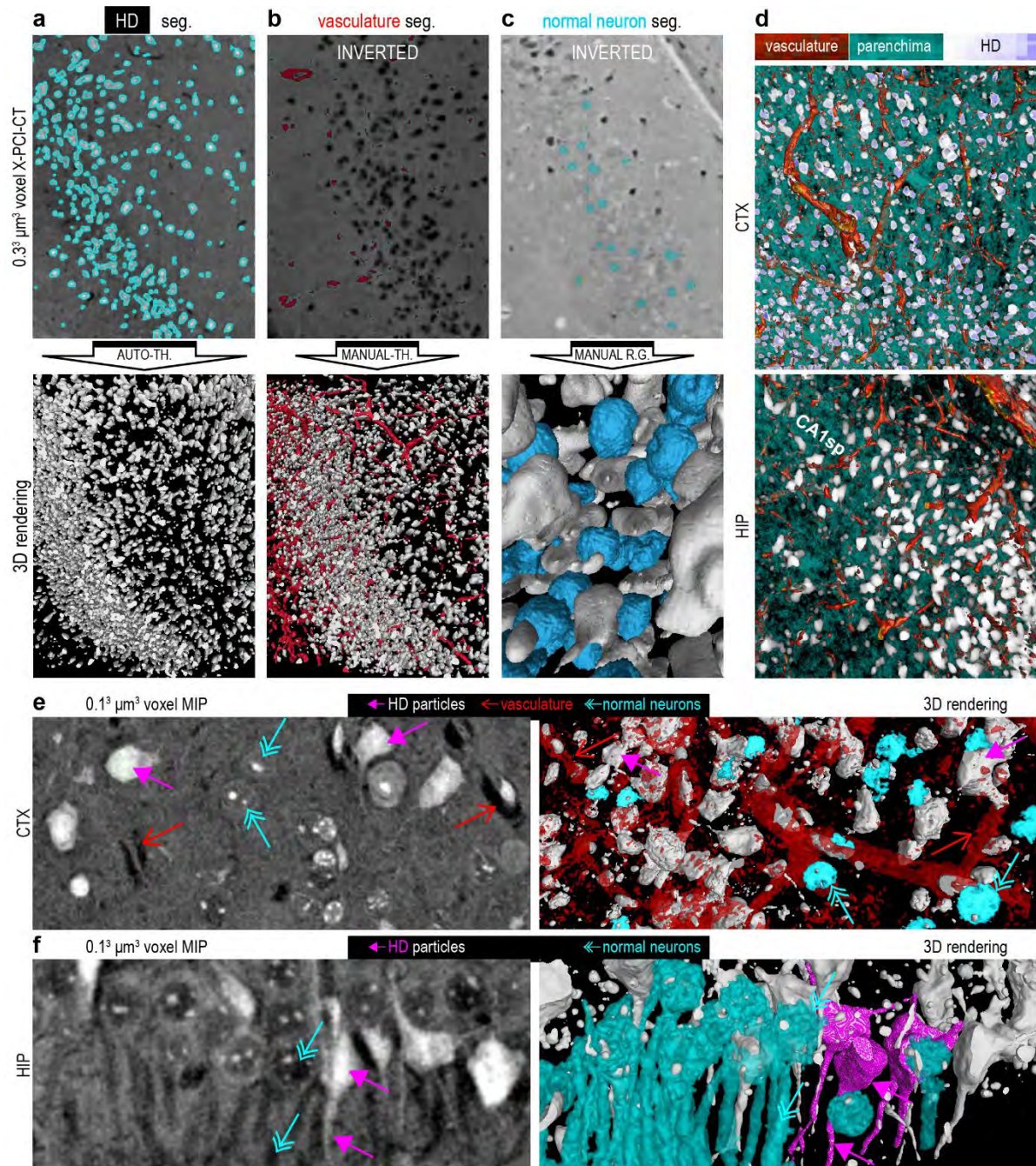


Suppl. Fig. 3 | Multiscale 3D X-PCI-CT. a-d, 3D renderings of (a) $3^3 \mu\text{m}^3$, (b) $0.7^3 \mu\text{m}^3$, (c) $0.3^3 \mu\text{m}^3$ and (d) $0.1^3 \mu\text{m}^3$ voxel X-PCI-CT data, after threshold-based gray-level segmentation and GFB LUT recoloring, showcasing the volumetric morphology of HD-particles at the organ- to intra-cellular level. e, $3^3 \mu\text{m}^3$ voxel sagittal MIP (50 consecutive CT-slices), enhances HD neuronal populations, e.g. within CTX ENT 2, HIP CA1sp and CA3sp layers. f, coronal $0.3^3 \mu\text{m}^3$ voxel MIP + minimum intensity projections (mIP, 200 consecutive CT-slices) highlighting hypodense vasculature development alongside cellular HD deposition within the cerebrum in pseudo-3D. g-k, 3D rendering of HD particles (white) with cell-like morphology, alongside local vasculature (red), in (g, k) $3^3 \mu\text{m}^3$ and (h-j) $0.3^3 \mu\text{m}^3$ voxel X-PCI-CT datasets.



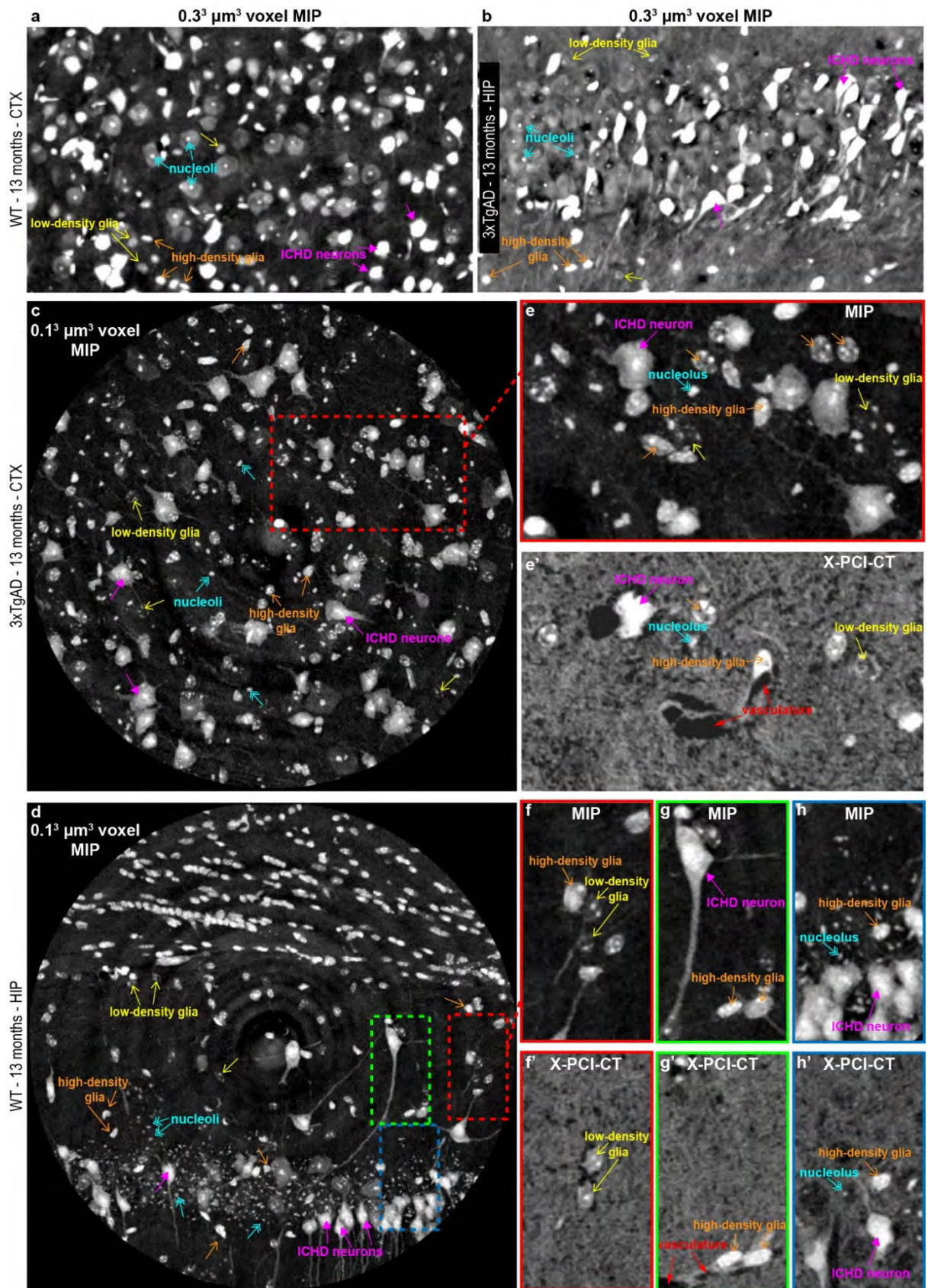
Suppl. Fig. 4 | MIPs of the hippocampal formation highlight HD in CAsp and DGsg. a-c, $3^3 \mu\text{m}^3$ voxel coronal MIPs of the HIP region, collected from several 13-month-old mouse brains. a, dorsal to ventral HIP slices show layer-level HD cell-groups (magenta arrows) in CAsp and DGsg, compared to contiguous less-dense same-layer cell-groups (azure arrows). b, Different choices of gray-level windowing (brightness/contrast 1 vs. 2) increasingly enhance the visualization of local cell-layer HD (magenta arrows) in MIPs, compared to contiguous less-dense

cell-groups (azure arrows). **c**, MIP-slices of HD-bearing HIP CAsp and DGsg cell-layers (magenta arrows), compared to same-level slices, bearing normal CAsp and DGsg cell-layers, that are relatively more HD-free (azure arrows).



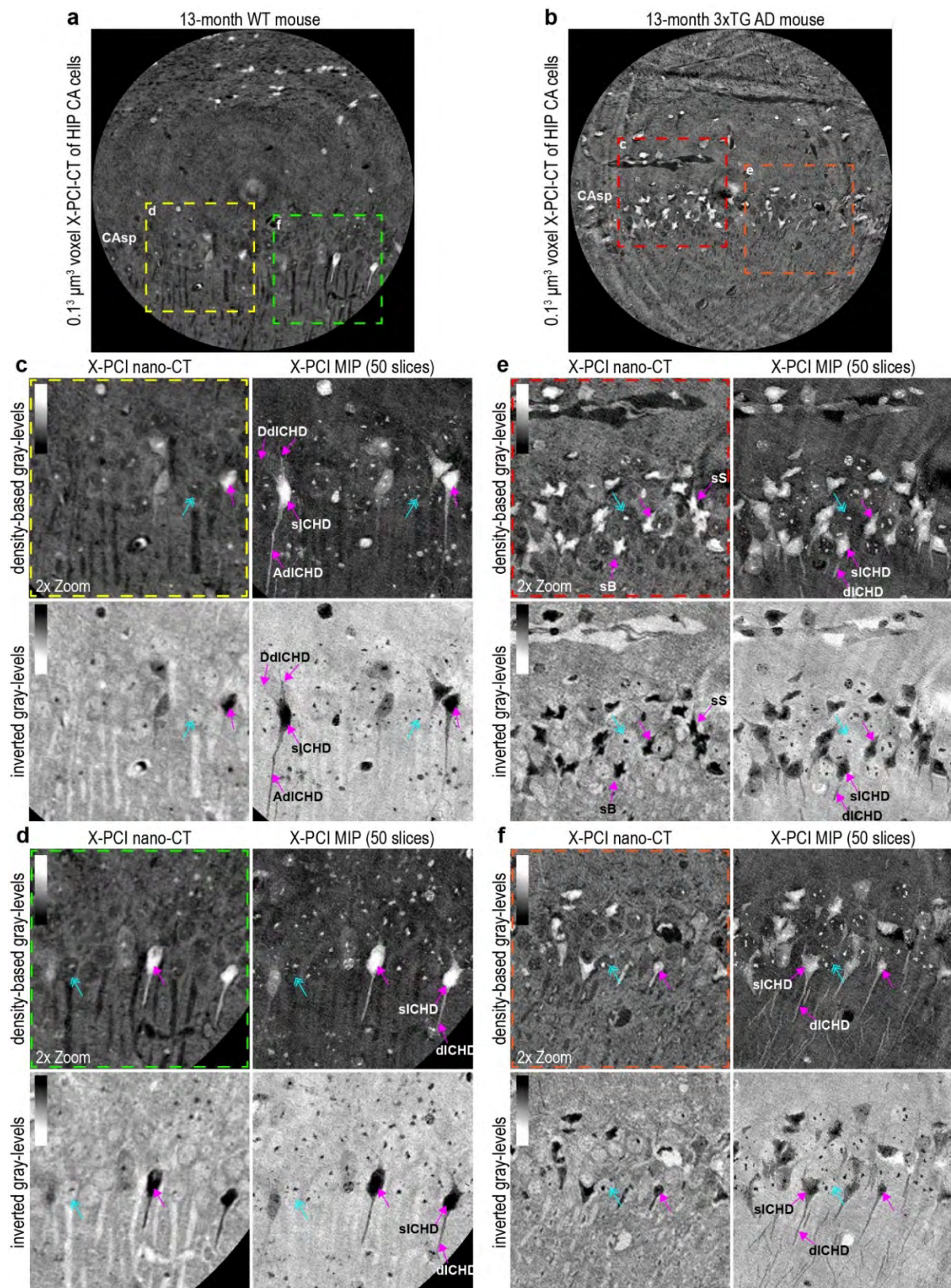
Suppl. Fig. 5 | Segmentation methods for X-PCI-CT-measured neuro-morphology. **a-c**, Representative (a) automated threshold-based (AUTO-TH), (b) manual threshold-based (MANUAL-TH) or (c) manual region-growing (MANUAL R.G.) segmentations (segmentation borders highlighted) obtained from (a) normal- or (b-c) inverted-contrast 0.3³ μm³ voxel X-PCI-CT images pertaining to HIP CA cells. Below the 3D rendering of (a) ICHD-bearing (white in 3D), (b) + vasculature (red in 3D) or (c) + normal cells (azure in 3D), obtained after each type of segmentation. **d**, 3D rendering of 0.3³ μm³ X-PCI-CT data visualizing CTX, HIP CA and HIP DG regions, including individual ICHD-bearing cells alongside local micro-vasculature, obtained after application of the segmentation methodology described in (a-c). High gray-levels pertaining to ICHD-bearing cells are visualized in white/magenta, lower gray-levels pertaining to normal brain parenchyma in azure, and the very low gray-levels pertaining to vascular features in red/yellow (See Calibration Bar). **e-f**, 2D 0.1³ μm³ voxel MIPs vs. 3D renderings

of ICHD-bearing cells (white in **e**, white or magenta in **f**), vasculature (red), and normal cells (azure), within volumes containing CTX or HIP cell-groups, after application of the segmentation methodology described in (**a-c**). Magenta, red and azure arrows point to respectively ICHD-bearing neurons, vasculature and normal neurons. In (**f**), arrows point to the same cells and cellular processes rendered in pseudo-3D (left, MIP map) vs. 3D (right, 3D rendering).



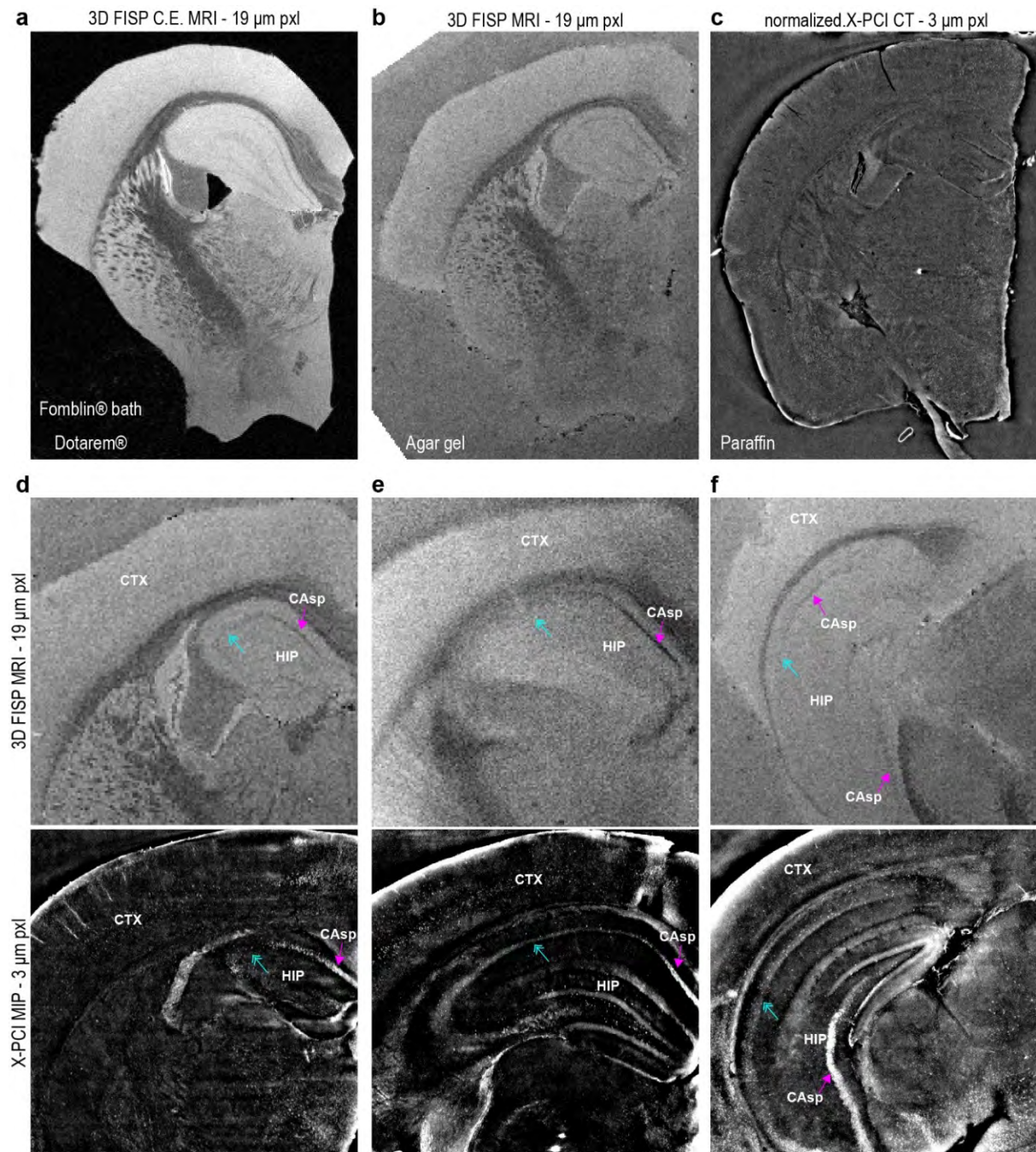
Suppl. Fig. 6 | HD particles represent ICHD-bearing neurons, glia & normal nucleoli. a-d, (a,b) $0.3^3 \mu\text{m}^3$ vs. (c,d) $0.1^3 \mu\text{m}^3$ voxel-size cellular-level X-PCI-CT-based MIP data, showing morphology- and size-based annotations of visible HD particles in (a,c) CTX and (b,d) HIP layers. At least three main differently-sized neuronal and non-neuronal cellular populations are present: (1) strongly ICHD-bearing neurons (largest HD-particles, magenta

arrows); (2) variedly-dense glial cells (intermediate size, yellow and brown arrows); (3) dense nucleoli at the center of smooth-circular hypo-dense nuclei in normal neurons (smallest HD-particles, azure arrows). Differences in both morphology and density within mid-sized non-neuronal cells, likely pertaining to different glial species, are visible: low-density glia presenting hypo-dense somas (yellow arrows, likely astrocytes), compared to higher-density glia presenting signs of abundant nuclear chromatin clumping (brown arrows, likely oligodendrocytes or microglia). **e** vs. **e'**, **f** vs. **f'**, **g** vs. **g'** and **h** vs. **h'** compare respectively MIPs vs. single-slice X-PCI-CTs of zoomed data from (**c-d**), containing HD-particles from all labelled cellular populations described in (**a-d**).



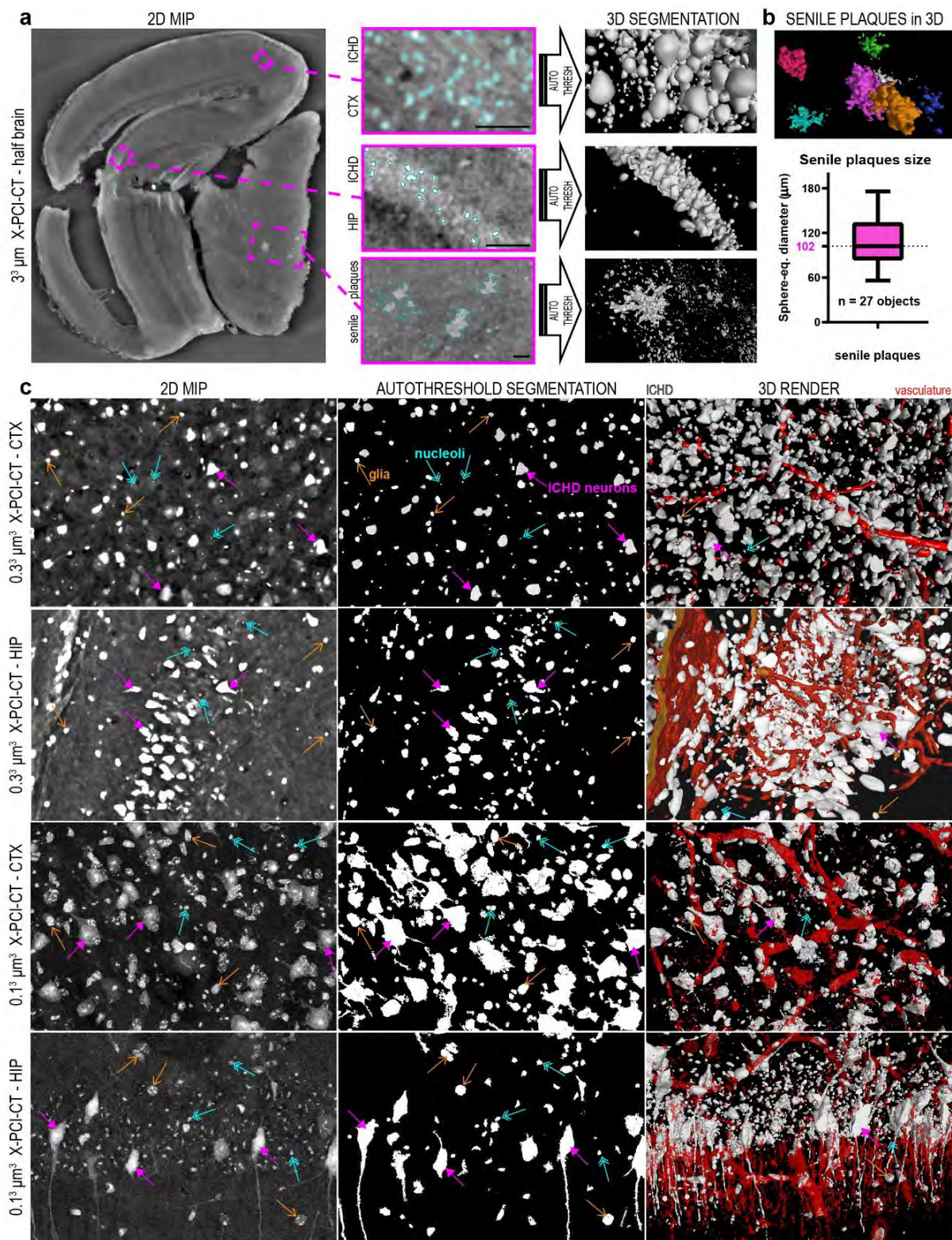
Suppl. Fig. 7 | Intra-cellular nano-anatomy of ICHD-bearing neurons. **a-b**, Label-free 0.1³ μm³ voxel X-PCI-CT visualization of HIP CAsp pyramidal neurons in the brain of **(a)** a 13-month-old WT and **(b)** a 13-month-old 3xTgAD mice. **c-f**, 2x Zooms and MIPs (50 contiguous CT slices) visualize the local intra-cellular nano-anatomy of cells in **(a,b)**. Individual ICHD-bearing neurons (magenta arrows), compared to normal relatively more hypodense cells (azure arrows), are visible in both aged WT and aged 3xTgAD mice. MIPs show rounded cell-body-

like somatic ICHD (sICHD), as well as dendritic/axonal ICHD depositions (dICHD), recognizable as hyper-intense branch-like extensions departing the HD somas. In (c) both axonal dICHD (AdICHD) and dendritic dICHD (DdICHD) are visible. Several ICHD-bearing somas in 3xTgAD samples (e-f) present peculiar pathological cyto-morphology, e.g. signs of cell blebbing (sB) and shrinkage (sS), typical features of cellular neurodegeneration. Inverted gray-level CT slices and MIPs show the same cellular populations, but with inverted feature contrast.



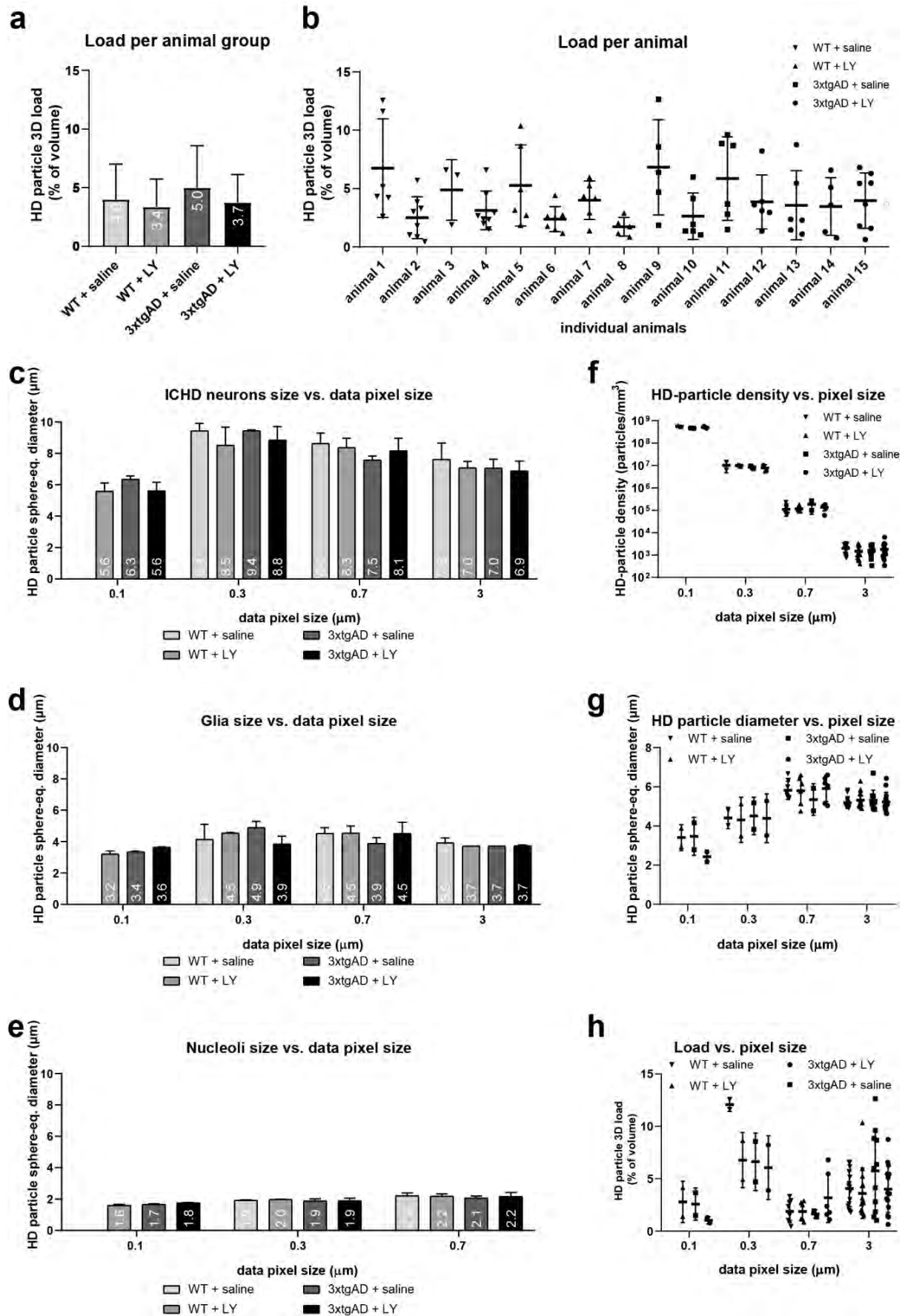
Suppl. Fig. 8 | X-PCI-CT vs. 9.4 T MRI. a-b, Comparative imaging of aged 3xTgAD half-brain samples, using either (a-b) high-field 9.4 Tesla (T) volumetric ($19^3 \mu\text{m}^3$ voxel) MRI, measured after placement of the excised brain sample in either (a) a contrast-enhancing Dotarem® bath (Gadolinium-based MRI contrast agent) and then in an artifact-reducing Fomblin® bath or (b) only within Agarose gel, or (c) $3^3 \mu\text{m}^3$ voxel X-PCI-CT, measured with the excised brain sample embedded in paraffin. d-f, Local dorsal (d) to ventral (f) CTX and HIP zooms of MRI data, measured using the same sequence and sample preparation as in (b), vs. X-PCI-CT MIP data of comparable CTX/HIP layers, measured as in (c). In CTX layers, little sign of aberrant hypo-density is visible at this resolution via MRI, compared to some sparse CTX ICHD visible in X-PCI-based MIPs. In HIP layers, instead, layer-like hypo-

density within cell-groups in the key AD-linked CA₅p layer (magenta arrows), compared to contiguous less-hypo-dense same-layer cells (azure arrows), are visible in the MRI data. Similar patterns of CA₅p layer morphology, featuring layer-like ICHD (magenta arrows), compared to contiguous more-hypo-dense CA₅p layer areas populated by normal pyramidal cells (azure arrows), are visible in the X-PCI-based MIPs.



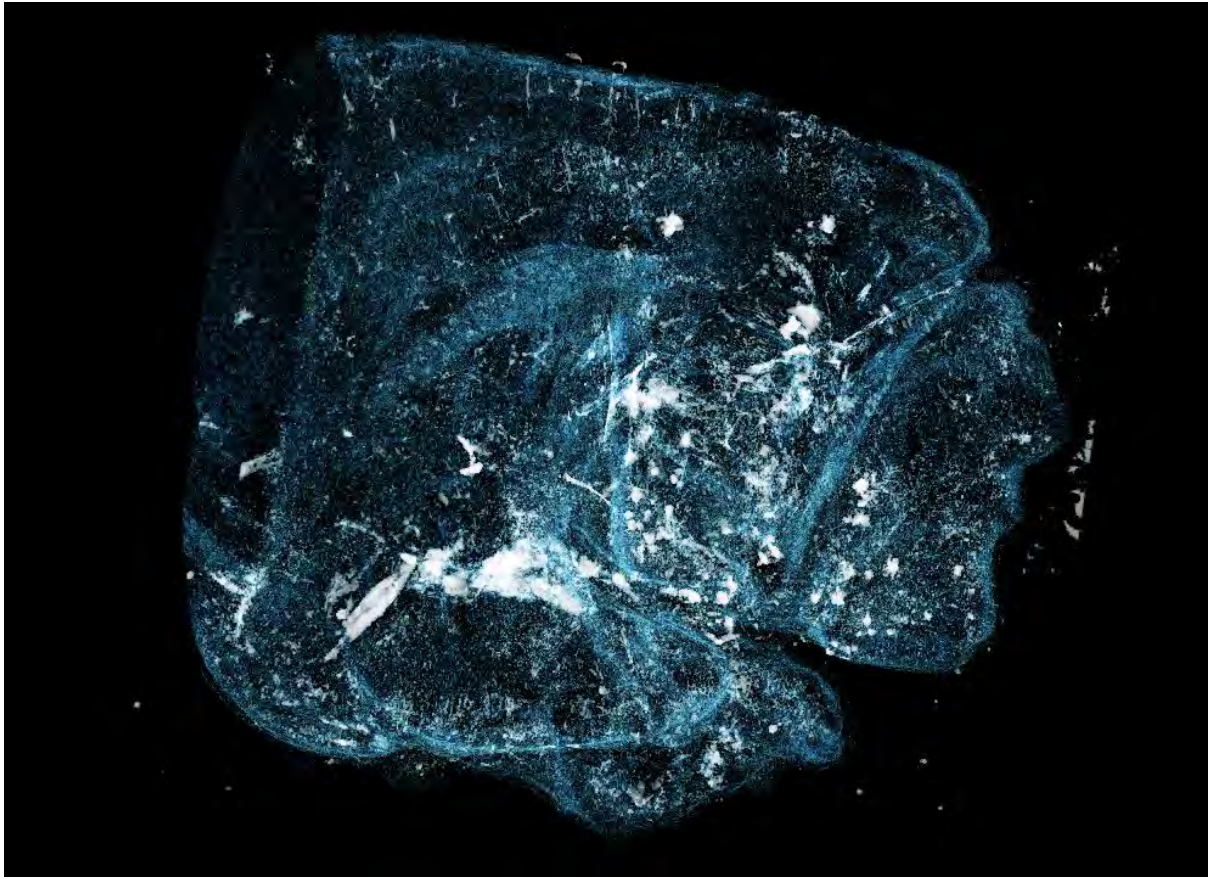
Suppl. Fig. 9 | Segmentation & quantification of plaque-like HD vs. auto-segmentation of ICHD. a, preliminary auto-threshold segmentation of $3^3 \mu\text{m}^3$ voxel X-PCI-CT half-brain data, with extraction of 1. $\sim 10 \mu\text{m}$ -big ICHD with particle-like morphology within CTX and HIP layers, and 2. of macroscopic $\sim 100 \mu\text{m}$ large HD clusters of

plaque-like morphology. Black scale-bars measure 50 μm . **b**, One-off quantification of individual macroscopic plaque-like HD clusters ($n=27$) within three 13-month-old mice, including 1 WT and 2 3xTgAD mice, after manual region-growing segmentation. Data are mean \pm SD. **c**, Representative panels of auto-threshold segmentations and 3D renderings of HD particles within HIP and CTX layers, using $0.3^3 \mu\text{m}^3$ and $0.1^3 \mu\text{m}^3$ voxel X-PCI-CT data and Max-Entropy-based auto-threshold segmentation methodology. 3D renderings visualize HD particles (white) and local hypo-dense vasculature (red), instead extracted with a manual threshold-based segmentation. HD particles pertain to three different cellular populations, (1) larger ICHD-bearing cells (magenta arrows), (2) intermediate-size HD glial cells (brown arrows) and (3) small dense nucleoli in the nucleus of normal hypo-dense neurons (azure arrows).



Suppl. Fig. 10 | More on the proof-of-principle drug-test with the group II metabotropic glutamate receptor agonist LY379268. **a**, group mean HD-particle 3D load (bar-graph shows group mean total HD-particle volume as % of total sample-volume \pm SD) in all four experimental groups, using all extracted sample-volumes independently of tissue area of origin. No significant difference in load between animal groups could be calculated by way of ANOVA testing (test details as in **Fig. 8**). **b**, HD-particle 3D load (graph shows individual sample-volume values and mean total-HD-particle volume % of total sample-volume \pm SD) for each animal used in the study. Note the high load variability within individual animals. **c-e**, comparison of group mean particle size (bar-graphs show group mean HD-particle size \pm SD) for each of the three HD-particle populations, i.e. (**c**) ICHD neurons, (**d**) microglia and (**e**) normal neuron nucleoli, with sample-volumes further subdivided by effective pixel size of the sample data. No significant difference in mean particle size between animal groups, or for different pixel sizes, could be calculated by way of ANOVA testing (test details as in **Fig. 8**). **f-h**, analysis of (**f**) HD-particle density (graph shows individual sample-volume values and mean HD-particle density \pm SD), (**g**) HD particle sizes (equivalent-sphere diameters, data as individual sample-volume values and group mean HD-particle eq.-sphere diameter \pm SD) and (**h**) HD-particle 3D load (graph shows individual sample-volume values and mean total-HD-particle volume % of total sample-volume \pm SD) in the four animal groups, further sub-divided by the effective pixel size of the sample-volume data. Note how smaller imaging-system pixel sizes portray higher densities (**f**), since they detect more, though smaller on average (see (**g**)), HD particles.

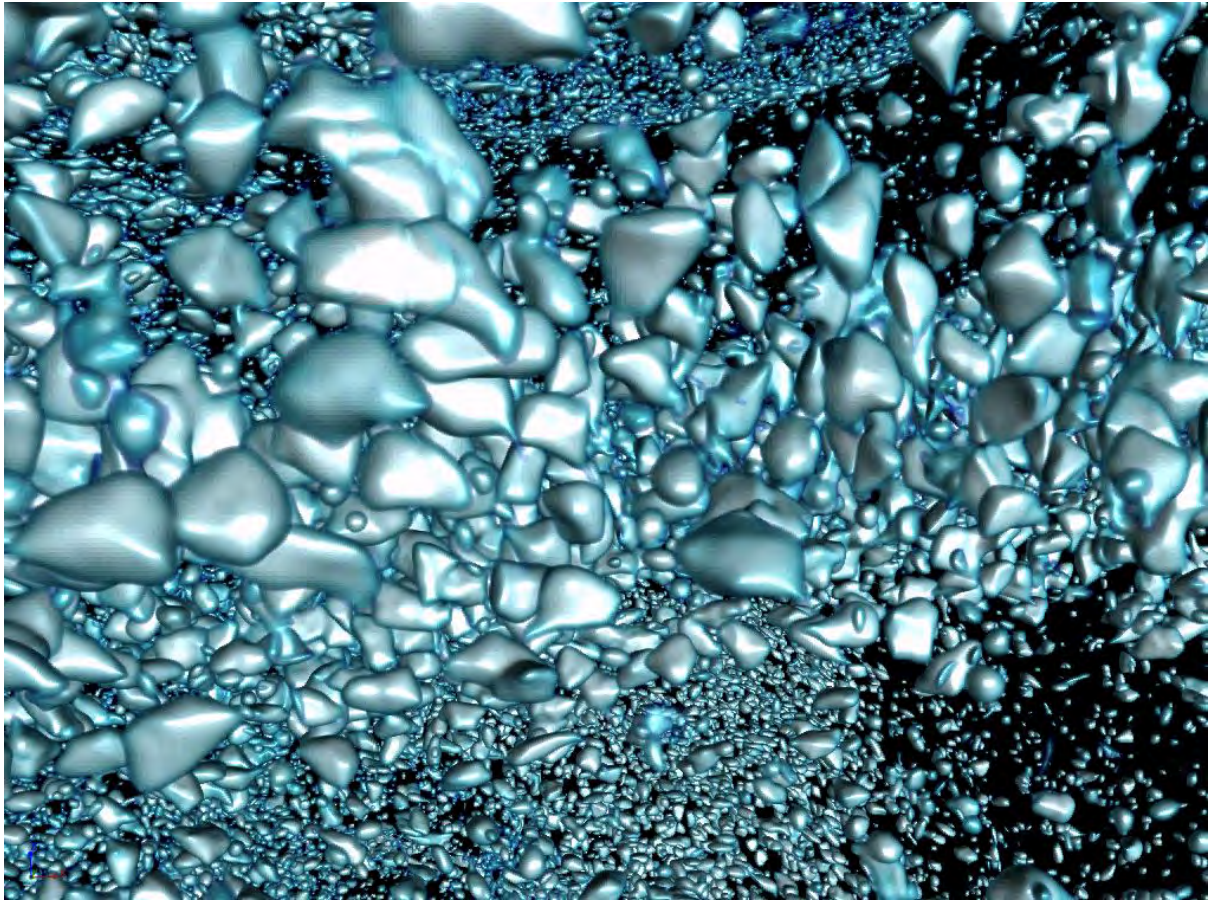
5.7.3 SUPPLEMENTARY VIDEOS



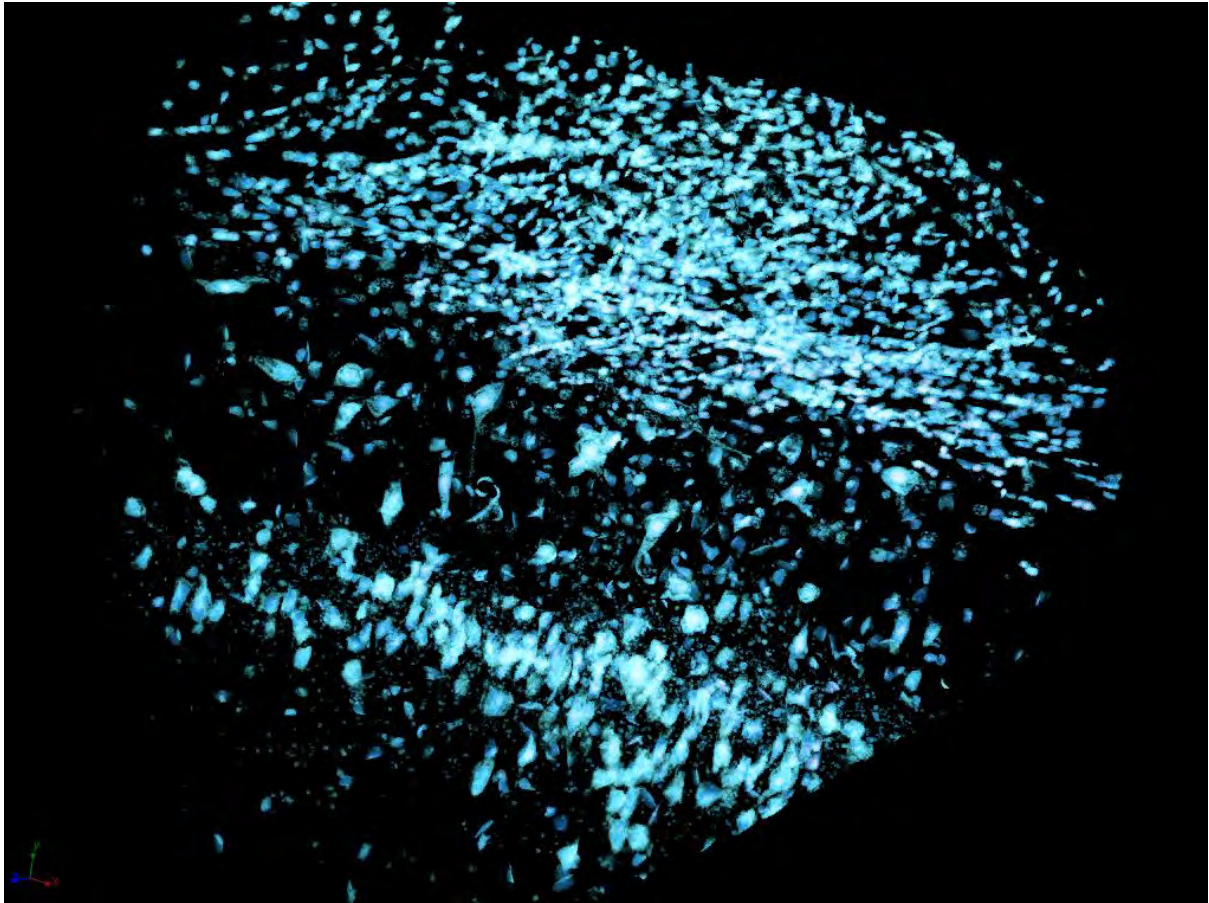
Suppl. Video 1 | 3D rendering of a $3^3 \mu\text{m}^3$ voxel X-PCI-CT dataset from a 13-month-old WT mouse. A half murine brain is visualized.



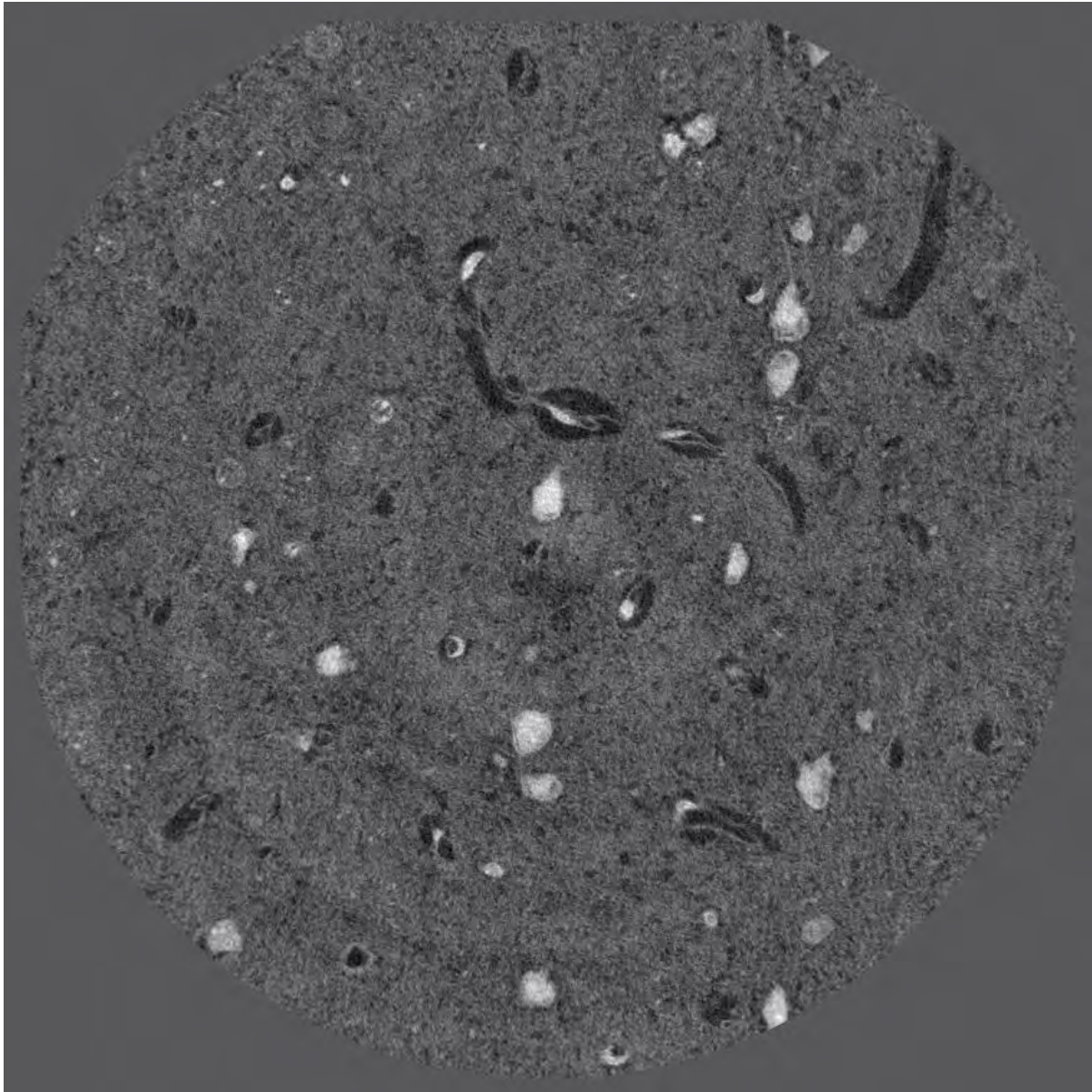
Suppl. Video 2 | 3D rendering of a $0.7^3 \mu\text{m}^3$ voxel X-PCI-CT dataset from a 13-month-old WT mouse. Cortical and hippocampal areas are visualized.



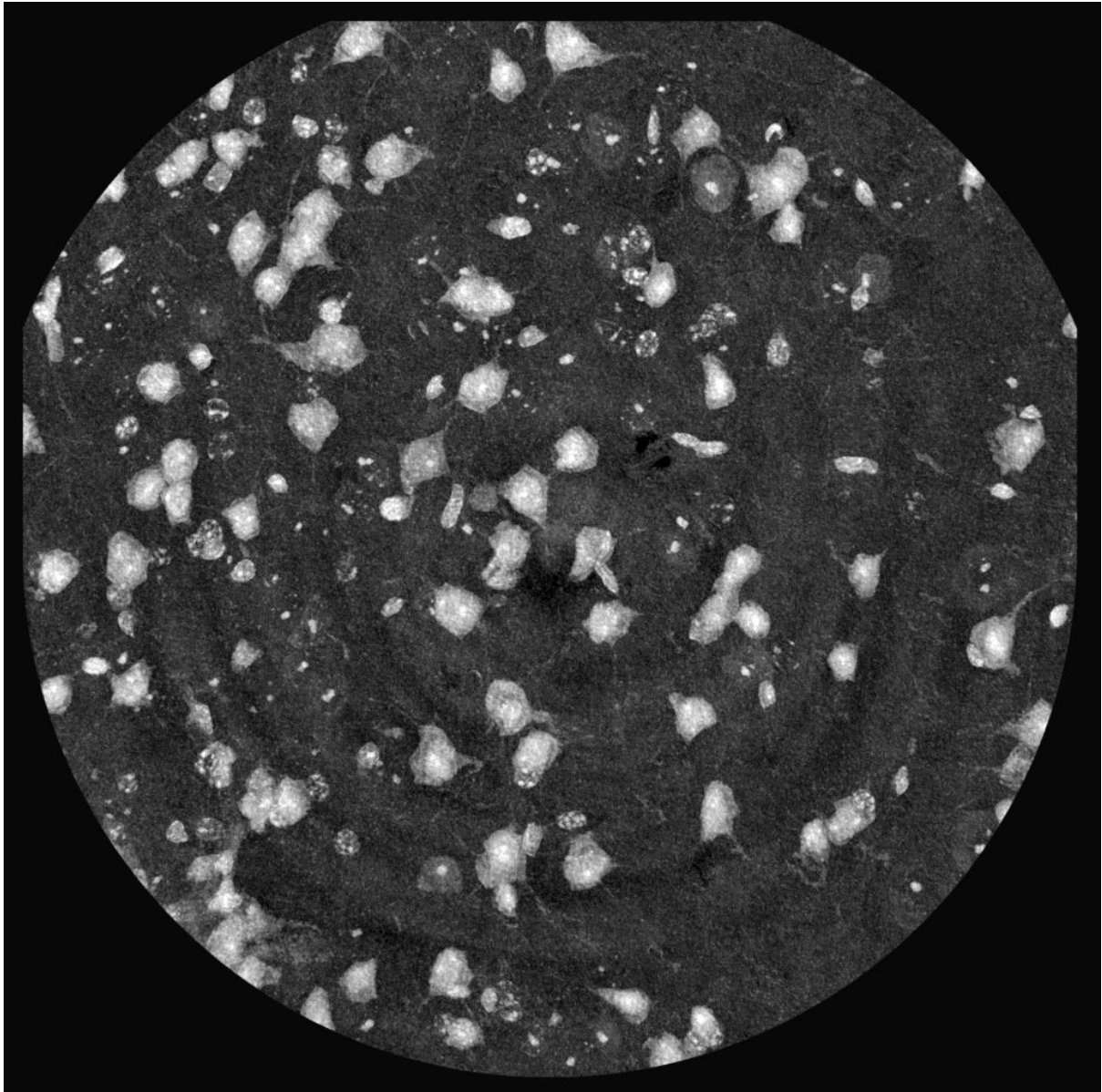
Suppl. Video 3 | 3D rendering of a $0.3^3 \mu\text{m}^3$ voxel X-PCI-CT dataset from a 13-month-old WT mouse. Hippocampal layers are visualized.



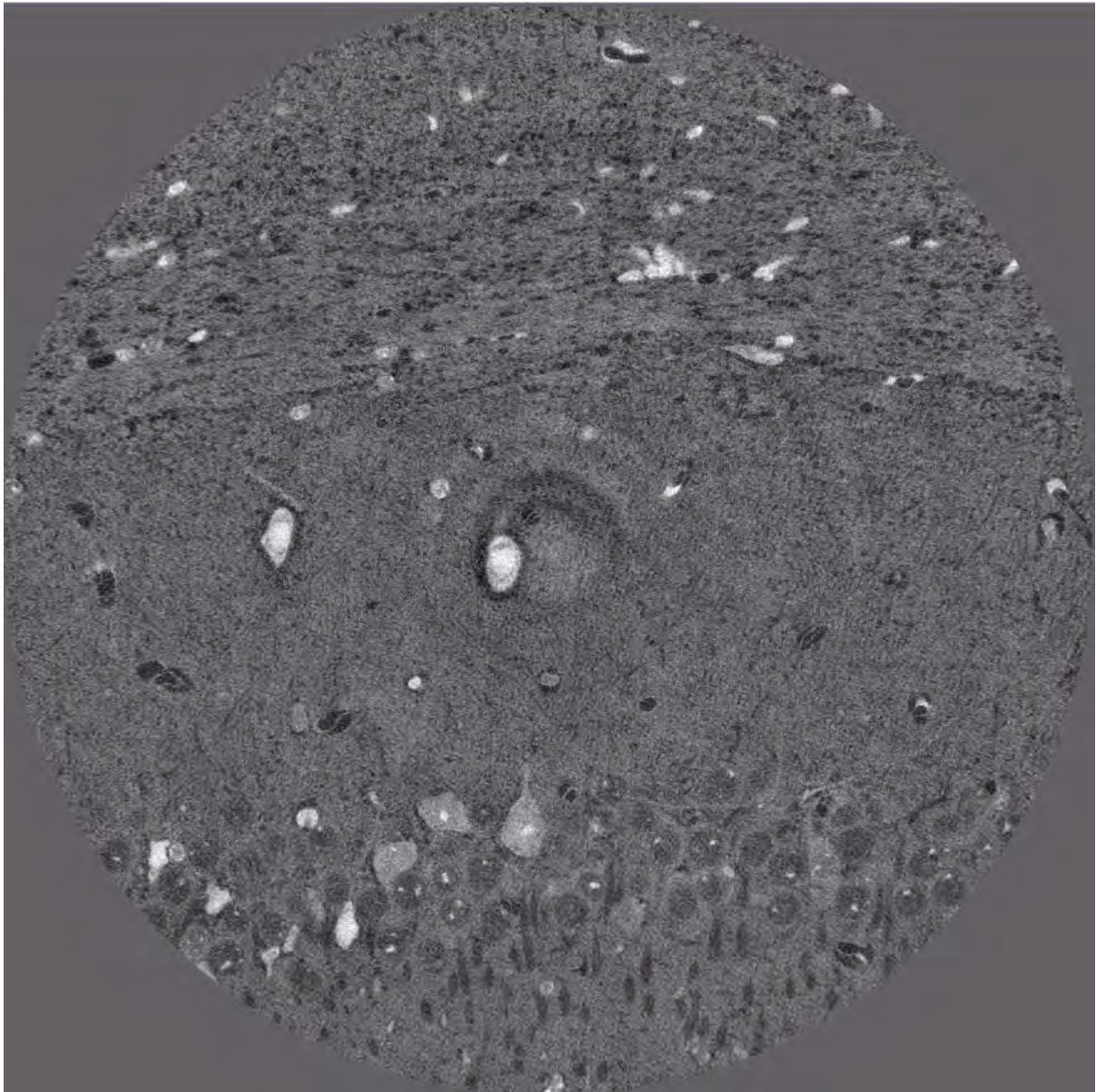
Suppl. Video 4 | 3D rendering of a $0.1^3 \mu\text{m}^3$ voxel X-PCI-CT dataset from a 13-month-old WT mouse. Hippocampal cells are visualized.



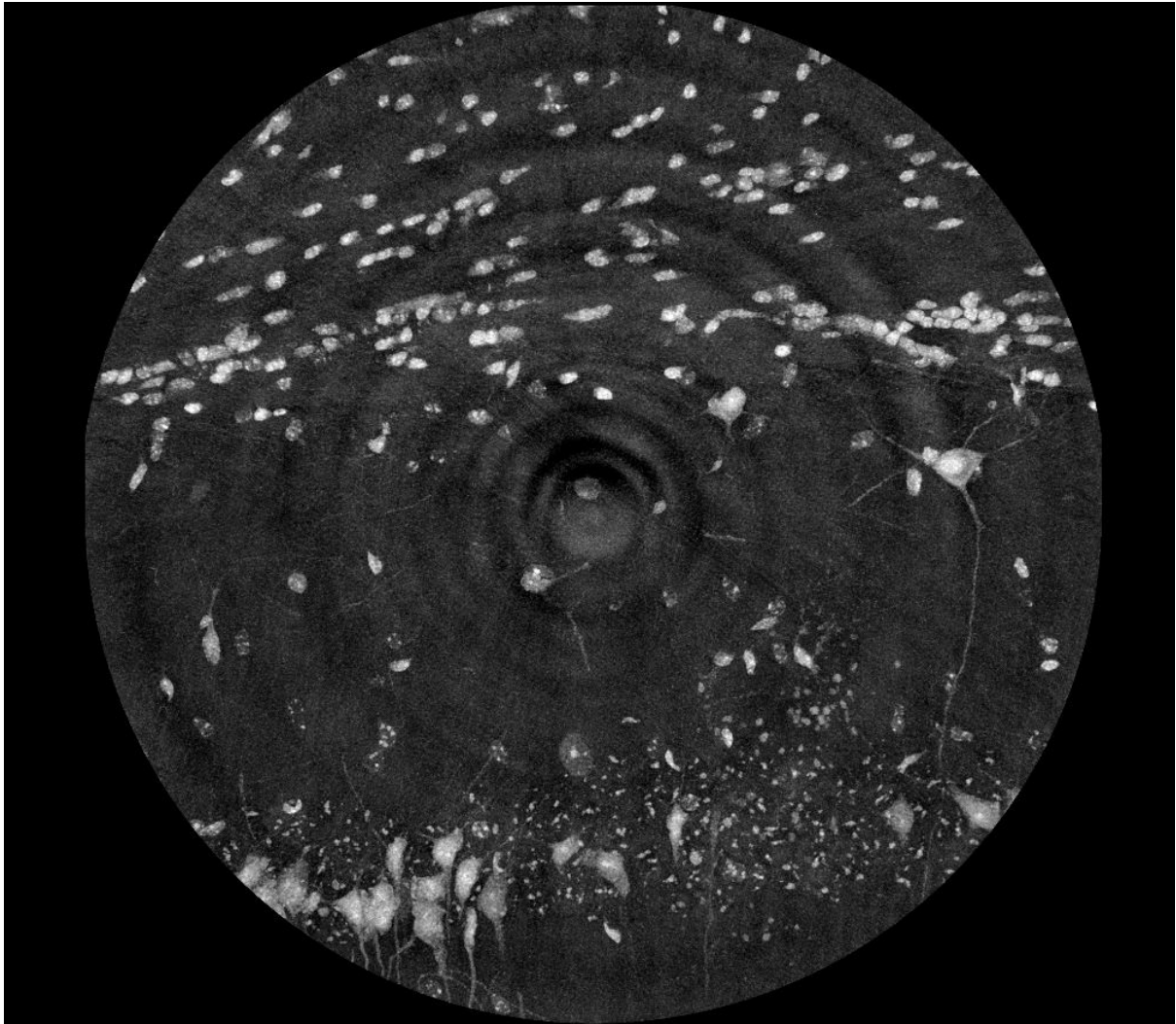
Suppl. Video 5 | CT image stack of a $0.1^3 \mu\text{m}^3$ voxel X-PCI-CT dataset from a 13-month-old 3xtgAD mouse. A dorsal cortical layer is visualized.



Suppl. Video 6 | Stack of consecutive $0.1^3 \mu\text{m}^3$ voxel X-PCI-CT cortical MIPs, computed with the dataset in Suppl. Video 5.



Suppl. Video 7 | CT image stack of a $0.1^3 \mu\text{m}^3$ voxel X-PCI-CT dataset from a 13-month-old WT mouse. A hippocampal CAsp layer is visualized.



Suppl. Video 8 | Stack of consecutive $0.1^3 \mu\text{m}^3$ voxel X-PCI-CT hippocampal MIPs, computed with the dataset in Suppl. Video 7.

REFERENCES:

- Astolfo, A. *et al.* (2016) ‘Amyloid-beta plaque deposition measured using propagation-based X-ray phase contrast CT imaging’, *Journal of Synchrotron Radiation*, 23, pp. 813–819. doi: 10.1107/S1600577516004045.
- Atrophy, N. (2015) ‘Seven-Tesla MRI and neuroimaging biomarkers for Alzheimer’s disease’, 39(November). doi: 10.3171/2015.9.FOCUS15326.
- Barbone, G. E. *et al.* (2018) ‘Micro-imaging of Brain Cancer Radiation Therapy Using Phase-contrast Computed Tomography’, *International Journal of Radiation Oncology Biology Physics*, 101(4), pp. 965–984. doi: 10.1016/j.ijrobp.2018.03.063.
- Bartels, M. *et al.* (2015) ‘Myelinated mouse nerves studied by X-ray phase contrast zoom tomography’, *Journal of Structural Biology*, 192(3), pp. 561–568. doi: <https://doi.org/10.1016/j.jsb.2015.11.001>.
- Beltran, M. a *et al.* (2011) ‘Interface-specific x-ray phase retrieval tomography of complex biological organs’, *Physics in Medicine and Biology*, 56, pp. 7353–7369. doi: 10.1088/0031-9155/56/23/002.
- Benavides-Piccione, R. *et al.* (2005) ‘Dendritic Size of Pyramidal Neurons Differs among Mouse Cortical Regions’, *Cerebral Cortex*, 16(7), pp. 990–1001. doi: 10.1093/cercor/bhj041.
- Bleuet, P. *et al.* (2009) ‘A hard x-ray nanoprobe for scanning and projection nanotomography’, *Review of Scientific Instruments*. American Institute of Physics, 80(5), p. 56101. doi: 10.1063/1.3117489.
- Boche, D. *et al.* (2010) ‘Reduction of aggregated Tau in neuronal processes but not in the cell bodies after A β 42 immunisation in Alzheimer’s disease’, *Acta Neuropathologica*, 120(1), pp. 13–20. doi: 10.1007/s00401-010-0705-y.
- Bolte, S. and Cordelières, F. P. (2006) ‘A guided tour into subcellular colocalization analysis in light microscopy’, *Journal of Microscopy*. John Wiley & Sons, Ltd (10.1111), 224(3), pp. 213–232. doi: 10.1111/j.1365-2818.2006.01706.x.
- Bon, P. *et al.* (2018) ‘Self-interference 3D super-resolution microscopy for deep tissue investigations’, *Nature Methods*. Springer US, 15(June). doi: 10.1038/s41592-018-0005-3.
- Braak, H. and Braak, E. (1991) ‘Neuropathological staging of Alzheimer-related changes’, *Acta Neuropathologica*, 82(4), pp. 239–259. doi: 10.1007/BF00308809.
- Bravin, A., Coan, P. and Suortti, P. (2013) ‘X-ray phase-contrast imaging: from pre-clinical applications towards clinics.’, *Physics in Medicine and Biology*, 58(1), pp. R1–R35. doi: 10.1088/0031-9155/58/1/R1.
- Bruno, V. *et al.* (2001) ‘Metabotropic Glutamate Receptor Subtypes as Targets for Neuroprotective Drugs’, *Journal of Cerebral Blood Flow & Metabolism*. SAGE Publications Ltd STM, 21(9), pp. 1013–1033. doi: 10.1097/00004647-200109000-00001.
- Bruno, V. *et al.* (2017) ‘The impact of metabotropic glutamate receptors into active neurodegenerative processes: A “dark side” in the development of new symptomatic treatments for neurologic and psychiatric disorders’, *Neuropharmacology*, 115, pp. 180–192. doi: <https://doi.org/10.1016/j.neuropharm.2016.04.044>.
- Cammalleri, M., Bagnoli, P. and Bigiani, A. (2019) ‘Molecular and Cellular Mechanisms Underlying Somatostatin-Based Signaling in Two Model Neural Networks, the Retina and the Hippocampus’, *International journal of molecular sciences*. MDPI, 20(10), p. 2506. doi: 10.3390/ijms20102506.
- Caraci, F. *et al.* (2011) ‘Targeting Group II Metabotropic Glutamate (mGlu) Receptors for the Treatment of Psychosis Associated with Alzheimer’s Disease: Selective Activation of mGlu2 Receptors Amplifies β -Amyloid Toxicity in Cultured Neurons, Whereas Dual Activation of mGlu2’, *Molecular Pharmacology*, 79(3), pp. 618 LP – 626. doi: 10.1124/mol.110.067488.

- Castillo-Carranza, D. L. *et al.* (2015) 'Tau Immunotherapy Modulates Both Pathological Tau and Upstream Amyloid Pathology in an Alzheimer's Disease Mouse Model', *The Journal of Neuroscience*, 35(12), pp. 4857 LP – 4868. doi: 10.1523/JNEUROSCI.4989-14.2015.
- Cedola, A. *et al.* (2017) 'X-Ray Phase Contrast Tomography Reveals Early Vascular Alterations and Neuronal Loss in a Multiple Sclerosis Model', *Scientific Reports*, 7(1), p. 5890. doi: 10.1038/s41598-017-06251-7.
- Cloetens, P. *et al.* (1996) 'Phase objects in synchrotron radiation hard x-ray imaging', *J. Phys. D: Appl. Phys.*, 29, pp. 133–146. doi: 10.1088/0022-3727/29/1/023.
- Cloetens, P. *et al.* (1999) 'Holotomography: Quantitative phase tomography with micrometer resolution using hard synchrotron radiation x rays', *Applied Physics Letters*. American Institute of Physics, 75(19), pp. 2912–2914. doi: 10.1063/1.125225.
- Connor, D. M. *et al.* (2009) 'Computed tomography of amyloid plaques in a mouse model of Alzheimer's disease using diffraction enhanced imaging', *NeuroImage*. Elsevier Inc., 46(4), pp. 908–914. doi: 10.1016/j.neuroimage.2009.03.019.
- Davis, B. M. *et al.* (2017) 'Characterizing microglia activation: a spatial statistics approach to maximize information extraction', *Scientific Reports*, 7(1), p. 1576. doi: 10.1038/s41598-017-01747-8.
- Delatour, B. *et al.* (2010) 'In vivo imaging biomarkers in mouse models of Alzheimer's disease: are we lost in translation or breaking through?', *International journal of Alzheimer's disease*. SAGE-Hindawi Access to Research, 2010, p. 604853. doi: 10.4061/2010/604853.
- Dyer, E. L. *et al.* (2017) 'Quantifying Mesoscale Neuroanatomy Using X-ray Microtomography', *eNeuro*, 4(5)(e0195-17.2017). doi: 10.1523/ENEURO.0195-17.2017 1.
- Eberle, A. L. *et al.* (2015) 'High-resolution, high-throughput imaging with a multibeam scanning electron microscope', *Journal of microscopy*. 2015/01/27. John Wiley & Sons, Ltd, 259(2), pp. 114–120. doi: 10.1111/jmi.12224.
- Economou, M. N. *et al.* (2016) 'A platform for brain-wide imaging and reconstruction of individual neurons', *eLife*. Edited by D. D. Ginty. eLife Sciences Publications, Ltd, 5, p. e10566. doi: 10.7554/eLife.10566.
- Farley, K. I. *et al.* (2015) 'Determinants of mammalian nucleolar architecture', *Chromosoma*. 2015/02/12, 124(3), pp. 323–331. doi: 10.1007/s00412-015-0507-z.
- Fitzgerald, R. (2000) 'Phase-Sensitive X-ray Imaging', *Physics Today*, 7(23). doi: 10.1063/1.1292471.
- Flood, D. G. and Coleman, P. D. (1988) 'Neuron numbers and sizes in aging brain: Comparisons of human, monkey, and rodent data', *Neurobiology of Aging*, 9, pp. 453–463. doi: [https://doi.org/10.1016/S0197-4580\(88\)80098-8](https://doi.org/10.1016/S0197-4580(88)80098-8).
- Frost, B., Bardai, F. H. and Feany, M. B. (2016) 'Lamin Dysfunction Mediates Neurodegeneration in Tauopathies', *Current biology : CB*. 2015/12/24, 26(1), pp. 129–136. doi: 10.1016/j.cub.2015.11.039.
- Gramaccioni, C. *et al.* (2020) 'Cryo-nanoimaging of Single Human Macrophage Cells: 3D Structural and Chemical Quantification.', *Analytical Chemistry*. United States, 92(7), pp. 4814–4819. doi: 10.1021/acs.analchem.9b04096.
- Honavar, M. and Lantos, P. L. (1987) 'Ultrastructural changes in the frontal cortex and hippocampus in the ageing marmoset', *Mechanisms of Ageing and Development*, 41(1), pp. 161–175. doi: [https://doi.org/10.1016/0047-6374\(87\)90060-1](https://doi.org/10.1016/0047-6374(87)90060-1).
- Honda, K. *et al.* (2004) 'Oxidative Stress and Redox-Active Iron in Alzheimer's Disease', *Annals of the New York Academy of Sciences*. John Wiley & Sons, Ltd (10.1111), 1012(1), pp. 179–182. doi: 10.1196/annals.1306.015.
- Honson, N. S. *et al.* (2007) 'Differentiating Alzheimer disease-associated aggregates with small molecules', *Neurobiology of disease*. 2007/07/28, 28(3), pp. 251–260. doi: 10.1016/j.nbd.2007.07.018.

- Hussain, R. Z. *et al.* (2017) ‘Laquinimod has no effects on brain volume or cellular CNS composition in the F1 3xTg-AD/C3H mouse model of Alzheimer’s disease’, *Journal of Neuroimmunology*. Elsevier, 309, pp. 100–110. doi: 10.1016/j.jneuroim.2017.05.017.
- Iulita, M. F. *et al.* (2014) ‘Intracellular A β pathology and early cognitive impairments in a transgenic rat overexpressing human amyloid precursor protein: a multidimensional study’, *Acta neuropathologica communications*. BioMed Central, 2, p. 61. doi: 10.1186/2051-5960-2-61.
- Johnson, G. A. *et al.* (2007) ‘High-throughput morphologic phenotyping of the mouse brain with magnetic resonance histology’, *NeuroImage*. Elsevier Inc., 37(1), pp. 82–89. doi: 10.1016/j.neuroimage.2007.05.013.
- Kapur, J. N., Sahoo, P. K. and Wong, A. K. C. (1985) ‘A new method for gray-level picture thresholding using the entropy of the histogram’, *Computer Vision, Graphics, and Image Processing*, 29(3), pp. 273–285. doi: [https://doi.org/10.1016/0734-189X\(85\)90125-2](https://doi.org/10.1016/0734-189X(85)90125-2).
- Khimchenko, A. *et al.* (2018) ‘Hard X-Ray Nanoholotomography: Large-Scale, Label-Free, 3D Neuroimaging beyond Optical Limit’, *Advanced Science*, 5, p. 1700694. doi: 10.1002/advs.201700694.
- Kim, Y. *et al.* (2017) ‘Brain-wide Maps Reveal Stereotyped Cell-Type- Based Cortical Architecture and Subcortical Sexual Dimorphism’, *Cell*, 171, pp. 456–469. doi: 10.1016/j.cell.2017.09.020.
- Komulainen, E. *et al.* (2014) ‘JNK1 controls dendritic field size in L2/3 and L5 of the motor cortex, constrains soma size, and influences fine motor coordination’, *Frontiers in cellular neuroscience*. Frontiers Media S.A., 8, p. 272. doi: 10.3389/fncel.2014.00272.
- Kuchibhotla, K. V *et al.* (2008) ‘A β plaques lead to aberrant regulation of calcium homeostasis in vivo resulting in structural and functional disruption of neuronal networks’, *Neuron*, 59(2), pp. 214–225. doi: 10.1016/j.neuron.2008.06.008.
- Landfield, P. W. *et al.* (1981) ‘Hippocampal aging in rats: A morphometric study of multiple variables in semithin sections’, *Neurobiology of Aging*, 2(4), pp. 265–275. doi: [https://doi.org/10.1016/0197-4580\(81\)90034-8](https://doi.org/10.1016/0197-4580(81)90034-8).
- Landfield, P. W., Baskin, R. K. and Pitler, T. A. (1981) ‘Brain Aging Correlates: Retardation by Hormonal-Pharmacological Treatments’, *Science*. American Association for the Advancement of Science, 214(4520), pp. 581–584. Available at: <http://www.jstor.org.ezp-prod1.hul.harvard.edu/stable/1687317>.
- Lathuilière, A. *et al.* (2016) ‘A subcutaneous cellular implant for passive immunization against amyloid- β reduces brain amyloid and tau pathologies’, *Brain*, 139(5), pp. 1587–1604. doi: 10.1093/brain/aww036.
- Lichtman, J. W. and Denk, W. (2011) ‘The Big and the Small: Challenges of Imaging the Brain’s Circuits’, *Science*, 334(6056), pp. 618 LP – 623. doi: 10.1126/science.1209168.
- Loo, D. T. *et al.* (1993) ‘Apoptosis is induced by beta-amyloid in cultured central nervous system neurons’, *Proceedings of the National Academy of Sciences*, 90(17), pp. 7951 LP – 7955. doi: 10.1073/pnas.90.17.7951.
- Lyckegaard, A., Johnson, G. and Tafforeau, P. (2011) ‘Correction of ring artifacts in X-ray tomographic images’, *International Journal of Tomography and Statistics*, 18(F11), pp. 1–9.
- Mader, K. *et al.* (2011) ‘High-throughput full-automatic synchrotron-based tomographic microscopy’, *Journal of synchrotron radiation*. 2011/01/20. International Union of Crystallography, 18(Pt 2), pp. 117–124. doi: 10.1107/S0909049510047370.
- Massimi, L. *et al.* (2019) ‘Exploring Alzheimer’s disease mouse brain through X-ray phase contrast tomography: From the cell to the organ’, *NeuroImage*. Elsevier Ltd, 184, pp. 490–495. doi: 10.1016/j.neuroimage.2018.09.044.
- Masuda, T. *et al.* (2019) ‘Spatial and temporal heterogeneity of mouse and human microglia at single-cell resolution’, *Nature*, 566(7744), pp. 388–392. doi: 10.1038/s41586-019-0924-x.

- Mattson, M. P. (2007) 'Calcium and neurodegeneration', *Aging Cell*. John Wiley & Sons, Ltd (10.1111), 6(3), pp. 337–350. doi: 10.1111/j.1474-9726.2007.00275.x.
- McLachlan, G. and Peel, D. (2000) *Finite Mixture Models*. John Wiley & Sons, Inc. doi: 10.1002/0471721182.
- Meadowcroft, M. D. *et al.* (2009) 'MRI and histological analysis of beta-amyloid plaques in both human Alzheimer's disease and APP/PS1 transgenic mice', *Journal of magnetic resonance imaging : JMRI*, 29(5), pp. 997–1007. doi: 10.1002/jmri.21731.
- Mikula, S. and Denk, W. (2015) 'High-resolution whole-brain staining for electron microscopic circuit reconstruction', *Nature Methods*. Nature Publishing Group, a division of Macmillan Publishers Limited. All Rights Reserved., 12, p. 541. Available at: <https://doi.org/10.1038/nmeth.3361>.
- Mirone, A. *et al.* (2014) 'The PyHST2 hybrid distributed code for high speed tomographic reconstruction with iterative reconstruction and a priori knowledge capabilities', *Nuclear Instruments and Methods in Physics Research Section B*, 324, pp. 41–48. doi: <https://doi.org/10.1016/j.nimb.2013.09.030>.
- Mittone, A. *et al.* (2017) 'Characterization of a sCMOS-based high-resolution imaging system', *Journal of Synchrotron Radiation*, 24(6), pp. 1226–1236. doi: 10.1107/S160057751701222X.
- Moffitt, J. R. *et al.* (2018) 'Molecular, spatial, and functional single-cell profiling of the hypothalamic preoptic region', *Science*, 362(6416), p. eaau5324. doi: 10.1126/science.aau5324.
- Mokso, R. *et al.* (2007) 'Nanoscale zoom tomography with hard x rays using Kirkpatrick-Baez optics', *Appl. Phys. Lett.*, 90, p. 144104. doi: 10.1063/1.2719653.
- Murakami, T. C. *et al.* (2018) 'A three-dimensional single-cell-resolution whole-brain atlas using CUBIC-X expansion microscopy and tissue clearing', *Nature Neuroscience*, 21(4), pp. 625–637. doi: 10.1038/s41593-018-0109-1.
- Musiek, E. S. and Holtzman, D. M. (2015) 'Three dimensions of the amyloid hypothesis : time , space and “ wingmen ”', *Nature Neuroscience*, 18(6), pp. 800–806. doi: 10.1038/nn.4018.
- Noda-Saita, K. *et al.* (2006) 'Quantitative analysis of amyloid plaques in a mouse model of Alzheimer's disease by phase-contrast X-ray computed tomography', *Neuroscience*, 138(4), pp. 1205–1213. doi: 10.1016/j.neuroscience.2005.12.036.
- Nordberg, A. *et al.* (2010) 'The use of PET in Alzheimer disease', *Nature Reviews Neurology*, 6(2), pp. 78–87. doi: 10.1038/nrneurol.2009.217.
- Nunomura, A. *et al.* (1999) 'RNA Oxidation Is a Prominent Feature of Vulnerable Neurons in Alzheimer's Disease', *The Journal of Neuroscience*, 19(6), pp. 1959 LP – 1964. doi: 10.1523/JNEUROSCI.19-06-01959.1999.
- Oddo, S., Caccamo, A., Kitazawa, M., *et al.* (2003) 'Amyloid deposition precedes tangle formation in a triple transgenic model of Alzheimer ' s disease', *Neurobiology of Aging*, 24, pp. 1063–1070. doi: 10.1016/j.neurobiolaging.2003.08.012.
- Oddo, S., Caccamo, A., Shepherd, J. D., *et al.* (2003) 'Triple-Transgenic Model of Alzheimer ' s Disease with Plaques and Tangles : Intracellular A β and Synaptic Dysfunction', *Neuron*, 39, pp. 409–421.
- Okamura, N. *et al.* (2016) 'Advances in the development of tau PET radiotracers and their clinical applications', *Ageing Research Reviews*, 30, pp. 107–113. doi: <https://doi.org/10.1016/j.arr.2015.12.010>.
- Ortega, R. *et al.* (2007) 'Iron storage within dopamine neurovesicles revealed by chemical nano-imaging', *PLoS one*. Public Library of Science, 2(9), pp. e925–e925. doi: 10.1371/journal.pone.0000925.
- Pacureanu, A. *et al.* (2018) 'Nanoscale three-dimensional imaging of biological tissue with x-ray holographic tomography', in *Proceedings of the SPIE*, p. 107112B. doi: 10.1117/12.2319477.
- Paganin, D. *et al.* (2002) 'Simultaneous phase and amplitude extraction from a single defocused image of a

- homogeneous object', *Journal of Microscopy*, 206(1), pp. 33–40. doi: 10.1046/j.1365-2818.2002.01010.x.
- Pan, C. *et al.* (2016) 'Shrinkage-mediated imaging of entire organs and organisms using uDISCO', *Nature Methods*, 13, pp. 859–867. doi: 10.1038/nmeth.3964.
- Paxinos, G. and Franklin, K. B. J. (2001) *Paxinos and Franklin's The mouse brain in stereotaxic coordinates*. 2nd ed. San Diego: Academic Press.
- Pfeiffer, F. *et al.* (2007) 'High-resolution brain tumor visualization using three-dimensional x-ray phase contrast tomography', *Physics in Medicine and Biology*, 52(23), pp. 6923–6930. doi: 10.1088/0031-9155/52/23/010.
- Pinton, P. *et al.* (2008) 'Ca²⁺ Signaling, Mitochondria and Cell Death', *Current Molecular Medicine*, 8(119). doi: 10.2174/156652408783769571.
- Pinzer, B. R. *et al.* (2012) 'Imaging brain amyloid deposition using grating-based differential phase contrast tomography', *NeuroImage*. Elsevier Inc., 61(4), pp. 1336–1346. doi: 10.1016/j.neuroimage.2012.03.029.
- Que, E. L. *et al.* (2014) 'Quantitative mapping of zinc fluxes in the mammalian egg reveals the origin of fertilization-induced zinc sparks', *Nature Chemistry*. Nature Publishing Group, 7, p. 130. Available at: <https://doi.org/10.1038/nchem.2133>.
- Rauch, J. N., Olson, S. H. and Gestwicki, J. E. (2017) 'Interactions between Microtubule-Associated Protein Tau (MAPT) and Small Molecules', *Cold Spring Harbor perspectives in medicine*, 7(7), p. a024034. doi: 10.1101/cshperspect.a024034.
- Rosenberg, R. N., Fu, M. and Lambracht-Washington, D. (2018) 'Active full-length DNA A β (42) immunization in 3xTg-AD mice reduces not only amyloid deposition but also tau pathology', *Alzheimer's research & therapy*. BioMed Central, 10(1), p. 115. doi: 10.1186/s13195-018-0441-4.
- De Samber, B. *et al.* (2018) 'Nanoscope X-ray fluorescence imaging and quantification of intracellular key-elements in cryofrozen Friedreich's ataxia fibroblasts', *PLOS ONE*. Public Library of Science, 13(1), p. e0190495. Available at: <https://doi.org/10.1371/journal.pone.0190495>.
- Sanchez-Cano, C. *et al.* (2017) 'Synchrotron X-Ray Fluorescence Nanoprobe Reveals Target Sites for Organo-Osmium Complex in Human Ovarian Cancer Cells', *Chemistry (Weinheim an der Bergstrasse, Germany)*. 2017/01/26. John Wiley and Sons Inc., 23(11), pp. 2512–2516. doi: 10.1002/chem.201605911.
- Schneider, C. A., Rasband, W. S. and Eliceiri, K. W. (2012) 'NIH Image to ImageJ: 25 years of image analysis', *Nature methods*, 9(7), pp. 671–675. Available at: <https://www.ncbi.nlm.nih.gov/pubmed/22930834>.
- Selkoe, D. J. (2011) 'Resolving controversies on the path to Alzheimer's therapeutics', *Nature Medicine*, 17(9). doi: 10.1038/nm.2460.
- Da Silva, J. C. *et al.* (2017) 'Efficient concentration of high-energy x-rays for diffraction-limited imaging resolution', *Optica*, 4(5), pp. 492–495.
- Singleton, M. K. *et al.* (2011) 'MeCP2 is required for global heterochromatic and nucleolar changes during activity-dependent neuronal maturation', *Neurobiology of disease*. 2011/03/21, 43(1), pp. 190–200. doi: 10.1016/j.nbd.2011.03.011.
- Smith, M. A. *et al.* (1997) 'Iron accumulation in Alzheimer disease is a source of redox-generated free radicals', *Proceedings of the National Academy of Sciences*, 94(18), pp. 9866 LP – 9868. doi: 10.1073/pnas.94.18.9866.
- Snigirev, A. *et al.* (1995) 'On the possibilities of x-ray phase contrast microimaging by coherent high-energy synchrotron radiation', *Review of Scientific Instruments*. American Institute of Physics, 66(12), pp. 5486–5492. doi: 10.1063/1.1146073.
- Solé, V. A. *et al.* (2007) 'A multiplatform code for the analysis of energy-dispersive X-ray fluorescence spectra', *Spectrochimica Acta Part B: Atomic Spectroscopy*, 62(1), pp. 63–68. doi: 10.1016/j.sab.2006.12.002.

- Stampanoni, M. *et al.* (2007) 'TOMCAT: A beamline for TOMographic Microscopy and Coherent rAdiology experimenTs', *AIP Conference Proceedings*. American Institute of Physics, 879(1), pp. 848–851. doi: 10.1063/1.2436193.
- Suortti, P. *et al.* (2000) 'Fixed-exit monochromator for computed tomography with synchrotron radiation at energies 18-90keV', *Journal of Synchrotron Radiation*, 7(5), pp. 340–347. doi: 10.1107/S0909049500008384.
- Tafoya, M. A., Madi, S. and Sillerud, L. O. (2017) 'Superparamagnetic nanoparticle-enhanced MRI of Alzheimer's disease plaques and activated microglia in 3X transgenic mouse brains: Contrast optimization', *Journal of Magnetic Resonance Imaging*. John Wiley & Sons, Ltd, 46(2), pp. 574–588. doi: 10.1002/jmri.25563.
- Töpperwien, M. *et al.* (2017) 'Three-dimensional mouse brain cytoarchitecture revealed by laboratory-based x-ray phase-contrast tomography', *Scientific Reports*. Nature Publishing Group, 7(42847). doi: 10.1038/srep42847.
- Töpperwien, M. *et al.* (2018) 'Three-dimensional virtual histology of human cerebellum by X-ray phase-contrast tomography', *Proceedings of the National Academy of Sciences*, 115(27), pp. 6940 LP – 6945. doi: 10.1073/pnas.1801678115.
- Töpperwien, M. *et al.* (2020) 'Correlative x-ray phase-contrast tomography and histology of human brain tissue affected by Alzheimer's disease', *NeuroImage*, 210, p. 116523. doi: <https://doi.org/10.1016/j.neuroimage.2020.116523>.
- Ullmann, J. F. P. *et al.* (2012) 'Segmentation of the C57BL/6J mouse cerebellum in magnetic resonance images', *NeuroImage*, 62(3), pp. 1408–1414. doi: <https://doi.org/10.1016/j.neuroimage.2012.05.061>.
- Vallet, P. G. *et al.* (1992) 'A comparative study of histological and immunohistochemical methods for neurofibrillary tangles and senile plaques in Alzheimer's disease', *Acta Neuropathologica*, 83(2), pp. 170–178. doi: 10.1007/BF00308476.
- Vanhoutte, G. *et al.* (2005) 'Noninvasive in vivo MRI detection of neuritic plaques associated with iron in APP[V717I] transgenic mice, a model for Alzheimer's disease', *Magnetic Resonance in Medicine*. Wiley-Blackwell, 53(3), pp. 607–613. doi: 10.1002/mrm.20385.
- Venkataramani, V. *et al.* (2018) 'Enhanced labeling density and whole-cell 3D dSTORM imaging by repetitive labeling of target proteins', *Scientific Reports*, 8(1), p. 5507. doi: 10.1038/s41598-018-23818-0.
- Wang, Y. *et al.* (2017) 'Myosin IIA-related Actomyosin Contractility Mediates Oxidative Stress-induced Neuronal Apoptosis', *Frontiers in Molecular Neuroscience*, p. 75. Available at: <https://www.frontiersin.org/article/10.3389/fnmol.2017.00075>.
- Wei, H. *et al.* (2016) 'Imaging whole-brain cytoarchitecture of mouse with MRI-based quantitative susceptibility mapping', *NeuroImage*. 2016/05/12, 137, pp. 107–115. doi: 10.1016/j.neuroimage.2016.05.033.
- Wyss-Coray, T. (2015) 'Ageing, neurodegeneration and brain rejuvenation', *Nature*, 539(7628), pp. 180–186. doi: 10.1038/nature20411.
- Yankner, B. A., Lu, T. and Loerch, P. (2008) 'The Aging Brain', *Annu. Rev. Pathol. Mech. Dis.*, 3, pp. 41–66. doi: 10.1146/annurev.pathmechdis.2.010506.092044.
- Zabler, S. *et al.* (2005) 'Optimization of phase contrast imaging using hard x rays', *Review of Scientific Instruments*. American Institute of Physics, 76(7), p. 73705. doi: 10.1063/1.1960797.

Chapter 6 – X-PCI-CT of the human spinal cord

High-Spatial-Resolution 3D imaging of human spinal cord and column anatomy by post-mortem X-ray phase-contrast micro-CT

This chapter reports on a first test on the use of synchrotron X-PCI-CT for the 3D virtual imaging of human spinal column samples. It documents the collection of several *post-mortem* CT datasets from spinal cords prepared with two different protocols, i.e. either non-dissected & Thiel-embalmed or dissected and formalin-fixed prior to the imaging experiments. Results are then evaluated in terms of qualitative image quality, and a brief discussion on the prospects of applicability of this approach is presented.

This work was performed in collaboration with Dr. Djonov at the Institute of Anatomy of the University of Bern, who was responsible for the harvesting and fixation of all the human samples involved in the study, with the team of Dr. Bravin at the ID17 beamline of the ESRF, who supported and made possible all the X-PCI-CT measurements in this study, with the team of Dr. Cavaletti at the School of Medicine and Surgery of the University Milano-Bicocca, who provided support in the evaluation and interpretation of the results, and with the team of Dr. Ricke at the LMU Radiology Department. I would like to express my gratitude to all parties involved in this international collaborative study.

A condensed version of this work has been published in 2020 in the journal [Radiology](#), [COPYRIGHT] (2020) as follows:

G.E. Barbone, A. Bravin, A. Mittone, S. Grosu, J. Ricke, G. Cavaletti, V. Djonov, P. Coan. “High-Spatial-Resolution Three-dimensional Imaging of Human Spinal Cord and Column Anatomy with Postmortem X-ray Phase-Contrast Micro-CT”, *Radiology*, Vol. 298, No. 1, pp. 135-146 (2021). <https://doi.org/10.1148/radiol.2020201622>.

This work was also presented orally at the Radiological Society of North America meeting in 2017 (RSNA 2017).

Summary Statement: This work investigates the application of *post-mortem* X-ray phase-contrast micro-CT for the volumetric ultrahigh-resolution imaging and 3D rendering of human cadaveric spinal cord and column samples.

Key Results:

1. Ultrahigh-resolution 3D imaging of the human spinal column based on X-ray phase-contrast micro-CT leads to the concurrent visualization of soft-tissue spinal cord neuroanatomy and vertebral bone structure
2. X-PCI-CT of formalin-fixed boneless cords led to much higher gray- vs. white-matter contrast compared to Thiel-embalmed column samples
3. Within extracted formalin-fixed spinal cord samples, deep microscale cellular and vascular structure can be detected contrast-agent-free and volumetrically

Abbreviations: Central Nervous System (CNS); X-ray Phase-Contrast Computed Tomography (X-PCI-CT); *Post-Mortem* MRI (PMMR); Spinal Cord (SC); Contrast-Enhanced (CE).

6.1 Abstract

Background: Modern high-resolution radiological methods enable increasingly-detailed volumetric *post-mortem* investigations of human neuroanatomy for diagnostic, research and educational purposes.

Purpose: In this designed-experiment study we evaluated *post-mortem* X-ray phase-contrast micro-CT (X-PCI-CT) 3D imaging of the human spinal cord and column as a tissue-conserving candidate for efficient ultrahigh-resolution neuro-radiological work. Specific focus was placed on assessing the detection of micrometric spinal cord soft-tissue structure and vasculature.

Materials and Methods: Three Thiel-embalmed human spinal column samples, unilaterally perfused with Angiofil® vascular contrast-agent, and three extracted formalin-fixed spinal cord samples were imaged *post-mortem* at a synchrotron radiation facility, using a propagation-based X-PCI-CT setup, monochromatic 60 keV X-rays and a detector with either 46 μm or 8 μm pixel sizes. A single-distance phase-retrieval algorithm was applied to the acquired CT projection images in advance of filtered-back projection CT reconstruction. The influence on image quality of Thiel- vs. formalin-embalming was examined, and images were qualitatively evaluated in terms of the value of their anatomical representations.

Results: X-PCI-CT of Thiel-embalmed samples resulted in soft-tissue contrast within the vertebral canal, despite evident nervous tissue deterioration post Thiel-embalming. Gross spinal cord anatomy, spinal meninges, contrast-enhanced spinal vasculature and spinal nerves were all well rendered alongside surrounding vertebral bone structure. On the other hand, X-PCI-CT of formalin-fixed boneless cords led to much higher gray- vs. white-matter contrast, and to the microscale visualization of deep medullary vasculature and gray-matter neuron-soma structure.

Conclusions: This work demonstrates the viability of X-PCI-CT for a detailed volumetric visualization of the anatomy within embalmed human spinal column samples. The main methodological novelty is the concurrent contrast-agent- and label-free 3D display of bone, nervous tissue and vasculature at microscale resolutions. Image quality was shown to strongly depend on sample type and sample preparation.

6.2 Introduction

High-resolution visualization of human neuroanatomy is paramount to a better understanding of human CNS structure, function and disease. Advancements in both *in-vivo* and *post-mortem* neuroimaging can widely impact modern medicine, from diagnostics to public health management, and to research assessing disease etiology (Van Horn and Toga, 2014). Moreover, there is increasing evidence that (neuro-)anatomy education can also be enriched by novel methods for computer-assisted learning (Estai and Bunt, 2016; Javaid *et al.*, 2018), especially by combining traditional cadaveric dissections, cornerstones of anatomical education (Ghosh, 2017; Hu, Wattchow and de Fontgalland, 2018), with modern 3D imaging technology (Sugand, Abrahams and Khurana, 2010; Peterson and Mlynarczyk, 2016).

Using conventional imaging techniques, it remains difficult to analyze large soft-tissue samples collected from human CNS organs in a tissue-conserving way, and especially to render the collected data in 3D for a global volumetric assessment. In fact, currently available approaches struggle to achieve an efficient and detailed imaging of brain and spinal cord soft-tissue that is concurrently sub-10- μm in spatial resolution, volumetric and contrast-agent- and label-free. Histological analyses of the CNS, for example, involve organ dissection (brain removal from the skull and spinal cord removal from the bony spinal canal) followed by tissue-preserving formalin fixation prior to tissue sectioning and sampling. These labor-intensive procedures avoid nervous-tissue maceration, autolysis, and structural demise, but they have evident drawbacks: tissue fixation protocols are long (in the order of several weeks), organ dissections cause sample structural disruption, and tissue sectioning intrinsically involves the physical destruction of the sample into 2D components (traditional histological slices), neglecting large portions of a sample total volume and coming short of a 3D and interactive examination of CNS tissue.

3D, more interactive, less-invasive and less 'lossy' *post-mortem* CNS investigation methods are being actively researched, and this effort is centered around the application of modern tissue-conserving volumetric radiological imaging methods, with *post-mortem* MRI (PMMR) at the forefront (Addison, Arthurs and Thayyil, 2014). Ultrahigh-resolution high-field PMMR, so-called PMMR microscopy, in fact, is particularly suitable for a dissection-free microscale CNS analysis of fixed human specimen, since it allows detailed human organ examinations free from the artifacts arising in histology without risk of tissue damage, and affords dense volumetric virtually-storable data, which can be re-audited, reconstructed and explored in arbitrary planes (Arthurs *et al.*, 2015). Unlike traditional (absorption-based) *post-mortem* CT, which struggles to detect even traumatic spinal cord injuries (Makino *et al.*, 2014), spinal cord

PMMR microscopy can provide exquisite 3D micrometric anatomical visualizations of spinal cords (Lycklama à Nijeholt *et al.*, 2001), up to entire extracted human spines (Calabrese *et al.*, 2018), and can detect and quantify small cord lesions and pathologic circuitry modifications characteristic of spinal cord diseases (Schmierer *et al.*, 2018), such as the axonal loss in the spinal cord typical of multiple sclerosis (Petrova *et al.*, 2018) (more in **Supplementary Introduction**). Still, PMMR microscopy is time-consuming (scan times in the tens of hours for sub- $20^3 \mu\text{m}^3$ voxel datasets) and has spatial-resolution limitations (difficulty in reaching sub- $10^3 \mu\text{m}^3$ voxel measurements) and field-of-view (FoV) constraints (in-plane FoVs up to few cm^2).

A potential candidate for tissue-conserving ultrahigh-resolution (Haddad *et al.*, 1994) 3D imaging of soft tissue alternative to PMMR microscopy may be recognized in *post-mortem* X-ray phase-contrast CT (Fitzgerald, 2000) (X-PCI-CT). Compared to traditional absorption-based CT, this technique exploits the phase shift of X-rays passing through the sample (Momose, 1995), rather than X-ray attenuation, to achieve enhanced image contrast within unstained soft-tissues (Lewis *et al.*, 2003) (more in **Supplementary Introduction**). Compared to PMMR microscopy, X-PCI-CT at synchrotron radiation facilities can be performed faster (scan times in the tens of minutes), can be used to acquire higher spatial resolution data with larger fields-of-view (sub- $10 \mu\text{m}$ pixel measurements with in-plane FoVs of $\sim 10 \text{cm}^2$ are routine). Table-top absorption-based micro-CT (Jorgensen, Demirkaya and Ritman, 1998) and nano-CT (Kampschulte *et al.*, 2016) systems, equipped with X-ray tubes, also efficiently afford sub- $10 \mu\text{m}$ resolution high-contrast imaging of various types of small samples in a laboratory setting, e.g. of mineralized murine bone samples (Kallai *et al.*, 2011), of contrast-perfused vasculature (Marxen *et al.*, 2004), or of murine organ soft-tissue specimens after incubation of the tissue in contrast agent (de Bournonville, Vangrunderbeeck and Kerckhofs, 2019; De Clercq *et al.*, 2019). Synchrotron X-PCI-CT, though, can be applied label- and staining-free for the imaging of much larger (human) soft-tissue samples, and this owing to:

- a. the wide beam available, which affords relatively wide fields-of-view and makes possible the 3D imaging of large objects at ultrahigh resolution.
- b. the high intensity of the synchrotron X-ray beam, which allows short detector integration times and time-efficient measurements,
- c. the high photon energies available (up to 150 keV), which permit penetration within thick bony specimens,
- d. the X-ray light coherence and monochromaticity achievable at synchrotron experimental stations, which enables high sensitivity to weakly-absorbing features within soft-tissues and minimizes beam hardening due to highly dense structures and the scattering component of the signal,

These characteristics make synchrotron X-PCI-CT especially fit for ultrahigh-resolution 3D renderings and analyses of anatomical structure within large human soft-tissue specimens, from which both basic research and human anatomy education could benefit. In fact, X-PCI-CT has already been applied for *post-mortem* visualization of various fixed human organ specimens, including normal (Arfelli *et al.*, 2000; Sztrókay *et al.*, 2012) and tumor-

bearing(Olivo *et al.*, 2009) human breast samples, human carotid artery specimens(Hetterich *et al.*, 2014), mummified human hands(Romell *et al.*, 2018) and human knee joints(Mollenhauer *et al.*, 2002; Majumdar *et al.*, 2004; Horng *et al.*, 2014). Clinical trials for *in-vivo* X-PCI-CT-based mammography with synchrotron radiation have also already been carried out(Castelli *et al.*, 2011).

At the price of reduced fields-of-view, cutting-edge synchrotron setups for X-PCI-CT(Mokso *et al.*, 2007; Mader *et al.*, 2011; Mittone *et al.*, 2017, 2020) can reach sub-micron spatial resolutions (with pixel sizes down to less than 100nm(Khimchenko *et al.*, 2018)), allowing the exploration in this case of (smaller) dissected rodent CNS organ samples without the need for any contrast media or label, an approach which can bridge the gap between light and electron microscopy(Kuan, 2020). These platforms for small-animal *post-mortem* 3D X-ray microscopy work are being used for experimental neuroimaging, e.g. in the study of microscale anatomy and tumor pathology within dissected rodent brains(Barbone *et al.*, 2018), and of microvascular(Cao *et al.*, 2016; Barbone *et al.*, 2020) and cellular structure(Fratini *et al.*, 2015; Hu *et al.*, 2017) within dissected rodent spinal cord specimen, pathological lesions included (Hu *et al.*, 2015; Miao *et al.*, 2016; Cedola *et al.*, 2017), successfully correlating X-PCI-CT results with histological ground truth.

In this study, we investigate the potential of X-PCI-CT as a tool for ultrahigh-resolution 3D anatomical imaging of large human spinal cord and column specimens, notoriously challenging due to the thick and complex bone structures surrounding the spinal cord environment(Stroman *et al.*, 2014). To evaluate the influence of sample embalming on X-PCI-CT-based spinal cord imaging results, we compared the image quality of X-PCI-CT data of non-dissected Thiel-embalmed human spines against X-PCI-CT images of extracted formalin-fixed human cords.

6.3 Materials and Methods

6.3.1 Specimen preparation

This *post-mortem* experimental study on human specimens was approved by the institutional review board, and written informed consent was obtained from all donors. Three non-dissected human spinal column specimens (10 vertebrae each, including bone and nervous tissue) and three dissected human spinal cords (30 cm long, nervous tissue only) were harvested following ethical approval and guidelines (more in **Supplementary Methods**). The non-dissected spinal columns (**Fig. 1a**) underwent Thiel-embalming(Thiel, 1992, 2002; Bangerter *et al.*, 2017), and their left vertebral arteries were injected with Angiofil® (Fumedica AG, Switzerland)(Grabherr *et al.*, 2008). The dissected nervous-tissue-only spinal cords (**Fig. 1b**) were extracted from the spinal canal, together with their meninges and short portions from spinal nerve roots, and formalin-fixed by standard(Waters, 2009) two-week immersion in 10% buffered formalin solution. All specimens were stored for 3 months before imaging.

6.3.2 Propagation-based X-PCI-CT

A diagram of the experimental setup is sketched in **Fig. 1c**. Briefly, measurements were carried out at the biomedical beamline (ID17) of the European Synchrotron Radiation Facility (ESRF). All samples were imaged in a vertical position, immersed in formalin 4% solution within sealed plastic cylindrical containers. CT acquisitions were performed using a quasi-parallel laminar monochromatic 60 keV X-ray beam (7 mm vertical size), and a propagation-based X-PCI-CT setup (Snigirev *et al.*, 1995) including a rotating sample station and a fixed FReLoN CCD detector (Coan *et al.*, 2006). Initial CT scans were performed at a sample-to-detector distance of 11 m and with an optical system affording an isotropic effective CT image voxel size of $46^3 \mu\text{m}^3$ (CT acquisition time ~ 3.5 min) and a resulting FoV of $90 \times 7 \text{ mm}^2$ (H x V). Vertical sample scanning (overall 60 CT acquisitions) permitted the full vertical coverage of the spine specimens (full-specimen acquisition time ~ 3.5 h). Then, $8^3 \mu\text{m}^3$ voxel size CT scans were completed by changing optics-system magnification and by setting the new sample-to-detector distance to 4 m. These CT scans had a smaller FoV ($32 \times 5.6 \text{ mm}^2$ H x V) than the sample lateral dimension, affording only partial sample coverage, aimed at intra-medullary soft-tissue structures with the aid of the already-collected $46^3 \mu\text{m}^3$ voxel data (CT acquisition time ~ 1 hour). Detailed CT scan parameters are provided as **Supplementary Methods**.

6.3.3 Data processing

After normalization of each CT projection against reference-beam images, the so-called Paganin phase retrieval algorithm (Paganin *et al.*, 2002) was applied to projection images to extract phase information. CT reconstruction was then performed using the standard filtered-back projection algorithm. A CT ring artifact correction procedure (Lyckegaard, Johnson and Tafforeau, 2011) was used to remove ring-like structures from all CT data. To remove cupping artifacts, arising due to acquisitions in local tomography, the $8^3 \mu\text{m}^3$ voxel data was further normalized by division against the Gaussian blurred version of the same CT slice (Gaussian sigma: 50 pixels), thereby suppressing the low-frequency image background. The commercial software VG Studio MAX (Volume Graphics GmbH., 2001) was used for volumetric exploration of the reconstructed data, as well as for all 3D renderings. Segmentation and 3D rendering of soft-tissue was achieved via a threshold-based segmentation approach, segmentation/rendering of vascular networks and bone structure via a region-growing approach (Pal and Pal, 1993). 2D maximum intensity projection (MIP) images, which project the brightest pixels within a stack of consecutive CT slices onto a 2D plane, were computed using the software ImageJ (National Institutes of Health, Bethesda, MD).

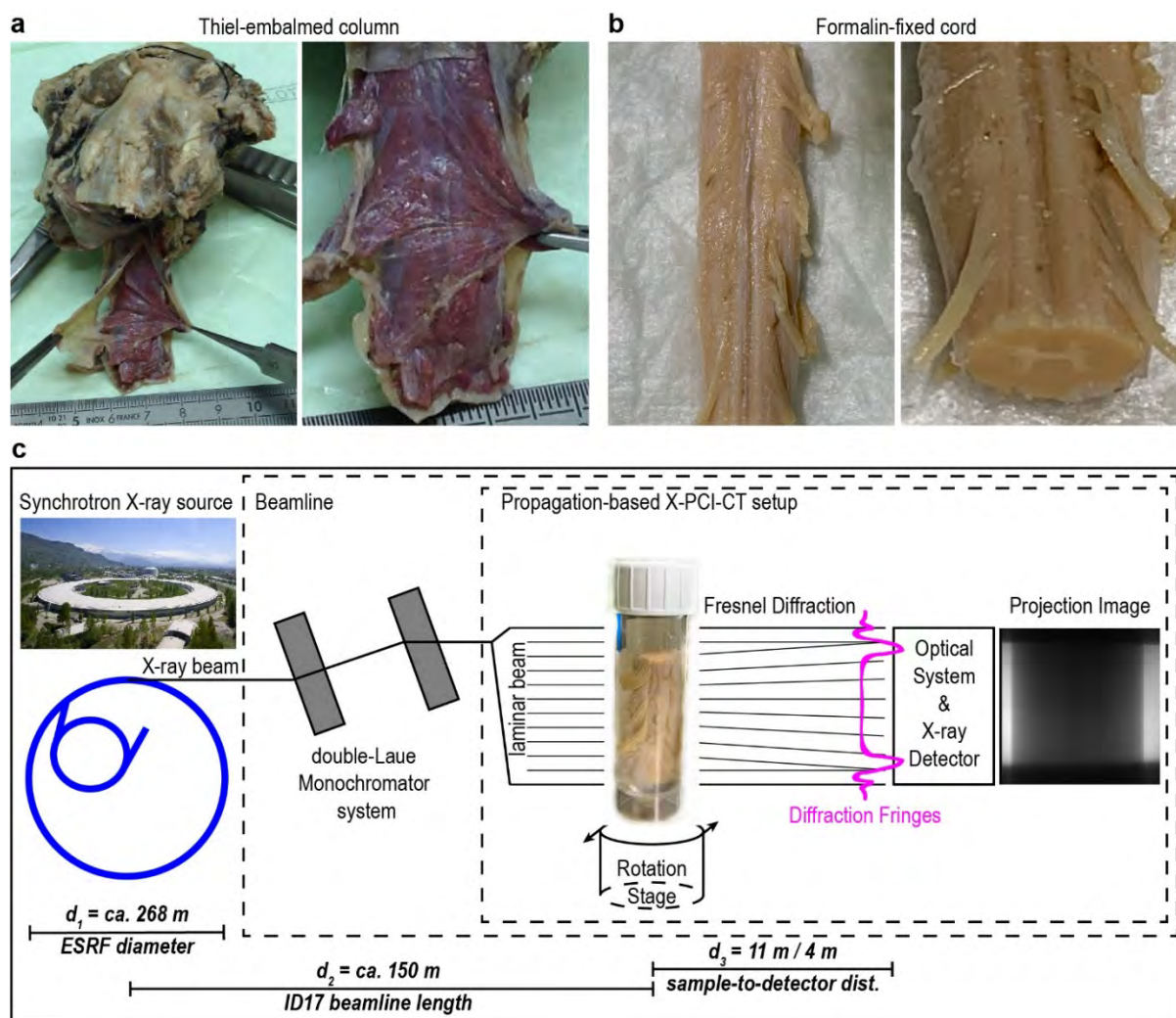


FIGURE 1: (a) Representative photographs of a Thiel-embalmed human spinal column specimen. The specimen was imaged via X-PCI-CT (both with the $46^3 \mu\text{m}^3$ and $8^3 \mu\text{m}^3$ voxel setups) before caudally sawing away part of the bony vertebral structure and removing part of the dura mater, procedures performed post-imaging to inspect cord nervous tissue preservation. Note how the zoomed-in photo shows preserved overall organ shape and spinal meninges, but limited intra-medullary structure. (b) Representative photographs of a formalin-fixed human spinal cord specimen, dissected from its spinal canal before X-PCI-CT (both with the $46^3 \mu\text{m}^3$ and $8^3 \mu\text{m}^3$ voxel setups). Note how the zoomed-in photo shows preserved cord radicular fila and intra-medullary structure - characteristic thoracic cord white funiculi vs. gray column anatomy is visible to the naked eye. (c) Schematic diagram and dimensions of the experimental setup for propagation-based X-PCI-CT at the European Synchrotron – beamline ID17 (photo credit: ESRF/Morel). The setup includes a double-Laue monochromator system, which affords a laminar monochromatic X-ray beam, the sample (here a human spinal cord sample in a cylindrical plastic container) placed on a rotation stage, and an optical system & X-ray detector. In addition to attenuation, the setup exploits the physical mechanisms of X-ray refraction, propagation and Fresnel diffraction to record sample-induced diffraction fringes in each CT projection image. d_3 , the sample-to-detector distance (often called propagation distance) was set to ~ 11 m in the case of $46^3 \mu\text{m}^3$ voxel imaging, to ~ 4 m in the case of $8^3 \mu\text{m}^3$ voxel imaging.

6.4 Results

6.4.1 Thiel-embalmed spinal column imaging

The collected isotropic $46^3 \mu\text{m}^3$ voxel X-PCI-CT data pertaining to Thiel-embalmed human spines (**Fig. 2-4, Supplementary Video 1**) allowed a qualitative evaluation of the suitability of this imaging technique and this embalming procedure for the *post-mortem* 3D visualization of spinal bone- and nervous-tissue anatomy. Propagation-based X-PCI-CT rendered the anatomical borders and internal structures of both spinal bones and spinal nervous tissues (**Fig. 2**), e.g. sharp tissue demarcations between bony vertebral body tissue, vertebral fat tissue and muscle tissues, but also between vertebral disk soft-matter structure, vertebral joint hyaline cartilage, and spinal cord soft-tissue. Much like PMMR data, X-PCI-CT data-volumes could be resliced in arbitrary planes (**Fig. 2a-d**) and explored volumetrically (with the aid of 3D rendering software).

As previously reported (Peyrin *et al.*, 1998; Yu *et al.*, 2020), trabecular architecture within the cancellous tissue of vertebral bodies is clearly visible by X-PCI-CT. Notably, the technique was also able to portray soft-tissue structures within spinal cord meningeal spaces (**Fig. 2e,f**), including all three spinal cord (SC) meninges, the spinal medulla, out-branching ventral & dorsal spinal nerve roots (*Radix anterior/posterior*), and nerve ganglions (*Ganglion sensorium nervi spinalis*) (**Fig. 2c**). Bone structure and Angiofil®-perfused contrast-enhanced (CE) vasculature could be differentiated, as the brightest image voxels, from lower-density soft-matter structures of the SC, such as vertebral disks, cartilage, interspinous ligaments and ligamenta flava, and medullary SC tissue (**Fig. 2**). However, almost no intra-medullary gray-vs. white-matter contrast could be visualized in Thiel-embalmed SC samples (**Fig. 2c**). Therefore, these images seem most fit to display the macroscopic anatomy of mineralized bone, soft-tissue and vasculature within the spinal canal, e.g. to study the progress of spinal nerve roots within bone-surrounded intervertebral foramina before their unification as spinal nerve, or to demonstrate the organization of different meningeal spaces around the spinal cord, e.g. epidural spaces padded by adipose tissue and occupied by their characteristic venous plexus (*Plexus venosi vertebrales interni anterior/posterior*). This combination of sample embalming, sample type and image resolution seems instead inappropriate for the visualization of intra-medullary structure, e.g. intra-cord microvasculature, cellularity and fibers.

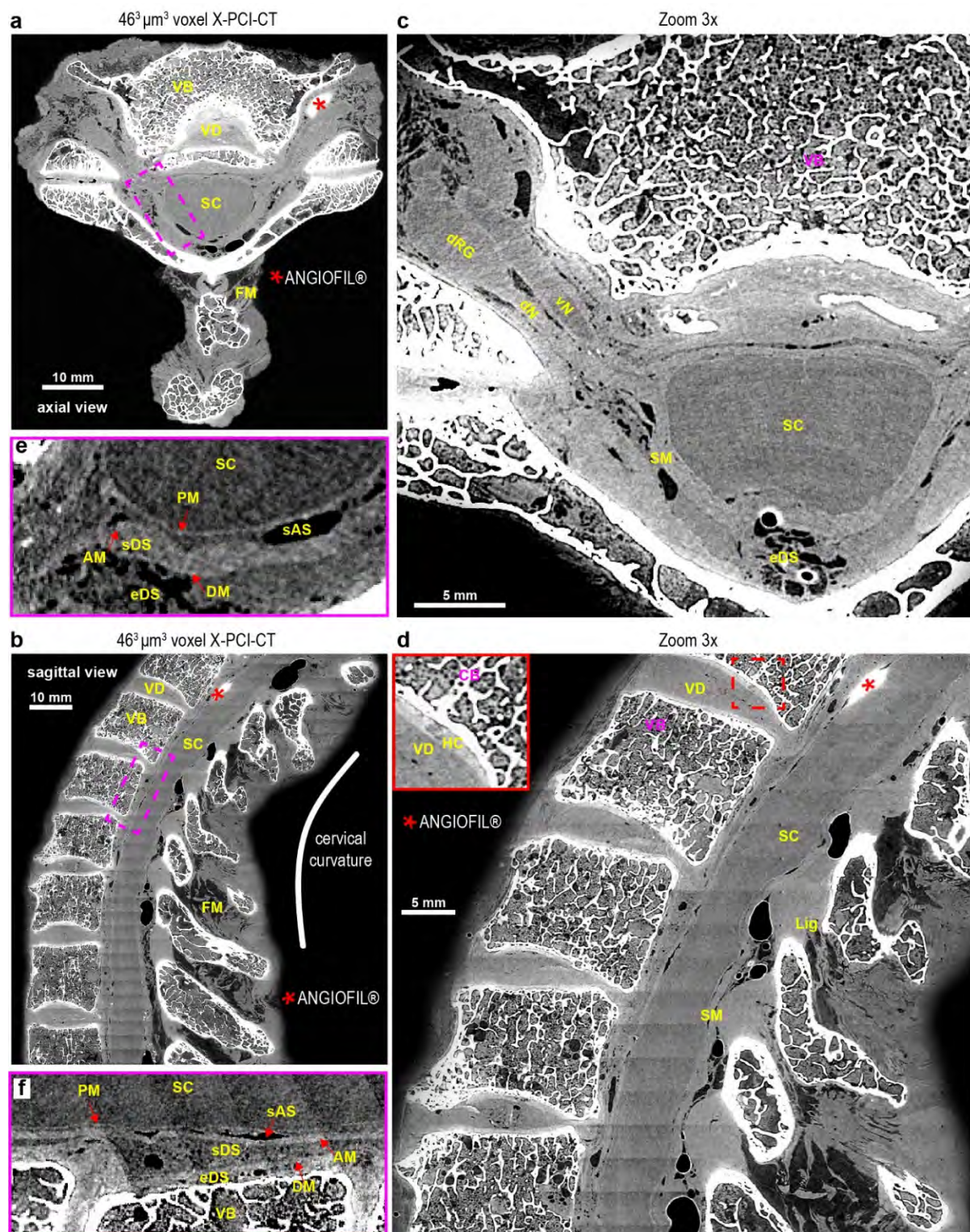


FIGURE 2: Axial (**a**) and sagittal (**b**) views from a *post-mortem* $46^3 \mu\text{m}^3$ voxel 3D X-PCI-CT dataset of a Thiel-embalmed human spine specimen. The technique permits the concurrent visualization of both bony vertebral bodies (VB) and soft-matter structures within spinal cords (SC), vertebral disks (VD) and spinal fat and muscles (FM). Zoom-ins of (**a,b**) respectively in (**c,d**) highlight and label SC structure visible in the spinal canal, including interspinous ligaments and ligamenta flava (Lig), the epidural space (eDS) with its adipose-tissue padding and venous plexus, spinal meninges (SM), ventral and dorsal nerves (vN, dN), and a dorsal root ganglion (dRG). The insert in (**d**) shows detail of vertebral joint tissue demarcation, including VD structure, hyaline cartilage plate structure (HC), and cancellous bone structure within the VB. Dashed rectangles in (**a,b**) are recapitulated at

higher magnification in **(e,f)** to demonstrate structure delineation in-between meningeal spaces (eDS, subdural space – sDS, subarachnoid space - sAS), including visible layer structures pertaining to all three CNS meninges (pia mater - PM, arachnoid mater - AM, dura mater - DM). Red asterisks highlight ANGIOFIL[®]-filled vasculature. Formalin background was masked in all CT data for clarity.

The volumetric nature of the collected CT data permitted 2D to 3D visualizations of spinal anatomy without the need for sample sectioning (**Fig. 3a-b**). Image contrast was sufficient to segment bone, CE vasculature and soft-tissue features and explore them in 3D (**Fig. 3b**). CE spinal vasculature (**Fig. 3c**) offered the contrast necessary for its extraction from surrounding soft-matter (**Fig. 3d-e**), compared to non-CE vasculature, which presented gray-levels hardly different from surrounding nerve structure (**Fig. 3c**) and was not easily segmented (by means of traditional segmentation approaches, see **Methods**) nor well rendered in 3D alongside extracted bone- and soft-tissues (**Fig. 3f**).

Measurements of Thiel-embalmed cervical to lumbar spinal segments (**Fig. 4**) demonstrated the feasibility of concurrent high-contrast soft-tissue and bone-tissue morphological visualizations using a single X-PCI-CT dataset. In fact, image gray-levels could be optimized alternatively for soft-tissue (**Fig. 4a-c**) or for bone-structure (**Fig. 4d-f**) visualizations (more in **Supplementary Results**), and datasets could be segmented to render soft-tissue and bone structures in 3D (**Supplementary Fig. 1**). Images recapitulated the structure of spinal vertebrae, of the spinal cord and of spinal nerves, and consistently detected CE microvasculature within subarachnoid spaces (**Fig. 4a-c**), including the unpaired anterior spinal artery, both posterior spinal arteries and the arterial vasocorona. Overall, these images afforded a clear virtual-anatomical visualization of the spinal-canal environment and the extra-medullary spinal cord arterial blood supply system.

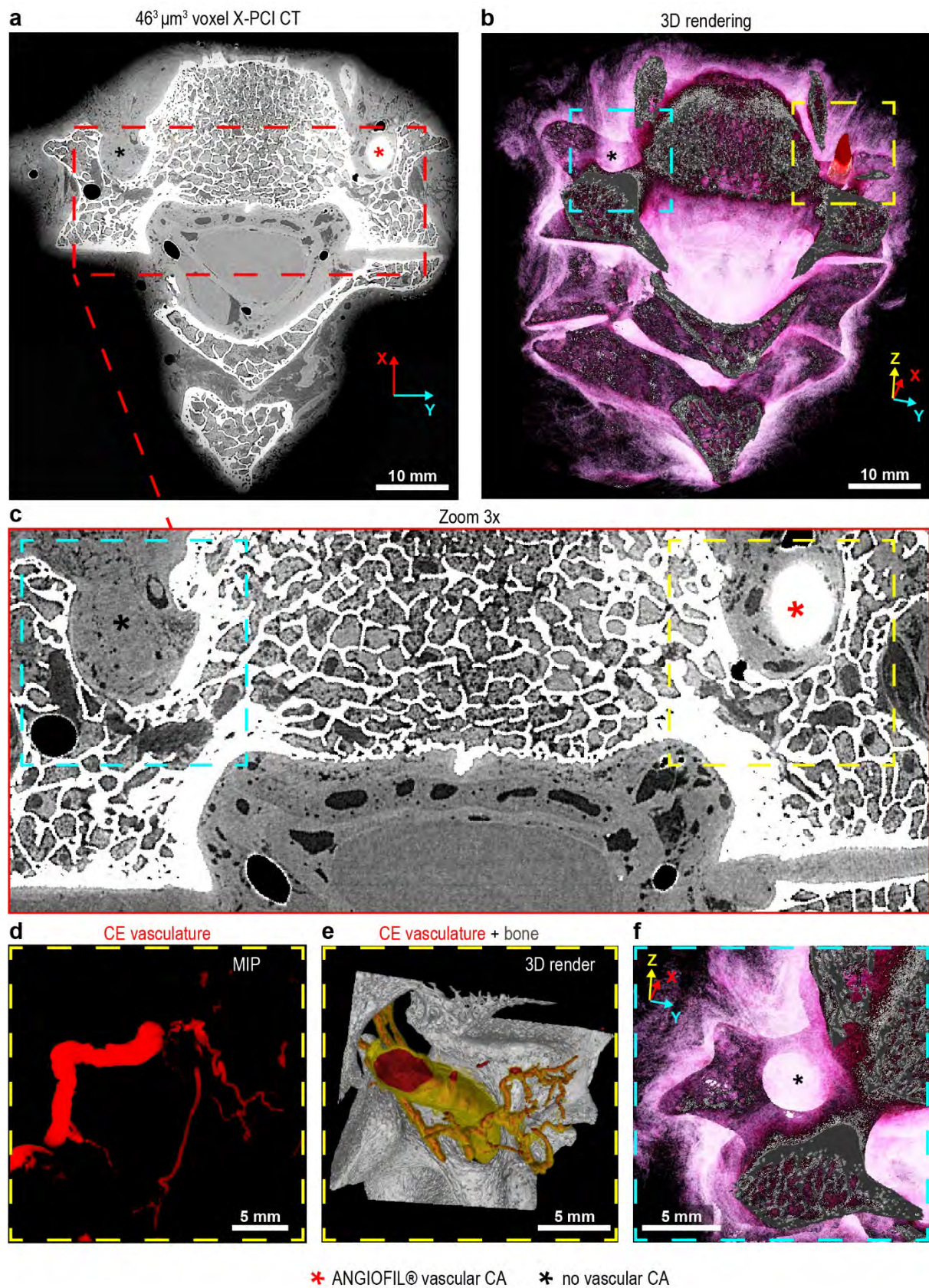


FIGURE 3: A $46^3 \mu\text{m}^3$ voxel X-PCI-CT dataset of a Thiel-embalmed human spine, portrayed in a 2D CT slice (a) or as a 3D rendering (b). In 2D, darker gray-levels pertain to soft-tissue, brighter gray-levels to bone structure. In 3D, bone structure is rendered as gray/white, soft-tissue as light-magenta, contrast-enhanced (CE) vasculature

as red. The zoom-in of (a) in (c) highlights unilateral vascular contrast enhancement in a spine specimen selectively perfused with ANGIOFIL® contrast agent in the left vertebral artery. Red vs. black asterisks label ANGIOFIL®-perfused vs. contralateral un-perfused vasculature. Data in (d-f) originates from the same dataset rendered in (b), with color-coded dashed rectangles showing the specific locations of origin. (d) shows the region-growing-based segmentation and 3D rendering of CE spinal vasculature (rendered in red), (e) a 3D rendering of the same segmented vertebral artery segment (rendered in red/yellow) as in (d), alongside its surrounding body structure (rendered in white/silver), also extracted with a region-growing segmentation approach. (f) shows a 3D rendering of the contralateral spinal area with respect to data in (d-e), with bone structure detail (rendered in white/silver) extracted via region-growing segmentation, and soft-tissue structure detail (rendered in light-magenta) extracted via a threshold-based segmentation approach. In (f), a much lower visibility of non-CE contralateral vasculature hindered the same vascular feature segmentation approach used in (d-e), and thus no vascular feature was rendered here. XYZ-arrows in (a,b,f) depict the relative orientations of the 2D CT slice in (a) vs. the 3D renderings in (b, f). Formalin background was masked in the CT data in (a) for clarity.

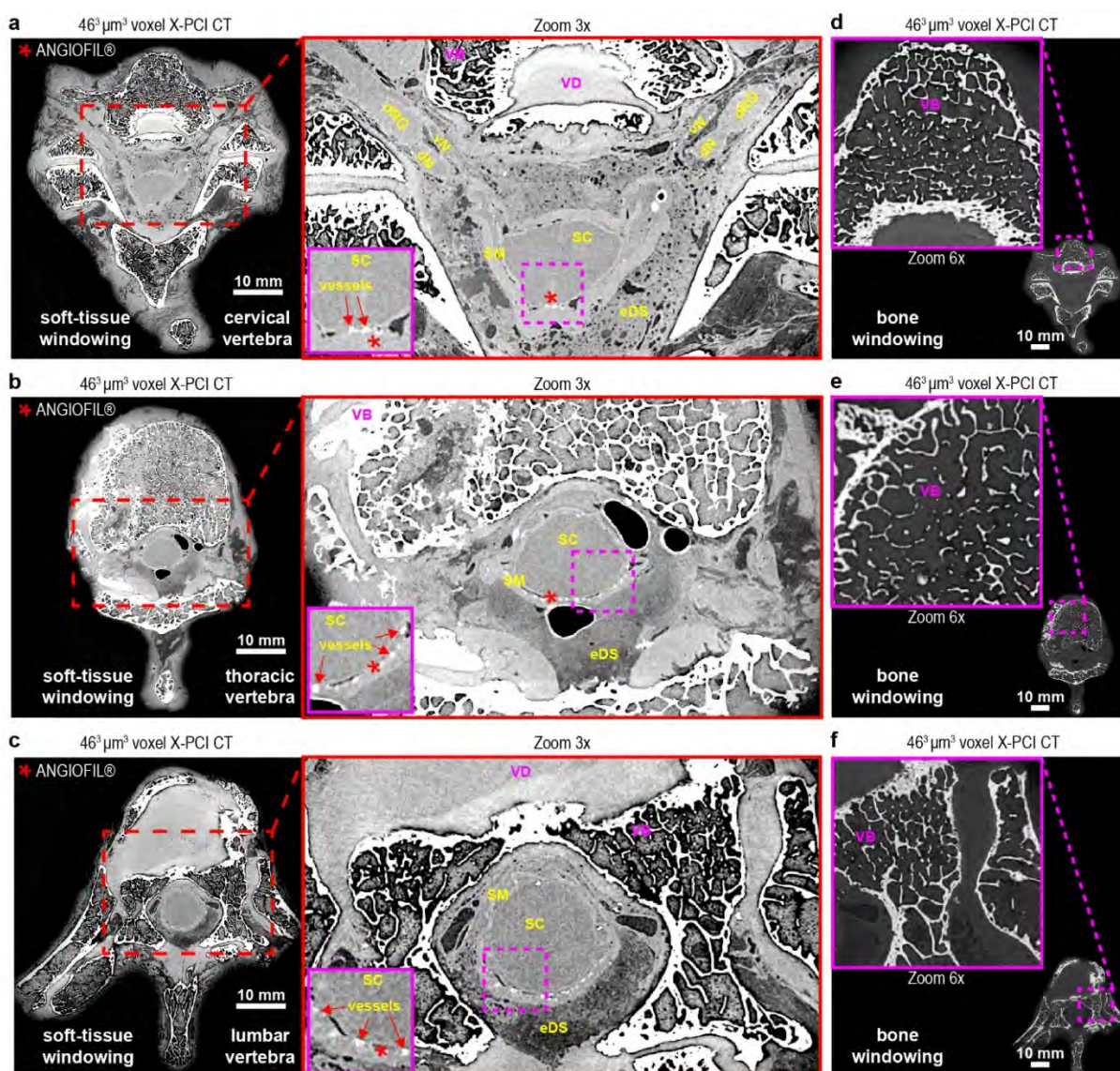


FIGURE 4: Representative *post-mortem* $46^3 \mu\text{m}^3$ voxel X-PCI-CT data of human Thiel-embalmed cervical (a), thoracic (b) and lumbar (c) vertebrae surrounding spinal cord (SC) soft-matter structure within the spinal canal. Image gray-level windowing was chosen for optimal soft-tissue contrast. Detailed spinal canal compartmentalization can be recognized within data 3x zoom-ins, including meningeal spaces (epidural spaces - eDS), spinal meninges (SM), dorsal and ventral nerves (dN, vN), and dorsal-root ganglions (dRG) alongside

bright vertebral body structure (VB). Vertebral disk structure is also visualized when present. Both SC and eDS show signs of possible deterioration, including deformation and air-bubble infiltration. Red asterisks, red arrows and further-zoomed image inserts highlight ANGIOFIL®-filled micro-vasculature (vessels) in the subarachnoid space, which pertain to the anterior spinal artery, both posterior spinal arteries and the arterial vasocorona. The same human spine data as in (a-c) is visualized in (d-f), but with a choice of image gray-level windowing more favorable to bone structure visualization. Notice how VB internal cancellous organization can be rendered without contrast saturation within the bone tissue. Formalin background was masked in all CT data for clarity.

6.4.2 Formalin-fixed spinal cord imaging

Still, almost no gray vs. white-matter contrast was visible in the bone-surrounded Thiel-embalmed cords, and neither vascular nor cellular microarchitecture could be resolved in intra-medullary compartments; moreover, evident epidural space deterioration could be recognized in all Thiel-embalmed samples including air-bubble infiltration, meningeal and medullary deformation, and fat tissue decomposition. These observations suggested likely incomplete nervous-tissue fixation and intra-medullary structural demise in these samples, which likely limited the depiction of intra-medullary anatomy achieved by X-PCI-CT. To study the role played by the insufficient nervous-tissue fixation in the Thiel-embalmed samples, we collected further $46^3 \mu\text{m}^3$ voxel X-PCI-CT datasets, this time of dissected bone-free formalin-fixed human spinal cords (**Fig. 5**), as well as higher-resolution $8^3 \mu\text{m}^3$ voxel data of specimens prepared with both embalming methods (**Fig. 5-6, Supplementary Video 2**).

Unlike non-dissected Thiel-embalmed ones, the dissected formalin-fixed human cords harvested for this study appeared histologically well-preserved upon visual inspection, and consistently presented at least some of the expected intra-SC gray- vs. white-matter contrast in both 46^3 and $8 \mu\text{m}^3$ voxel X-PCI-CT datasets (**Fig. 5a-b**). Notably, $8^3 \mu\text{m}^3$ voxel datasets could resolve micrometer-scale intra-medullary vascular and cellular structures (**Fig. 5c-e**). Maximum intensity projections (MIP, see **Methods**) visualized complex networks of intra-cord micro-vascular structure without need for contrast-agent injection (**Fig. 5f, h**) and enhanced intra-medullary motor neuron structure within gray-matter horns. These data permit the detailed examination of the medullary blood-supply system (both arteries and veins), and the recognition e.g. of the anterior spinal artery penetrating the cord at the anterior median fissure (**Fig. 5d,f**) as terminal sulcocommissural arteries, (alternatingly) each centrally-supplying a medulla-half. The arterial vasocorona system can be observed (**Fig. 5f**) surrounding the cord and peripherally supplying via terminal inward-branching radial arterioles the (white-matter) funiculi and gray columns. Neuron cell somas can be seen populating agglomerates in the anterior gray columns (**Fig. 5c-h**), and thereby forming e.g. the ventrolateral and dorsolateral gray matter nuclei, all cholinergic motor centers. These small intra-medullary neuro-anatomical features were easily rendered in 3D (**Fig. 5g**) after simple threshold-based segmentation. Zoom-ins and 3D renderings allow the volumetric inspection of deep microvasculature as it supplies specific gray-matter nuclei and individual motor neurons.

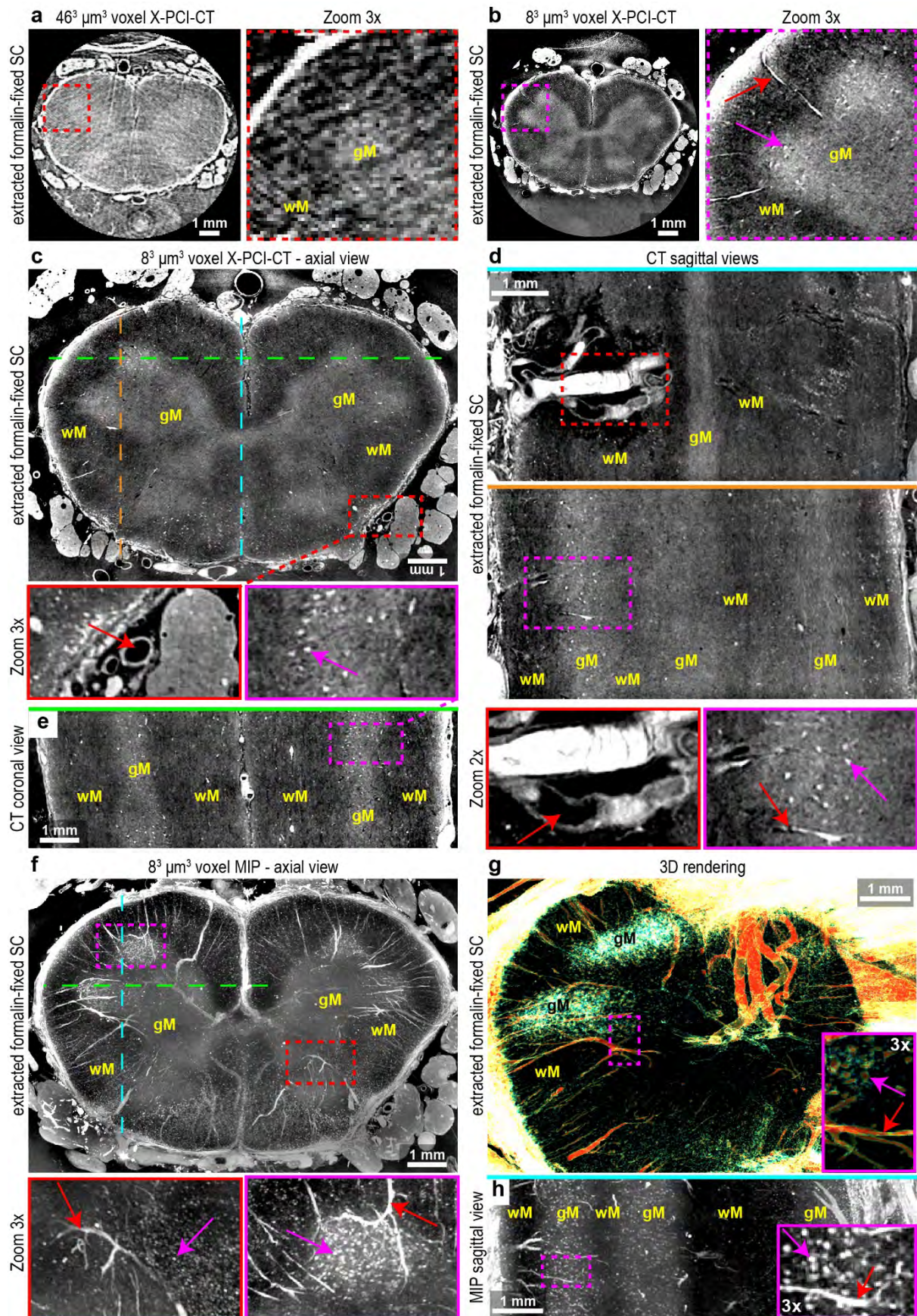


FIGURE 5: (a) $46^3 \mu\text{m}^3$ voxel vs. (b) $8^3 \mu\text{m}^3$ voxel axial X-PCI-CT data and zoom-ins of an extracted (dissected) formalin-fixed human spinal cord (SC). (c) Higher magnification axial image and zoom-in of the same SC as in (b). Both anterior and posterior spinal arteries and veins are rendered. (d-e) sagittal and corona volumetric virtual

re-slicing (+ zoom-ins) of the same 3D X-PCI-CT dataset as in (c). A blood-filled sulcocommissural artery penetrating the anterior median fissure is visible in (d). (f) 2D maximum intensity projection (MIP) axial map, obtained from 100 consecutive CT slices from the same 3D X-PCI-CT dataset as in (c). The MIP map highlights hyper-dense intra-cord (micro-)vasculature from both the anterior spinal artery and the arterial vasocorona systems, as well as cellularity in the SC ventral horns, populating (among others) the ventrolateral and dorsolateral gray-matter nuclei. (g) 3D rendering of hyper-intense intra-SC vascular and cellular features, extracted via threshold-based segmentation. Throughout the figure, X-PCI-CT data show intra-cord gray matter (gM) vs. white matter (Wm) contrast, vascular features (red arrows) and cellular features (magenta arrows).

6.4.3 Comparison Thiel vs. Formalin embalming

Direct comparison of Thiel-embalmed spinal column (**Fig. 6a-d**) vs. formalin-embalmed spinal cord (**Fig. 6e-h**) X-PCI-CT data showed noticeable differences in achieved sample preservation, soft-tissue contrast and feature delineation. Data from the Thiel-embalmed specimens effectively visualized macroscopic spinal column anatomy, detected inter-tissue boundaries and afforded area-contrast between bone-tissues, soft-tissues, and extra-medullary CE vasculature. Nevertheless, little to no intra-medullary structural information could be detected. Conversely, data pertaining to the formalin-fixed specimens exhibited good intra-medullary feature delineation, including both (micro-)vascular and cellular structures, and also some intra-SC white vs. gray matter contrast. Contrast as well as feature-detection were especially enhanced in the higher resolution $8^3 \mu\text{m}^3$ voxel acquisitions of boneless cords (**Fig. 6g-h**). The contrast-agent-free visualization of dense 3D micro-vascular networks within formalin-fixed dissected cords (**Fig. 6h**) was particularly noteworthy, especially compared to the rather poor vascular imaging result achieved for non-dissected Thiel-embalmed spines even after contrast-agent injection (**Fig. 6d**).

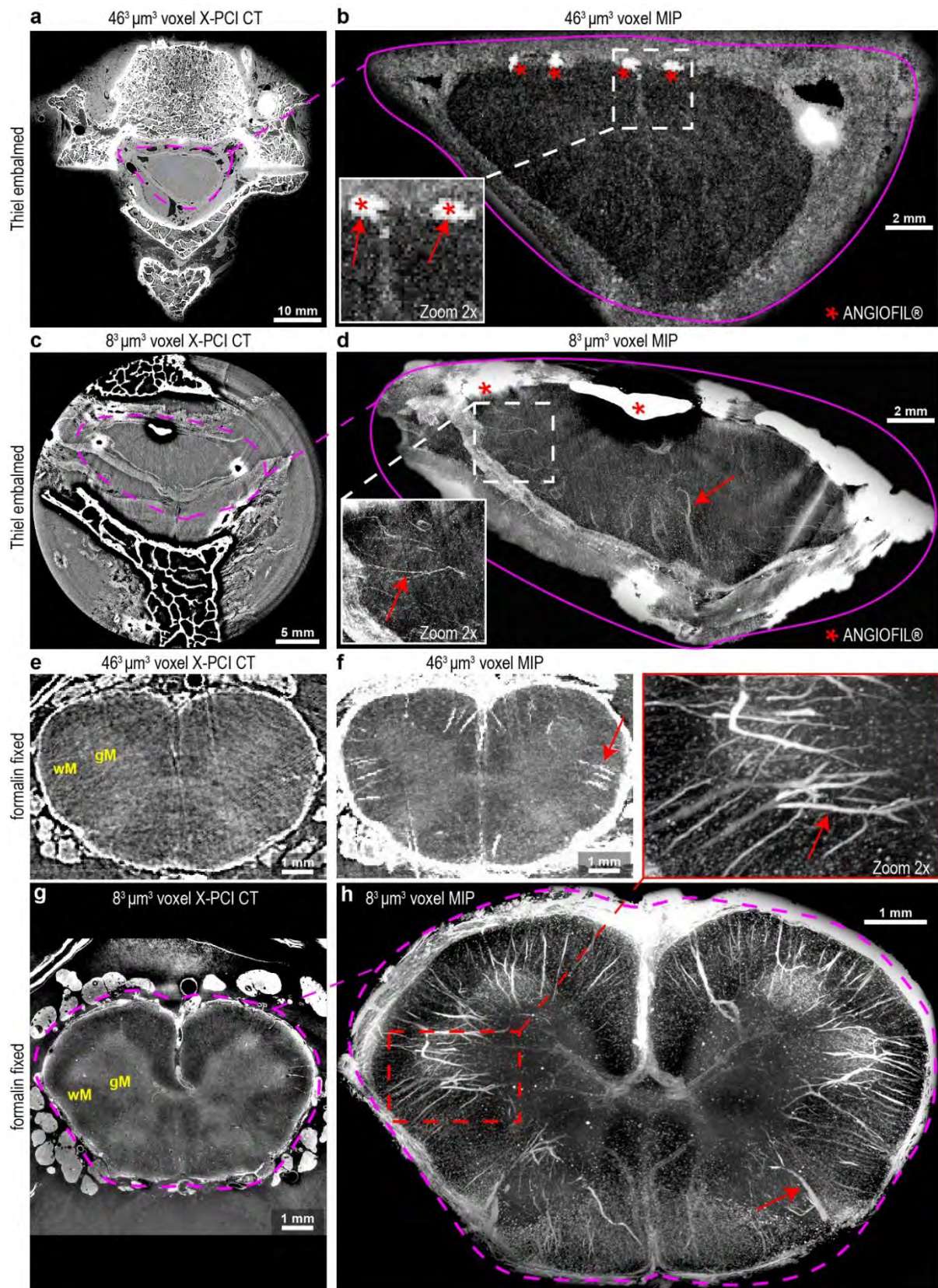


FIGURE 6: Comparison of X-PCI-CT data from (a-d) Thiel-embalmed non-dissected human spines (bone + soft-matter) perfused with ANGIOFIL® vs. (e-h) un-perfused dissected formalin-fixed human (soft-matter only) spinal cords (SC). (a) vs. (b) and (e) vs. (f) show $46^3 \mu\text{m}^3$ voxel axial spinal single-slice X-PCI-CT vs. 50-slice MIP data. (c) vs. (d) and (g) vs. (h) show $8^3 \mu\text{m}^3$ voxel axial spinal single-slice X-PCI-CT vs. 50-slice MIP data. Only X-PCI-CT data of dissected formalin-fixed SC shows some intra-cord gray matter (gM) vs. white matter (wM) contrast. Both

methods show at least some sign of vascular feature contrast (red arrows) in MIP maps, in (f-g) without contrast-agent. Red asterisks highlight likely ANGIOFIL®-filled vasculature. Formalin background was masked in most CT data for clarity.

6.5 Discussion

The complex structure and function of the vertebral column call for sensitive and high resolution imaging modalities. In this study, we used a multiscale synchrotron-radiation propagation-based X-PCI-CT setup to obtain tissue-conserving microscale-resolution volumetric *post-mortem* (46^3 and $8^3 \mu\text{m}^3$ voxel) datasets of human Thiel-embalmed spinal column and human formalin-embalmed spinal cord specimens. The volumetric nature of X-PCI-CT datasets permitted a 3D exploration of extended (tens of cm long) samples, from cervical to lumbar regions, which would have hardly been possible via traditional histological approaches. This 3D imaging approach yielded concurrent bone and soft tissue image contrast and sensitivity, key assets for the efficacious imaging of the spinal cord, a challenging organ physical environment completely encased in the bony vertebral structure of the spinal canal. When imaging Thiel-embalmed spinal columns with a $46^3 \mu\text{m}^3$ voxel system, X-PCI-CT generated precise virtual representations of the macroscopic anatomy of the spinal canal in 3D. This type of images could facilitate and enrich the study of spinal cord organ and vasculature structure for both anatomy education purposes as well as in basic science inquiries. Most notably, when applied to dissected boneless cord specimens with an $8^3 \mu\text{m}^3$ voxel system, this technique was able to measure arterial and venous intra-medullary spinal cord micro-vasculature in the absence of vascular contrast agent, and to resolve cellular structures within gray-matter layers, *de facto* providing quasi-histological micro-anatomical intra-cord morphological information.

The possibility to consecutively 3D-render first the macroscopic and then also the microscopic anatomy within a human cord specimen, as demonstrated here, makes evident the value of X-PCI-CT in medical imaging, i.e. that this imaging technique can bridge the gap between organ-level and cellular level anatomical visualizations, e.g. of the CNS, by a multiscale analysis of large human specimen. This type of datasets could facilitate anatomy learning for clinicians in training, and could promote a better volumetric understanding. For example, this method could be used, macroscopically, to study spinal cord blood supply and the path of spinal nerves with respect to surrounding meningeal compartments and supporting/protecting bone structure, and, microscopically, to study neuronal parenchymal cyto-architecture within cord columns and funiculi, and intra-medullary micro-vasculature. This neuroanatomical imaging approach could also be applied to the detailed rendering of typical osseous, disk and ligament failures of the vertebral column, of spinal canal stenosis and of macro- to microscopic neuron and nerve-fiber lesions.

This work also shows how proper nervous-tissue soft-matter embalming is of paramount importance in the optimization of tissue-conserving anatomical imaging via *post-mortem* X-PCI-CT, especially in the context of micro-scale imaging. Spinal column Thiel-embalming enabled the conservation of macroscopic organ compartments (**Fig. 2-4, Fig. 6a-d**), including

its soft-tissue components, but proved inadequate for the preservation of inner cord structure, and led to a quite limited depiction of intra-medullary nervous tissue architecture by X-PCI-CT in spinal cords left within the bony column. Conversely, the satisfactory internal spinal cord nervous-tissue sub-structural preservation achieved within dissected specimen by formalin-fixation, led to much higher medullary white vs. gray matter contrast and much more detailed microvasculature representations. X-PCI-CT sensitivity to intra-cord soft-tissue structure was thus verified here only for the case of dissected formalin-fixed specimens (**Fig. 5, Fig. 6e-h**). This experiment alone cannot confirm, instead, whether X-PCI-CT can afford high intra-SC white vs. gray matter contrast when measuring a non-dissected human spinal column specimen, since the poor conservation of micro-anatomical CNS integrity by Thiel-embalming likely played a crucial, detrimental, role here. The highly-absorptive, highly-scattering mineralized bony vertebral walls also affect X-ray light and will also likely influence soft-tissue X-PCI-CT imaging of non-dissected CNS soft-tissue. Nevertheless, the feasibility of neural soft-tissue imaging of organs encased within their thick surrounding bony structure (brains within the skull or spinal cords within the spinal canal) is an actively researched question, and X-PCI-CT methodology has already been shown to provide some brain gray vs. white matter differentiation within the skull of a *post-mortem* piglet model (Zamir *et al.*, 2016), and some brain sub-structure delineation within the skull of a *post-mortem* rabbit model (Croton *et al.*, 2018). In the case of *post-mortem* human spinal cord soft-tissue imaging by X-PCI-CT, an objective evaluation of whether a bone removal dissection step represents a necessary and thus limiting aspect, performed in this study in combination with formalin-fixation to produce intra-medullary contrast, will involve future testing of X-PCI-CT on non-dissected bone-surrounded spinal column specimens, either fresh/fresh-frozen, or fixed by immersion in formalin, or by means of combinations of aldehyde fixatives, as customary e.g. in electron microscopy.

The highly specialized setup and equipment, and the issues of access, cost and workflow involved in performing imaging at synchrotron radiation facilities make the presented X-PCI-CT imaging methods only remotely accessible for clinical, but also for educational and scientific work. A future more routine applicability of X-PCI-CT, which would be highly beneficial to anatomy education purposes, will rely on bringing the technique outside of a synchrotron radiation facility setting via technology which could fit within a pathology department building, a possibility that is offered nowadays by the spreading of novel miniaturized X-ray sources, e.g. compact X-ray light sources (Eggl *et al.*, 2015; Jacquet, 2016; Sung *et al.*, 2017; Cole *et al.*, 2018). Raising the scientific relevance of the X-PCI-CT technique for soft-tissue imaging, instead, involves a further increase in its spatial resolution capabilities within specimen of cubic-millimeters to cubic-centimeters sizes, something that is possible with bright synchrotron light and an effort already ongoing at specifically-designed synchrotron beamlines (Khimchenko *et al.*, 2018; Dejea *et al.*, 2019). X-PCI-CT 3D microscopy technology today can reach the sub-micron spatial regime, making the technique competitive compared to micro-imaging results achievable with commercial micro-CT on stained murine soft-tissue, and to the nano-imaging results achievable with traditional (sample-invasive and mostly-2D) histological and electron microscopy methodologies.

6.6 Conclusions

In conclusion, this proof-of-concept study demonstrates that *post-mortem* X-PCI-CT provides unique 3D knowledge of vertebral bone, soft-tissue and vasculature at ultrahigh resolution within a single CT image. This makes it an attractive novel method for multiscale anatomical imaging work on human spinal cord and column specimens in alternative to, or in combination with, traditional histological techniques or other complementary virtual 3D imaging techniques. Further experimental work is necessary in order to develop and verify a spinal column sample-preparation protocol that will optimize soft-tissue imaging results without requiring bone removal for the detection of inner cord micro-architecture.

6.7 Supplementary Material

6.7.1 Supplementary Text

Supplementary Introduction:

High-field PMMR microscopy:

High-resolution high-field PMMR, so-called PMMR microscopy, since it is less-restricted by scan duration constraints compared to *in-vivo* MRI, it can thereby fully exploit advanced MR pulse sequences to achieve sensitivity to diverse nervous tissue microstructures even beyond the anatomical resolution limit of the imaging system (e.g. spinal cord myelin content, axonal density(Mottershead *et al.*, 2003), neurite density(Grussu *et al.*, 2015), and gray matter lesions(Gilmore *et al.*, 2008)). CNS PMMR microscopy, compared to traditional (absorption-based) CT, affords superior white vs. gray matter soft-tissue contrast, arising from the water and lipid content differences between the two different tissue types, and can provide various types of diffusion-based nervous-tissue connectivity maps(Cohen, Anaby and Morozov, 2017), demonstrated to closely correlate to histology. Since whole-body high-field PMMR is a feasible option for fetuses(Thayyil *et al.*, 2009), the technique is being proposed as an alternative to perinatal autopsy.

X-PCI-CT:

Compared to traditional (absorption-based) CT, this experimental 3D imaging methodology(Snigirev *et al.*, 1995) simultaneously exploits both X-ray absorption and refraction while passing through tissue. Since refraction effects are larger than absorption effects at X-ray energies used in medical diagnostics, this technique can better visualize weakly-absorbing features within thick soft-tissue samples of biomedical interest(Lewis *et al.*, 2003; Bravin, Coan and Suortti, 2013). For example, excised rodent brain X-PCI-CT can afford quite high gray vs. white matter contrast(Pfeiffer *et al.*, 2007; Beltran *et al.*, 2011), complementary to MR contrast(Schulz *et al.*, 2012).

Supplementary Methods:

Specimens:

All human spinal cord specimens were provided by the Institute of Anatomy of the University of Bern, Switzerland. The use of the samples was performed according to the Swiss Federal Act on Research involving Human Beings (Human Research Act, HRA(Bundesgesetz 810.30 über die Forschung am Menschenforschungsgesetz, 2011)) and to the 2014 adapted ethical guidelines of the Swiss Academy of Medical Sciences (SAMS)(SAMW, 2014). Donors have formally agreed to the use of body parts for research purposes by signing the donation forms. There was no age limitation for the body donation. All further specimen study was carried out in accordance with the Declaration of Helsinki, after their use was approved by the institution's local ethical committee.

Thiel-embalming:

Thiel-embalming is reported to lead to excellent cadaver flexibility and is used by medical schools for education purposes as an alternative to formalin fixation (Eisma, Lamb and Soames, 2013; Bangerter *et al.*, 2017). *Post-mortem* delay until embalming was less than 24 hours. Angiofil® (Fumedica AG, Switzerland) is a highly radio-opaque oily vascular contrast agent, used here to enhance image contrast of anteroposterior spinal arteries in the left neck region. Briefly, full cadavers were initially perfused, and then immersed for more than 2 months in a fluid made up mainly of water, glycol and various salts, and containing only minimal quantity of formalin, chlorocresol and other substances with associated health risks. After embalming, extracted spinal specimens were stored in plastic bags for several months without cooling or vacuum packing. Spine samples were 30 cm in height and 8 cm in diameter, and included cervical, thoracic and lumbar sections.

Formalin fixation:

The used protocol is standard to achieve anatomical preservation for *post-mortem* human autopsies.

Propagation-based X-PCI-CT:

Briefly, a propagation-based X-PCI-CT setup can measure spatial variations in beam phase shifts induced by the sample under investigation, by capturing diffraction-driven beam intensity variations via a detector placed a specific distance away from the sample (Gureyev, Roberts and Nugent, 1995; Nugent *et al.*, 1996). It is the spatial propagation between the sample and the downstream detector of differently Fresnel-diffracted X-ray wave-front sections, in combination with their interference at the detector position, that converts the object-induced phase shifts into detectable signal intensity differences (Cloetens *et al.*, 1996).

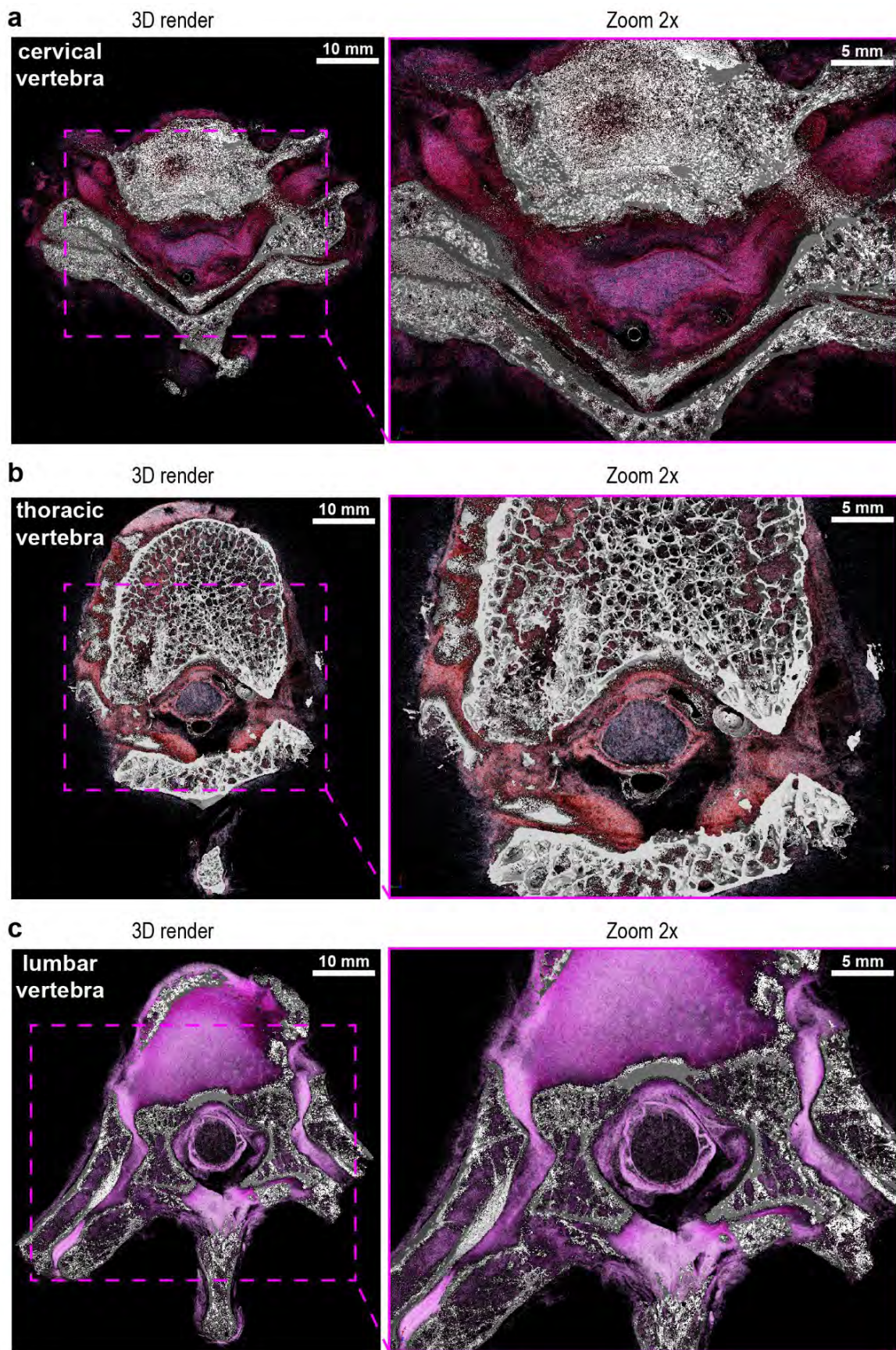
To perform propagation-based X-PCI-CT at the ESRF ID17 beamline, the X-ray beam, detector pixel matrix and sample stage are aligned, and the sample is rotated with the other setup components remaining fixed. $46^3 \mu\text{m}^3$ voxel size CT scans were performed over 180° with the center of rotation set (horizontally) to the center of the detector pixel matrix (full-acquisition mode). During each scan, 4000 angular projections with a 0.05 s detector integration time were acquired, all with an image matrix of 2048 x 160 pixels and a resulting field-of-view (FoV) of $90 \times 7 \text{ mm}^2$ (H x V). $8^3 \mu\text{m}^3$ voxel size CT scans were performed over 360° with the center of rotation set (horizontally) to one of the sides of the detector pixel matrix (half-acquisition mode), to extend the field of view. For these acquisitions, 6000 angular projections with a 0.6 s detector integration time were acquired, all with a projection image matrix of 2048 x 700 pixels and an extended CT FoV of 4000×700 pixels, $32 \times 5.6 \text{ mm}^2$ (H x V).

Supplementary Results:**Thiel-embalmed samples:**

As already reported (Willner *et al.*, 2016), fatty vs. muscle tissue differentiation could also be observed, with the darkest gray-level likely pertaining to lipid-rich adipose structure, whereas

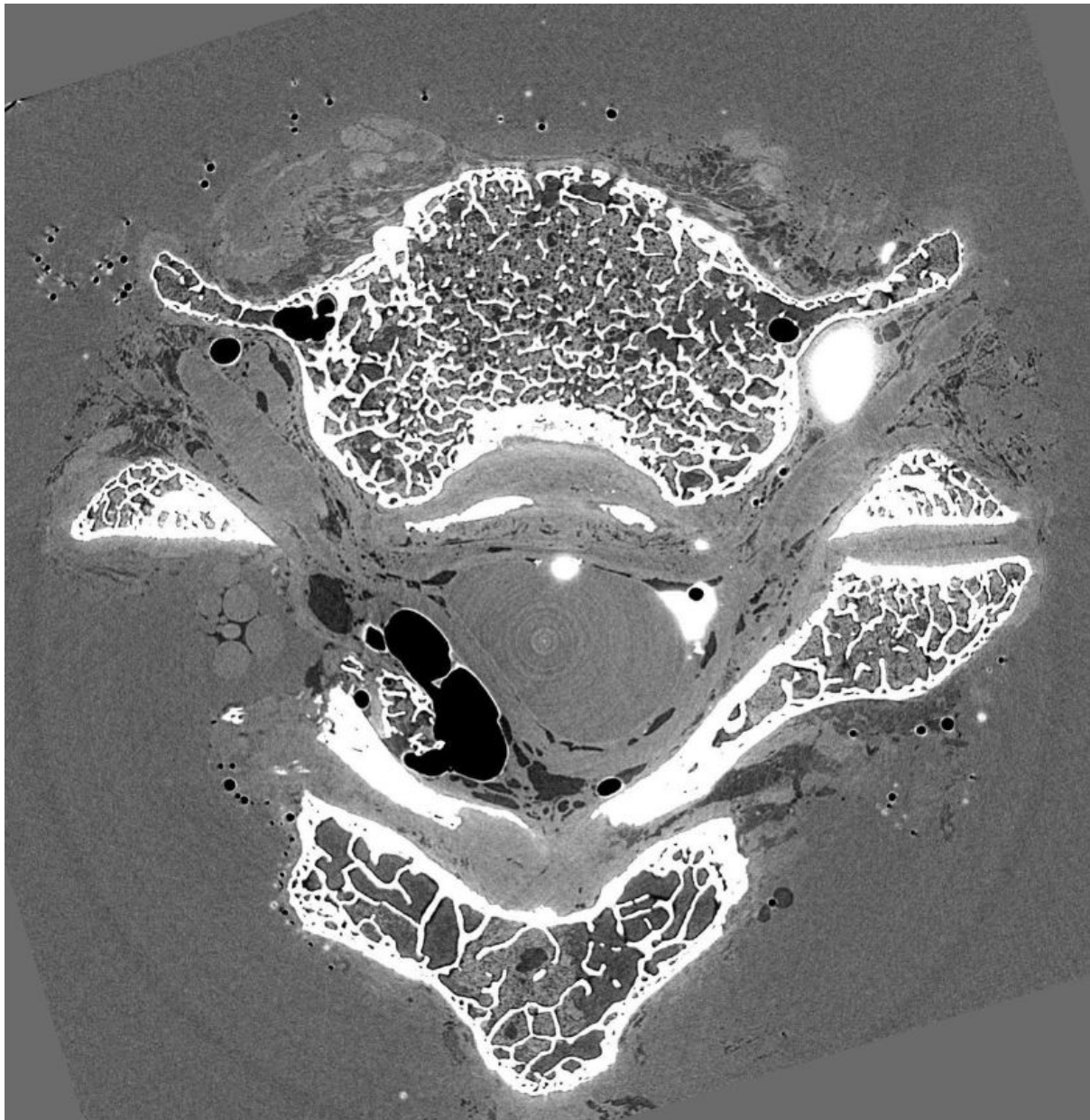
muscle structure likely corresponding to slightly brighter fibers. When image gray-level dynamic range was optimized for soft-tissue visualization, the Thiel-embalmed X-PCI-CT data of human spines showed appropriate soft-tissue contrast in all key soft-matter regions except the intra-SC medulla, where the anticipated presence of white vs. gray tissue contrast seems instead lacking. This soft-tissue-centric windowing choice leads to apparent gray-level saturation within the bony tissues of the human spine (**Fig. 4a-c**), but the observed saturation can be considered as a mere artifact of the selected windowing, since a different gray-level window choice, optimal for the visualization of pixels pertaining to more absorptive tissue, readily enables a visualization of internal bone structure within cancellous vertebral bodies that is completely saturation-free (**Fig. 4d-f**).

6.7.2 Supplementary Figures

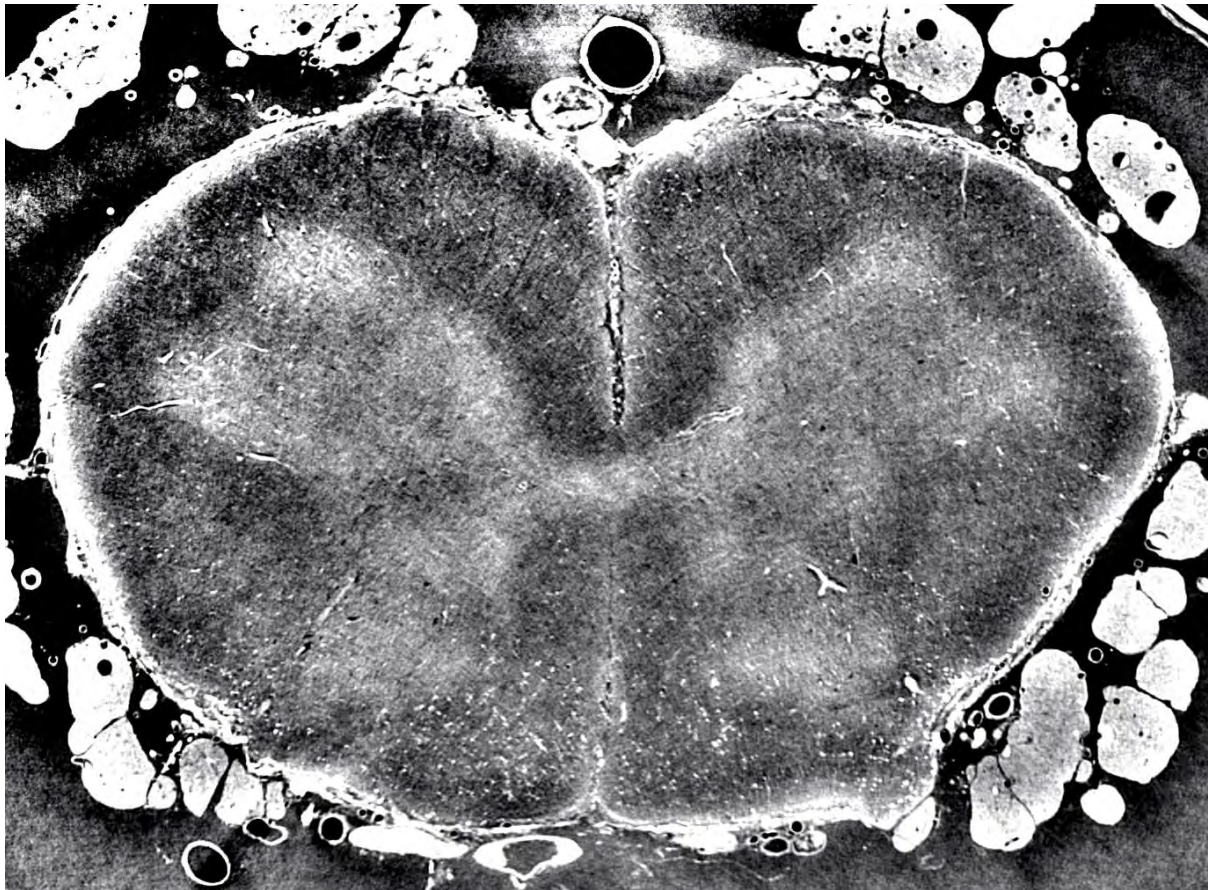


SUPPLEMENTARY FIGURE 1: 3D renderings of the *post-mortem* $46^3 \mu\text{m}^3$ voxel X-PCI-CT data in **Fig. 3**, capturing the volumetric development of a human Thiel-embalmed (a) cervical, (b) thoracic and (c) lumbar vertebra. First, bone and soft-matter structures were segmented via a threshold-based approach and two different threshold levels. Then, vertebral bone structure was rendered in white/silver and spinal cord (SC) soft-matter structure within the spinal canal was rendered in different shades of magenta. Note that these 3D renderings visualize only a small 3D portion of the volumetric X-PCI-CT datasets acquired.

6.7.3 Supplementary Videos



SUPPLEMENTARY VIDEO 1: Representative X-PCI-CT image stack of one of the measured Thiel-embalmed human spinal column specimens.



SUPPLEMENTARY VIDEO 2: Representative X-PCI-CT image stack of one of the measured formalin-fixed human spinal cord specimens.

References:

- Addison, S., Arthurs, O. J. and Thayyil, S. (2014) 'Post-mortem MRI as an alternative to non-forensic autopsy in fetuses and children: from research into clinical practice', *The British journal of radiology*. The British Institute of Radiology., 87(1036), p. 20130621. doi: 10.1259/bjr.20130621.
- Arfelli, F. *et al.* (2000) 'Mammography with Synchrotron Radiation: Phase-Detection Techniques', *Radiology*. Radiological Society of North America, 215(1), pp. 286–293. doi: 10.1148/radiology.215.1.r00ap10286.
- Arthurs, O. J. *et al.* (2015) 'Diagnostic accuracy and limitations of post-mortem MRI for neurological abnormalities in fetuses and children', *Clinical Radiology*. Elsevier, 70(8), pp. 872–880. doi: 10.1016/j.crad.2015.04.008.
- Bangerter, H. *et al.* (2017) 'Combined maceration procedure permits advanced microsurgical dissection of Thiel-embalmed specimens', *Annals of Anatomy - Anatomischer Anzeiger*, 210, pp. 9–17. doi: <https://doi.org/10.1016/j.aanat.2016.10.008>.
- Barbone, G. E. *et al.* (2018) 'Micro-imaging of Brain Cancer Radiation Therapy Using Phase-contrast Computed Tomography', *International Journal of Radiation Oncology Biology Physics*, 101(4), pp. 965–984. doi: 10.1016/j.ijrobp.2018.03.063.
- Barbone, G. E. *et al.* (2020) 'Establishing sample-preparation protocols for X-ray phase-contrast CT of rodent spinal cords: Aldehyde fixations and osmium impregnation', *Journal of Neuroscience Methods*, 339, p. 108744. doi: <https://doi.org/10.1016/j.jneumeth.2020.108744>.
- Beltran, M. A. *et al.* (2011) 'Interface-specific x-ray phase retrieval tomography of complex biological organs', *Physics in Medicine and Biology*. IOP Publishing, 56(23), pp. 7353–7369. doi: 10.1088/0031-9155/56/23/002.
- de Bournonville, S., Vangrunderbeeck, S. and Kerckhofs, G. (2019) 'Contrast-Enhanced MicroCT for Virtual 3D Anatomical Pathology of Biological Tissues: A Literature Review', *Contrast Media Molecular Imaging*. Edited by A. Roivainen. Hindawi, 2019, p. 8617406. doi: 10.1155/2019/8617406.
- Bravin, A., Coan, P. and Suortti, P. (2013) 'X-ray phase-contrast imaging: from pre-clinical applications towards clinics.', *Physics in Medicine and Biology*, 58(1), pp. R1–R35. doi: 10.1088/0031-9155/58/1/R1.
- Bundesgesetz 810.30 über die Forschung am Menschenforschungsgesetz (2011) *Human Research Act (HRA)*, www.admin.ch. Available at: <https://www.admin.ch/opc/de/classified-compilation/20061313/index.html> (Accessed: 19 September 2019).
- Calabrese, E. *et al.* (2018) 'Postmortem diffusion MRI of the entire human spinal cord at microscopic resolution', *NeuroImage: Clinical*. Elsevier, 18, pp. 963–971. doi: 10.1016/j.nicl.2018.03.029.
- Cao, Y. *et al.* (2016) 'Visualization of mouse spinal cord intramedullary arteries using phase- and attenuation-contrast tomographic imaging.', *Journal of synchrotron radiation*, 23(4), pp. 966–974. doi: 10.1107/S1600577516006482.
- Castelli, E. *et al.* (2011) 'Mammography with Synchrotron Radiation : First Clinical Experience with Phase-Detection Technique', *Radiology*, 259(3). doi: 10.1148/radiol.11100745.
- Cedola, A. *et al.* (2017) 'X-Ray Phase Contrast Tomography Reveals Early Vascular Alterations and Neuronal Loss in a Multiple Sclerosis Model', *Scientific Reports*, 7(1), p. 5890. doi: 10.1038/s41598-017-06251-7.
- De Clercq, K. *et al.* (2019) 'High-resolution contrast-enhanced microCT reveals the true three-dimensional morphology of the murine placenta.', *Proceedings of the National Academy of Sciences of the United States of America*, 116(28), pp. 13927–13936. doi: 10.1073/pnas.1902688116.
- Cloetens, P. *et al.* (1996) 'Phase objects in synchrotron radiation hard x-ray imaging', *Journal of Physics D: Applied Physics*, 29(1), pp. 133–146. doi: 10.1088/0022-3727/29/1/023.
- Coan, P. *et al.* (2006) 'Evaluation of imaging performance of a taper optics CCD "FReLoN" camera designed for medical imaging', *Journal of Synchrotron Radiation*, 13(3), pp. 260–270. doi: 10.1107/S0909049506008983.

- Cohen, Y., Anaby, D. and Morozov, D. (2017) 'Diffusion MRI of the spinal cord: from structural studies to pathology', *NMR in Biomedicine*. John Wiley & Sons, Ltd, 30(3), p. e3592. doi: 10.1002/nbm.3592.
- Cole, J. M. *et al.* (2018) 'High-resolution μ CT of a mouse embryo using a compact laser-driven X-ray betatron source', *Proceedings of the National Academy of Sciences of the United States of America*. 2018/06/05. National Academy of Sciences, 115(25), pp. 6335–6340. doi: 10.1073/pnas.1802314115.
- Croton, L. C. P. *et al.* (2018) 'In situ phase contrast X-ray brain CT', *Scientific reports*. Nature Publishing Group UK, 8(1), p. 11412. doi: 10.1038/s41598-018-29841-5.
- Dejea, H. *et al.* (2019) 'Comprehensive Analysis of Animal Models of Cardiovascular Disease using Multiscale X-Ray Phase Contrast Tomography', *Scientific Reports*, 9(1), p. 6996. doi: 10.1038/s41598-019-43407-z.
- Eggl, E. *et al.* (2015) 'X-ray phase-contrast tomography with a compact laser-driven synchrotron source', *PNAS*, 112(18), pp. 5567–5572. doi: 10.1073/pnas.1500938112.
- Eisma, R., Lamb, C. and Soames, R. W. (2013) 'From formalin to thiel embalming: What changes? One anatomy department's experiences', *Clinical Anatomy*. John Wiley & Sons, Ltd, 26(5), pp. 564–571. doi: 10.1002/ca.22222.
- Estai, M. and Bunt, S. (2016) 'Best teaching practices in anatomy education: A critical review.', *Annals of Anatomy*. Germany, 208, pp. 151–157. doi: 10.1016/j.aanat.2016.02.010.
- Fitzgerald, R. (2000) 'Phase-Sensitive X-ray Imaging', *Physics Today*, 7(23). doi: 10.1063/1.1292471.
- Fratini, M. *et al.* (2015) 'Simultaneous submicrometric 3D imaging of the micro-vascular network and the neuronal system in a mouse spinal cord.', *Scientific reports*, 5, p. 8514. doi: 10.1038/srep08514.
- Ghosh, S. K. (2017) 'Cadaveric dissection as an educational tool for anatomical sciences in the 21st century.', *Anatomical sciences education*. United States, 10(3), pp. 286–299. doi: 10.1002/ase.1649.
- Gilmore, C. P. *et al.* (2008) 'Spinal cord grey matter lesions in multiple sclerosis detected by post-mortem high field MR imaging', *Multiple Sclerosis Journal*. SAGE Publications Ltd STM, 15(2), pp. 180–188. doi: 10.1177/1352458508096876.
- Grabherr, S. *et al.* (2008) 'Angiofil®-mediated visualization of the vascular system by microcomputed tomography: A feasibility study', *Microscopy Research and Technique*. John Wiley & Sons, Ltd, 71(7), pp. 551–556. doi: 10.1002/jemt.20585.
- Grussu, F. *et al.* (2015) 'Neurite orientation dispersion and density imaging of the healthy cervical spinal cord in vivo', *NeuroImage*, 111, pp. 590–601. doi: <https://doi.org/10.1016/j.neuroimage.2015.01.045>.
- Gureyev, T. E., Roberts, A. and Nugent, K. A. (1995) 'Phase retrieval with the transport-of-intensity equation: matrix solution with use of Zernike polynomials', *Journal of the Optical Society of America A*. OSA, 12(9), pp. 1932–1941. doi: 10.1364/JOSAA.12.001932.
- Haddad, W. S. *et al.* (1994) 'Ultrahigh-Resolution X-ray Tomography', *Science*, 266(5188), pp. 1213 LP – 1215. doi: 10.1126/science.266.5188.1213.
- Hetterich, H. *et al.* (2014) 'Phase-Contrast CT: Qualitative and Quantitative Evaluation of Atherosclerotic Carotid Artery Plaque', *Radiology*. Radiological Society of North America, 271(3), pp. 870–878. doi: 10.1148/radiol.14131554.
- Van Horn, J. D. and Toga, A. W. (2014) 'Human neuroimaging as a "Big Data" science.', *Brain imaging and behavior*, 8(2), pp. 323–331. doi: 10.1007/s11682-013-9255-y.
- Hornig, A. *et al.* (2014) 'Cartilage and Soft Tissue Imaging Using X-rays: Propagation-Based Phase-Contrast Computed Tomography of the Human Knee in Comparison With Clinical Imaging Techniques and Histology', *Invest Radiol*, 49(9), pp. 627–634. doi: 10.1097/RLI.0000000000000063.
- Hu, J. *et al.* (2015) '3D angioarchitecture changes after spinal cord injury in rats using synchrotron radiation phase-contrast tomography.', *Spinal Cord*, 53(8), pp. 585–590. doi: 10.1038/sc.2015.49.

- Hu, J. *et al.* (2017) 'Nondestructive imaging of the internal micro-structure of vessels and nerve fibers in rat spinal cord using phase-contrast synchrotron radiation microtomography', *Journal of Synchrotron Radiation*, 24(2), pp. 482–489. doi: 10.1107/S1600577517000121.
- Hu, M., Wattchow, D. and de Fontgalland, D. (2018) 'From ancient to avant-garde: a review of traditional and modern multimodal approaches to surgical anatomy education.', *ANZ journal of surgery*. Australia, 88(3), pp. 146–151. doi: 10.1111/ans.14189.
- Jacquet, M. (2016) 'Potential of compact Compton sources in the medical field', *Physica Medica: European Journal of Medical Physics*. Elsevier, 32(12), pp. 1790–1794. doi: 10.1016/j.ejmp.2016.11.003.
- Javaid, M. A. *et al.* (2018) 'Understanding neurophobia: Reasons behind impaired understanding and learning of neuroanatomy in cross-disciplinary healthcare students.', *Anatomical sciences education*. United States, 11(1), pp. 81–93. doi: 10.1002/ase.1711.
- Jorgensen, S. M., Demirkaya, O. and Ritman, E. L. (1998) 'Three-dimensional imaging of vasculature and parenchyma in intact rodent organs with X-ray micro-CT.', *The American journal of physiology*. United States, 275(3), pp. H1103-14. doi: 10.1152/ajpheart.1998.275.3.H1103.
- Kallai, I. *et al.* (2011) 'Microcomputed tomography-based structural analysis of various bone tissue regeneration models.', *Nature protocols*. England, 6(1), pp. 105–110. doi: 10.1038/nprot.2010.180.
- Kampschulte, M. *et al.* (2016) 'Nano-Computed Tomography: Technique and Applications.', *RoFo : Fortschritte auf dem Gebiete der Rontgenstrahlen und der Nuklearmedizin*. Germany, 188(2), pp. 146–154. doi: 10.1055/s-0041-106541.
- Khimchenko, A. *et al.* (2018) 'Hard X-Ray Nanoholotomography: Large-Scale, Label-Free, 3D Neuroimaging beyond Optical Limit', *Advanced Science*, 5, p. 1700694. doi: 10.1002/adv.201700694.
- Kuan, A. T. (2020) 'Dense Neuronal Reconstruction through X-ray Holographic Nano-Tomography', *Biophysical Journal*. Elsevier, 118(3), p. 290a. doi: 10.1016/j.bpj.2019.11.1647.
- Lewis, R. A. *et al.* (2003) 'X-ray refraction effects: application to the imaging of biological tissues', *The British Journal of Radiology*. The British Institute of Radiology, 76(905), pp. 301–308. doi: 10.1259/bjr/32889803.
- Lyckegaard, A., Johnson, G. and Tafforeau, P. (2011) 'Correction of ring artifacts in X-ray tomographic images', *International Journal of Tomography and Statistics*, 18(F11), pp. 1–9.
- Lycklama à Nijeholt, G. J. *et al.* (2001) 'Post-mortem high-resolution MRI of the spinal cord in multiple sclerosis: A correlative study with conventional MRI, histopathology and clinical phenotype', *Brain*, 124(1), pp. 154–166. doi: 10.1093/brain/124.1.154.
- Mader, K. *et al.* (2011) 'High-throughput full-automatic synchrotron-based tomographic microscopy', *Journal of synchrotron radiation*. 2011/01/20. International Union of Crystallography, 18(Pt 2), pp. 117–124. doi: 10.1107/S0909049510047370.
- Majumdar, S. *et al.* (2004) 'Diffraction enhanced imaging of articular cartilage and comparison with micro-computed tomography of the underlying bone structure', *European Radiology*, 14(8), pp. 1440–1448. doi: 10.1007/s00330-004-2355-8.
- Makino, Y. *et al.* (2014) 'Spinal Cord Injuries With Normal Postmortem CT Findings: A Pitfall of Virtual Autopsy for Detecting Traumatic Death', *American Journal of Roentgenology*. American Roentgen Ray Society, 203(2), pp. 240–244. doi: 10.2214/AJR.13.11775.
- Marxen, M. *et al.* (2004) 'MicroCT scanner performance and considerations for vascular specimen imaging.', *Medical physics*. United States, 31(2), pp. 305–313. doi: 10.1118/1.1637971.
- Miao, P. *et al.* (2016) 'Synchrotron Radiation X-Ray Phase-Contrast Tomography Visualizes Microvasculature Changes in Mice Brains after Ischemic Injury', *Neural plasticity*. 2016/07/31. Hindawi Publishing Corporation, 2016, p. 3258494. doi: 10.1155/2016/3258494.
- Mittone, A. *et al.* (2017) 'Characterization of a sCMOS-based high-resolution imaging system', *Journal of Synchrotron Radiation*, 24(6), pp. 1226–1236. doi: 10.1107/S160057751701222X.

- Mittone, A. *et al.* (2020) 'Multiscale pink beam microCT imaging at the ESRF-ID17 biomedical beamline', *Journal of Synchrotron Radiation*, Submitted.
- Mokso, R. *et al.* (2007) 'Nanoscale zoom tomography with hard x rays using Kirkpatrick-Baez optics', *Appl. Phys. Lett.*, 90, p. 144104. doi: 10.1063/1.2719653.
- Mollenhauer, J. *et al.* (2002) 'Diffraction-enhanced X-ray imaging of articular cartilage', *Osteoarthritis and Cartilage*, 10(3), pp. 163–171. doi: <https://doi.org/10.1053/joca.2001.0496>.
- Momose, A. (1995) 'Demonstration of phase-contrast X-ray computed tomography using an X-ray interferometer', *Nuclear Instruments and Methods in Physics Research Section A: Accelerators, Spectrometers, Detectors and Associated Equipment*, 352(3), pp. 622–628. doi: [https://doi.org/10.1016/0168-9002\(95\)90017-9](https://doi.org/10.1016/0168-9002(95)90017-9).
- Mottershead, J. P. *et al.* (2003) 'High field MRI correlates of myelin content and axonal density in multiple sclerosis', *Journal of Neurology*, 250(11), pp. 1293–1301. doi: 10.1007/s00415-003-0192-3.
- Nugent, K. A. *et al.* (1996) 'Quantitative Phase Imaging Using Hard X Rays', *Physical Review Letters*. American Physical Society, 77(14), pp. 2961–2964. doi: 10.1103/PhysRevLett.77.2961.
- Olivo, A. *et al.* (2009) 'Phase contrast imaging of breast tumours with synchrotron radiation', *Applied Radiation and Isotopes*, 67(6), pp. 1033–1041. doi: <https://doi.org/10.1016/j.apradiso.2009.01.075>.
- Paganin, D. *et al.* (2002) 'Simultaneous phase and amplitude extraction from a single defocused image of a homogeneous object', *Journal of Microscopy*, 206(1), pp. 33–40. doi: 10.1046/j.1365-2818.2002.01010.x.
- Pal, N. R. and Pal, S. K. (1993) 'A review on image segmentation techniques', *Pattern Recognition*, 26(9), pp. 1277–1294. doi: [https://doi.org/10.1016/0031-3203\(93\)90135-J](https://doi.org/10.1016/0031-3203(93)90135-J).
- Peterson, D. C. and Mlynarczyk, G. S. A. (2016) 'Analysis of traditional versus three-dimensional augmented curriculum on anatomical learning outcome measures.', *Anatomical sciences education*. United States, 9(6), pp. 529–536. doi: 10.1002/ase.1612.
- Petrova, N. *et al.* (2018) 'Axonal loss in the multiple sclerosis spinal cord revisited', *Brain Pathology*. John Wiley & Sons, Ltd (10.1111), 28(3), pp. 334–348. doi: 10.1111/bpa.12516.
- Peyrin, F. *et al.* (1998) 'Micro-CT examinations of trabecular bone samples at different resolutions: 14, 7 and 2 micron level', *Technology and Health Care*. IOS Press, 6, pp. 391–401. doi: 10.3233/THC-1998-65-611.
- Pfeiffer, F. *et al.* (2007) 'High-resolution brain tumor visualization using three-dimensional x-ray phase contrast tomography', *Physics in Medicine and Biology*, 52(23), pp. 6923–6930. doi: 10.1088/0031-9155/52/23/010.
- Romell, J. *et al.* (2018) 'Soft-Tissue Imaging in a Human Mummy: Propagation-based Phase-Contrast CT', *Radiology*. Radiological Society of North America, 289(3), pp. 670–676. doi: 10.1148/radiol.2018180945.
- SAMW (2014) *Medizin-ethische Richtlinien*, www.samw.ch. Available at: <https://www.samw.ch/de/Publikationen/Richtlinien.html> (Accessed: 19 September 2019).
- Schmierer, K. *et al.* (2018) 'Quantifying multiple sclerosis pathology in post mortem spinal cord using MRI', *NeuroImage*, 182, pp. 251–258. doi: <https://doi.org/10.1016/j.neuroimage.2018.01.052>.
- Schulz, G. *et al.* (2012) 'Multimodal imaging of human cerebellum - merging X-ray phase microtomography, magnetic resonance microscopy and histology.', *Scientific Reports*, 2, p. 826. doi: 10.1038/srep00826.
- Snigirev, A. *et al.* (1995) 'On the possibilities of x-ray phase contrast microimaging by coherent high-energy synchrotron radiation', *Review of Scientific Instruments*. American Institute of Physics, 66(12), pp. 5486–5492. doi: 10.1063/1.1146073.
- Stroman, P. W. *et al.* (2014) 'The current state-of-the-art of spinal cord imaging: methods', *NeuroImage*. 2013/05/14, 84, pp. 1070–1081. doi: 10.1016/j.neuroimage.2013.04.124.
- Sugand, K., Abrahams, P. and Khurana, A. (2010) 'The anatomy of anatomy: a review for its modernization.', *Anatomical sciences education*. United States, 3(2), pp. 83–93. doi: 10.1002/ase.139.

- Sung, Y. *et al.* (2017) 'Phase-contrast imaging with a compact x-ray light source: system design', *Journal of medical imaging (Bellingham, Wash.)*. 2017/11/23. Society of Photo-Optical Instrumentation Engineers, 4(4), p. 43503. doi: 10.1117/1.JMI.4.4.043503.
- Sztróky, A. *et al.* (2012) 'High-resolution breast tomography at high energy: a feasibility study of phase contrast imaging on a whole breast.', *Physics Med. Biol.*, 57(10), pp. 2931–2942. doi: 10.1088/0031-9155/57/10/2931.
- Thayyil, S. *et al.* (2009) 'Post-mortem examination of human fetuses: a comparison of whole-body high-field MRI at 9.4 T with conventional MRI and invasive autopsy', *The Lancet*. Elsevier, 374(9688), pp. 467–475. doi: 10.1016/S0140-6736(09)60913-2.
- Thiel, W. (1992) 'Die Konservierung ganzer Leichen in natürlichen Farben', *Annals of Anatomy - Anatomischer Anzeiger*, 174(3), pp. 185–195. doi: [https://doi.org/10.1016/S0940-9602\(11\)80346-8](https://doi.org/10.1016/S0940-9602(11)80346-8).
- Thiel, W. (2002) 'Ergänzung für die Konservierung ganzer Leichen nach W. Thiel', *Annals of Anatomy - Anatomischer Anzeiger*, 184(3), pp. 267–269. doi: [https://doi.org/10.1016/S0940-9602\(02\)80121-2](https://doi.org/10.1016/S0940-9602(02)80121-2).
- Volume Graphics GmbH. (2001) 'VGStudio MAX 2.2'. doi: www.volumegraphics.com.
- Waters, B. L. (2009) 'Fixation and Transport of Autopsy Material BT - Handbook of Autopsy Practice', in Waters, B. L. (ed.). Totowa, NJ: Humana Press, pp. 145–149. doi: 10.1007/978-1-59745-127-7_15.
- Willner, M. *et al.* (2016) 'Quantitative three-dimensional imaging of lipid, protein, and water contents via x-ray phase-contrast tomography', *PLoS ONE*, 11(3), pp. 1–13. doi: 10.1371/journal.pone.0151889.
- Yu, B. *et al.* (2020) 'Assessment of the human bone lacuno-canalicular network at the nanoscale and impact of spatial resolution', *Scientific Reports*, 10(1), p. 4567. doi: 10.1038/s41598-020-61269-8.
- Zamir, A. *et al.* (2016) 'X-ray phase contrast tomography; proof of principle for post-mortem imaging', *The British journal of radiology*. 2015/11/27. The British Institute of Radiology., 89(1058), p. 20150565. doi: 10.1259/bjr.20150565.

Chapter 7 – Fixatives for rodent spinal cord X-PCI-CT

Optimization of rodent spinal cord sample preparation for synchrotron X-ray phase-contrast computed tomography using a combination of aldehyde fixatives & osmium impregnation

This chapter discusses an *post-mortem* study focused on the visualization of the gross anatomy of the rodent spinal cord via synchrotron X-PCI-CT, after preparation of the dissected medullary sampled with different nervous tissue fixation protocols. Moreover, the study explored the potential of sub-micron X-PCI-CT data for the detection of local cellular structure and the complex vascular network of the rodent spinal cord within extended 3D samples, in comparison to traditional histological approaches as well as high-field 9.4T MRI. The spinal cord cellular and micro-vascular networks play key roles in many neuro-functional and neurodegenerative diseases; their 3D visualization, still limited today by conventional imaging modalities, is fundamental for detecting and better understanding CNS pathologies, and evaluating their treatment.

This work was performed in collaboration with the team of Dr. Bravin at the ID17 beamline of the ESRF, who hosted and supported the majority of the X-PCI-CT measurements in this study, with the team of Dr. Cavaletti at the School of Medicine and Surgery of the University Milano-Bicocca, including Dr. Ceresa, Dr. Rodriguez Menendez and Dr. Ballarini, who provided and prepared the rodent spine samples, strongly contributed in the design of the study, and performed the histological analysis. Last, the high-field MRI images were acquired with the support of the German Mouse Clinic of the Helmholtz Center – Munich, in collaboration with Dr. Kraiger. I would like to express my gratitude to all parties involved in this international collaborative study.

This work has been published in 2020 in the [Journal of Neuroscience Methods](#), [COPYRIGHT] (2020), as follows:

G.E. Barbone, A. Bravin, A. Mittone, M.J. Kraiger, M. Hrabě de Angelis, M. Bossi, E. Ballarini, V. Rodriguez-Menendez, Cecilia Ceresa, Guido Cavaletti, Paola Coan. “Establishing sample-preparation protocols for X-ray phase-contrast CT of rodent spinal cords: Aldehyde fixations and osmium impregnation”, *Journal of Neuroscience Methods*, Vol. 339, 108744 (2020). <https://doi.org/10.1016/j.jneumeth.2020.108744>

This work was also presented orally at the Radiological Society of North America meeting in 2017 (RSNA 2017).

Work Highlights:

- X-ray phase-contrast CT (X-PCI-CT) enables label-free 3D nervous-tissue microscopy
- Multiscale X-PCI-CT captures full-organ to intra-cellular spinal cord neuroanatomy
- Combination of aldehyde fixatives optimizes visualizations of deep micro-vasculature
- Osmium impregnation highlights white-matter and individual motor neuron perikarya
- Post-mortem X-PCI-CT resolving power can exceed that of post-mortem high-field MRI

7.1 Abstract

Background: Dense and unbiased cellular-resolution representations of extended volumetric central nervous system soft-tissue anatomy are difficult to obtain, even in experimental *post-mortem* settings. Interestingly, X-ray phase-contrast computed tomography (X-PCI-CT), an emerging soft-tissue-sensitive volumetric imaging technique, can provide multiscale organ- to cellular-level morphological visualizations of neuroanatomical structure.

New Method: Here, we tested different nervous-tissue fixation procedures, conventionally used for transmission electron microscopy, to better establish X-PCI-CT-specific sample-preparation protocols. Extracted rat spinal medullas were alternatively fixed with a standard paraformaldehyde-only aldehyde-based protocol, or in combination with glutaraldehyde. Some specimens were additionally post-fixed with osmium tetroxide. Multiscale X-PCI-CT datasets were collected at several synchrotron radiation facilities, using state-of-the-art setups with effective image voxel sizes of 3.0^3 to $0.3^3 \mu\text{m}^3$, and compared to high-field magnetic resonance imaging, histology and vascular fluorescence microscopy data.

Results: Multiscale X-PCI-CT of aldehyde-fixed spinal cord specimens resulted in dense histology-like volumetric representations and quantifications of extended deep spinal micro-vascular networks and of intra-medullary cell populations. Osmium post-fixation increased intra-medullary contrast between white and gray-matter tissues, and enhanced delineation of intra-medullary cellular structure, e.g. axon fibers and motor neuron perikarya.

Comparison with Existing Methods: Volumetric X-PCI-CT provides complementary contrast and higher spatial resolution compared to 9.4 T MRI. X-PCI-CT's advantage over planar histology is the volumetric nature of the cellular-level data obtained, using samples much larger than those fit for volumetric vascular fluorescence microscopy.

Conclusions: Deliberately choosing (post-)fixation protocols tailored for optimal nervous-tissue structural preservation is of paramount importance in achieving effective and targeted neuroimaging via the X-PCI-CT technique.

7.2 Introduction

The diagnosis and study of spinal vascular diseases, such as hemorrhage and vasculitis, and of complex neurodegenerative disorders involving the spinal cord, such as amyotrophic lateral sclerosis (ALS) or multiple sclerosis (MS), require first of all the localization of small pathological lesions within the extended anatomy of the central nervous system (CNS), followed by the detailed examination of microstructural and even molecular content within identified pathological tissues. Up to now, though, a non-destructive 3D technique for the multiscale investigation of CNS tissue anatomy and pathology, i.e. which can provide both organ-level and cellular-level 3D structural information, is still not available amongst cutting-edge neuroimaging techniques, both in clinical and research settings.

Histological methods at the technological forefront of cellular-level structural and functional interrogations, for example, are still limited by an intrinsically 2D analysis of thin planar tissue sections and by labor-intensive protocols, lasting up to tens of hours when the goal is a 3D reconstruction (Annese *et al.*, 2014). Even the whole human brain histological atlases achievable today (Ding *et al.*, 2016), with in-plane cellular-resolution approaching 1 μ m/pixel, come short of a fully-volumetric CNS network representation. First, the resolution of the third dimension is restricted by the slice thickness, which determines a minimal sampling interval usually of around 50 μ m. Second, alleged 3D histological datasets need to face the error-prone challenge of slice-to-slice alignment, and, last, the projection of volumetric tissue structures within an individual histological slice onto a 2D plane leads to at least some degree of stereological bias (Schmitz and Hof, 2005) of histology-based neuro-morphological quantifications. Besides, tissue sectioning is notoriously sample-invasive and frequently causes tissue disruption and artifact formation in tissue sections, including both larger cracks as well as smaller tears in white and gray matter alike. Last, despite their undisputed and invaluable role in neuroscience, histological techniques rely heavily on staining and labeling of tissues to derive structural contrast and functional information, and thus fail to deliver a completely direct and dense characterization of CNS structure. Electron microscopy (EM) technology, for its part, enables unprecedented visualizations of even ultra-structural nervous tissue components, e.g. brain neuropil or spinal cord axonal microstructure (Duval *et al.*, 2019), and arguably affords the densest and most detailed representations of nervous tissue morphology available today. EM too, though, normally involves osmium staining, and is limited by tissue-sectioning procedures even more challenging than those required for histology.

The leading non-destructive 3D neuroimaging technique is high-field MRI, which, instead, trades less spatial resolution (compared to histology) for less sample-invasiveness. MRI, unlike histological neuroimaging work, can remain free from staining and labeling, and can produce truly-volumetric nervous tissue maps composed of (possibly) thousands of virtual slices. Ultra-high field MRI scanners are equipped with strong gradients, which permit access to 3D nervous tissue mesoscopic (Sear *et al.*, 2015) bio-scale structure without the need for sample sectioning, and afford high CNS soft-tissue contrast already in-vivo (Loureiro *et al.*, 2018). *Post-mortem* high-field MRI (PMMR) can efficiently reach, though obviously at the cost

of long measurement times, even higher CNS image quality(Calabrese *et al.*, 2018), and obtain e.g. exquisite soft-tissue contrast and ultra-high resolution within large human brain specimens(Sengupta *et al.*, 2018) (isotropic pixel sizes in the order of 50 μm), or even full rodent CNS visualizations(Harrison *et al.*, 2013) (isotropic pixel sizes in the order of 25 μm). For these reasons PMMR is finding increasing application as a tool for non-invasive virtual autopsy(Arthurs *et al.*, 2015), a setting where long image acquisition times (in the order of tens of hours) are still acceptable. Interestingly, PMMR can effectively characterize microstructures even beyond the resolution limit of the imaging system. This possibility exists due to the fact that signal intensity in CNS PMMR microscopy is influenced in different ways by the complex underlying microstructural environment within nervous tissue(Pallebage-Gamarallage *et al.*, 2018) (including for example axon fibers and cell density, but also myelin, gliosis or iron content) and since different state-of-the-art MRI modalities (e.g. structural, diffusion and susceptibility scanning modes) in combination with advanced MRI data reconstruction techniques can be applied to infer specific CNS connectivity and microstructure(Beaujoin *et al.*, 2018). For example, diffusion-based techniques, such as tractography, can be employed to infer the micro-connectivity of tens-of-micron-thick white-matter tracts even while employing imaging system pixel sizes only in the order of hundreds of microns(Plantinga *et al.*, 2016). These PMMR-based structural deductions are grounded on intense multimodal work, which has correlated MRI neuroimaging to ground-truth histological microstructural identifications; thanks to it, PMMR can be applied today to the study of disease-specific pathological CNS structural changes(Schmierer *et al.*, 2018). The indirect nature of these measurements, though, makes PMMR microstructural imaging intrinsically somewhat unreliable. Overall, both histology-based and MRI-based neuroimaging approaches available today still fail to capture direct and unbiased volumetric information on cellular structure and microvasculature within full-organ CNS samples.

Micro-CT technology can also play a role in CNS imaging, since, especially *post-mortem*, it can be efficiently used as a tool for 3D-virtual-histology of biological tissues(de Bournonville, Vangrunderbeeck and Kerckhofs, 2019), or to guide 3D histology(Senter-Zapata *et al.*, 2016): produced datasets correlate well to brain(Chen *et al.*, 2018) and spinal cord(Saito *et al.*, 2012) tissue histology, and can be routinely applied for dissection-free volumetric investigations e.g. of CNS lesions(Masís *et al.*, 2018), tumor(Kirschner *et al.*, 2016) and microvasculature(Unnikrishnan *et al.*, 2019). Traditional CT methodology, though, is based on X-ray absorption and, therefore, affords only weak soft-tissue contrast within low-absorbing biomaterials. For this reason, micro-CT neuroimaging typically involves the implementation of tailored contrast enhancement protocols, and can suffer from issues of inadequate stain penetration.

X-ray phase-contrast tomography (X-PCI-CT), for its part, is a label- and dissection-free experimental 3D imaging technique for biomedical research(Bravin, Coan and Suortti, 2013), which is emerging as an added-value technology for *post-mortem* neuroimaging. X-PCI-CT synchrotron radiation setups, by capturing X-ray phase modulations within a measured sample(Cloetens *et al.*, 1996) in addition to the absorption modulations of traditional (absorption-based) X-ray CT, can achieve increased CNS soft-matter morphological contrast(Beltran *et al.*, 2011) complementary to MRI(Schulz *et al.*, 2012). This method has

been proven sensitive to the underlying cellularity of nervous and tumor tissue and to microvasculature(Barbone *et al.*, 2018), and, by means of sub-micron pixel size imaging systems, can provide *post-mortem* cellular-resolution visualizations(Khimchenko *et al.*, 2018) fit for direct dense characterizations of nervous-tissue microstructure within extended samples. Spinal neuronal-network contrast at the single-neuron and single-vessel level, obtained via X-PCI-CT, differs from advanced in-vivo (window-based(Haghayegh Jahromi *et al.*, 2017)) and *post-mortem* (tissue-clearing-based(Soderblom *et al.*, 2015)) spinal cord fluorescence microscopy (FM) technology, in that it arises in the absence of any transgenic, antibody, chemical or viral fluorescent labeling agent. In this way, label-free X-PCI-CT measurements achieve dense and direct morphological 3D maps of neural microstructural connectivity, more limited compared to molecular cell-specific FM signals in terms of the provided functional information and resolution, but also freed from the sparse-labeling and limited sample-thickness issues of FM techniques. For all these reasons, it can be said that X-PCI-CT, a sectioning- and labelling-free volumetric dense & direct high resolution method for CNS analysis, holds the potential to provide a new perspective to the study of CNS vascular(Massimi *et al.*, 2016) and neurodegenerative diseases(Pinzer *et al.*, 2012; Massimi *et al.*, 2019), and supplement that of other more-established cutting-edge neuroimaging technologies.

Extensive *post-mortem* X-PCI-CT work on dissected spinal cord (SC) samples from rodent animal models has, thus far, been able to characterize anatomical intramedullary vascular structure(Cao *et al.*, 2016; Massimi *et al.*, 2016), mesoscale white- and gray-matter nerve fibers and neuron somas(Fratini *et al.*, 2015; Hu *et al.*, 2017), nanoscale axonal and myelin substructures(Bartels *et al.*, 2015), as well as pathological signs of various cord vascular injuries(Hu *et al.*, 2015; Miao *et al.*, 2016; Cao *et al.*, 2017) and of spinal cord neurodegeneration(Cedola *et al.*, 2017). These exploratory synchrotron X-PCI-CT studies demonstrate the impact this experimental technique can have on various spinal cord neuroimaging applications. And, as has already been the case for other now-established *post-mortem* CNS imaging techniques, it will be of paramount importance for the optimization of *post-mortem* spinal cord tissue contrast in X-PCI-CT images to develop adequate, goal-oriented, technique- and organ-specific CNS sample-preparation and tissue-fixation(Fix and Garman, 2000) protocols.

Interestingly, the X-PCI-CT research community has already evaluated several options to improve *post-mortem* X-PCI-CT soft-tissue imaging, for example by comparing ethanol vs. paraformaldehyde CNS tissue perfusion-fixation protocols(Stefanutti *et al.*, 2018), by testing multiple staining protocols based on iodine and heavy ions(Saccomano *et al.*, 2018), and even by trying different sample embedment procedures(Töpperwien *et al.*, 2019) and imaging parameters(Strotton *et al.*, 2018). In this work, we test the state-of-the-art multi-step nervous tissue sample-preparation procedure historically designed for transmission EM(Park *et al.*, 2016) (TEM), i.e. immersion-fixation with a combination of aldehydes, followed by osmium tetroxide impregnation. Conventional multi-aldehyde fixation with paraformaldehyde and glutaraldehyde is used to optimally preserve fast-degrading neuronal tissues, and is compatible with histological stains. Post-fixation by osmium staining, for its part, marks lipid, membrane and intracellular structures, and has traditionally been used to both enhance

image contrast and further fix neuronal white-matter structure. Here, we study the influence of each of these preparation steps on intra-medullary vascular- and neuronal-network contrast within multiscale X-PCI-CT images of excised rat spinal cord samples. In this way, we hope to enhance the quality of X-PCI-CT-based microstructural CNS imaging, and thereby help direct future sample-preparation design specific for spinal-cord *post-mortem* X-PCI-CT of both small animals and human origin.

7.3 Materials and Methods

7.3.1 Animals

For ethical reasons, spinal cords were obtained from 10 healthy wild-type Sprague-Dawley female rats already sacrificed as part of previously approved *in-vitro* neurotoxicity studies (Chiorazzi *et al.*, 2009) at the Milano-Bicocca University. All experimental procedures involving animals were approved by the local ethical committee and performed in accordance with all European laws on animal care.

7.3.2 Sample preparation

Nine of the animals were sacrificed under deep anesthesia with CO₂, followed by cervical dislocation. One-centimeter-long spinal cord samples, including the lumbar enlargement, were harvested by dissecting the medullary soft-matter from the bony spinal canal. Then, the 9 extracted SC samples were fixed by immersion following three alternative protocols (a-c), which represent the three consecutive steps traditionally employed for the preservation of CNS tissue and its preparation for TEM analysis:

- a. **PFA 4%**: 3 cord samples were immersed in 4% paraformaldehyde (PFA) phosphate-buffered solution 0.12M for 2 hours at room temperature.
- b. **PFA 4%, Glu 2%**: 3 cord samples were immersed in PFA 4% in combination with 2% glutaraldehyde (Glu) phosphate-buffered solution 0.12M for 2 hours at room temperature.
- c. **PFA 4%, Glu 2% + OsO₄**: 3 cord samples were immersed in PFA 4% in combination with Glu 2% for 2 hours at room temperature, and then post-fixed with osmium tetroxide (OsO₄) 2% in cacodylate buffer solution 0.12M for another 2 hours at room temperature.

After fixation, lumbar SC samples were divided in two portions, rostral and caudal. Rostral lumbar portions were embedded in epoxy resin for further histological analysis. Caudal lumbar portions, instead, were stored in PBS for several weeks until synchrotron-radiation X-ray phase-contrast CT imaging sessions. Right before imaging, samples were included in agar-agar gel within a sealed plastic Eppendorf tube to reduce sample dehydration and movement

during CT scans. Finally, one Sprague-Dawley female rat was used to reveal the vascular structure of the spinal cord via vascular fluorescence, as explained below (see Section 2.7).

7.3.3 Synchrotron X-PCI-CT imaging acquisitions

X-PCI-CT scans were carried out with the propagation-based (Snigirev *et al.*, 1995; Cloetens *et al.*, 1996) micro-X-PCI-CT setups of two synchrotron beamlines, the biomedical beamline (ID17) of the European Synchrotron (ERSF – Grenoble, France) and the TOMCAT beamline (Stampanoni *et al.*, 2007; Mader *et al.*, 2011) of the Swiss Light Source (SLS, Paul Scherrer Institute, Villigen, Switzerland). Both setups include a sCMOS PCO.Edge 5.5 (PCO AG, Germany) detector camera (Mittone *et al.*, 2017), mounted at a specific distance downstream of a sample stage, in turn equipped with translation and rotation precision motors used for fine 3D sample positioning, alignment and rotation. During scans, the sample-containing Eppendorf plastic tubes were mounted vertically on the sample stage and rotated around an axis perpendicular to the X-ray beam propagation plane, while keeping the X-ray source and detector fixed. Projection images at different angles were recorded to obtain CT datasets of the scanned samples. Three different effective detector voxel sizes, i.e. 3.0^3 , 0.7^3 and 0.3^3 μm^3 , were used to enable a multiscale morphological analysis of each soft-matter cord sample. The osmium-fixed samples were the only ones not imaged with the 0.3^3 μm^3 setup. The different effective voxel sizes were obtained by coupling the detector to Optique Peter™ indirect-conversion optics systems (Optique Peter, 2019) affording different options for magnification (2x, 10x, 20x magnification respectively for 3.0^3 , 0.7^3 and 0.3^3 μm^3 voxel systems). In all scans, the X-ray beam was shaped by tungsten slits to obtain a laminar beam, which impinged first on the samples, and then on the sCMOS detectors, equipped with 2560 x 2160 (H x V) 2D pixel matrices and either GGG, YAG:Ce (at ID17) or LuAG:Ce (at TOMCAT) scintillators to convert the X-rays into visible light. At 3.0^3 μm^3 , the entire 1 cm vertical length of the rodent cord samples was covered, by acquiring CT scans at 2 vertically-contiguous heights on the sample. At higher spatial resolution, only partial vertical sample coverage was obtained by the acquired 2 to 5 vertically-contiguous stacks.

micro-X-PCI-CT with 3^3 μm^3 voxel at ID17, ESRF: these scans were performed in the imaging hutch of the ID17 beamline, around 150 m away from a wiggler X-ray source, using a quasi-parallel monochromatic 40 keV incident X-ray beam issued from a double Si(111) Laue crystal monochromator system (Suortti *et al.*, 2000). Wiggler opening gaps were set to 55 and 45 mm respectively for w150 and w125 wiggler magnets; movable absorber filters included aluminum (1 mm) and carbon (0.8 mm). The propagation sample-to-detector distance was set to ~ 200 cm (Weitkamp *et al.*, 2011). CT scan parameters included: detector exposure time per angular projection, 150 ms; detector field of view (FoV), 7.7×6.5 mm^2 (H x V); number of equally-spaced CT angular projections, 3000; rotation angular range, 180° ; rotation axis position, center of the CT projection (so-called full-acquisition mode); single-stack scan time, 7.5 min; number of vertical stacks, 2; total sample scan time, 15 min.

micro-X-PCI-CT with 0.7^3 μm^3 voxel at ID17, ESRF: these scans were performed in the so-called Microbeam Radiation Therapy hutch of the ID17 beamline, around 45 m away from the wigglers, using a quasi-parallel pink X-ray beam with peak at 40 keV and a broad spectrum (Mittone *et al.*, 2020). Wiggler opening gaps were in this case set to 70 and 200 mm;

movable absorber filters included aluminum (1.0 mm), copper (0.7 mm) and carbon (1.15 mm). The propagation sample-to-detector distance was set to 50 cm. CT scan parameters included: detector exposure time per angular projection, 80 ms; detector FoV, 1.9 x 1.5 mm² (H x V); number of equally-spaced CT projections, 3000; rotation angular range, 360°; rotation axis position, at the edge of the CT projection (so-called half-acquisition mode); single stack scan time, 4 min; number of vertical stacks, 5; total sample scan time, 20 min.

micro-X-PCI-CT with 0.3³ μm³ voxel at TOMCAT, PSI: these scans were performed in the imaging hutch of the TOMCAT beamline, using a quasi-parallel monochromatic 21 keV incident X-ray beam, obtained via a W/Si double multilayer monochromator system (Mader *et al.*, 2011). The propagation sample-to-detector distance was set to 5 cm. CT scan parameters included: detector exposure time per angular projection, 120 ms; detector FoV, 0.86 x 0.70 mm² (H x V); number of equally-spaced CT projections, 3000; rotation angular range, 180°; rotation axis position, center of the CT projection; single stack scan time, 6 min; vertical stacks, 2; total sample scan time, 12 min.

7.3.4 X-PCI-CT image processing

Tomographic reconstructions were computed from collected projection images, using in-house software available at the respective beamlines, including the ESRF PyHST2 (Mirone *et al.*, 2014) software package and the TOMCAT tomographic reconstruction pipeline (Marone *et al.*, 2017). Briefly, the conventional filtered-back projection algorithm was used after application of the single-distance Paganin (Paganin *et al.*, 2002) phase-retrieval algorithm, in order to transform image edge-enhancement into pseudo-quantitative area-contrast (phase-images). We removed cupping artifacts, likely due to the local-tomography configuration of CT scans (i.e. with sample sizes larger than the detector FoV), via slice-by-slice normalization: CT images were divided by their Gaussian-blurred version (ImageJ (Schneider, Rasband and Eliceiri, 2012) Gaussian filter, sigma: 50 pixels), thereby suppressing the low-frequency image background. Moreover, we removed most CT ring artifacts by means of a published ring-removal approach (Lyckegaard, Johnson and Tafforeau, 2011), based on the ring-reducing subtraction of angularly filtered CT images from the original ones. Maximum intensity projections (MIPs) were computed by summing 50-100 consecutive reconstructed CT slices, using the ImageJ maximum intensity z-projection function, which projects 3D bright features onto a 2D plane. Minimum intensity projections (mIPs) were obtained in a similar way, but using the minimum intensity z-projection function instead, and thereby projecting dark image features. Different ImageJ preset lookup tables (LUTs) were used to recolor CT data (e.g. Viridis & Fire LUTs) and highlight different cord microstructural features. 3D renderings of CT data were computed using the commercial software VG Studio Max 3.2 (Volume Graphics GmbH, Heidelberg, Germany). Threshold-based segmentation approaches were used to extract cellular vs. vascular features, and the semi-transparent 'X-ray' 3D rendering algorithm, available in VG Studio Max, was chosen to render the segmented structures in 3D.

7.3.5 X-PCI-CT image analysis

Using an automatic threshold algorithm (Max Entropy(Kapur, Sahoo and Wong, 1985)) available in ImageJ, we could segment 3D masks of cell-like features from 0.7^3 and $0.3^3 \mu\text{m}^3$ voxel datasets. The same auto-threshold algorithm was applied to datasets from all three sample-preparation group. Obtained masks included all closed objects above the automatically-determined threshold (mainly cell somas, but also interrupted portions of neighboring blood-vessels). These masks were then analyzed with the '3D Object Counter' ImageJ plugin(Bolte and Cordelières, 2006) to quantify the volumes of unconnected segmented objects, and thereby obtain distributions of cell-like object sizes, expressed as equivalent-sphere diameters (after assumption of a spherical object shape). Manual threshold selection, instead, was used to extract 3D masks of vascular features only from both 0.7^3 and $0.3^3 \mu\text{m}^3$ voxel datasets. These vessel network masks were analyzed with the 'Local Thickness' ImageJ plugin(Hildebrand and Rügsegger, 1997), to obtain quantitative distributions of vascular thickness sizes. Violin plots of extracted cellular size and vascular thickness distributions were produced with the commercially available software GraphPad Prism (GraphPad Prism 8.0.0, GraphPad Software Inc., San Diego, CA, USA).

7.3.6 High-field MRI

The same Eppendorf plastic tubes used for X-PCI-CT, containing the agar-embedded rodent cords, were also used to acquire *post-mortem* high-field MRI with a preclinical 9.4 T MRI scanner (BioSpec 94/21; Bruker Biospin, Ettlingen, Germany). Axial spinal cord images were collected using a transceiver cryogenic quadrature RF surface probe (CryoProbe, catalog number Z125365, Bruker Biospin, Ettlingen, Germany). Two osmium-free samples were imaged with this MRI setup, one from the PFA 4% group and one from the PFA 4%, Glu 2% group. The acquired contrast-agent free MRI datasets were obtained using the following parameters: sequence, 3D FISP; repetition time (TR), 30 ms; echo time (TE), 11 ms; excitation pulse angle 20° ; FOV, $8 \times 8 \times 6 \text{ mm}^3$; acquisition matrix, $400 \times 400 \times 300$ voxels; voxel size, $20 \times 20 \times 20 \mu\text{m}^3$; number of averages, 16; scan time, ~ 19 hrs.

7.3.7 Histological stainings

Briefly, resin embedded samples were cut on a microtome (Leica RM2265, Leica Microsystems GmbH, Wetzlar, Deutschland) into $1.5\text{-}\mu\text{m}$ -thick sections, and then stained with toluidine blue. Due to the absence of osmium impregnation, which normally aids membrane preservation, we were obliged to use (non-standard) high staining times for both the PFA 4% sample preparation group (5 min) and the PFA 4%, Glu2% sample preparation group (2 min). A motorized Olympus BX63 equipped with DP80 camera and software cellSens (Shinjuku Monolith, Tokyo, Japan) was used for analyzing the slices and acquiring 20x reconstructed images after photo stitching.

Moreover, one healthy Sprague-Dawley rat, not involved in the X-PCI-CT measurements, was used to collect vascular fluorescence data. Briefly, after deep animal anesthesia with

ketamine and xylazine, a dose of 2 $\mu\text{gr}/\mu\text{l}$ Tomato Lectin (Robertson *et al.*, 2015) (FITC conjugated, Sigma-Aldrich, Saint Louis, USA) was injected into the proximal tail vein of the rat 2 minutes before its perfusion with PFA 4%. The dissected spinal cord was collected and a 0.1 mm slice observed using a Meta710 confocal microscope (Zeiss, Oberkochen, Germany).

7.4 Results

7.4.1 Impact of different fixation protocols

The 3D synchrotron X-PCI-CT data collected with the $3.0^3 \mu\text{m}^3$ voxel propagation-based setup (**Fig. 1**) permits a side-by-side qualitative comparison of image quality between each of the three steps in the rodent spinal cord sample preparation procedure, i.e. paraformaldehyde 4% (PFA 4%) fixation vs. PFA 4% + glutaraldehyde 2% (PFA 4%, Glu 2%) fixation vs. PFA 4%, Glu 2% + osmium tetroxide 1% impregnation (PFA 4%, Glu 2% + OsO_4). Within axial views of the medulla spinalis (**Fig. 1a**), all three sample preparations allow an at-least partial delineation of gross full-organ spinal cord anatomy, including spinal fissures, septa and sulci, the central canal, spinal funiculi, (superficial) extra-medullary spinal arteries and the anterior, lateral and posterior gray horns. Moreover, signs of intra-medullary vascular (red arrows in **1a** zooms 3x) and cellular (yellow arrows, likely motor neurons, in **1a** zooms 3x) microstructure are already visible at this resolution in all sample types, without need for vascular contrast-agent injection. OsO_4 post-fixation stains myelin sheaths within nerve fibers; this impregnation leads to the direct 3D visualization via X-PCI-CT of both (hypo-dense) unmyelinated axons (**Suppl. Fig. 1**) and osmicated (hyper-dense) myelinated nerve fibers (magenta arrows point to nerve fibers in **Fig. 1a** Zooms 3x, **Suppl. Fig. 1**).

In terms of image area contrast, some gray vs. white matter contrast is evident in all measured medullary axial and coronal SC virtual CT slices (**Fig. 1a-b**). Moreover, within osmium-free cords (PFA 4% and PFA 4%, Glu 2% preparation groups) the brightest image gray-level values arise from non-perfused blood-filled vessels and their thick endothelial cell walls, followed in order by the gray levels of cell-soma structures, of gray-matter parenchyma and, last, of white matter. The addition of osmium (PFA 4%, Glu 2% + OsO_4 preparation group), for its part, leads to an inversion of intramedullary nervous tissue contrast. The osmium impregnation itself becomes the highest-Z material present, leading to enhanced white-matter brightness compared to gray matter tissue intensity. This inversion influences also the signal intensity within cell-like structures (zooms 3x in **Fig. 1a**, inserts in **Fig. 1b**), with neurons in osmicated samples appearing as the darkest structures, compared to neurons in staining-free samples, which instead look mildly denser than surrounding neuropil. Vascular feature gray-level brightness, instead, seems unperturbed by the osmium metal fixative.

Maximum and minimum intensity projection (MIP and mIP, see **Methods**) images were calculated to highlight and compare the volumetric development of respectively the brightest and darkest image features within different extended axial and sagittal CT data volumes (**Fig. 1 c-d**). In these pseudo-volumetric maps, we can observe extended vascular tree morphology (red arrows) as well as local cyto-architecture (yellow arrows) within samples of all

preparation groups. Within MIP datasets of osmium-free samples (PFA 4% and PFA 4%, Glu 2% preparation groups), extensive deep micro-vasculature can be recognized within both gray and white-matter tissues. MIPs of osmium-stained medullas, instead, allow good renderings of vascularization within gray-matter, but only little vascular structure visualization within the white-matter. In its place, they portray the detailed volumetric structure of white-matter nerve bundles, e.g. the pseudo-3D out-branching of individual white-matter fibers (magenta arrows) toward more-internal medullary gray-matter tissue (**Figs. 1d, 2d-e, 2i**). Deep motor neuron populations are revealed within MIP maps of osmium-free spinal cords and within MIP of osmicated ones (yellow arrows, **Fig. 1d**).

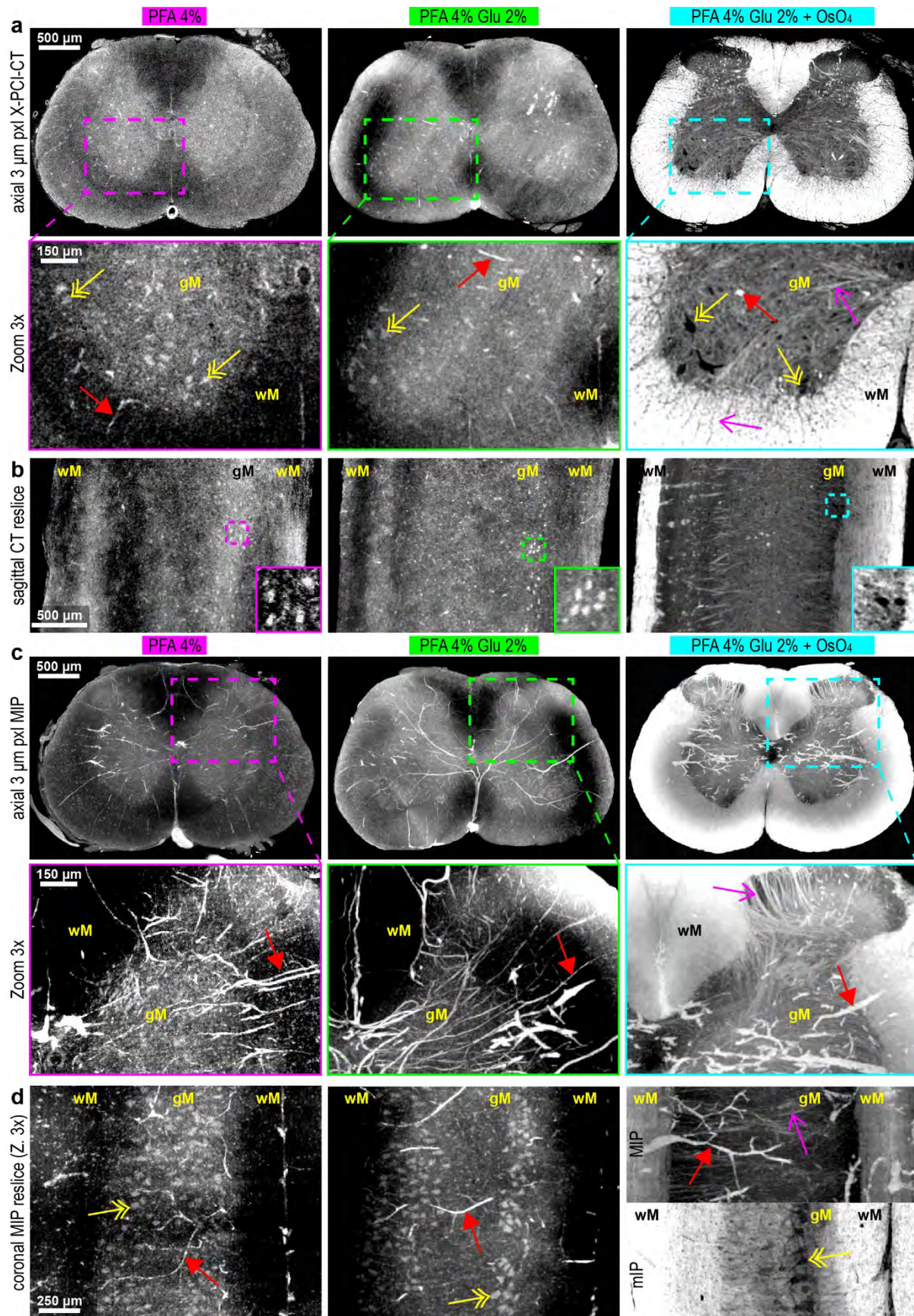


FIGURE 1. Impact of aldehyde fixation and osmication of rat spinal cords on X-PCI-CT with $3.0^3 \mu\text{m}^3$ voxels. Representative (a) axial and (b) sagittal views from *post-mortem* $3.0^3 \mu\text{m}^3$ voxel 3D X-PCI-CT datasets of rodent spinal cord specimens fixed by immersion respectively with paraformaldehyde 4% only (PFA 4%), with PFA 4%

and glutaraldehyde 2% (PFA 4%, Glu 2%), and with PFA 4%, Glu 2% plus post-fixation in osmium tetroxide (PFA 4%, Glu 2% + OsO₄). Zoomed 3x images in **(a)** show axial gray vs. white matter contrast (gM, wM), and vascular (red arrows), cellular (yellow arrows) and nerve fiber (magenta arrows) microstructures. Inserts in **(b)** show sagittal cellular features. Note nervous tissue and structure contrast inversion in the osmicated samples. **(c)** Axial and **(d)** zoomed 3x sagittal MIP maps (plus one mIP map) highlight bright (dark) features pseudo-volumetrically. Again, vascular, cellular and fiber structure detail within gM and wM is indicated with red vs. yellow vs. magenta arrows. Agar gel background was masked in all presented CT images for clarity.

7.4.2 X-PCI-CT with osmium

X-PCI-CT imaging data on extended sections of osmium-stained (PFA 4%, Glu 2% + OsO₄) cord medullas (**Fig. 2**) confirms that an efficacious homogeneous penetration of the Os metal within small rodent spinal cord samples was obtained, leading to very high-contrast nervous tissue visualizations. These measurements enable the 3D exploration of micrometric medullary anatomy in axial, sagittal and coronal views (**Fig. 2a**). Moreover, pseudo-volumetric MIP- and mIP-based rendering of vascular, fiber (**Fig. 2b**) and cellular (**Fig. 2c**) structures, well-visible in zoomed multi-view displays (**Fig. 2d-f**), demonstrate the ability of the method to capture extended feature-specific 3D networks deep within soft-matter CNS tissue. mIP maps of dark cellular features can be recolored to mimic cellular fluorescence microscopy data (**Fig. 2g**), and their virtual re-slicing in all 3 orthogonal planes proves that dissection-free full-organ rodent cord 3D cellular imaging is possible with this sample preparation and imaging approach. Moreover, the differential recoloring of MIP vs. mIP maps (**Fig. 2h**) makes it evident that the achieved image contrast within these contrast-enhanced osmium-stained medullas is sufficient to separate, and independently study, bright hyper-dense vasculature and fiber networks, recolored to red-violet tones, vs. dark hypo-dense neuron populations, recolored to green-yellow tones. The high level of organ-wide CNS structure morphological detail attainable is evident in the zoomed-in displays (**Fig. 2i-j**), extracted from the full-sample MIP and mIP maps (**Fig. 2b-c**): the fine structure of individual osmium-stained nerve fibers, of individual intra-medullary micro-vessels (**Fig. 2i**), and even of individual differently-sizes neurons and their somatic and dendritic sub-structure (**Fig. 2j**), appears quite well defined.

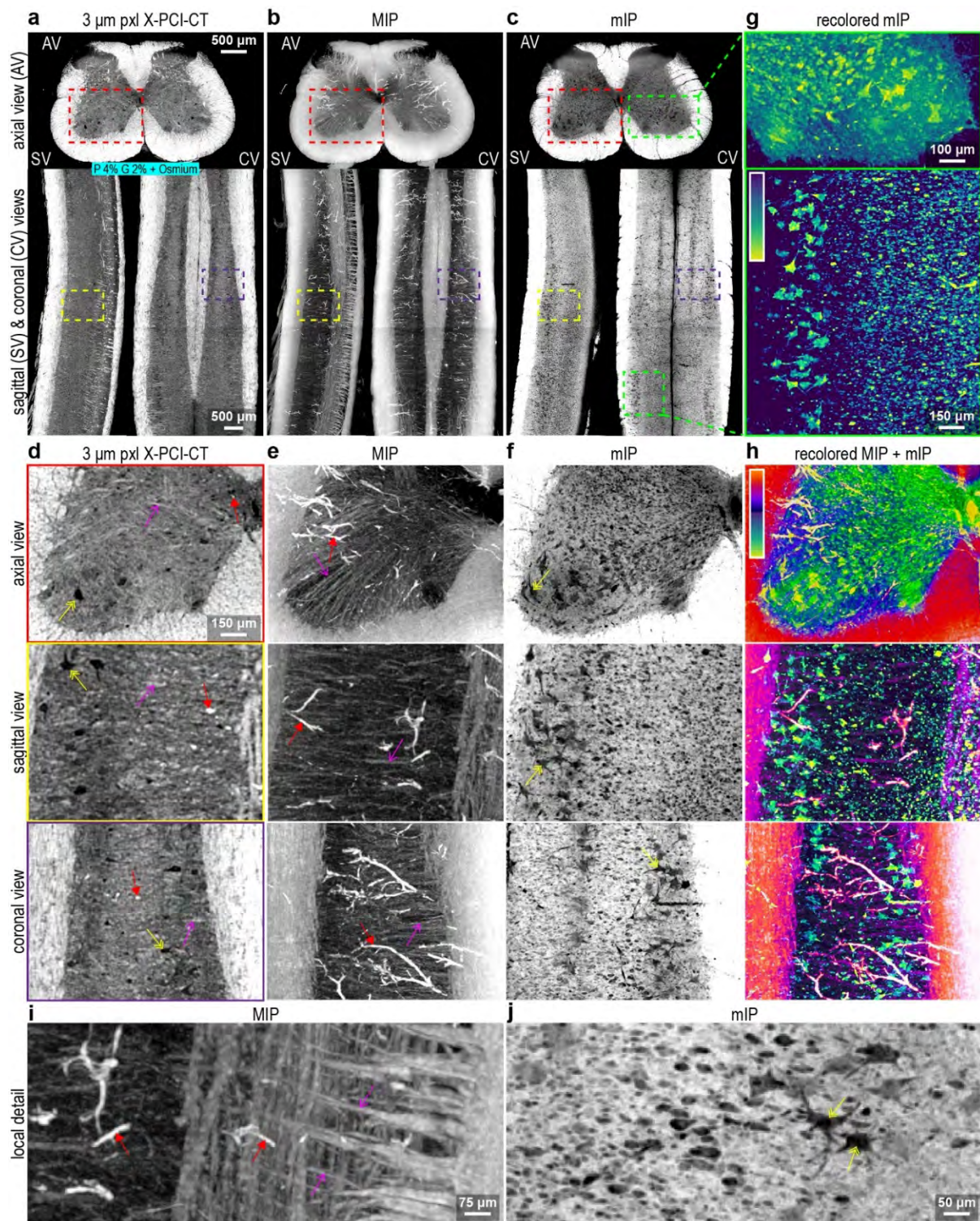


FIGURE 2. X-PCI-CT with $3.0^3 \mu\text{m}^3$ voxels of osmicated rat spinal cords. (a) CT vs. (b) MIP vs. (c) mIP X-PCI-CT maps showing axial, sagittal and coronal views of a PFA/Glu aldehyde-fixed & osmium-stained rat spinal cord (PFA 4%, Glu 2% + OsO₄ sample preparation group). (d-f) axial, sagittal and coronal zoomed (2x) views of image data from the color-associated dashed rectangles in (a-c). Red, yellow and magenta arrows indicate respectively vascular, cellular and fiber microstructure. (g) Zoomed views of mIP maps within the connected dashed rectangles in (c), recolored with the 'Viridis' LUT. (h) Sum of the MIP data in (e), recolored with the 'Fire' LUT, plus the mIP data in (f), recolored with the 'Viridis' LUT. In (g-h) color bars specify the recoloring of low-to-high CT gray-levels. (i-j) 4x ultra-zooms of (i) MIP and (j) mIP data, extracted respectively from (b) and (c), display

detailed local morphology of vascular (red arrows), cellular (yellow arrows) and fiber (magenta arrows) microstructure. Agar gel background was masked in all presented CT images for clarity.

7.4.3 Sub-micron X-PCI-CT of the spinal cord

To further explore the potential of each sample preparation method for morphologic 3D spinal cord X-PCI-based neuroimaging, we collected sub-micron voxel size synchrotron X-PCI-CT data on selected rat cord samples (**Fig. 3**). $0.7^3 \mu\text{m}^3$ voxel MIP and mIP data shows that the feature contrast already observed in micro-CT datasets (**Fig. 1**) can be similarly recapitulated also in sub-micron CTs. Again, vasculature generates the brightest voxel values in all cords, and osmium-stained nervous tissues produce inverted gray vs. white-matter contrast compared to unstained ones. Motor neuron somas within gray-matter horns, in particular, appear within aldehyde-only fixed samples (PFA 4% and PFA 4%, Glu 2% preparation groups) as mildly hyper-intense pyramidal structures containing bright nucleoli, whereas as dark similarly-shaped features containing dark nucleoli within osmium-stained samples (PFA 4%, Glu 2% + OsO_4 preparation group) (**Fig. 3a**). Furthermore, since they have slightly-differing gray-levels, cellular vs. vascular anatomical structures can be manually segmented based on their gray-level threshold, enabling the color-coded 3D rendering and volumetric differentiation of cellular and vascular features present within extended nervous-tissue datasets (**Fig. 3b**, **Suppl. Fig. 2a-c**).

Non-osmicated medullas (PFA 4% and PFA 4%, Glu 2% preparation groups) were analyzed also with a $0.3^3 \mu\text{m}^3$ voxel X-PCI-CT setup (**Fig. 3c**) in order to verify cellular-level tissue preservation and demonstrate that sub-cellular-level structural visualizations are achievable by *post-mortem* sub-micron X-PCI-CT. At this ultra-high resolution, we recognize single neuronal cells perfused by surrounding micro-vasculature, as well as some intra-cellular structure: cell bodies of individual motor neurons, including their bright/dense cell nucleoli and their dendritic components, as well as other smaller likely glial cells, are visible deep within un-sectioned SC samples (from both types of aldehyde-fixation) without need for staining or contrast agent injection (**Fig. 3c**). Furthermore, these microstructural data show that both fixation procedures preserved nervous tissue structural integrity. Therefore, they could be used to visualize intra-cord vascular and cellular networks in 3D (**Fig. 3d**, **Suppl. Fig. 2d-e**), by applying manual threshold segmentation approaches to separate vascular vs. cellular features based on their gray-level. These 3D representations characterize the volumetric arrangement of local cells and capillaries, and even display some intra-cellular detail, e.g. nucleolar detail.

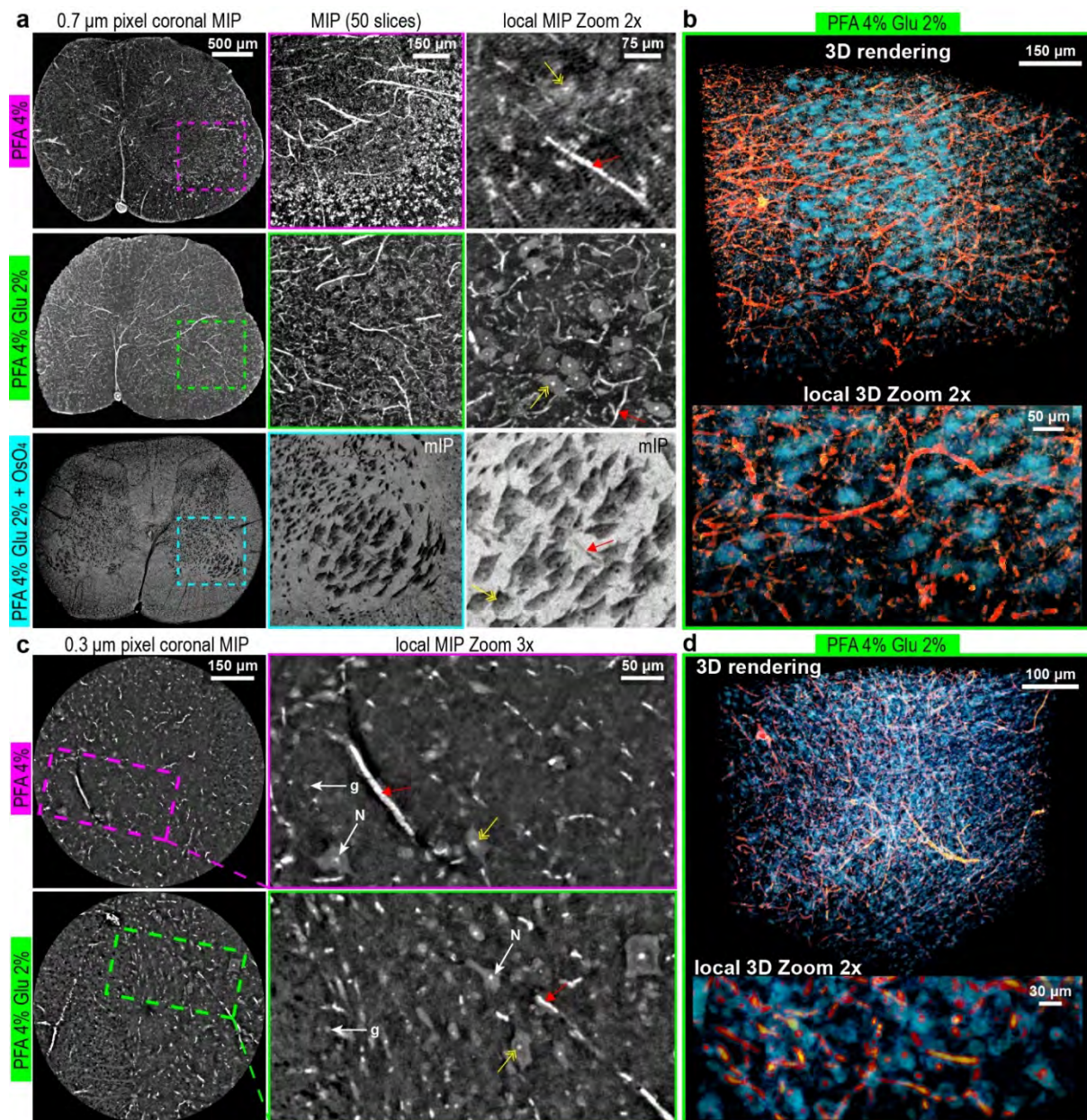


FIGURE 3. Impact of aldehyde fixation and osmication of rat spinal cords on X-PCI-CT with sub-micron voxels. (a) Representative axial views from *post-mortem* $0.7^3 \mu\text{m}^3$ voxel 3D X-PCI-CT MIP datasets of rat spinal cord medullas fixed by immersion respectively with paraformaldehyde 4% only (PFA 4% preparation group), with PFA 4% and glutaraldehyde 2% (PFA 4%, Glu 2% preparation group), or with PFA 4%, Glu 2% plus post-fixation in osmium tetroxide (PFA 4%, Glu 2%, OsO₄ preparation group). 50-slice MIP maps (or mIP maps for the third group), computed from image data within the dashed rectangles in the left-most panel column, highlight bright (or dark in the mIPs) features pseudo-volumetrically. Zooms 2x show local vascular and cellular detail, labelled respectively with red and yellow arrows. (b) 3D rendering, after threshold-based segmentation, of a 100-slice $0.7^3 \mu\text{m}^3$ voxel CT dataset from a PFA 4%, Glu 2% preparation group spine, showing vascular features, colored in shades of red, and cellular features, colored in shades of blue. The 2x zoom shows 3D detail of local medullary tissue microstructure. (c) Representative axial $0.3^3 \mu\text{m}^3$ voxel *post-mortem* local X-PCI-CT MIP data of rat cords fixed with PFA 4% or PFA 4% + Glu 2% in combination. Local MIP zooms (3x) visualize vascular vs. cellular detail (red vs. yellow arrows), neurons (N) vs. glial cells (g). Note that intra-cellular microstructure is resolved here. (d) 3D rendering, obtained as in (b), of a 150-slice $0.3^3 \mu\text{m}^3$ voxel X-PCI-CT dataset of fixed medullary tissue from a PFA 4%, Glu 2% preparation group specimen. Note that bright/dense intra-cellular nucleoli are rendered in red, like local micro-vasculature, and neuronal cell bodies in blue. Agar gel background was masked in all CT images for clarity.

7.4.4. Morphological quantifications

The collected multiscale 3D X-PCI-CT datasets imaging CNS tissue seem well suited for structural analyses of various kinds. Here, by selecting and analyzing volumes of lateral gray horn spine tissue data, we performed a proof-of-principle quantification of cell-like and vascular image features (**Fig. 4, Suppl. Fig. 3**). All three spinal cord sample-preparation procedures were included in the analysis of $0.7^3 \mu\text{m}^3$ data (**Fig. 4a**), whereas the quantification of $0.3^3 \mu\text{m}^3$ data (**Suppl. Fig. 3a**) was limited to fixed unstained cord samples (PFA 4% and PFA 4%, Glu 2% preparation groups). Procedurally, from the gray-level datasets (**Fig. 4a, Suppl. Fig. 3a**), masks containing cell-like microstructures (**Fig. 4b, Suppl. Fig. 3b**) were extracted via an automatic (Kapur, Sahoo and Wong, 1985) threshold-based segmentation technique, masks containing vascular features (**Fig. 4c, Suppl. Fig. 3c**) instead via manual thresholding (see **Methods**). The applied auto-threshold algorithm, which extracts all types of closed objects within a certain gray-level regime, did not always discriminate well between voxels pertaining to hyper-dense cell somas, and neighboring voxels, pertaining to local vasculature. This is especially evident in the segmentations obtained from 0.7^3 (**Fig. 4b**) and $0.3^3 \mu\text{m}^3$ (**Suppl. Fig. 3b**) voxel data of PFA/Glu samples, due to the high vascular-feature contrast in these images. Therefore, cell-like object masks contained also some extraneous local vessels. Since they were obtained manually, vascular masks (**Fig. 4c, Suppl. Fig. 3c**), instead, did not contain extraneous objects.

ImageJ (Schneider, Rasband and Eliceiri, 2012) implementations of established 3D object measurement algorithms (Hildebrand and Rügsegger, 1997; Bolte and Cordelières, 2006) were used to quantify the size of the extracted cell-like objects (**Fig. 4b, Suppl. Fig. 3b**) and the thickness of the extracted vasculature (**Fig. 4c, Suppl. Fig. 3c**), obtaining distributions for each type of sample preparation. The analysis of cell-like microstructure (graphs in **Fig. 4b, Suppl. Fig. 3b**) measured that a majority of detected cell-like objects has diameters falling within a 2-20 microns range, which is appropriate for various types of rodent neural cells (Flood and Coleman, 1988). Vessel thickness distributions (graphs in **Fig. 4c, Suppl. Fig. 3c**), for their part, measured detected vascular diameters in the 2-10 microns range. Obviously, higher-resolution datasets (**Suppl. Fig. 3**), which enable the detection of smaller objects than lower-resolutions scans (**Fig. 4**), overall led to cell-like objects being quantified as smaller and to vasculature-like tubular structures as thinner. Overall, these microstructure quantifications resulted in comparatively quite similar distributions for each of the three different cord sample preparation protocols (**Fig. 4b-c, Suppl. Fig. 3**).

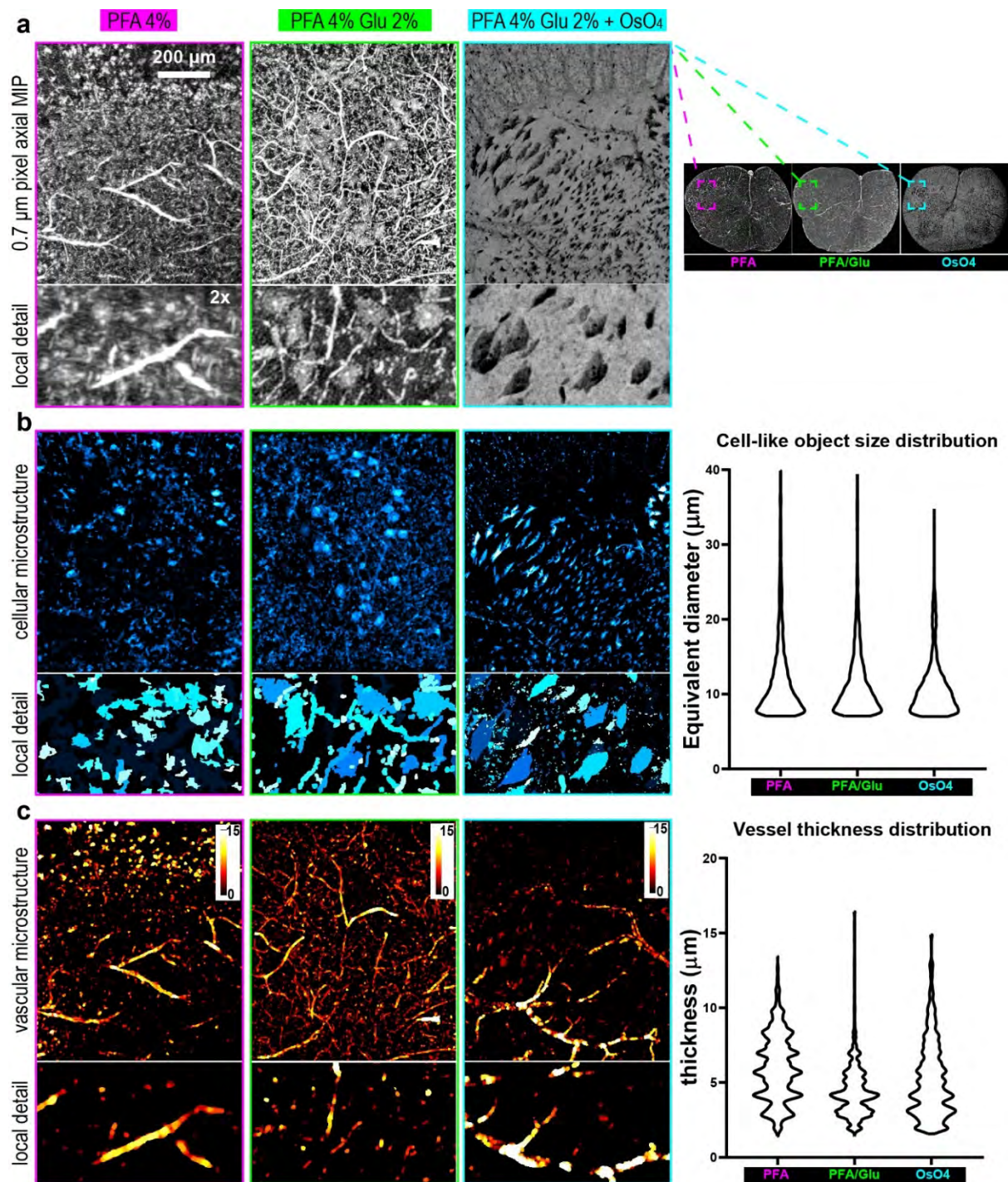


Figure 4. Quantification of cellular and vascular parameters using X-PCI-CT data with $0.7^3 \mu\text{m}^3$ voxels. (a) $0.7^3 \mu\text{m}^3$ voxel axial X-PCI-CT MIP data of lateral horn gray-matter tissue, collected from cords prepared with all three different sample-preparation protocols (PFA fixation vs. combined PFA/Glu fixation vs. PFA/Glu fixation + OsO₄ impregnation). (b) recolored masks of X-PCI-CT MIP data from (a), segmented via an automated threshold algorithm (see **Methods**) to extract cell-like microstructure. Local (2x zoomed) mask detail is also displayed to better visualize the result of the segmentations. Especially in the PFA/Glu data, some of the segmented objects or voxels actually pertained to vascular structure. Violin plots report size distributions obtained by extracting the equivalent diameter of each distinct 3D object in the masks, quantified via an image analysis plugin of ImageJ specific for populations of 3D objects (see **Methods**). (c) quantitatively-recolored masks of X-PCI-CT MIP data from (a), segmented by manual threshold selection to extract vascular microstructure. Color-coding quantifies the internal thickness of tubular structures (calibration bar in μm), computed with an ImageJ image-analysis plugin specific for tubular 3D structures (see **Methods**). Local mask detail is displayed to better visualize the

goodness of the segmentations. Violin plots report vessel thickness distributions, obtained by combining all voxel values in the corresponding image masks in (c).

7.4.5 X-PCI-CT vs. MRI vs. histology

To better benchmark our multiscale *post-mortem* spinal cord X-PCI-CT imaging results (**Fig. 1-3**), we imaged the same (caudal) lumbar SC samples also with a 9.4 T PMMR setup, i.e. state-of-the-art non-invasive volumetric imaging technology. Moreover, we analyzed the set-aside rostral SC samples with traditional toluidine blue histology in combination with optical microscopy (OM), i.e. state-of-the-art 2D cellular imaging technology. A side-by-side comparison of histological vs. X-PCI-CT-based vs. MRI-based medullary axial views is presented in **Fig. 5**. The $3^3 \mu\text{m}^3$ voxel X-PCI-CT panels of non-osmicated cords (PFA 4% and PFA 4%, Glu 2% preparation groups) display the potential of this technique for a staining-free full-organ 3D examination, which detects local vascular and cellular microstructure (**Fig. 5a-b**). Comparatively, the $20^3 \mu\text{m}^3$ voxel PMMR data show superior gray vs. white matter contrast but also an only at-best pre-cellular resolving power, leading to only partial visualizations of underlying SC cellular and fiber structure (see inserts in **Fig. 5a-b**). Cord impregnation with osmium (PFA 4%, Glu 2%, OsO_4 preparation group), for its part, leads to much-enhanced white-matter contrast within X-PCI-CT data (**Fig. 5c**), as well as a clear delineation of white-matter fiber structure, surpassing the quality of the white-matter visualizations recapitulated in both X-PCI-CTs and PMMR images (both 3D FISP and 3D FISP phase maps, **Fig. 5a-c**) of non-osmicated SC samples.

The full medullary views of toluidine blue-stained 2D histology data (**Fig 5a-c**) served, first of all, as ground-truth for the correct interpretation of the 3D imaging datasets, and were used to assess the white vs. gray matter contrast obtained via X-PCI-CT and PMMR: though histological toluidine blue staining seems undeniably superior in terms of nervous-tissue differentiation capability, especially after osmium post-fixation, acceptable histology-like macroscopic gray vs. white-matter tissue delineation seems indeed possible also via both virtual-histological imaging techniques. Once again, the most striking differences can be recognized in the unequal possibilities for cellular-resolution imaging of the three techniques (inserts in **Fig. 5a-c**). Already without need for further magnification, the histological optical-microscopy approach affords the most detailed cellular-level visualizations, with boundaries of individual neural cells appearing very well defined by the histological stain. Label-free density-based detection of cellular structure by X-PCI-CT, for its part, enables at least some cell-soma visualization already within isotropic $3.0^3 \mu\text{m}^3$ voxel data, though at the price of less cell-structure boundary definition compared to the histological approach. Last, the isotropic $20^3 \mu\text{m}^3$ voxel PMMR data, instead, comes completely short of resolving any well-defined cell structure, with underlying cord structural micro-anatomy only vaguely perceptible within pixelated data visualizations.

Moreover, the toluidine blue histology, collected from the same organs used to produce the samples analyzed via X-PCI-CT, was essential to verify and compare (at the cellular scale) the degree of nervous-tissue preservation in the three different rodent cord sample groups. Overall, gross anatomical structures (e.g. gray-matter horns, white matter columns, etc.)

within spinal cord tissues from all three sample-preparation groups (PFA 4% vs. PFA 4%, Glu2% vs. PFA4%, Glu2% + OsO₄) are well preserved and easily distinguishable within 2D toluidine blue histological slices (first column in **Fig. 5a-c**). Nevertheless, higher-magnification OM images of the same sections (**Fig. 5d-e**, **Suppl. Fig. 4**) provide the cyto-structural information necessary to observe protocol-dependent differences in cellular-level tissue preservation within both white- (**Fig. 5d**) and gray-matter (**Fig. 5e**) tissues areas. Evident similarities and differences between fixation protocols can be noted: sub-cellular motor neuron structure within ventral horns, such as nuclei and nucleoli, are well distinguishable in histological slices from all preparation cases; unsurprisingly, they are thus detectable via X-PC-CT (yellow arrows in **Fig. 5d**). Also motor efferent nerve fibers, passing through the white matter, can be recognized in histology data from all three cases, and are visible – though only barely – also within X-PCI-CT data (azure arrows in **Fig. 5e**, **Suppl. Fig. 4b**). Upon closer inspection of the histological data, however, it is evident that samples from the PFA 4%, Glu 2% + OsO₄ group are the best preserved ones: osmication, which aids the fixation of lipid-rich cell structures (e.g. cellular membranes) in this group, visibly marks myelination at the level of single nerve sheaths (**Suppl. Fig. 4**). Instead, the poor lipid preservation in non-osmicated samples (PFA 4% and PFA 4%, Glu2% samples-preparation groups), which imposed higher staining times for acceptable cellular structure during preparation (see **Methods**), is responsible for the excessively dark blue-staining of motor neurons in the non-osmicated slices compared to neurons in osmicated ones (**Fig. 5d**). Moreover, such lipid wash-out appears especially evident in dorsal horn neuropil, where sensory afferent fibers were found to be well preserved only within osmicated samples (green arrow in **Suppl. Fig. 4a**). This histological finding explains the almost complete lack of fiber visualization in dorsal horn X-PCI-CT images of non-osmicated cords, and instead the quite rich fiber networks visible in osmicated ones (green arrow in **Suppl. Fig. 4a**). Last, the lack of complete lipid fixation determines also the scarcity in dark blue myelin sheaths, which can be observed around axons in white matter areas within PFA 4% and PFA 4%, Glu2% samples (magenta arrows in **Fig. 5e**, **Suppl. Fig. 4b-c**). Such a poor lipid-layers preservation is thus likely at least partially responsible for the overall weak structural definition and contrast of white-matter structures (e.g. minute individual sections of nerve fibers) within X-PCI-CT images of non-osmicated SC samples (magenta arrows in **Fig. 5e**, **Suppl. Fig. 4b-c**).

Much subtler differences can be appreciated between the PFA-only group aldehyde fixation group and the mixed PFA/Glu, with the latter expectedly preserving the morphology of individual white-matter bundles slightly better than the former (**Fig. 5e**). Overall, the comparison of cellular toluidine blue histology to sub-micron X-PCI-CT data (**Fig. 5d-e**) shows that, at sub-micron resolutions, X-PCI-CT can provide cellular and micro-vascular visualizations comparable to histological ones (**Fig. 5d**) already within non-osmicated cords. Distinctive of X-PCI-CT, though, is that these structures reside deep within un-sectioned rodent spinal medullas and are detected based on local density levels without need for any cellular staining or labeling. Addition of osmium impregnation in pre-imaging protocols leads to superior lipid fixation within samples, and thus to enhancement of contrast and structural detail in X-PCI-CT data of white-matter tissues (magenta arrows in **Fig. 5**, **Suppl. Fig. 4b-c**). Interestingly, though, the osmium reduces the visibility of individual blood-filled sharp-

boundary-rich micro-vessels, which are clearly identifiable only in data from osmium-free samples (red arrows in **Fig. 5, Suppl. Fig. 4a**).

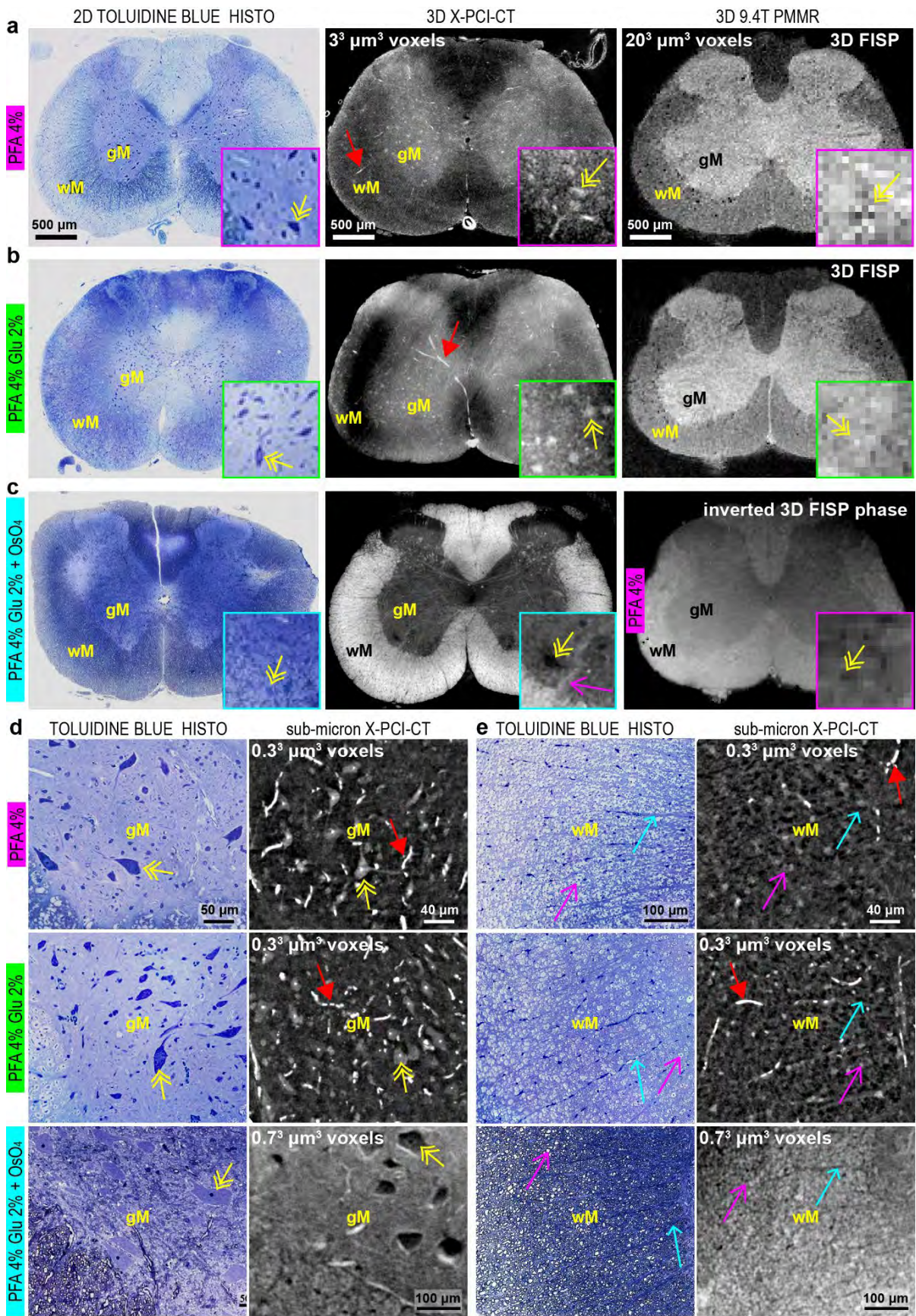


Figure 5. 3D X-PCI-CT vs. 3D PMMR and 2D cellular histology. (a-c) Comparison of rodent spinal medulla axial views, obtained via 2D toluidine blue histology vs. $3^3 \mu\text{m}^3$ voxel 3D X-PCI-CT vs. $20^3 \mu\text{m}^3$ voxel 3D 9.4 T PMMR (3D FISP sequence), using cords prepared *post-mortem* via (a) PFA 4%, or (b) PFA 4%, Glu 2%, or (c) PFA 4%, Glu 2% fixation + Osmium impregnation. In (c), the PMMR 3D FISP phase image was acquired from a PFA 4% sample, and inverted to best match the inverted-contrast of osmicated cord X-PCI-CT data. Note the display of gray-matter (gM) vs. white-matter (wM) contrast in all cases, and of high-contrast vascular structure only in X-PCI-CT datasets of non-osmicated samples (red arrows). Inserts (3x zooms of the larger images) show differences between techniques and preparations in the visualization of cellular structure (yellow arrows) within ventral gray-horn tissues. X-PCI-CT of osmicated cords also displays local enhanced white-matter fiber delineation (magenta arrow). (d-e) Magnified (20x with respect to data in (a-c)) optical microscopy data of toluidine blue-stained histological slices vs. isometric sub-micron (0.7^3 to $0.3^3 \mu\text{m}^3$ voxel) X-PCI-CT data of un-sectioned cord tissue, centered respectively on (d) ventral horn gM and (e) lateral column wM tissues. Sample data from all three sample-preparation protocols as in (a-c) are included in (d-e). Note the abundance of micro-morphology detail, with vascular vs. cellular vs. white-matter (e.g. minute individual sections of nerve fibers) structures indicated respectively by red vs. yellow vs. magenta arrows, as well as motor efferent fibers passing through the white matter (marked with azure arrows). Agar gel background was masked in several of the presented CT and MRI images for clarity.

7.4.6 Multiscale 3D X-PCI-CT vs. 2D histology & 3D fluorescence-histology

Last, we compared multiscale X-PCI-CT data (Fig. 6a-b), obtained by scanning the same staining-free PFA/Glu-fixed rodent spinal cords with 3 to $0.3^3 \mu\text{m}^3$ voxel setups in succession, to cutting-edge neuroimaging technology for the investigation of cellular and vascular microstructure within CNS tissue (Fig. 6c-d), i.e. respectively to traditional 2D histology (Fig. 6c) and 3D confocal fluorescence microscopy (Fig. 6d). Multiscale X-PCI-CTs can reach pre-cellular to intra-cellular resolutions and display pseudo-histological detail in the imaging of both neurons (Fig. 6a) and microvasculature (Fig. 6b). Comparatively, 2D toluidine blue histological staining of cord tissue, combined with optical microscopy imaging of thin slices, affords pre-cellular to intra-cellular structure visualizations that are superior in their (nanometric) spatial resolution, compared to sub-micron X-PCI-CT data (Fig. 6c). Histological views, though, are mono-directional and 2D, compared to 3D X-PCI-CTs, which enable, via virtual reslicing and 3D segmentation of data, morphological explorations of individual cells within deep neuronal populations in arbitrary planes and in 3D (Fig. 6c).

PFA-perfused & Tomato Lectin-labelled vessels within a $100 \mu\text{m}$ -thick slice of rat cord tissue were imaged with a confocal microscope at two different levels of magnification (Fig. 6d). This technology delivers 3D vascular representations that volumetrically outline endothelial-cell vessel-walls, rendering tube-like structures, especially well visible at the highest magnifications. Similar 3D vascular imaging was also achieved via X-PCI-CT, by locally scanning nervous tissues deep within extended PFA/Glu-fixed SC samples with sub-micron resolution setups, and then by segmenting out masks of hyper-intense voxels. This approach resulted in much more extended and dense vascular network representations (Fig. 6d).

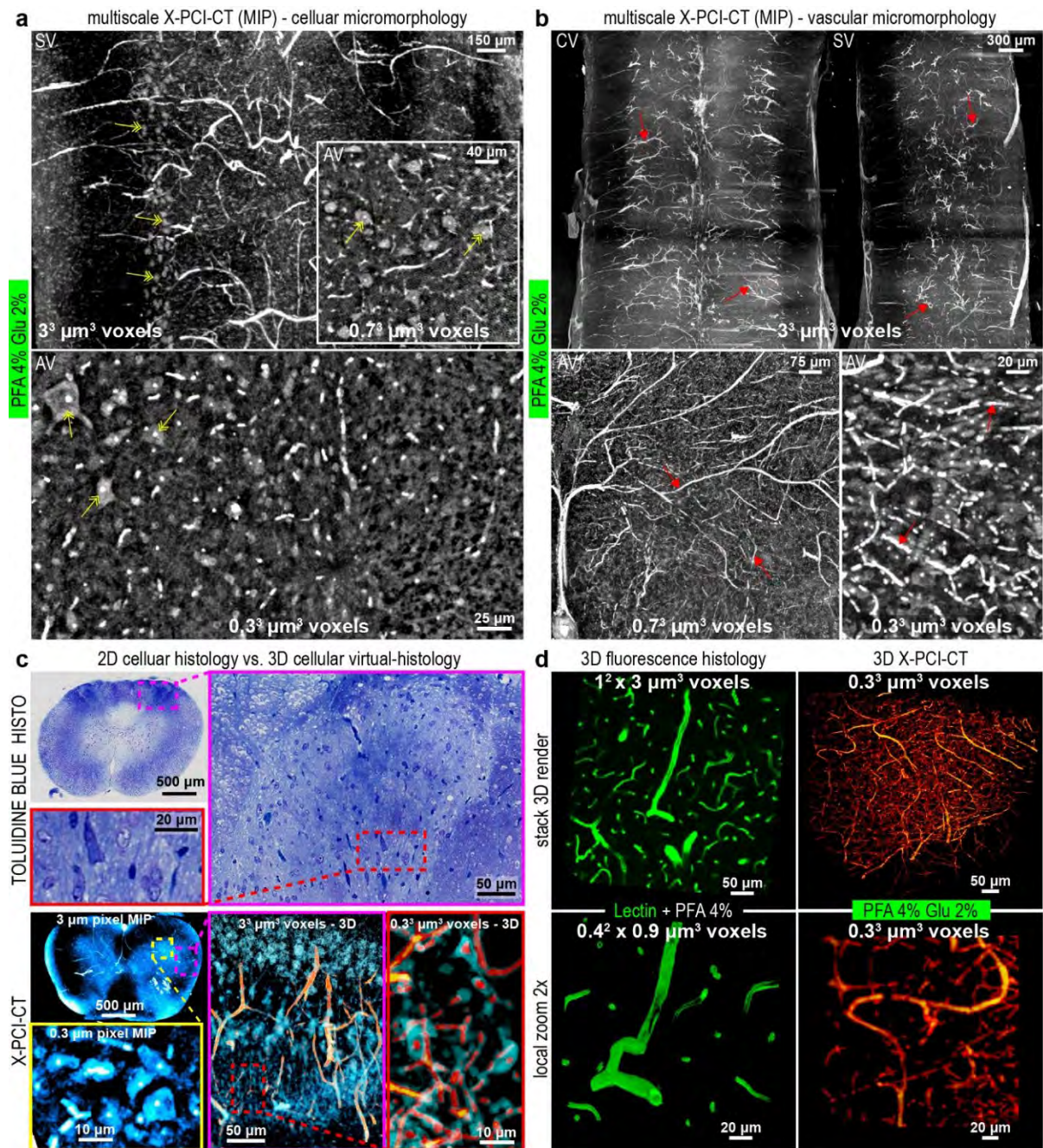


Figure 6. Multiscale 3D X-PCI-CT vs. 2D cellular histology and 3D vascular fluorescence-histology. (a-b) sagittal (SV), coronal (CV) and axial (AV) views of 3^3 to $0.3^3 \mu\text{m}^3$ voxel multiscale 3D X-PCI-CT MIP maps of a dissected rat spinal cord fixed with PFA 4% + Glu 2%. MIPs computed with few (20-50) consecutive CT slices, in (a), visualize primarily cellular morphology. Adding more (50-200) consecutive CT slices to MIP maps, in (b), highlights extended vascular network morphology. Yellow arrows point to cellular microstructure at different scales, red arrows to vascular microstructure at different scales. (c-d) state-of-the-art (c) 2D cellular imaging, i.e. 2D toluidine blue histology staining cellular structure (rendered in shades of blue), and (d) 3D vascular imaging, i.e. confocal fluorescence microscopy of Tomato-Lectin (Lectin) labelled & PFA-perfused vasculature (rendered green), vs. (c) recolored 2D MIP maps and 3D renderings of 3^3 to $0.3^3 \mu\text{m}^3$ voxel multiscale X-PCI-CT data, emphasizing together cellular (rendered in shades of blue) & vascular anatomy (rendered red), and vs. (d) 3D renderings of $0.3^3 \mu\text{m}^3$ voxel X-PCI-CT data, emphasizing only vascular anatomy (rendered red).

7.5 Discussion

7.5.1 Image contrast in multiscale X-PCI-CT of the spinal cord

Gray-levels and image contrast in propagation-based X-PCI-CT images can be easily interpreted, since phase-contrast arises due to differences in the electron density (Cloetens *et al.*, 1996) within the imaged object, which in turn depends on the atomic number (Z) of the material (Zachariasen, 1945). Further, X-ray refraction effects make the technique very sensitive to object interfaces (Cloetens *et al.*, 1999), and thus to internal object structures (Betz *et al.*, 2007). X-PCI-CT can be made quantitative by implementing specific image acquisition and post-processing procedures (Nugent *et al.*, 1996). The phase-retrieval algorithm for single-distance propagation-based X-PCI-CT used here is fully-quantitative only in the limit of a monochromatic X-ray source and a homogenous object (Paganin *et al.*, 2002), but can still successfully deliver interpretable semi-quantitative measurements also of heterogeneous soft-tissue matter after irradiation with quasi-monochromatic to pink X-ray beams, as is our case here.

Within the native (unstained) soft-matter CNS tissues analyzed in this study, X-PCI-CT image soft-tissue contrast relates to small local differences in mass density, and can arise between different nervous tissue types (e.g. white vs. gray matter vs. cancerous tissue), due to high- Z material deposition (e.g. calcifications, blood) or due to internal anatomical structures with sharp edges (e.g. cells, vasculature) (Barbone *et al.*, 2018). In the non-osmicated cord samples (**Fig. 1,3**), the observed image contrast is congruent with medullary local density differences and embedded structural features: denser gray-matter tissue yields higher gray-level values than white-matter, and denser somatic and nuclear structures (e.g. nucleoli) appear brighter than surrounding neuropil. The osmicated cords (**Fig. 1-2**), for their part, show how lipid cross-linkage, at the molecular level, by (strongly X-ray absorbing) OsO_4 metal leads, at the tissue level, to an (expected) enhancement of X-PCI-CT signal within stained myelinated white-matter, and thus to an inversion of white vs. gray matter image contrast.

As far as vascular structure imaging with X-PCI-CT goes, the sharp borders created by thick endothelial-cell vascular walls, as well as any deposits of dense iron-rich blood, concur to provide the highest image contrasts in unstained PFA- and PFA/Glu-fixed cords. Vascular gray-levels are followed by those of slightly hyper-dense cellular features, especially from motor neurons in spinal gray-matter horns. After osmium post-fixation, instead, white matter fiber and vascular structures contend the brightest image signals, and cellular features end up generating the lowest intra-medullary signals amongst these three structure types (**Fig. 2**).

When comparing different X-PCI-CT setups, gray vs. white matter contrast obtained using monochromatic X-rays (e.g. the data in **Fig. 1** & **Fig. 3c** with 3.0^3 and $0.3^3 \mu\text{m}^3$ voxel sizes) was found generally higher than in X-PCI-CT data, obtained using pink X-ray beams (e.g. the data in **Fig. 3a** with $0.7^3 \mu\text{m}^3$ voxel size). Structure contrast, instead, seems largely unaffected by the degree of mono-chromaticity (monochromatic vs. pink beams) of the X-rays used, and adequate microstructural characterization could be achieved using both beam types.

7.5.2 Sample preparation vs. image quality and microstructure detection

Overall, some evident image quality differences arise depending on the carried-out cord sample-preparation technique: osmium staining affords the most distinct delineations of neural structural boundaries and greatly enhances white vs. gray matter contrast (**Fig. 1, 3**). Especially well-visible after osmication is the fine structure of white matter fiber bundles, as well as individual nerve fibers intruding within the gray matter (**Fig. 2**). Vascular structure, instead, is better rendered within osmium-free medullas (**Fig. 1, 3**), and particularly after aldehyde fixation in combination (PFA 4%, Glu 2%). Compared to PFA 4% alone, the mixed aldehyde fixation protocol seems to lead to less image noise and more complete and detailed vascular trees (**Fig. 1**). OsO₄ impregnation, too, allows the visualization of vascular detail, mainly within gray-matter tissue. With this protocol, though, vessels compete against the bright osmium signal of myelin-rich areas, which hinders the visibility of vasculature within white-matter and leads to less complete vascular maps. Likewise, the quality of cellular structure visualizations appears as heterogeneous among differently prepared cords, with osmicated samples delivering the best portraits of cyto-architecture morphology, including some dendritic and axonal detail in addition to well-delineated hypo-dense cell-soma structure (**Fig. 2, Suppl. Fig. 1**). Glutaraldehyde fixation in combination with PFA, for its part, seems beneficial to staining-free cellular imaging, leading to somewhat better motor neuron soma demarcation within gray matter compared to gray-matter tissues fixed only with PFA, where local neuron soma structure appears more indistinct (**Fig. 1, 3**). Glutaraldehyde, and its superior protein cross-linking ability compared to PFA (Fix and Garman, 2000), is likely also responsible for the observed improved vascular and cellular visualizations in PFA/Glu-fixed samples, compared to just PFA-fixed ones. The Glu-component of this mixed-fixative protocol excels at preserving cellular and tissue microstructure (Park *et al.*, 2016), while the PFA-component makes the tissue penetration of the PFA/Glu combination quite quick. The benefits of a PFA/Glu fixation in combination are evident in the histological-resolution X-PCI-CT images obtained here (**Fig. 3**), showing well-defined (label-free & dense) cellular and intracellular structure alongside deep vasculature, all in 3D. Moreover, these imaging results are well recapitulated also in the collected cellular-level 2D toluidine blue-stained histological data (**Fig. 5**), which shows better-preserved nervous-tissue structures in the PFA/Glu case than in the PFA-only case.

While perfusion is considered the gold standard approach for CNS tissue fixation, *post-mortem* fixation by immersion, as performed here, is a viable alternative when specimens are small enough to allow effective fixative penetration, as is the case for the rodent SC samples. Fixation by immersion is also compatible with a possible future application of this imaging technology to human spine specimens *post-mortem*, a case for which perfusion would not constitute a viable option.

Still, no aldehyde fixative (or combination of aldehyde fixatives) can completely fix lipid components in CNS tissue, such as mixed protein/lipid structures within cell membranes: this result is, instead, normally achieved in CNS tissue sample-preparation protocols for TEM via post-fixation by osmium impregnation. The advantages of osmication, i.e. better cell-membrane preservation in addition to white-matter contrast enhancement, are well visible

in the acquired cellular-level spinal nervous tissue X-PCI-CT data (**Fig. 2-3**) and histological data (**Fig. 5**), which capture the morphology of neuronal and axonal matter with the highest detail, owing to the superior degree of feature preservation and delineation afforded by the osmium staining. In conclusion, in this study osmium-stain cords proved to be the highest-quality samples for myelinated white-matter imaging and cellular sub-structure imaging (neuron perikarya, dendrites, axons), whereas PFA/Glu-fixed unstained cord samples proved to be the most reliable for multiscale vascular network imaging, including some local cellular and intra-cellular structure. Its independence from labels & contrast agents, and the relative protocol ease compared to osmium post-fixation, make the PFA/Glu the most readily-available and user-friendly of the sample-preparation techniques tested here.

7.5.3 3D quantification of CNS microstructure

The quantification of selected cellular and vascular parameters (**Fig. 4**), including sizes of cell-like structures and vascular thicknesses, demonstrates the possible use of X-PCI-CT data in the context of virtual-histological evaluations of 3D tissue volumes. In fact, based on the improved obtainable soft-tissue image contrast compared to absorption CTs, the collected spinal cord X-PCI-CT data could be masked to separate different 3D anatomical features within un-sectioned medullas. After segmentation, 3D masks could be analyzed with various 3D image analysis algorithms to extract quantitative distributions of meaningful morphological parameters.

For rodent spinal cord samples, such cellular-level analyses are limited (partially) by the duration of X-PCI-CT scans and synchrotron beam-time availability, and most of all by the size of collected CT volumes and by the computation durations of segmentation and analysis algorithms. Conversely, they are not limited by setup constraints, since the imaging FoV of the $3.0^3 \mu\text{m}^3$ voxel setup is sufficient for the imaging of full soft-matter rodent cords, and the $0.7\text{-}0.3^3 \mu\text{m}^3$ voxel setups can achieve image resolutions sufficient for cell imaging. Last, these X-PCI-CT-based quantifications are not hindered by sample-related constraints, since the fixed dissected SC samples are measured with no absolute prerequisite of either sample labeling, staining or sectioning.

The automatically-segmented masks of cellular structure presented here (**Fig. 4**), though, noticeably contain some unwanted microvasculature and other nervous tissue structure, which of course influence the resulting cellular-size distributions, at least to some degree. The manually-segmented masks used in vessel thickness measurements, for their part, seem to do a better job at extracting vascular features preferentially, this though at the price of a more arbitrary determination of threshold, and thus to a more biased quantification of extracted vascular network structure. It is to be expected, though, that the application of a more advanced segmentation methodology compared to the threshold-based one used in this study, may likely lead to more precise microstructure extractions and quantifications. A post-segmentation solution may, instead, involve filtering objects of different biological origin based on differing morphological parameters: rod-like vascular objects likely differ from spherical/oval cell-somas e.g. in terms of their surface/volume ratios. Any further design and

implementation of segmentation methodology was deemed beyond the scope of this work, but will represent a necessary and important step in the future development of X-PCI-CT-based virtual-histological approaches for the automated 3D quantification of CNS tissue structure. Of interest to us, the performed data analysis seems sufficient to demonstrate that a quantification of deep 3D cellular-level features of the size of few microns is, at least in principle, feasible based on the multiscale datasets acquired here, for all sample preparation protocols.

7.5.4 X-PCI-CT vs. established volumetric and histological neuroimaging technologies

Post-mortem X-PCI-CT neuroimaging most closely relates to high-field PMMR neuroimaging, in that they both represent little-invasive soft-tissue-sensitive volumetric technologies. As highlighted in this work (**Fig. 5**), the foremost main advantage of X-PCI-CT with respect to PMMR is the higher achievable spatial resolution in measurements of CNS soft-tissue structure. Multiscale X-PCI-CT, in fact, enables intra-medullary micro-morphological visualizations of rodent neuron and intra-neuronal detail, which are beyond the possibility of current MRI technology. Second, X-PCI-CT seems better suited for vascular network imaging, owing to its high sensitivity to sharp internal sample borders and localized high-Z material dense deposits, as is the case for blood-filled (unperfused) multi-boundary vascular structures. Moreover, the generated density-based maps deliver complementary physical information with respect to PMMR. Last, the acquisition times for high-resolution synchrotron X-PCI-CT datasets are more moderate, in the order of tens of minutes, compared to PMMR datasets, which necessitate long measurement times in the order of tens of hours.

PMMR, for its part, achieves higher white vs. gray-matter contrast (**Fig. 5**), functional maps in addition to morphological ones, and a multiplicity of contrasts related to different physical parameters (e.g. relaxometry vs. diffusion vs. susceptibility maps, etc.). An advantage of PMMR specific to CNS imaging is an easier access to intra-skull and intra-spinal canal detail without the need for sample dissection, compared to X-PCI-CT measurements of CNS organs, for which the encasement within highly-absorbing and refracting bony structure represents a challenge (Zamir *et al.*, 2016). More generally, PMMR has the undeniable further advantage of relatively compact one-room measurement setups, especially compared to synchrotron beamline X-PCI-CT setups, which exploit the brilliant X-rays of a dedicated large-scale scientific facility several hundreds of meters in diameter. More compact one-room X-ray light sources for X-PCI-CT applications (Eggl *et al.*, 2015) as well as simplified more-robust X-PCI-CT setups (Zamir *et al.*, 2017) are under development, with the objective to take the technique outside synchrotron facilities and thereby make the method more widely available. Overall though, since these two techniques provide, notably, complementary physical information, one based on tissue density and the other on nuclear spin systems, their side-by-side application may prove useful for future multimodal studies of CNS microanatomy.

PMMR aside, X-PCI-CT technology is naturally quite close to traditional 3D micro-CT neuroimaging, which also enables histology-like virtual 3D imaging. Compared to micro-CT, though, which relies heavily on contrast-enhancing impregnations and contrast-agent

injections for brain and spinal cord (respectively) anatomical and vascular imaging, the work presented here shows that high intra-medullary vascular and cellular-feature contrast can be achieved in contrast-agent-free images by using the X-PCI-CT method. Further clear advantages of the X-PCI-CT measurements are the quickness and sub-micron resolution of the acquisitions, both unfeasible via traditional micro-CT in the absence of contrast agent.

The established possibility to image cellular and intra-cellular soft-tissue detail, including nervous tissue (Töpperwien *et al.*, 2017), allows referring to X-PCI-CT as a 3D virtual-histological technique (Töpperwien *et al.*, 2016). Therefore, a direct comparison of X-PCI-CT data to established histological approaches for spinal cord structural imaging seemed warranted in this study (**Fig. 5-6**). Compared to virtual imaging with X-PCI-CT setups, traditional histological approaches to small-animal CNS micro-anatomical measurements involve the sectioning and eventual destruction of the CNS sample under analysis. Moreover, histological workups necessitate technically challenging manual procedures, and commonly lead to only mainly-2D visualizations, to anatomical distortions and subjective 3D reconstructions, to quantification-biasing artifacts of sample preparation, and to limits in the sample size due to constraints in the penetration of stains and dyes. On the contrary, X-PCI-CT allows for non-destructive virtual spatially-aligned 3D visualizations of CNS tissue in arbitrary planes of evaluation, and for staining- and label-free dense quantifications of microstructure with fewer (at least theoretical) limits in sample size, and less-biased (since dense and label-free) morphological representations. Admittedly, though, image artifacts due to *post-mortem* nervous tissue fixation (Fix and Garman, 2000), such as artifactual dark neurons, differential neuropil retraction and shrinkage, mucocytes or other white-matter artifacts, are present also in CNS X-PCI-CT datasets, since they depend on pre-imaging sample-preparation procedures related to fixation. Moreover, a relatively complex dissection of the cord before sample fixation was necessary also to collect the X-PCI-CT data in this study. Last, the osmium-stained visualizations presented here suffer from the same dye/label tissue-penetration issues typical of other histological imaging approaches, such as TEM or immunohistology, or traditional absorption-based micro-CT. Homogenous osmium-penetration within non-dissected rodent spinal cords, for example, might prove a challenging step prior to X-PCI-CT scanning, so that, depending on the sample, X-PCI-CT may also have to face sample-size limitations due to sample-preparation issues, when osmium impregnation is involved.

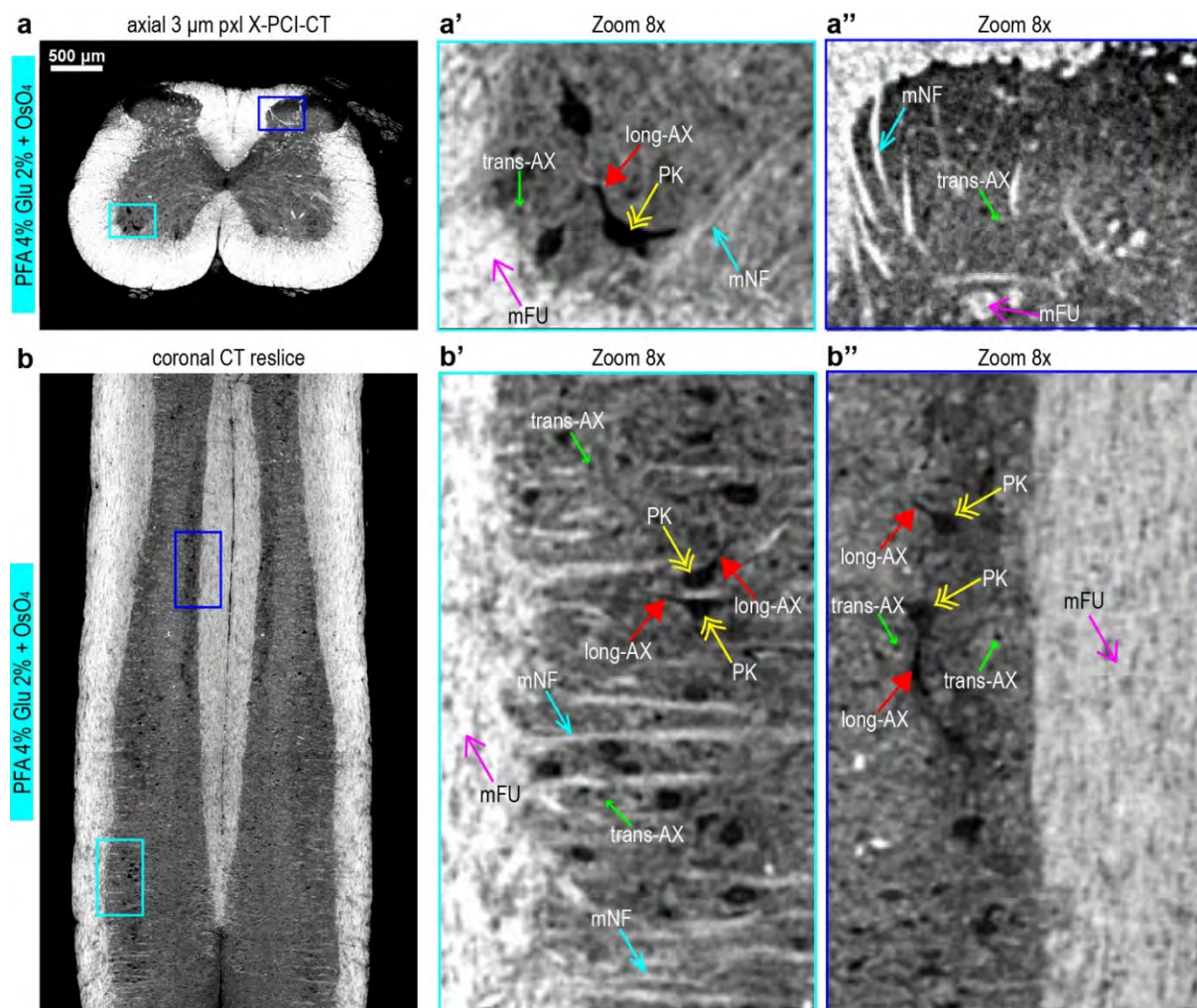
Perhaps, the most interesting results from spinal cord X-PCI-CT, both here and in previous works, relate to vascular imaging. Here, vascular networks were extracted from CT datasets based on threshold segmentations, with vascular gray-levels relating to the intrinsic density of blood-filled vascular structure and to the edges created by thick endothelial-cell vascular wall linings. This vessel detection method is simple, completely independent of labels or contrast agents, and delivers unbiased dense and quantitative 3D representations of extended vascular networks at relatively high spatial resolution. Compared to this approach, fluorescence microscopy of vascular networks (**Fig. 6**), which relies on indirect label-based measurements for vascular structure sensitivity, suffers from sparse labelling issues and labelling-related bias (Farhoodi, Lansdell and Kording, 2019). Moreover, the spatial extension of (Lectin)-labelled vascular networks is limited by the initial choice of tissue slice thickness,

and this vascular imaging approach becomes increasingly more complicated with increasingly larger sample sizes. The sample size allowed for similar X-PCI-CT-based acquisitions of 3D contrast-agent-free vasculature, instead, is limited only by the number of contiguous datasets acquired during imaging (and thus by the overall measurement times) and by the increasingly large datasets, which will arise for increasingly large samples, leading to a rise in post-processing times (e.g. data reconstruction and analysis duration) and in the needed virtual storage-space. Last, while fluorescence-microscopy-based vascular measurements can currently still achieve the highest spatial resolutions, X-PCI-CT and its 3D renderings of capillary-level microstructure were shown here to not trail too far behind in terms of resolving power, and thus in terms of measurable level of micro-vascular detail.

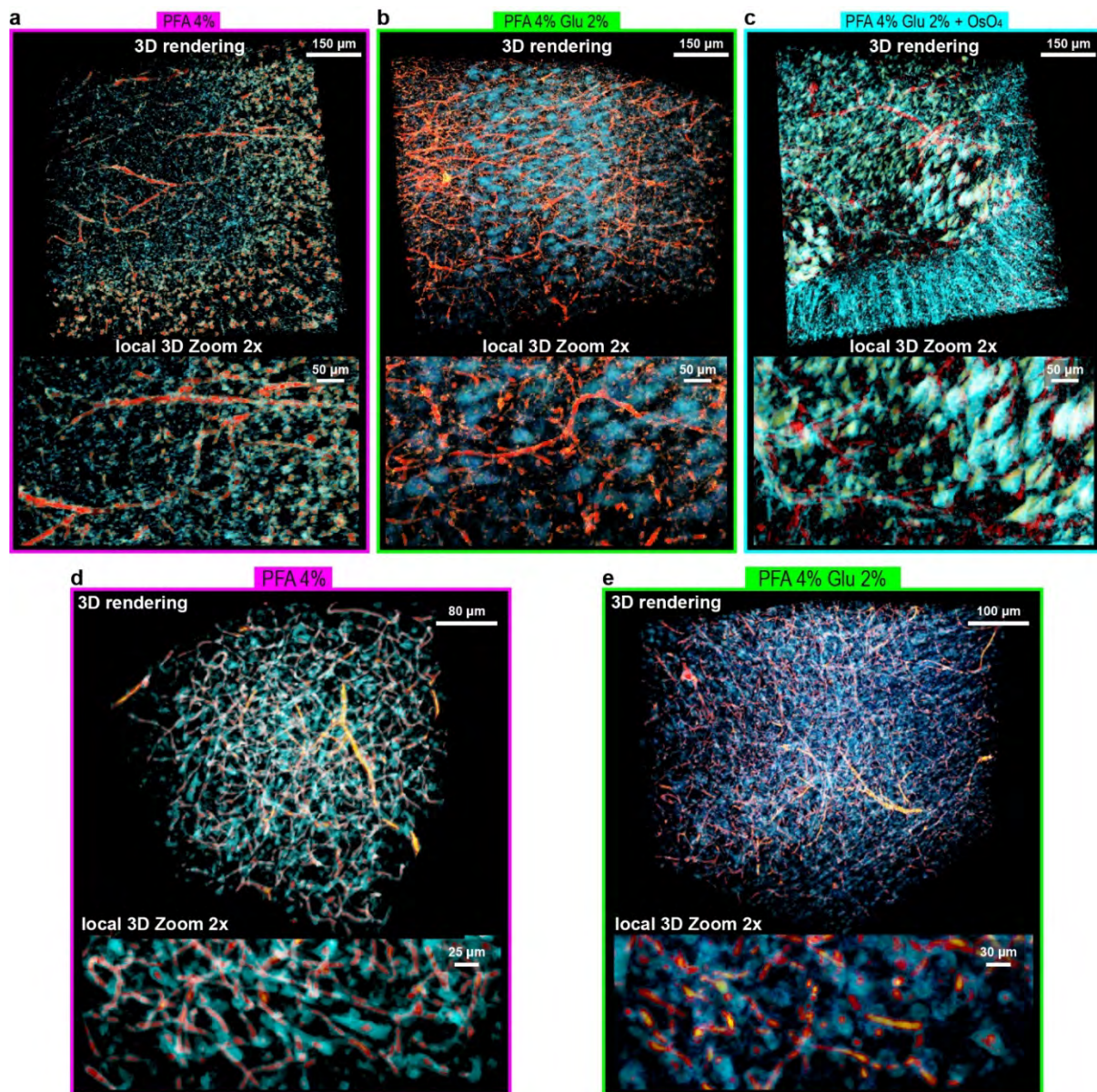
7.6 Conclusions

Non-invasive 3D visualizations of full-organ CNS micro-vascularization and of neuronal cellular microstructure are fundamental in the preclinical study of vascular and neurodegenerative diseases, and yet they are still difficult to obtain with current cutting edge imaging technology. In this study, carried out *post-mortem* on extracted animal-model spinal cord samples, we demonstrate that multiscale X-PCI-CT permits a unique volumetric histology-like analysis & quantification of intra-medullary neuronal and vascular microstructure. The technique, in fact, can detect the micromorphology of deep single cells and single micro-vessels within extended soft-matter samples, after little sample preparation and in the absence of any neuronal labeling or staining. Interestingly, the crucial role of an adapted and robust nervous tissue fixation protocol for the development of better-designed and more specific neuroimaging approaches was (once more) made evident by the analysis of the effect on image quantity of different aldehyde fixation and post-fixation protocols performed as part of this study. A comparative qualitative evaluation of the imaging results for differently-prepared SC samples led to valuable insight on the suitability of the tested sample preparation procedures for differently-oriented CNS microstructural studies: for example, a PFA/Glu fixation in combination was deemed most effective for spinal cord micro-vascular studies. PFA/Glu with the addition of osmium post-fixation, instead, was deemed ideal for studies on myelination and white-matter fiber structure. Last, these results confirm that the application of synchrotron radiation X-PCI-CT for non-invasive volumetric *post-mortem* CNS tissue imaging, i.e. the employment of a technique, which can achieve the cellular resolution of histological approaches combined with the 3D soft-tissue sensitivity of PMMR, may arguably be able to provide new opportunities for neuroimaging. Several advantages of an X-PCI-CT-based approach to neuroimaging, compared to established PMMR, traditional micro-CT, histology and fluorescence microscopy approaches, was discussed in detail. For all these reasons, X-PCI-CT seems fit to potentially improve current micrometric neuro-anatomical investigations of the CNS in animal models, and impact both neuroanatomical and neuropathological research.

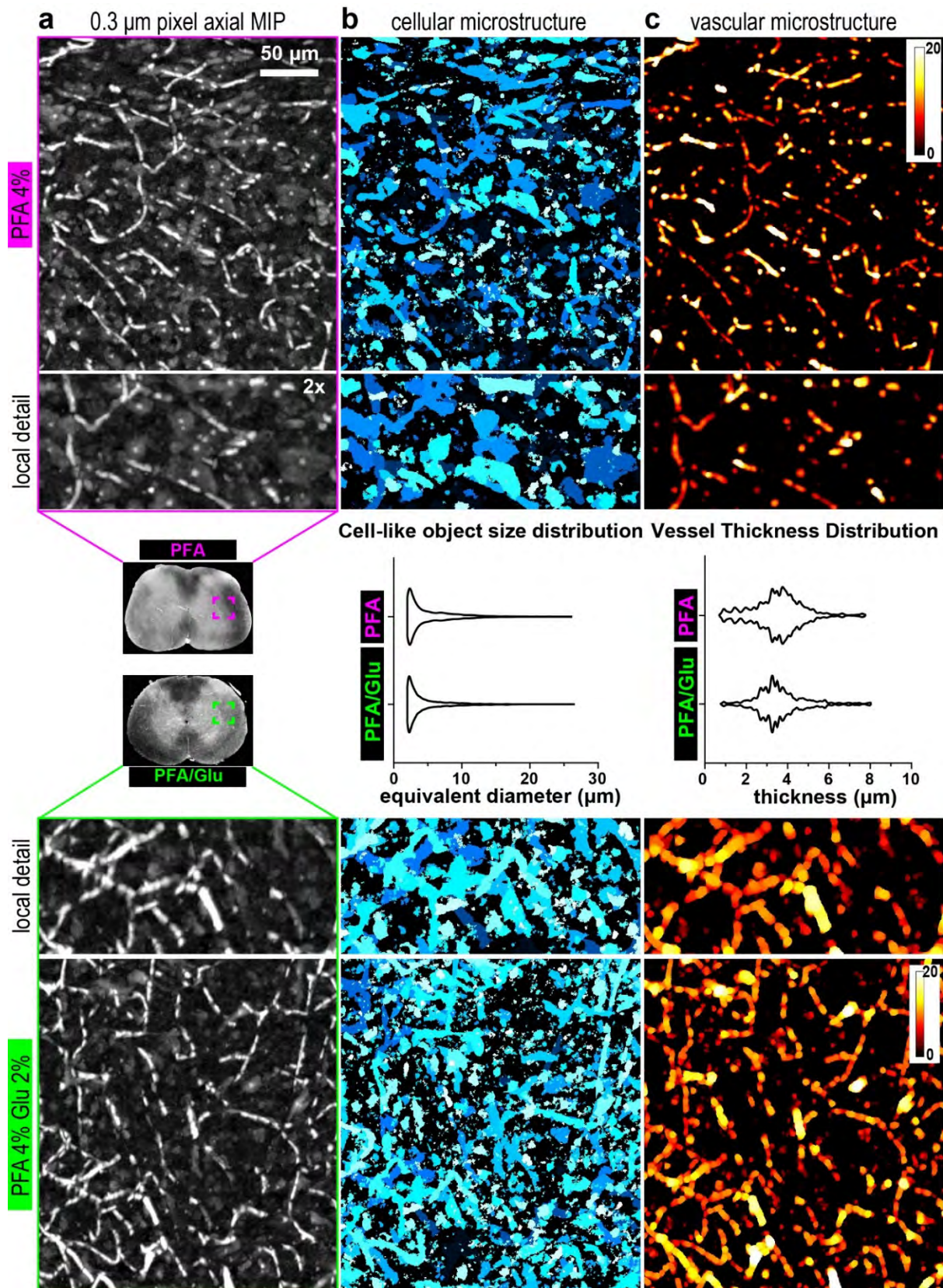
7.7 Supplementary Figures



Suppl. Fig. 1: Annotated cellular micro-structure visible within osmicated cords. (a) Axial and (b) sagittal X-PCI-CT data of osmium-stained cords. (a'-a'') and (b'-b'') are annotated 8x Zooms of (a) and (b), showing cellular-level microstructure. Striped osmicated columnar white-matter structures represent hyper-dense myelinated funiculi (mFU) within spinal cord tracts. Branch-like osmicated structures represent hyper-dense individual or multiple myelinated nerve fibers (mNF). Cell-like hypo-dense objects represent motor neuron perikarya (PK). Hypo-dense branchlike extensions from the cell somas represent longitudinally-sliced un-myelinated axons or axon hillocks (long-AX). Hypo-dense point-like features represent transversely-sliced un-myelinated axons (trans-AX). Only few of each structure-type are labelled, but many more are present.

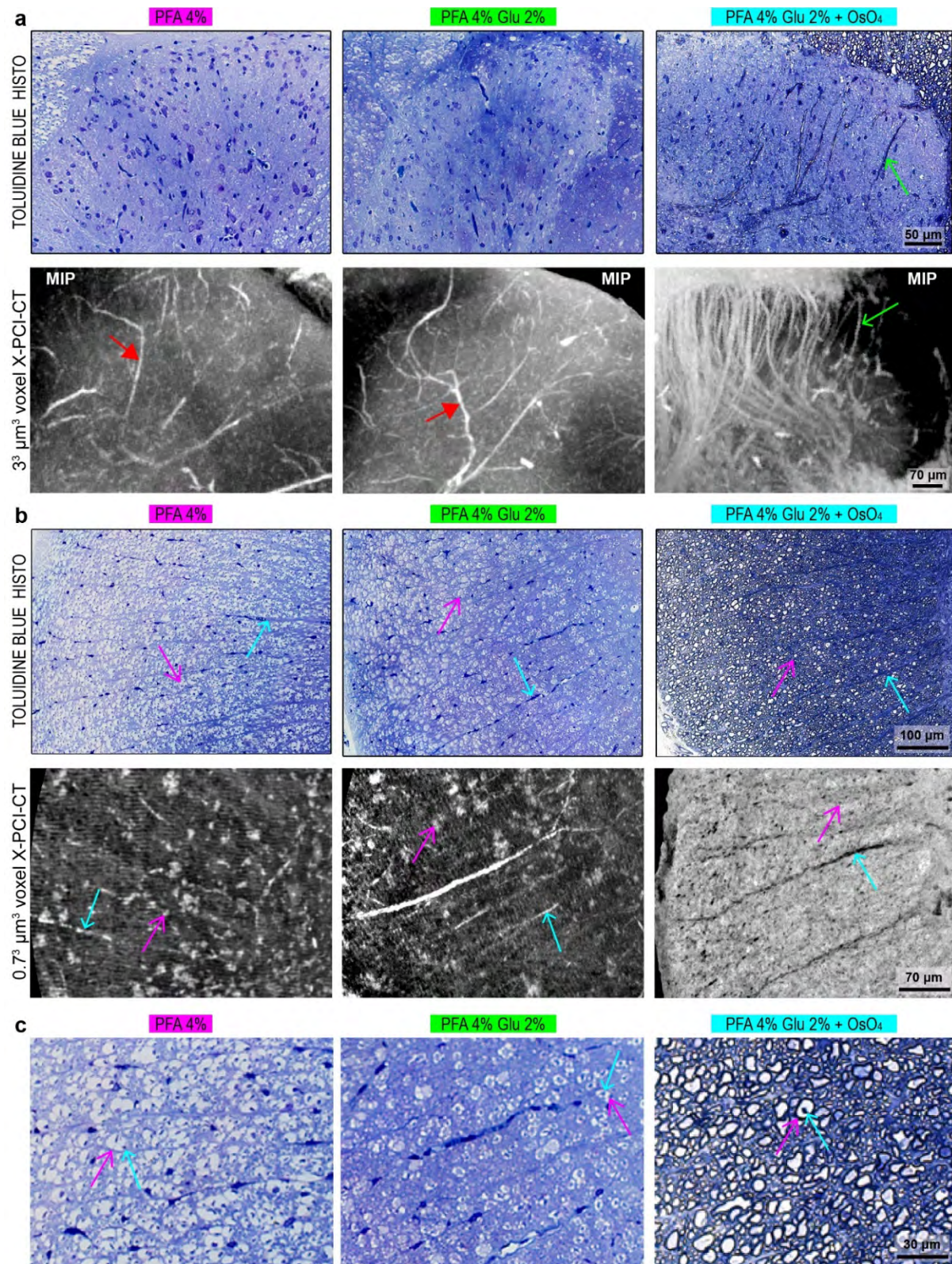


Suppl. Figure 2. 3D renderings of X-PCI-CT with sub-micron voxels. (a-c) 3D renderings, after threshold-based segmentation, of 50- to 100-slice $0.7^3 \mu\text{m}^3$ voxel X-PCI-CT datasets of fixed medullary tissue from (a) a PFA 4% preparation group specimen, (b) a PFA 4%, Glu 2% preparation group specimen and (c) a PFA 4%, Glu 2%, OsO₄ preparation group specimen, showing vascular features, colored in shades of red, and cellular features, colored in shades of blue. The 2x zoom shows 3D detail of local medullary tissue microstructure. (d-e) 3D renderings, obtained as in (a-c), of 50- to 150-slice $0.3^3 \mu\text{m}^3$ voxel X-PCI-CT datasets of fixed medullary tissue from (d) a PFA 4% preparation group specimen and (e) a PFA 4%, Glu 2% preparation group specimen. Note that intra-cellular microstructure is resolved here, and that bright/dense intra-cellular nucleoli are rendered in red, like local microvasculature, and neuronal cell bodies in blue. Agar gel background was masked in all CT images for clarity.



Suppl. Figure 3. Quantification of cellular and vascular parameters using X-PCI-CT data with $0.7^3 \mu\text{m}^3$ voxels. (a) $0.3^3 \mu\text{m}^3$ voxel axial X-PCI-CT MIP data of lateral horn gray-matter tissue collected from cords prepared with two of the three sample-preparation protocols (PFA fixation vs. combined PFA/Glu fixation). (b) recolored masks of X-PCI-CT MIP data from (a), segmented via an automated threshold algorithm (see **Methods**) to extract cell-like microstructure. Local (2x zoomed) mask detail is also displayed, to better visualize the result of the

segmentations. Especially in the PFA/Glu data, some of the segmented objects or voxels actually pertained to vascular structure. Violin plots report size distributions obtained by extracting the equivalent diameter of each distinct 3D object in the masks, quantified via an image analysis plugin of ImageJ specific for populations of 3D objects (see **Methods**). (c) quantitatively-recolored masks of X-PCI-CT MIP data from (a), segmented by manual threshold selection to extract vascular microstructure. Local mask detail is displayed to better visualize the goodness of the segmentations. Color-coding quantifies the internal thickness of tubular structures (calibration bar in μm), computed with an ImageJ image-analysis plugin specific for tubular 3D structures (see **Methods**). Violin plots report thickness distributions obtained by combining all voxel values in the corresponding image masks in (c).



Suppl. Figure 4. X-PCI-CT vs. cellular histology of gray- and white-matter spinal cord tissues. (a-b) magnified toluidine blue-stained histological slices vs. sub-micron ($0.7^3 \mu\text{m}^3$ and $0.3^3 \mu\text{m}^3$ voxel) X-PCI-CT data from all three sample-preparation protocols (PFA 4% vs. PFA 4%, Glu 2% vs. PFA 4%, Glu 2% + OsO_4), centered respectively on (a) dorsal horn gM and (b) lateral column wM tissues. Agar gel background was masked in several of the X-PCI-CT images for clarity. In (a), note the visualization of micro-vasculature features in the MIPs of the aldehyde-only fixed samples (red arrows), of individual sensory afferent myelinated nerve fibers in the histology and MIPs of the osmicated samples (green arrows). In (b), note the visualization of myelinated white-matter structure

(magenta arrows) vs. motor efferent fibers passing through the white matter (azure arrows). (c) Zooms 3x of histological data in (b), showing single myelin sheaths (magenta arrows) and their axons (if present, blue arrows) in the three different sample-preparation groups.

REFERENCES:

- Annese, J. *et al.* (2014) 'Postmortem examination of patient H.M.'s brain based on histological sectioning and digital 3D reconstruction', *Nature Communications*. The Author(s), 5, p. 3122. Available at: <https://doi.org/10.1038/ncomms4122>.
- Arthurs, O. J. *et al.* (2015) 'Diagnostic accuracy and limitations of post-mortem MRI for neurological abnormalities in fetuses and children', *Clinical Radiology*. Elsevier, 70(8), pp. 872–880. doi: 10.1016/j.crad.2015.04.008.
- Barbone, G. E. *et al.* (2018) 'Micro-imaging of Brain Cancer Radiation Therapy Using Phase-contrast Computed Tomography', *International Journal of Radiation Oncology Biology Physics*, 101(4), pp. 965–984. doi: 10.1016/j.ijrobp.2018.03.063.
- Bartels, M. *et al.* (2015) 'Myelinated mouse nerves studied by X-ray phase contrast zoom tomography', *Journal of Structural Biology*, 192(3), pp. 561–568. doi: <https://doi.org/10.1016/j.jsb.2015.11.001>.
- Beaujoin, J. *et al.* (2018) 'Post-mortem inference of the human hippocampal connectivity and microstructure using ultra-high field diffusion MRI at 11.7 T', *Brain structure & function*. 2018/01/31. Springer Berlin Heidelberg, 223(5), pp. 2157–2179. doi: 10.1007/s00429-018-1617-1.
- Beltran, M. a *et al.* (2011) 'Interface-specific x-ray phase retrieval tomography of complex biological organs', *Physics in Medicine and Biology*, 56, pp. 7353–7369. doi: 10.1088/0031-9155/56/23/002.
- Betz, O. *et al.* (2007) 'Imaging applications of synchrotron X-ray phase-contrast microtomography in biological morphology and biomaterials science. I. General aspects of the technique and its advantages in the analysis of millimetre-sized arthropod structure', *Journal of Microscopy*. John Wiley & Sons, Ltd (10.1111), 227(1), pp. 51–71. doi: 10.1111/j.1365-2818.2007.01785.x.
- Bolte, S. and Cordelières, F. P. (2006) 'A guided tour into subcellular colocalization analysis in light microscopy', *Journal of Microscopy*. John Wiley & Sons, Ltd (10.1111), 224(3), pp. 213–232. doi: 10.1111/j.1365-2818.2006.01706.x.
- de Bournonville, S., Vangrunderbeeck, S. and Kerckhofs, G. (2019) 'Contrast-Enhanced MicroCT for Virtual 3D Anatomical Pathology of Biological Tissues: A Literature Review', *Contrast Media Molecular Imaging*. Edited by A. Roivainen. Hindawi, 2019, p. 8617406. doi: 10.1155/2019/8617406.
- Bravin, A., Coan, P. and Suortti, P. (2013) 'X-ray phase-contrast imaging: from pre-clinical applications towards clinics.', *Physics in Medicine and Biology*, 58(1), pp. R1–R35. doi: 10.1088/0031-9155/58/1/R1.
- Calabrese, E. *et al.* (2018) 'Postmortem diffusion MRI of the entire human spinal cord at microscopic resolution', *NeuroImage: Clinical*. Elsevier, 18, pp. 963–971. doi: 10.1016/j.nicl.2018.03.029.
- Cao, Y. *et al.* (2016) 'Visualization of mouse spinal cord intramedullary arteries using phase- and attenuation-contrast tomographic imaging.', *Journal of synchrotron radiation*, 23(4), pp. 966–974. doi: 10.1107/S1600577516006482.
- Cao, Y. *et al.* (2017) 'Three Dimensional Quantification of Microarchitecture and Vessel Regeneration by Synchrotron Radiation Microcomputed Tomography in a Rat Model of Spinal Cord Injury', *Journal of Neurotrauma*, 34(6), pp. 1187–1199. doi: <http://doi.org/10.1089/neu.2016.4697>.
- Cedola, A. *et al.* (2017) 'X-Ray Phase Contrast Tomography Reveals Early Vascular Alterations and Neuronal Loss in a Multiple Sclerosis Model', *Scientific Reports*, 7(1), p. 5890. doi: 10.1038/s41598-017-06251-7.
- Chen, K.-C. *et al.* (2018) 'High-definition neural visualization of rodent brain using micro-CT scanning and non-local-means processing', *BMC medical imaging*. BioMed Central, 18(1), p. 38. doi: 10.1186/s12880-018-0280-6.
- Chiorazzi, A. *et al.* (2009) 'Experimental epothilone B neurotoxicity: Results of in vitro and in vivo studies', *Neurobiology of Disease*, 35(2), pp. 270–277. doi: <https://doi.org/10.1016/j.nbd.2009.05.006>.
- Cloetens, P. *et al.* (1996) 'Phase objects in synchrotron radiation hard x-ray imaging', *Journal of Physics D: Applied*

Physics, 29(1), pp. 133–146. doi: 10.1088/0022-3727/29/1/023.

Cloetens, P. *et al.* (1999) 'Holotomography: Quantitative phase tomography with micrometer resolution using hard synchrotron radiation x rays', *Applied Physics Letters*. American Institute of Physics, 75(19), pp. 2912–2914. doi: 10.1063/1.125225.

Ding, S.-L. *et al.* (2016) 'Comprehensive cellular-resolution atlas of the adult human brain', *The Journal of comparative neurology*. John Wiley and Sons Inc., 524(16), pp. 3127–3481. doi: 10.1002/cne.24080.

Duval, T. *et al.* (2019) 'Axons morphometry in the human spinal cord', *NeuroImage*, 185, pp. 119–128. doi: <https://doi.org/10.1016/j.neuroimage.2018.10.033>.

Eggl, E. *et al.* (2015) 'X-ray phase-contrast tomography with a compact laser-driven synchrotron source', *PNAS*, 112(18), pp. 5567–5572. doi: 10.1073/pnas.1500938112.

Farhoodi, R., Lansdell, B. J. and Kording, K. P. (2019) 'Quantifying How Staining Methods Bias Measurements of Neuron Morphologies', *Frontiers in neuroinformatics*. Frontiers Media S.A., 13, p. 36. doi: 10.3389/fninf.2019.00036.

Fix, A. S. and Garman, R. H. (2000) 'Practical Aspects of Neuropathology: A Technical Guide for Working with the Nervous System', *Toxicologic Pathology*. SAGE Publications Inc, 28(1), pp. 122–131. doi: 10.1177/019262330002800115.

Flood, D. G. and Coleman, P. D. (1988) 'Neuron numbers and sizes in aging brain: Comparisons of human, monkey, and rodent data', *Neurobiology of Aging*, 9, pp. 453–463. doi: [https://doi.org/10.1016/S0197-4580\(88\)80098-8](https://doi.org/10.1016/S0197-4580(88)80098-8).

Fratini, M. *et al.* (2015) 'Simultaneous submicrometric 3D imaging of the micro-vascular network and the neuronal system in a mouse spinal cord.', *Scientific reports*, 5, p. 8514. doi: 10.1038/srep08514.

Haghighy Jahromi, N. *et al.* (2017) 'A Novel Cervical Spinal Cord Window Preparation Allows for Two-Photon Imaging of T-Cell Interactions with the Cervical Spinal Cord Microvasculature during Experimental Autoimmune Encephalomyelitis', *Frontiers in Immunology*, 8, p. 406. doi: 10.3389/fimmu.2017.00406.

Harrison, M. *et al.* (2013) 'Vertebral landmarks for the identification of spinal cord segments in the mouse', *NeuroImage*, 68, pp. 22–29. doi: <https://doi.org/10.1016/j.neuroimage.2012.11.048>.

Hildebrand, T. and Rügsegger, P. (1997) 'A new method for the model-independent assessment of thickness in three-dimensional images', *Journal of Microscopy*. John Wiley & Sons, Ltd (10.1111), 185(1), pp. 67–75. doi: 10.1046/j.1365-2818.1997.1340694.x.

Hu, J. *et al.* (2015) '3D angioarchitecture changes after spinal cord injury in rats using synchrotron radiation phase-contrast tomography.', *Spinal Cord*, 53(8), pp. 585–590. doi: 10.1038/sc.2015.49.

Hu, J. *et al.* (2017) 'Nondestructive imaging of the internal micro-structure of vessels and nerve fibers in rat spinal cord using phase-contrast synchrotron radiation microtomography', *Journal of Synchrotron Radiation*, 24(2), pp. 482–489. doi: 10.1107/S1600577517000121.

Kapur, J. N., Sahoo, P. K. and Wong, A. K. C. (1985) 'A new method for gray-level picture thresholding using the entropy of the histogram', *Computer Vision, Graphics, and Image Processing*, 29(3), pp. 273–285. doi: [https://doi.org/10.1016/0734-189X\(85\)90125-2](https://doi.org/10.1016/0734-189X(85)90125-2).

Khimchenko, A. *et al.* (2018) 'Hard X-Ray Nanoholotomography: Large-Scale, Label-Free, 3D Neuroimaging beyond Optical Limit', *Advanced Science*, 5, p. 1700694. doi: 10.1002/adv.201700694.

Kirschner, S. *et al.* (2016) 'Imaging of Orthotopic Glioblastoma Xenografts in Mice Using a Clinical CT Scanner: Comparison with Micro-CT and Histology', *PloS one*. Public Library of Science, 11(11), p. e0165994. doi: 10.1371/journal.pone.0165994.

Loureiro, J. R. *et al.* (2018) 'In-vivo quantitative structural imaging of the human midbrain and the superior colliculus at 9.4T', *NeuroImage*, 177, pp. 117–128. doi: <https://doi.org/10.1016/j.neuroimage.2018.04.071>.

Lyckegaard, A., Johnson, G. and Tafforeau, P. (2011) 'Correction of ring artifacts in X-ray tomographic images',

International Journal of Tomography and Statistics, 18(F11), pp. 1–9.

Mader, K. *et al.* (2011) 'High-throughput full-automatic synchrotron-based tomographic microscopy', *Journal of synchrotron radiation*. 2011/01/20. International Union of Crystallography, 18(Pt 2), pp. 117–124. doi: 10.1107/S0909049510047370.

Marone, F. *et al.* (2017) 'Towards on-the-fly data post-processing for real-time tomographic imaging at TOMCAT', *Advanced Structural and Chemical Imaging*, 3(1), p. 1. doi: 10.1186/s40679-016-0035-9.

Masís, J. *et al.* (2018) 'A micro-CT-based method for quantitative brain lesion characterization and electrode localization', *Scientific Reports*, 8(1), p. 5184. doi: 10.1038/s41598-018-23247-z.

Massimi, L. *et al.* (2016) 'Characterization of mouse spinal cord vascular network by means of synchrotron radiation X-ray phase contrast tomography', *Physica Medica*. Elsevier, 32(12), pp. 1779–1784. doi: 10.1016/j.ejmp.2016.09.015.

Massimi, L. *et al.* (2019) 'Exploring Alzheimer's disease mouse brain through X-ray phase contrast tomography: From the cell to the organ', *NeuroImage*. Elsevier Ltd, 184, pp. 490–495. doi: 10.1016/j.neuroimage.2018.09.044.

Miao, P. *et al.* (2016) 'Synchrotron Radiation X-Ray Phase-Contrast Tomography Visualizes Microvasculature Changes in Mice Brains after Ischemic Injury', *Neural plasticity*. 2016/07/31. Hindawi Publishing Corporation, 2016, p. 3258494. doi: 10.1155/2016/3258494.

Mirone, A. *et al.* (2014) 'The PyHST2 hybrid distributed code for high speed tomographic reconstruction with iterative reconstruction and a priori knowledge capabilities', *Nuclear Instruments and Methods in Physics Research Section B*, 324, pp. 41–48. doi: <https://doi.org/10.1016/j.nimb.2013.09.030>.

Mittone, A. *et al.* (2017) 'Characterization of a sCMOS-based high-resolution imaging system', *Journal of Synchrotron Radiation*, 24(6), pp. 1226–1236. doi: 10.1107/S160057751701222X.

Mittone, A. *et al.* (2020) 'Multiscale pink beam microCT imaging at the ESRF-ID17 biomedical beamline', *Journal of Synchrotron Radiation*, Submitted.

Nugent, K. A. *et al.* (1996) 'Quantitative Phase Imaging Using Hard X Rays', *Physical Review Letters*. American Physical Society, 77(14), pp. 2961–2964. doi: 10.1103/PhysRevLett.77.2961.

Optique Peter (2019). Available at: <http://www.optiquepeter.com> (Accessed: 10 April 2020).

Paganin, D. *et al.* (2002) 'Simultaneous phase and amplitude extraction from a single defocused image of a homogeneous object', *Journal of Microscopy*, 206(1), pp. 33–40. doi: 10.1046/j.1365-2818.2002.01010.x.

Pallebage-Gamarallage, M. *et al.* (2018) 'Dissecting the pathobiology of altered MRI signal in amyotrophic lateral sclerosis: A post mortem whole brain sampling strategy for the integration of ultra-high-field MRI and quantitative neuropathology', *BMC neuroscience*. BioMed Central, 19(1), p. 11. doi: 10.1186/s12868-018-0416-1.

Park, C.-H. *et al.* (2016) 'How to Get Well-Preserved Samples for Transmission Electron Microscopy', *Applied Microscopy*. Korean Society of Microscopy, 46(4), pp. 188–192. doi: 10.9729/AM.2016.46.4.188.

Pinzer, B. R. *et al.* (2012) 'Imaging brain amyloid deposition using grating-based differential phase contrast tomography', *NeuroImage*. Elsevier Inc., 61(4), pp. 1336–1346. doi: 10.1016/j.neuroimage.2012.03.029.

Plantinga, B. R. *et al.* (2016) 'Ultra-High Field MRI Post Mortem Structural Connectivity of the Human Subthalamic Nucleus, Substantia Nigra, and Globus Pallidus', *Frontiers in neuroanatomy*. Frontiers Media S.A., 10, p. 66. doi: 10.3389/fnana.2016.00066.

Robertson, R. T. *et al.* (2015) 'Use of labeled tomato lectin for imaging vasculature structures', *Histochemistry and Cell Biology*, 143(2), pp. 225–234. doi: 10.1007/s00418-014-1301-3.

Saccomano, M. *et al.* (2018) 'Synchrotron inline phase contrast μ CT enables detailed virtual histology of embedded soft-tissue samples with and without staining', *Journal of Synchrotron Radiation*, 25(4), pp. 1153–1161. doi: 10.1107/S1600577518005489.

- Saito, S. *et al.* (2012) 'High-resolution ex vivo imaging in mouse spinal cord using micro-CT with 11.7T-MRI and myelin staining validation', *Neuroscience Research*, 73(4), pp. 337–340. doi: <https://doi.org/10.1016/j.neures.2012.05.004>.
- Schmierer, K. *et al.* (2018) 'Quantifying multiple sclerosis pathology in post mortem spinal cord using MRI', *NeuroImage*, 182, pp. 251–258. doi: <https://doi.org/10.1016/j.neuroimage.2018.01.052>.
- Schmitz, C. and Hof, P. R. (2005) 'Design-based stereology in neuroscience', *Neuroscience*, 130(4), pp. 813–831. doi: <https://doi.org/10.1016/j.neuroscience.2004.08.050>.
- Schneider, C. A., Rasband, W. S. and Eliceiri, K. W. (2012) 'NIH Image to ImageJ: 25 years of image analysis', *Nature methods*, 9(7), pp. 671–675. Available at: <https://www.ncbi.nlm.nih.gov/pubmed/22930834>.
- Schulz, G. *et al.* (2012) 'Multimodal imaging of human cerebellum - merging X-ray phase microtomography, magnetic resonance microscopy and histology.', *Scientific Reports*, 2, p. 826. doi: 10.1038/srep00826.
- Sear, R. P. *et al.* (2015) 'Life at the mesoscale : the self-organised cytoplasm and nucleoplasm', *BMC Physiology*, 8(4), pp. 4–9. doi: 10.1186/s13628-015-0018-6.
- Sengupta, S. *et al.* (2018) 'High resolution anatomical and quantitative MRI of the entire human occipital lobe ex vivo at 9.4T', *NeuroImage*. 2017/03/20. Academic Press, 168, pp. 162–171. doi: 10.1016/j.neuroimage.2017.03.039.
- Senter-Zapata, M. *et al.* (2016) 'The Role of Micro-CT in 3D Histology Imaging', *Pathobiology*, 83(2–3), pp. 140–147. doi: 10.1159/000442387.
- Snigirev, A. *et al.* (1995) 'On the possibilities of x-ray phase contrast microimaging by coherent high-energy synchrotron radiation', *Review of Scientific Instruments*. American Institute of Physics, 66(12), pp. 5486–5492. doi: 10.1063/1.1146073.
- Soderblom, C. *et al.* (2015) '3D Imaging of Axons in Transparent Spinal Cords from Rodents and Nonhuman Primates', *eNeuro*, 2(2), p. e.0001-15.2015. doi: 10.1523/ENEURO.0001-15.2015.
- Stampanoni, M. *et al.* (2007) 'TOMCAT: A beamline for TOMographic Microscopy and Coherent rAdiology experimenTs', *AIP Conference Proceedings*. American Institute of Physics, 879(1), pp. 848–851. doi: 10.1063/1.2436193.
- Stefanutti, E. *et al.* (2018) 'Assessment of the effects of different sample perfusion procedures on phase-contrast tomographic images of mouse spinal cord', *JINST*. IOP Publishing, 13(03), p. C03027. doi: 10.1088/1748-0221/13/03/c03027.
- Strotton, M. C. *et al.* (2018) 'Optimising complementary soft tissue synchrotron X-ray microtomography for reversibly-stained central nervous system samples', *Scientific reports*. Nature Publishing Group UK, 8(1), p. 12017. doi: 10.1038/s41598-018-30520-8.
- Suortti, P. *et al.* (2000) 'Fixed-exit monochromator for computed tomography with synchrotron radiation at energies 18-90keV', *Journal of Synchrotron Radiation*, 7(5), pp. 340–347. doi: 10.1107/S0909049500008384.
- Töpperwien, M. *et al.* (2016) 'Laboratory-based x-ray phase-contrast tomography enables 3D virtual histology', in *Proceedings of the SPIE*, p. 99640I. Available at: <https://doi.org/10.1117/12.2246460>.
- Töpperwien, M. *et al.* (2017) 'Three-dimensional mouse brain cytoarchitecture revealed by laboratory-based x-ray phase-contrast tomography', *Scientific Reports*. Nature Publishing Group, 7(42847). doi: 10.1038/srep42847.
- Töpperwien, M. *et al.* (2019) 'Contrast enhancement for visualizing neuronal cytoarchitecture by propagation-based x-ray phase-contrast tomography', *NeuroImage*, 199, pp. 70–80. doi: <https://doi.org/10.1016/j.neuroimage.2019.05.043>.
- Unnikrishnan, G. *et al.* (2019) 'A 3-D Rat Brain Model for Blast-Wave Exposure: Effects of Brain Vasculature and Material Properties', *Annals of biomedical engineering*. 2019/05/03. Springer US, 47(9), pp. 2033–2044. doi: 10.1007/s10439-019-02277-2.
- Weitkamp, T. *et al.* (2011) 'ANKAphase: software for single-distance phase retrieval from inline X-ray phase-

contrast radiographs', *Journal of Synchrotron Radiation*, 18(4), pp. 617–629. doi: 10.1107/S0909049511002895.

Zachariasen, W. (1945) *Theory of X-ray diffraction in crystals*. New York: J. Wiley & Sons Inc.

Zamir, A. *et al.* (2016) 'X-ray phase contrast tomography; proof of principle for post-mortem imaging', *The British journal of radiology*. 2015/11/27. The British Institute of Radiology., 89(1058), p. 20150565. doi: 10.1259/bjr.20150565.

Zamir, A. *et al.* (2017) 'Recent advances in edge illumination X-ray phase-contrast tomography', *Journal of Medical Imaging*, 4(4), p. 040901. doi: 10.1117/1.JMI.4.4.040901.

Chapter 8 - Other pioneering studies

This chapter is intended to present three additional case-studies and their results, which were not already included in the previous Results **Chapters 4-7**. They involve respectively a comparative analysis of data acquired using a table-top liquid-metal X-ray source vs. synchrotron X-ray source, a characterization of AD amyloid-PET signal and the 3D analysis of vascular remodeling in an animal model of hypertension.

8.1 A liquid metal jet vs. synchrotron X-ray source

During a short scientific mission at the Department of Applied Physics (Biomedical & X-Ray Physics) of the KTH Royal Institute of Technology in Stockholm, Sweden, I performed a preliminary comparative study of X-ray phase-contrast CT imaging for biomedical applications using two quite different sources:

1. a liquid metal jet compact X-ray source available at KTH (source commercialized by Exillum (Excillum, 2019a))
2. a synchrotron X-ray source, i.e. the ID17 beamline of the European Synchrotron (ESRF)

As extensively discussed, X-PCI can provide non-invasive high-resolution imaging of soft-tissue organ anatomy, making it a very interesting imaging technique for biomedicine. Still, for this technique to really make a difference in both pre-clinical and clinical imaging, a successful validation of PCI methodologies using more widely available compact X-ray light sources is of paramount importance. This preliminary test was planned to contribute to the ongoing technical feasibility efforts towards compact and lab-compatible X-PCI micro-CT setups.

8.1.1 Project goals

A. The **first objective** was to use high resolution PCI to study prenatal anatomical deformations of the abdomen and thorax in *post-mortem* embryos from a rat model. Most clinically relevant congenital malformations arise during early to mid-embryonic stages: congenital diaphragmatic hernia (CDH), for example, though its origin still controversial, consists in the failure of normal closure of the canal in the developing embryo, and is an invalidating, often deadly, congenital disease that affects about one child over 3,500 live birth. Abdominal contents herniate in-utero and progressively compress the ipsilateral developing lung in the thorax, causing pulmonary hypoplasia and hypertension. Longitudinal investigations on embryo development could have great impact in the understanding of the human embryo and the genesis of fetal diseases like CDH.

The sample to be imaged in this preliminary study was a rat embryo fixed in formalin, extracted from a nitrofen-induced CDH pregnant Sprague Dawley rat model 13 days post conception. Features of interest include the extension of diaphragmatic hernia in the abdomen and thorax, as well as internal organs such as lungs, stomach, liver and intestines. This project also included the *in-vivo* and *post-mortem* measurement of pregnant rats, but only some representative *post-mortem* results are included here.

B. The **second objective** was to use multi-source data to compare PCI methodology at a synchrotron facility (the ESRF) vs. that obtained via a compact X-ray light source (the Excillum liquid metal jet X-ray source).

8.1.2 Methods and Results

ESRF:

Methods: the PB-X-PCI-CT setup at ID17 was used with 30 keV beam energy and a FReLoN camera as detector set 11 m away from the sample; scan parameters included 46 and 8 μm effective voxel sizes, 3000 CT projections in 360-degree half-acquisition mode.

Results: High resolution embryo synchrotron X-PCI-CT data (see **Fig. 8.1.1**) were acquired by our group both *in-utero* and *post-mortem*: PCI images show soft-tissue contrast in both the abdominal and thoracic regions of the embryo. These preliminary images led to detailed portraits of the local micro-morphology of the abdomen and thorax, which could be of key importance in enabling precise quantitative longitudinal studies of CDH development.

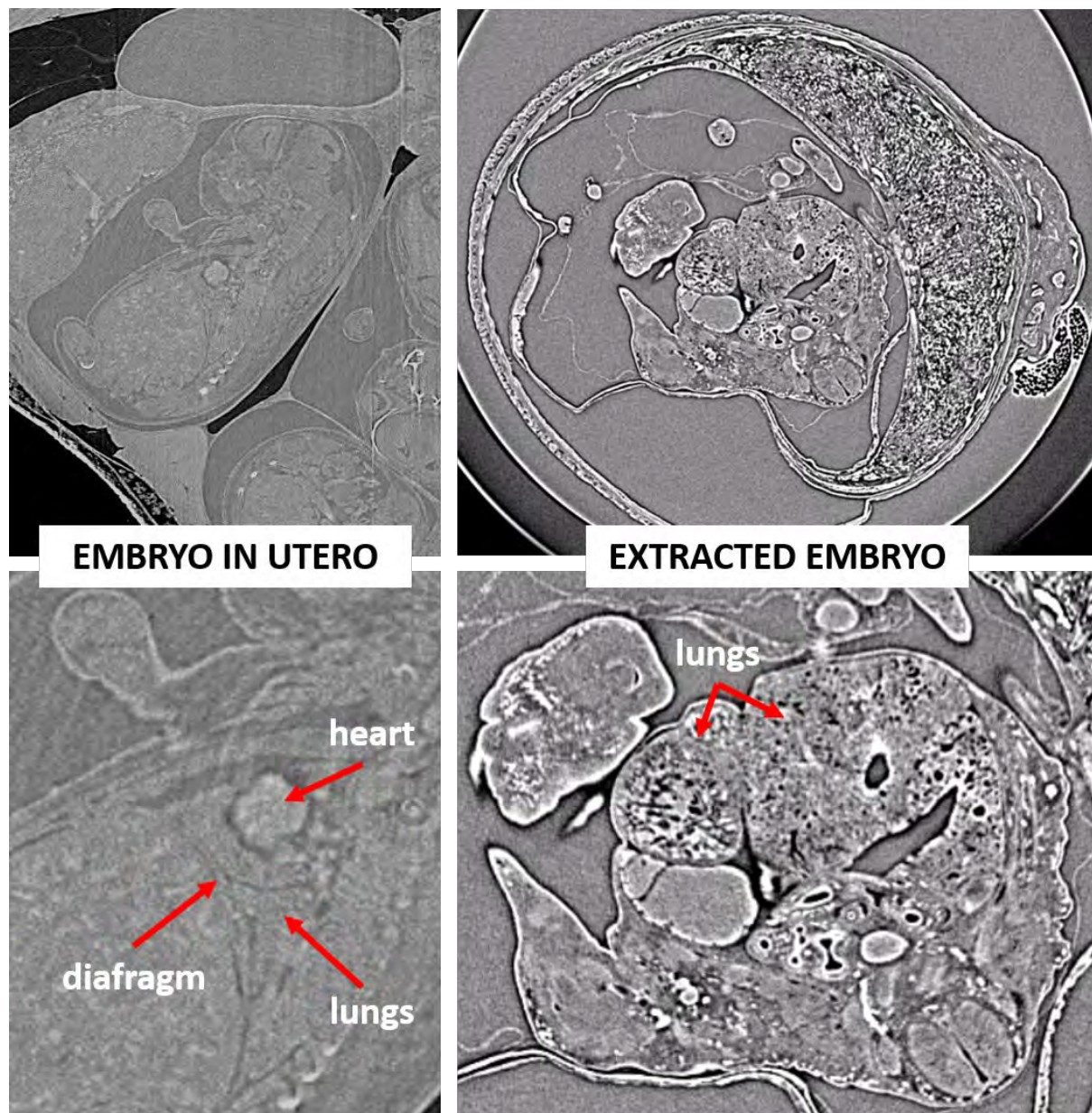


Figure 8.1.1: *in-utero* 46-micron pixel (left) vs. *post-mortem* 8-micron pixel PCI of a rodent embryo from a CDH pregnant Sprague Dawley rat model, acquired with the PB-PCI setup at the ID17 beamline of the ESRF. Images show good delineation of lung micro-anatomy. Scale bars: 4 mm.

KTH:

At KTH, in collaboration with Jenny Romell, PhD student of Prof. Hans Hertz, we performed several imaging experiments using the new Excillum MetalJet D2 + 70 kV source (Excillum, 2019b), the most brilliant liquid-metal jet source on the market at the moment of the experiment. First, we tested and optimized experimental parameters for cone-beam propagation-based phase contrast CT scans of two different samples. Despite some difficulties with source alignment, we were able to perform complete CTs of:

1. 1 rat embryo extracted from a nitrofen-induced CDH pregnant Sprague Dawley rat model fixed in formalin solution.
2. 1 extracted human lumbar spinal cord sample fixed in formalin solution.

Methods: We removed the formalin and imaged the samples in air, to decrease absorption. We refined source-sample and sample-detector distances to increase magnification and maintain reasonable detector counts. CT images were performed in local CT mode to maximize the resolution and also to simplify the phase retrieval (only two materials in the field-of-view).

Results: Fig. 8.1.2 is a summary of our PCI results for both samples, using the MetalJet D2 + 70 kV source. Within the rat embryo, microscopic organ anatomy could be visualized, including the alveolar system of the lungs. Within the human spinal cord sample, the characteristic pattern of medullary white vs. gray matter was rendered, at least to some degree.

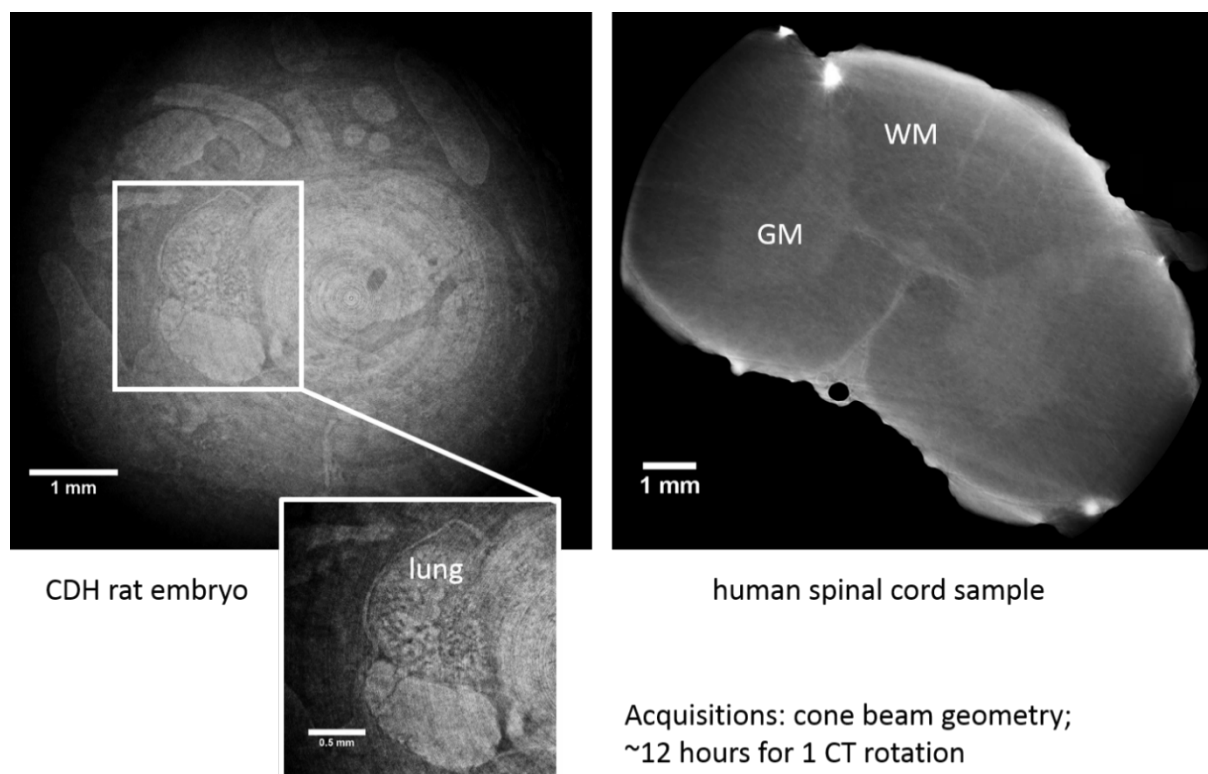


Figure 8.1.2: rodent embryo (left) and human spinal cord sample (right), both imaged in local-tomography mode with the PB-PCI setup in cone-beam geometry at the KTH laboratory for Biomedical and X-ray physics, using the MetalJet D2 + 70 kV liquid-metal jet as X-ray source. GM – gray matter, WM – white matter.

After collection of PCI datasets with both X-ray sources, we were able to compare the *post-mortem* synchrotron data with *post-mortem* compact source data (see **Fig. 8.3** below).

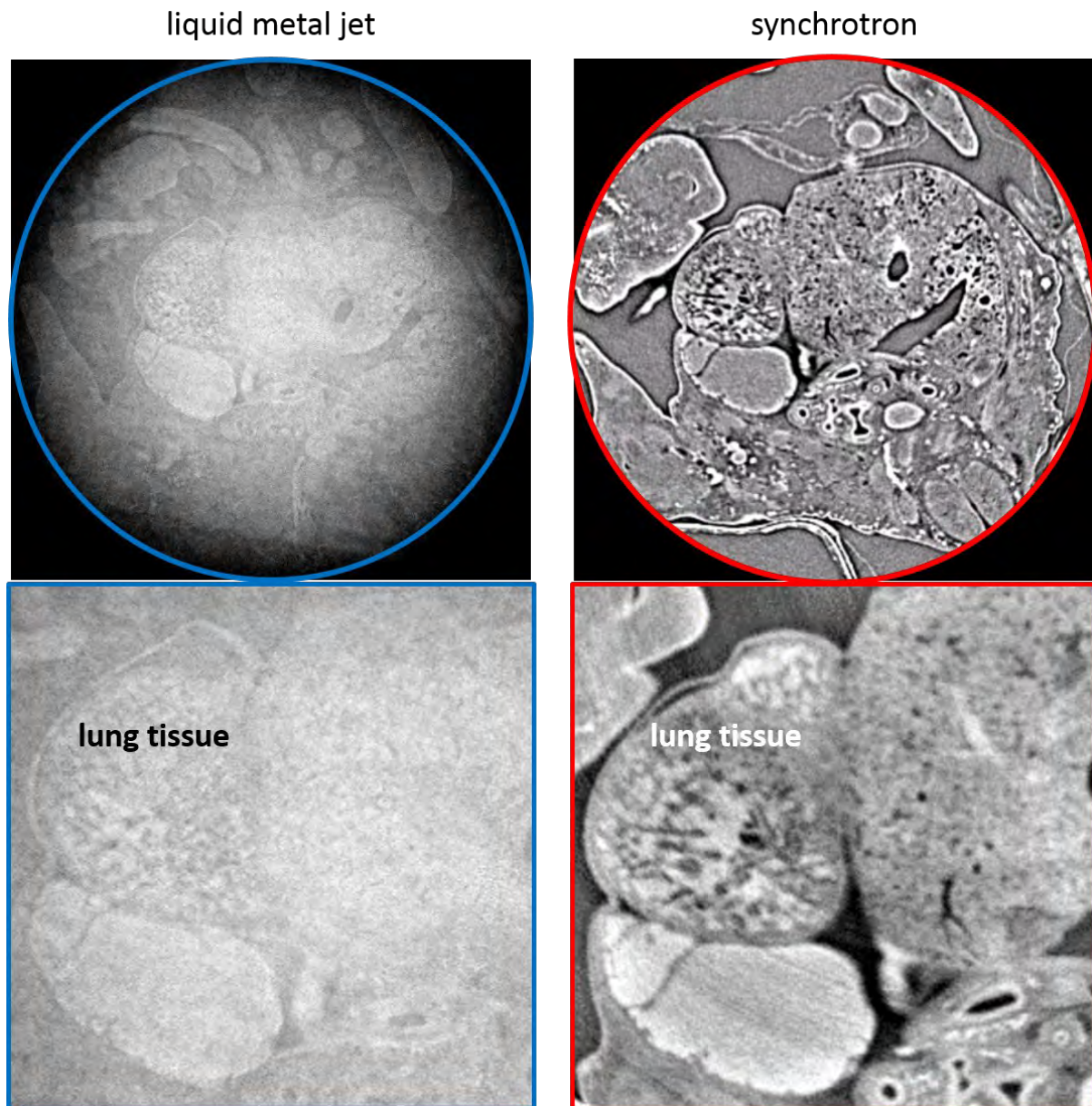


Figure 8.1.3: X-PCI-CT data showing extended anatomy (top) and local lung tissue detail (bottom) from the same rodent embryo, collected using a liquid-metal jet (left) vs. synchrotron (right) X-ray source.

8.1.3 Conclusions

Imaging both a human spinal cord and a rat embryo's soft tissue anatomy with a compact X-ray source proved to be something feasible with a table-top PB setup and a liquid-metal jet X-ray source. Further experimental work, though, seems still necessary to optimize the PCI experimental set-up and source, and thereby reduce the current long acquisition times. Synchrotron-based PCI data are superior in terms of quickness of acquisition and image contrast within micrometric soft-tissue details. This was only a very preliminary test, and the collection of more evidence is necessary to deliver a more complete comparison and a more objective evaluation of the possibilities offered by compact X-ray sources.

Thank you: I would like to thank the MP1207 COST Action for economically supporting this project, as well as the Biomedical and X-ray physics department and Prof. Hertz for hosting me, inviting me to various department seminars, and most importantly for the collaboration in setting up these preliminary measurements.

8.2 X-PCI-CT to study amyloid-PET signal

Further experimental beam-time awarded at the ESRF ID17 beamline led to another study concerning Alzheimer's Disease (AD) neuropathology, titled "*On the establishment of quantitative relationships between A β plaque burden detected via phase-contrast CT, PET and MRI in a mouse model of AD*", this time focused on the characterization of *in-vivo* amyloid positron emission tomography (PET) signal, via a PCI-based *post-mortem* 3D quantification of amyloid deposition.

8.2.1 Project goals

Scientific Case: As already described in **Chapter 5**, Alzheimer's disease is a chronic neurodegenerative disorder that represents the leading cause of dementia. AD is characterized by the formation of amyloid- β (A β) plaques in the brain, which are considered the underlying cause of disease. For decades, the only way to detect A β plaques was invasive *post-mortem* immune-histopathology (IHC). At present, the only available non-invasive *in-vivo* imaging method, i.e. PET, relies on A β -binding tracers to diagnose AD in patients (Nordberg *et al.*, 2010). This technique is also extensively used in clinical trials to monitor treatment effects (Weiner *et al.*, 2010; Seignyn *et al.*, 2016). The morphologic detection of A β plaque burden, however, still relies on *post-mortem* IHC. Previous studies demonstrated that the specific plaque frequency and topographic distribution in the brain is linked to the symptoms of AD (Cummings and Cotman, 1995; Cummings *et al.*, 1996). Aside from distribution, plaque size has been shown to be heterogeneous but its clinical significance has not been established. Regarding PET imaging, it is unclear whether the tracer signal depends on plaque distribution, frequency or size (Brendel *et al.*, 2015). The main advantages of PCI compared to IHC are complete spatial coverage and non-destructive analysis of the AD brain, and, as work in **Chapter 5** proves, PCI-CT represents an accurate method for the non-invasive *post-mortem* detection and analysis of A β plaques.

Objectives: In collaboration with the Radiology and Nuclear Medicine departments of the LMU Klinikum, our group set out to measure via PCI several brain samples from different mouse AD models, for which *in-vivo* PET and *post-mortem* MRI data were also available. The experimental design is schematized in **Fig. 8.2.1**, and involves the direct comparison of hyper-intense X-PCI signal within bright local spots (individual amyloid plaques), which can be segmented in 3D and quantified, against PET signal from the same brain areas.

By means of this experimental design, three main goals could be pursued:

1. characterization and quantification of A β plaque burden in AD brain tissue using PCI-CT
2. interpretation of pre-clinical amyloid-PET signal
3. comparison of PCI- vs. MRI-based *post-mortem* high-resolution morphological imaging

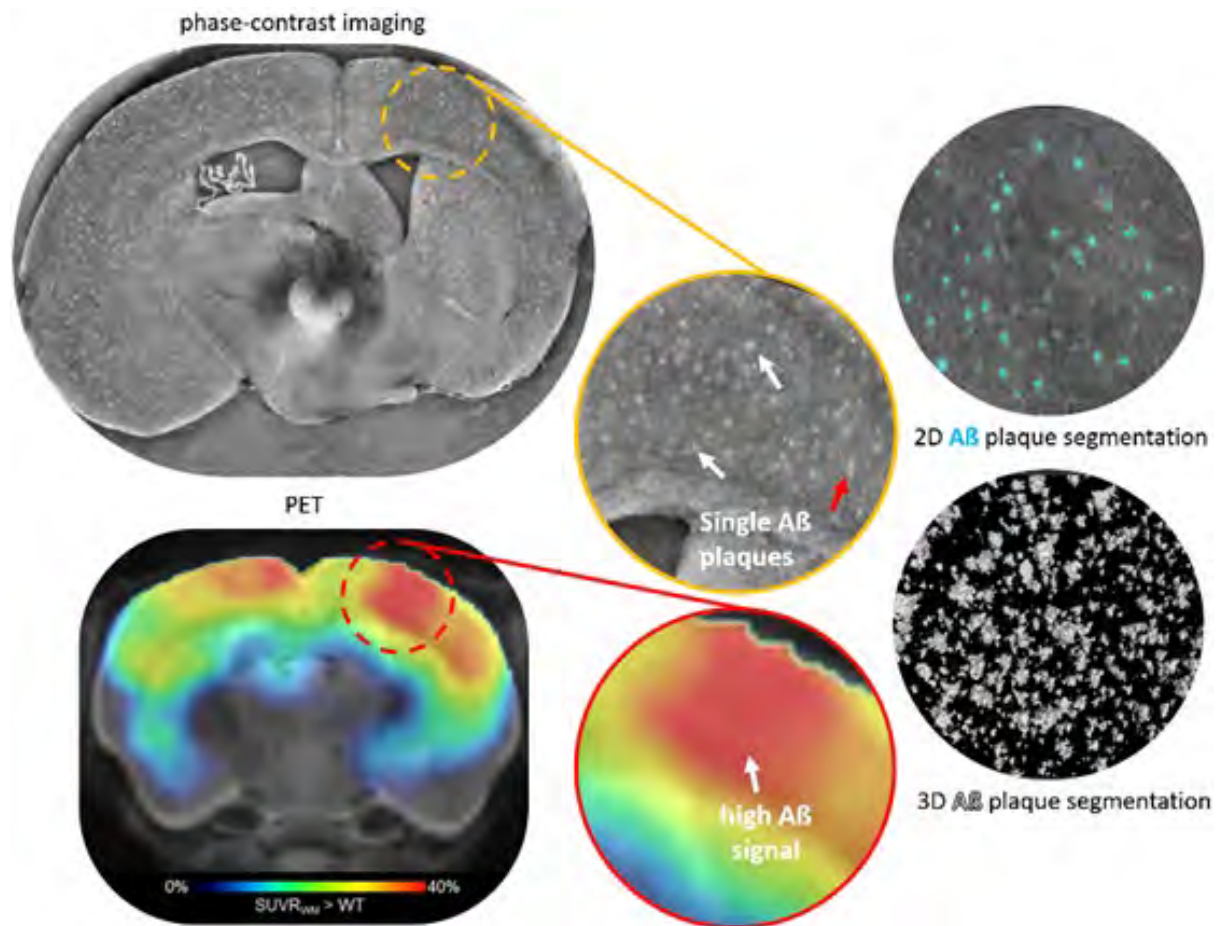


Figure 8.2.1: experimental design for this experiment involves the acquisition of *in-vivo* 3D amyloid-PET data and *post-mortem* 3D X-PCI-CT data. The segmentation bright/hyper-dense structure within PCI images will lead to a possible 3D quantification of amyloid deposition and precise characterization of the PET signal measured in the same areas.

8.2.2 Methods

Animals: 12 months old transgenic mice from the AD animal models APP/PS1 (Radde *et al.*, 2006), APP/PS2 (Richards *et al.*, 2003) and APP/SL (Löffler *et al.*, 2014) were used in this study. These rodents all develop amyloid plaque deposition in the neocortex, hippocampus, striatum, thalamus and brainstem.

***In-vivo* PET:** PET image acquisition and reconstruction was carried out *in-vivo* at the Nuclear Medicine Department at the Großhadern Klinikum of the University of Munich, and followed a standardized protocol as described in (Brendel *et al.*, 2015). Briefly, mice were anesthetized and received a bolus injection of the amyloid ^{18}F -labeled imaging tracer florbetaben to a tail vein. They were then scanned with a small-animal X-Ray CT device (Siemens Inveon P120 DPET) first with a transmission scan for 15 min, and then a single PET frame emission scan for 30-60 min. While still anesthetized, the mice were sacrificed immediately after the PET scan, and the brain were extracted from their skull *post-mortem*. Manual rigid-body co-registration of reconstructed PET emission images to a 3T MRI template, as well as a manual rigid-body

re-alignment of individual ^{18}F -florbetaben images on a ^{18}F -florbetaben healthy mice template were done using the PMOD fusion tool (PMOD Technologies Ltd., 2019).

Post-mortem X-PCI-CT: X-PCI-CT scans were performed on the extracted and formalin-fixed brain samples at the ID17 beamline of the ESRF. The monochromatic-beam PB-PCI setup of the imaging hutch was used, at 40 keV beam energy, with 2m sample-to-detector-distance, the PCO-Edge 5.5 camera and optics to acquire $3^3 \mu\text{m}^3$ voxel datasets of full-organ rodent brain 3D morphology. Local $0.7^3 \mu\text{m}^3$ voxel X-PCI-CT datasets were instead acquired in the MRT hutch in pink-beam mode.

Post-mortem MRI: high resolution 9.4T MRI images were collected at the German Mouse Clinic in Munich. Different MRI sequences and resolutions were tested (e.g. EPI, FLASH, RARE and FISP; 77–20 μm pixel sizes), and the 3D FISP sequence with pixel size of 26 μm was selected, since it gave rise to the best results in terms of plaque contrast. Acquired images were Gaussian-normalized and served as basis for PCI vs. MRI inter-modality comparison.

8.2.3 Results & Conclusions

Preliminary reconstruction and exploration of X-PCI-CT made evident, that the acquired 3D image datasets can well-visualize amyloid deposits and single $\text{A}\beta$ plaques as hyper-dense (bright) spots within multiple cerebral brain regions, as illustrated in **Fig. 8.2.2**.

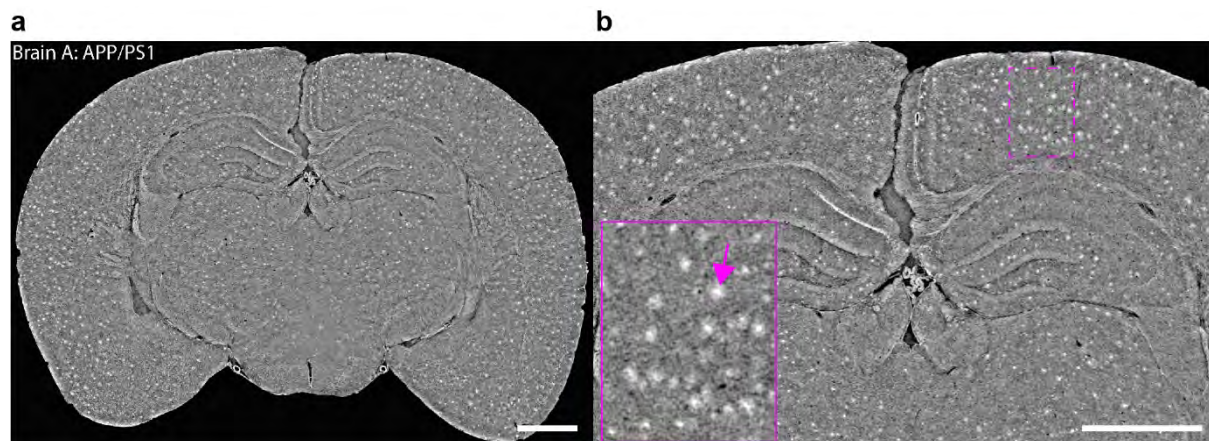


Figure 8.2.2: (a) *post-mortem* X-PCI-CT of an APP/PS1 mouse brain at 12 months of age, exhibiting extended amyloid pathology in the form of bright spots in several key AD brain regions (cortex, hippocampus, thalamus). (b) 2x & 3x zooms of (a) show individual hyper-dense amyloid deposits (magenta arrow). Scale bars: 1 mm.

These PCI-based 3D visualizations sensitive to $\text{A}\beta$ plaque morphology could lead to the precise quantification of amyloid burden, provided that an unbiased analysis methodology is designed, which will extract structural and morphological information from these image datasets.

An extraction of structural parameters related to $\text{A}\beta$ plaque burden (e.g. plaque distribution, frequency and size) from full-sample X-PCI-CT datasets, and a characterization of the relationships between PCI-CT data and MRI and PET data was carried out as part of the Master Thesis work by Christine Schmeichel, entitled “**Quantitative Interpretation of ^{18}F -Florbetaben Amyloid-PET Signal in Alzheimer’s Disease using X-Ray Phase-Contrast micro-**

CT”, which I co-supervised (Master Thesis, Physics Department of the LMU (Schmeichel, 2019)). In her thesis, Schmeichel describes and performs an original in-depth multi-parametric analysis of the relationships between PCI-CT-based quantitative information on A β plaque burden vs. either in-vivo amyloid PET signal or *post-mortem* MRI signal.

A sketch of the workflow used for the comparative study of PET vs. PCI amyloid imaging is outlined in **Fig. 8.2.3**. Briefly, after masking of PCI-CT images of AD animal-model brain samples, a 3D grid of local cubes was defined for each brain volume. Within each grid cube, dense-cored amyloid deposits were segmented (with an automated method) and the amyloid particle load and particle mean size (diameter) were extracted. By populating new 3D grids with these two morphological parameters, the X-PCI-CT data was converted in 3D maps of amyloid-particle load and amyloid-particle size. PET data of the same AD samples had been previously collected *in-vivo*, and were then normalized against a control (wild-type) brain sample to extract Z-score maps of the local PET signal. By overlaying the PET Z-Score maps to the two PCI-based morphological parameters, information from the two different imaging modalities could be correlated and both global and local trends could be comparatively evaluated.

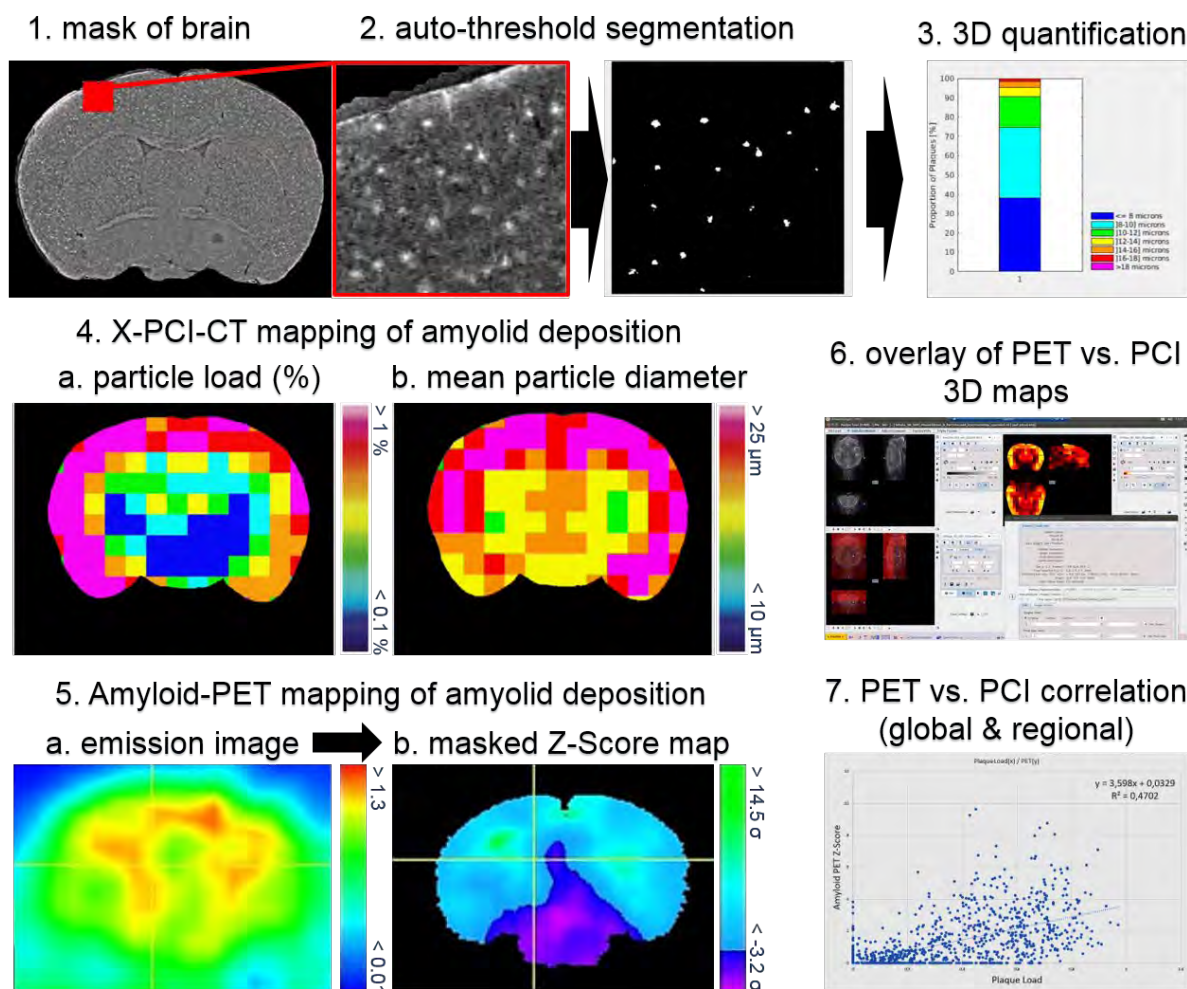


Figure 8.2.3: Workflow used to correlate amyloid-PET tracer data vs. X-PCI-CT morphological data. A 3D grid was defined for each (1) masked AD brain volume analyzed by *post-mortem* X-PCI-CT. Within each grid cube, (2) auto-threshold segmentation and (3) 3D quantification was performed, as described in **Chapters 3 & 5**, to extract dense-cored amyloid plaques and compute local measures of (4a) amyloid parenchymal load and (4b) particle

mean size (diameter). (5a) Emission images of the same AD brain samples had also been previously collected *in-vivo*, and their values normalized against the PET signal of a control brain, thereby computing (5b) a so-called “Z-Score” map (each voxel represents the normalized deviation of the recorded PET emission signal in the AD sample from that one of the control [$z = (x-m)/\sigma$, with x the AD sample value, m the local control mean signal, and σ the standard deviation of the control distribution]). PET and PCI 3D maps were then (6) registered (i.e. overlaid) against one another, in order to perform a cube-by-cube correlation of PET signal vs. X-PCI-CT-measured local amyloid-plaque morphological parameters.

Our main results are illustrated here in **Fig. 8.2.4** and discussed in detail in (Schmeichel, 2019). As performed in (Brendel *et al.*, 2015), correlations were computed after computation of regional PET and morphological-parameter values, here for 14 different brain regions and three different AD APP/PS1 mouse brain samples. Intra-cellular deposits were excluded from the PCI-based quantification, both because the image voxel size ($3^3 \mu\text{m}^3$ voxel) just barely small enough to detect such deposits, and especially because the used PET-radiotracer Florbetaben binds to fibrillar, dense-cored-plaques, but not to diffuse intra-cellular plaques (Fodero-Tavoletti *et al.*, 2012), which would then not have contributed to the amyloid PET-signal.

The relationship between the X-PCI-CT-based measurements of plaque load and amyloid-PET tracer signal was found to be linear (**Fig. 8.2.4 a**), since a decent correlation ($R^2 \sim 65\%$) could be demonstrated already when considering all data-points together, independently of brain region. Moreover, especially good linear relationships ($R^2 > 85\%$) were found in hippocampal and cortical regions, known key AD brain areas. The linearity shown in these results matches well with the linear relationship reported between Florbetaben amyloid-PET signal in APP/PS1 mice and histology-based 2D quantification of amyloid-plaque load in cortical areas (Matthias Brendel *et al.*, 2015).

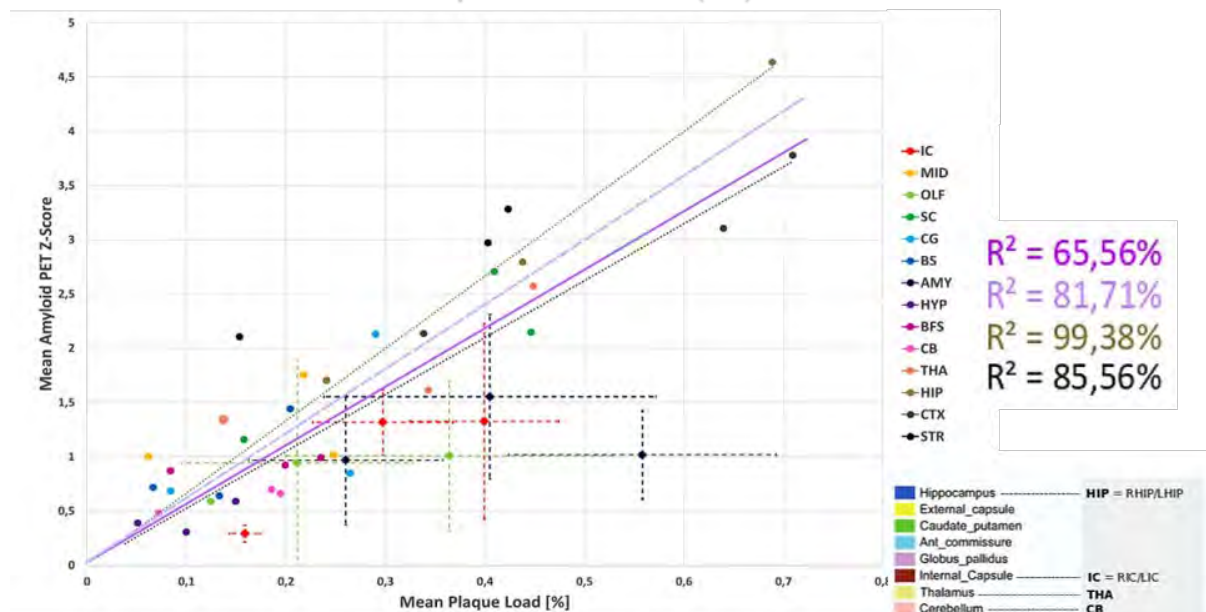
A much less well-investigated topic is the possible influence of amyloid-plaque size on the amyloid PET-signal. In this study, we showed that both an exponential ($R^2 = 63.81\%$) and a quadratic correlation ($R^2 = 61.85\%$) fit well between the X-PCI-CT-based evaluations of plaque size and the PET Z-score signal (**Fig. 8.2.4 b**), when neglecting the outlier regions IC, OLF, AMY and HYP. A quadratic relationship seems especially plausible, based on the known structure of plaque constituents (the amyloid fibrils), since the quantity of available amyloid PET-tracer binding sites likely depends on the size of local amyloid fibril surface. A quadratic relationship between plaque diameter and PET signal seems thus warranted.

Further necessary steps to substantiate this study should involve the processing of many more brain samples (to increase current the samples size of 3), as well as the extension of these observations to different AD animal models (e.g. by exploiting the already collected APP/PS1, APP/PS2, and APP/SL X-PCI-CT data). Further interesting work may arise from the use of even higher-resolution X-PCI-CT data, in order to better characterize the shape (and thus surface) of individual deposits, moving beyond the spherical model preliminarily used here.

In conclusion, this study offered new insight on the interpretation of PET data in preclinical models of AD. Moreover, it showcased the evident benefit and flexibility of the use of X-PCI-CT for 3D morphological quantifications, which was applied to perform a label-free full-organ murine brain analysis inaccessible to traditional histological and other neuroimaging methods. This study, therefore, further established X-PCI-CT as a novel non-destructive

method for the quantification of A β plaque burden and for more detailed interpretations of conventional neuroimaging datasets.

a. PET vs. particle load (%)



b. PET vs. mean particle diameter (μm)

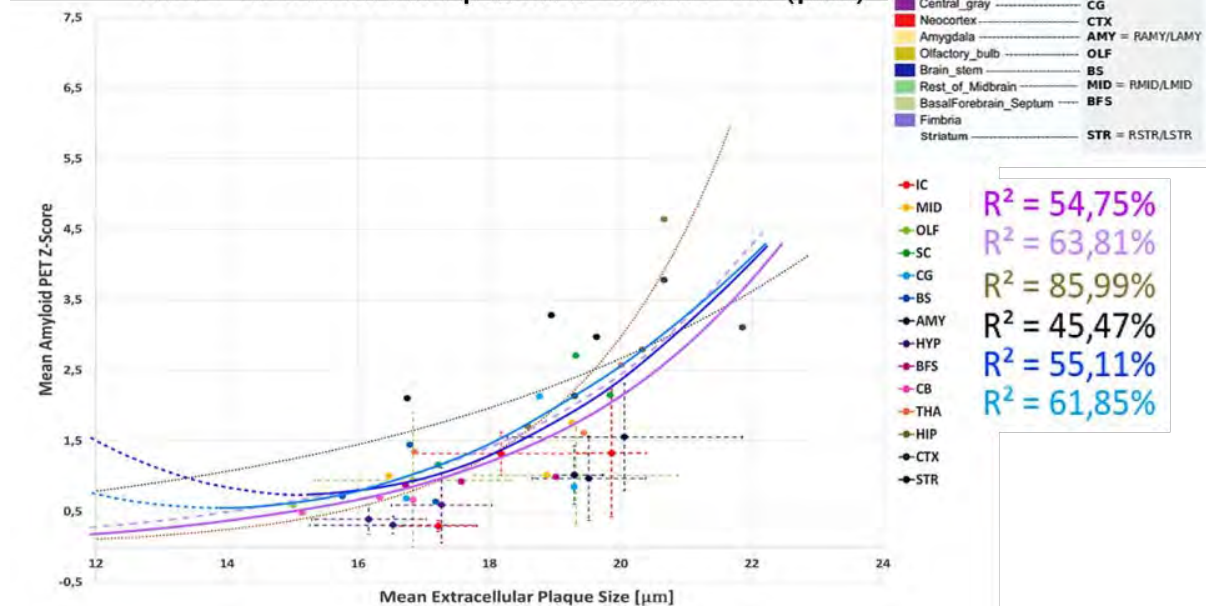


Figure 8.2.4: Plots of the mean amyloid PET Z-Score values vs. (a) the mean plaque load or (b) the mean plaque size for each of 14 brain regions (see legend) and for each of three APP/PS1 AD brain samples. In (a), the dotted gray and dark beige trend lines correspond to proposed linear correlations in the CTX and HIP area, respectively. The solid dark purple trend line corresponds to the linear correlation, when considering all data points. The dashed light purple line neglects the brain regions IC, OLF and AMY, which, as shown in this plot with their respective error bars (standard deviations), are regions that most strongly deviate from a linear correlation. In (b), the dotted gray and dark beige trend lines show proposed exponential correlations in the CTX and HIP area, respectively. The solid dark purple trend line corresponds to the exponential correlation, when considering all data points. The dashed light purple line, again, neglects the brain regions IC, OLF, AMY and HYP. The dark and light blue partially-solid trend lines correspond to a proposed quadratic correlation, respectively when including

all data points or after excluding the outlier regions. The regression-analysis coefficients of determination R^2 ($p < 0.001$) are given. Plots were adapted from (Schmeichel, 2019).

8.3 X-PCI-CT to study hemorrhage

This research project, titled “*Characterization of brain blood-vessel remodeling in an experimental model of hypertension by X-ray phase-contrast micro-CT and nano-holotomography*”, was carried out in collaboration with Dr. Battaglia, and his team at the Neuromed Institute in Pozzilli, Italy, and Dr. Bravin, and his team at the ESRF, and was presented at the European Congress of Radiology 2019 (ECR 2019) as “Voice of EPOS Poster” number C-2056.

8.3.1 Project goals

In this study we apply X-PCI micro-CT to deep brain vessel imaging, and specifically to the detection and evaluation of hypertension-mediated vascular remodeling in the brain of a rodent animal model of hypertension. Hypertension is the most prevalent risk factor for stroke in humans, and cardiovascular complications are related to endothelial damage or dysfunctional angiogenesis (Felmeden *et al.*, 2003). Neuroangiogenesis and infarction studies in animal models almost exclusively rely on sample-invasive 2D immunohistochemistry for the morphologic detection and evaluation of pathologic angio-structure in the brain. Moreover, non-invasive preclinical neuroimaging techniques (e.g. MRI) often lack the adequate spatial resolution, or are limited in terms of sample coverage. We expect, instead, that the presence of neuronal and vascular damage can be less-invasively detected and quantified *post-mortem* via X-PCI, by examining the morphology of 3D brain tissues and cellularity, and the integrity of vascular trees.

We report here on the results of a preliminary X-PCI neuroimaging study, exploring the intracerebral vascular network of brain samples extracted from C57BL/6J mice, developing hypertension following angiotensin II treatment. The long-term goal is to develop and apply the same methodology for a more systematic aid to mechanistic and therapeutic stroke research studies involving small-animal models of hypertension.

8.3.2 Methods

Animal model preparation: Hypertension was induced in 5 C57BL/6J male mice by subcutaneous infusion of angiotensin II (0.5 mg/kg/day) for 6 months via osmotic mini-pumps (Model 2004, ALZET). Thereafter, all animals were sacrificed. Full rodent brains were extracted out from the skull, embedded in paraffin and stored in cylindrical Eppendorf plastic tubes in preparation for CT imaging.

Data acquisition: 3D *post-mortem* rodent brain neuroimaging was performed at several synchrotron facilities, using X-PCI setups for both micro- and nano-CT (ID17 Biomedical beamline and ID16A-NI nanoimaging beamline (Mokso *et al.*, 2007) of the European

Synchrotron (ESRF) in Grenoble, France; TOMCAT beamline (Stampanoni *et al.*, 2007) of the Swiss Light Source, Paul Scherrer Institute, Villigen, Switzerland).

Micro-imaging parameters included 20-30 keV X-rays, sCMOS-sensor PCO cameras, optics systems with effective voxel sizes of 3^3 , 0.7^3 and $0.3^3 \mu\text{m}^3$, and single-distance propagation-based setups (Wilkins *et al.*, 1996). The experimental configuration of the $3^3 \mu\text{m}^3$ CT allowed the acquisition of full organ rodent brain datasets: horizontal field-of-view (FOV) of ~ 1.5 cm, vertical FOV (after multiple vertical sample scanning) of ~ 3 cm (i.e. 1.5 cm x 3 cm H x V), 4000 angular projections over 360 degrees in half acquisition mode, total acquisition times ~ 0.5 hours per full brain sample. $0.7^3 \mu\text{m}^3$ and $0.3^3 \mu\text{m}^3$ CT acquisitions presented instead proportionally reduced FOVs (~ 3.5 mm x 1.5 mm H x V at $0.7^3 \mu\text{m}^3$ in half acquisition mode, ~ 0.86 mm x 0.70 mm H x V at $0.3^3 \mu\text{m}^3$ in full acquisition mode), which enabled increasingly reduced rodent brain coverage.

Nano-CT imaging parameters included 17keV X-rays, a charge-coupled device (CCD) camera (FReLoN, ESRF, Grenoble, France), an optics system with effective voxel sizes of 100^3nm^3 and a 4-propagation distance X-ray nano-holotomography (XNH) setup (Da Silva *et al.*, 2017; Pacureanu *et al.*, 2018). 100^3nm^3 XNH datasets were acquired after sample dissection into ~ 0.5 mm x 0.5 mm x 3 mm micro-rods with an experimental configuration optimized for imaging intra-rod local brain nano-anatomy post-dissection (Khimchenko *et al.*, 2018): 1800 angular projections over 180 degrees in full acquisition mode, total acquisition time of ~ 3 -4 hours per micro-rod, and image FOVs of ~ 0.2 mm x 0.2 mm H x V.

Data analysis: X-PCI-CT images were reconstructed using the standard filtered back-projection algorithm for CT. The so-called Paganin algorithm (Paganin *et al.*, 2002) for single-distance propagation-based X-PCI was used for the phase retrieval of micro-CT datasets. CT ring artifacts (due to non-uniformities of the X-ray beam or to the uneven response of individual detector pixels) were removed using a reported correction algorithm (Lyckegaard, Johnson and Tafforeau, 2011). CT cupping artifacts (present in local tomography acquisitions) were mostly removed by normalization of individual CT slices against their Gaussian-blurred version (filter sigma size: 50). Note that, while it is successful in the removal of the cupping artifacts, this normalization procedure also flattens and reduces area contrast while enhancing high-frequency signals, such as object interfaces and feature borders. This effect is an evident drawback of this normalization approach, leading to images that can afford effective feature detection and analysis (i.e. in analyses of high-frequency image components), but that cannot be used if the interest is obtaining an area contrast measurement between different broad sample components (i.e. in analyses of low-frequency image components).

To better visualize vasculature volumetrically, 2D pseudo-volumetric minimum Intensity Projections (mIP) images were computed by summing 100 consecutive 3-microns-pixel slices with the minimum intensity z-projection function in open source software ImageJ (Schneider, Rasband and Eliceiri, 2012). Moreover, 3D renderings were produced using the commercially available software VG Studio MAX (Volume Graphics GmbH., 2001). Brain vessel trees were obtained by threshold-based data segmentation. Vessel thickness distributions were computed using the ImageJ plugin 'Local Thickness' (Hildebrand and Rüeggsegger, 1997) on

the segmented datasets. Particle size distributions were also extracted using the ImageJ plugin '3D Objects Counter' (Bolte and Cordelières, 2006). Vascular segmentations were further skeletonized with ImageJ and skeleton branch length distributions were extracted using the ImageJ plugin 'AnalyzeSkeleton' (Arganda-Carreras *et al.*, 2010).

8.3.3 Results

Label-free high-resolution X-PCI-CT images with effective voxel size of $3^3 \mu\text{m}^3$ (**Fig. 8.3.1-6**) of an extracted brain sample from a representative hypertensive rodent showcase the achievable sensitivity of these micro-CT imaging setups and methodology to brain vascular detail. Brain vascularization, both healthy and pathological, appears strongly hypo-intense compared to surrounding brighter normal tissue parenchyma (**Fig. 8.3.1**) without the need to use any contrast agent. Relative hypo-intensity is also present in the abundant fiber tracts of the caudoputamen, and smaller hypo-intense cell-like structures can also be recognized within several macroscopic brain regions (e.g. in the cerebellum, brain stem, cortex). Hypo-intense vascular details, bearing aberrant morphology, show signs of occurred vascular hemorrhage: several cyst-like infarctions are visible in the cerebellum (pink arrows in **Fig. 8.3.1a', 1b', 1b''**), and edematous formations appear within cortical layers (pink arrow in **Fig. 8.3.1a''**).

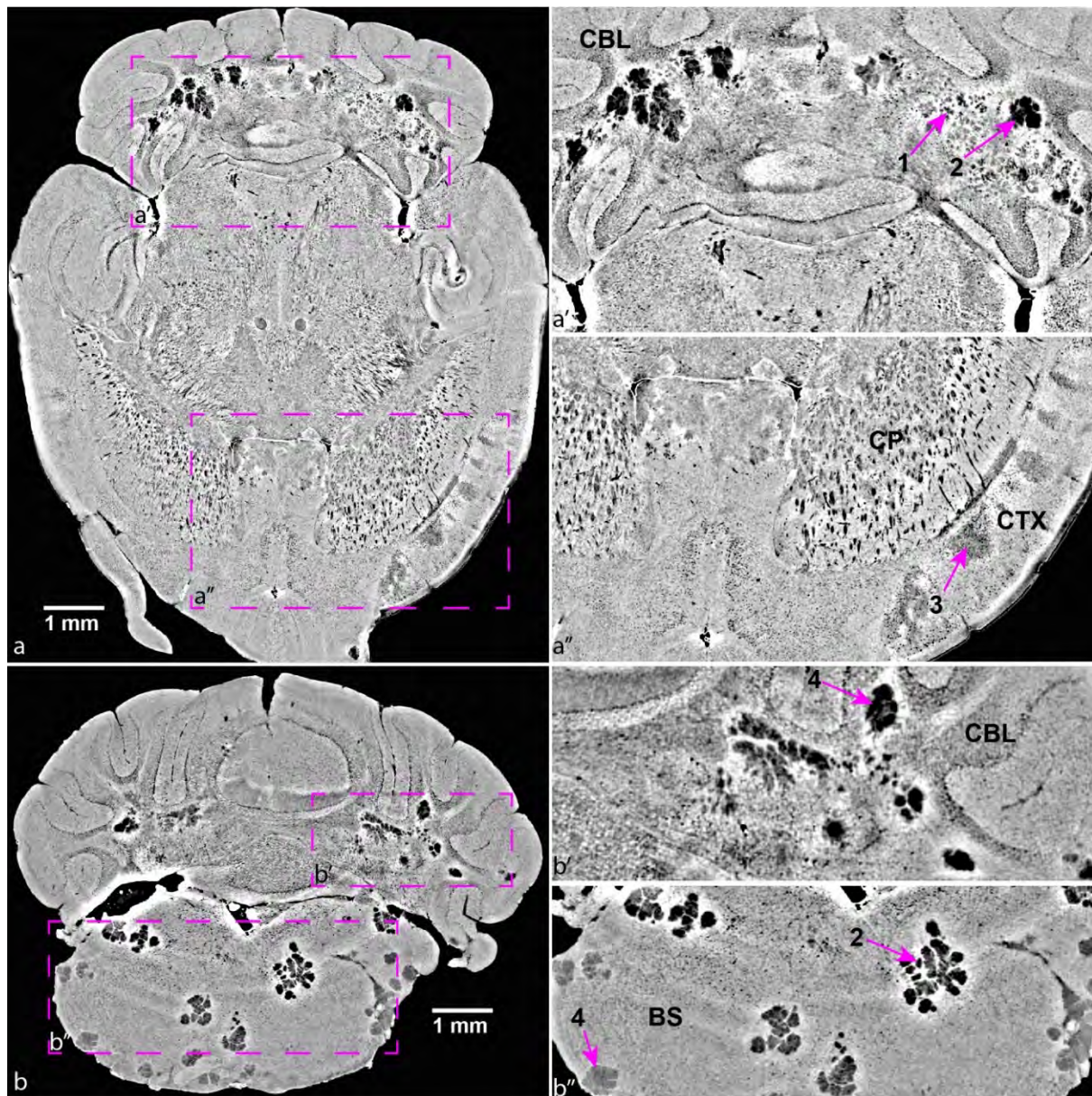


Figure 8.3.1: Representative 3-micron-pixel X-PCI micro-CT images of an extracted brain sample from a hypertensive rodent (**a** frontal view and **b** coronal view) and zoom-ins (**a'-a''** and **b'-b''**). Pink arrows point to signs of vascular hemorrhage (both (1) micrometric ischemic foci and (2) extra-cellular vacuoles), (3) edematous formations and (4) several large cysts. CP – caudoputamen, CBL – cerebellum, CTX – cortex, BS – brain stem.

Within the brains of the hypertensive rodents, the occurrence of localized hemorrhages and ischemic stroke leads to extravasation, to cerebral vasogenic edema, and to the formation of single micrometric ischemic foci, of extracellular vacuoles, of infarcts and of larger cysts, which can all be recognized and distinguished from healthy vasculature in X-PCI-based pseudo-volumetric mIPs. In **Fig. 8.3.2**, such vascular remodeling (of heterogeneous sizes) can be observed diffusely in the brain stem and cerebellum (**Fig. 2a-a'-a''**), in the periaqueductal gray of the midbrain and within fiber tracts adjacent to the pons (**Fig. 2b-b'-b''**), in the hippocampal formation and adjacent fiber tracts (**Fig. 2c-c'-c''**) and in the dorsal cortex (**Fig. 2d-d'-d''**).

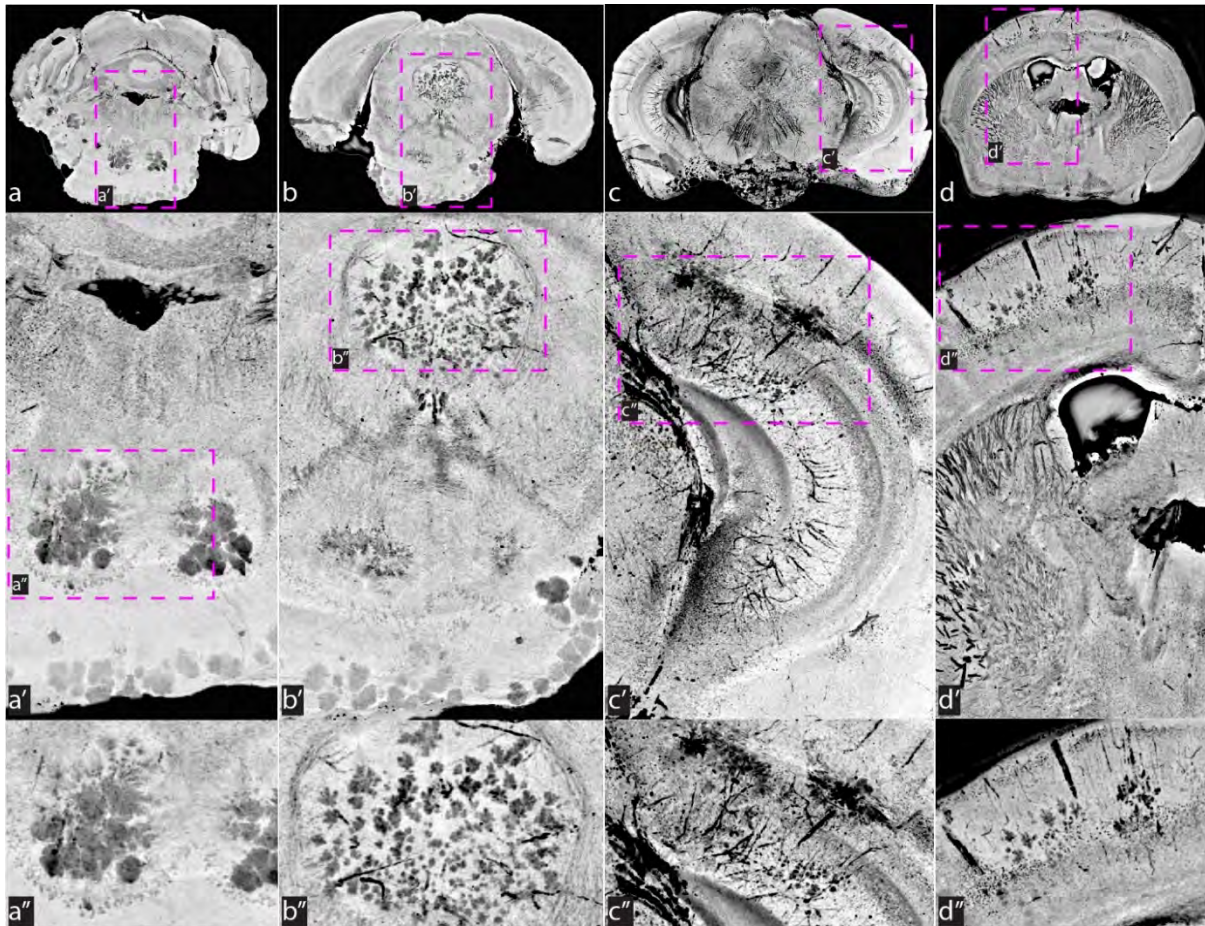


Figure 8.3.2: Posteroanterior sequential brain coronal sums of 100 consecutive 3-micron-pixel X-PCI micro-CT slices (pseudo-volumetric mIP images, **a-d**) and zoom-ins (**a'-d'** & **a''-d''**) show diffused vascular remodeling. **a-a''** highlight macroscopic cysts in the medulla. **b-b''**: micro-hemorrhages in the periaqueductal gray of the midbrain. **c-c''**: vascular damage of heterogeneous sizes in the hippocampal formation and adjacent fiber tracts. **d-d''**: micro-hemorrhages in the dorsal cortex.

X-PCI 3D datasets can be virtually resliced or also explored pseudo-volumetrically (e.g. via 2D mIP slices as in **Fig. 8.3.3**) without need for sample dissection. These mIP representations allow the visualization of vascular paths within different brain regions, as well as of the distribution of differently-sized vascular hemorrhages in the analyzed brains. Moreover, threshold-based segmentation of the most hypo-intense vascular features in label-free X-PCI images enable a fully-volumetric rendering of 3D vessel trees (as in **Fig. 8.3.4**).

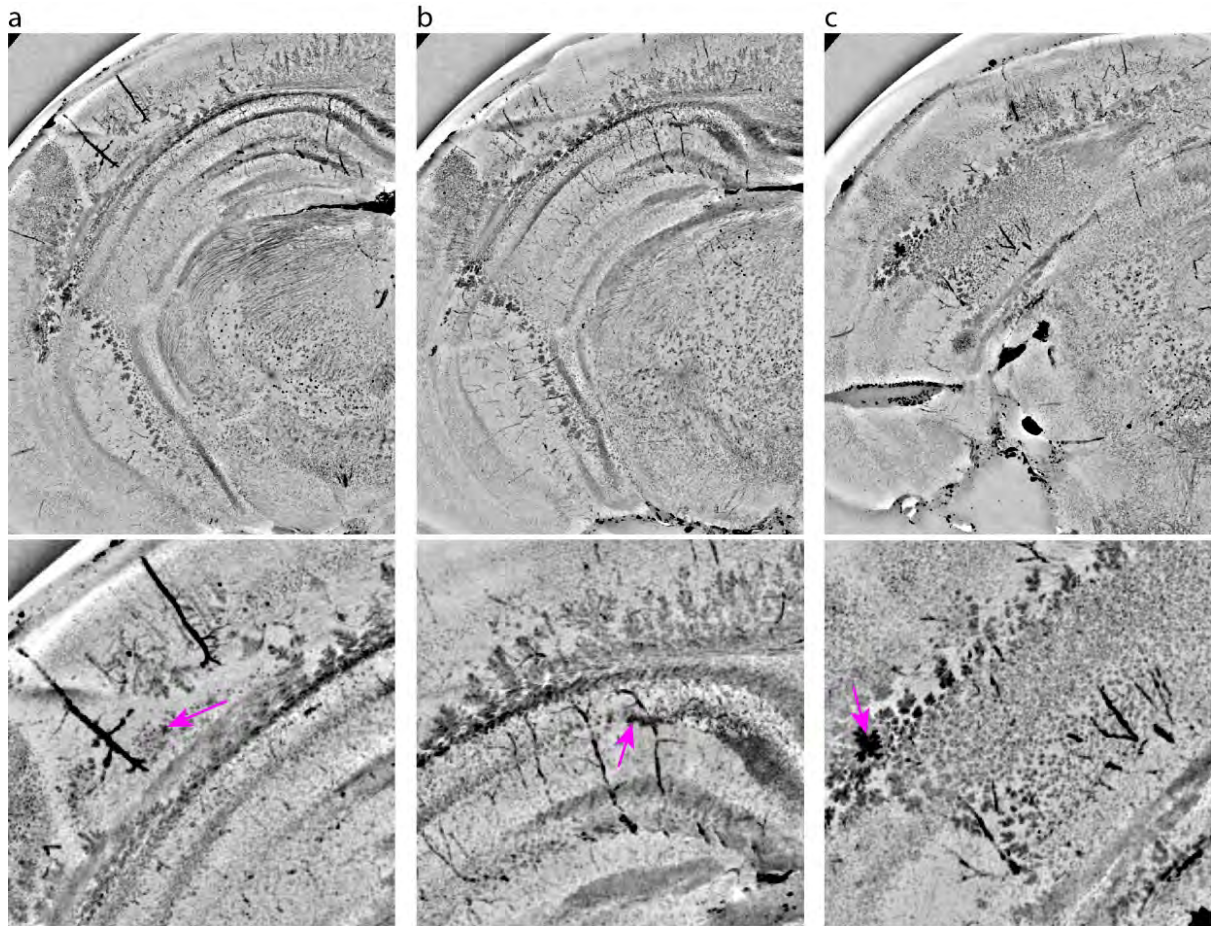


Figure 8.3.3: a-c, series of pseudo-volumetric mIP images, i.e. 2D projections of 50 consecutive X-PCI slices, showing pseudo-volumetric signs of hemorrhage (pink arrows) and edematous formation within and in the vicinity of cortical and hippocampal brain vasculature of a hypertensive rodent brain.

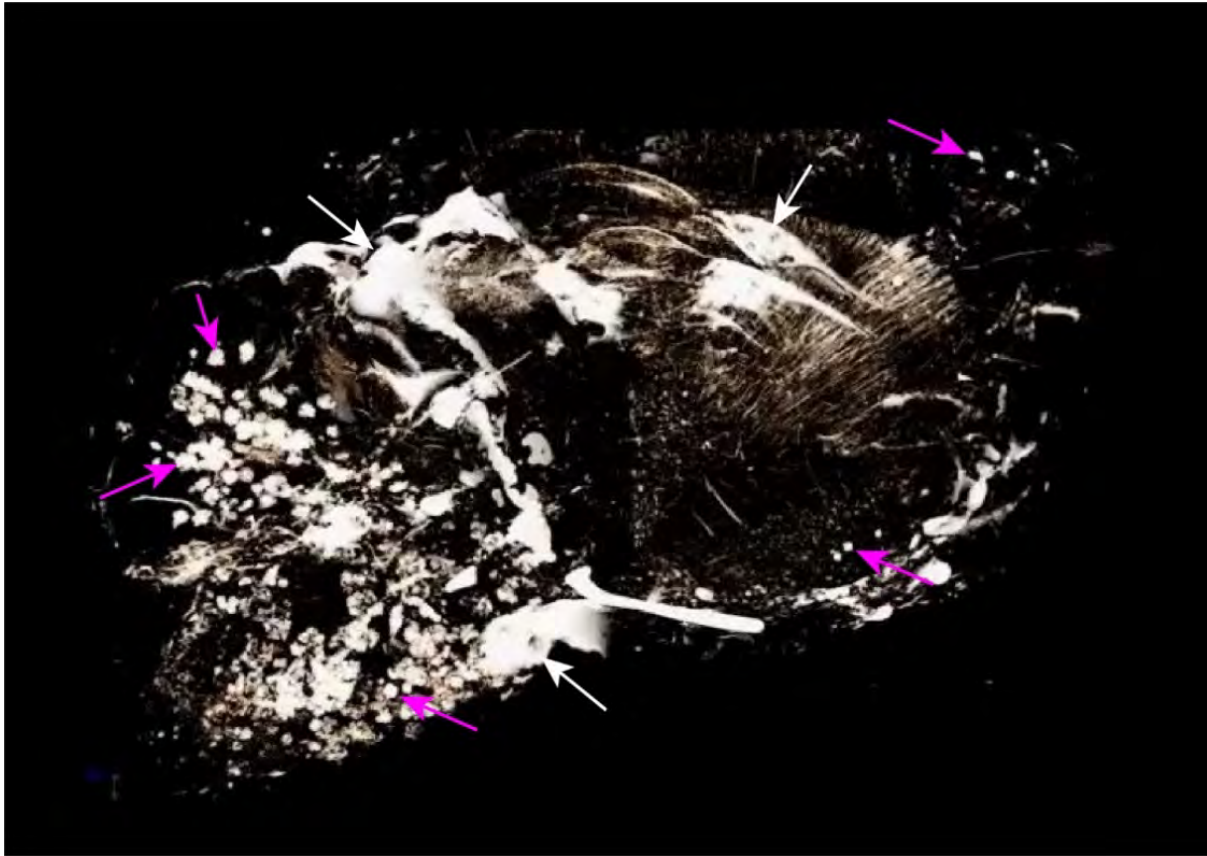


Figure 8.3.4: a representative full-organ threshold-based segmentation and 3D rendering of X-PCI data, showing the 3D brain vessel tree of a hypertensive rodent brain. Signs of pathologic vasculature (pink arrows) are evident within cerebellar and cortical layers. Applied on a full brain sample, the segmentation includes also some large non-vascular features (white arrows), which would need to be removed before performing any meaningful quantitative analysis of this vascular tree.

Fig. 8.3.5 shows how both pseudo-volumetric mIP images (**a-a'** and **c-c'**) and corresponding 3D renderings (**b-b'** and **d-d'**) enable an easily localization of deep brain vascular remodeling and micro-infarction (see pink arrows), and highlights the intrinsically three-dimensional development of such neurologic features. In many cases, this capability for volumetric analysis may lead to observations of pathological features, which could have potentially been missed by standard 2D histological analyses.

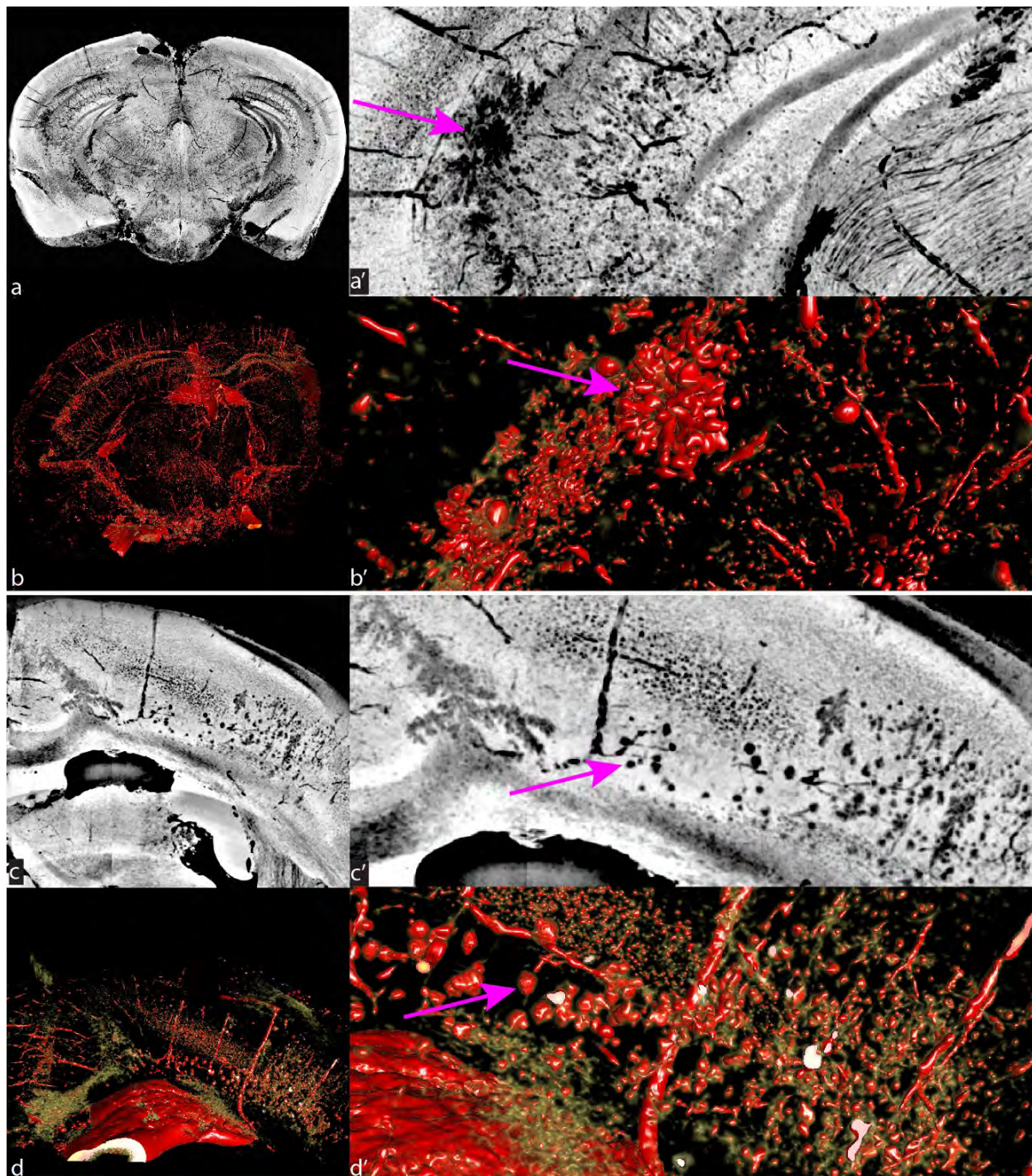


Figure 8.3.5: 2D projections of 3D X-PCI brain data (mIP images in **a-a'** and **c-c'**), and corresponding vessel-tree 3D renderings (**b-b'** and **d-d'**) show the volumetric development of vascular remodeling and individual microinfarcts (magenta arrows point toward them).

Furthermore, a quantitative image analysis of several morphological features related to the effects of hypertension was performed on a X-PCI dataset with effective voxel size of $3^3 \mu\text{m}^3$ (**Fig. 8.3.6**). Exhibited local cortical and hippocampal vascular remodeling (**a-a'-a''**) was first characterized in terms of its local vessel thickness (**b-b'-b''**): interestingly, the largest distribution values (thickness > 10 microns) can be observed within aberrant burst-shaped infarcts. Local infarctions can also be treated as particle-like objects (**c-c'**). Individual particle volumes were then measured to obtain a distribution of local particle sizes (**c''**): the presence of diffuse microscopic (<20 micron lesions) and sparse macroscopic (>100micron lesions)

vascular damage can be inferred both from the particle map and from the extracted distribution. The same vascular segmentation was also skeletonized to obtain a 3D map of vessel connectivity (**d-d'**) and extract a branch length distribution (**d''**).

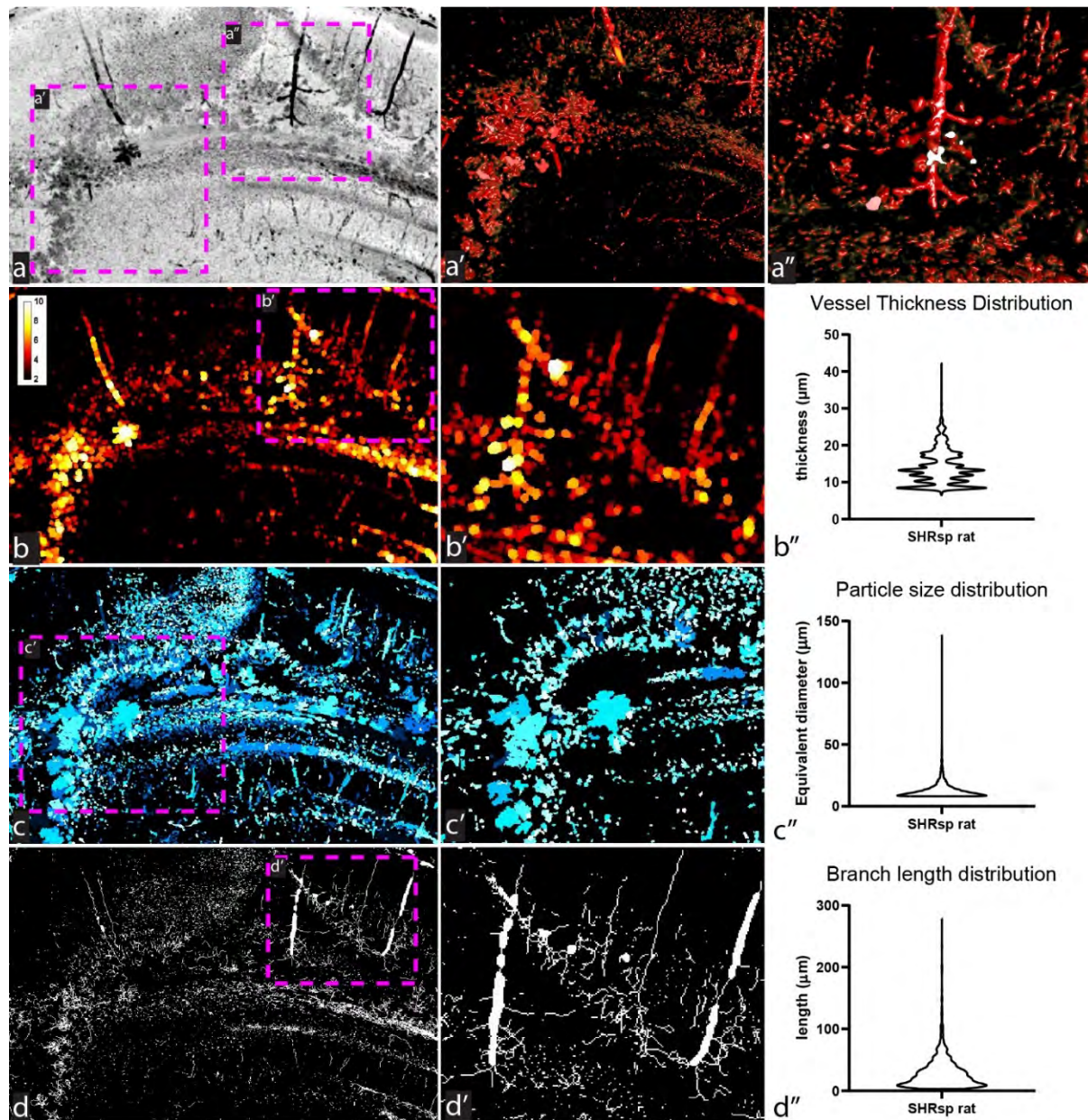


Figure 8.3.6: 2D Vascular damage in the cortex and hippocampal formation of a hypertensive rodent, i.e. hemorrhagic foci, vasogenic edema and (lacunar) micro-infarcts, captured by X-ray PCI micro-CT in pseudo-3D (**a**) and 3D (**a'-a''**), was segmented and quantified volumetrically. **b-b''**: vessel thickness 3D maps (**b-b'**, calibration bar in microns) and vessel thickness distribution (**b''**). **c-c''**: 3D particle maps (**c-c'**) and extracted particle size distribution (**c''**, particle volume converted to the diameter of its volumetrically-equivalent sphere). **d-d''**: 3D vascular skeleton maps (**d-d'**) and extracted skeleton branch length distribution (**d''**).

Last, we explored the potential of localized sub-micron-resolution neuroimaging (**Fig. 8.3.7**), beyond the full-organ imaging at $3^3 \mu\text{m}^3$ (**a-a'**), by collecting datasets of effective voxel sizes of $0.7^3 \mu\text{m}^3$, $0.3^3 \mu\text{m}^3$ and 100^3nm^3 (respectively **b-b'**, **c-c'-c''**, **d-d'-d''**). X-PCI sub-micron-CT can detect subtle tissue morphological and density differences possibly corresponding to local ischemia and edema (pink arrow in **b'** and **c'-c''**). XNH-based nanoimaging of vascular

hemorrhage resolves local pathological perfusion (pink arrow in **d''**), deep single neuronal cells (**d'**), and both intra-vascular and intra-cellular detail.

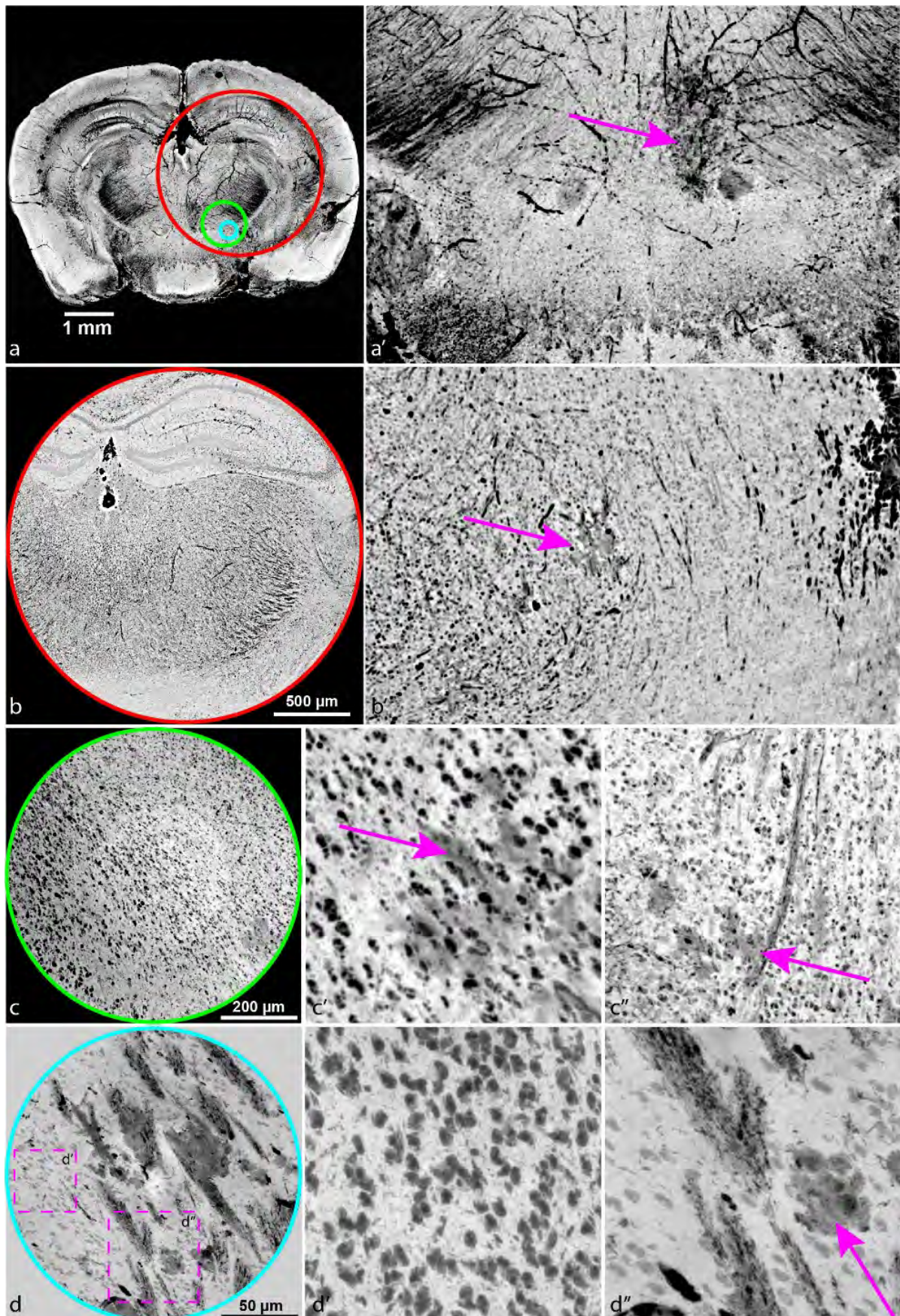


Figure 8.3.6: Multiscale sub-micron-resolution X-PCI. **a-a'**: 3-micron-pixel PCI datasets capture full-organ anatomical morphology. **b-b'**: 0.7-micron-pixel PCI datasets visualize high-resolution tissue morphology. **c-c'**: 0.3-micron-pixel PCI datasets show intra-tissue cellularity. **d-d'**: 100-nanometer-pixel PCI datasets image nanometric morphological detail. Pink arrows point to signs of vascular hemorrhage at different imaging resolutions.

8.3.4 Conclusions

In conclusion, this work represents a successful preliminary proof-of-principle *post-mortem* imaging study on the potential of X-PCI micro- and nano-CT techniques to visualize micro-hemorrhage, stroke and vascular remodeling in a rodent animal model of hypertension. We showed how X-PCI provides precise and high-contrast volumetric morphological representations of deep brain vasculature and ischemia, and permits relatively simple full-organ vascular segmentations leading to the quantification of vascular structural parameters of interest to stroke research. A more thorough methodological study on the *post-mortem* quantification via X-PCI-CT scanning of vascular abnormalities in the same animal model was carried out by Laurent Jacques in his Master Thesis entitled “**Methodology for Characterisation of Vascular Abnormalities in a Mouse Model of Hypertension by X-ray Phase-Contrast micro-CT**”, which I co-supervised and which was turned in in the Physics Department of the LMU in July 2019 (Jacques, 2019). In the future, this imaging and quantification technique could be used e.g. to quantitatively evaluate the role of genes involved in stroke or angiogenesis, and for the development of drugs that may prevent vascular injury in animal models of hypertension.

REFERENCES:

- Arganda-Carreras, I. *et al.* (2010) '3D reconstruction of histological sections: Application to mammary gland tissue', *Microscopy Research and Technique*. John Wiley & Sons, Ltd, 73(11), pp. 1019–1029. doi: 10.1002/jemt.20829.
- Boite, S. and Cordelières, F. P. (2006) 'A guided tour into subcellular colocalization analysis in light microscopy', *Journal of Microscopy*. John Wiley & Sons, Ltd (10.1111), 224(3), pp. 213–232. doi: 10.1111/j.1365-2818.2006.01706.x.
- Brendel, Mathias *et al.* (2015) 'Amyloid-PET predicts inhibition of de novo plaque formation upon chronic γ -secretase modulator treatment.', *Molecular psychiatry*, 20(10), pp. 1179–1187. doi: 10.1038/mp.2015.74.
- Brendel, Matthias *et al.* (2015) 'Cross-sectional comparison of small animal [18F]-florbetaben amyloid-PET between transgenic AD mouse models', *PloS one*. Public Library of Science, 10(2), pp. e0116678–e0116678. doi: 10.1371/journal.pone.0116678.
- Cummings, B. J. *et al.* (1996) 'Beta-amyloid deposition and other measures of neuropathology predict cognitive status in Alzheimer's disease.', *Neurobiology of aging*. United States, 17(6), pp. 921–933. doi: 10.1016/s0197-4580(96)00170-4.
- Cummings, B. J. and Cotman, C. W. (1995) 'Image analysis of beta-amyloid load in Alzheimer's disease and relation to dementia severity.', *Lancet (London, England)*. England, 346(8989), pp. 1524–1528. doi: 10.1016/s0140-6736(95)92053-6.
- Excillum, A. (2019a) *excillum.com*. Available at: www.excillum.com (Accessed: 9 September 2019).
- Excillum, A. (2019b) *MetalJet D2+ 70 kV*. Available at: <https://www.excillum.com/products/metaljet-sources/metaljet-d2-70-kv/> (Accessed: 9 September 2019).
- Felmeden, D. C. *et al.* (2003) 'Endothelial damage and angiogenesis in hypertensive patients: relationship to cardiovascular risk factors and risk factor management*', *American Journal of Hypertension*, 16(1), pp. 11–20. doi: 10.1016/S0895-7061(02)03149-7.
- Fodero-Tavoletti, M. T. *et al.* (2012) 'In vitro characterization of [18F]-florbetaben, an A β imaging radiotracer.', *Nuclear medicine and biology*. United States, 39(7), pp. 1042–1048. doi: 10.1016/j.nucmedbio.2012.03.001.
- Hildebrand, T. and Rügsegger, P. (1997) 'A new method for the model-independent assessment of thickness in three-dimensional images', *Journal of Microscopy*. John Wiley & Sons, Ltd (10.1111), 185(1), pp. 67–75. doi: 10.1046/j.1365-2818.1997.1340694.x.
- Jacques, L. (2019) *Methodology for Characterisation of Vascular Abnormalities in a Mouse Model of Hypertension by X-ray Phase-Contrast micro-CT*. Ludwig-Maximilian-University Munich.
- Khimchenko, A. *et al.* (2018) 'Hard X-Ray Nanoholotomography: Large-Scale, Label-Free, 3D Neuroimaging beyond Optical Limit', *Advanced Science*, 5, p. 1700694. doi: 10.1002/advs.201700694.
- Löffler, T. *et al.* (2014) 'Neuroinflammation and related neuropathologies in APPSL mice: further value of this in vivo model of Alzheimer's disease.', *Journal of neuroinflammation*, 11, p. 84. doi: 10.1186/1742-2094-11-84.
- Lyckegaard, A., Johnson, G. and Tafforeau, P. (2011) 'Correction of ring artifacts in X-ray tomographic images', *International Journal of Tomography and Statistics*, 18(F11), pp. 1–9.
- Mokso, R. *et al.* (2007) 'Nanoscale zoom tomography with hard x rays using Kirkpatrick-Baez optics', *Appl. Phys. Lett.*, 90, p. 144104. doi: 10.1063/1.2719653.
- Nordberg, A. *et al.* (2010) 'The use of PET in Alzheimer disease', *Nature Reviews Neurology*, 6(2), pp. 78–87. doi: 10.1038/nrneurol.2009.217.
- Pacureanu, A. *et al.* (2018) 'Nanoscale three-dimensional imaging of biological tissue with x-ray holographic tomography', in *Proceedings of the SPIE*, p. 107112B. doi: 10.1117/12.2319477.

Paganin, D. *et al.* (2002) 'Simultaneous phase and amplitude extraction from a single defocused image of a homogeneous object', *Journal of Microscopy*, 206(1), pp. 33–40. doi: 10.1046/j.1365-2818.2002.01010.x.

PMOD Technologies Ltd. (2019) *Image Registration and Fusion Tool*. doi: <https://www.pmod.com/web/?portfolio=22-image-processing-pfus>.

Radde, R. *et al.* (2006) 'Abeta42-driven cerebral amyloidosis in transgenic mice reveals early and robust pathology.', *EMBO reports*, 7(9), pp. 940–946. doi: 10.1038/sj.embor.7400784.

Richards, J. G. *et al.* (2003) 'PS2APP Transgenic Mice, Coexpressing hPS2mut and hAPPswe, Show Age-Related Cognitive Deficits Associated with Discrete Brain Amyloid Deposition and Inflammation', *The Journal of Neuroscience*, 23(26), pp. 8989 LP – 9003. doi: 10.1523/JNEUROSCI.23-26-08989.2003.

Schmeichel, C. (2019) *Quantitative Interpretation of 18F-Florbetaben Amyloid-PET Signal in Alzheimer's Disease using X-Ray Phase-Contrast micro-CT*. Ludwig-Maximilian-University Munich.

Schneider, C. A., Rasband, W. S. and Eliceiri, K. W. (2012) 'NIH Image to ImageJ: 25 years of image analysis', *Nature methods*, 9(7), pp. 671–675. Available at: <https://www.ncbi.nlm.nih.gov/pubmed/22930834>.

Sevigny, J. *et al.* (2016) 'The antibody aducanumab reduces A β plaques in Alzheimer's disease', *Nature*. Macmillan Publishers Limited, part of Springer Nature. All rights reserved., 537, p. 50. Available at: <https://doi.org/10.1038/nature19323>.

Da Silva, J. C. *et al.* (2017) 'Efficient concentration of high-energy x-rays for diffraction-limited imaging resolution', *Optica*, 4(5), pp. 492–495.

Stampanoni, M. *et al.* (2007) 'TOMCAT: A beamline for TOMographic Microscopy and Coherent rAdiology experimenTs', *AIP Conference Proceedings*. American Institute of Physics, 879(1), pp. 848–851. doi: 10.1063/1.2436193.

Volume Graphics GmbH. (2001) 'VGStudio MAX 2.2'. doi: www.volumegraphics.com.

Weiner, M. W. *et al.* (2010) 'The Alzheimer's disease neuroimaging initiative: progress report and future plans.', *Alzheimer's & dementia: the journal of the Alzheimer's Association*, 6(3), pp. 202–11.e7. doi: 10.1016/j.jalz.2010.03.007.

Wilkins, S. W. *et al.* (1996) 'Phase-contrast imaging using polychromatic hard X-rays', *Nature*, 384(6607), pp. 335–338. doi: 10.1038/384335a0.

Conclusions

The several different scientific projects, which together form this PhD Thesis work, have been meant as exploratory efforts in the evaluation of X-PCI-CT, an experimental 3D imaging technique, for neuroimaging applications. In this exploration, several major topics of interest to neuroscience and nervous-system biomedicine have been incorporated, including the anatomic rendering of brain and spinal cord tissue, the study of tumor structure, and the detection and quantification of cellular and vascular CNS pathologies.

Take-away points, applications & limitations

Overall, a few **major take-away points** can be recognized thanks to these experiments:

1. **Post-mortem X-PCI-CT** is highly sensitive to soft-tissue local density variations, leads to enhanced soft-tissue contrast, and **can detect the 3D morphology of CNS anatomy and pathology in a little-invasive, unbiased & “dense” way**, i.e. without the need for extensive sample preparation and sectioning, without structural labelling, and by direct quantitative (easily-interpretable) measurement of all intra-sample structures.
2. Compared to other neuroimaging technology, current limits in X-PCI-CT spatial resolution lie between those of TEM and of high-field *post-mortem* MRI. These limits mean that the obtained 3D X-PCI-CT dataset can capture **full-organ to intra-cellular nervous-tissue anatomy** in the case of rodent brain and spinal cord samples. Altogether, **a multiscale approach to X-PCI-CT-based neuroimaging** (covering the 50 μm to ~ 10 nm pixel-size range), **can bridge an important spatial resolution gap**, i.e. between lower-resolution tissue-scale MRI visualizations (in the 1 mm to 10 μm pixel-size range) and higher-resolution TEM-based renderings (with sub-nm pixel-sizes) of organelle sub-structure, and thereby provide a new perspective for neuroscientific investigations.

Given these results, productive neuroscience and biomedical **applications of the technique** may be:

1. **X-PCI employment to precede and guide histological analysis of rodent CNS samples.** Since X-PCI technology provides “one-shot” (i.e. within one acquisition) 3D images of normal CNS tissues and tumor tissues, and of intra-sample micrometric angio-structure and AD intra-cellular pathology, it enables the post-mortem full-organ localization and visualization of morphological features deep within un-sectioned samples, which would otherwise prove extremely laborious if at all possible with standard histological techniques. X-PCI-CT datasets can provide information, e.g. on the precise location of effects of high-dose ionizing radiation or of cellular neurodegeneration within specific tissues (as demonstrated in **Chapters 4 and 5**). The detection of radiation damage can be used to verify the correct spatial delivery of CNS

tumor treatment protocols in quantitative animal model studies of different radiotherapies. Moreover, these datasets help locate unexpected abnormal intra-sample structure, and thereby can inspire and direct histological analysis.

2. **X-PCI-based 3D depiction and quantifications of microscopic CNS morphology.** X-PCI's sensitivity to brain and spinal cord tissue and tissue abnormality allows for volumetric quantifications of embedded tissue structure, e.g. vascular and cellular micro-structure, as well as tissue modifications and pathologies, which have the potential for unprecedented precision in extended 3D structural evaluations (as demonstrated in **Chapter 5** and **7**). These novel quantification procedures could impact, for example, new studies on cancer tissue survival following radiotherapy, or on the assessment of the efficacy of new AD drugs in reducing neurodegeneration.
3. **Label-free X-PCI-CT use in cases where CNS contrast agents and labels fail.** In a *post-mortem* setting this is the case, for example, for thick CNS samples (as demonstrated in **Chapter 6**), where achieving homogeneous contrast-agent impregnation within the deepest sample layers proves difficult. Label-free morphological neuroimaging becomes even more important in an in-vivo setting, where non-vascular contrast agents are impossible to apply, and where fluorescent labels are difficult to observe within native-state organs.
4. **Application of X-PCI technology for the 3D analysis of dissection-free human soft-tissue specimens: a higher-resolution alternative to *post-mortem* high-field MRI.** As demonstrated in **Chapter 6** for the case of human spinal cord samples, detailed volumetric visualizations of human anatomy could positively impact both anatomy education and anatomy research. 3D rendering of unperturbed organ- to cellular- and vascular-level structure, still a difficult task for cutting-edge neuroimaging, could be decisive in enhanced comprehension of the organization and the complex spatial relationship between different anatomical components.

The results of this PhD Thesis also highlight **some limitations for the technique**:

1. One of the major road-blocks for the use of X-PCI-CT setups for neuroimaging is the **accessibility and specificity of synchrotron-based PCI setups**. Beam time at synchrotrons is awarded on the basis of scientific proposals, a process which lasts 6 months (at best), and which slows-down progress on specific imaging applications. Much progress in this area could come with the design and establishment of beamlines specifically dedicated to micro- and nano-X-PCI-CT of small animal soft-matter sample investigations. Moreover, a future more routine applicability of X-PCI-CT will rely on bringing the technique outside of a synchrotron radiation facility setting. In this sense, the ongoing development of miniaturized synchrotron-like high-flux X-ray source technology, which can fit e.g. within a pathology department building, is crucial. Novel compact X-ray light sources based on inverse Compton scattering are indeed already spreading, e.g. the Munich Compact Light Source

- (MUCLS)¹, THOMX² or BriXS and STAR³. Progress in the development of advanced X-ray tubes for table-top *post-mortem* micro-CT, e.g. nano-focused and liquid-metal-jet X-ray sources, is also ongoing and could play a decisive role in future X-PCI-CT work.
2. Specific to neuroimaging is the **difficulty of X-PCI-CT to image *post-mortem* CNS tissue** in their native environments **in the absence of organ dissection and extraction**. Their surrounding bony structures lead to extensive scattering and absorption of X-rays, and thus may cause artefacts and decreased soft-tissue signal within X-PCI-CT images, especially at high (sub-micron) resolutions. Progress on this issue may come from novel multi-material phase-retrieval algorithms, already currently under development by researchers in this field.
 3. High-resolution **X-PCI-CT has yet to be demonstrated for *in-vivo* neuroimaging** applications, mainly due to the aforementioned issues related to intra-skull and intra-vertebral soft-tissue imaging. Progress in this area would pave the way to the future application of X-PCI-CT in longitudinal micron-resolution neuroimaging studies, something which would represent a considerable breakthrough in the context of cellular-level neuroscientific research.

In conclusion, this PhD Thesis work demonstrated that *post-mortem* X-PCI-CT can serve as a unique multiscale method for high-resolution neuroimaging in alternative to, or in combination with, traditional histological techniques or other complementary virtual 3D imaging techniques. In a series of experiments involving the investigation CNS anatomy and pathology, it was proved that X-PCI-CT can provide advantages in the 3D analysis of nervous system structure. By bridging a crucial gap in current available technologies, this novel avenue for neuroimaging was shown to be fit to impact basic neuroscience research, animal model studies of CNS disease, and experimental drug development studies, and also to bring added value to anatomy medical education and to brain radiation therapy research.

¹ <https://doi.org/10.1107/S1600577520008309>

² <https://doi.org/10.1117/12.2530995>

³ <https://doi.org/10.1117/12.2531168>